Transactions of the ASME®

Journal of Turbomachinery

Published Quarterly by The American Society of Mechanical Engineers

VOLUME 117 • NUMBER 1 • JANUARY 1995

Technical Editor, **T. H. OKIISHI (1998)**
Associate Technical Editors
Aeromechanical Interaction
R. E. KIELB (1996)
Gas Turbine
C. J. RUSSO (1995)
Heat Transfer
M. G. DUNN (1996)
Nuclear Engineering
H. H. CHUNG (1996)
Power
P. H. GILSON (1996)
Turbomachinery
N. A. CUMPSTY (1995)

BOARD ON COMMUNICATIONS
Chairman and Vice-President
R. D. ROCKE

Members-at-Large
T. BARLOW, N. H. CHAO, A. ERDMAN, G. JOHNSON, L. KEER, W. MORGAN, E. M. PATTON, S. PATULSKI, R. E. REDER, S. ROHDE, R. SHAH, F. WHITE, J. WHITEHEAD

OFFICERS OF THE ASME
President, **P. J. TORPEY**
Executive Director
D. L. BELDEN
Treasurer
R. A. BENNETT

PUBLISHING STAFF
Mng. Dir., Publ.,
CHARLES W. BEARDSLEY
Managing Editor,
CORNELIA MONAHAN
Sr. Production Editor,
VALERIE WINTERS
Production Assistant,
MARISOL ANDINO

Transactions of the ASME, Journal of Turbomachinery (ISSN 0889-504X) is published quarterly (Jan., Apr., July, Oct.) for $150.00 per year by The American Society of Mechanical Engineers, 345 East 47th Street, New York, NY 10017. Second class postage paid at New York, NY and additional mailing offices. POSTMASTER: Send address change to Transactions of the ASME, Journal of Turbomachinery, c/o THE AMERICAN SOCIETY OF MECHANICAL ENGINEERS, 22 Law Drive, Box 2300, Fairfield, NJ 07007-2300.
CHANGES OF ADDRESS must be received at Society headquarters seven weeks before they are to be effective. Please send old label and new address.
PRICES: To members, $40.00, annually; to nonmembers, $150.00.
Add $24.00 for postage to countries outside the United States and Canada.
STATEMENT from By-Laws. The Society shall not be responsible for statements or opinions advanced in papers or . . . printed in its publications (B7.1, Par. 3).
COPYRIGHT © 1995 by The American Society of Mechanical Engineers. Authorization to photocopy material for internal or personal use under circumstances not falling within the fair use provisions of the Copyright Act is granted by ASME to libraries and other users registered with the Copyright Clearance Center (CCC) Transactional Reporting Service provided that the base fee of $3.00 per article is paid directly to CCC, 222 Rosewood Dr., Danvers, MA 01923. Request for special permission or bulk copying should be addressed to Reprints/Permission Department.
INDEXED by Applied Mechanics Reviews and Engineering Information, Inc.
Canadian Goods & Services
Tax Registration #126148048

TECHNICAL PAPERS

(Contents Continued on p. 11)

Downloaded 01 Jun 2010 to 171.66.16.52. Redistribution subject to ASME license or copyright; see http://www.asme.org/terms/Terms_Use.cfm

(Contents Continued)

TECHNICAL BRIEFS

ANNOUNCEMENTS

Darryl E. Metzger Memorial Session Paper

Y. W. Kim
Dept. of Mechanical and Aerospace Eng.,
Arizona State University,
Tempe, AZ 85287

J. P. Downs

F. O. Soechting

United Technologies Corp.,
Pratt & Whitney,
West Palm Beach, FL 33410

W. Abdel-Messeh
United Technologies Corp.,
Pratt & Whitney,
Longueuil, Quebec, Canada

G. D. Steuber

S. Tanrikut

United Technologies Corp.,
Pratt & Whitney,
East Hartford, CT 06108

A Summary of the Cooled Turbine Blade Tip Heat Transfer and Film Effectiveness Investigations Performed by Dr. D. E. Metzger

The clearance gap between the stationary outer air seal and blade tips of an axial turbine allows a clearance gap leakage flow to be driven through the gap by the pressure-to-suction side pressure difference. The presence of strong secondary flows on the pressure side of the airfoil tends to deliver air from the hottest regions of the mainstream to the clearance gap. The blade tip region, particularly near the trailing edge, is very difficult to cool adequately with blade internal coolant flow. In this case, film cooling injection directly onto the blade tip region can be used in an attempt to directly reduce the heat transfer rates from the hot gases in the clearance gap to the blade tip. The present paper is intended as a memorial tribute to the late Professor Darryl E. Metzger, who made significant contributions in this particular area over the past decade. A summary of this work is made to present the results of his more recent experimental work, which was performed to investigate the effects of film coolant injection on convection heat transfer to the turbine blade tip for a variety of tip shapes and coolant injection configurations. Experiments are conducted with blade tip models that are stationary relative to the simulated outer air seal based on the result of earlier works that found the leakage flow to be mainly a pressure-driven flow, which is related strongly to the airfoil pressure loading distribution, and only weakly, if at all, to the relative motion between blade tip and shroud. Both heat transfer and film effectiveness are measured locally over the test surface using a transient thermal liquid crystal test technique with a computer vision data acquisition and reduction system for various combinations of clearance heights, clearance flow Reynolds numbers, and film flow rates with different coolant injection configurations. The present results reveal a strong dependency of film cooling performance on the choice of the coolant supply hole shapes and injection locations for a given tip geometry.

Introduction

In the development of modern high-performance gas turbines, convective heat transfer aspects relating to the active cooling schemes of turbine components continue to be a major focus. Current efforts to improve overall engine performance almost always involve gas path temperature increases. In particular, increases in turbine inlet temperature require improved cooling designs to keep the temperature level and thermal gradients in various turbine components within acceptable limits.

The sought-after temperature levels and thermal gradients control must be achieved with a minimum use of coolant due to the resulting engine cyclic penalties associated with the extraction of costly high-pressure air from the engine compressor stages for use as coolant. Minimization of cooling air is one of the primary motivations for the development of improved convection heat transfer knowledge and predictive capability.

One of the critical areas of gas turbine engines, in terms of durability and cooling air use, is the blade tip region. In axial turbine stages under almost all operating conditions, a clearance gap exists between the blade tips and the stationary outer seal. Even with sophisticated clearance control methods, this gap is never eliminated at all operating conditions (Hennecke, 1984). Thus, in normal operation, the pressure difference be-

---

Contributed by the International Gas Turbine Institute and presented at the 39th International Gas Turbine and Aeroengine Congress and Exposition, The Hague, The Netherlands, June 13-16, 1994. Manuscript received by the International Gas Turbine Institute February 15, 1994. Paper No. 94-GT-167. Associate Technical Editor: E. M. Greitzer.

tween the convex and concave sides of the blades drives a leakage flow across the tip that has detrimental effects on both aerodynamic performance and heat transfer. Near the pressure side of the gap, hot mainstream flow is turned into the gap with high acceleration levels and thin boundary layers (Mayle and Metzger, 1982; Metzger and Rued, 1989). Because of this boundary layer thinning, and together with strong secondary flows within the blade hot gas path, the flow entering a gap is often primarily composed of fluid at or near the maximum temperature of the hot gases, particularly in the downstream tip region near the trailing edge. The resultant thermal loading at the blade tip can be very significant and detrimental to tip durability, especially since the blade tip region near the trailing edge can be difficult to cool adequately with blade internal cooling flows.

As a result of their effects on turbine efficiency and performance, blade tip leakage flows have been the subject of fairly intense investigation for more than a decade (Allen and Kofskey, 1955; Booth et al., 1982; Bindon, 1986; Moore and Tilton, 1988); but only in more recent years has attention focused on the heat transfer aspects of these leakage flows (Mayle and Metzger, 1982; Metzger and Rued, 1989; Rued and Metzger, 1989; Moore et al., 1989). One of the results of these more recent studies has been demonstration that convection heat transfer on the blade tip is virtually independent of the relative velocity between the tip and the stationary outer ring seal. Despite the fact that the clearance gap is normally very small (the order of one percent of blade height), this independence has been established for both plane and grooved blade tip configurations both experimentally and numerically (Chyu et al., 1986, 1987) over a range of relative velocities including those greater than expected in practice. This independence has been previously used to enable the experimental study of tip heat transfer with stationary test sections (Metzger and Bunker, 1989). Recently, these previous studies have been extended to the case with film coolant injection from the simulated plane blade tips to show local convection coefficient and film cooling effectiveness distributions downstream of an array of discrete slots (Kim and Metzger, 1995). The present study is a continuation of these efforts at Arizona State University to include variations in blade tip geometry and coolant injection schemes. The modeled situation is generically depicted in the sketch of Fig. 1 together with the three basic tip film cooling configurations considered in the present study. Film coolant can be injected from the blade tip surface, from the airfoil pressure side face near the tip, or from a grooved-tip cavity, representative of a squealer blade tip, to protect the tip from the deleterious effects of the hot leakage flow.

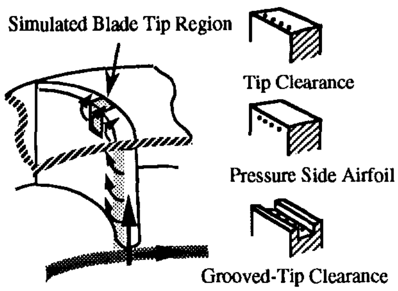

Fig. 1 Clearance gap leakage and blade tip film cooling configurations

In the present experiments, the simulated blade tips are constructed of acrylic plastic and are coated with a thin liquid crystal layer capable of providing a visual color indication of the local test surface temperature distribution. A transient test procedure is used, with differentially heated primary and secondary flows applied to the test surface to cause the coating to display colors that are locally viewed and processed with a workstation-based computer vision system. The test method allows the determination of detailed local convection coefficient and film cooling effectiveness distributions, and these distributions have been acquired over an extensive range of clearance heights, clearance flow Reynolds numbers, and film flow rates.

Experimental Apparatus and Procedures

Experimental Apparatus. A schematic of the test setup is shown in Fig. 2. The apparatus consists of a plenum chamber containing a calming section, which supplies mainstream flow to a narrow channel with the bottom, or test surface, representing a turbine blade tip surface. Heated flow can be provided to both the primary and secondary flow systems through diverter ball valves, which allow sudden application of the flow(s) to the test section. The test surface is coated with temperature-sensitive liquid crystals, and the display from this coating is viewed and processed by the computer vision system components shown in the figure. The test section is constructed en-

Nomenclature

A = heat transfer area
c_p = specific heat
D_h = channel hydraulic diameter
G = mass velocity = ρV
G_m = main flow mass velocity
G_f = film flow mass velocity
m_m = main flow mass flow rate
m_f = film flow mass flow rate
H = clearance gap height
h = local convection coefficient in $q = h(T_r - T_w)$
h_{avg} = cross-stream-averaged heat transfer coefficient
h_{fd} = fully developed heat transfer coefficient
k = test surface thermal conductivity
k_f = fluid thermal conductivity
L = test plate length in streamwise direction
L_c = simulated grooved-tip cavity width
M = blowing parameter = G_f/G_m
Nu_D = cross-stream-averaged Nusselt number = $h_{av}D_h/k_f$
Nu_{fd} = fully developed Nusselt number = $h_{fd}D_h/k_f$
Pr = Prandtl number = $\mu c_p/k_f$
q = heat flux
Re_m = Reynolds number = $G_m D_h/\mu$
R = mass flow rate ratio = m_f/m_m
s = cross-stream coordinate
t = time
T_{aw} = adiabatic wall temperature
T_f = film temperature
T_i = initial temperature
T_{mix} = mixed-mean temperature
T_r = reference temperature
T_w = wall temperature
T_{wg} = wall temperature indicated by green display
T_{wb} = wall temperature indicated by blue display
T_m = mainstream temperature
U = fundamental solution
w = length of injection hole in cross-stream direction
x = streamwise coordinate
x_0 = distance from channel entrance to upstream edge of injection hole
α = surface material thermal diffusivity
β = injection angle
γ = flare angle
η = film cooling effectiveness = $(T_r - T_m)/(T_f - T_m)$
η_{mix} = film cooling effectiveness = $(T_r - T_{mix})/(T_f - T_{mix})$
μ = fluid viscosity
ρ = density
τ = time step

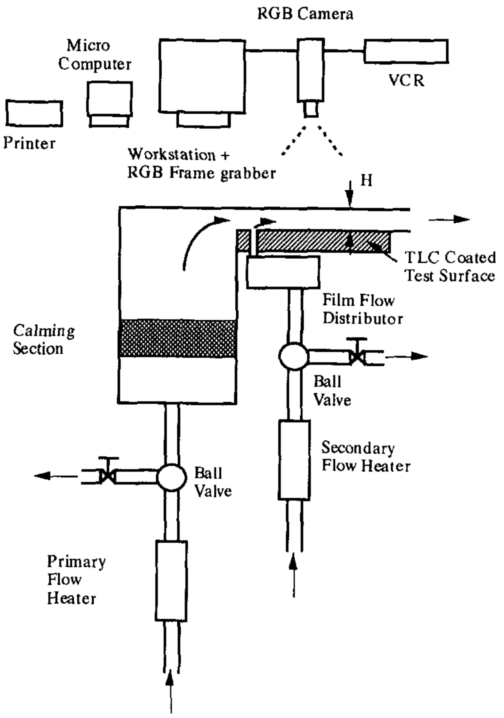

Fig. 2 Apparatus schematic

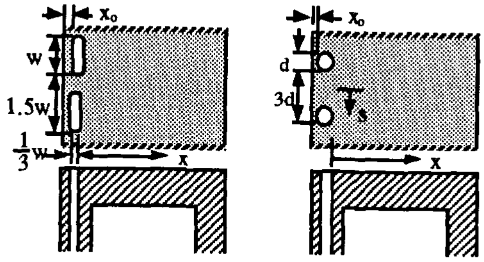

(a) Discrete Slot (b) Round Hole

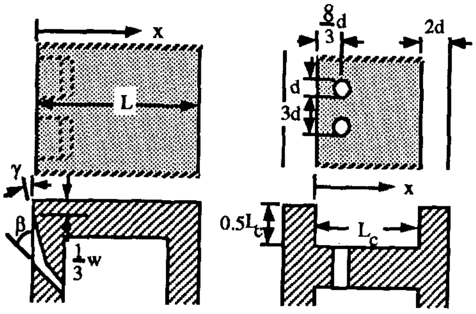

(c) Pressure Side (d) Grooved-Tip

Fig. 3 Blade tip geometry and film injection configurations

tirely of acrylic plastic: transparent on the top of the clearance gap channel to allow viewing of the test surface from outside the channel, and painted black on the test surface itself to provide an optimum background for the liquid crystal coating display.

The working fluid used in the main flow circuit consists of filtered and dried laboratory compressed air, which flows through an in-line electric heater with autotransformer-controlled power input, and a three-way ball-type flow diverter valve. The diverter valve is used to bypass the heated air from the test section until the heated air temperature reaches a desired value. The diverted air passes through the balancing valve, which is adjusted to equalize the flow resistance between the test section and bypass circuit so that the flow rate is unchanged when the flow is suddenly routed to the test section.

The thermal liquid crystal coating used is a commercially available, micro-encapsulated chiral nematic thermochromic liquid crystal (TLC), which is applied to the test surface using an airbrush. This TLC displays colors in response to temperature changes as a result of lattice reorientation of the crystal. When applied as a thin layer, the TLC is essentially clear, showing the black background, and displays color with increasing temperature in sequence of red, green, and blue, and returning to clear. The nominal temperatures for red, green, and blue displays of the TLC formulation used are 38.4°C, 39.8°C, and 43.5°C, respectively. It is expected that this coating, which is on the order of 10^{-3} cm thick, will have a response time of only a few milliseconds, as shown by Ireland and Jones (1987). This time is negligible in comparison with the duration of the thermal transients used in the present study.

To minimize experimental uncertainties, the temperatures of the supplied flows are chosen so that the color threshold is not reached until sufficient time has elapsed after the start of flow (usually 15 seconds or more) to insure that the elapsed time can be determined accurately. Also, the primary and secondary flow temperatures are chosen so that the elapsed time (usually less than 60 seconds), and corresponding depth of heat penetration into the test surface, will permit the assumption of a semi-infinite solid, as discussed below, to be valid. Experimental uncertainties have been assessed by the methods of Kline and McClintock (1953) and are estimated to be ±8 percent for convection coefficients, h, and ±10 percent for film cooling effectiveness, η.

Table 1 Tip model dimensions

Configuration	Dimensions [cm]
Discrete Slot	xo=0.25, w=0.95
Round Hole	xo=0.25, d=0.48
Pressure Side	w=0.95, γ=12°, β=45°
Grooved Tip	d=0.48, Lc=5.08

The present computer vision system employs the following three major components: (*i*) SUN SPARC station2 with ethernet mainframe connection, (*ii*) RasterOps RGB color frame grabber, and (*iii*) Pulnix RGB CCD color video camera. Additional auxiliary components include a video cassette recorder, microcomputer, and color printer. The use of the system to evaluate film cooling performance is described in the following section.

The cross sections and plane views of the test surfaces are shown in Fig. 3. The basic dimension of the test surface for all blade tip configurations is 8.26 cm wide in the cross-stream direction and 7.24 cm long in the streamwise direction from the simulated pressure-to-suction side. Two clearance gap heights have been considered in the present test program, resulting in clearance gap ratios (L/H) of 9.12 and 15.2, respectively. The detailed dimensions of the test surfaces are summarized in Table 1. Secondary film flow is supplied from the heater to a manifold, which, in turn, distributes the film flow equally to a single array of injection holes. The test surfaces for discrete slot, round hole, and pressure side injection configurations each have an array of five equally spaced injection holes, whereas the grooved tip configuration employed four holes. The spacing and hole cross section upstream of the flared exit for the pressure side injection model are identical to those of the discrete slot configuration. For each configuration, primary channel flow Reynolds numbers, based on channel hydraulic diameter, were set at values of 15×10^3, 30×10^3, and 45×10^3, and secondary film flow rates were set to provide values of film-to-mainstream mass flow rate ratio ranging from 0.016 to 0.223.

Measurement Theory and Procedures. The measurement of the test surface convection characteristics and evaluation of the performance of the film coolant injection follow the methods of Vedula and Metzger (1991) with local heat transfer rate expressed as:

$$q = h(T_r - T_w) \tag{1}$$

where T_w is the local test surface temperature and T_r is the reference, or convection driving, temperature that renders the convection coefficient, h, independent of the temperatures. For small temperature differences and constant fluid properties, the appropriate T_r reduces the convection coefficient h to a function of the aerodynamic character of the flow field alone, and allows a local surface convection behavior to be condensed into a constant of proportionality (h) for a given flow field.

In two-temperature convection situations, with a single convecting fluid at temperature T_m, the reference temperature is simply T_m, and only h must be determined in the experiments. In film cooling with two flows present, the reference temperature is at some generally unknown level that depends on the supply temperatures of the two interacting streams and the degree of mixing that has occurred between them before they arrive at the various locations on the surface. For these situations, both h and T_r must be considered unknowns to be determined by experiment. Note that in general if the surface is locally adiabatic, $T_r = T_{aw}$ (adiabatic wall temperature). Thus traditionally T_r distributions over the surface have been obtained on adiabatic surfaces, but separate testing on a nonadiabatic surface is required to determine the h distribution. With the present test method, both T_r and h are determined with use of the same surface.

In the present experiments, the test surface is suddenly exposed to the flow(s) and the transient response of the test surface as indicated by the TLC color display is observed. The wall material including the test surface is initially at a uniform temperature at all depths, and the initial response near the surface is governed by a semi-infinite formulation of the transient heat conduction where the temperature at the surface is given by the classical solution:

$$\frac{T_w - T_i}{T_r - T_i} = 1 - \exp\left[\frac{h^2 \alpha t}{k^2}\right] \operatorname{erfc}\left[\frac{h\sqrt{\alpha t}}{k}\right] \tag{2}$$

The semi-infinite description is appropriate as long as the transient temperature penetration does not exceed the thickness of the wall material being used, and thus the penetration time becomes the criterion for deciding test wall thickness and subsequent allowable transient test duration. The solution is applied locally at all points on the surface in accordance with the findings of Metzger and Larson (1986), and Vedula et al. (1988), which showed that lateral conduction effects within the test surface are very small, even with strong variations of h over the surface.

For situations where T_r is known, for example tests in the present program conducted without secondary flow present, h can be determined from Eq. (2) by measuring the time t required for the surface temperature to reach a prescribed value as indicated by the coating color display. The method is extended to film cooling and other three-temperature situations (Vedula and Metzger, 1991) by noting that both h and T_r can be obtained as the simultaneous solution of two equations of the form of Eq. (2) obtained either from a single transient test with two surface temperature indications at different times during the transient, or from two separate related transient tests. For example, if during the transient a liquid crystal surface coating indicates one surface temperature T_{wg} at time t_g corresponding to the green display and another T_{wb} corresponding to the blue display at t_b, then h and T_r are determined from the simultaneous solution of:

$$\frac{T_{wg} - T_i}{T_r - T_i} = 1 - \exp\left[\frac{h^2 \alpha t_g}{k^2}\right] \operatorname{erfc}\left[\frac{h\sqrt{\alpha t_g}}{k}\right] \tag{3}$$

$$\frac{T_{wb} - T_i}{T_r - T_i} = 1 - \exp\left[\frac{h^2 \alpha t_b}{k^2}\right] \operatorname{erfc}\left[\frac{h\sqrt{\alpha t_b}}{k}\right] \tag{4}$$

In the experiments, for both two- and three-temperature situations, an additional complication is introduced since true step changes in the applied fluid temperatures are usually not possible and the reference temperatures are thus functions of time. This complication is accounted for by modifying the equations through the use of superposition and Duhamel's theorem (Metzger and Larson, 1986). The actual gradual change is obtained by using a series of steps. The solution is represented as:

$$T - T_i = \sum_{j=1}^{N} U(t - \tau_j)\,(T_r - T_i)_j \tag{5}$$

where

$$U(t - \tau_j) = 1 - \exp\left[\frac{h^2}{k^2}\,\alpha(t - \tau_j)\right] \operatorname{erfc}\left[\frac{h}{k}\sqrt{\alpha(t - \tau_j)}\right] \tag{6}$$

Here, T_r is time varying and unknown but related to the time variation in T_m and T_f, and to the film cooling effectiveness η such that:

$$T_r - T_i = (1 - \eta)(T_m - T_i) + \eta(T_f - T_i) \tag{7}$$

The two simultaneous equations are solved in the form of Eqs. (5)-(7) to obtain the two unknowns, h and η.

It is appropriate here to mention that a distinct advantage of the testing scheme described is that all wetted surfaces are thermally active. This is in contrast to many other testing techniques, where only the test surface itself is thermally active, and adjacent surfaces that may interact through convection with the test surface have unrealistic thermal boundary conditions. Moreover, the thermal boundary conditions on the test and adjacent surfaces are close to spatially isothermal, which is the wall surface condition usually desired in gas turbine engine component design.

Results and Discussion

The immediate results of the test procedures described in the preceding section are two color-coded maps displayed on the workstation monitor, which describe the local distributions of both convection coefficients and film cooling effectiveness over the entire test surface downstream of injection (Kim and Metzger, 1992). Each map is produced from a 100 × 75 raw data matrix. Figure 4 shows a typical set of local convection coefficient and film cooling effectiveness maps in gray levels acquired from the discrete slot, normal injection configuration.

A significant advantage of the present experimental technique concerns the degree of detail available for providing both qualitative and quantitative results of the highly complex convective heat transfer phenomena under consideration. For comparison purposes, various linear variations and averages can be derived from these maps, and samplings of those are presented in this section to describe the character of the film cooling performance for each configuration.

Flat Surface With No Injection. Figure 5 shows the cross-stream-averaged convection coefficients in the form of Nusselt numbers obtained on the test surface in the absence of coolant injection. Local cross-stream-averaged Nusselt numbers have been normalized with respect to fully developed values calculated from the Dittus-Boelter correlation for fully developed flow in a duct ($\mathrm{Nu}_{fd} = 0.023\,\mathrm{Re}_m^{0.8}\mathrm{Pr}^{0.4}$) and are plotted as a function of channel length divided by hydraulic diameter. Also

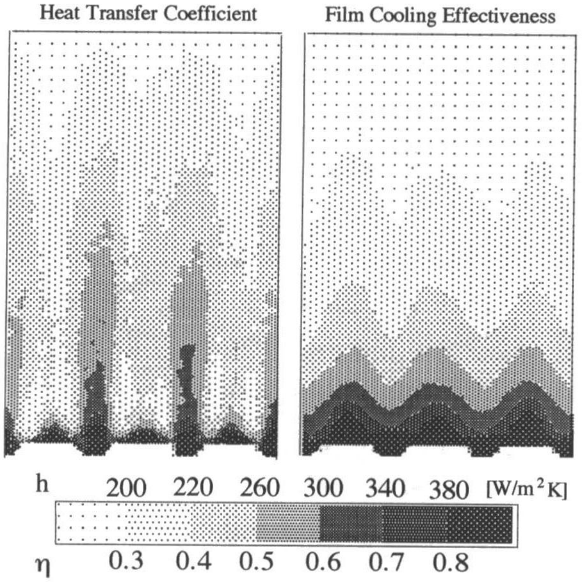

Fig. 4 Local heat transfer and film cooling effectiveness distributions, Re_m = 45,000, R = 0.124, L/H = 9.12

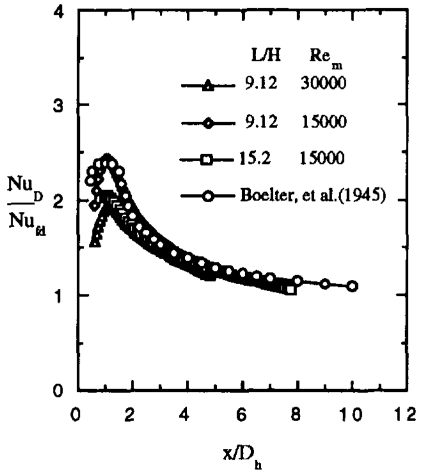

Fig. 5 No-injection cross-stream-averaged Nu_D

shown is the result of Boelter et al. (1945) for a sharp-edged duct entry as given by Kays and Crawford (1980). The data obtained with Re_m = 15,000 and L/H = 9.12 are in excellent agreement with the classical results, particularly near the entry region, whereas other results obtained for higher mean velocity, or a smaller channel height, tend to fall below the classical values. This trend is in general agreement with the expectation that the present geometry, which simulates a sharp-edged entry on only one side of the channel, will approach the duct entry situation at low inlet speeds and large channel heights where a better symmetry of flow can be established. In general, the present results are in good agreement with expected values for a duct flow entry region, providing confidence in the present test procedures.

Discrete Slot Normal Injection. A detailed discussion of the results for this configuration has been given by Kim and Metzger (1993). To facilitate comparisons with other configurations evaluated, some of the results of that work are repeated here. Figures 6 and 7 show the local distributions of heat transfer and film cooling effectiveness at four streamwise locations downstream of injection for a typical set of results obtained with Re_m = 45,000, R = 0.124, and L/H = 9.12. To minimize the channel end wall effects, the range of data

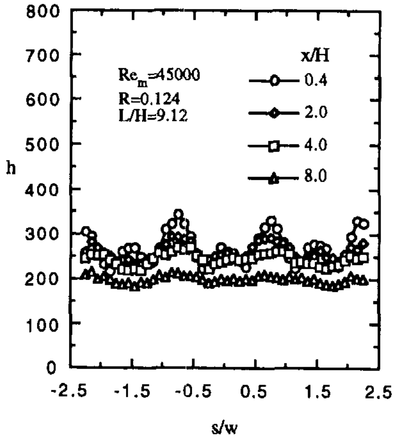

Fig. 6 Local convection coefficient distributions, discrete slot injection

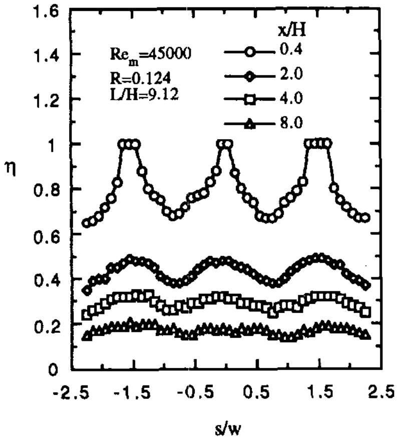

Fig. 7 Local film cooling effectiveness distributions, discrete slot injection

presented is restricted to a nominal three-pitch distance centered at the cross-stream midpoint of the slot array (s/w = 0). Also, data obtained near the film supply slots ($x/H < 0.4$) were excluded due to the local invalidation of one-dimensional heat flow assumption. In Fig. 6, it appears that local convection coefficients vary significantly in the region close to the injection location. The observed peaks and valleys of the local heat transfer distribution at x/H = 0.4 correlate well with the locations of the three slots whose centers are positioned at s/w = −1.5, 0.0, and 1.5, respectively. The data indicate heat transfer is relatively low immediately downstream of each slot compared with the values in the space between two neighboring slots. This trend is in accord with the expected boundary layer thickening associated with film injection which tends to reduce local heat transfer. The initial periodic heat transfer distributions eventually smear out far downstream as indicated by values at x/H = 8.0. This observation suggests the discrete film flows spaced relatively close to each other may have merged in the far downstream region.

The corresponding set of film cooling effectiveness data for the same conditions and locations is given in Fig. 7. The effectiveness data also show a large variation at the streamwise location closest to injection. Film cooling effectiveness immediately downstream of each slot is as high as 1.0 at some locations and drops to approximately 65 percent of the peak value between the slots. The lowest value, however, still reads above 0.6. This means that the present film cooling configuration, with film injection slots spaced relatively close to each other, contains no totally uncooled region downstream of the injection location. The local distributions presented in Fig. 7

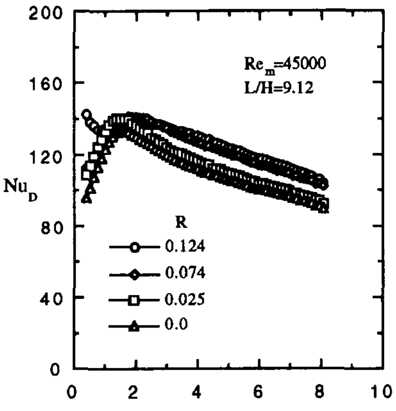

Fig. 8 Effect of R on cross-stream-averaged Nusselt numbers, discrete slot injection

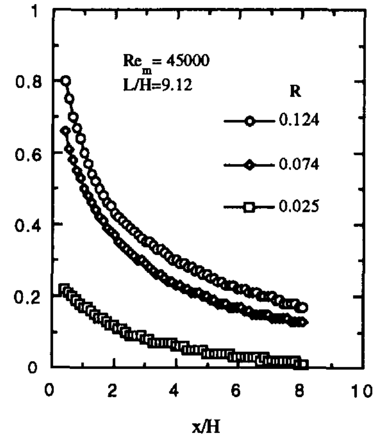

Fig. 9 Effect of R on cross-stream-averaged effectiveness, discrete slot injection

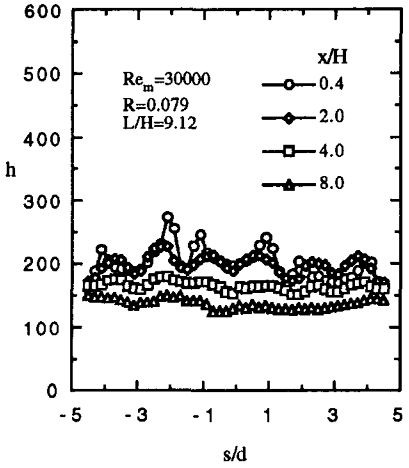

Fig. 10 Local convection coefficient distributions, round hole injection

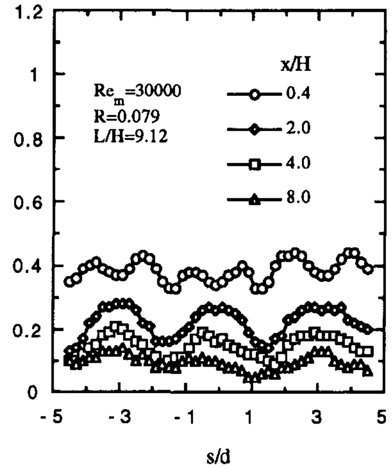

Fig. 11 Local film cooling effectiveness distributions, round hole injection

are typical of all the film cooling effectiveness data obtained with the present configuration for L/H = 9.12 and for an intermediate range of mass flow rate ratios. In general, the cross-stream variations tend to be highest at the highest blowing rates, with higher cross-stream-averaged effectiveness values close to injection, and monotonically decreasing in the downstream direction. In all cases, the close cross-stream spacing of the holes prevents any zero-effectiveness regions between the holes.

The overall effects of coolant injection rate on measured heat transfer and film cooling performance are shown in Figs. 8 and 9, respectively. Figure 8 gives the heat transfer variation in terms of cross-stream-averaged Nusselt number with respect to increasing mass flow rate ratio for Re_m = 45,000 and L/H = 9.12. All data sets, with the exception of the highest values of R, show a classical sharp-edged channel entrance distribution with low values close to the entrance corner, which is attributable to flow separation. The values rise abruptly, peaking at x/H = 1.5 due to the expected flow reattachment onto the test surface. It is clear that increasing coolant injection rate generally enhances the convection coefficients at all streamwise locations. Relative to the no-injection values, an increase of up to 20 percent is observed in cross-section-average convection coefficients measured downstream of injection as a result of coolant injection into the gap. This injection-induced convection coefficient increase means that if the film injection temperature is not low enough, relative to the clearance leakage flow temperature, injection can actually increase thermal loading on the tip, which is opposed to the desired effect. The nonmonotonic behavior near the pressure side corner observed for R = 0.124 is an evidence of locally complex flow interactions between the accelerating main flow and injected coolant flow, which warrants further study. The corresponding film cooling effectiveness variations are given in Fig. 9. It is observed that the cross-stream-averaged film cooling effectiveness monotonically increases with increasing coolant injection rate over all of the protected surface. This trend is typical of all the data sets obtained thus far.

Round Hole Injection. The cross-stream variations of local heat transfer and film cooling effectiveness at four streamwise locations downstream of injection obtained with Re_m = 30,000, R = 0.079, and L/H = 9.12 are shown in Figs. 10 and 11, respectively. The heat transfer distribution given in Fig. 10 shows a trend similar to that observed in the previous discrete slot injection case, i.e., a large cross-stream variation immediately downstream of a discrete hole array followed by gradual decay of the resulting periodic structure in the downstream direction. It is of interest to note the existence of six peaks in the cross-stream distribution close to the hole array corresponding to the injection hole locations now at $s/d = -3.0$, 0.0, and 3.0, where d is the injection hole diameter. This observation suggests the presence of horseshoe-type vortex pairs downstream of each hole, which are typical of round hole flow injection into a moving gas stream (Goldstein, 1971). The corresponding film cooling effectiveness data for the same conditions are given in Fig. 11. It is noted that the cross-sectional local film cooling effectiveness distributions also be-

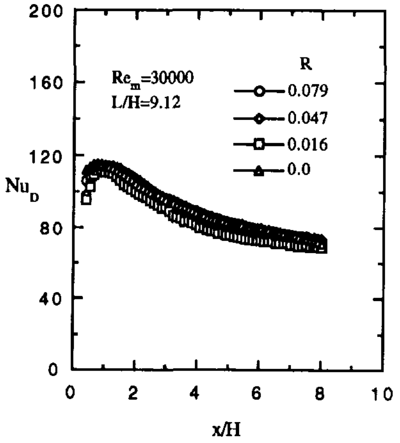

Fig. 12 Effect of R on cross-stream-averaged Nusselt numbers, round hole injection

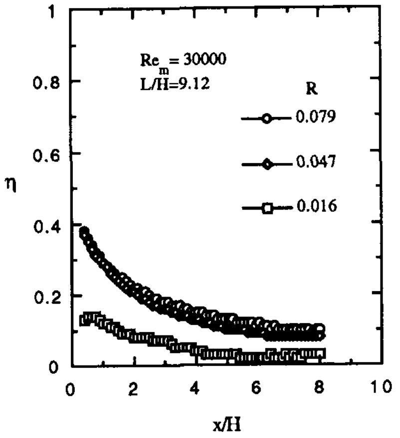

Fig. 13 Effect of R on cross-stream-averaged effectiveness, round hole injection

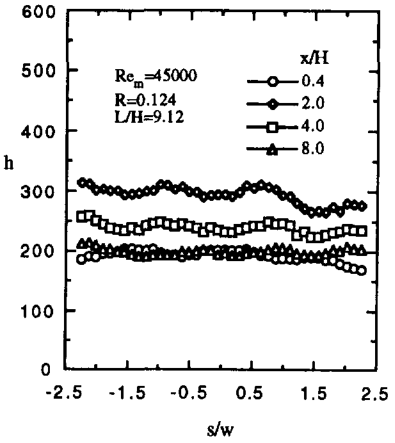

Fig. 14 Local convection coefficient distributions, pressure side flared hole injection

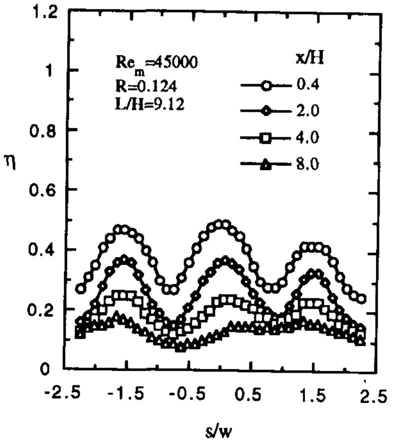

Fig. 15 Local film cooling effectiveness distributions, pressure side flared hole injection

gin with six distinct peaks close to the injection location, which are similar to those observed in the heat transfer data. In contrast to the convection coefficient distributions, the periodic pattern, again plausibly caused by horseshoe-type vortices, rapidly changes to a more expected three-peak distribution similar to that observed in the previous discrete slot injection case as indicated by the data set for $x/H = 2.0$. The transition in the shape of the local distribution is believed to be an indication that significant mainstream gas entrainment occurs in the region downstream of injection between two neighboring injection holes, which is driven by local secondary flow motions. It is generally observed that the present round hole injection results exhibit less-diminished periodic structure in the far downstream region when compared with the previous discrete slot injection results. Although a direct comparison is not possible due to differences in flow parameters, this trend may be attributable to the relatively large hole spacing of the present round hole configuration, which results in a larger initially unprotected region between injection holes. Nevertheless, the measured film cooling effectiveness values indicate that no unprotected surface exists downstream of injection with the present round hole injection configuration.

Figures 12 and 13 show the overall effect of increasing injection rate on measured cross-stream-averaged Nusselt number and film cooling effectiveness. The Nusselt number distributions show only a small variation with respect to increasing injection rate. Also noticeable is that the Nusselt number variation is not monotonic with respect to the increasing value of R, although the entrance behavior is clearly observed and appears to be insensitive to the injection rate. The cross-stream-averaged film cooling effectiveness data in Fig. 13 show a strong variation with increasing injection rate. It is of interest to observe that the data set obtained for $R = 0.047$ shows little difference compared with the values for $R = 0.079$ regardless of nearly a 70 percent increase in the coolant mass flow rate. Such behavior highlights the need for a detailed investigation of film injection rate for a given leakage flow Reynolds number and injection configuration to identify an optimum.

Pressure Side Flared Hole Injection. The local cross-stream variations of convection coefficients and film cooling effectiveness for a configuration that injects air on the simulated pressure side through flared slots are shown in Figs. 14 and 15 for conditions of $\mathrm{Re}_m = 45{,}000$, $R = 0.124$, and $L/H = 9.12$. In the present injection configuration, the film coolant is injected into the mainstream as angled jets upstream of the test surface and into the supply plenum where local mainstream velocity is relatively low.

Based on the mean velocity within the plenum for the given mass flow rate ratio, the local velocity ratio of the mainstream to injected film flow can be as low as 1/13. In this situation, one may expect the film flow to travel far into the mainstream and become embodied into the leakage flow entering the clearance gap. Unless the film flows reattach before they enter the clearance gap, the local transport characteristics will be dominated by the entrance behavior of the accelerating tip leakage flow. Figure 14 suggests that both the mainstream and film

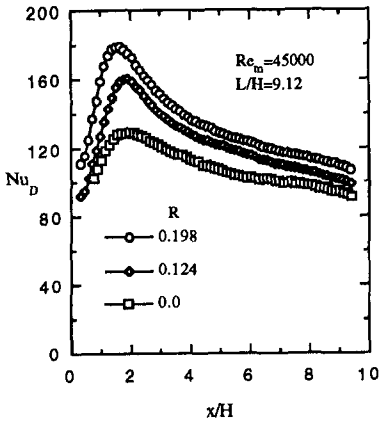

Fig. 16 Effect of R on cross-stream-averaged Nusselt numbers, pressure side flared hole injection

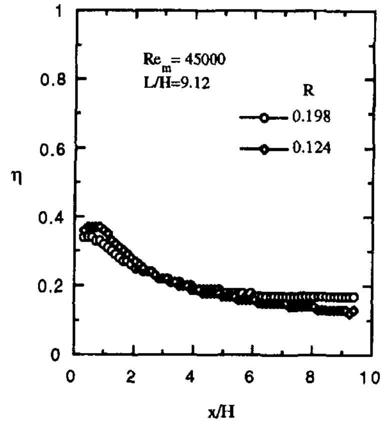

Fig. 17 Effect of R on cross-stream-averaged effectiveness, pressure side flared hole injection

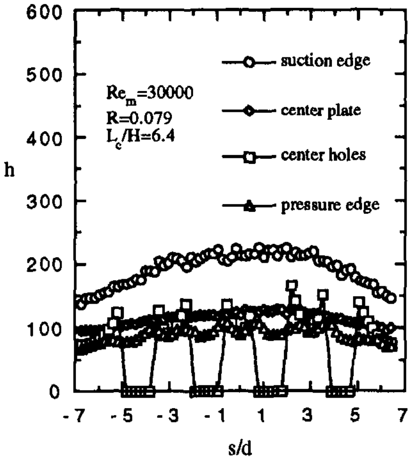

Fig. 18 Local convection coefficient distributions, grooved-tip cavity injection

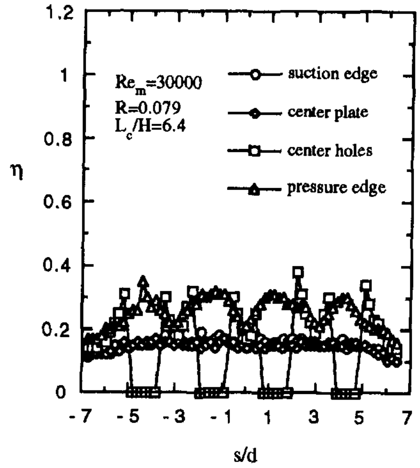

Fig. 19 Local film cooling effectiveness distributions, grooved-tip cavity injection

flows separate at the pressure-side tip corner and reattach far into the clearance gap as indicated by the low values at $x/H = 0.4$. The measured cross-section heat transfer distributions show no significant effect of upstream film injection as they appear fairly uniform at all four streamwise locations. On the other hand, the cross-section film cooling effectiveness distributions given in Fig. 15 show large variations at all streamwise locations, clearly showing the trace of upstream fluid temperature distributions along the cross-stream direction. Although the transport characteristics due to discrete film flow injection appear to have been smeared out, at least near the test surface of interest, this observation suggests the local reference temperature distributions are retained in the clearance leakage flow even after a sharp, 90 deg turn over the pressure-side tip. This large difference in local heat transfer and film effectiveness distribution characteristics provides strong evidence that information for both heat transfer and film cooling effectiveness is needed to predict thermal loading accurately.

Figures 16 and 17, respectively, show the effect of varying injection rate on measured cross-stream-averaged Nusselt number and film cooling effectiveness distributions in the streamwise direction. As shown in Fig. 16, the measured convection coefficient distributions appear highly sensitive to the increase in injection rate, particularly in the reattachment region. Comparing the present data with those obtained for the discrete slot injection case given in Fig. 8, one finds that the difference between the values in the reattachment region obtained with and without injection is significantly larger for the present pressure side injection configuration. The local Nusselt numbers obtained with $R = 0.124$ near the reattachment region show an increase of nearly 25 percent over the no-injection values, whereas the corresponding increase in Fig. 8 for the same mass flow rate ratio is no more than 5 percent. This is apparently due to the lack of flow interactions that would exist for the discrete slot injection case. Figure 17 shows the matching film cooling effectiveness variation with respect to increasing injection rate. It is noted that measured cross-stream-averaged effectiveness values show no evidence of significant enhancement with nearly a 60 percent increase in coolant injection rate. In fact, values near the pressure side, at a higher injection rate, read slightly lower than those for a lower injection rate.

Grooved-Tip Cavity Injection. The local convection coefficient and film cooling effectiveness distributions within the grooved-tip cavity floor are shown in Figs. 18 and 19, respectively, for the pressure-side cavity injection case. Four streamwise locations on the cavity floor surface are chosen to show local cross-section variations in each figure, i.e., pressure-edge and suction-edge each signifying the data set taken at streamwise locations: $x/L_c = 0.05$ and 0.95 (approximately one-half the hole diameter from the pressure-side and suction-side cavity walls), center-plate: $x/L_c = 0.5$ (representing the data set along the midpoints on the cavity floor), and center-holes: $x/L_c = 0.25$ (representing the data set along the line passing the centers of the injection holes). This data presentation format should provide at least an overall view of the complex heat

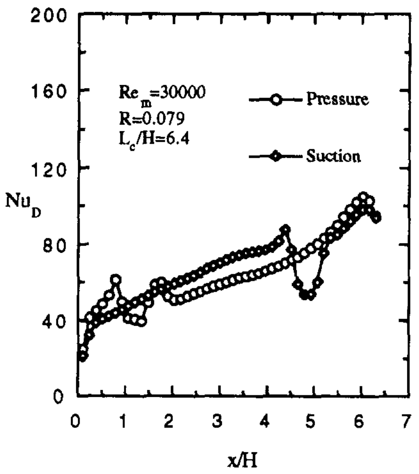

Fig. 20 Effect of injection location on cross-stream-averaged Nusselt numbers, grooved-tip cavity injection

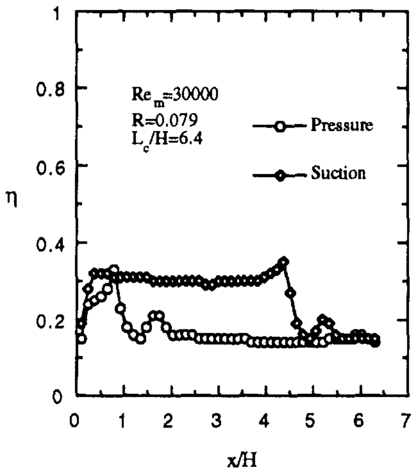

Fig. 21 Effect of injection location on cross-stream-averaged effectiveness, grooved-tip cavity injection

transfer phenomenon within the grooved-tip cavity region. The local convection coefficient distributions shown in Fig. 18 do reveal many interesting features of local transport characteristics. First, it is noted that relatively high convection coefficients are found near the suction-side cavity wall, which suggests the existence of a circulation bubble typically found in the groove-tip cavity. Based on the local heat transfer map produced from the raw data matrix, a large circulation bubble, located near the suction-side cavity wall, is identified for all test results for the present configuration. The mild cross-stream variation of the data set for suction-edge, showing a maximum at midspan is due to the finite cross-stream length of the grooved-tip cavity, which necessarily introduces three dimensionality into the test results.

The values measured along the hole centerlines (centerhole) clearly show a periodic cross-stream variation, which is apparently caused by the discrete hole injection. Data points acquired on the hole edges have been removed to exclude the edge effects. Therefore, the peak values near the injection holes located at $s/d = \pm 1.5$ and ± 4.5 do represent injection-induced local heat transfer enhancement. The pressure-edge values also show a periodic variation, which indicates the circulation bubble, with its mean motion directly opposite to the leakage flow direction near the cavity floor surface, tends to sweep the film flows toward the pressure-side cavity wall. The matching film cooling effectiveness data in Fig. 19 reveal this flow phenomenon within the cavity more clearly. Local film cooling effectiveness values for pressure-edge show four distinct peaks aligned with the center of each hole, whereas data obtained near the suction corner indicate no periodic variations. Nevertheless, the values in the region between the injection location and suction-side wall are all found to be above 0.1, suggesting that the circulation bubble present within the grooved-tip does carry coolant flows to the opposite end of the cavity floor.

One of the main objectives for the present grooved-tip configuration study was to investigate the effect of varying injection location on the measured heat transfer and film cooling performance.

A typical set of results, showing the effect of varying injection location, is presented in Figs. 20 and 21 in terms of cross-stream-averaged channel Nusselt numbers and film effectiveness on the cavity floor.

The two injection locations considered are the pressure-side injection, in which the hole array is located at $x/L_c = 0.25$, and the suction-side injection at $x/L_c = 0.75$. The Nusselt number distributions shown in Fig. 20 indicate that the suction-side injection results are slightly higher than those of the pressure-side injection over the majority of the test surface. The effectiveness data, however, show a significant difference in the overall film cooling performance. Data obtained with suction-side injection consistently show a twofold increase over those with pressure-side injection on virtually all locations of the cavity floor. This trend is apparently due to the flow interaction between the injected film flows and the circulation bubble present within the cavity. As pointed out in the previous cross-stream distribution results, the air motion associated with the circulation bubble tends to sweep the injected coolant toward the pressure-side cavity wall where it is forced to be in direct contact with the leakage flow moving in the opposite direction. In this situation, one may expect a rapid degradation in the cooling capability of the film flows due to the inevitable mixing with the mainstream while traveling to the upstream end of the cavity floor. Since the fluid motion on the cavity floor is opposed to the leakage flow, this surface will therefore never have the opportunity to be protected by fresh coolant flows in the case of pressure-side injection. For the case of suction-side injection, however, the same circulation bubble tends to bend the coolant jets toward the cavity floor, and if the local flow momentum of the circulation bubble is strong enough relative to that of the coolant flow, the injected flow may cover a substantial portion of the cavity floor. The raw data corresponding to the suction-side injection configuration, which are presented in Fig. 21, actually show four distinct film traces downstream of the injection holes, meaning the film flows do attach to the downstream region after being injected. This trend is consistently observed with the present grooved-tip cavity configuration for an intermediate range of injection rates. More complete film cooling performance characterization should also include the data obtained on the cavity walls. For instance, when high thermal loading on the pressure-side cavity wall is of concern, pressure-side injection may be preferred over the suction-side injection. These points should warrant future studies that include an evaluation of film cooling performance on these areas.

Comparison Between Various Injection Configurations. In this section, a comparison of the results between different injection configurations based on the film cooling data obtained from the first three cases is discussed. The film cooling performances of the three injection configurations are compared for a given mass flow rate ratio and the results are presented in terms of the cross-stream-averaged film cooling effectiveness values at three downstream locations in Fig. 22. In order to delineate the surface film effectiveness characteristics from the mixing phenomena associated with the inter-

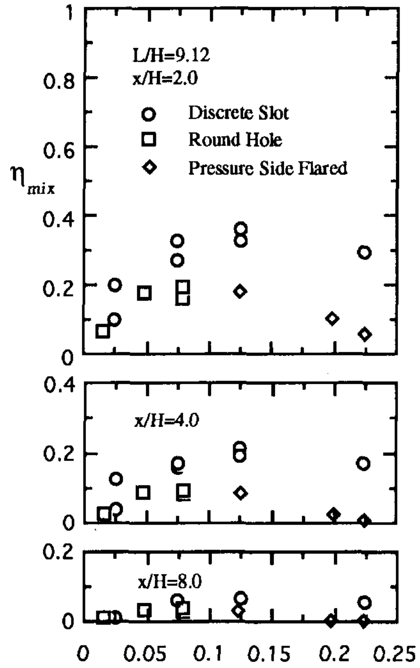

Fig. 22 Film cooling performance comparisons using mixed-mean correlation

action of the primary leakage and injected cooling flows, an attempt is made to correlate the results using a film cooling effectiveness definition based on the channel mixed-mean temperature, which is given as:

$$\eta_{mix} = \frac{T_r - T_{mix}}{T_f - T_{mix}} \tag{8}$$

From a simple energy balance for flow through a channel bounded by adiabatic walls, the following correlation can be used to relate the overall film cooling effectiveness, η, and the effectiveness based on the channel mixed-mean temperature, η_{mix}:

$$\eta_{mix} = \eta + (\eta - 1)R \tag{9}$$

The utility of this definition of film cooling effectiveness is that it indicates the magnitude of local fluid mixing characteristics for a given injection scheme separate from the overall channel cooling performance due to the decrease in leakage flow temperature within the channel as a result of coolant injection. With this definition, η_{mix} will be zero wherever the mainstream and film flows are fully mixed. In the other extreme, η_{mix} will read 1.0 wherever the local surface is exposed to pure, unmixed coolant fluid, so that the local driving temperature is equal to that of coolant at the hole exit. In Fig. 22, it is clearly shown that for a given coolant-to-mainstream mass flow rate ratio the discrete slot injection scheme provides the highest surface thermal protection performance at all downstream locations. This is undoubtedly the result of the special hole geometry and close cross-stream spacing, which provides better film coverage over the test surface. An interesting trend is observed regarding the variation of mixed-mean-based film cooling effectiveness with respect to increasing mass flow rate ratio. The discrete slot injection data clearly show a maximum point near $R = 0.125$ indicating that further mass flow rate ratio increases actually result in diminished efficiency of the film protection system.

The lower value obtained with $R = 0.224$ suggests that the coolant may not be used effectively, even though a higher overall cooling effectiveness can be obtained with increased coolant injection rate. It is of interest to note that η_{mix} values obtained in the far downstream region tend to approach zero, particularly at smaller mass flow rate ratios. This trend agrees with the expected behavior of η_{mix} in the far downstream region where substantial mixing between mainstream and coolant flows must have occurred.

Closure

The results of this study indicate that film cooling performance with coolant injection near the pressure side corner on plane blade tips varies significantly with blade tip geometry and injection locations. For the case of film injection at the blade tip pressure-side corner, the average film cooling effectiveness downstream of injection is found to increase with injection rate in general, whereas the same is not necessarily true for the airfoil pressure side injection. It is also observed that convection coefficients also vary substantially with injection rate for a given configuration. The results for the grooved-tip cavity injection indicate that overall film cooling performance varies significantly with injection locations. Among the three plane-tip film injection configurations considered in the present study, the discrete slot injection is found to provide a superior film protection capability over others for a given film-to-mainstream mass flow rate ratio. Although some of the results display unexplained trends and complexities that warrant further study, the overall results are in reasonable accordance with expectations, and should aid designers in predicting the film cooling performance on turbine blade tips.

Acknowledgments

The authors wish to pay the greatest respect to the late Professor Darryl E. Metzger for his distinguished contributions in the gas turbine heat transfer research field that resulted in many technological advances. Sponsorship for a significant portion of this work from the U.S. Air Force Wright Laboratory Aero Propulsion and Power Directorate at Wright Patterson Air Force Base, through United Technologies Corporation—Pratt & Whitney, is greatly appreciated.

References

Allen, H. W., and Kofskey, M. G., 1955, "Visualization Study of Secondary Flows in Turbine Rotor Tip Regions," NACA TN 3519.

Bindon, J. P., 1986, "Visualization of Axial Turbine Tip Clearance Using a Linear Cascade," Report No. CUED/A-Turbo TR122, Whittle Laboratory, Cambridge University, United Kingdom.

Boelter, L. M. K., Young, G., and Iverson, H. W., 1945, "An Investigation of Aircraft Heaters, XXXVII—Distribution of Heat Transfer Rate in the Entrance Region of a Tube," NACA TN 1451.

Booth, T. C., Dodge, P. R., and Hepworth, H. K., 1982, "Rotor-Tip Leakage: Part I—Basic Methodology," ASME *Journal of Engineering for Power*, Vol. 104, pp. 154-161.

Chyu, M. K., Moon, H. K., and Metzger, D. E., 1986, "Heat Transfer in the Tip Region of a Rotor Blade Simulator," *Turbine Engine Hot Section Technology*, NASA CP 2444, pp. 177-192.

Chyu, M. K., Metzger, D. E., and Hwan, C. L., 1987, "Heat Transfer in Shrouded Rectangular Cavities," *AIAA J. Thermophysics and Heat Transfer*, Vol. 1, pp. 247-252.

Goldstein, R. J., 1971, "Film Cooling," *Advances in Heat Transfer*, Academic Press, New York-London, Vol. 7, pp. 321-379.

Hennecke, D. K., 1984, "Heat Transfer Problems in Aeroengines," *Heat and Mass Transfer in Rotating Machinery*, Hemisphere Publishing Company, Washington, DC, pp. 353-379.

Ireland, P. T., and Jones, T. V., 1987, "The Response Time of a Surface Thermometer Employing Encapsulated Thermochromic Liquid Crystals," *Journal of Physics E*, Vol. 20, pp. 1195-1199.

Kays, W. M., and Crawford, M. E., 1980, *Convective Heat and Mass Transfer*, McGraw-Hill, New York.

Kim, Y. W., and Metzger, D. E., 1992, "Advanced Turbine Tip Film Cooling Studies—Phase II Final Report, Part 1, Normal Tip Injection Results," Technical Report No. 92055, Arizona State University.

Kim, Y. W., and Metzger, D. E., 1995, "Heat Transfer and Effectiveness on Film Cooled Turbine Blade Tip Models," ASME JOURNAL OF TURBOMACHINERY, Vol. 117, this issue, pp. 12-21.

Kline, S. J., and McKlintock, F. A., 1953, "Describing Uncertainties in Single Sample Experiments," *Mechanical Engineering*, Vol. 75, Jan., pp. 3-8.

Mayle, R. E., and Metzger, D. E., 1982, "Heat Transfer at the Tip of an Unshrouded Turbine Blade," *Proceedings, Seventh International Heat Transfer Conference*, Vol. 3, pp. 87-92.

Metzger, D. E., and Larson, D. E., 1986, "Use of Melting Point Surface Coatings for Local Convection Heat Transfer Measurements in Rectangular Channels With 90-degree Turns," ASME *Journal of Heat Transfer*, Vol. 108, pp. 48-54.

Metzger, D. E., and Bunker, R. S., 1989, "Cavity Heat Transfer on a Transverse Grooved Wall in a Narrow Flow Channel," ASME *Journal of Heat Transfer*, Vol. 111, pp. 73-79.

Metzger, D. E., and Rued, K., 1989, "The Influence of Turbine Clearance Gap Leakage on Flowpath Velocities and Heat Transfer, Part I: Sink Flow Effects on Blade Pressure Sides," ASME JOURNAL OF TURBOMACHINERY, Vol. 111, pp. 284-292.

Moore, J., and Tilton, J. S., 1988, "Tip Leakage Flow in a Linear Turbine Cascade," ASME JOURNAL OF TURBOMACHINERY, Vol. 110, pp. 18-26.

Moore, J., Moore, J. G., Henry, G. S., and Chaudhry, U., 1989, "Flow and Heat Transfer in Turbine Tip Gaps," ASME JOURNAL OF TURBOMACHINERY, Vol. 111, pp. 301-309.

Rued, K., and Metzger, D. E., 1989, "The Influence of Turbine Clearance Gap Leakage on Flowpath Velocities and Heat Transfer, Part II: Source Flow Effects on Blade Suction Sides," ASME JOURNAL OF TURBOMACHINERY, Vol. 111, pp. 293-300.

Vedula, R. J., Metzger, D. E., and Bickford, W. B., 1988, "Effects of Lateral and Anisotropic Conduction on the Determination of Local Convection Heat Transfer Characteristics With Transient Tests and Surface Coatings," *Collected Papers in Heat Transfer 1988*, ASME HTD-Vol. 104, pp. 21-28.

Vedula, R. J., and Metzger, D. E., 1991, "A Method for the Simultaneous Determination of Local Effectiveness and Heat Transfer Distributions in Three-Temperature Convection Situations," ASME Paper No. 91-GT-345.

Heat Transfer and Effectiveness on Film Cooled Turbine Blade Tip Models

Y. W. Kim

D. E. Metzger[1]

Department of Mechanical and Aerospace
Engineering,
Arizona State University,
Tempe, AZ 85287

In unshrouded axial turbine stages, a small but generally unavoidable clearance between the blade tips and the stationary outer seal allows a clearance gap leakage flow to be driven across the blade tip by the pressure-to-suction side pressure difference. In modern high-temperature machines, the turbine blade tips are often a region prone to early failure because of the presence of hot gases in the gap and the resultant added convection heating that must be counteracted by active blade cooling. The blade tip region, particularly near the trailing edge, is often very difficult to cool adequately with blade internal coolant flow, and film cooling injection directly onto the blade tip region can be used in an attempt to reduce the heat transfer rates directly from the hot clearance flow to the blade tip. An experimental program has been designed and conducted to model and measure the effects of film coolant injection on convection heat transfer to turbine blade tips. The modeling approach follows earlier work that found the leakage flow to be mainly a pressure-driven flow related strongly to the airfoil pressure loading distribution and only weakly, if at all, to the relative motion between blade tip and shroud. In the present work the clearance gap and blade tip region is thus modeled in stationary form with primary flow supplied to a narrow channel simulating the clearance gap above a plane blade tip. Secondary film flow is supplied to the tip surface through a line array of discrete normal injection holes near the upstream or pressure side. Both heat transfer and effectiveness are determined locally over the test surface downstream of injection through the use of thin liquid crystal coatings and a computer vision system over an extensive test matrix of clearance heights, clearance flow Reynolds numbers, and film flow rates. The results of the study indicate that film injection near the pressure-side corner on plane turbine blade tips can provide significant protection from convection heat transfer to the tip from the hot clearance gap leakage flow.

Introduction

Convection heat transfer phenomena continue to play an important role in the development of improved gas turbine engines, for both aerospace and terrestrial applications. Improvements in overall engine performance almost always involve increases in hot gas temperature, necessitate the development of better cooling schemes and more efficient use of the cooling air that is used to control temperatures in the engine components. To achieve acceptable durability, both temperature levels and temperature gradients must be controlled in the components exposed to the hot gas stream.

The sought-after temperature and temperature gradient control must be achieved with a minimum use of coolant, since most modern engines, regardless of application, use costly compressed air diverted from the engine compressor stages. Minimization of cooling air use is one of the primary motivations for the development of improved convection heat transfer knowledge and predictive ability.

One of the critical areas of gas turbine engines, in terms of durability and use of cooling air, is the blade tip region. In axial turbine stages under almost all operating conditions, a clearance gap exists between the blade tips and the outer stationary seal. Even with sophisticated clearance control methods and hardware this gap is never eliminated at all operating conditions (Hennecke, 1984). Thus in normal operation the pressure difference between the convex and concave sides of the blades drives a leakage flow across the tip, which has detrimental effects on both aerodynamic performance and heat transfer. Near the pressure side of the gap, hot mainstream flow is turned into the gap (Fig. 1) with high acceleration levels and thin boundary layers (Mayle and Metzger, 1982; Metzger and Rued, 1989). Because of this boundary layer thinning and together with strong secondary flows within the hot gas blade path, the flow entering the gap is often primarily composed of fluid at or near the maximum

---

[1] Deceased.

Contributed by the International Gas Turbine Institute and presented at the 38th International Gas Turbine and Aeroengine Congress and Exposition, Cincinnati, Ohio, May 24–27, 1993. Manuscript received at ASME Headquarters March 3, 1993. Paper No. 93-GT-208. Associate Technical Editor: H. Lukas.

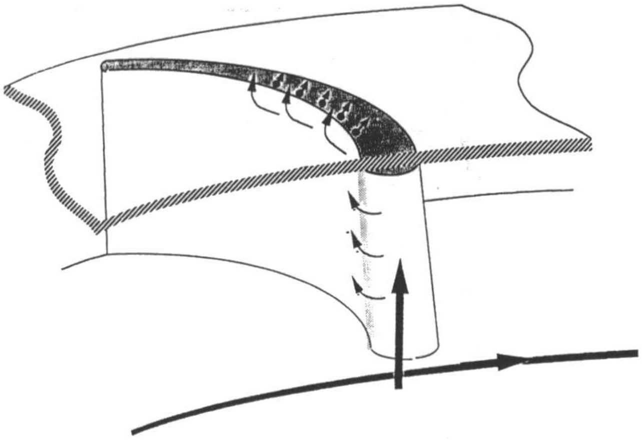

Fig. 1 Clearance gap leakage and plane tip film cooling

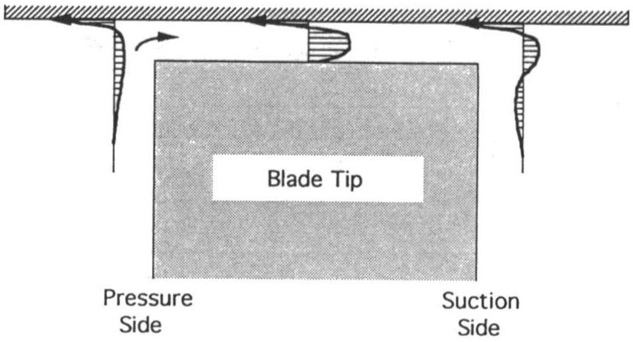

Fig. 2 Character of the clearance gap flow

temperature of the hot gases, particularly in the downstream tip region near the trailing edge. The resultant thermal loading at the blade tip can be very significant and very detrimental to tip durability, especially since the blade tip region near the trailing edge can be difficult to cool adequately with blade internal cooling flows.

As a result of their effects on turbine efficiency and performance, blade tip leakage flows have been the subject of fairly intense investigation for more than a decade (Allen and Kofskey, 1955; Booth et al., 1982; Bindon, 1986; Moore and Tilton, 1988); but only in more recent years has attention focused on the heat transfer aspects of these leakage flows (Mayle and Metzger, 1982; Metzger and Rued, 1989; Rued and Metzger, 1989; Moore et al., 1989). One of the results of these more recent studies has been demonstration that convection heat transfer on the blade tip itself is virtually independent of the relative velocity between the tip and the stationary outer ring seal. Despite the fact that the clearance gap is normally very small (the order of 1 percent of blade height), this independence has been established for both plane and grooved blade tip configurations both experimentally and numerically (Chyu et al., 1986, 1987) for relative velocities greater than those expected in practice. The essence of the situation is sketched in Fig. 2, where the effects of the relative velocity are seen to be confined to a thin layer next to the shroud, with the velocity profile near the tip virtually unchanged from the shape it would have without relative seal motion. This independence has been previously used to enable the experimental study of tip heat transfer with stationary test sections (Metzger and Bunker, 1989), and the present study is a continuation of those efforts with film coolant injection onto simulated plane blade tips. The plane tip configuration is representative of a large class of turbine blade designs practice, particularly for larger engine sizes where the size of the clearance gap relative to blade span can be kept smaller. The situation modeled is shown generally in the sketch of the Fig. 1, where film coolant injection is provided at the tip from within the blade along the pressure-side corner to protect the tip from the deleterious effects of the hot leakage flow.

In the present experiments, the simulated blade tip surface downstream of a single line of film cooling injection sites is constructed of acrylic plastic and coated with a thin liquid crystal layer capable of giving a visual color indication of the local test surface temperature distribution. A transient test procedure is used, with heated primary and secondary flows applied to the test surface to cause the coating to display colors that are locally viewed and processed with a workstation-based computer vision system. The test method allows determination of detailed local convection coefficient and film cooling effectiveness distributions, and these distributions have been acquired over an extensive test range of clearance heights, clearance flow Reynolds numbers, and film flow rates.

Experimental Apparatus and Procedures

Experimental Apparatus. A schematic arrangement of the test setup is shown in Fig. 3. The test section consists of a plenum chamber with calming section feeding a narrow channel with the bottom, or test, surface of this channel representing a plane turbine blade tip surface. Heated flow can be provided to both the primary and secondary lines through diverter ball valves, which allow sudden application of the flow(s) to the test section. The test surface is liquid crystal

Nomenclature

A = heat transfer area
c_p = specific heat
b = injection hole width
D_h = channel hydraulic diameter
G = mass velocity $= \rho V$
G_m = main flow mass velocity
G_f = film flow mass velocity
H = clearance gap height
h = local convection coefficient in $q = h(T_r - T_w)$
h_{av} = spanwise averaged convection coefficient
k = test surface thermal conductivity
k_f = fluid thermal conductivity
m = mass flow rate

M = blowing parameter $= G_f/G_m$
Nu_D = spanwise-averaged Nusselt number $= h_{av}D_h/k_f$
Pr = Prandtl number $= \mu c_p/k_f$
q = heat flux
Re_m = Reynolds number $= G_m D_h/\mu$
t = time
T_i = initial temperature
T_f = film temperature
T_r = reference temperature
T_w = wall temperature
T_{wg} = wall temperature indicated by green display
T_{wb} = wall temperature indicated by blue display
T_m = mainstream temperature

U = fundamental solution, Eq. (6)
w = length of injection hole in spanwise direction
x = streamwise coordinate, from downstream edge of injection hole
x_o = distance from channel entrance to upstream edge of injection hole
α = surface material thermal diffusivity
η = film cooling effectiveness $= (T_r - T_m)/(T_f - T_m)$
μ = fluid viscosity
ρ = density
τ = time step

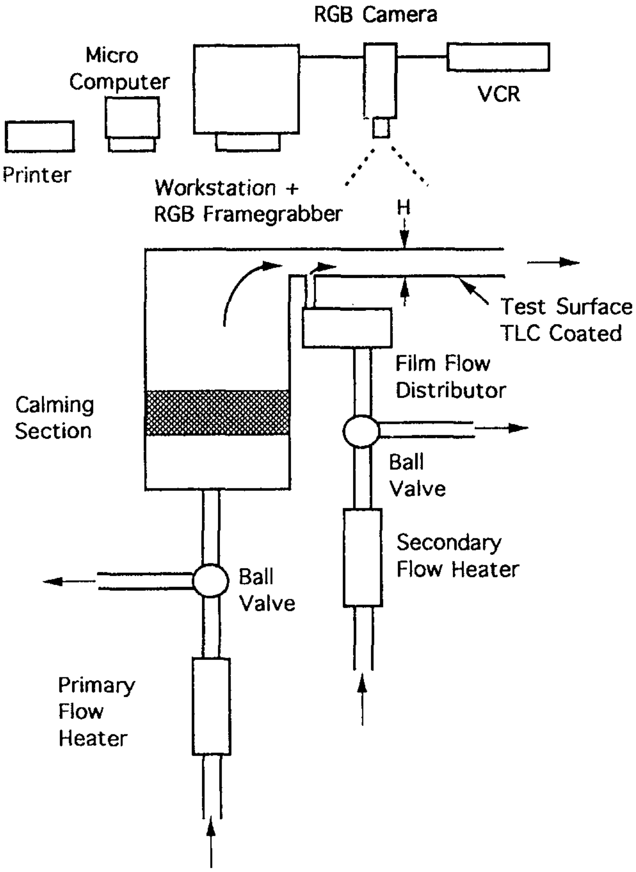

Fig. 3 Apparatus schematic

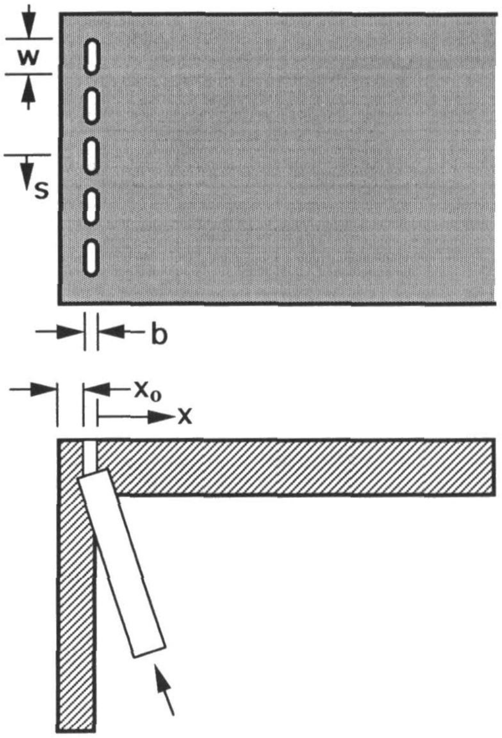

Fig. 4 Test surface details

coated, and the display from this coating is viewed and processed by the vision system components shown in the figure. The test section is constructed entirely of acrylic plastic: transparent on the top of the clearance gap channel to allow viewing of the surface from outside the channel, and black on the test surface itself to provide an optimum visual background for the liquid crystal coating display.

The main flow circuit consists of filtered and dried laboratory compressed air feeding an in-line electric air heater with autotransformer-controlled power input, a three-way ball-type flow diverter valve, and a flow balancing valve (not shown). The diverter valve is used to bypass the heated air from the test section until the heated air temperature reaches a desired value. The diverted air passes through the balancing valve, which is adjusted to equalize the flow resistance between the test section and bypass circuit so that the flow rate is unchanged when the flow is suddenly routed to the test section.

The coating used is a commercially available micro-encapsulated chiral nematic thermochromic liquid crystal (TLC), applied to the test surface using an airbrush. This TLC displays colors in response to temperature changes as a result of lattice reorientation of the crystal. When sprayed as a thin layer, the TLC is essentially clear (showing the black background) and displays color with increasing temperature in sequence of red, green, blue, and back to clear. The nominal temperatures for red, green, and blue displays of the TLC formulation used are nominally 38.4° C, 39.8° C, and 43.5° C, respectively. It is expected that this coating (the order of 10^{-3} cm thick) will have a response time of only a few milliseconds as shown by Ireland and Jones (1987). This time is negligible in comparison with the length of the thermal transients used in the present study.

To minimize experimental uncertainties, the temperatures of the supplied flows are chosen so that the color threshold is not reached until sufficient time has elapsed after the start of flow (usually 15 seconds or more) to insure that the elapsed time can be determined accurately. Also, the flow temperature is chosen so that the elapsed time and corresponding penetration of the temperature pulse into the surface are small enough (usually less than 60 seconds) to insure that the test surface can be treated as semi-infinite as discussed above. Experimental uncertainties have been assessed by the methods of Kline and McClintock (1953) and are estimated to be ±8 percent for convection coefficients, h, and ±10 percent for film cooling effectiveness, η.

The present computer-vision system employs the following three major components: (*i*) SUN SPARC II workstation with ethernet mainframe connection, (*ii*) RasterOps RGB color frame grabber, and (*iii*) Pulnix RGB CCD color video camera. Additional auxiliary components include a video cassette recorder, microcomputer, and color printer. The use of the system to evaluate film cooling performance is described in the following section.

A cross section and plan view of the test surface is shown in Fig. 4. The test surface is 4 in. (10.16 cm) wide in the spanwise direction and 3.125 in. (7.94 cm) long in the streamwise direction across the simulated blade tip from pressure side to suction side. Secondary film flow is supplied from the heater to a manifold, which in turn distributes the film flow equally to a single line of five elongated injection holes, 0.125 in. (0.318 cm) wide (b) in the streamwise direction and 0.375 in. (0.953 cm) long in the spanwise direction. The five holes are equally spaced in the spanwise direction on a pitch of 0.5625 in. (1.429 cm), and the upstream edge of the hole array is located at a distance, x_o, of 0.1 in. (0.254 cm) from the pressure side corner. The channel height, H (clearance gap), is set in the present tests to give values of H/b of both 1.5 and 2.5. For each value of H/b, primary channel flow Reynolds numbers were set at values of 15×10^3, 30×10^3, and 45×10^3, and secondary film flow rates were set to give values of M equal to 0.01, 0.3, 0.5, and 0.9.

Measurement Theory and Procedures. The measurement of the test surface convection characteristics and evaluation of the performance of the film coolant injection follows the methods of Vedula and Metzger (1991) with local heat transfer rate expressed as:

$$q = h(T_r - T_w) \tag{1}$$

where T_w is local test surface temperature and T_r is the reference, or convection driving, temperature that renders h independent of the temperatures. For small temperature differences and constant fluid properties, the appropriate T_r reduces the convection coefficient h to a function of the aerodynamic character of the flowfield alone, and allows local surface convection behavior to be condensed into a constant of proportionality (h) for a given flowfield.

In two-temperature convection situations, with a single convecting fluid at temperature T_m, the reference temperature is simply T_m, and only h must be determined in the experiments. In film cooling with two flows present, the reference temperature is at some generally unknown level that depends on the supply temperatures of the two interacting streams and the degree of mixing that has occurred between them before they arrive at the various locations on the surface. For these situations, both h and T_r must be considered unknowns to be determined by experiment. Note that in general if the surface is locally adiabatic, $T_r = T_w$ (adiabatic wall temperature). Thus traditionally T_r distributions over the surface have been obtained on adiabatic surfaces, but separate testing on a nonadiabatic surface is required to determine the h distribution. With the present test method, both T_r and h are determined with use of the same surface.

In the present experiments, the test surface is suddenly exposed to the flow(s) and the transient response of the test surface as indicated by the TLC color display is observed. The wall material including the test surface is initially at a uniform temperature at all depths, and the initial response near the surface is governed by a semi-infinite formulation of the transient heat conduction where the temperature at the surface is given by the classical solution:

$$\frac{T_w - T_i}{T_r - T_i} = 1 - \exp\left[\frac{h^2 \alpha t}{k^2}\right] \operatorname{erfc}\left[\frac{h\sqrt{\alpha t}}{k}\right] \tag{2}$$

The semi-infinite description is appropriate as long as the transient temperature penetration does not exceed the thickness of the wall material being used, and thus the penetration time becomes the criterion for deciding test wall thickness and subsequent allowable transient test duration. The solution is applied locally at all points on the surface in accordance with the findings of Metzger and Larson (1986) and Vedula et al. (1988), which showed that lateral conduction effects within the test surface are very small, even with strong variations of h over the surface.

For situations where T_r is known, for example tests in the present program conducted without secondary flow present, h can be determined from Eq. (2) by measuring the time, t, required for the surface temperature to reach a prescribed value as indicated by the coating color display. The method is extended to film cooling and other three-temperature situations (Vedula and Metzger, 1991) by noting that both h and T_r can be obtained as the simultaneous solution of two equations of the form of Eq. (2) obtained either from a single transient test with two surface temperature indications at different times during the transient, or from two separate related transient tests. For example, if during the transient a liquid crystal surface coating indicates one surface temperature T_{wg} at time t_g corresponding to the green display and another T_{wb} corresponding to the blue display at t_b, then h and T_r are determined from the simultaneous solution of:

$$\frac{T_{wg} - T_i}{T_r - T_i} = 1 - \exp\left[\frac{h^2 \alpha t_g}{k^2}\right] \operatorname{erfc}\left[\frac{h\sqrt{\alpha t_g}}{k}\right] \tag{3}$$

$$\frac{T_{wb} - T_i}{T_r - T_i} = 1 - \exp\left[\frac{h^2 \alpha t_b}{k^2}\right] \operatorname{erfc}\left[\frac{h\sqrt{\alpha t_b}}{k}\right] \tag{4}$$

In the experiments, for both two- and three-temperature situations, an additional complication is introduced, since true step changes in the applied fluid temperatures are usually not possible and the reference temperatures are thus functions of time. This complication is accounted for by modifying the equations through use of superposition and Duhamel's theorem (Metzger and Larson, 1986). The actual gradual change is obtained by using a series of steps. The solution is represented as:

$$T - T_i = \sum_{i=1}^{N} U(t - \tau_i)\Delta T_r \tag{5}$$

where

$$U(t - \tau_i) = 1 - \exp\left(\frac{h^2}{k^2}\alpha(t - \tau_i)\right) \operatorname{erfc}\left(\frac{h}{k}\sqrt{\alpha(t - \tau_i)}\right) \tag{6}$$

Here, T_r is time-varying and unknown but related to the time variation in T_m and T_f and to the film cooling effectiveness η such that:

$$\Delta T_r = (1 - \eta)\Delta T_m + \eta \Delta T_f \tag{7}$$

So:

$$T - T_i = \sum_{i=1}^{N} U(t - \tau_i)\big((1 - \eta)\Delta T_m + \eta \Delta T_f\big) \tag{8}$$

The two simultaneous equations are solved in the form of Eq. (8) to obtain the two unknowns, η and h.

It is appropriate here to mention that a distinct advantage of the testing scheme described is that all wetted surfaces are thermally active. This is in contrast to many other testing techniques where only the test surface itself is thermally active and adjacent surfaces that may interact through convection with the test surface have unrealistic thermal boundary conditions. Moreover, the thermal boundary conditions on the test and adjacent surfaces are close to spatially isothermal, which is the wall surface condition usually desired in gas turbine engine component design.

Results and Discussion

The immediate results of the test procedures described in the preceding section are two color-coded maps displayed on the workstation screen describing the local distributions of both convection coefficients and film cooling effectiveness over the entire test surface downstream of injection for the various parameter combinations included in the test program (Kim and Metzger, 1992). For the purposes of clarity and comparison, various linear variations and averages can be derived from these maps, and a sampling of those sufficient to describe the character of the film cooling performance are presented in this section.

Typical Local Convection Coefficient and Effectiveness Variations. Figure 5 shows variations in convection coefficients along the spanwise direction over a nominal three-pitch distance centered at the spanwise center of the hole array ($s = 0$) for a typical set of results acquired with $\mathrm{Re}_m = 30{,}000$, $M = 0.3$, and $H/b = 1.5$. Data and results were acquired for this case and for all others over the entire test surface span

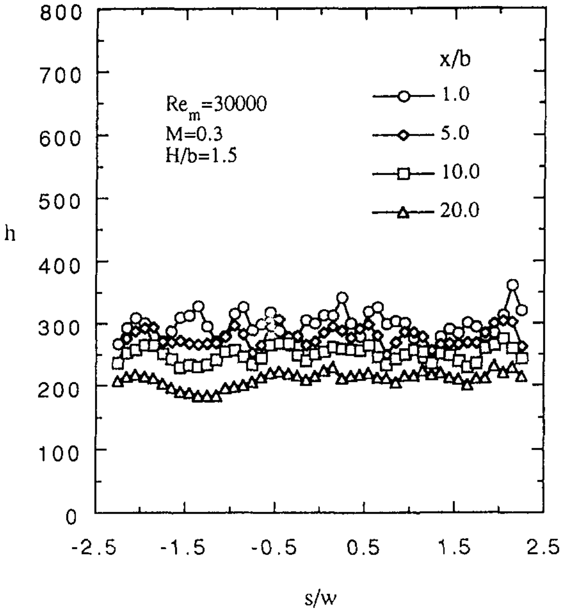

Fig. 5 Typical local convection coefficient distributions

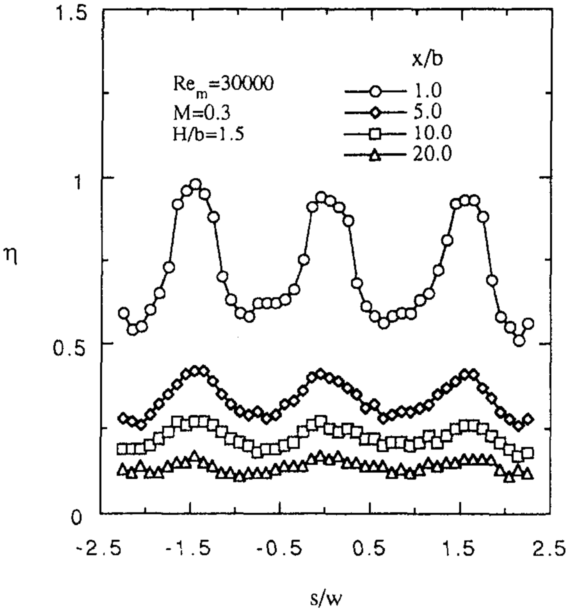

Fig. 6 Typical local effectiveness distributions

but this central spanwise zone is used for presentation purposes to minimize array and test channel end effects. The distributions of Fig. 5 are presented for four streamwise locations downstream of injection presented in terms of number of hole widths, x/b.

It is evident from this Fig. 5 that the overall variation in h across the central test span is small at the injection location and remains so at all stations downstream. The local variation is also quite small: no more than ±10–15 percent. This spanwise variation is typical of the intermediate blowing rates examined in this study for both $H/b = 1.5$ and 2.5. The local spanwise variations for $M = 0.1$ are very small, the order of ±5 percent, while the variations for $M = 0.9$ range upward of 30–40 percent at the streamwise locations closest to the holes. As a general observation, however, it can be said that the spanwise variations in convection coefficient are small, particularly when compared with the corresponding variations in effectiveness. The small spanwise variation is probably attributable to the fact that the coefficients are elevated and dominated by the channel entrance effect, and are only elevated significantly by injection at the highest values of film flow rate.

In contrast to the situation for convection coefficients, Fig. 6 shows the corresponding variation in film cooling effectiveness for the same conditions and locations of Fig. 5. At the streamwise location closest to injection, and aligned with the center of the injection holes, effectiveness values of nearly 1.0 are recorded. Even exactly halfway between the holes only one hole width downstream of injection, the minimum local effectiveness is above 0.5. This lack of any totally uncooled region is of course an objective of the film cooling configuration design and is undoubtedly the result of the close spanwise spacing of the injection holes. Again, the local distributions presented in Fig. 6 are typical. In general, the spanwise variations tend to be highest at the highest blowing rates, with higher spanwise-averaged effectiveness values close to injection, monotonically decreasing in the downstream direction. In all cases, the close spanwise spacing of the holes prevents any zero-effectiveness regions between the holes, with spanwise variations in local η at $x/b = 1.0$ varying from ±10–50 percent and decreasing with increasing x/b.

Another way to visualize the spanwise variation in local effectiveness is with linear cuts through the surface effectiveness map aligned in the downstream direction and positioned at various positions on the span. Figure 7 is such a presentation, again for a typical, but different, set of conditions: $Re_m = 45{,}000$, $M = 0.5$, and $H/b = 1.5$. Here there cuts at three positions on the span are presented: one aligned with the center of the holes, one aligned at the edge of the holes, and the third aligned halfway between the holes. The values shown are averages of results from similar positions within the center-span region defined in the discussion of Figs. 5 and 6. The behavior shown is again typical, with spanwise differences in effectiveness for this set of conditions varying somewhat with downstream distance, but in the range of ±20 percent.

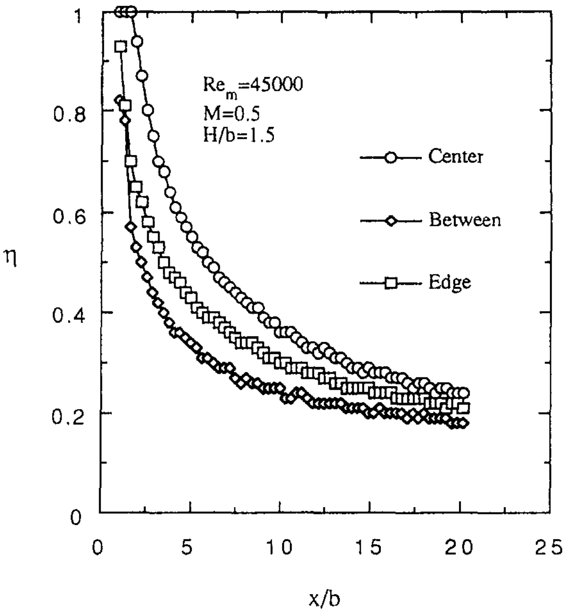

Fig. 7 Streamwise local effectiveness variations, $Re_m = 45{,}000$, $M = 0.5$, $H/b = 1.5$

The spanwise variations in effectiveness are important in practice since they play a major role in establishing the magnitude of local metal temperature gradients on the cooled surface, and in turn the size of the thermal stresses. In general, the present set of results show that the spanwise

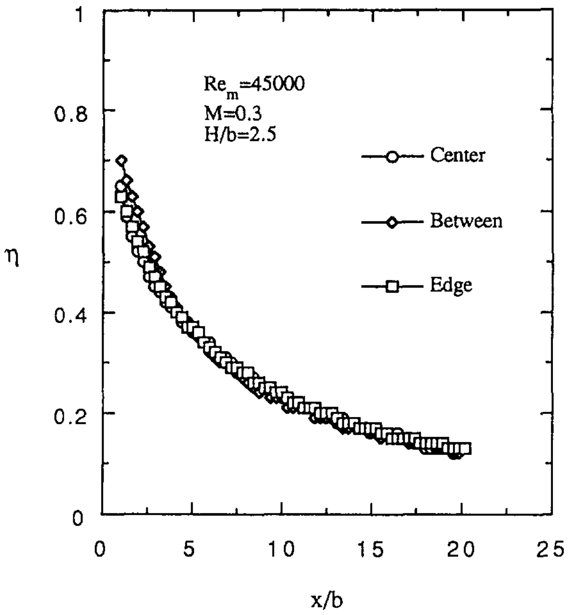

Fig. 8 Streamwise local effectiveness variations, Re_m = 45,000, M = 0.3, H/b = 2.5

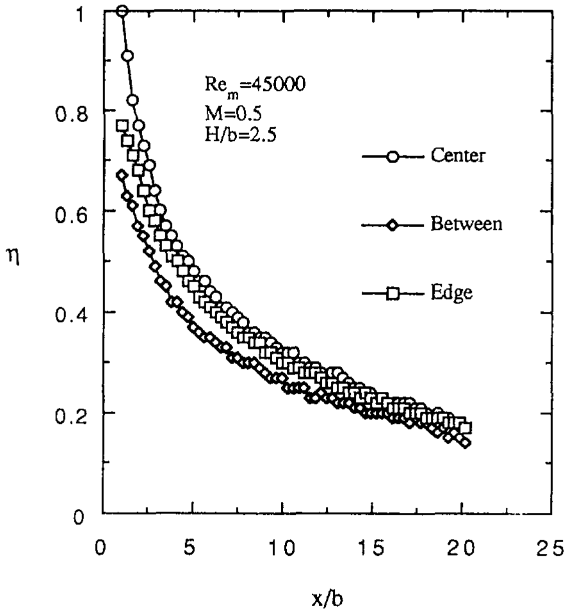

Fig. 10 Streamwise local effectiveness variations, Re_m = 45,000, M = 0.5, H/b = 2.5

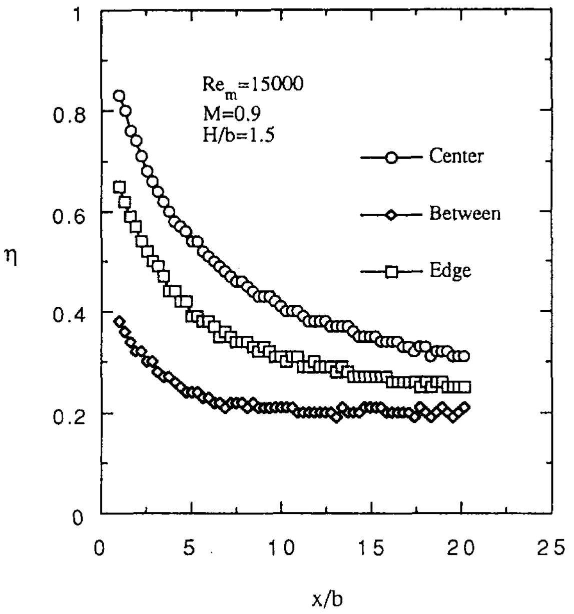

Fig. 9 Streamwise local effectiveness variations, Re_m = 15,000, M = 0.9, H/b = 1.5

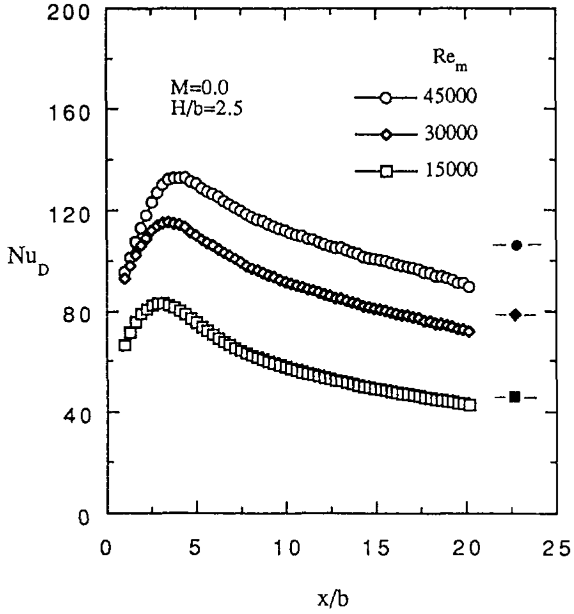

Fig. 11 No-injection spanwise-averaged Nu_D, H/b = 2.5

differences in effectiveness are very small for $M = 0.1$ and 0.3, but increase with increasing values of M to a maximum at $M = 0.9$. Also for all other parameters held constant, the spanwise differences are greater for $H/b = 1.5$ than for $H/b = 2.5$. Figures 8–10 illustrate and quantify these trends.

Spanwise-Averaged Distributions

Baseline Results, $M = 0$. Figure 11 shows results conducted in the absence of film injection for the larger clearance gap, $H/b = 2.5$, for all three values of Reynolds numbers used throughout the study. The convection coefficients, presented here in Nusselt number form, display a classical sharp-edge channel entrance distribution with low values immediately downstream of the entrance (pressure side) corner attributable to flow separation. The values then rise abruptly in the streamwise direction, peaking at values of x/b that monotonically increase from 2.5 to 3.5 as Reynolds numbers increase, as expected and attributable to reattachment on the test surface. As flow develops streamwise, Nusselt numbers decrease, and are generally in agreement with expected fully established values near the downstream end of the channel. Fully established Colburn equation predictions are shown as solid symbols near the right edge of the figure, and show that the predictions systematically overpredict the measured downstream values as Reynolds number increases, although the overall agreement is good and establishes confidence in the experimental procedures used.

Figure 12 shows corresponding zero film injection results for the smaller clearance gap configuration, $H/b = 1.5$, and these values differ significantly both in character and in magnitude from the wider gap results. The values are generally lower than those in the previous figure, and the peak Nu behavior evident in that figure is absent, suggesting that the greater confinement associated with the narrow channel de-

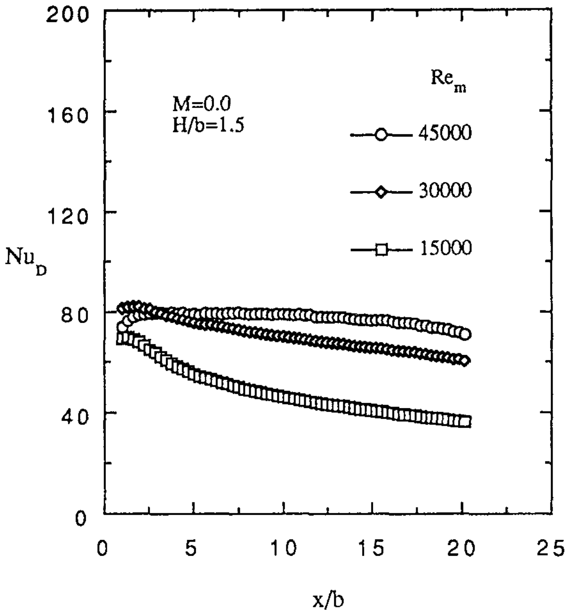

Fig. 12 No-injection spanwise-averaged Nu_D, $H/b = 1.5$

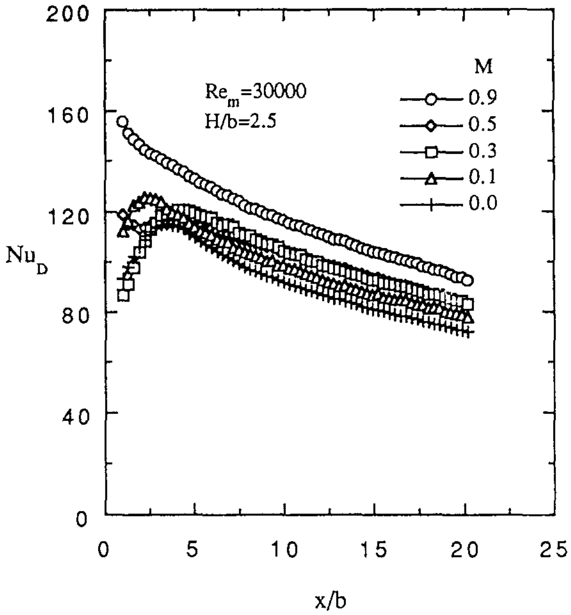

Fig. 14 Effect of M on spanwise-averaged Nusselt numbers, $H/b = 2.5$, $Re_m = 30{,}000$

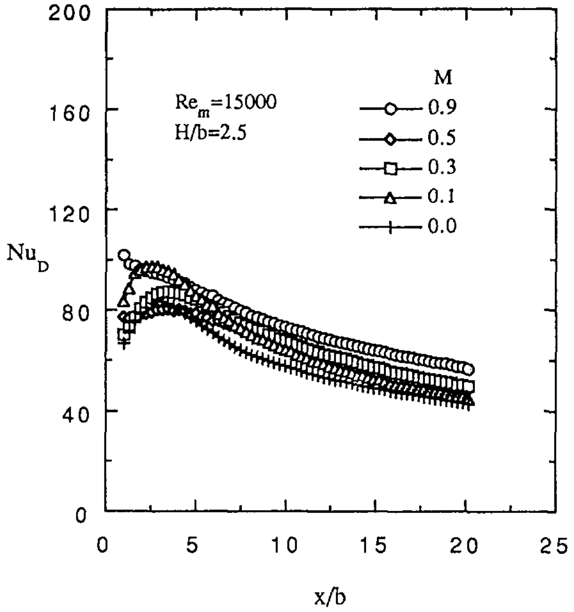

Fig. 13 Effect of M on spanwise-averaged Nusselt numbers, $H/b = 2.5$, $Re_m = 15{,}000$

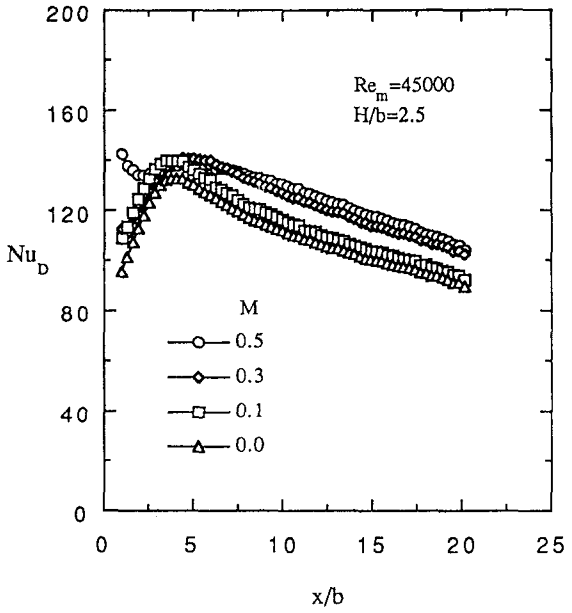

Fig. 15 Effect of M on spanwise-averaged Nusselt numbers, $H/b = 2.5$, $Re_m = 45{,}000$

creases the size of the separated zone to the extent that it is contained within the narrow region upstream of $x = 0$. This may also place reattachment within the injection holes, which are present on the test surface even though zero film flow is injected. Also, it should be noted that acceleration levels associated with the contracting of the flow into the narrow clearance gap are high (Mayle and Metzger, 1982), and are higher as Reynolds number increases at constant gap spacing and higher for the narrow gap than for the wide gap. The degree of suppression of the Nu_D distributions below expected fully established values appears to increase as acceleration increases, suggesting that relaminarization may be a factor, but this speculation will need to be examined in future work. Also left for future work is the issue of unsteadiness and embedded vorticity within the ingested flow, as can exist in practice. For the purposes of the present work, Figs. 11 and 12 represent the no-injection Nu behavior that will be used as baselines to compare with cases with injection present.

Effect of Injection Rate on Nu_D. Figures 13–15 and 16–18 display the measured effects of sequentially increasing coolant injection rates on the spanwise-averaged Nusselt numbers, with the $M = 0$ baseline values represented on each figure for reference. The important effect for all parameter combinations is the general tendency for convection coefficients to increase with increasing injection rate over virtually all of the protected surface. The increases for the maximum values of M used in the study are in the range of 30–50 percent, and this is a significant factor for use of these results in assessing the probable effect of film cooling on blade tip thermal loading in practice. This injection-induced elevation in convection coefficients means that if the film injection temperature is not low enough, relative to the clearance leakage flow

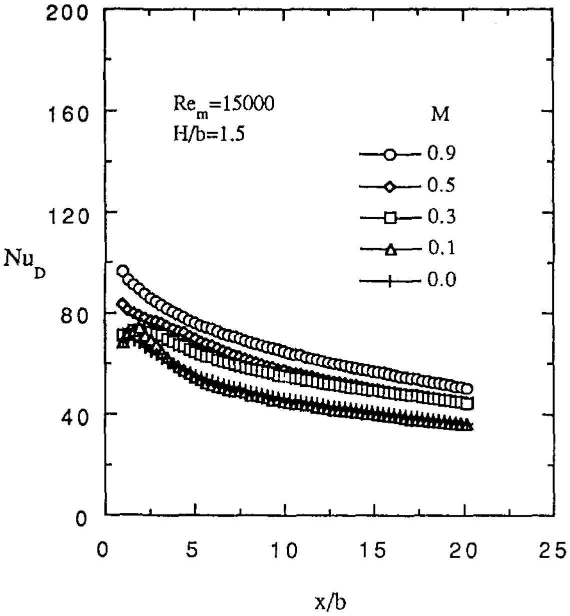

Fig. 16 Effect of M on spanwise-averaged Nusselt numbers, $H/b = 1.5$, $Re_m = 15{,}000$

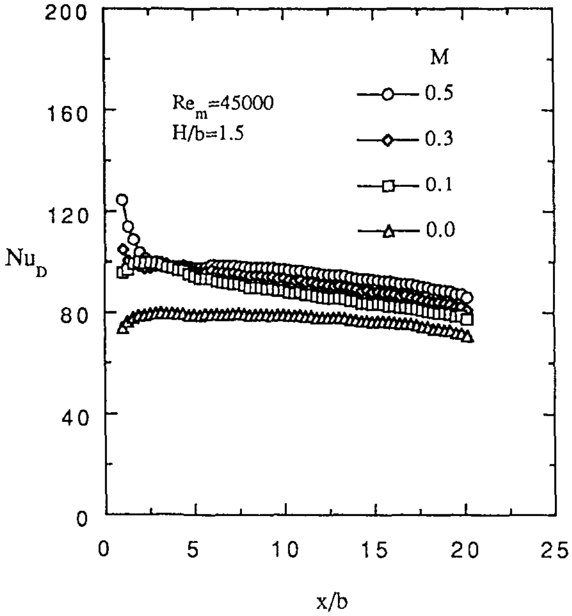

Fig. 18 Effect of M on spanwise-averaged Nusselt numbers, $H/b = 1.5$, $Re_m = 45{,}000$

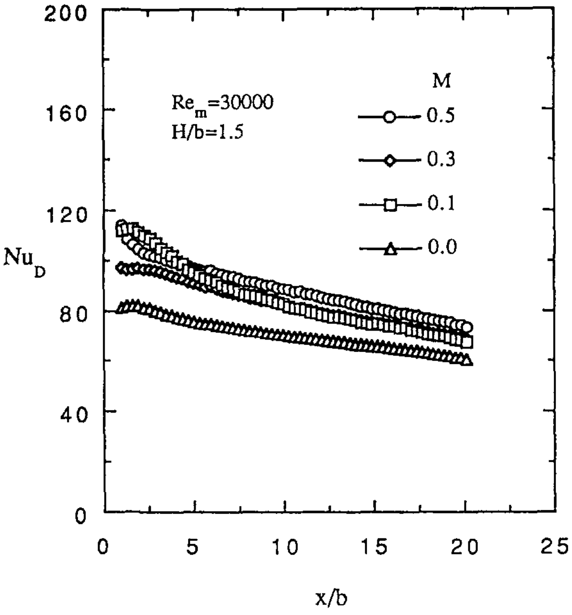

Fig. 17 Effect of M on spanwise-averaged Nusselt numbers, $H/b = 1.5$, $Re_m = 30{,}000$

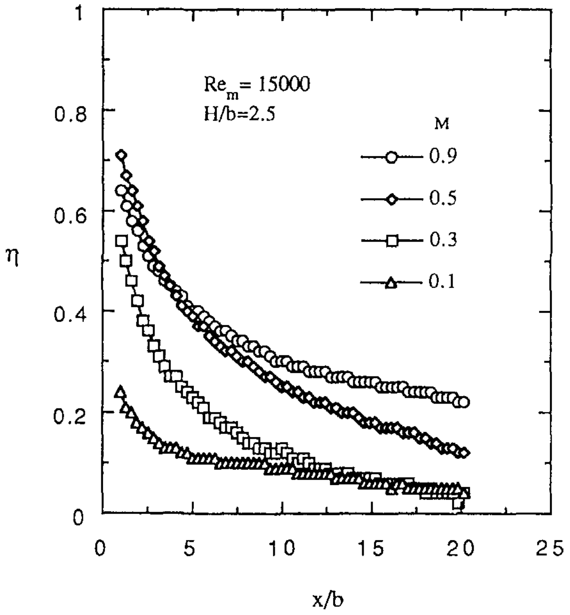

Fig. 19 Effect of M on spanwise-averaged effectiveness, $H/b = 2.5$, $Re_m = 15{,}000$

temperature, injection can actually increase the thermal loading on the tip, opposite to the desired effect.

The effect of injection rate on Nusselt number near the pressure side corner is more complex than the overall simple effect discussed above, but does appear reasonably consistent across the set of results for each channel height. In Figs. 13–15 for $H/b = 2.5$, the lower injection rates apparently allow the distribution of initial low Nu_D values followed by a peak to be retained at elevated values over $M = 0$, but the elevation in this zone near the pressure corner is not always monotonic with M. For the higher injection rates, $M = 0.5$ and 0.9, this pattern is broken and the heat transfer coefficients in the separated flow zone are elevated. In Figs. 16–18 for $H/b = 1.5$, the higher M values, particularly for the highest velocity flows of Fig. 18, appear to allow the local coefficient values to emerge from their suppressed levels right at injection, but they return to their suppressed levels almost immediately. In this regard it should be noted that at $Re_m = 45{,}000$ at $M = 0.5$ in Fig. 18, Nu_D is still below even the fully developed Colburn values over almost all the test surface.

Effect of Injection Rate on Effectiveness. Figures 19–21 and 22–24 display the measured effects of sequentially increasing coolant injection rates on spanwise-averaged effectiveness values for $H/b = 2.5$ and 1.5, respectively. These display essentially expected trends, but establish both the maximum values at injection and the decay rates for this particular family of configurations. Spanwise-averaged effectiveness increases essentially monotonically with increasing blowing rate up to $M = 0.5$. At all cases where the higher rate $M = 0.9$ was included in the test sequence, this rate resulted in slightly lower effectiveness near the injection site, but higher effectiveness downstream. This behavior is proba-

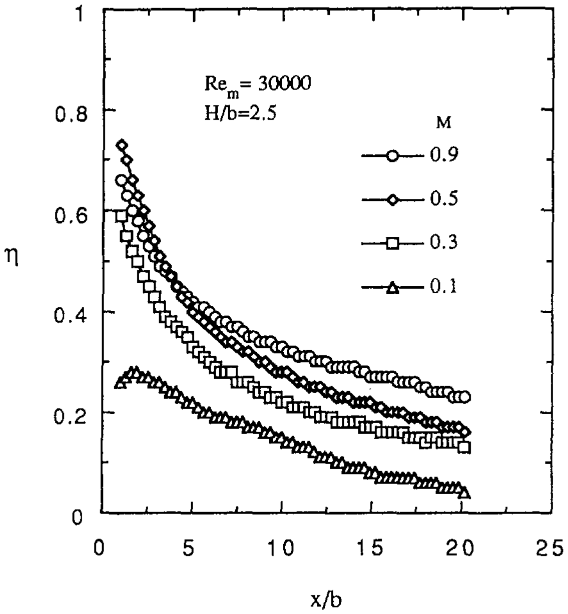

Fig. 20 Effect of *M* on spanwise-averaged effectiveness, *H/b* = 2.5, Re_m = 30,000

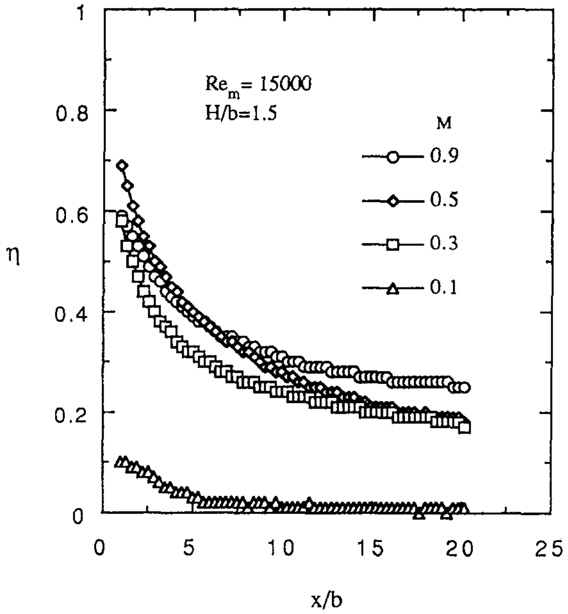

Fig. 22 Effect of *M* on spanwise-averaged effectiveness, *H/b* = 1.5, Re_m = 15,000

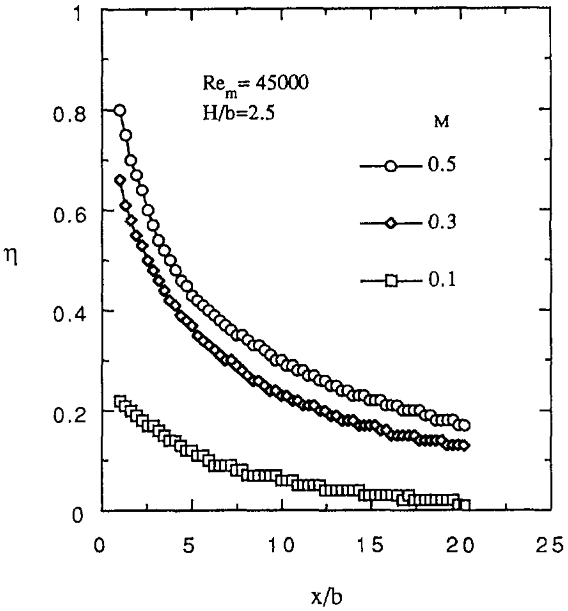

Fig. 21 Effect of *M* on spanwise-averaged effectiveness, *H/b* = 2.5, Re_m = 45,000

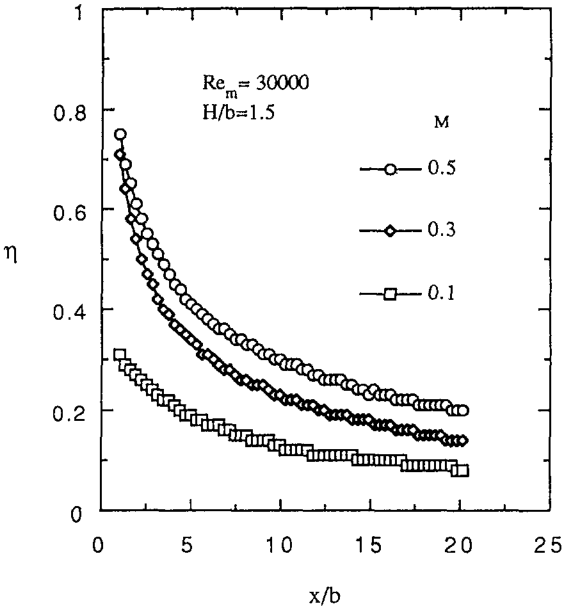

Fig. 23 Effect of *M* on spanwise-averaged effectiveness, *H/b* = 1.5, Re_m = 30,000

bly explained in terms of more separation of coolant jet from the surface at small x/b, together with enhanced entrainment of the primary stream toward the surface at the edges of each film jet. The film subsequently reattaches to the surface, and the greater amount of injected coolant provides better downstream coverage. An anomalous set of results is noted in Fig. 22 for $M = 0.1$, where effectiveness is unexpectedly low upstream, and drops off to essentially zero almost immediately. This could again be the result of some interaction between the injection site and initial entrance separation and reattachment, and provides a further reason for future more detailed investigation of the behavior right at the pressure side corner.

Effect of Reynolds Number on Effectiveness. Finally, Fig. 25 shows a set of results displaying the relative independence of the spanwise effectiveness values from changes in Reynolds number. This is behavior typical of the present results set, although close examination of Figs. 19–24 will show that the spread of the results with Re_m is sometimes greater than shown in Fig. 25.

Closure

The results of the study indicate that film injection near the pressure-side corner on plane turbine blade tips can provide significant protection from convection heat transfer to the tip from the hot clearance gap leakage flow. The results, for a closely spaced single row of elongated injection sites, indicates that injection provides nearly continuous spanwise film coverage, and for a high enough blowing rate, effectiveness should remain significantly above zero over the

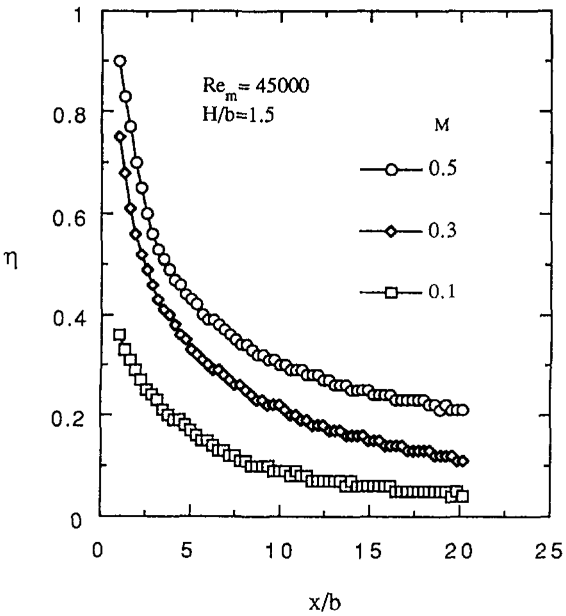

Fig. 24 Effect of M on spanwise-averaged effectiveness, H/b = 1.5, Re_m = 45,000

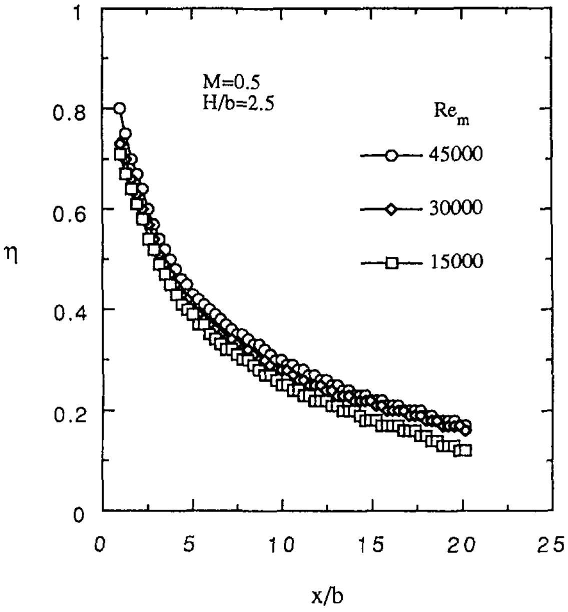

Fig. 25 Typical effect of Re_m on spanwise-averaged effectiveness

entire distance to the suction-side corner. Injection generally increases the convection coefficients in a straightforward manner over most of the covered surface. The results for the smallest clearance spacing investigated indicate some unexplained trends and complexities that warrant further study, but the overall results are in reasonable accord with expectations, and should aid designers in predicting the film cooling performance on plane turbine blade tips.

Acknowledgments

This work was supported by funds provided by the U.S. Air Force Wright Laboratory, Aeropropulsion and Power Directorate, through United Technologies Corporation, Pratt and Whitney Government Engine Business. The technical monitors for this effort are Matt Meininger and Jim Downs.

References

Allen, H. W., and Kofskey, M. G., 1955, "Visualization Study of Secondary Flows in Turbine Rotor Tip Regions," NACA TN 3519.

Bindon, J. P., 1986, "Visualization of Axial Turbine Tip Clearance Using a Linear Cascade," Report No. CUED/A-Turbo TR122, Whittle Laboratory, Cambridge University, United Kingdom.

Booth, T. C., Dodge, P. R., and Hepworth, H. K., 1982, "Rotor-Tip Leakage: Part I—Basic Methodology," ASME *Journal of Engineering for Power*, Vol. 104, pp. 154–161.

Chyu, M. K., Moon, H. K., and Metzger, D. E., 1986, "Heat Transfer in the Tip Region of a Rotor Blade Simulator," *Turbine Engine Hot Section Technology* 1986, NASA CP 2444, 177-92.

Chyu, M. K., Metzger, D. E., and Hwan, C. L., 1987, "Heat Transfer in Shrouded Rectangular Cavities," *J. Thermophysics and Heat Transfer*, Vol. 1, pp. 247–252.

Hennecke, D. K., 1984, "Heat Transfer Problems in Aero-engines," *Heat and Mass Transfer in Rotating Machinery*, Hemisphere Publishing Company, Washington, DC, pp. 353–379.

Ireland, P. T., and Jones, T. V., 1987, "The Response Time of a Surface Thermometer Employing Encapsulated Thermochromic Liquid Crystals," *Journal of Physics E*, Vol. 20, pp. 1195–1199.

Kim, Y. W., and Metzger, D. E., 1992, "Advanced Turbine Tip Film Cooling Studies—Phase II Final Report, Part 1, Normal Tip Injection Results," Technical Report No. 92055, Arizona State University.

Kline, S. J., and McKlintock, F. A., 1953, "Describing Uncertainties in Single Sample Experiments," *Mechanical Engineering*, Vol. 75, Jan., pp. 3–8.

Mayle, R. E., and Metzger, D. E., 1982, "Heat Transfer at the Tip of an Unshrouded Turbine Blade," *Proceedings, Seventh International Heat Transfer Conference*, Vol. 3, pp. 87–92.

Metzger, D. E., and Larson, D. E., 1986, "Use of Melting Point Surface Coatings for Local Convection Heat Transfer Measurements in Rectangular Channels With 90-deg Turns," ASME *Journal of Heat Transfer*, Vol. 108, pp. 48–54.

Metzger, D. E., and Bunker, R. S., 1989, "Cavity Heat Transfer on a Transverse Grooved Wall in a Narrow Flow Channel," ASME *Journal of Heat Transfer*, Vol. 111, pp. 73–79.

Metzger, D. E., and Rued, K., 1989, "The Influence of Turbine Clearance Gap Leakage on Flowpath Velocities and Heat Transfer, Part I: Sink Flow Effects on Blade Pressure Sides," ASME JOURNAL OF TURBOMACHINERY, Vol. 111, pp. 284–292.

Moore, J., and Tilton, J. S., 1988, "Tip Leakage Flow in a Linear Turbine Cascade,' ASME JOURNAL OF TURBOMACHINERY, Vol. 110, pp. 18–26.

Moore, J., Moore, J. G., Henry, G. S., and Chaudhry, U., 1989, "Flow and Heat Transfer in Turbine Tip Gaps," ASME JOURNAL OF TURBOMACHINERY, Vol. 111, pp. 301–309.

Rued, K., and Metzger, D. E., 1989, "The Influence of Turbine Clearance Gap Leakage on Flowpath Velocities and Heat Transfer, Part II: Source Flow Effects on Blade Suction Sides," ASME JOURNAL OF TURBOMACHINERY, Vol. 111, pp. 293–300.

Vedula, R. J., Metzger, D. E., and Bickford, W. B., 1988, "Effects of Lateral and Anisotropic Conduction on the Determination of Local Convection Heat Transfer Characteristics With Transient Tests and Surface Coatings," *Collected Papers in Heat Transfer* 1988, American Society of Mechanical Engineers, Heat Transfer Div., Vol. 104, pp. 21–28.

Vedula, R. J., and Metzger, D. E., 1991, "A Method for the Simultaneous Determination of Local Effectiveness and Heat Transfer Distributions in Three-Temperature Convection Situations," ASME Paper No. 91-GT-345.

J. D. Bryce

M. A. Cherrett

P. A. Lyes

Defence Research Agency,
Pyestock, Farnborough,
Hampshire, United Kingdom

Three-Dimensional Flow in a Highly Loaded Single-Stage Transonic Fan

Tests have been conducted at DRA Pyestock on a single-stage transonic fan with a very high level of aerodynamic loading at the hub. The objective of the tests was to survey the flow field in detail, with emphasis on studying the three-dimensional viscous aspects of the flow. The test module was highly instrumented. Detailed flow traversing was provided at rotor and stator exit, and replaceable stator cassettes allowed various types of on-blade instrumentation to be fitted. The test rig and instrumentation are described and detailed flow measurements, taken at peak efficiency operation on the design speed characteristic, are presented. These measurements, which are supplemented by flow visualization results, indicate the presence of a severe endwall corner stall in the stator hub flow field. The fan was modeled using the DRA S1-S2 method and these results are also discussed.

Introduction

The performance and surge margin of highly loaded, high-speed compressors and fans can be seriously eroded by the complex, unsteady three-dimensional viscous flows in the blade endwall region and wake regions. Detailed investigation and improved understanding of these complex flows are required before better numerical models can be developed and validated. This will, in turn, lead to improved axial compressor aerodynamic design accompanied by reductions in engine weight and cost.

The problem is particularly acute in the highly loaded military style transonic fan where the demand for high pressure rise per stage leads to high levels of Mach number with strong shocks and severe diffusion requirements. This has particular implications for the first stator hub region where the high deflection, exacerbated by near-sonic inlet Mach number, can lead to the condition known as hub stalling. Here the flow separates in the corner regions between the stator suction surface and endwall. This phenomenon has been investigated in low-speed compressors by Joslyn and Dring (1985), Dong et al. (1987), and Schultz and Gallus (1988). However, because the task is much more difficult, the endwall flows have not been measured with sufficient detail in high-speed (engine relevant) compressors and fans.

The Aerodynamics and Propulsion Department of the Defence Research Agency (DRA Pyestock) is currently engaged in a research program to investigate these problems in a very highly loaded single-stage transonic fan known as C148. 350 hours of testing have been completed on the first build, which was extensively instrumented with steady-state and high-frequency response instrumentation. This paper introduces the extensive test program and analysis and describes the rig and instrumentation. Results from extensive traversing with three-dimensional pneumatic probes are also presented. The measurements indicate that severe hub stalling occurs in the stator. This is confirmed by oil flow visualization. In addition, the results of preliminary modeling of the fan, using the DRA *S*1-*S*2 method, are presented and discussed in reference to the measured flowfield.

C148 Single-Stage Transonic Fan

Design Concept. C148 employed the first stage of an existing Rolls-Royce multistage transonic fan. Table 1 lists the overall design point parameters along with some relevant dimensions. Figure 1 illustrates the radial variation of quantities defining the aerodynamic duty of the stage. It is clear from the above that, although the levels of rotor tip speed, rotor

Table 1 C148 parameters

Number of rotor blades	25
Rotor pitch/ chord ratio (mid span)	0.65
Number of stator blades	52
Stator pitch/ chord ratio (mid span)	0.55
Corrected mass flow (kg/s)	53.3
Stage pressure ratio	1.807
Stage temperature rise ratio ($\Delta T/T$)	0.214
Stage hub loading ($\Delta H/U^2$)	1.21
Rotor tip speed (m/s)	442
Rotor inlet tip diameter (mm)	633
Stage inlet hub/tip ratio	0.39
Stage exit hub/tip ratio	0.62

Contributed by the International Gas Turbine Institute and presented at the 38th International Gas Turbine and Aeroengine Congress and Exposition, Cincinnati, Ohio, May 24-27, 1993. Manuscript received at ASME Headquarters February 12, 1993. Paper No. 93-GT-3. Associate Technical Editor: H. Lukas.

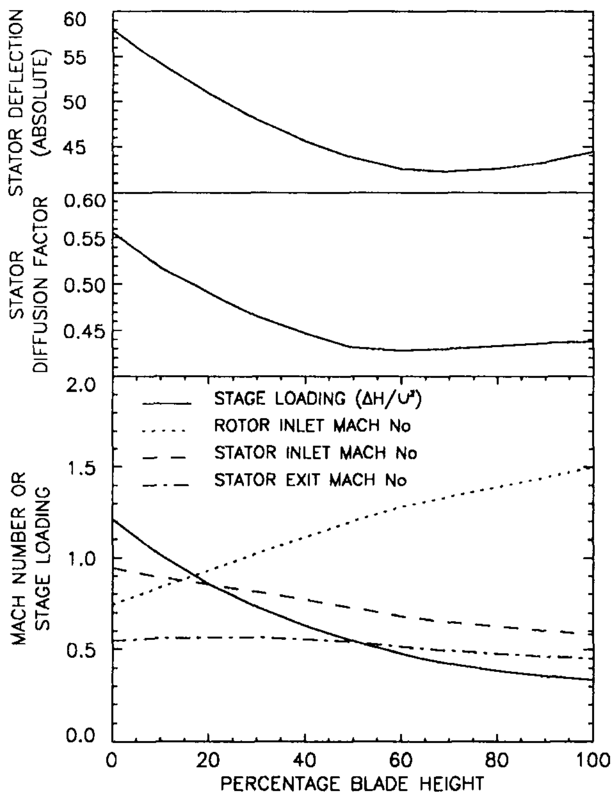

Fig. 1 C148 aerodynamic design parameters

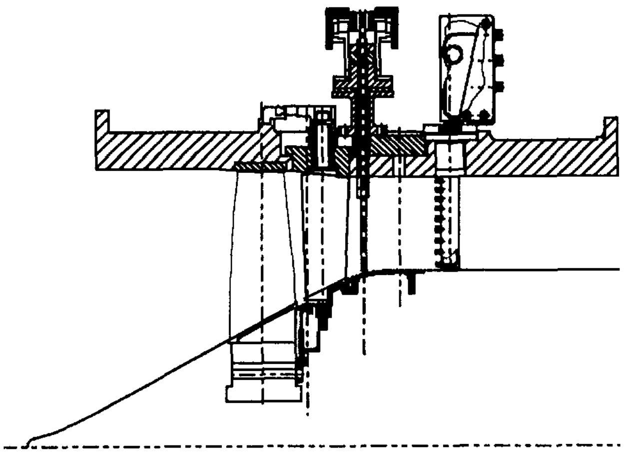

Fig. 2 The C148 single-stage transonic fan

Mach number, and mass flow per unit area are well within current engine experience, the aerodynamic stage loading at the hub is very high and well in advance of present levels. This was a deliberate design intent, setting a very challenging aerodynamic task exemplified by the near-sonic Mach number at inlet to the stator hub and the high diffusion factor (>0.55) and high deflection (>57 deg turning, relative to axial at stator exit) required.

The aerodynamic design of the fan was conducted some 10 years ago at a time when the computational codes were less well developed than today. Therefore, the design may lack the refinement that modern computational methods would bring to bear on optimizing blade profiles. Nevertheless, it employed cubic and parabolic aerofoil sections that more recent *S*1–*S*2 analysis indicate as being acceptable and on a par with the best of transonic fans designed at that time. Therefore, on account of its challenging aerodynamics, the stage was considered a very appropriate vehicle for investigation of three-dimensional viscous endwall flows and unsteady flow effects.

Fan Test Module. The test module (see Fig. 2) has no inlet guide vanes and has a 0.63-m-dia rotor at inlet. The rotor has no snubber while the stator has an inner shroud ring. The running tip clearance of the rotor was less than 1 percent. The strongly rising hub line and small rotor–stator gap are notable features. The stator angle is adjustable but was fixed at the design value during the work described here. The rig is highly instrumented and has the flexibility of allowing easy insertion and removal of single and twin stator cassettes. These permit various types of on-blade instrumentation to be used. The rig also has the provision for detailed flow traversing. Radial traversing can be conducted at rotor exit employing a stator (with a cut-back leading edge) in one of the single stator cassette positions. Full area traverses may be conducted at stator exit through circumferential traverse slots at 36 and 118 percent stator axial chord downstream of the trailing edge.

Experimental Procedure

Test Installation and Instrumentation. The C148 fan was installed and tested in the DRA Pyestock compressor test facility. Ambient air was drawn through a silencer and contraction duct before entering a constant-diameter calibrated airmeter. The air was then passed to the fan, which was driven by an 11 MW steam turbine via a 1.3 ratio step-up gearbox. Overall pressure and temperature rise were measured by six Pitot rakes and six calibrated Keil thermocouple rakes positioned approximately two axial chords downstream of the stator trailing edge. Alternate pressure and temperature rakes were equispaced about the annulus with each rake having nine spanwise measuring points. Clearly, the measurement of delivery pressure and temperature at only six circumferential stations provides a source of uncertainty when quantifying the fan performance. This is a particular concern in C148 where, as will be shown in this paper, the flow is highly distorted at stator exit and the losses are not fully mixed out upstream of the rake measurement plane. However, both sets of rakes were indexed across one stator pitch.

Compressor rotational speed was measured, along with drive shaft torque, by a phase-shift torquemeter. The air left the fan in a single stream and discharged, via an annular duct, into an exhaust collector. It then passed via a hydraulically operated (butterfly) throttle valve through a silencer to atmosphere.

Various instrumented stators were inserted during the test program. Single stators each with 10 leading edge Pitots or Keil thermocouples were used to measure the absolute total pressure and total temperature at exit from the rotor.

Traverse Probes and Calibration. Several probes were employed to measure the three-dimensional flows in C148. Some of these have been reported by Cherrett et al. (1992). The current paper concentrates on measurements taken with two probes, a four-hole wedge design similar to that described by Heneka (1983) and Bubeck and Wachter (1987) and a pyramid probe similar to that reported by Shepherd (1981). Both probes, which are shown in Fig. 3, have been traversed at stator exit with their sensing heads at the 36 percent (stator chord) downstream plane. The four-hole wedge probe has a triangular cross section with an included angle of 25 deg and a true chord of 5.6 mm. This cross section is maintained for a height of 25 mm before blending into a 6.4-mm-dia support stem. This arrangement was chosen in an attempt to minimize the aerodynamic interference of the stem. The bottom face of the sensing head is inclined downward by 20 deg to the horizontal and provided with a static pressure tapping to facilitate pitch angle measurement. All of the probe static tappings are 0.5-mm-dia holes drilled perpendicular to the probe surfaces.

The pyramid probe has a sensing head shaped like the frus-

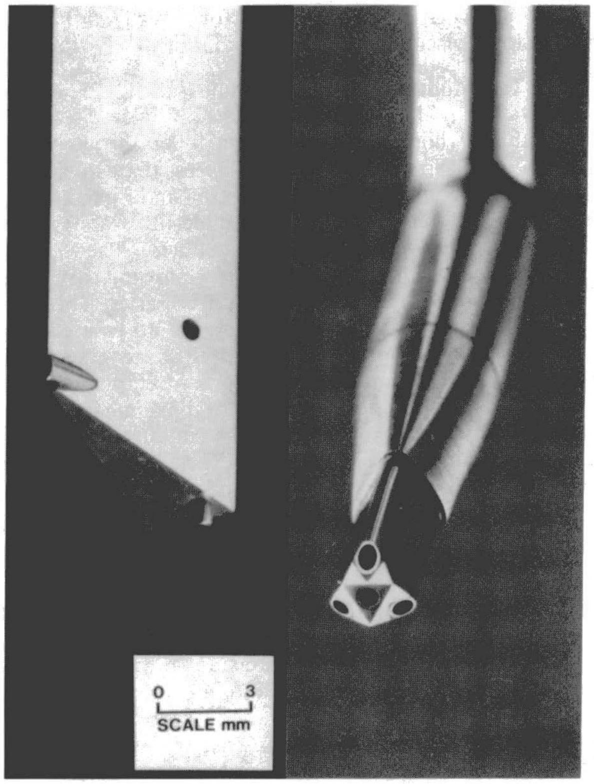

Fig. 3 The pyramid and four-hole wedge probes

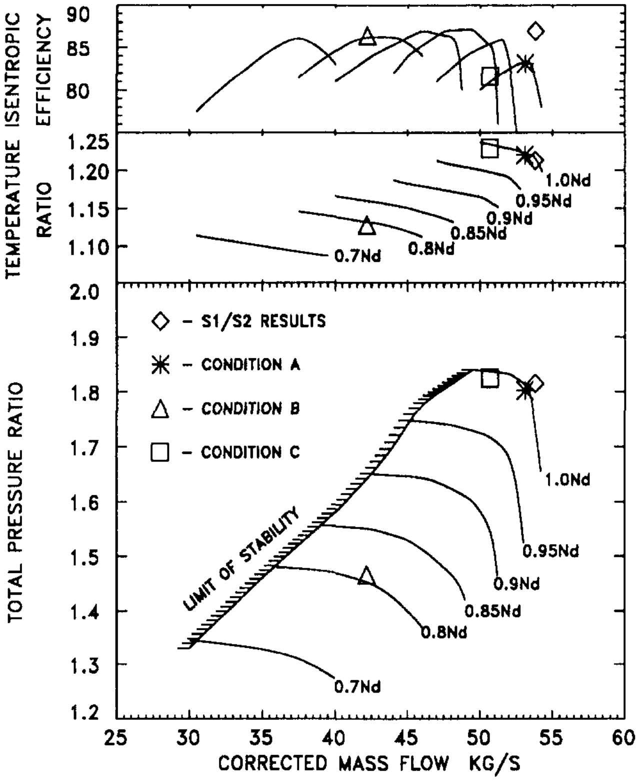

Fig. 4 The C148 transonic fan performance characteristic

tum of a three-sided pyramid, with faces at 45 deg. The three static pressure holes are positioned on a pitch circle diameter of 3.0 mm around the central axes of the probe. All of the static tappings were forward facing rather than being perpendicular to their respective pyramid faces. The sensing head was mounted on a sting 41 mm upstream of the probe support stem to reduce probe blockage. Two versions were manufactured: one with a horizontal sting for surveying the outer span region and one inclined downward by 15 deg to match stator hub annulus geometry. Only measurements taken with the inclined probe are presented in this paper.

All of the three-dimensional probes used on C148 were calibrated for the effects of Mach number, yaw angle, and pitch angle in the Transonic Cascade Test Facility at the Whittle Laboratory, Cambridge University (Gostelow and Watson, 1976). The test section was fitted with a two-dimensional transonic nozzle with perforated upper and lower walls similar to that developed by Baines (1983). The probes were calibrated at a Reynolds number of 55×10^3 (using the probe sensing head diameter of 3.5 mm as the characteristic length). This corresponded to the Reynolds number at C148 stator exit. The calibrations covered the Mach number range between 0.2 and 0.9 and yaw and pitch angle ranges of ±35 deg (as described by Cherrett et al.).

When used in C148, the probes were traversed at a fixed yaw angle setting. No attempt to null the probes into the flow was made, although the fixed traversing angle was chosen to be close to that expected at the corresponding operating point. The algorithm used by Dominy and Hodson (1992) was employed to derive stagnation pressure, static pressure, yaw angle, and pitch angle from the four probe pressures.

Measurement Accuracy. At rig inlet, pressure was measured to better than 0.1 percent, temperature to better than ±0.5 K, and mass flow to better than ±0.5 percent. However, accurate pressure and temperature measurement in the highly unsteady and distorted flow downstream of high-speed transonic fans is problematic. A complex array of factors gives rise to measurement uncertainty, which, in practice, is difficult to quantify. While a rigorous audit of measurement uncertainty has not been carried out for the C148, confidence in downstream pressure measurements can be gained from comparing data taken with a wide range of probes coupled to different measurement systems. Downstream of the stator, area-averaged total pressure measurements at midheight were found to agree to better than ±0.8 percent of the delivery pressure (Cherrett et al.). Similarly, angle measurement uncertainty was found to be better than ±0.5 deg. A similar rationale cannot be used to quantify temperature measurement uncertainty due to the limited number of measurement sources available. However, as individually calibrated thermocouples were used in association with empirically derived recovery factor corrections, the C148 temperature measurements are thought to be representative of current recommended procedure.

Results

Overall Performance. The overall performance characteristics of C148 are shown in Fig. 4 for nondimensional speeds between 70 and 100 percent of design. A wide flow range was achieved, particularly at up to 95 percent speed and the fan stable operating limit was well defined at all speeds. The envelope of maximum isentropic efficiencies fell sharply above 95 percent speed. (The efficiencies shown in Fig. 4 are based on temperature rise measurements.) The detailed flowfield measurements presented in this paper were taken at the peak efficiency operating point (A) and near-surge point (C) on the design speed characteristic and at the peak efficiency point (B) on the 80 percent speed characteristic. These are shown in Fig. 4.

Fan performance at the design speed, peak efficiency, operating point was modeled using the DRA $S1$–$S2$ system (Calvert, 1991). This system couples an essentially inviscid throughflow ($S2$) calculation to an inviscid–viscous blade-to-blade ($S1$) calculation. Iteration between the $S1$ and $S2$ calculations produces an axisymmetric quasi-three-dimensional

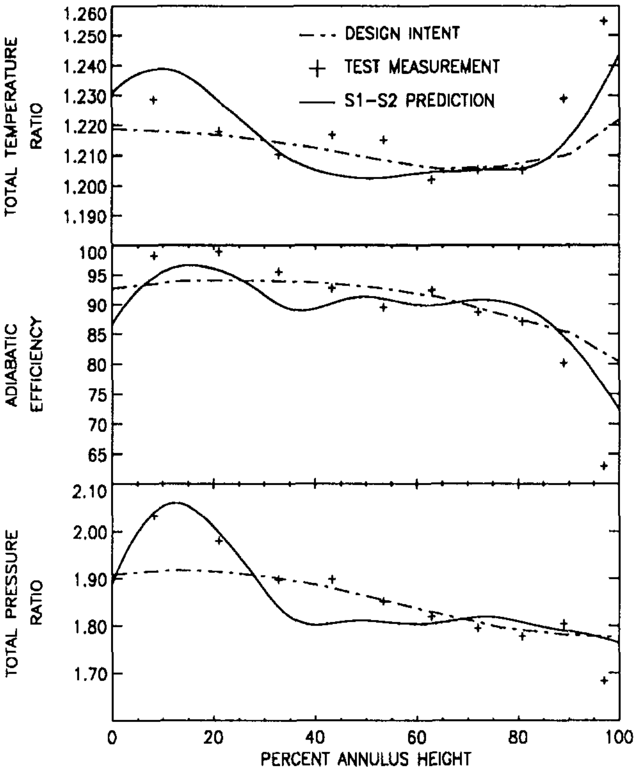

Fig. 5 C148 rotor exit flow field

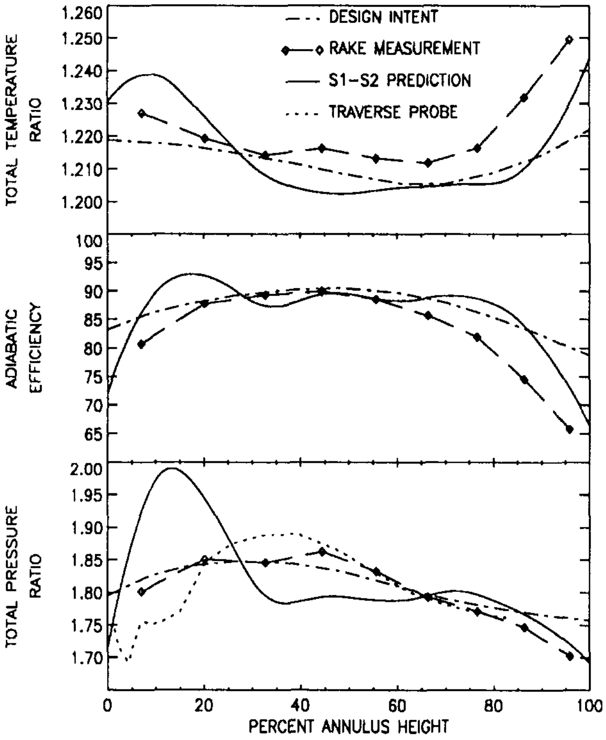

Fig. 6 C148 stator exit flow field

model of the compressor/fan. The system models shock waves and blade boundary layer development and predicts their loss contributions. Endwall boundary layer blockage and loss are modeled by empirical inputs based on previous experience. The system has been used, with considerable success, to design and analyze compressors and fans in the United Kingdom. Calvert (1991) gives a fuller description of the method and presents details of its application to a wide range of test cases.

The primary inputs to the system are inlet stagnation pressure and temperature, exit flow function $(m\sqrt{T}/P)$, rotational speed, and compressor geometry. The values used to set up the model were taken from the overall performance measurement shown in Fig. 4. The predicted performance is also shown in Fig. 4, and is seen to agree reasonably well with the measured pressure ratio and mass flow. However, the predicted efficiency is 3.5 percent higher than the measured value of 83.1 percent.

At this point it is to be noted that the S1-S2 system was used as a preliminary analysis tool for the work reported here. The model could have been tuned to provide more realistic modeling of the compressor performance by attempting to model hub endwall blockage more realistically using measurements taken in C148. However, this was not attempted because it was felt that three-dimensional viscous modeling of the flow was required in future work.

Rotor Exit Measurements. Figure 5 shows spanwise distributions of absolute total temperature ratio, total pressure ratio, and efficiency at rotor exit. Included in this figure are: the spanwise variations intended in the design; the measured variation (using stator leading edge mounted Pitots and Keil thermocouples); the variation predicted by the S1-S2 model.

Qualitative comparison of the measurements with the design intent and S1-S2 prediction gives insight into the rotor performance. Reasonable agreement is found between the design intent and the measurements over much of the span. However, between the hub (0 percent) and 30 percent span, there is a marked disagreement between design intent and measured rotor exit flow. A localized "tongue" of high-pressure fluid is measured and predicted by the S1-S2 model. It is thought that the reason for this departure from design intent is due to shortcomings in the deviation corrections used when the rotor was designed in the early 1980s.

The S1-S2 prediction does not compare well with the consensus achieved between the design intent and measured flow between 30 and 60 percent span. This is due to a very severe predicted boundary layer separation at the 40 percent span calculating plane. In reality such behavior is relieved by three-dimensional redistribution of the flow. Total temperature prediction near the endwalls does not compare well with measurement indicating that endwall loss distribution input to the model needs modifying.

Stator Exit Measurements. Figure 6 shows similar information to that given in Fig. 5 only at stator exit. The measurements in this case are derived from the six Pitot and six thermocouple rakes situated approximately two chords downstream of the stator trailing edge. In addition, total pressure measurements taken with the four-hole wedge probe at 36 percent axial stator chord downstream are shown. This has been determined by circumferentially averaging full area traverse measurements over one stator pitch. Qualitative differences between this and the rake measurements are due to streamwise mixing of the fluid in the intervening duct.

In general the measurements show fair agreement with the design intent over much of the span. The good agreement found in the stator hub region is somewhat surprising given the disagreement at rotor exit. The S1-S2 model again predicts a tongue of localized high pressure fluid at the hub and does not model the high loss found in this region of the flow in reality. This discrepancy arises because the high loss region is fundamentally three dimensional in nature, and as such it cannot be modeled adequately by the S1-S2 method. This becomes clear from consideration of the stator exit traverse measurements shown in Fig. 7.

The data in Fig. 7 were taken from a full area traverse with the four-hole wedge probe. Total pressure, Mach number, yaw angle, and pitch angle are shown. In this figure the stator is viewed from behind looking upstream. Positive yaw angle is in the same sense as rotor rotation (i.e., clockwise in Fig. 7)

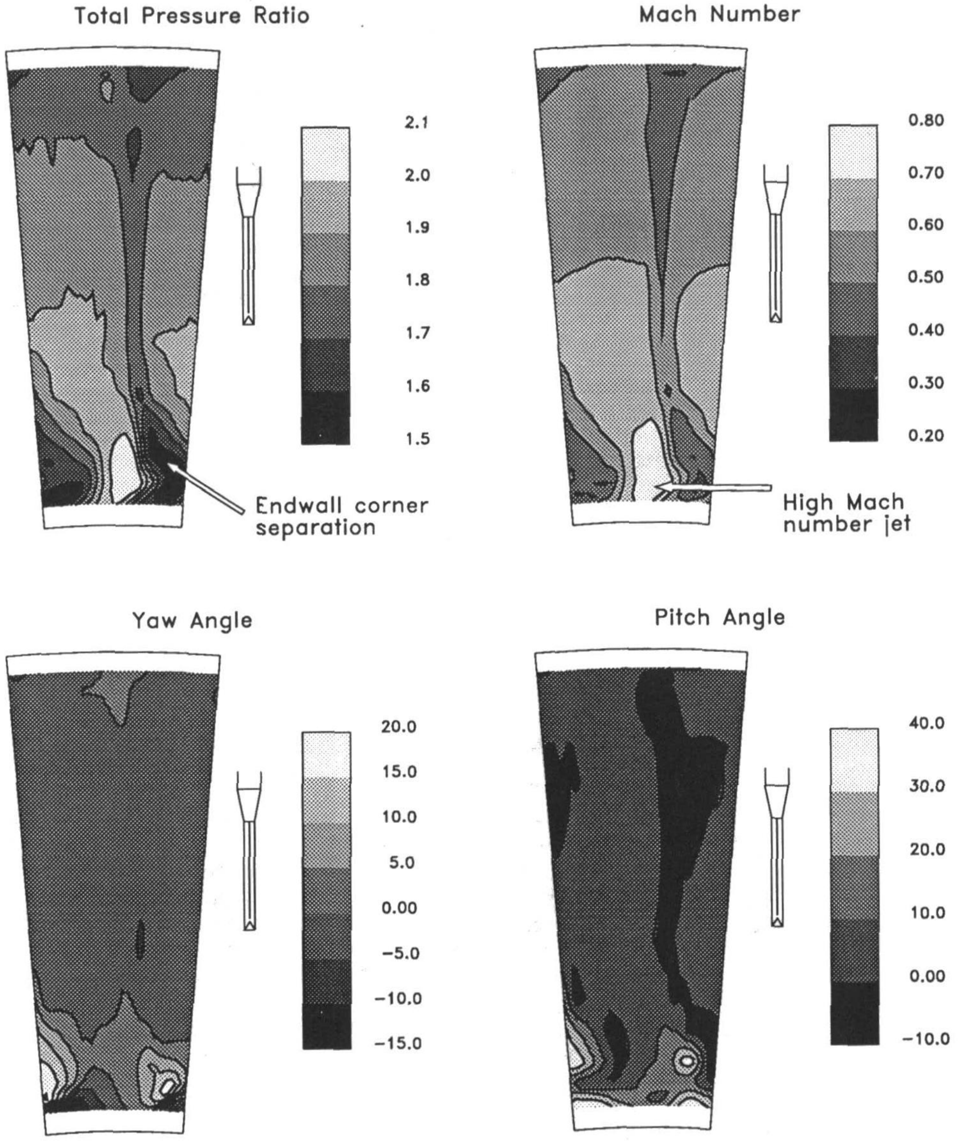

Fig. 7 Stator exit traverse measurements

and positive pitch angle is radially outward from the hub. A schematic view of the four-hole wedge probe is included at the same scale as the annulus.

The measurements show that the stator hub region of the flow is dominated by an endwall corner stall. This produces a high loss (low pressure) region that extends up to 25 percent span. The reduced passage area, due to the blockage caused by this phenomenon, induces a high Mach number jet of fluid between the separated flow and the pressure surface of the adjacent stator blade. This is undoubtedly exacerbated by the excess pressure at stator inlet induced by the off-design performance of the rotor.

Large velocity gradients and high unsteadiness levels are associated with the shear layer that separates the high loss and high-pressure regions of the flow. Such conditions make accurate intrusive measurements with traverse probes difficult. However, it is clear that the flow is highly three dimensional in this region and that large variations of yaw and pitch angle are recorded. Away from the hub region the stator wakes are observed to thicken with increasing span. In addition, there is evidence of an endwall corner separation at the casing, although it is far less pronounced than at the hub.

Stator Surface Flow Visualization. The surface flow characteristics were investigated using a fluorescing dye technique similar to that used by Hodson and Dominy (1987). Monochrome pictures of the colored oil flow patterns on the pressure and suction surfaces are shown in Fig. 8. This illustrates that on the aerofoil pressure surface the flow is essentially two-dimensional and streamline (but with strong annulus geometry induced radial components). On the suction surface, there is evidence of a strong separation in the hub-endwall/suction surface corner extending from about 20 percent chord to the trailing edge. This extends to about 25 percent of span, which is consistent with the stator exit traverse measurements. A less pronounced separation appears to occur at the casing end of the blade, which again supports the traverse probe measurements. By using different colored dyes on the aerofoil and endwall surfaces, the flow patterns showed that there is significant migration of flow from the endwall into the separated regions. Also there is some evidence of vortex action reminiscent of the passage vortex in the turbine nozzle guide vane cascade of Dominy and Harding (1989), "scrubbing" a path over the separation zone and then migrating up the trailing edge of the blade, where the flow may be separating. Evidence to support this latter hypothesis is contained in the high values of boundary layer shape factor (over 5) close to the trailing edge produced by the $S1$–$S2$ calculations.

The Effect of Compressor Operating Point. Figure 9 shows Mach number measurements taken with the sting-mounted pyramid probe at three compressor operating points; i.e., 80 percent speed (peak efficiency—condition *B*), 100 percent speed (peak efficiency—condition *A*), and 100 percent speed (near-surge—condition *C*). It is clearly evident that the endwall corner separation increases greatly in size as stator diffusion is increased in moving from the 80 percent speed to 100 percent speed characteristic. A further significant growth in extent of the separation is seen as diffusion is further increased in moving to the near surge condition. The Mach number deficit within the separation also becomes deeper. Moving from peak efficiency to near surge on the 100 percent speed characteristic sees the high Mach number jet between adjacent separations become more compressed with increasing separation size. However, the peak Mach numbers attained are not seen to increase accordingly, because of the reduction in axial velocity through the fan with increasing loading. Good quantitative agreement is observed between the wedge probe measurements (in Fig. 7) and the pyramid probe, at design speed peak efficiency operation, in the inviscid core flow of the passage. Measurements in the viscous flow regions are in good qualitative agreement although the lowest Mach numbers recorded, by both probes, in the wake and corner separation differ.

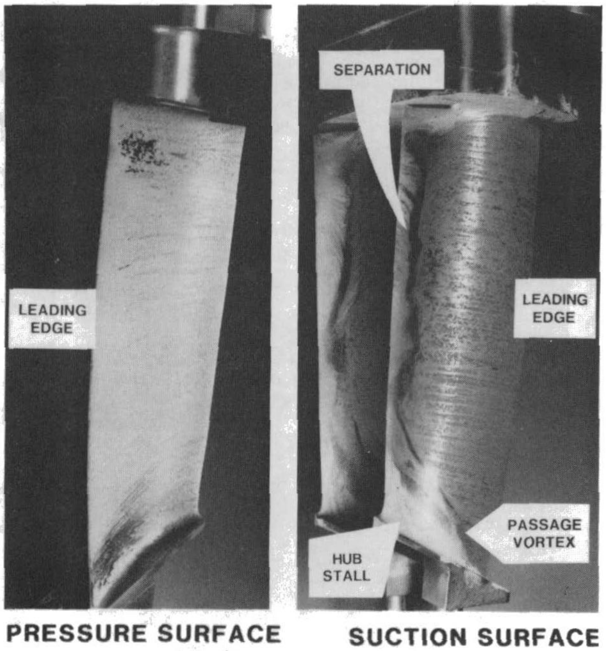

Fig. 8 C148 stator flow visualization

Discussion

Clearly, the very pronounced viscous flow features measured in the stator exit flow field create significant difficulties for a theoretical method to predict accurately. The *S*1–*S*2 method, which assumes that local flows are essentially two dimensional, coped adequately with the rotor exit flow but was unable to model the stator hub region adequately. To model the stator flow, it is apparent that the better physical modeling offered by three-dimensional Navier–Stokes methods needs to be applied in future work.

The complexity of the three-dimensional flow features and the strong velocity gradients occurring in the exit flow make accurate measurements by pneumatic probes very difficult, particularly close to endwalls. This points to the need for developing smaller probes and making corroborating measurements using nonintrusive techniques such as laser anemometry and particle image velocimetry (PIV). However, while the fine detail of the flow (particularly flow angles) varied significantly, the overall qualitative and quantitative agreement achieved between the measurements made at stator exit using different types of traverse probe (not presented here) gives confidence in their quality and their value to CFD code development.

Clearly, the highly three-dimensional and viscous flow field identified at exit from the stator makes the aerodynamic task of a downstream second stage extremely difficult. Future work will investigate and then test an improved aerodynamic design of first-stage stator with the objective of ameliorating the hub stall problem.

Conclusions

Complex, unsteady viscous flows limit the performance of highly loaded transonic compressors. DRA is carrying out a program to investigate such flows in a single-stage transonic fan known as C148. Build 1 of C148 has been tested extensively

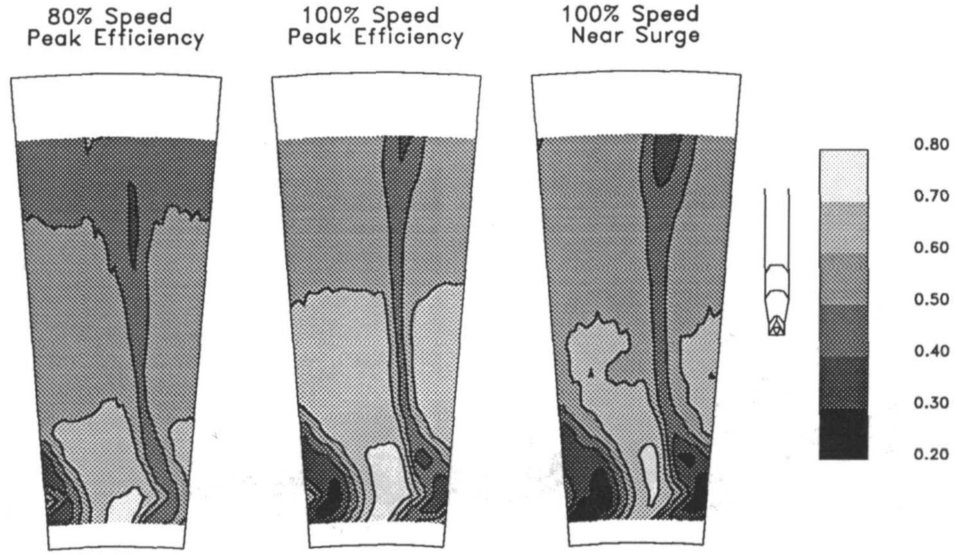

Fig. 9 The effect of compressor operating point on endwall corner separation growth (Mach number plots are shown)

in the compressor test facility at DRA Pyestock. The rig was comprehensively instrumented and a wide range of steady and unsteady flow measurements have been carried out that will provide a data base for current and future code development. In the current paper some steady-state measurements of the rotor and stator exit flow fields have been presented as well as stator surface flow visualization. These results have been compared with an $S1$–$S2$ prediction of the fan flow field at the nominal design condition. Major conclusions are as follows:

1 At rotational speeds up to 100 percent corrected speed the fan operates over a wide stable flow range, with the limit of stability sharply defined at all speeds. At design speed, peak efficiency, the $S1$–$S2$ model agreed well with the measured mass flow and pressure but predicted isentropic efficiency was 3.5 percent greater than measured.

2 The rotor was found to produce greater total pressure rise than intended by design between the hub and 35 percent span. This localized excess of total pressure was also predicted by the $S1$–$S2$ model indicating that two-dimensional phenomena, rather than three-dimensional viscous phenomena, were responsible for this behavior.

3 Stator exit area traverse measurements show that the stator hub region is dominated by an endwall corner separation. The resulting high loss region reduces the passage area and induces a high Mach number region of flow between the corner separation and the pressure surface of the adjacent stator blade. Confirmation of this behavior has been given by oil flow visualization.

4 The inability of the $S1$–$S2$ method to model adequately the flow in the stator hub region emphasizes that the endwall corner stall is a fundamentally three-dimensional phenomenon.

5 Further measurements and analysis will be reported in subsequent papers.

Acknowledgments

The successful completion of the C148 test series owes much to the contributions of many colleagues at DRA Pyestock. However, special acknowledgment is made to the efforts of Mr. I. R. McKenzie and Miss J. M. Parker. In addition, due acknowledgment is given to Dr. H. P. Hodson and Dr. O. C. Jadayel who carried out the probe calibration work at the Whittle Laboratory, Cambridge University (Dr. Jadayel now works at Birmingham University, United Kingdom).

References

Baines, N. C., 1983, "Development of a Perforated Nozzle for Calibrating Transonic Probes," *Proc. of 7th Symposium on Measurement Techniques for Transonic & Supersonic Flows in Cascades and Turbomachines*, Aachen, Federal Republic of Germany.

Bubeck, H., and Wachter, J., 1987, "Development and Application of a High Frequency Wedge Probe," ASME Paper No. 87-GT-216.

Calvert, W. J., 1991, "Application of S1BYL2 to the AGARD WG18 Compressor Test Cases," AGARD CP-510-3.

Cherrett, M. A., Bryce, J. D., and Hodson, H. P., 1992, "3D Pneumatic and 2D Dynamic Probes: Their Development and Subsequent Use in a Transonic Fan," *Proc. of 11th Symposium on Measuring Techniques for Transonic and Supersonic Flows in Cascades & Turbomachines*, Munich, Federal Republic of Germany.

Dominy, R. G., and Harding, S. C., 1989, "An Investigation of Secondary Flows in Nozzle Guide Vanes," AGARD CP-469.

Dominy, R. G., and Hodson, H. P., 1993, "An Investigation of Factors Influencing the Calibration of Five-Hole Probes for Three-Dimensional Flow Measurements," ASME JOURNAL OF TURBOMACHINERY, Vol. 115, pp. 513–519.

Dong, Y., Gallimore, S. J., and Hodson, H. P., 1987, "Three-Dimensional Flow and Loss Reduction in Axial Compressors," ASME JOURNAL OF TURBOMACHINERY, Vol. 109, pp. 359–361.

Gostelow, J. P., and Watson, J. P., 1976, "A Closed Circuit Variable Density Air Supply for Turbomachinery Research," ASME Paper No. 76-GT-62.

Heneka, A., 1983, "Instantaneous Three-Dimensional Four-Hole Wedge Probe," *Proc. of 7th Symposium on Measurement Techniques for Transonic & Supersonic Flows in Cascades & Turbomachines*, Aachen, Federal Republic of Germany.

Hodson, H. P., and Dominy, R. G., 1987, "Three-Dimensional Flow in a Low-Pressure Turbine Cascade at Its Design Condition," ASME JOURNAL OF TURBOMACHINERY, Vol. 109, pp. 177–185.

Joslyn, H. D., and Dring, R. P., 1985, "Axial Compressor Stator Aerodynamics," ASME *Journal of Engineering for Gas Turbines and Power*, Vol. 107, pp. 485–493.

Schulz, H. D., and Gallus, H. D., 1988, "Experimental Investigation of the Three-Dimensional Flow in an Annular Cascade," ASME JOURNAL OF TURBOMACHINERY, Vol. 110, pp. 467–478.

Shepherd, I. C., 1981, "A Four-Hole Pressure Probe for Fluid Flow Measurements in Three-Dimensions," ASME *Journal of Fluids Engineering*, Vol. 103, pp. 590–594.

Measurements of the Flow Field Within a Compressor Outlet Guide Vane Passage

J. F. Carrotte

K. F. Young[1]

S. J. Stevens

Department of Transport Technology,
Loughborough University,
Loughborough, Leicestershire,
United Kingdom

A series of tests have been carried out to investigate the flow in a Compressor Outlet Guide Vane (OGV) blade row downstream of a single-stage rotor. The subsequent flow field that developed within an OGV passage was measured, at intervals of 10 percent axial chord, using a novel design of miniature five-hole pressure probe. In addition to indicating overall pressure levels and the growth of regions containing low-energy fluid, secondary flow features were identified from calculated axial vorticity contours and flow vectors. Close to each casing the development of classical secondary flow was observed, but toward the center of the annulus large well-defined regions of opposite rotation were measured. These latter flows were due to the streamwise vorticity at inlet to the blade row associated with the skewed inlet profile. Surface static pressures were also measured and used to obtain the blade pressure force at three spanwise locations. These values were compared with the local changes in flow momentum calculated from the measured velocity distributions. With the exception of the flow close to the outer casing, which is affected by rotor tip leakage, good agreement was found between these quantities indicating relatively weak radial mixing.

Introduction

In the continuing quest for increased power plant performance, considerable attention is being focused on ways of improving component efficiency. This means that manufacturers must investigate in greater detail the aerodynamic processes taking place within the engine both by measurements and through the development and utilization of sophisticated three-dimensional design techniques. In the case of a compressor, for example, all the flow mechanisms occurring within the rotor and stator blade passages must be fully understood and included in the design process. With this aim in mind an experimental investigation has been carried out to establish the detailed performance of an Outlet Guide Vane (OGV) stator row, which is incorporated within a single-stage axial flow compressor.

A substantial amount of data obtained from compressor cascade tests has already been reported by a wide variety of authors (e.g., Lieblein [1]), which provides a baseline for the influence of such parameters as blade profile, camber, stagger angle, etc., on overall blade row performance. From these numerous investigations consideration has also been given to the flow mechanisms that occur within a blade passage. For example, Gostelow [2] describes how streamline curvature at the center of a blade passage represents a balance between centrifugal forces ($\rho V^2/r_s$) and the pitchwise pressure gradient between the blade suction and pressure surfaces. By incorporating a more representative inlet profile with wall boundary layers, it has also been shown how the pitchwise pressure gradient prevails through these shear layers, so that the lower velocity (V) of this fluid results in differing amounts of streamline curvature (r_s). The resulting relative movement of flow, from pressure to suction surface, close to each casing has therefore been noted and described by many authors (e.g., Horlock [3]), and in this paper it is termed the classical secondary flow effect. However, simple two-dimensional cascade tests cannot fully simulate the flow conditions to a stator row that are provided by a rotor in which the following features are present:

- (*i*) Radial variation of incidence, i.e., a skewed inlet boundary layer
- (*ii*) High levels of turbulence and unsteadiness associated with rotor blade wakes
- (*iii*) Rotor tip leakage fluid
- (*iv*) Thick and often asymmetric wall boundary layers
- (*v*) Radial pressure gradients.

Several authors have reported tests conducted on a stator blade row downstream of a rotor, although measurements have been limited to blade inlet and exit planes. In the case of Joslyn and Dring [4], flow visualization and pressure probe measurements indicated that if a hub corner stall is present, this can dominate the flow field and have a significant impact on loss, deviation, and blockage. An ethylene tracer gas was injected at stator inlet by Gallimore and Cumpstey [5] who inferred secondary flows, fluid migration, and turbulent diffusion from the location of this gas at the exit of the blade row. These measurements were performed in the third stage of a four-

---

[1] Present address: Rolls Royce PLC, Derby, United Kingdom.

Contributed by the International Gas Turbine Institute and presented at the 38th International Gas Turbine and Aeroengine Congress and Exposition, Cincinnati, Ohio, May 24–27, 1993. Manuscript received at ASME Headquarters February 12, 1993. Paper No. 93-GT-22. Associate Technical Editor: H. Lukas.

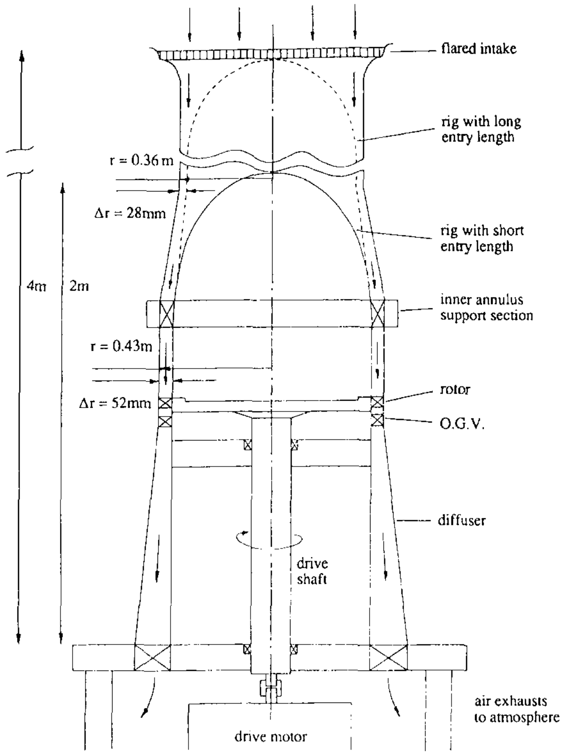

Fig. 1 Experimental facility—general layout

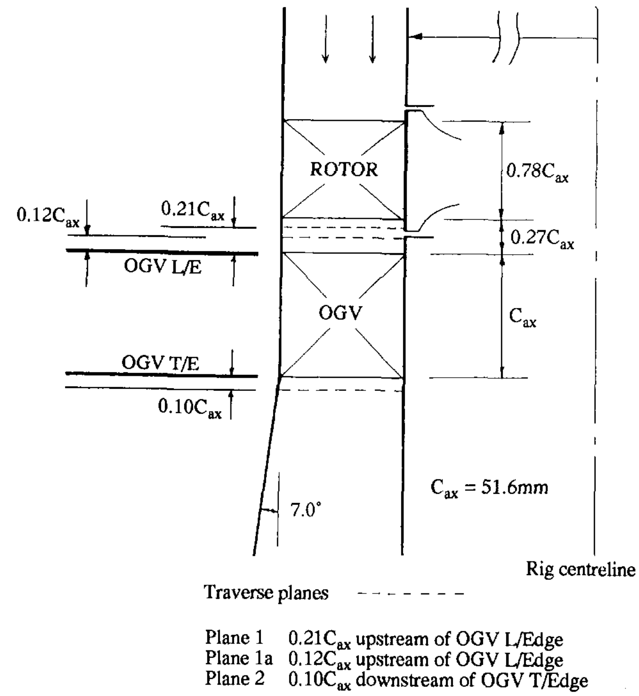

Fig. 2 Experimental facility—working section

stage axial compressor and they concluded that while secondary flows may be responsible for a significant circumferential transport of fluid, mixing in the radial direction was dominated by turbulent diffusion. In addition to a tracer gas, Wisler et al. [6] also used hot-wire anemometry to measure velocities and turbulence intensities at the exit of a third-stage stator row. This work also confirmed the importance of secondary flows and turbulent diffusion, although close to each casing ($r_n < 0.2$ and $r_n > 0.8$) the authors concluded that secondary flows may also affect the radial mixing of fluid.

The present paper reports on the results of traverses performed within an OGV blade row downstream of a rotor. Since data were acquired with mean pressure probes and surface tappings only, no information on flow turbulence is available. However, a detailed qualitative description of the mean pressure and velocity fields within the OGV passage is given.

Experimental Facility

A comprehensive description of the experimental facility has already been given by Stevens and Young [7]. Air is drawn from atmosphere into a plenum chamber prior to passing through a honeycomb flow straightener sited upstream of a long annular entry length (Fig. 1). This is followed by the working section (Fig. 2), which contains the rotor and fully shrouded stator blades, both of which are of constant axial chord from hub to tip. The blade geometry and aerodynamic test conditions are summarized in Table 1. A 45 kW DC motor is used to drive the rotor at a constant nondimensional operating speed ($N/\sqrt{T}$) of 117.8, this corresponding to a rotor speed of 2000 rpm at a reference inlet temperature of 288 K. The speed is controlled by a thyristor drive unit to within ±3 rpm of a given setting. Sited immediately downstream of the OGVs is a single-sided diffuser, area ratio 3.06, with the outer wall diverging at an angle of 7.0 deg. At diffuser exit the air is dumped into an exhaust plenum from which it is discharged to atmosphere via a throttle.

Measurements were mainly obtained using miniature five-hole pressure probes of overall diameter 1.7 mm, hole bore 0.25 mm, and were used in a nonnulled mode as outlined by Wray [8]. Inlet conditions were obtained from two traverse

Nomenclature

C = blade true chord
C_{ax} = blade axial chord
C_p = static pressure rise coefficient = $(\tilde{p}_2 - \tilde{p}_1)/(\tilde{P}_1 - \tilde{p}_1)$
N = rotor speed, rpm
P, p = total, static pressure
OGV = outlet guide vane
r = radius measured from rig centerline
r_i = inner casing radius
r_o = outer casing radius
r_n = nondimensional annulus height = $(r - r_i)/(r_o - r_i)$
r_s = radius of flow streamline curvature
T = temperature
V = velocity
α = flow angle relative to axial direction (Fig. 3)
γ = yaw angle relative to blade camberline
θ = angle
λ = loss coefficient = $(\tilde{P}_1 - \tilde{P}_2)/(\tilde{P}_1 - \tilde{p}_1)$
ρ = density
τ = blade pitch
Ω = vorticity

Superscripts

$\bar{}$ = area average
$\tilde{}$ = mass-weighted average
p = pitch (circumferential) average

Subscripts

n = coordinate perpendicular to streamwise direction
m = blade midspan location
s = coordinate in streamwise direction, parallel to blade camber line (Fig. 3)
z, r, ax = coordinates in the rig tangential, radial, and axial directions
1, 2 = traverse plane upstream/downstream of blade row (Fig. 2)

Table 1 Midspan blade geometry and design conditions (free vortex blading)

Mean radius	405.9mm
Hub/Tip radius ratio	0.88
Mass flow	5.4Kg/s
Rotor	
Rotor speed	2000rpm
Flow coefficient (ϕ)	0.425
Tip clearance/blade height	1.0%
OGV	
Blade inlet angle	41° (relative to axial direction)
Blade outlet angle	-8° (relative to axial direction)
Estimated deviation	8°
Design incidence	0°
Stagger angle	16.5°
True chord	53.9mm
Re	$1.8\text{x}10^5$
Nos. of blades	92
Profile	C5
Camber line	Circular arc
Thickness/chord ratio	0.1
Space/chord ratio	0.515
Diffusion factor	0.41

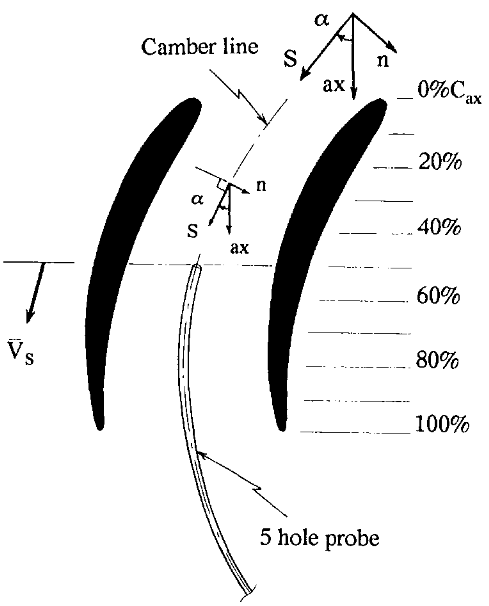

Fig. 3 Data acquisition within the OGV passage

stations located at 21 and 12 percent of the OGV axial chord upstream of the OGV leading edge but downstream of the rotor (Fig. 2). A traverse station at 10 percent axial chord downstream of the OGV trailing edge provided information on blade exit conditions. The carrier ring containing the shrouded OGVs could be rotated over two blade spaces and this, combined with radial movement of the instrumentation probes, allowed a full area traverse to be performed. The downstream flow conditions were defined from 42 radially spaced data points recorded at each of 21 circumferential locations spaced over one blade pitch. Traversing between the stator blades was accomplished using a probe constructed in such a fashion as to follow the mean blade camber line (Fig. 3), the 1.7 mm probe tip representing less than 0.5 percent of the area at each axial plane within the OGV passage. The probe was mounted within the facility approximately one blade chord downstream of the OGVs and an externally mounted manual traverse mechanism provided radial movement via a small shaft. In this way flow leakage through the outer casing was virtually eliminated. Flow conditions at eleven equispaced chordwise intervals (Fig. 3) were defined from 12 radially spaced data points at 11 circumferential locations. Information on the blade surface pressure distribution was given by static tappings at 10, 50, and 90 percent annulus height for six chordwise locations on both the pressure and suction surfaces.

Data Reduction

At each traverse point, five hole probes provide information on total and static pressure in addition to velocity magnitude and direction. The overall mean velocity at a traverse plane is calculated using an area weighting method, whereas other mean quantities such as total and static pressures are derived from mass weighting of the data. For radial distributions of pitch-averaged quantities, this weighting is performed in the pitchwise (i.e., circumferential) direction only. All flow angles presented are derived from the mass-weighted tangential and area-weighted axial velocity components as outlined by Dring and Spear [9]. It should be noted that all these averaged quantities were derived by numerical integration of the data to which had been fitted a spline curve. Furthermore, a linear extrapolation of the static pressure was performed to casing and blade surfaces with the velocity at these locations being set to zero.

Vorticity contours are used to identify the presence, location, and relative strength of secondary flow features within the OGV passage. Only axial vorticity values are presented on planes of constant axial location, these values being given by:

$$\Omega_{ax}=\frac{\partial V_z}{\partial r}+\frac{V_z}{r}-\frac{1}{r}\frac{\partial V_r}{\partial \theta} \tag{1}$$

which for large radii reduces to

$$\Omega_{ax}=\frac{\partial V_z}{\partial r}-\frac{\partial V_r}{r\partial \theta}=\frac{\partial V_z}{\partial r}-\frac{\partial V_r}{\partial z} \tag{2}$$

where z is the coordinate in the circumferential direction. At a given location, gradients for each velocity component are derived by fitting a three-term lagrange polynomial both in the radial and circumferential directions from which the axial vorticity is calculated. It should be noted that the axial vorticity (Ω_{ax}) includes contributions from both the streamwise component (Ω_s) and the vorticity component (Ω_n) perpendicular to the mean flow direction (Fig. 3). The relative contribution of these components depends on the angle of the mean flow to the axial direction (α).

Over one blade pitch, the tangential and axial momentum of the flow upstream and downstream of the blade row and within the OGV passage is calculated using the method outlined by Dring [10]:

$$M_{ax}=\int_{r_i}^{r_o}\tau_m\frac{r}{r_m}\,(\overline{p}^p+\rho\overline{V}_{ax}^p\tilde{V}_{ax}^p)dr \tag{3}$$

$$M_z=\int_{r_i}^{r_o}\tau_m\frac{r}{r_m}\,(\rho\overline{V}_{ax}^p\tilde{V}_z^p)rdr \tag{4}$$

At a given spanwise location, the change in flow momentum is compared with the axial and tangential force on the stator blades. These forces are calculated at 10, 50, and 90 percent span from the measured surface static pressure distributions. Since the skin friction force is relatively small, these pressure forces are representative of the forces being applied to the flow at that radial location.

Estimate of Experimental Errors

At a given data point the experimental accuracy is influenced by:

(*i*) the spatial error associated with the finite distance between the five holes on the probe tip; this was eliminated

Table 2 Mass flow errors

a) within OGV passage (relative to passage mean value)

Axial Chord :	0.%	10.%	20.%	30.%	40.%	50.%
Error :	-0.2%	+2.1%	+2.7%	+1.6%	+1.7%	+1.6%
Axial Chord :	60.%	70.%	80.%	90.%	100.%	
Error :	+0.5%	-0.7%	-1.8%	-3.3%	-4.3%	

b) overall (relative to plane 1)

Plane 1 (reference)	0.0%
within the OGV passage (Mean value)	-4.8%
Plane 2	-0.3%

by radial and circumferential interpolation of the side pressures onto the central measurement hole [8].

(*ii*) the proximity of the casing and blade surfaces to a measurement location; and

(*iii*) recording of the pressure signals via transducers and an analogue-to-digital converter.

Young [11] estimates that the aforementioned sources of error mean that total and static pressures are accurate to within 2 percent of the inlet dynamic head, with flow angles being measured to within 2 deg of their true value.

Since the interblade traverse probe followed the blade camberline, bending due to aerodynamic loading was not thought to be a significant problem. However, of some concern with these measurements was the presence of interference effects when the probe was located far into the blade passage. This may be indicated by differences in the mass flow recorded at each traverse plane (Table 2*a*), and a trend clearly exists of lower mass flows being recorded in the latter stages of the passage. However, since all values are within 4.3 percent of the mean, it is thought that such effects, although present, do not invalidate the test results. It should also be noted that the average mass flow derived from the interblade traverse data is 4.8 percent less than that recorded at plane 1 (Table 2*b*). This may be due to probe blockage effects, but also of significance will be the errors associated with the extrapolation of data to the blade surface. This is because the instrumentation probe could not touch these surfaces at certain chordwise stations. For this reason no quantitative performance figures (e.g., total pressure loss, static pressure rise coefficients, etc.) are quoted for the interblade traverse measurements due to lack of data in high loss regions close to each blade surface and endwall.

Results and Discussion

Inlet Conditions. Measurements were made at two traverse stations in the space between the rotor and stator blade rows, the axial velocity distributions (Fig. 4) illustrating the sheared nature of the flow in this region. OGV incidence is represented by the difference between the flow and blade inlet angles, with relatively high values being recorded close to each casing while incidence is negative in the central region of the passage ($0.2 < r_n < 0.7$). Stevens and Young [7] present distributions of rotor incidence and deviation, which indicate that close to the outer wall, the large flow angles may be attributable to a rotor tip stall caused by the combined effects of tip leakage and localized high incidence. Furthermore, since rotor incidence at the hub and tip is comparable, it therefore follows that the inferior flow behavior close to the outer wall must be due to the influence of tip leakage flows.

Comparison of the data recorded at each upstream traverse plane indicates the change in axial velocity and flow incidence with downstream location, this being particularly noticeable close to the outer wall where axial velocity increases and incidence decreases. This is further confirmed by the data at the OGV leading edge, although the validity of the measured values adjacent to the end walls is thought questionable since they do not follow the trend for the overall distribution at this plane. However, differences between the measured distributions at all three planes reflect the decay of flow swirl, due to viscous effects, downstream of the rotor stage and means that actual OGV incidence is dependent on the rotor-stator axial spacing. Cascade predictions outlined by Stevens and Young [7] suggest a stalling incidence of about 14 deg for this blading and on this basis OGV stall might be expected in very localized regions near the end walls.

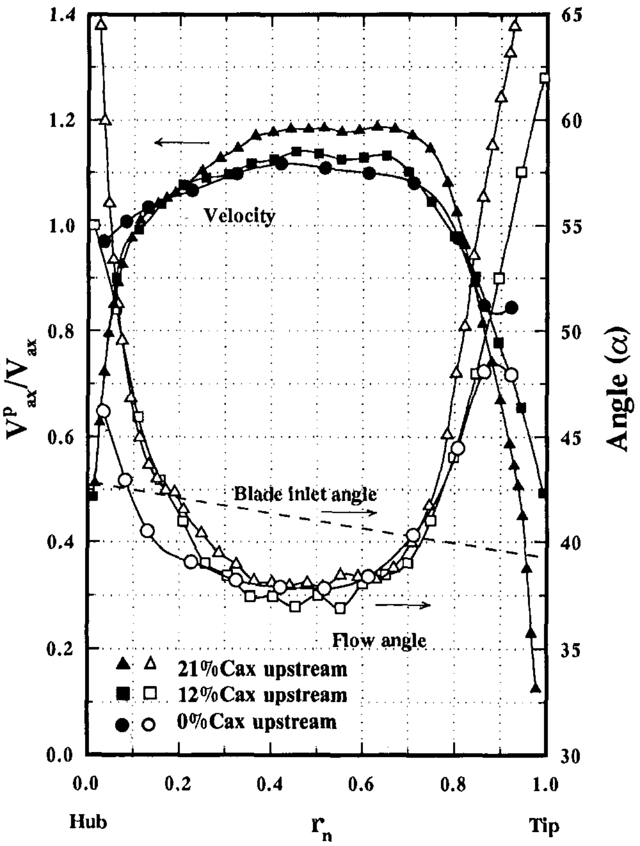

Fig. 4 Axial velocity and flow angles at OGV inlet

Overall Performance. The overall performance of the OGV blade row has already been described in detail by Stevens and Young [7]. The stator blades are not highly loaded and the total pressure loss (λ) of 0.083 and static pressure rise coefficient (C_p) of 0.418 are in good agreement with published empirical correlations. The mean flow deviation angle of 11 deg was derived from measurements downstream of the OGVs (plane 2) and compared with an 8 deg estimated value based on two-dimensional cascade correlations. Axial velocity contours [7] at this same location also indicate no significant regions of flow separation within the blade passage. This was also confirmed by small wool tufts observed through the Perspex casings and through an endoscope located downstream of the blade row. These tufts were attached to both end walls and on the blade surfaces at five chordwise locations for each of six spanwise positions.

The pitch (circumferentially) averaged axial velocity profiles indicate the radial distribution of mass flow and comparison of the profiles upstream and downstream (planes 1 and 2) of the OGVs shows a radially outward movement of fluid across the stator row (Fig. 5*a*). Differences between the upstream (plane 1) and OGV leading edge (0 percent chord) profiles show that some of this redistribution occurs within the intense mixing region immediately upstream of the OGV blade row, as has already been discussed. Between the OGV leading and trailing edges the axial velocity profiles also indicate a change in flow distribution (Fig. 5*b*). This occurs at a reasonably

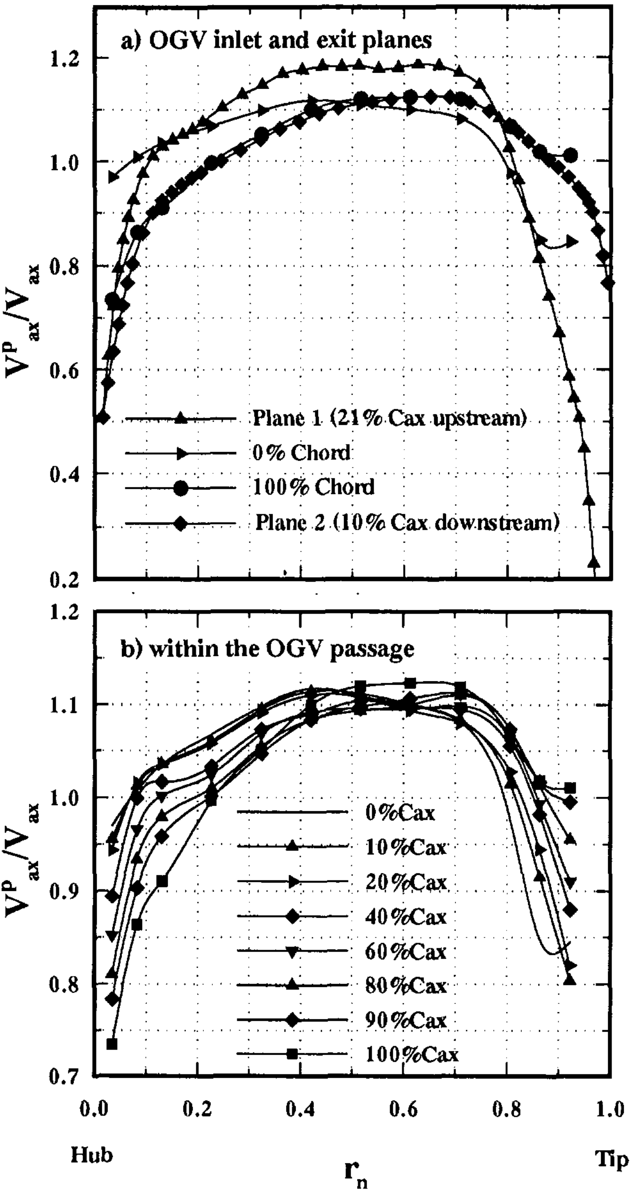

Fig. 5 Radial variation of axial velocity

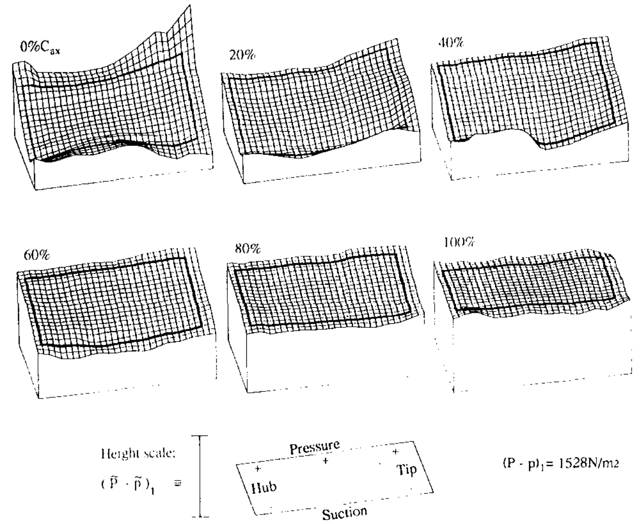

Fig. 6 Static pressure distributions within the OGV passage

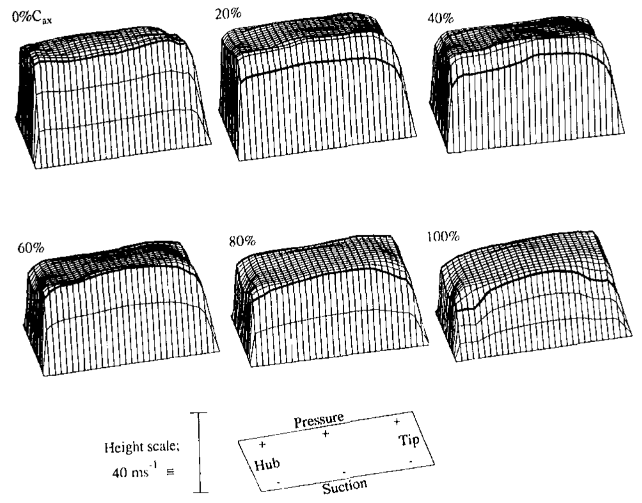

Fig. 7 Velocity distributions within the OGV passage

uniform rate throughout the blade passage, although slightly higher rates of change occur within the first and last 10 percent regions of the passage.

Blade Passage Flows. Measurements were made at intervals of 10 percent axial chord, but for the sake of brevity relief maps of passage velocity, stagnation, and static pressure are presented at 20 percent chord intervals only. The experimental data grids from which these distributions have been derived are indicated by the vector plots to be presented later. However, for reasons of clarity, an interpolation of the data was performed in order to produce a large number of nodes on the surface of each map. In addition, the proximity of the measured data to each blade surface and endwall is indicated by the bold lines, and a linear extrapolation of this data is performed to generate the nodes adjacent to each surface.

Static Pressure. As would be expected in a diffusing passage, there is a static pressure rise (Fig. 6) and a corresponding reduction in the overall mean velocity (Fig. 7) through the blade row. However, these changes are not progressive since over the first 30 percent of the passage any diffusion caused by the change in swirl is approximately balanced by the reduced area as the blade thickness increases to its maximum value. It is only downstream of this location that significant changes occur in the average static pressure and velocity levels. The pitchwise gradients of static pressure and velocity through the passage reflect the different velocities on the blade passage and suction surfaces, the resulting pressure gradient causing the mean flow to approximately follow the blade camber line. In addition, over the first 30 percent of the blade chord a positive radial pressure gradient is discernible, the pressure increasing with radius. This gradient is necessary to maintain radial equilibrium of the swirling flow, the gradient therefore decreasing as the swirl is progressively reduced through the passage.

The pitchwise static pressure gradient is also indicated by the difference between the static tapping values on the blade suction and pressure surfaces (Fig. 8). In addition, a linear extrapolation of the five-hole probe data to each surface allows a comparison between these measurements. Agreement between the two independent sets of data is good, the only significant discrepancy occurring between 20 and 40 percent chord on the blade suction surface. The five-hole probe data suggest the presence of a suction surface bubble, but this was not confirmed with wool tufts. Instead, examination of the data revealed that the anomaly was most likely associated with the extrapolation of the five-hole probe data to the blade surface since it is in this region where the gradient in static pressure is strongest. A smaller effect is thought to be the presence of

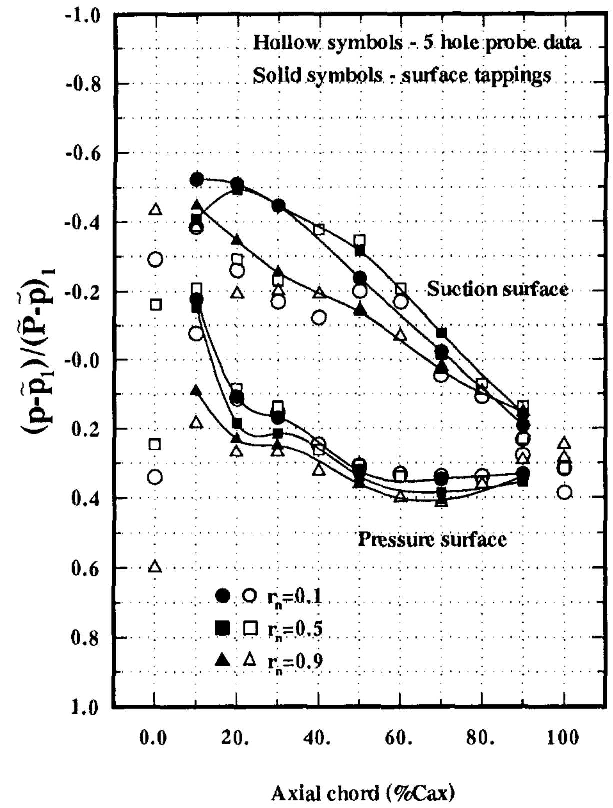

Fig. 8 Blade surface static pressure distributions

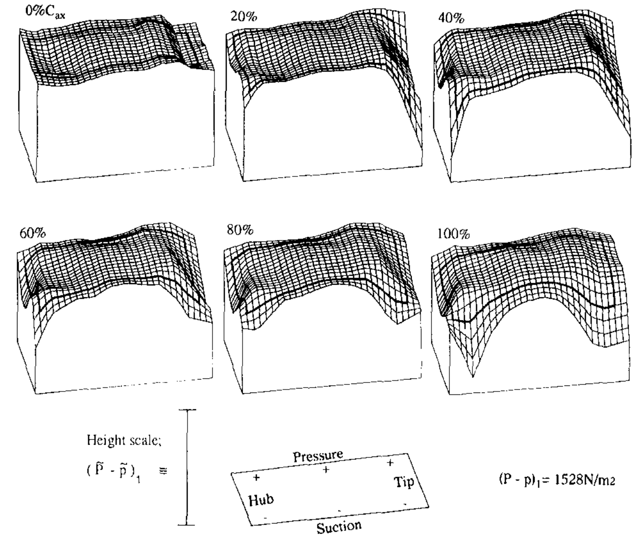

Fig. 9 Total pressure distributions within the OGV passage

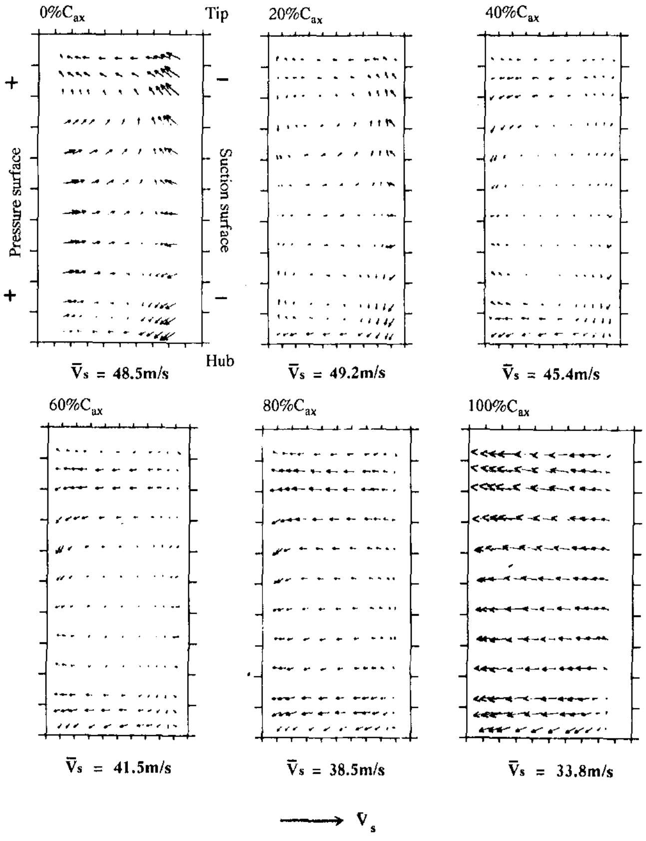

N.B. All vectors are scaled with respect to the local streamwise velocity at that plane (V_s). The magnitude of the streamwise vector is indicated above.

Fig. 10 Flow vector plots within the OGV passage

the probe, its influence on measured static pressure being greatest in this region of minimum flow area.

Total Pressure. Over a significant proportion of the annulus, the stagnation pressure at 0 percent chord is uniform but near the outer wall a noticeable decrease in total pressure occurs (Fig. 9). This is due to the effects and mixing out of tip leakage flows and although not presented here, the distribution at 10 percent blade chord indicates a continuing decrease of total pressure. These effects are thought to give a significant contribution to the radial redistribution of fluid noted earlier. Farther downstream the low-pressure region close to the outer wall can still be observed, but comparison of the distributions at 20 and 100 percent axial chord shows that its prominence decreases. This is particularly the case midway between blades and close to the blade pressure surface, and is probably due to radial redistribution of fluid. The total pressure distribution also indicates losses associated with the casing boundary layer, with localized regions of low-energy fluid being observed in the corners formed by the suction surface and end wells. These can be observed at the 20 percent chord location and grow progressively in the chordwise direction, correlating well with the velocity distributions. In addition, midway between the blade surfaces near the inner wall, a region of lower velocity and total pressure develops that is still present at the 100 percent chord position. The higher rate of change of the pitch-averaged velocity profile over the last 10 percent chord, near the inner wall, that was noted earlier (Fig. 5*b*) is thought to be associated with the presence of this region but from the data available it is not known why this feature occurs.

These observations agree with the radial distribution of total pressure loss presented by Stevens and Young [7]. This was obtained by calculating the difference in total pressure between blade inlet and exit at a given nondimensional height. Whereas a fairly constant loss across the blade row is observed between 15 and 80 percent annulus height, near the inner wall the loss increases sharply. However, in the vicinity of the outer wall the loss is reduced, indicating that end wall boundary layer effects are being offset by the radial redistribution of flow.

Secondary Flows. To a limited extent secondary flows within the OGV passage are indicated by vector plots (Fig. 10). The relative magnitude of these flows can be assessed by comparison with the length of the vector representing the overall mean streamwise velocity component measured for that plane in the direction of the camberline. However, it should be noted that although the interblade data points lie on traverse planes of constant axial chord, each vector has been obtained by resolving onto a plane perpendicular to the camberline at that

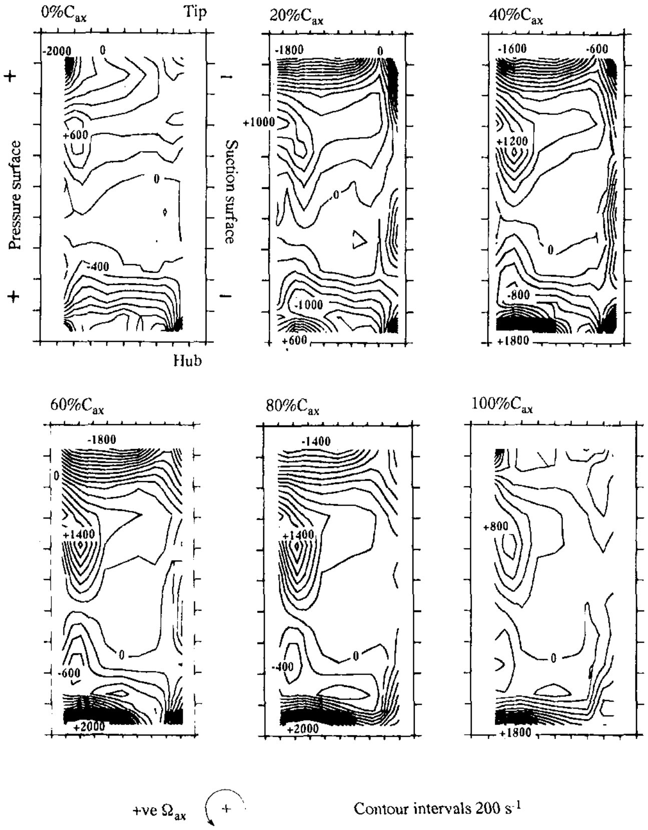

Fig. 11 Axial vorticity contours within the OGV passage

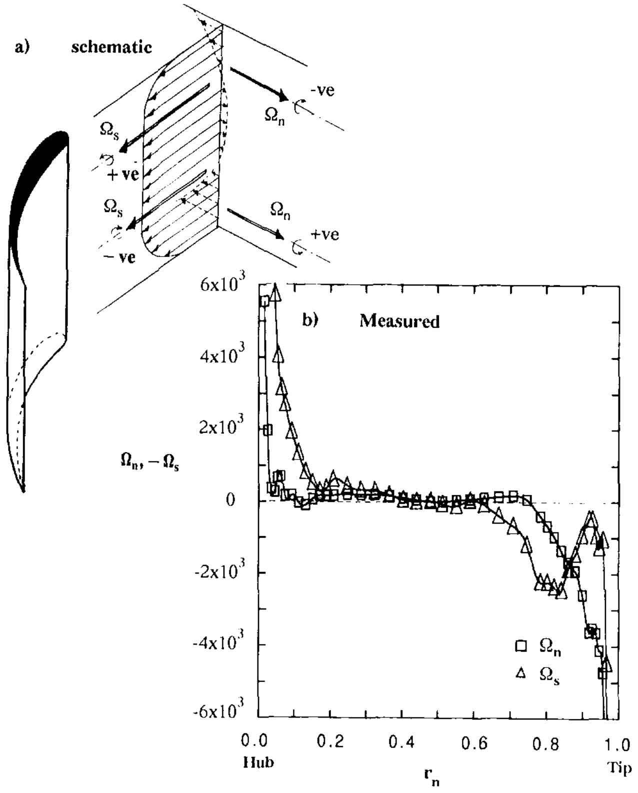

Fig. 12 Inlet vorticity

location (Fig. 3). In this way a "dot" represents flow following the blade camberline. Towards the rear of the OGV passage though a large movement of fluid from the blade pressure to suction surface will be indicated (e.g., 100 percent C_{ax}). This is associated with flow deviation and can be seen to dominate the vector plots in this region, with any fluid movement relative to the bulk motion becoming difficult to distinguish. However, such motion, associated with the secondary flows, can be identified using axial vorticity contours (Fig. 11).

The vector plots at 0 and 20 percent axial chord show considerable secondary flow movement as the flow accelerates around the leading edge of the blade toward the passage center (Fig. 10). At 20 percent axial chord large secondary flows of counterclockwise and clockwise rotation exist in the upper ($0.5 < r_n < 0.85$) and lower ($0.5 < r_n < 0.1$) half of the blade passage, respectively. This is also indicated by the positive and negative vorticity values in these regions (Fig. 11). Although farther downstream the vector plot becomes dominated by flow deviation, these features can still be distinguished by the axial vorticity contours. At OGV exit they are located adjacent to the blade pressure surface and for identification purposes these flows have been termed inlet vortices. It should be noted that the associated flow movement close to each casing ($r_n = 0.1$ and $r_n = 0.85$) is in the opposite direction to that of classical secondary flow. However, as already indicated by the radial variation of blade incidence (Fig. 4) there is significant skewing of the OGV inlet profile and, as described by Horlock [12], such rotor-generated vorticity will produce secondary flows within the downstream blade passage. In compressors, the changes between the rotating and stationary end wall surfaces results in the inlet skewing being of opposite sign to that of the classical secondary flow generated by flow turning. This is confirmed by the streamwise vorticity derived from measurements at plane 1 (Fig. 12), with the magnitude and sign of the vorticity accounting for the presence of the inlet vortices within the OGV passage. While skewing of the inlet profile occurs close to both casings, its effect near the outer wall is modified by the rotor tip vortex whose presence is indicated by the streamwise vorticity distribution at 90 percent span (Fig. 12).

The vorticity perpendicular to the streamwise direction (Ω_n) at OGV inlet (Fig. 12) is associated with the casing boundary layers and, as already noted, the curvature of this slower moving fluid within the blade passage varies from that of the mainstream flow. However, as shown by Moore and Richardson [13], skewing of the inlet profile results in the flow close to each sidewall having initial momentum, which opposes the blade pressure forces perpendicular to the mainstream direction. Close to the inner casing this produces little classical secondary flow, as indicated by the velocity vectors and regions of positive vorticity, in the early stages of the OGV passage. However, eventually this initial momentum is overcome and, together with the thickening of the boundary layer, leads to a well-developed classical flow. At OGV exit, the vectors close to the hub ($r_n = 0.04$) clearly indicate a fluid movement from blade pressure to suction surface relative to the bulk motion, which is dominated by flow deviation. These observations are confirmed by the pitch-averaged yaw angles (Fig. 13), with classical flow overturning close to the inner casing only being observed downstream of the 60 percent chord location. Close to the outer casing classical secondary flow is indicated by regions of negative vorticity, and its development is enhanced by the rotor tip leakage. A more rapid generation of classical secondary flow is therefore observed, with flow overturning close to the outer wall being indicated by the flow angles at the 20 percent axial chord location (Fig. 13). Farther downstream, the thickness of the outer wall boundary layer is reduced by the radial flow redistribution. Hence, downstream of the 80 percent chord location flow overturning decreases and is at a minimum at the OGV trailing edge.

Airfoil Force and Flow Momentum Change. As indicated by Dring [10], at a given radius the difference between the force on an airfoil and the change in fluid momentum across

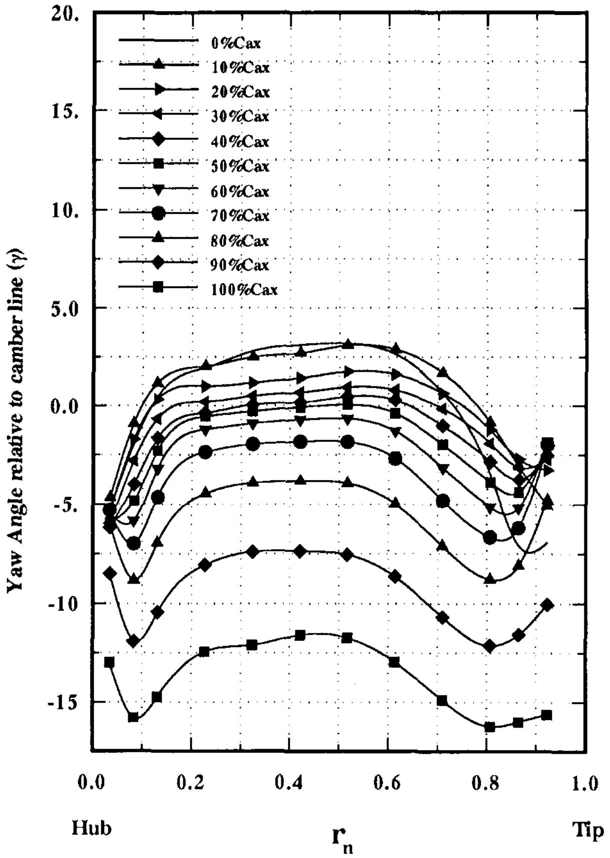

Fig. 13 Yaw angles within the OGV passage

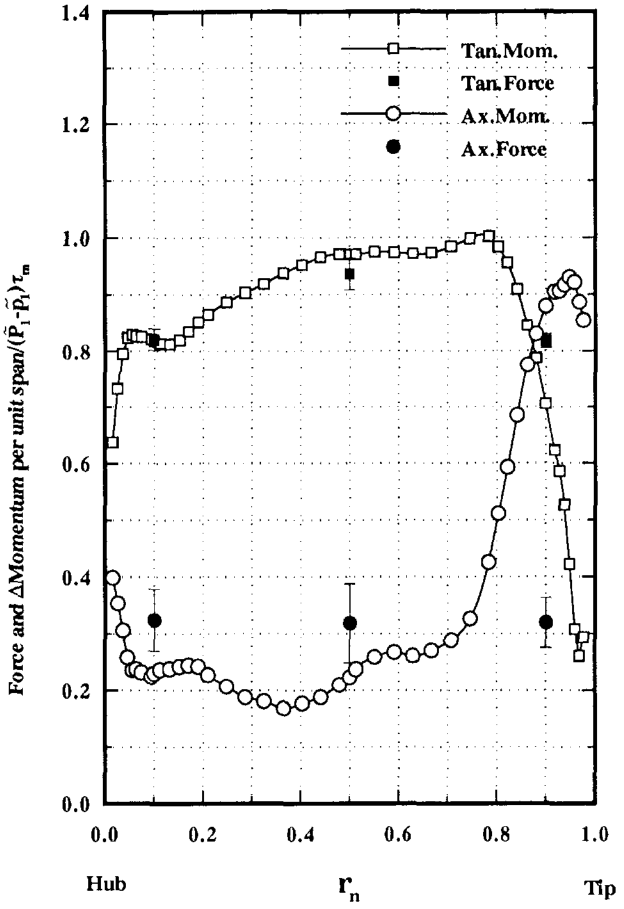

Fig. 14 Blade force and flow momentum change

the OGV row is a good indication of the radial transport and mixing within the blade passage. The measured surface static pressure distributions were used to calculate the axial and tangential components of force on the OGVs at 10, 50, and 90 percent spanwise locations. These forces were compared with the measured changes in flow momentum, which could be computed across the complete blade height. In Figs. 14 and 15, a solid symbol indicates a blade pressure force while a hollow symbol shows the change in flow momentum at a given radius between the upstream station (plane 1) and the plane downstream of the OGVs (Fig. 14) or within the blade passage (Fig. 15). The errors associated with the calculation of the blade force, shown in Fig. 14 by error bars, are due to the finite number of static tappings on the OGVs and their proximity to the blade leading edge. It can also be seen the axial force calculation is more sensitive to these error sources than the tangential component. An additional error of unknown magnitude must also occur for the calculation of flow momentum at planes within the OGV passage. This is due to the lack of information close to the airfoils with the data being extrapolated to the blade surface. The same method of presentation has been adopted as that outlined by Dring [10], with the axial component of momentum being the dimensionless form of the integrand in Eq. (3) while the tangential momentum is the dimensionless form of the integrand in Eq. (4) but without the final factor r. The differences between these radial distributions of force and momentum change therefore indicate the strength of the radial transport.

The changes in flow momentum observed across the airfoil row (Fig. 14) are similar to those observed by Dring [10] for his second-stage stator operating with a relatively large rotor tip clearance. Large variations in momentum change are observed close to the outer wall, which differ from that of the blade force being applied in this region. This is associated with the strong radial transport and mixing caused by rotor tip leakage. However, across the rest of the passage there appears to be reasonable agreement, within experimental error, between the blade forces and the changes in flow momentum. This is also confirmed by the changes in tangential momentum of the flow within the OGV passage and the forces that have been applied by the blade up to a given chordwise location (Fig. 15). This therefore suggests that, outside of the region affected by rotor tip leakage, radial transport is relatively weak. This is in contrast to the results of Dring [10] who found that near the hub, changes in tangential momentum exceeded the tangential blade force by a factor of 2.0. However, a hub corner stall was present in these tests and this stalled region is therefore thought to be the driving mechanism for the strong radial transport of fluid. The absence of such a region in the data presented here is therefore thought to account for the much smaller differences between the local blade force and momentum changes. This weaker radial mixing is thought to reflect that the dominant mechanism for this mixing is probably due to secondary flow and/or turbulent diffusion.

The total pressure distributions already presented (Fig. 9) indicate regions of relatively high loss on the blade suction surface close to each end wall, and also close to the inner casing midway between the blade surfaces. In two-dimensional cascade tests such pressure loss distributions have often been attributed to the convection of low-energy boundary layer fluid into these corner regions by secondary flows. However, measurements made on the third stage of a compressor by Gallimore and Cumpsty [5] indicated that, for their configuration, mixing was dominated by a turbulent diffusion process with secondary flows thought to be of limited significance in the circumferential direction only. The present investigation has measured well-defined secondary flow features in an OGV blade row downstream of a rotor. However, the magnitude of the sec-

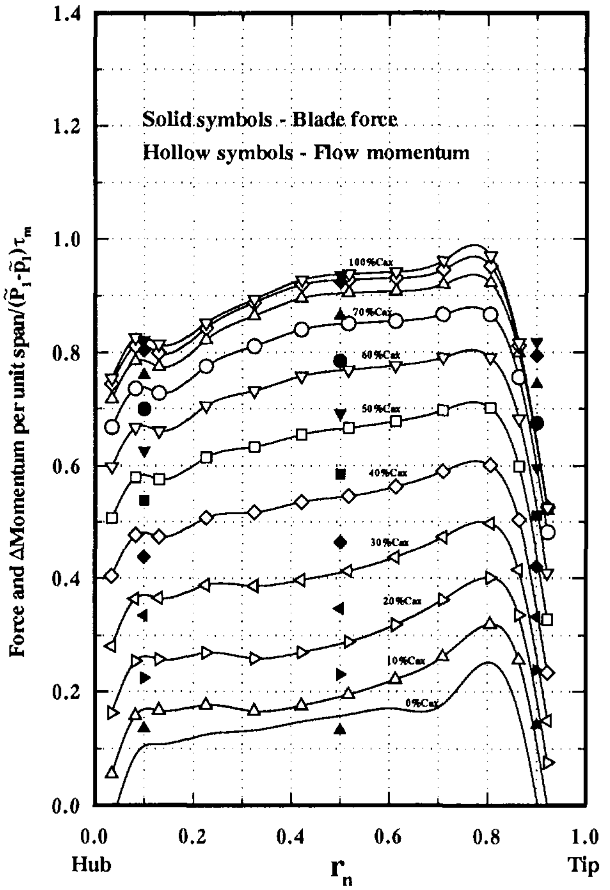

Fig. 15 Tangential blade force and flow momentum change within the OGV passage

ondary flow velocities in comparison with the streamwise component appears to be relatively small, as illustrated by the velocity components in the plane closest to the suction surface (Fig. 16). It should be noted that the distance of this plane from the blade surface varied from approximately 1 mm to 2.5 mm between the 20 and 80 percent axial chord locations. On this plane, radial convection of fluid by secondary flows is only discernible in the early stages of the passage and is limited to a few millimeters, this being of a similar order of magnitude to that observed by Gallimore and Cumpsty [5]. Similar effects were observed on the planes closest to the pressure surface and inner casing, although the latter case was complicated by the effects of flow deviation. This means that:

(*i*) Significant convection of low-energy fluid by secondary flows only occurs close to the blade surface and casing walls, which is outside the region surveyed in the present investigation; and/or

(*ii*) Mixing of fluid is dominated by turbulent diffusion. This is despite a single rotor stage, which will provide a modest turbulence level and differing amounts of inlet skew relative to the third stage of the compressor tested by Gallimore and Cumpsty [5].

Conclusions

Detailed measurements have been made of the flow field at inlet to, within, and downstream of an OGV blade row with inlet conditions being generated by a single-stage rotor. The following conclusions have been drawn:

- In the gap between rotor trailing edge and OGV leading edge significant changes in axial velocity and flow angle occurred, particularly close to the outer wall. The radial variation of incidence indicated skewing of the inlet profile to the OGVs.
- The blade pressure loss (λ) was 8.3 percent of the inlet dynamic head, and no areas of flow separation were observed within the OGV passage. Regions of relatively high loss were located on the suction surface close to each casing, and on the inner wall midway between blades. In the early stages of the blade passage a pressure drop occurred close to the outer wall, which was associated with rotor tip leakage flow.
- Significant changes in the overall level of velocity and static pressure only occurred downstream of the location of maximum blade thickness.
- At a given radius, differences between the blade force and the change in fluid momentum are small over most of the blade height indicating that radial transport and mixing is relatively weak.
- Classical secondary flow was observed close to each casing, while flows of opposite rotation occurred at greater immersion from the casings. These latter flows were due to the streamwise vorticity at inlet to the blade row associated with the skewed inlet profile.

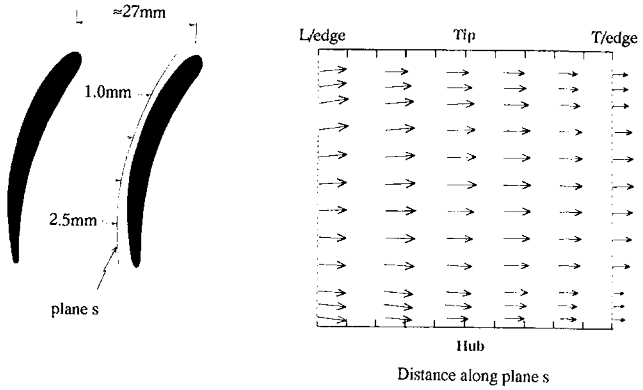

Fig. 16 Vector plot on plane closest to OGV suction surface

Acknowledgments

This work was supported by The Ministry of Defence, D.R.A., Pyestock, Farnborough, Contract No. AT/2170/090/XR. The authors also wish to express their thanks to Messrs. G. Hodson, R. Marson, and D. Glover for their assistance in the construction of the test rig, and to J. Hallet for his help in processing some of this data. The comments and suggestions put forward by R. P. Dring of UTRC prior to submission of this paper were also greatly appreciated by the authors.

References

1 Lieblein, S., "Experimental Flow in Two-Dimensional Cascades," NASA SP-36, 1965.

2 Gostelow, J. P., *Cascade Aerodynamics*, Pergamon Press, 1984.

3 Horlock, J. H., *Axial Flow Compressors*, Butterworths, 1958.

4 Joslyn, H. D., and Dring, R. P., "Axial Compressor Stator Aerodynamics," ASME *Journal of Engineering for Gas Turbines and Power*, Vol. 107, 1985, pp. 485-492.

5 Gallimore, S. J., and Cumpsty, N. A., "Spanwise Mixing in Multistage Axial Flow Compressors: Part I—Experimental Investigation," ASME JOURNAL OF TURBOMACHINERY, Vol. 108, pp. 2-9.

6 Wisler, D. C., Bauer, R. C., and Okiishi, T. H., "Secondary Flow, Turbulent Diffusion, and Mixing in Axial Flow Compressors," ASME JOURNAL OF TURBOMACHINERY, Vol. 109, 1987, pp. 455-482.

7 Stevens, S. J., and Young, K. F., "Axial Compressor Outlet Guide Vane Aerodynamics," AIAA Paper No. AIAA-87-1744, 1987.

8 Wray, A. P., "The Analysis of 5-Hole Probe Data Using Generalised Computer Software," Dept. of Transport Technology, Loughborough University, Report No. TT86R06, 1986.

9 Dring, R. P., and Spear, D. A., "The Effects of Wake Mixing on Compressor Aerodynamics," ASME JOURNAL OF TURBOMACHINERY, Vol. 113, 1991, pp. 600-607.

10 Dring, R. P., "Radial Transport and Momentum Exchange in an Axial Compressor," ASME JOURNAL OF TURBOMACHINERY, Vol. 115, pp. 477-486.

11 Young, K. F., "The Performance of Compressor Outlet Guide Vanes and Downstream Diffuser," Ph.D. Thesis, Loughborough University of Technology, Dec. 1988.

12 Horlock, J. H., "Annulus Wall Boundary Layers in Axial Compressor Stages," ASME *Journal of Basic Engineering*, Vol. 85, 1963, pp. 55-65.

13 Moore, R. W., and Richardson, D. L., "Skewed Boundary-Layer Flow Near the End Walls of a Compressor Cascade," *Trans. ASME*, Vol. 79, Nov. 1957.

T. R. Camp[1]
Rolls-Royce plc,
Derby DE24 8BJ,
United Kingdom

H.-W. Shin
General Electric Aircraft Engines,
Cincinnati, OH 45215

Turbulence Intensity and Length Scale Measurements in Multistage Compressors

This paper describes the measurement and processing of turbulence data from multistage low-speed compressors. Measurements were made at the same relative positions in three four-stage compressors, each having different levels of the design stage loading coefficient. A new method of data processing to calculate turbulence intensities and integral length scales is outlined. Using this method, integral length scales have been measured in turbomachinery flows for the first time. It is shown how the turbulence intensity and integral length scale vary with position in the blade passage, with changing flow coefficient and with the value of the design stage loading coefficient. The results have been used to specify representative inlet conditions for experimental rigs and to improve the application of CFD turbulence models to turbomachinery modeling.

Introduction

Compressor blading in aircraft gas turbine engines typically operates at low blade Reynolds numbers, at which condition transition of the boundary layers can occur over a wide range of chordwise positions. The exact position of the transition region has a strong influence on the performance of each blade row and, cumulatively, on the performance of the whole compressor. The position of transition depends heavily on the properties of the surrounding flow and, in particular, on the degree of turbulence.

There are two specific reasons why quantitative information about the turbulent nature of the flow inside multistage compressors is needed. The first stems from the requirement to model various aspects of the compressor flow field experimentally. Many experiments, in both rotating and stationary rigs, require the turbulence of the inlet flow to be representative of the levels occurring inside high-speed compressors to ensure representative results. An example of such an experiment is a wind tunnel at the Whittle Laboratory for modeling compressor blade leading-edge separation bubbles. Using the turbulence results presented here, the correct turbulence-generating grids were selected to provide representative turbulence intensity and scale in the inlet flow (described by Walraevens and Cumpsty, 1995).

A second reason for acquiring turbulence data is to enable more realistic applications of turbulence models to compressor CFD codes. In the past, the effects of wakes from an upstream blade row and of the turbulence between wakes (the background turbulence) have been modeled with the same turbulence parameters. As the significance of wake interaction on the blade boundary layers becomes clearer, however, more advanced CFD codes are beginning to model the wake effects separately from the background turbulence. Quantitative information about each of the two effects is therefore needed.

Velocity measurements in the multistage environment have strong periodic components at the blade passing frequency and at a number of its harmonics. Traces of velocity against time do not, however, show an exactly repeating pattern; there is a degree of "randomness" that makes each trace individual. The velocity fluctuations due to the components of the signal at blade passing frequency and its harmonics are usually known as "unsteadiness," while those due to the random component are described as "turbulence." Cherrett and Bryce (1991) found that wakes could be discerned at least two stages downstream of the blade row in which they were created, before being mixed into the background turbulence. The principal challenge in processing turbulence parameters from velocity measurements made in turbomachinery is to subtract the effects of unsteadiness from the raw data so that the turbulent components alone may be measured.

The two most significant turbulence parameters in this context are the turbulence intensity and the integral length scale. If we express a velocity signal as the sum of a time-mean component ($\bar{u}$) and a perturbation component (u') then the turbulence intensity is simply the root-mean-square of the perturbation component divided by the magnitude of the mean component.

That is, if $u_i = \bar{u} + u'_i$ then

$$\text{Turbulence intensity} = \frac{1}{\bar{u}} \sqrt{\frac{1}{N} \sum_{i=1}^{N} u_i'^2} \qquad (1)$$

The turbulence intensity expresses the "strength" of the

---

[1] Former address: Whittle Laboratory, Cambridge University, Cambridge, United Kingdom.

Contributed by the International Gas Turbine Institute and presented at the 39th International Gas Turbine and Aeroengine Congress and Exposition, The Hague, The Netherlands, June 13–16, 1994. Manuscript received by the International Gas Turbine Institute January 31, 1994. Paper No. 94-GT-4. Associate Technical Editor: E. M. Greitzer.

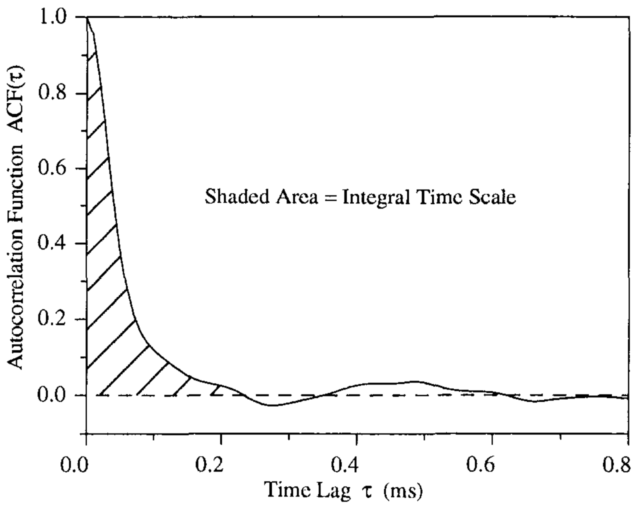

Fig. 1 Example autocorrelation function

turbulence while the integral length scale assigns a spatial dimension to the turbulence structure, often identified as the average eddy size. The route to calculating the integral length scale lies through the correlation of two velocity signals or, if Taylor's hypothesis is assumed as here, through the autocorrelation of a single velocity signal.

The autocorrelation function (ACF) is given by:

$$\mathrm{ACF}(\tau)=\frac{\frac{1}{\Delta T}\int_0^{\Delta T}u(t)u(t+\tau)dt}{\frac{1}{\Delta T}\int_0^{\Delta T}u^2(t)dt} \tag{2}$$

where ΔT is large compared to the period of the lowest frequency component of the signal with significant amplitude.

To calculate the integral length scale, the autocorrelation function is integrated with respect to the time lag (τ) to obtain the integral time scale, which is then multiplied by the mean velocity to give the length scale

$$\text{Integral length scale} = \bar{u}\int_0^{\infty}\mathrm{ACF}(\tau)d\tau \tag{3}$$

Figure 1 shows an autocorrelation function calculated from measured data. In practice, the integral was evaluated from $\tau = 0$ to the value at τ at which ACF(τ) first became zero, as indicated in the figure.

One can see that the definition of integral length scale is only valid for "random" signals (those with no periodic order) because the autocorrelation of a periodic signal is itself periodic and does not tend to zero as τ increases. This condition places a significant restriction on signals measured in turbomachinery environments and was the motivation for the new method of data processing, described in this paper.

Previous measurements of turbulence in turbomachinery have involved the measurement of turbulence intensity only. De Haller (1953) and Schlichting and Das (1969) measured the total unsteadiness (i.e., unsteadiness plus turbulence) inside multistage compressors and both reported values of about 6 percent. Evans (1976) measured turbulence intensity as a function of rotor position and showed how the unsteadiness and the turbulence levels changed as a function of flow coefficient. More recently, Wisler et al. (1987) measured turbulence intensity in a compressor of modern blading and showed that the turbulence intensity in the wakes and endwall regions can be as high as 27 percent. The effects of turbulence on transition (and subsequent loss and turning) in cascades were reported by Schlichting and Das (1969) and by Evans (1971).

Evans (1976) and Wisler et al. (1987) used the ensemble-averaging technique to separate the contributions due to unsteadiness from those due to turbulence. This technique requires the capture of many velocity traces, triggered as the rotor passes a fixed position, to calculate an ensemble-averaged velocity trace. By then subtracting the ensemble-averaged trace from each measured trace the perturbations attributed to the moving rotor field are removed, leaving the perturbations due to turbulence. It is then possible to calculate the intensity of the true turbulence at each rotor-locked position. Unfortunately it is not possible to use an identical method to calculate the turbulent length scale. To calculate an integral length scale we require long, continuously sampled measurements of a random signal. The technique of subtracting the ensemble-averaged trace to remove the periodic components does not suffice in this case because the data at each rotor-locked position are not part of one continuous time series. The calculation of turbulent length scales in a turbomachinery environment requires a more sophisticated method of data processing, such as the method described in this paper.

In this paper we describe the measurement and processing of turbulence data from three low-speed, four-stage compressor rigs. The data were used to calculate values of turbulence intensity and integral length scale within an embedded stage in each of the three compressors. The results show how the values of turbulence intensity and length scale change with position in the blade passage, with flow coefficient and with the value of the design stage loading coefficient. The paper describes a new method of data processing that enables the turbulence intensity and integral length scale to be calculated. In particular, this method has allowed integral length scales to be measured in turbomachinery flows for the first time.

Experimental Procedure

Turbulence measurements were made on three low-speed compressor rigs: the C106 compressor at the Whittle Laboratory, Cambridge, United Kingdom, the four-stage compressor at the Cranfield Institute of Technology (C.I.T.), Bedford, United Kingdom, and the Low-Speed Research Compressor (L.S.R.C.) at the G.E. Aerodynamics Research Laboratory, Cincinnati, OH. Each compressor rig contained four stages of blading plus inlet guide vanes, all having modern profiles and the same level of stage loading coefficient ($\Delta H/U^2$) for each stage. Table 1 gives details of the rotor diameters, tip speeds, and design stage loading coefficients for each compressor.

The flow velocity was measured at two axial locations in

Nomenclature

ACF = autocorrelation function
H = total enthalpy
i, j = index integers
M = number of samples
N = number of traces
Re = Reynolds number

T = time
Tu = turbulence intensity
U = blade speed
t = time
u = flow velocity
τ = time lag

ϕ = flow coefficient = Vx/U

Superscripts

$\_'$ = perturbation
$\_$ = time average
$\tilde{}$ = ensemble average

Table 1 Design details of the three test compressors

Compressor	Rotor Diameter (m)	Tip Speed (m/s)	Design Stage Loading
C106	0.508	77.4	0.40
C.I.T.	1.219	53.8	0.45
L.S.R.C.	1.524	47.9	0.54

Table 2 Stator 3 velocities and Reynolds numbers for the three test compressors

Compressor	Mean Velocities (m/s)		Re ($x10^5$)	
	Stator 3 inlet	Stator 3 exit	Rotor	Stator
C106	48.5	38.3	1.7	1.2
C.I.T.	53.5	39.0	1.8	2.1
L.S.R.C.	40.4	33.2	5.0	2.7

each compressor: upstream of the third stator (between stator three and rotor three) and downstream of the third stator (between stator three and rotor four). At both axial locations the radial position of the sensing element was midspan and the circumferential position was chosen to be in the middle of the stator passage, thereby avoiding strong potential effects near the stator leading edge and the stator wake at exit. Each set of velocity measurements was made while the compressor was running at its design operating point.

Table 2 gives the mean velocities upstream and downstream of the third stator and the rotor and stator Reynolds numbers (based on midspan chord) for each of the three compressors.

In the C106 and C.I.T. compressors, a subminiature single-element hot-wire probe was used to measure the velocities, whereas a hot-film probe of similar geometry was used in the L.S.R.C. To allow accurate comparisons of the results from each compressor, the measurement procedure and data processing techniques were the same in each case.

In each compressor the sensing element of the probe was aligned to be perpendicular to the radial direction and to the mean flow direction in the axial-tangential plane. With this orientation, perturbations in the radial and mean flow directions were detected, whereas perturbations normal to the mean flow direction in the axial-tangential plane (parallel to the sensing element) made only a very small contribution to the measured velocity. Measurements by Wisler et al. (1987), however, found the turbulence in an embedded stage to be very nearly isotropic and so it was decided that the use of single-element sensors would provide sufficient accuracy (to about two significant figures) as well as considerable simplification to the experimental procedure.

At each probe position, data were collected in two formats using the same data acquisition software. In the first "short" format, 300 velocity traces were measured, each long enough to record two blade passing periods (70 samples for the C106, 180 for the C.I.T. compressor, and 370 for the L.S.R.C.). The sampling of these traces was triggered by a rotor "once per rev." signal so that each trace was locked to the same rotor position. These datasets were processed with the conventional ensemble-averaging technique to calculate turbulence intensity as a function of rotor position. The second format was a "long" format containing a single, continuously sampled set of velocity measurements. For the C106 and C.I.T. compressors 4096 samples were recorded, while 16384 samples were measured on the L.S.R.C. These datasets were used as input to the Fourier analysis method of data processing to calculate both the turbulence intensity and the integral length scale.

Table 3 Blade passing frequencies and mean chords

Compressor	Blade Passing Frequency (kHz)	Mean R & S Chord at mid height (mm)
C106	2.814	36.0
C.I.T.	1.109	58.6
L.S.R.C.	0.540	118.6

The signals for both datasets were filtered at the same frequencies. A high pass filter of 0.1 Hz was used to remove the d.c. component from the signal, which was measured separately, allowing the a.c. component to be amplified for maximum resolution. Signals were low-pass filtered at 30 kHz and then sampled at 100 kHz (30 kHz is just over ten times the blade passing frequency for the C106 and much greater for the other two compressors). Considering the "long" format datasets, the sampling rate and length of the measured traces gave a resolution in the frequency domain of, at most, 24 Hz. The length of sampling for the C.I.T. compressor covered 45 blade passing periods; this was the lowest value of the three compressors but was still sufficiently large to ensure accurate calculation of the Fourier coefficients down to frequencies much lower than the blade passing frequency.

Along with these measurements, which were made on each of the three compressors, two extra sets of turbulence measurements were made on the C106 compressor. The first of these was a series of three area traverses of a hot wire in the stator 3 exit plane. The traverse grid consisted of 39 radial points by 43 circumferential points and covered two stator passages. Traverses were done at three values of flow coefficient: $\phi = 0.493$ (near stall), $\phi = 0.521$ (design), and $\phi = 0.758$ (high flow). At each traverse point the hot wire was rotated until perpendicular to the mean flow direction (in the axial-tangential plane) and then 4096 velocity samples were recorded. The data were processed using the Fourier analysis technique to obtain the turbulence intensity and integral length scale at each traverse point.

The second extra set of measurements on the C106 was a series of turbulence measurements made over a wide range of flow coefficients. During these measurements the hot wire was held fixed at midspan, perpendicular to the mean flow direction at the design point.

The Choice of Nondimensionals

Presenting the results of the experiments in a nondimensional form enables the turbulence values from the three compressors to be compared, and the results to be used in other applications, such as CFD.

It is worthwhile to consider how best to nondimensionalize the turbulence parameters and the frequencies at which the velocity signal was filtered and sampled. The choices here are based on the proposition that the main mechanisms for turbulence creation in turbomachinery are wake generation and wake chopping, i.e., the action of fluid flowing past a blade and the action of blades passing blades. The fundamental time scale in this mechanism is the blade passing period (the fundamental frequency therefore being the blade passing frequency). The travel time of a particle through a blade passage is another suitable choice, and is of similar magnitude to the blade passing period. Here we use the blade passing frequency to nondimensionalize the sampling and filtering frequencies.

We would expect the turbulence levels to correlate well with wake thickness but, when choosing a length scale for the mechanism, a more convenient dimension is the blade chord. Here we use the average of the rotor and stator chords at midheight to nondimensionalize the measured length scales.

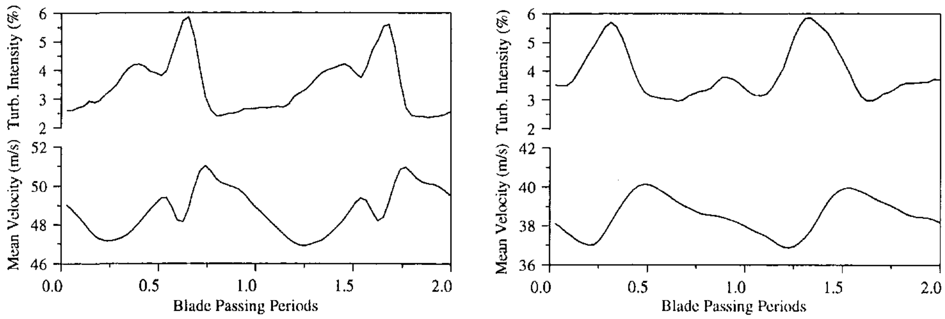

a) Upstream of Stator 3

b) Downstream of Stator 3

Fig. 2 Ensemble-averaged results—C106 compressor

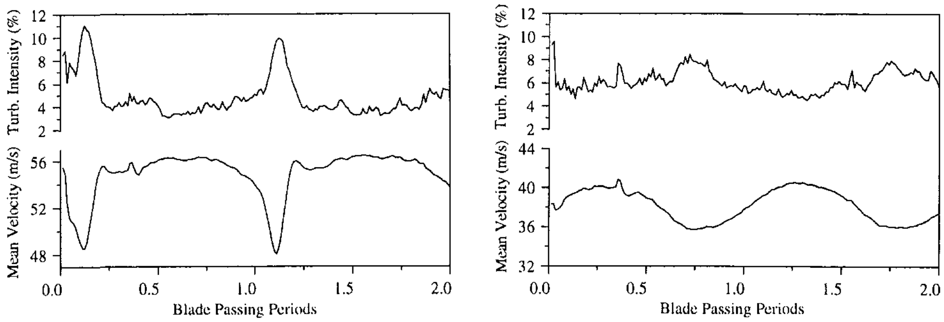

a) Upstream of Stator 3

b) Downstream of Stator 3

Fig. 3 Ensemble-averaged results—C.I.T. compressor

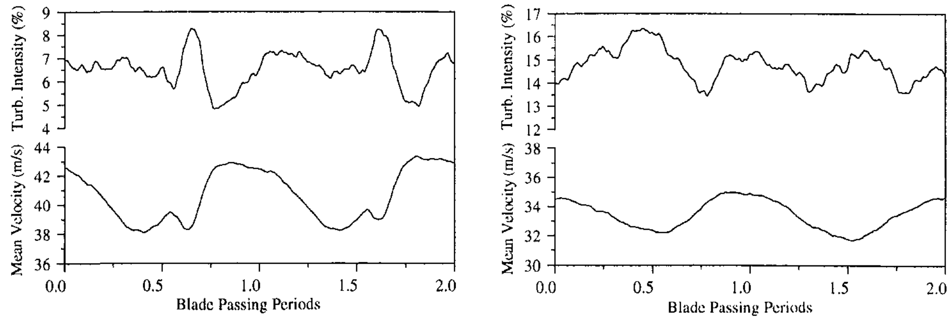

a) Upstream of Stator 3

b) Downstream of Stator 3

Fig. 4 Ensemble-averaged results—L.S.R.C.

Table 3 gives the blade passing frequencies and the mean chords for each of the three test compressors.

As can be seen from the definition of turbulence intensity given in the introduction, this parameter has no dimensions: The rms velocity perturbation is nondimensionalized by dividing it by the mean velocity. If the velocity *u* is thought of as a vector, the rms term is constant and does not depend on whether the velocity is measured in a rotating or stationary frame of reference. The mean velocity, however, does depend on the frame of reference and dividing by this quantity means that the turbulence intensity is itself dependent on the frame of reference.

Considering the length scale, the integral time scale is independent of the frame of reference, but the introduction of the mean velocity into the length scale definition causes the value of the integral length scale to depend on the frame of reference. The complication introduced by the choice of reference frame sometimes makes it simpler to use the rms perturbation and integral time scale directly.

Calculation Procedures and Results

The datasets in the "short" and "long" formats, recorded at the same measuring positions, were processed separately. The short datasets were processed with the conventional ensemble-averaging technique while the long datasets were processed using a new technique based on Fourier analysis of the velocity signal. Section (1) below describes the processing of and results from the short format datasets, while the processing and results of the long format datasets are described in section (2). The variation of the turbulence intensity and integral length scale with position in the stator passage and with flow coefficient are described in sections (3) and (4), respectively.

(1) Data Processing and Results From the Short Datasets. This process was used to calculate turbulence intensity as a function of rotor position. The short format datasets were processed using the ensemble-averaging technique, as summarized below:

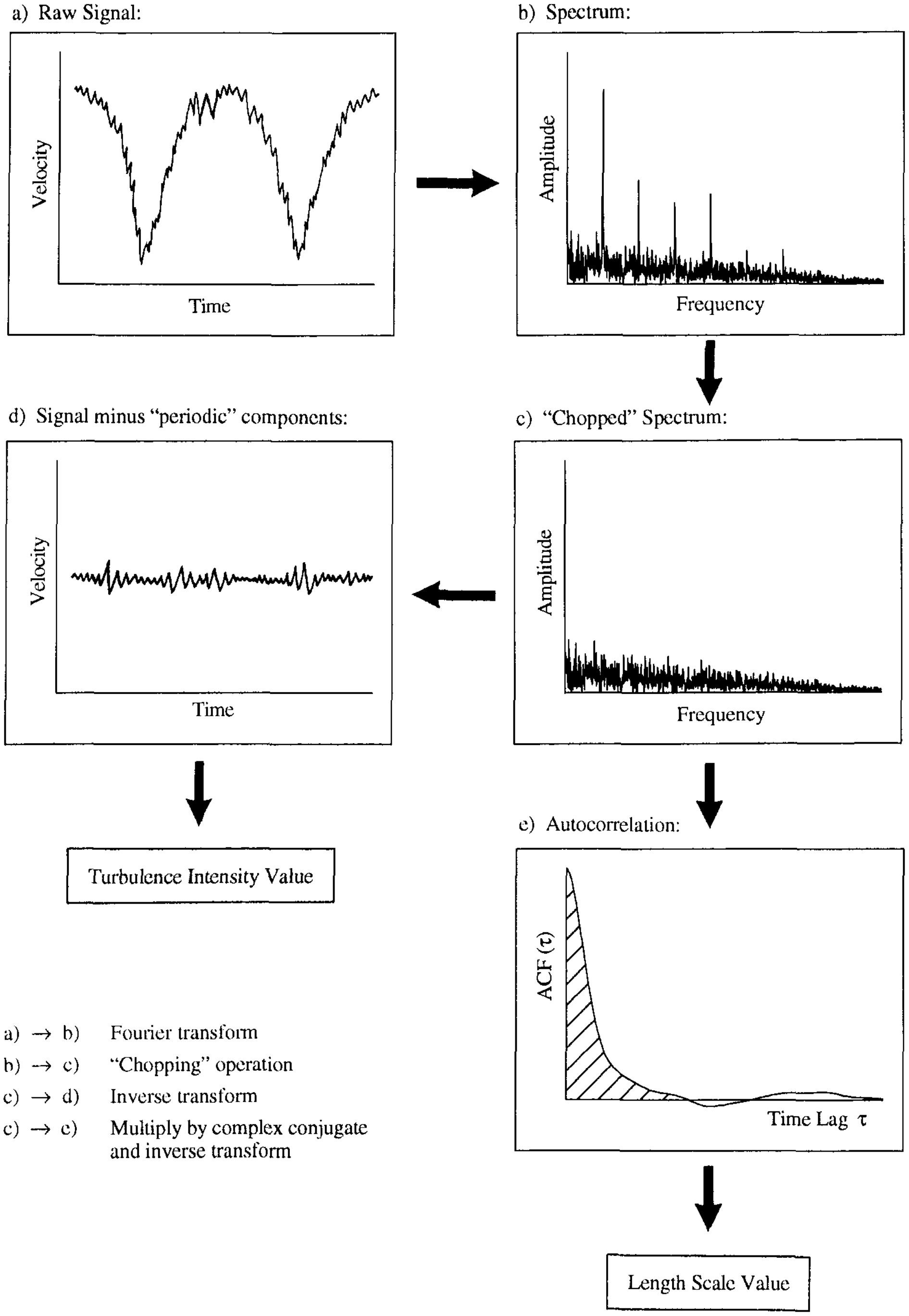

Fig. 5 Fourier transform calculation procedure

Consider N velocity traces:

$$u_i(t) \quad \text{where} \quad i = 1, N$$

The ensemble-averaged velocity is given by:

$$\tilde{u}(t) = \frac{1}{N} \sum_{i=1}^{N} u_i(t)$$

and the time-averaged velocity by:

$$\bar{u} = \frac{1}{M} \sum_{j=1}^{M} \tilde{u}(t_j)$$

where M is the number of samples recorded during an integer number of blade passing periods.

By subtracting the ensemble-averaged trace from the raw data, the periodic component of the signal is removed, leaving the perturbation velocity $u_i'(t)$:

$$u_i'(t) = u_i(t) - \tilde{u}(t)$$

The turbulence intensity can then be calculated at each rotor position as:

$$Tu(t) = \frac{1}{\bar{u}} \sqrt{\frac{1}{N} \sum_{i=1}^{N} u_i'^2(t)^2} \tag{4}$$

Figure 2 shows the turbulence intensity and mean velocity results processed using this technique from data measured upstream and downstream of the third stator in the C106 compressor. Figures 3 and 4 show equivalent results from the C.I.T. and L.S.R.C. compressors.

Each set of results from the upstream measuring position shows features that are periodic with blade passing frequency. The rotor 3 wakes are seen as peaks in the turbulence intensity traces, which are slightly nearer the suction surface of the rotor blades relative to the velocity minima. The shape of each trace is very sensitive to the angular orientation of the probe and this may explain some of the differences in the shapes of the traces between the three compressors. Differences are also due to the stage loading coefficient, as can be seen from the L.S.R.C. velocity trace in Fig. 4(*a*), which shows a much wider wake owing to the higher level of loading (and therefore turning). Other differences in the traces can be assigned to the different values of the nondimensional sampling frequency (sampling frequency/blade passing frequency) for each compressor. This, for example, caused the C106 traces, measured with a lower nondimensional sampling frequency, to appear smoother than the traces from the other two compressors.

The turbulence intensity results from each compressor show smaller secondary peaks in intensity between the peaks corresponding to the wakes from rotor 3. It seems likely that these secondary peaks are the remains of the chopped wakes from stator 2. The C106 traces, which show these peaks clearly, show them to be close to the pressure surface of the rotor blades. This is consistent with the higher incidence with which the slower moving wake fluid from stator 2 impinges onto rotor 3 (the "negative-jet" effect).

Downstream of stator 3 (Figs. 2*b*, 3*b*, and 4*b*) the wake from rotor 3 is less evident as it is more mixed out. Consequently the mean velocity traces are less "spiky" and the C.I.T. and L.S.R.C. velocity traces are nearly sinusoidal in shape. The intensity traces also show much smaller variations with rotor position.

(2) Data Processing and Results From the Long Datasets. To calculate the length scale of the turbulence as well as the intensity, a new method of data processing was developed to overcome the restriction on periodic signals imposed by the definition of the integral length scale. In this method the "periodic" components of the signal (those components at blade passing frequency and its harmonics) were digitally filtered out by Fourier transforming the signal into the frequency domain and then setting the components at blade passing frequency and its harmonics (up to five harmonics in practice) to zero amplitude.

This method for calculating the turbulence intensity and integral length scale from the long datasets is shown schematically in Fig. 5. Figure 5(*a*) represents a section of the raw velocity trace, as recorded. Fourier transformation of this signal into the frequency domain reveals the spectrum, shown in Fig. 5(*b*). At this point the amplitudes of the components at blade passing frequency and its harmonics are set to zero. This operation gives the "chopped" spectrum shown in Fig. 5(*c*). This spectrum is now transformed back into the time domain to give the turbulent signal, shown in Fig. 5(*d*) from which the turbulence intensity is calculated. The Fourier coefficients of the "chopped" spectrum are also used directly, using the Wiener–Khinchin Theorem, to calculate the autocorrelation function (Fig. 5*e*) from which the length scale is calculated.

This method requires a comparatively small amount of data (4096 velocity samples for the C106 and C.I.T. compressors) and the use of the Fourier coefficients to calculate the autocorrelation function directly makes the calculation procedure very fast. The storage and speed advantages of the technique made it possible to implement the method on an 80386 personal computer, and also made it possible to measure turbulence at a large number of points over the stator passage (as reported in section (3), following).

The turbulence intensity and length scale results from the long format datasets are summarized in Tables 4 and 5.

Table 4 RMS and turbulence intensity results from the Fourier transform technique

	RMS velocity (m/s)		Turbulence Intensity (%)	
Compressor	Stator 3 inlet	Stator 3 exit	Stator 3 inlet	Stator 3 exit
C106	1.75	1.65	3.6	4.3
C.I.T.	2.03	2.03	3.8	5.2
L.S.R.C.	2.83	3.69	7.0	11.1

Table 5 Integral time scale and length scale results from the Fourier transform technique

	Time Scale (μs)		Length Scale (% of mean Chord)	
Compressor	Stator 3 inlet	Stator 3 exit	Stator 3 inlet	Stator 3 exit
C106	26.8	37.4	3.6	4.0
C.I.T.	52.4	94.5	4.8	6.3
L.S.R.C.	207.4	370.0	7.1	10.4

It can be seen that as the flow passes through the stator blade passage, the level of turbulence intensity increases slightly. This is primarily a consequence of the mean velocity falling while the rms perturbation size stays approximately constant. The length scales are seen to increase through the stator passage, which is consistent with measurements made downstream of turbulence-generating grids where the scale increases in the downstream direction as the smaller eddies are dissipated faster (as reported by Roach, 1987, and by Baines and Peterson, 1951).

Tables 4 and 5 also show that, while the intensities and length scales are similar for the C106 and C.I.T. compressors, the values of both parameters are significantly higher for the L.S.R.C. As the main mechanism for turbulence creation in turbomachinery is wake generation and wake chopping, one would expect the turbulence levels to correlate strongly with wake thickness and therefore with stage loading coefficient. This is confirmed by Figs. 6 and 7, which show the intensity and length scale results plotted as functions of design stage loading coefficient.

(3) Area Traverse Results. Using the C106 compressor, area traverses were performed midway between stator 3 and rotor 4 at three flow coefficients. The data were processed using the Fourier transform technique to give values of turbulence intensity and length scale over the stator passage at each flow coefficient. The results of these traverses are shown in Fig. 8, where the intensity and length scale results have been plotted as shaded contours over maps of the traverse area.

Figure 8(*b*) shows the traverse results at the design value of flow coefficient. Here the stator wake is clearly distinguishable as a region of high turbulence intensity (up to 30 percent). The wake region thickens toward the hub, where velocity traverse results showed a region of separation on the stator suction surface. High values of turbulence intensity are also present at a separation in the suction surface/casing corner and on the hub endwall. In the mainstream, the turbulence intensity has a trend, which decreases from 16 percent near the hub to 4 percent near the casing. As expected, the lowest values of length scale are seen to occur in the stator wakes, which contain recent boundary layer fluid and therefore eddies that are similar in scale to the boundary layer thickness.

Figure 8(*a*) shows the results of a traverse conducted at a flow coefficient near stall ($\phi = 0.493$). At this flow rate, the separated region on the stator suction surface has become

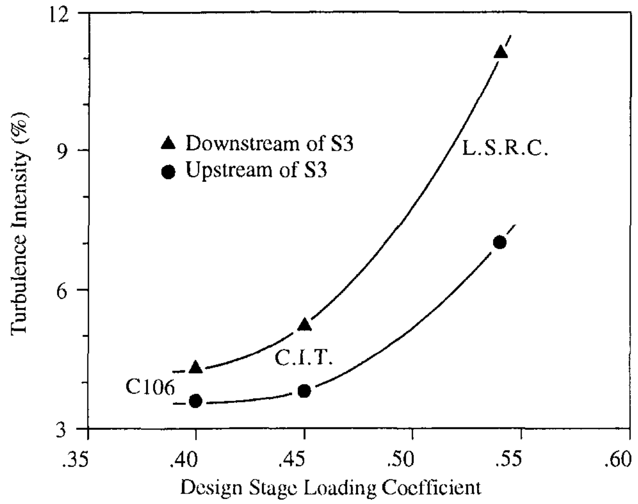

Fig. 6 Turbulence intensity as a function of design stage loading coefficient

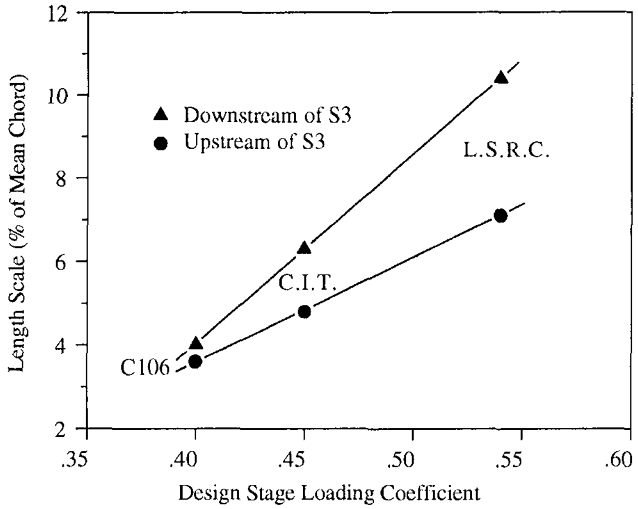

Fig. 7 Length scale as a function of design stage loading coefficient

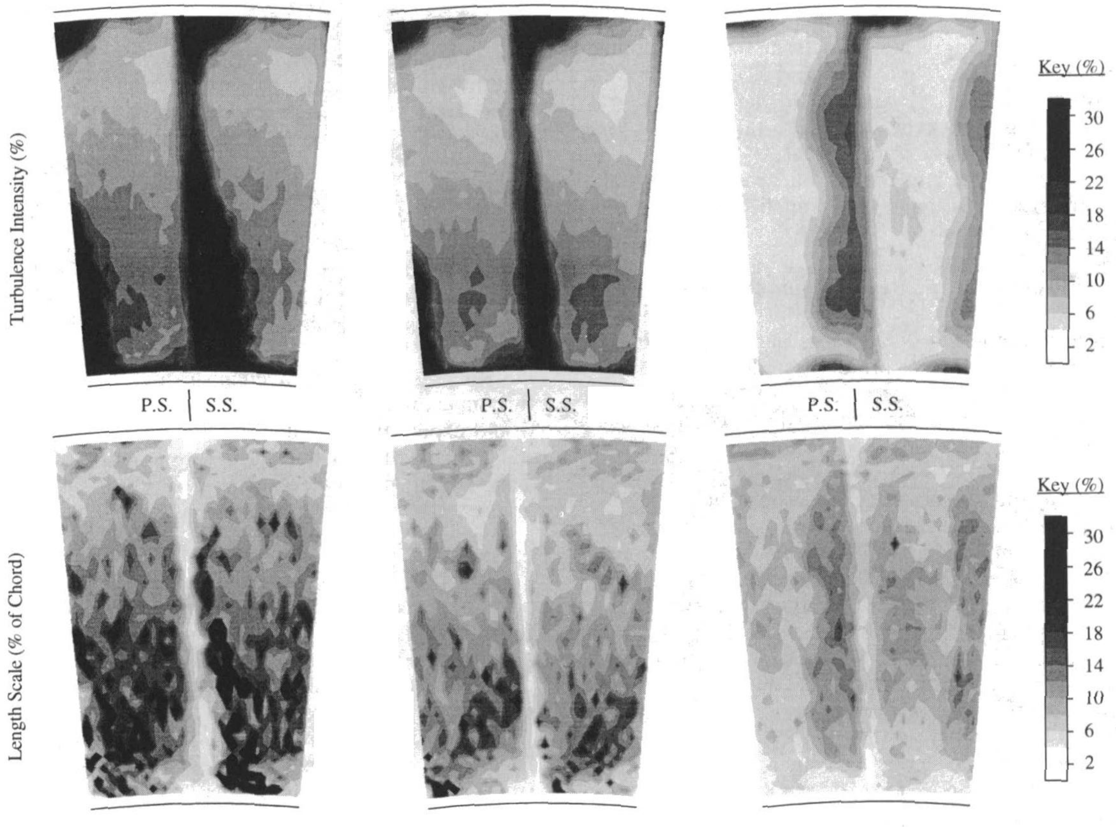

a) ϕ = 0.493 (near stall)

b) ϕ = 0.521 (design)

c) ϕ = 0.758 (high flow)

Fig. 8 Area traverse results

significantly larger and this is seen as a wide region of high turbulence intensity near the hub. The separated region at the casing, however, has not increased in size. The length scale results show that the largest length scales were measured at the boundary between the separated region on the suction surface and the mainstream flow. This implies the creation of new eddies in the shear layer between the separated region and the mainstream flow.

The results from the traverse at a high flow coefficient ($\phi = 0.758$), Fig. 8(c), show a very different distribution of the turbulence properties owing to the large negative incidence angle at this condition. The turbulence intensity results show thick regions of high intensity on the stator pressure surfaces, corresponding to regions of separation on the pressure surfaces. Intensity values in the midpassage are generally lower than those at the design flow coefficient. Endwall effects are much smaller at this high flow condition and consequently the flow is much more uniform across the span. Length scales are also generally lower; the wakes are just discernible as regions of smaller length scale while the separated regions on the pressure surfaces appear as regions of slightly larger scale.

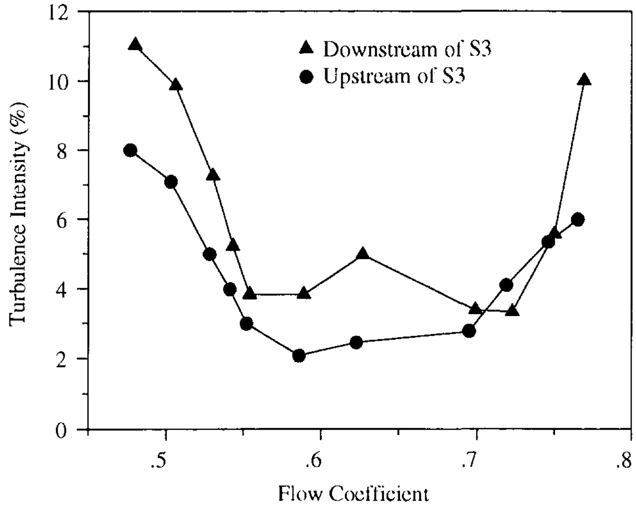

Fig. 9 Turbulence intensity as a function of flow coefficient

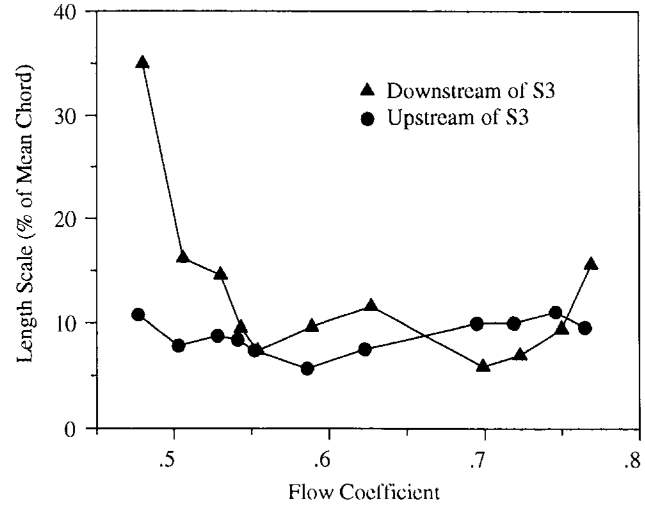

Fig. 10 Length scale as a function of flow coefficient

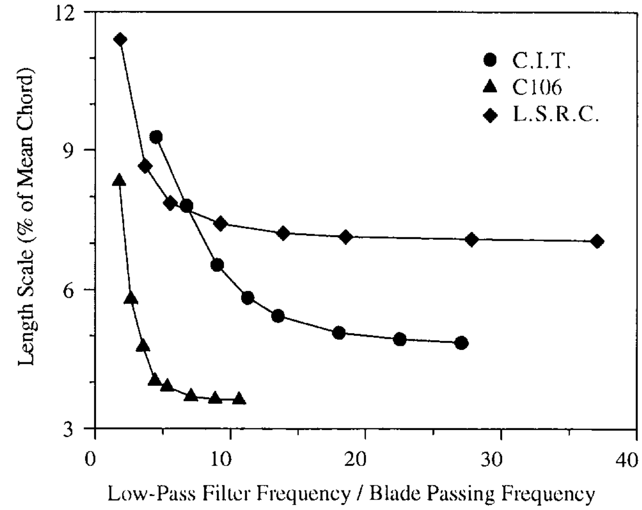

Fig. 11 Calculated upstream length scales as a function of theoretical low-pass filter setting

(4) Turbulence Variation With Flow Coefficients. The C106 compressor was also used to study how turbulence values at midpassage changed over the whole compressor characteristic. For these measurements the hot-wire probe was positioned perpendicular to the mean flow direction at the design point and velocity traces were recorded at a range of flow coefficients over the compressor's characteristic. These results are plotted in Figs. 9 and 10. The turbulence intensities measured at the upstream and downstream positions are approximately constant between flow coefficients of 0.55 and 0.70 and increase rapidly at lower and higher flows. The length scale measured downstream of stator three shows a similarly "bucket-shaped" variation over the characteristic whereas the upstream length scale remains approximately constant. Evans (1971) measured the changes in turbulence intensity in a similar manner but over a much smaller range of flow coefficient ($\Delta\phi = 0.1$). Consequently, he observed only the increasing turbulence intensity at low flow coefficients.

The increases in turbulence at low and high flow coefficients may be explained in terms of thicker wakes being shed from upstream blade rows, as revealed by the area traverses described above.

Discussion

(1) The Importance of Sampling Frequency. The measurements made during the course of this study highlighted the importance of the sampling and low-pass filter frequencies during data acquisition.

To calculate the turbulence intensity, no low-pass filtering of the velocity signal is required. The only considerations are that sufficient samples are taken to ensure statistical accuracy and that the sampling time is long compared to the period of the lowest frequency component of the signal. Data for length scale calculations, on the other hand, do require careful low-pass filtering to eliminate the effects of aliasing. This is due to the inherent "reconstruction" of the signal in the autocorrelation calculation from which the length scale is found. From the sampling theorem, the sampling rate must be at least twice the cut-off frequency of the low-pass filter.

The question arises as to how high the low-pass filter frequency should be, and therefore how fast one must sample to obtain accurate measurements of intensity and scale. To find the answer to this question, measured data from each of the three compressors were reprocessed to simulate the effects of using low-pass filters with lower cut-off frequencies. The Fourier transform method of data processing was used, but instead of only removing the components at blade passing frequency and its harmonics, a range of components were removed from the highest frequency recorded down to a new theoretical low-pass filter setting. Length scales calculated by this method for the upstream position are shown plotted against nondimensional low-pass filter setting in Fig. 11. As one would expect, elimination of the higher frequency components in the signal (those with the smallest wavelengths) leads to a higher value of length scale, the true values corresponding to the flat regions of the curves. Figure 11 shows that the required low-pass filter setting is (at least) 20 times the blade passing frequency. A plot of turbulence intensity, calculated from the same datasets, against low-pass filter setting led to the same conclusion.

The fact that very high frequencies are required to measure turbulence in turbomachinery means that the speeds of suitable test compressors are restricted by the frequency response of the instrumentation. The ability of a hot wire, for example, to measure high-frequency velocity perturbations depends on the length of the wire and the velocity of the oncoming flow. This kinematic effect was first considered by Frenkiel (1948), and in more detail by Uberoi and Kovasznay (1953) and Wyngaard (1968, 1969). If we consider the maximum frequency signal that can be measured accurately by a subminiature hot wire at typical flow rates to be at 60 kHz, this implies a low pass filter setting of 30 kHz and therefore a limit of 1.5 kHz on blade passing frequency (dividing by the ratio of 20 described above). The C106 is the only one of the three compressors in this study to exceed this speed and this fact may explain the steeper fall of the C106 line in Fig. 11. The requirement is therefore for high-frequency response instrumentation and/or large-scale experimental rigs.

(2) Filtering Considerations. It has been suggested that, during the processing of the long format datasets, components of the velocity in the range from 0 Hz to blade passing frequency should be removed, as well as those at blade passing frequency and its harmonics. This would remove unwanted contributions from sources such as rough bearings, nonuniformity in blade spacing, resonances in ducting, etc. Generally, however, this would not be correct because, although the main input into the mechanism of turbulence creation (the action of blades passing blades) occurs at the blade passing frequency, this can excite responses at lower frequencies in a nonlinear system. In cases where unwanted sources such as signals at shaft frequency are large, these can be identified in the velocity spectrum and should be removed individually.

The three compressor rigs that were used in this study each had equal numbers of rotor blades in all stages, thus giving a unique blade passing frequency for each machine. It was relatively easy, therefore, to remove the components of the signal at blade passing frequency and its harmonics. For compressors with different numbers of rotor blades in each row, and therefore several blade passing frequencies, the removal of the "periodic" components from the velocity spectrum (including beat frequencies) would be more difficult. In this case it would be possible to use a method based on the ensemble-averaging technique whereby a large number of long format data sets were recorded, the acquisition of each one being triggered by a "once per rev." signal. An ensemble-averaged trace could then be calculated and subtracted from any one of the raw data traces to provide input data for the length scale calculation. The autocorrelation function in this case could be calculated using the Fourier transform of the signal or by the shift-and-multiply method. The disadvantage of this procedure compared to the Fourier transform method described here, however, is that a great deal more data storage is required.

Conclusions

From the measurements of turbulence intensity and integral length scale described in this paper, the following conclusions can be drawn:

1 Turbulence levels in an embedded stage of a compressor of typical stage loading coefficient (0.45) are:

At bladerow inlet: Turbulence intensity = 3.8 percent
Integral length scale/mean chord = 4.8 percent
At bladerow exit: Turbulence intensity = 5.2 percent
Integral length scale/mean chord = 6.3 percent

2 The levels of turbulence intensity and integral length scale both increase significantly with an increasing value of design stage loading coefficient.

3 To measure turbulence intensity and length scale in a compressor flow it is necessary to record frequencies up to 20 times the blade passing frequency. A corollary of this is that, with current instrumentation, the full turbulence spectrum may only be measured on low-speed compressors.

4 A new method of processing turbulence data has been developed that uses the Fourier transform of the velocity signal. This allows both integral length scale and turbulence intensity to be calculated from a small amount of data in a short computational time.

Acknowledgments

The authors are very grateful to several people for their help, and for their permission to make the measurements described in this paper.

For permission to use and publish data from the C106, the L.S.R.C., and the C.I.T. compressor, we are very grateful to Rolls-Royce plc, G.E. Aircraft Engines and Dr. Paul Ivey. We are also grateful to Mr. David Barlow, Mr. Donald Menner, and Mr. Bernard Charnley for their technical assistance during the course of the experiments.

We would like to thank Mr. James Place for his help during the development of the data processing techniques.

Finally, we would like to acknowledge the financial support of Rolls-Royce plc and of G.E. Aircraft Engines for the first and second authors, respectively.

References

Baines, W. D., and Peterson, E. G., 1951, "An Investigation of Flow Through Screens," *Trans. ASME*, Vol. 73, pp. 467-480.

Cherrett, M. A., and Bryce, J. D., 1991, "Unsteady Viscous Flow in a High Speed Core Compressor," ASME JOURNAL OF TURBOMACHINERY, Vol. 114, pp. 287-294.

Evans, B. J., 1971, "Free-Stream Turbulence Effects in a Compressor Cascade," Ph.D. Dissertation, University of Cambridge, United Kingdom.

Evans, R. L., 1976, "Some Turbulence and Unsteadiness Effects in Turbomachinery," in: S.N.B. Murphy, *Turbulence in Internal Flows*, Hemisphere Publishing Corp., New York.

Frenkiel, F. N., 1948, "Etude Statistique de la turbulence, 1 Mesure de la turbulence avec un fil chaud non-compense, 2 Influence de la longueur d'un fil chaud compense sur la mesure de la turbulence," O.N.E.E.A. Rapp. Tech. 37.

De Haller, P., 1953, "Das Verhalten von Tragflugelgittern in Axialverdichtern und in Windkanal," *Brennstoff-Warme-Kraft*, Vol. 5, No. 10.

Roach, P. E., 1987, "The Generation of Nearly Isotropic Turbulence by Means of Grids," *Journal of Heat and Fluid Flow*, Vol. 8, No. 2, pp. 82-92.

Schlichting, H., and Das, A., 1969, "On the Influence of Turbulence Level on the Aerodynamic Losses in Axial Turbomachines," *Proceedings of the Symposium on Flow Research on Blading*, Brown Boveri and Co. Ltd., Baden, Switzerland; also in: L. S. Dzung, ed., *Flow Research on Blading*, Elsevier Publishing Company, 1970.

Uberoi, M. S., and Kovasznay, L. S. G., 1953, "On Mapping and Measurement of Random Fields," *Quarterly of Applied Mathematics*, Vol. 10, pp. 375-393.

Walraevens, R. E., and Cumpsty, N. A., 1995, "Leading Edge Separation Bubbles on Turbomachine Blades," ASME JOURNAL OF TURBOMACHINERY, Vol. 117, this issue, pp. 115-125.

Wisler, D. C., Bauer, R. C., Okiishi, T. H., 1987, "Secondary Flow, Turbulent Diffusion and Mixing in Axial-Flow Compressors," ASME JOURNAL OF TURBOMACHINERY, Vol. 109, pp. 455-482.

Wyngaard, J. C., 1968, "Measurement of Small-Scale Turbulence Structure With Hot Wires," *Journal of Physics E*, Vol. 1, pp. 1105-1108.

Wyngaard, J. C., 1969, "Spatial Resolution of the Vorticity Meter and Other Hot-Wire Arrays," *Journal of Physics E*, Vol. 2, pp. 983-987.

Control-Oriented High-Frequency Turbomachinery Modeling: Single-Stage Compression System One-Dimensional Model

O. O. Badmus
Graduate Student,
School of Chemical Engineering.

S. Chowdhury
Graduate Student,
School of Aerospace Engineering.

K. M. Eveker[1]
Air Force Laboratory
Graduate Fellow,
School of Aerospace Engineering.

C. N. Nett[1]
Associate Professor;
Director, Laboratory for Identification
and Control of Complex Highly
Uncertain Systems (LICCHUS),
School of Aerospace Engineering.

Georgia Institute of Technology,
Atlanta, GA 30332-0150

In this paper, a one-dimensional unsteady compressible viscous flow model of a generic compression system previously developed by the authors is applied to a multistage axial compressor experimental rig configured for single-stage operation. The required model parameters and maps are identified from experimental data. The resulting model is an explicit system of nine first-order ODEs. The model inputs are compressor speed, nozzle area, compressor discharge bleed area, plenum bleed area, inlet total pressure and entropy, and nozzle and bleed exit static pressures. The model and experimental data are compared with respect to both open-loop uncontrolled and closed-loop controlled behaviors. These comparisons focus on (i) forced transients and (ii) global nonlinear dynamics and bifurcations. In all cases the agreement between the model and experimental data is excellent. Of particular interest is the ability of the model, which does not include any hysteretic maps, to predict experimentally observed hysteresis with respect to the onset and cessation of surge. This predictive capability of the model manifests itself as the coexistence of a stable equilibrium (rotating stall) and a stable periodic solution (surge) in the model at a single fixed set of system input values. Also of interest is the fact that the controllers used for closed-loop comparisons were designed directly from the model with no a posteriori tuning of controller parameters. Thus, the excellent closed-loop comparisons between the model and experimental data provide strong evidence in support of the validity of the model for use in direct model based controller design. The excellent agreement between the model and experimental data summarized above is attributed in large part to the use of effective lengths within the model, as functions of axial Mach number and nondimensional compressor rotational speed, as prescribed by the modeling technique. The use of these effective lengths proved to be far superior to the use of physical lengths. The use of these effective lengths also provided substantial improvement over the use of physical lengths coupled with fixed first-order empirical lags, as proposed by other authors for the modeling of observed compressor dynamic lag. The overall success of this model is believed to represent a positive first step toward a complete experimental validation of the approach to control-oriented high-frequency turbomachinery modeling being developed by the authors.

1 Introduction

In [1, 2] the authors presented the theoretical foundations of a new approach for control-oriented high-frequency turbomachinery modeling. This approach was subsequently used by the authors in [3] to develop one-dimensional unsteady compressible viscous flow models for a generic turbojet engine and a generic compression system. In this paper, the generic compression system model presented in [3] is applied to the LICCHUS ("like us")[2] multistage axial compressor rig [4], configured for single-stage operation. The main goal of this study is to take some first steps toward a complete experimental validation of the approach to control-oriented high-frequency turbomachinery modeling being developed by the authors.

The required model parameters and maps are identified from experimental data using the techniques described in [1, 2]. The resulting model is an explicit system of nine first-order

---

[1] Current address: United Technologies Research Center, East Hartford, CT.

Contributed by the International Gas Turbine Institute and revised from a paper presented at the 38th International Gas Turbine and Aeroengine Congress and Exposition, Cincinnati, Ohio, May 24-27, 1993. Manuscript received at ASME Headquarters February 12, 1993. Paper No. 93-GT-18. Associate Technical Editor: H. Lukas.

[2] Acronym for the Laboratory for Identification and Control of Complex Highly Uncertain Systems, School of Aerospace Engineering, Georgia Institute of Technology.

ODE's. The model inputs are compressor speed, nozzle area, compressor discharge bleed area, plenum bleed area, inlet total pressure and entropy, and nozzle and bleed exit static pressures.

The model and experimental data are compared with respect to both open-loop uncontrolled and closed-loop controlled behaviors. These comparisons focus on (*i*) forced transients and (*ii*) global nonlinear dynamics and bifurcations [5]. In all cases the comparison between the model and experimental data is excellent. Of particular interest is the ability of the model, which does not include any hysteretic maps, to predict experimentally observed hysteresis with respect to the onset and cessation of surge. This predictive capability of the model manifests itself as the coexistence of a stable equilibrium (rotating stall) and a stable periodic solution (surge) in the model at a single fixed set of system input values.

Also of interest is that the controllers used for closed-loop comparisons were designed directly from the model with no a posteriori tuning of controller parameters. Thus, the excellent closed-loop comparisons between the model and experimental data provide strong evidence in support of the validity of the model for use in model-based controller design.

The excellent agreement between the model and experimental data summarized above is attributed in large part to the use of effective lengths within the model, as functions of axial Mach number and nondimensional compressor rotational speed, as prescribed by the modeling technique [3]. The use of these effective lengths proved to be far superior to the use of physical lengths. The use of these effective lengths also provided substantial improvement over the use of physical lengths coupled with fixed first-order empirical lags, as proposed in [6] and used in [7–11] for the modeling of observed compressor dynamic lag.

1.1 Historical Perspective. Many one-dimensional high-frequency turbomachinery models have been presented in the literature. For quasi-one-dimensional incompressible flow in compression systems, models of this type are given in [6, 12, 13, 10]. For quasi-one-dimensional compressible flow in compression systems, models of this type can be found in [14, 15, 7, 11]. For quasi-one-dimensional compressible flow in full engine systems, models of this type are given in [9, 16–19]. The model given in this paper is a quasi-one-dimensional compressible flow model. The advantages of the model presented in this paper over others of this type presented in the literature include: (1) a rigorous procedure for embedding steady-state experimental data into the model, and (2) the ability to obtain explicit models that incorporate natural system boundary conditions. Models of the type developed in this paper are primarily used in the design of surge control and integrated surge control/rotating stall avoidance schemes. Control schemes of these types have been reported in [20, 8, 21–25], respectively. The preliminary controllers given in this paper have the advantage of being model-based controllers. This means that they are designed directly from the model with no a posteriori tuning of controller parameters. Stabilization of surge using these model-based controllers represents, to the best of our knowledge, the first experimental demonstration of direct active control of surge in an axial flow compression system. In [26], a demonstration was given of the indirect control of surge, through the direct control of rotating stall, in an axial compression system.

For studying the two-dimensional phenomena of rotating stall, a two-dimensional model that can model and predict rotating stall is required. For incompressible flow, the models given in [27–31] have this capability. Extension of models of this type to compressible flow is discussed in [32]. These two-dimensional models are used in the design of rotating stall control schemes [20, 33, 31, 34, 26, 35]. Extensions of the one-dimensional model presented in this paper to a two-dimensional model will be undertaken in the future, using a parallel compressor concept [36], so that rotating stall control schemes can be investigated.

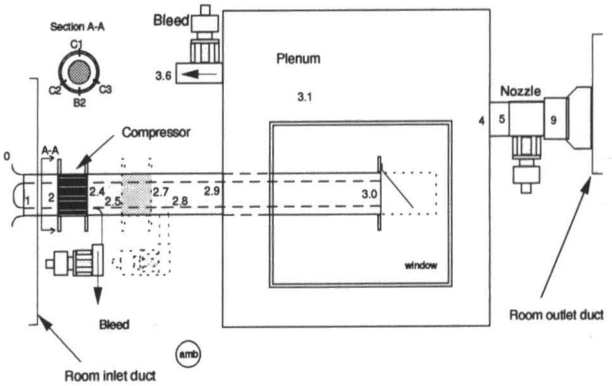

Fig. 1 Diagram of LICCHUS axial compressor rig

Nonlinear dynamic/bifurcation analyses (similar to those performed here) of various models discussed above have also been given in the literature [37–43]. Experimental observation of the coexistence of surge and rotating stall has been presented previously in the literature [12]. To our knowledge, however, this paper is the first to point out that experimentally observed hysteresis in the onset and cessation of surge can be predicted using a one-dimensional model, which does not include any hysteretic maps.

1.2 Outline. An outline of this paper is as follows: Section 2 gives a description of the LICCHUS axial compressor rig. Section 3 describes the development of the model for the LICCHUS axial compressor rig. Also, a discussion of model computation is given along with a discussion of how the parameters and maps required for the model are identified from experimental data. Section 4 discusses the open-loop validation of the model through comparisons between the model and experimental data for both forced transients and nonlinear dynamics/bifurcations. In Section 5, closed-loop validation of the model is presented through comparisons between the model and experimental data for closed-loop systems based on controllers designed at three different operating conditions. Finally, conclusions and future work are discussed in Section 6.

2 LICCHUS Axial Compressor Rig

The LICCHUS axial compressor experimental rig shown in Fig. 1 is designed with the capability to exhibit the typical compression system instabilities of surge and rotating stall. It is equipped with high bandwidth actuators, variable compressor duct length, and variable plenum volume. The rig can be configured with 1–3 compressor stages, and the speed of each compressor can be varied independently. In this paper we consider a single-stage configuration in which only a single compressor is used. The compressor is driven by a three-phase AC motor and is designed to run at a maximum speed of 10,500 rpm with a 400 Hz excitation frequency. A peak total pressure ratio of 1.01 is achieved at an axial flow Mach number of 0.06 with the compressor operating at the maximum speed. The speed set points may be controlled either manually or via a computer control interface. For reference, the B parameter [6] for this system can be varied through a range of 0.54 (4700 rpm) to 1.32 (10,500 rpm).

The compressor duct is connected to the compressor. Each section of the compressor duct consists of two concentric cylinders made out of plexiglass. Sections of duct can be

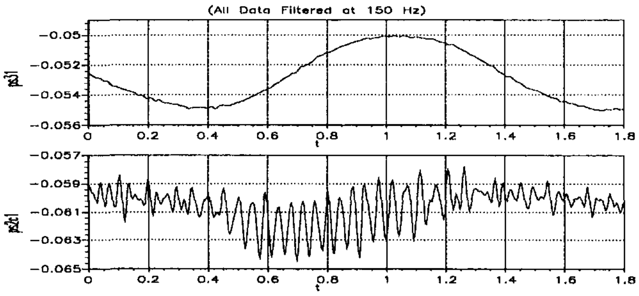

Fig. 2 Mixed surge / rotating stall mode

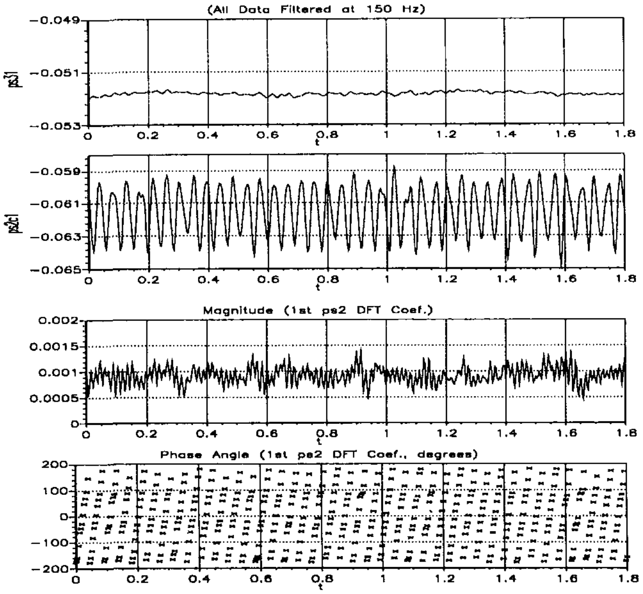

Fig. 3 Pure rotating stall mode

added on to the compressor duct to modify the system configuration as desired (shown in Fig. 1 as dotted lines at the end of the compressor duct). The ducts are connected to a downstream plenum, which has two plexiglass windows. The plexiglass ducts and plenum windows are used to facilitate flow visualization. An example of this flow visualization is an inverted "T" of balsa wood (shown in Fig. 1 as a solid line extending from the compressor duct), which oscillates with the flow when the system is surging.

This rig exhibits a strong rotating stall mode with a 90 Hz fundamental frequency. Depending on the various plenum and duct geometry, a strong surge mode is also observed at a fundamental frequency between 2 and 10 Hz. These behaviors are exhibited in Figs. 2 and 3 where plots of various experimentally measured dimensionless variables (defined in Table 2) are given. Figure 2 shows the experimentally measured static pressure in the plenum during a surge cycle along with the static pressure at a point on the circumference of the duct at the inlet of the compressor. As can be seen, a mixed surge/rotating stall mode is exhibited by the system. Figure 3 shows the experimentally measured static pressure in the plenum during pure rotating stall along with the static pressure at a point on the circumference of the duct at the inlet of the compressor. Also shown are the magnitude and phase of the first mode in rotating stall, which were obtained by doing spatial fourier transform on the static pressure signals at three circumferential locations around the duct at the inlet of the compressor. As can be seen, the rotating stall is moving at constant speed (approximately one half of the compressor rotational speed) around the circumference of the compressor.

In the single-stage configuration, this rig is equipped with three actuators: an exit nozzle, a plenum bleed, and a com-

Table 1 Dimensional variables

Variable	Description
$\tilde{x}$	position
$\tilde{t}$	time
$\tilde{L}$	length
$\tilde{A}(\tilde{x},\tilde{t})$	area
R	ideal gas constant
c_v	heat capacity at constant volume
c_p	heat capacity at constant pressure
$\tilde{u}(\tilde{x},\tilde{t})$	fluid velocity
$\tilde{\rho}_s(\tilde{x},\tilde{t})$	static density
$\tilde{p}_s(\tilde{x},\tilde{t})$	static pressure
$\tilde{T}_s(\tilde{x},\tilde{t})$	static temperature
$\tilde{e}(\tilde{x},\tilde{t})$	specific internal energy
$\tilde{w}(\tilde{x},\tilde{t})$	mass flow rate
$\tilde{Q}(\tilde{x},\tilde{t})$	volumetric heat transfer rate (into fluid)
$\tilde{f}_w(\tilde{x},\tilde{t})$	specific wall friction force (on fluid, does no work)
$\tilde{f}_s(\tilde{x},\tilde{t})$	specific force (on fluid, does work)
$\bar{t}$	reference time
$\bar{p}$	reference pressure
$\bar{T}$	reference temperature
$\tilde{N}(\tilde{t})$	shaft speed
μ	viscosity
k	thermal conductivity
$\tilde{T}_w(\tilde{x},\tilde{t})$	wall temperature

Table 2 Dimensionless variables

Variable	Description
$x = \tilde{x}/\tilde{L}$	dimensionless position
$t = \tilde{t}/\bar{t}$	dimensionless time
$A = ln\left[\tilde{A}/(\bar{t}^2\gamma R\bar{T})\right]$	dimensionless area
$L = \tilde{L}/\left(\bar{t}\sqrt{\gamma R\bar{T}}\right)$	dimensionless length
$\gamma = c_p/c_v$	ratio of specific heats
$M = \tilde{u}/\sqrt{\gamma R\tilde{T}_s}$	Mach number
$p = ln(\tilde{p}/\bar{p})$	dimensionless total pressure
$s = \tilde{s}/c_p$	dimensionless specific entropy
$T = ln(\tilde{T}/\bar{T})$	dimensionless total temperature
$Q = \tilde{Q}\tilde{L}/\left(\bar{p}\sqrt{\gamma R\tilde{T}}\right)$	dimensionless volumetric heat transfer rate
$f_w = \tilde{f}_w\tilde{L}/\left(\gamma R\tilde{T}\right)$	dimensionless specific wall friction force
$f_s = \tilde{f}_s\tilde{L}/\left(\gamma R\tilde{T}\right)$	dimensionless specific force
$N = \tilde{N}\sqrt{\tilde{A}/\left(\gamma R\tilde{T}\right)}$	dimensionless shaft speed
$Re = \tilde{\rho}_s\tilde{u}\sqrt{\tilde{A}}/\mu$	Reynolds number
$Pr = c_p\mu/k$	Prandtl Number
$T_w = ln(\tilde{T}_w/\bar{T})$	dimensionless wall temperature

Table 3 LICCHUS axial compressor rig: location of sensors and actuators

Sensor Number	Sensor	Sensor Number	Sensor	Sensor Number	Sensor	Actuator Number	Actuator
1	PS0	16	PS24B2	31	PD3	1	Bleed Valve Angle
2	PS2C1	17	PD24B2	32	PD3V	2	Nozzle Valve Angle
3	PD2C1	18	PS27C1	33	PS31	3	Compressor Discharge Bleed Valve Angle
4	PD2C1V	19	PD27C1	34	PS91		
5	PS2C2	20	PD27C1V	35	Pamb		
6	PD2C2	21	PS27C2	36	T0		
7	PS2C3	22	PD27C2	37	T31		
8	PD2C3	23	PS27C3	38	N2		
9	PS24C1	24	PD27C3	39	N25		
10	PD24C1	25	PS27B2	40	THA36		
11	PD24C1V	26	PD27B2	41	THA9		
12	PS24C2	27	PS29	42	THAB25		
13	PD24C2	28	PD29	43	NA36		
14	PS24C3	29	PD29V	44	NA9		
15	PD24C3	30	PS3	45	NAB25		

Table 4 LICCHUS axial compressor rig: geometric parameters and constants

Description	Parameter	Value	Parameter	Value
Compressor Inlet Area	$\tilde{A}_2$	0.0046 m^2	A_2	−14.4117
Compressor Exit Area	$\tilde{A}_{24}$	0.0046 m^2	A_{24}	−14.4117
Compressor Bleed Area (full open)	$\tilde{A}_{24bd}$	0.00046 m^2	A_{24bd}	−16.7143
Compressor Duct Area	$\tilde{A}_3$	0.0046 m^2	A_3	−14.4117
Plenum Area at Duct Discharge	$\tilde{A}_{31}$	1.1148 m^2	A_{31}	−8.93109
Plenum Bleed Area (full open)	$\tilde{A}_{36b}$	0.0020 m^2	A_{36b}	−20.539
Plenum Area Before Exit Nozzle	$\tilde{A}_4, \tilde{A}_{41}$	1.1148 m^2	A_4, A_{41}	−8.93109
Throttle Valve Area (full open)	$\tilde{A}_9$	0.0081 m^2	A_9	−13.8544
Compressor Length	$\tilde{L}_c$	0.1079 m	L_c	0.00124
Rotor Length	$\tilde{L}_r$	0.06349 m	L_r	0.00073
Stator Length	$\tilde{L}_s$	0.04445 m	L_s	0.00051
Rotor Tip Radius	$\tilde{r}_{tip}$	0.05715 m	r_{tip}	0.00065
Compressor Duct Length	$\tilde{L}_{cd}$	0.9652 m	L_{cd}	0.0111
Plenum Length	$\tilde{L}_p$	0.8270 m	L_p	0.00947
Compressor Speed	$\tilde{N}_2$	4700,10500 rpm	N_2	0.10,0.22
Reference Time	$\bar{t}$	0.256602 s	-	-
Reference Pressure	$\bar{p}$	101.3 KPa	-	-
Reference Temperature	$\bar{T}$	288 °K	-	-

pressor discharge bleed. The nozzle assembly consists of a low inertia, high tolerance butterfly valve driven by an electric motor. The plenum bleed and the compressor discharge bleed are identical to the nozzle except that the flow cross-sectional areas are less than that of the nozzle. The nozzle and plenum bleed valves are both located in the plenum, while the compressor discharge bleed valve is located at the exit of the compressor. Frequency response studies of the nozzle actuator depict achievable 3 dB bandwidth of about 70 Hz, which is several times the surge frequency. The plenum bleed valve and the compressor discharge bleed valve have similar 3 dB bandwidths.

This rig is equipped with 45 sensors consisting of compressor speed, total temperature, static pressure, and total-static differential pressure sensors located at different circumferential and axial positions. An augmented SAE notation is utilized in labeling the sensors and actuators installed on the LICCHUS axial compressor rig. A listing of these sensors and actuators is given in Table 3. Here, *PD* denotes total-static differential pressure, *PS* denotes static pressure, *T* denotes total temperature, and *N* denotes the compressor speed. Additional notations are used to identify the array of circumferentially located sensors, which detect rotating stall traveling waves, and reverse flow sensors, which measure backflow in deep surge mode. For example, *PS*23*C*2 is a static pressure (the *PS*) sensor at station 2.4 (the 24) located in the second circumferential position (the 2 in *C*2) of a two-dimensional flow sensing array employing three uniformly spaced sensors (*C* corresponding to three). Similarly, *PD*2*C*1*V* is a reverse (the *V*) total-static differential pressure sensor at the station 2 (the 2) located in the first circumferential position (the 1 in *C*1) of a two-dimensional flow sensing array employing three (*C* corresponding to three) uniformly spaced sensors around the duct annulus. All variables in this paper are annulus averaged unless specifically labeled in the manner discussed here.

The speed of the compressors is measured using a photo-optic sensor. This sensor provides a frequency signal to a tachometer, which in turn produces a voltage output with a ±0.5 percent accuracy at full speed. The temperature sensors are type K thermocouples, which have a time constant of 0.1 seconds. However, an error of ±3.6°C (±2°C) is present in the temperature measurements at ambient conditions. Therefore, the temperature measurements obtained from these thermocouples cannot be used for accurate measurement of the change in entropy or efficiency in this low-pressure ratio rig.

Fast, piezoresistive low-pressure sensors having a time constant of 1 ms are used to measure all pressures. The static-ambient pressure sensors have a range of 0–0.689 kPa (0–1 psi), while the total-static differential pressure sensors have a range of 0–2.48 kPa (0–0.36 psi). The Mach number and the dimensionless pressure rise are computed directly from the ambient pressure and the readings from these sensors. The maximum error incurred in computing Mach number at peak operating condition, based on manufacturer [44] specified error limits on sensors, is 2.5 percent. The corresponding error in dimensionless pressure is 2.3 percent.

The geometric parameters and constants of the LICCHUS axial compressor rig are listed in Table 4. The reference parameters ($\bar{p}$, $\bar{T}$, and $\bar{t}$) listed in this table were required for nondimensionalization of variables. Sea level standard conditions were chosen for $\bar{p}$ and $\bar{T}$, while $\bar{t}$ was chosen as the Helmholtz period of the system based on a $\tilde{L}/\tilde{A}$ and $\tilde{V}$ for the compressor duct and plenum combination, i.e.,

$$\bar{t} = \frac{2\pi}{\sqrt{\gamma R\bar{T}}}\sqrt{\left(\tilde{L}_{cd}/\tilde{A}_{cd} + \tilde{L}_p/\tilde{A}_p\right)\left(\tilde{L}_{cd}\tilde{A}_{cd} + \tilde{L}_p\tilde{A}_p\right)}\,.$$

To choose $\bar{t}$ to get one surge cycle to occur in one dimensionless time unit, effective lengths would need to be used for this calculation [3]. However, the effective lengths are time varying quantities, so this could not be done. Therefore, the dimensionless time period required for a surge cycle gives an indication of the difference between the physical lengths used to compute $\bar{t}$ and the effective lengths used in the model of the system.

3 One-Dimensional Model Development

The generic compression system model of [3] was applied to the LICCHUS multistage axial compressor rig [4] configured for single-stage operation. The discussion of this development given here is quite brief, and the reader is referred to [1] for further details. A diagram of this rig is shown in Fig. 1 with the station numbers indicated. When configured for single-stage operation, the rig is made up of the following components: inlet, single-stage compressor, compressor discharge bleed, compressor duct, abrupt area change, plenum, plenum bleed, nozzle duct, and nozzle. When discretizing the spatial domain of this system, it was found that all that was required was a single element for each component (models with multiple elements for each component gave identical results [45]). Thus, all components in which dynamics are not residualized are modeled with three first-order ODEs. Of the components above, the dynamics are residualized in the compressor discharge bleed, abrupt area change, plenum bleed, and nozzle. Therefore, the developed model consists of 15 first-order ODEs [45]. Using this model, excellent agreement between the model and experimental data was obtained [45]. It was found, however, that model order could be reduced by eliminating the inlet and nozzle duct components from the model without sacrificing the agreement between the model and experimental data [45]. Therefore, the inlet and nozzle duct are not considered as components in the model given here, and the resulting model consists of nine first-order ODEs. The model for this rig is now given along with some of the foundational equations used in its development [1, 2].

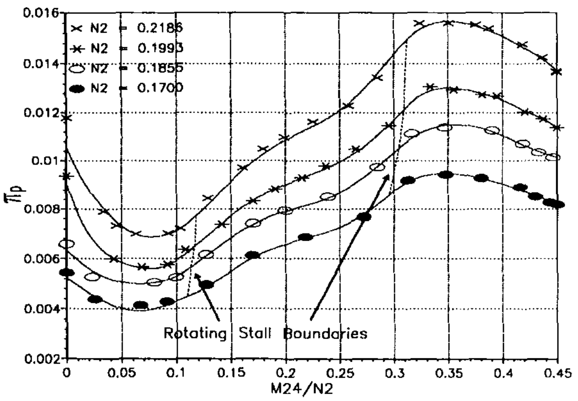

Fig. 4 Compressor dimensionless total pressure change map

3.1 Foundational Equations. In this section we list some foundational equations developed in [1, 2], which were used in the development of the model given in this paper. We first define some notation in Tables 1 and 2 for dimensional and dimensionless variables, respectively. In addition, we define the notation that $M_{k-1}(t) := M(x_{k-1}, t)$ and $M_k(t) := M(x_k, t)$, where x_{k-1} is the position of the entrance of the kth element, x_k is the position of the exit of the kth element. Similar notation is used for other variables. Now, the discretized form of the dimensionless equations for unsteady compressible viscous quasi-one-dimensional flow of a calorically perfect single species gas in the kth finite element of a component can be written as [2]:

$$\epsilon(s_{k-1}, p_{k-1}, L_k, \gamma)\frac{d}{dt}\begin{bmatrix} M_{k-1} \\ p_k \\ s_k \end{bmatrix} = \Xi(M_k, \gamma)\left\{\begin{bmatrix} M_k - M_{k-1} \\ p_k - p_{k-1} \\ s_k - s_{k-1} \end{bmatrix}\right.$$

$$\left. - \begin{bmatrix} m_4(M_k, e^{A_{k-1}}/L_k^2, A_k - A_{k-1}, N_{k-1}, \gamma, \mathrm{Re}_{k-1}, \mathrm{Pr}, T_{w,k-1} - T_{k-1}) \\ m_5(M_k, e^{A_{k-1}}/L_k^2, A_k - A_{k-1}, N_{k-1}, \gamma, \mathrm{Re}_{k-1}, \mathrm{Pr}, T_{w,k-1} - T_{k-1}) \\ m_6(M_k, e^{A_{k-1}}/L_k^2, A_k - A_{k-1}, N_{k-1}, \gamma, \mathrm{Re}_{k-1}, \mathrm{Pr}, T_{w,k-1} - T_{k-1}) \end{bmatrix}\right\} + \epsilon(s_{k-1}, p_{k-1}, L_k, \gamma)\begin{bmatrix} 0 \\ -1 \\ \frac{\gamma-1}{\gamma} \end{bmatrix}\frac{d}{dt}A_k. \quad (1)$$

The matrix $\Xi(M, \gamma)$ is made up of influence coefficient functions ξ_{ij} which are known functions of M and γ defined in [1, 2], and

$$\epsilon(s, p, L) = L\, e^{-(1/2)[s+(\gamma-1/\gamma)p]},$$

and

$$T_{k-1} = s_{k-1} + \frac{\gamma-1}{\gamma}p_{k-1}.$$

The maps, m_4, m_5, and m_6, in these equations account for the forcing terms Q, f_s, and f_w, in the quasi-one-dimensional flow equations. They are equal in steady state to the differences $M_k - M_{k-1}$, $p_k - p_{k-1}$, and $s_k - s_{k-1}$ across the element, respectively. Identification of these functions is discussed further in [1, 2].

3.2 Model Equations. In this section, we list the equations that form the model for the axial rig. These equations were obtained by applying the model developed for a generic compression system in [3] to the LICCHUS axial compressor rig in a single-stage configuration. This model assumes that the flow consists of a calorically perfect single species gas at all points in the system. Air ($\gamma = 1.4$), being a uniform mixture of nonreacting gases for temperatures encountered in this system, is regarded as the single species gas of interest for this model.

Compressor. For this model, the compressor is the first component considered. The experimentally determined maps required in the compressor model are listed as follows:

$$\pi_M = 0, \quad (2)$$

$$\pi_p = f_{c2}(M_{24}, N_2) \quad (3)$$

$$\pi_s = f_{c2}(M_{24}, N_2)/\gamma \quad (4)$$

The steady-state Mach number change across the compressor was found to be negligible. The map f_{c2} depends only on the flow Mach number and the dimensionless compressor speed and is plotted in Fig. 4. The Mach number axis of this plot is scaled by N_2 to keep the range for each speed on a similar scale. Other variable dependencies were determined to be negligible for this system and were dropped. The steady-state dimensionless entropy change is computed from the corresponding pressure rise by assuming that the fluid density is essentially constant across the compressor (i.e., $\tilde{\rho}_2 = \tilde{\rho}_{24}$) and using the ideal gas law. This computation was required because the very low temperature rise across the compressor was within the precision of the thermocouples and could not be measured. Hence, in dimensionless form, the steady-state entropy change across the compressor is:

$$\pi_s = (T_{24} - T_2) - \frac{\gamma-1}{\gamma}(p_{24} - p_2)$$

$$= (p_{24} - p_2)/\gamma = f_{c2}(M_{24}, N_2)/\gamma.$$

The dynamic equations for the compressor stage can then be written as:

$$\frac{d}{dt}M_2 = \frac{e^{(1/2)T_2}}{L_{c,e}}[\xi_{11}(M_{24}, \gamma)(M_{24} - M_2) + \xi_{12}(M_{24}, \gamma)(p_{24} - p_2 - \pi_p) + \xi_{13}(M_{24}, \gamma)(s_{24} - s_2 - \pi_s)] \quad (5)$$

$$\frac{d}{dt}p_{24} = \frac{e^{(1/2)T_2}}{L_{c,e}}[\xi_{21}(M_{24}, \gamma)(M_{24} - M_2) + \xi_{22}(M_{24}, \gamma)(p_{24} - p_2 - \pi_p) + \xi_{23}(M_{24}, \gamma)(s_{24} - s_2 - \pi_s)] \quad (6)$$

$$\frac{d}{dt}s_{24} = \frac{e^{(1/2)T_2}}{L_{c,e}}[\xi_{33}(M_{24}, \gamma)(s_{24} - s_2 - \pi_s)]. \quad (7)$$

Since this is the first component of the system, p_2 and s_2 are inputs to the system and to this component.

Compressor Discharge Bleed. The equations for this component are:

$$M_{24} = f_{spl}(c_{24}) \quad (8)$$

where

$$c_{24} = \mathrm{M}_{25}\left(1 + \frac{\gamma - 1}{2}\mathrm{M}_{25}^2\right)^{-[(\gamma+1)/2(\gamma-1)]}$$

$$+e^{(A_{24b}-A_{24})}\mathrm{M}_{24b}\left(1 + \frac{\gamma - 1}{2}\mathrm{M}_{24b}^2\right)^{-[(\gamma+1)/\{2(\gamma-1)\}]}$$

$$p_{25} = p_{24} \qquad s_{25} = s_{24}$$

$$p_{24b} = p_{24} \qquad s_{24b} = s_{24},$$

where

$$\mathrm{M}_{24b} = \sqrt{\frac{2}{\gamma - 1}[e^{[(\gamma-1)/\gamma](p_{24b}-p_{s24b})} - 1]}, \quad \mathrm{M}_{24b} \le 1. \tag{9}$$

Here, M_{24b} is the Mach number at the exit of the compressor discharge bleed valve. The dimensionless static pressure at the compressor discharge bleed, p_{s24b}, is an input to the system and to this component. It is defined in the same manner as dimensionless total pressure in Table 2 (i.e., $p_{s24b} = \ln(\tilde{p}_{s24b}/\bar{p})$).

Compressor Duct. This component consists of ducting with frictional losses. The experimentally determined maps required for the duct model are:

$$\chi_p = f_{d2}(\mathrm{M}_3, N_2), \tag{10}$$

$$\chi_M = \mathrm{M}_3 - f_{\mathrm{con}}(c_{25}), \tag{11}$$

where

$$c_{25} = e^{\chi_p}\mathrm{M}_3\left(1 + \frac{\gamma - 1}{2}\mathrm{M}_3^2\right)^{-[(\gamma+1)/\{2(\gamma-1)\}]},$$

and

$$\chi_s = -\frac{\gamma - 1}{\gamma}\chi_p.$$

The map f_{d2} depends only on the flow Mach number and the dimensionless compressor speed and is plotted in Fig. 5. The dependence on N_2 is due to the swirl that exists in the compressor duct since the flow does not exit the compressor in an axial direction. The Mach number axis of this plot is scaled by N_2 to keep the range for each speed on a similar scale. Other variable dependencies were determined to be negligible for this system and were dropped. The map $f_{\mathrm{con}}(c_{25})$ is given in [3]. The dynamic equations for the compressor duct are:

$$\frac{d}{dt}\mathrm{M}_{25} = \frac{e^{(1/2)T_{25}}}{L_{cd,e}}[\xi_{11}(\mathrm{M}_3, \gamma)(\mathrm{M}_3 - \mathrm{M}_{25} - \chi_M) + \xi_{12}(\mathrm{M}_3, \gamma)(p_3 - p_{25} - \chi_p) + \xi_{13}(\mathrm{M}_3, \gamma)(s_3 - s_{25} - \chi_s)] \tag{12}$$

$$\frac{d}{dt}p_3 = \frac{e^{(1/2)T_{25}}}{L_{cd,e}}[\xi_{21}(\mathrm{M}_3, \gamma)(\mathrm{M}_3 - \mathrm{M}_{25} - \chi_M) + \xi_{22}(\mathrm{M}_3, \gamma)(p_3 - p_{25} - \chi_p) + \xi_{23}(\mathrm{M}_3, \gamma)(s_3 - s_{25} - \chi_s)] \tag{13}$$

$$\frac{d}{dt}s_3 = \frac{e^{(1/2)T_{25}}}{L_{cd,e}}[\xi_{33}(\mathrm{M}_3, \gamma)(s_3 - s_{25} - \chi_s)]. \tag{14}$$

Abrupt Area Change. This component models the abrupt area change from the compressor duct discharge into the plenum. This area change occurs over a very short axial distance; therefore, the dynamics are residualized. For forward flow, the equations for this component are:

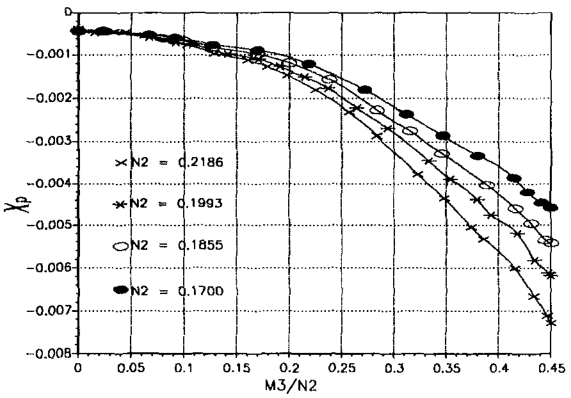

Fig. 5 **Compressor duct dimensionless total pressure loss map**

$$\mathrm{M}_3 = f_{aac}(c_3) \tag{15}$$

where

$$c_3 = e^{A_{31}-A_3}\mathrm{M}_{31}\left(1 + \frac{\gamma - 1}{2}\mathrm{M}_{31}^2\right)^{1/2},$$

$$p_{31} = p_3 + \frac{\gamma}{\gamma - 1}\ln\left[\frac{2 - \mathrm{M}_{31}^2 + \gamma\mathrm{M}_{31}^2}{2 - \mathrm{M}_3^2 + \mathrm{M}_3^2\gamma}\right],$$

and

$$s_{31} = s_3 - \ln\left[\frac{2 - \mathrm{M}_{31}^2 + \gamma\mathrm{M}_{31}^2}{2 - \mathrm{M}_3^2 + \gamma\mathrm{M}_3^2}\right].$$

The map $f_{aac}(c_{aac})$ is given in [3]. As explained in [3], the equations for reverse flow in this component are:

$$\mathrm{M}_3 = f_{ac}(c_{3r}) \tag{16}$$

where

$$c_{3r} = e^{(A_{31}-A_3)}\mathrm{M}_{31}\left(1 + \frac{\gamma - 1}{2}\mathrm{M}_{31}^2\right)^{-[(\gamma+1)/\{2(\gamma-1)\}]},$$

$$p_{31} = p_3, \quad \text{and} \quad s_{31} = s_3.$$

Plenum. This component consists of ducting in which all forcing is negligible, and the dynamic equations are:

$$\frac{d}{dt}\mathrm{M}_{31} = \frac{e^{(1/2)T_{31}}}{L_p}[\xi_{11}(\mathrm{M}_4, \gamma)(\mathrm{M}_4 - \mathrm{M}_{31}) + \xi_{12}(\mathrm{M}_4, \gamma)(p_4 - p_{31}) + \xi_{13}(\mathrm{M}_4, \gamma)(s_4 - s_{31})] \tag{17}$$

$$\frac{d}{dt}p_4 = \frac{e^{(1/2)T_{31}}}{L_p}[\xi_{21}(\mathrm{M}_4, \gamma)(\mathrm{M}_4 - \mathrm{M}_{31}) + \xi_{22}(\mathrm{M}_4, \gamma)(p_4 - p_{31}) + \xi_{23}(\mathrm{M}_4, \gamma)(s_4 - s_{31})] \tag{18}$$

$$\frac{d}{dt}s_4 = \frac{e^{(1/2)T_{31}}}{L_p}[\xi_{33}(\mathrm{M}_4, \gamma)(s_4 - s_{31})]. \tag{19}$$

Plenum Bleed. The equations for this component are:

$$\mathrm{M}_4 = f_{spl}(c_4) \tag{20}$$

where

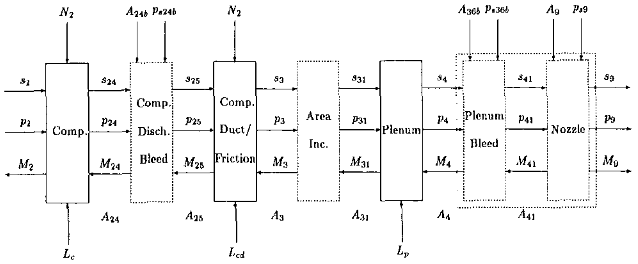

Fig. 6 Model computational diagram

$$c_4 = \mathrm{M}_{41}\left(1 + \frac{\gamma - 1}{2}\mathrm{M}_{41}^2\right)^{-[(\gamma+1)/\{2(\gamma-1)\}]}$$

$$+e^{(A_{36b}-A_4)}\mathrm{M}_{36b}\left(1 + \frac{\gamma - 1}{2}\mathrm{M}_{36b}^2\right)^{-[(\gamma+1)/\{2(\gamma-1)\}]}$$

$$p_{41} = P_4 \qquad s_{41} = s_4$$

$$p_{36b} = p_4 \qquad s_{36b} = s_4.$$

$$\mathrm{M}_{36b} = \sqrt{\frac{2}{\gamma - 1}\left[e^{[(\gamma-1)/\gamma](p_{36b}-p_{s36b})} - 1\right]}, \quad \mathrm{M}_{36b} \leq 1 \tag{21}$$

Here, M_{36b} is the Mach number at the exit of the plenum bleed valve. p_{s36b} is an input to the system and to this component.

Nozzle. In this component, the fluid undergoes an isentropic area change, which occurs over a very short axial distance; therefore the dynamics are residualized. The resulting equations for this component are:

$$\mathrm{M}_{41} = f_{ac}(c_{41}) \tag{22}$$

where

$$c_{41} = e^{(A_9-A_{41})}\mathrm{M}_9\left(1 + \frac{\gamma - 1}{2}\mathrm{M}_9^2\right)^{-[(\gamma+1)/\{2(\gamma-1)\}]}$$

$$p_9 = p_{41} \qquad s_9 = s_{41}.$$

$$\mathrm{M}_9 = \sqrt{\frac{2}{\gamma - 1}\left[e^{[(\gamma-1)/\gamma](p_9-p_{s9})} - 1\right]}, \quad \mathrm{M}_9 \leq 1. \tag{23}$$

p_{s9} is an input to the system and to this component.

3.3 Model Computation. Equations (2)–(23) constitute the overall compression system model, which consists of nine ODEs with related algebraic equations. A model computation flow diagram is given in Fig. 6. In this diagram, solid blocks represent elements that have dynamics associated with them, and dashed blocks represent elements in which dynamics have been residualized. All inputs to a dynamic element are required in order to do a state update, and all inputs to a static element are required to compute the outputs of the static element. Inputs that do not originate from any of the blocks are external inputs to the model. The states of the model are outputs of the solid blocks (dynamic elements). Explicit model computation requires that all inputs to the dynamic elements can be computed without iteration using the initial conditions of the states (outputs of the dynamic blocks) and the various inputs to the model. Critical points for the development of an explicit model occur if there are two static blocks next to each other in the computational flow diagram requiring possible iteration to obtain the inputs to neighboring dynamic elements. For this model there is only one point where there are two static blocks next to each other (plenum bleed and nozzle). However, the dashed box around these two static blocks indicates that they can be considered as a single static block. This means that if all inputs to the large dashed block are known, all outputs can be computed as well as any internal variables. Now, it can easily be seen that all inputs to the dynamic elements can be obtained from the initial conditions of the states and the various model inputs. Thus, our model is explicit. Model simulations can then be done using any explicit ODE solver with the model equations. The FORTRAN subroutine LSODA [46] is used for simulation results in this paper. This routine solves both stiff (using backward difference formula method) and nonstiff (using predictor-corrector method) systems of differential equations and automatically switches between the methods as required while solving a system of equations.

3.4 Parameter and Map Identification From Experimental Data. In this section, we describe the procedure used in experimental identification of various parameters and maps for the developed model.

Data Acquisition. Since this rig, in the configuration considered here, exhibits a strong rotating stall mode at a 90 Hz fundamental frequency as well as a strong surge mode at around 3 Hz fundamental frequency, data are acquired at two different rates. All of the circumferentially distributed pressure sensors located close to the compressor, namely at stations 2, 24, and 27, are filtered with two-pole low-pass Butterworth filters that have cut-off frequencies of 1000 Hz. These fast sensors are then sampled at a very high rate of 10,000 samples per second to avoid aliasing. All other sensors are filtered similarly at a cut-off frequency of 100 Hertz and are then sampled at a rate of 1000 samples per second to once again avoid aliasing. The data are finally digitally filtered using a two-pole Butterworth filter with an appropriate cut-off frequency. This cut-off frequency is chosen to eliminate signal noise and to emphasize the specific physical phenomenon of interest.

Experimental Determination of Forcing Maps. In order to measure the steady-state compressor performance map, π_p, and the steady-state compressor duct pressure loss map, χ_p, at several constant speed values, a temporary modification was made to the system configuration. A duct was made to connect the compressor discharge duct directly to the exit nozzle, thus bypassing the plenum entirely. The absence of a large downstream volume enabled the system to operate stably (annulus average) without surge over the entire range of system operating conditions. This global annulus average stability results because the compliance of the fluid in the plenum has been eliminated from the system. Approximately 40 steady-state data points were taken for each speed line. Each of these data points was obtained by time averaging of nearly 300 raw data points. The boundaries of rotating stall are also shown on the compressor map in Fig. 4 for reference. There is a slight hysteresis associated with the onset and cessation of rotating stall in this rig. However, the region is so small that for the purposes of the one-dimensional model developed in this paper, it can be assumed to be negligible. Of course, when considering a two-dimensional model for use in rotating stall control, this will not be the case. In addition, for a multistage configuration this region of hysteresis may not be small and thus cannot be neglected.

Model Parameter Identification. In the developed model, all area parameters were identified by using physical values (Table 4), while the length parameters were identified by calculating effective lengths as discussed in [3]. The effective lengths account for the helical path of the flow as it travels through components where swirl or rotation is present. For the compressor, there is rotation in the rotor, and the effective length of the rotor path is computed as follows:

$$L_{r,e} = L_r\sqrt{1 + \frac{N_2^2}{M_{24}^2} r_{\text{tip}}^2 e^{-A_2} \underbrace{e^{-(T_{24}-T_2)}\left(1+\frac{\gamma-1}{2}M_{24}^2\right)}_{\approx 1}}\,,$$

$$L_{r,e} \approx L_r\sqrt{1 + \frac{N_2^2}{M_{24}^2} r_{\text{tip}}^2 e^{-A_2}}\,, \tag{24}$$

where r_{tip} is the dimensionless tip radius of the compressor and L_r is the axial length of the rotor. Therefore, the effective length of the compressor becomes

$$L_{c,e} = L_{r,e} + L_s, \tag{25}$$

where L_s is the axial length of the stator, where no rotation/swirl can exist. In the compressor duct, however, while swirl does exist and an effective length must also be calculated, the rotational speed of the flow is not directly defined by the rotor speed and hence must be estimated. Therefore, a similar relation to that for the compressor was used with an added parameter to define this speed. This parameter is tuned to give good matching between model and experimental data. This parameter gives the ratio of the average duct rotational speed to the compressor rotational speed and is called ϵ_d. Therefore, the effective length of the compressor duct is

$$L_{cd,e} = L_{cd}\sqrt{1 + \frac{(\epsilon_d N_2)^2}{M_3^2} r_{\text{tip}}^2 e^{-A_3}}\,, \tag{26}$$

where L_{cd} is the axial length of the compressor duct. A table of tuned values for ϵ_d as a function of compressor rotational speed is as follows:

N_2	0.170	0.186	0.199	0.218
ϵ_d	0.10	0.11	0.115	0.120

The fact that ϵ_d is approximately constant speaks well for the utility of the empirical relation (26). For the plenum, no rotation/swirl is present, and thus no effective length needs to be computed.

4 Open-Loop Model Validation

In this section, open-loop model validation is addressed through comparisons of the model to experimental data. These comparisons focus on forced transients and nonlinear dynamics/bifurcations.

4.1 Forced Transients. In this section, some open-loop behaviors of the compression system are demonstrated. These behaviors involve the transient responses to changes in the nozzle area. Transient responses to changes in the other actuators in the system (compressor discharge and plenum bleeds) give similar results to those shown here for the nozzle [45]; however, for brevity they are not shown. All open-loop model simulations presented in this paper have been generated using actual experimental data for the various inputs to the model.

In Fig. 7, a comparison between model and experiment is given for $N_2 = 0.218$ in which the system starts out in a stable operating condition and the nozzle is closed causing the system to surge. As can be seen, the match between model and experimental data is quite good. The error at very low Mach numbers (see M_3 traces) can be attributed to sensor accuracy/limitations. The dotted lines in the phase plane plots are steady-state maps from the model, which are plotted for reference. For brevity, plots for this scenario at other speeds are not given here, but they show agreement as good as that shown in Fig. 7 [45].

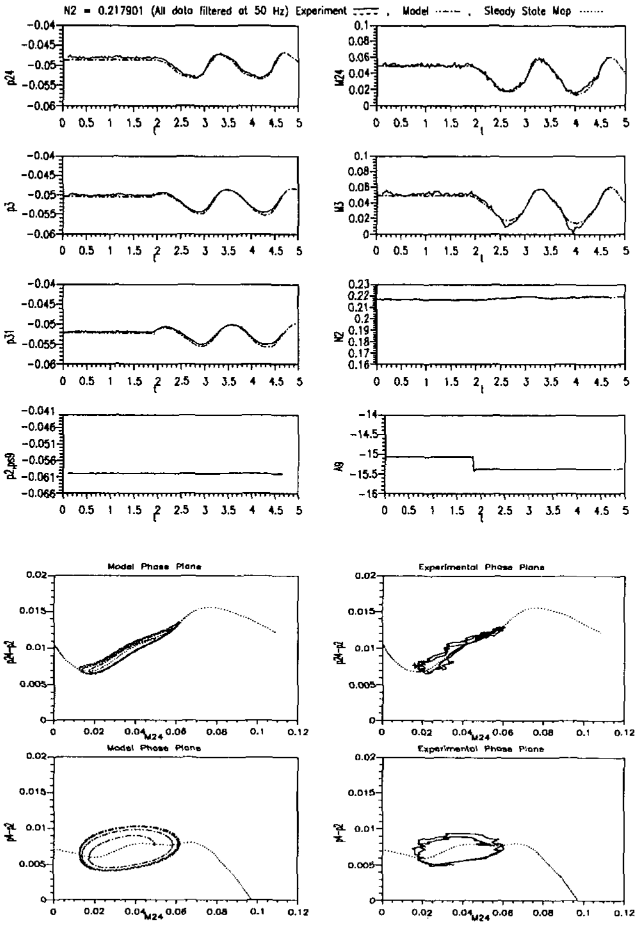

Fig. 7 Transient into surge (high speed)

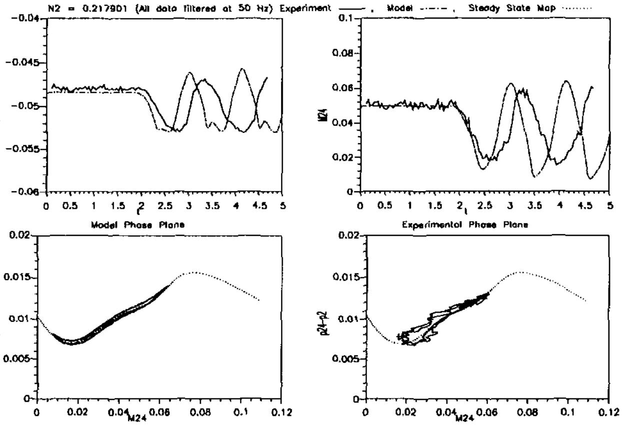

Fig. 8 Transient into surge (high speed) using physical lengths

The nonlinear model was modified and run using physical lengths instead of effective lengths to see the effect. In Fig. 8, it can be seen that the surge frequency of the model no longer matches the experimental surge frequency, and the lag in the compressor pressure rise is no longer present in the model phase plane plot. Inputs for these plots are the same as in Fig. 7. A first-order lag on the compressor pressure rise [6] was then added to the model with physical lengths to see if a better match between the model and experimental data could be obtained. The lag was tuned to get a match in frequency with experimental data. As can be seen in Fig. 9,

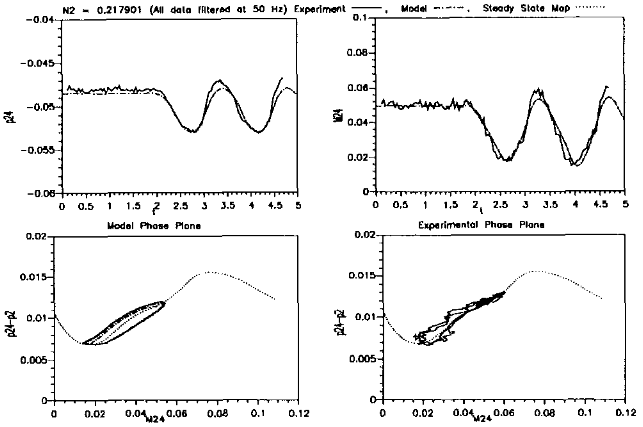

Fig. 9 Transient into surge (high speed) using physical lengths with first-order lag

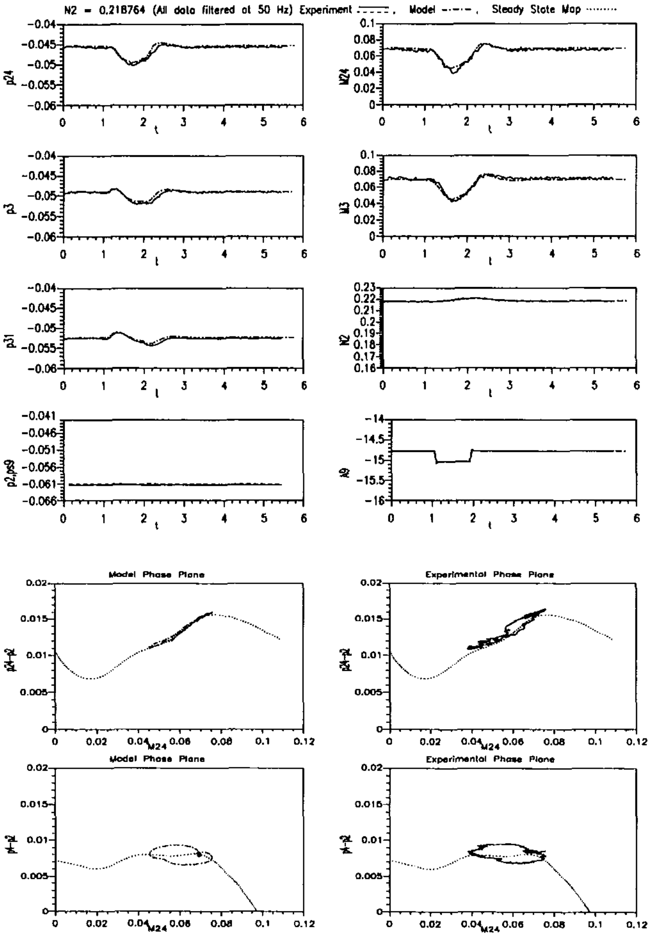

Fig. 10 Stable transient near transition to rotating stall

the amplitude and nonlinear character of the time traces of p_{24} and M_{24} do not match the experimental data as well as the time traces match in Fig. 7. Also, the nonlinear characteristic of the lag in compressor pressure rise is not pear shaped (see phase plane plots) as it is in the experiment and the model using effective lengths. This is due to the fact that the lag is fixed in this model instead of varying with Mach number and dimensionless compressor speed. Inputs for Fig. 9 are the same as in Fig. 7. As is indicated by the above comparisons, the best match between model and experimental data is obtained when effective lengths are used in the model.

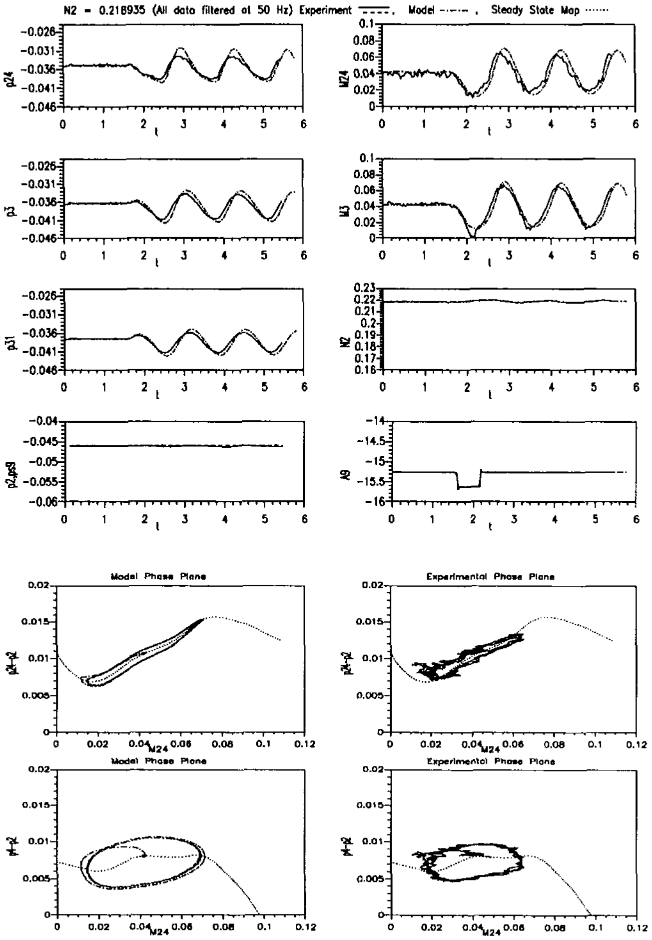

Fig. 11 Transient showing coexistent stable equilibrium and stable periodic solution

In Fig. 10, a transient is shown that begins with stable operation where no rotating stall exists. Then, a nozzle perturbation is introduced that moves the operating condition temporarily to a point where rotating stall does exist [45], and then returns the system to its original point. The match between model and experiment in this transient indicates the ability of the model to accurately predict the annulus average behavior of the system in the region of transition between axisymmetric and nonaxisymmetric flow. In the experimental phase plane plot of this figure, there seems to be a lag in the compressor pressure rise, which is not present in the model. This lag seems to be associated with the onset of rotating stall, and a two-dimensional model is probably required to predict this lag. Another possibility to account for this lag in some way is to add another input associated with rotating stall to the one-dimensional model. However, except for this lag, the match between the model and experimental data is quite good.

The comparison of model and experiment in Fig. 11 shows an interesting behavior of the model near the region of system instability. As can be seen, the system starts out in stable operation, and the nozzle area is perturbed for a short period of time and returned to its original position. The system does not, however, return to stable operation; it enters surge instead. Thus, at these parameter settings there exists both a stable equilibrium point and a stable periodic solution. Further discussion of this behavior is given in Section 4.2.

4.2 Nonlinear Dynamics and Bifurcations. In this section, we discuss the global nonlinear dynamic behavior of the compression system model given in Section 3. To do so, we turn to bifurcation theory. Bifurcation theory addresses the qualitative changes in system behavior, characterized by changes in stability and number of steady states, as the parameters of the system are varied.

The application of bifurcation theory involves first determining the steady state solutions of the system as a parameter is varied [5]. Then, the eigenvalues of the linearized system are computed, at each value of the parameter, to determine the local stability of the steady state. However, at some equilibrium points the eigenvalues of the linear system provide no information about the local behavior of the system. These equilibrium points are termed bifurcation points, and are characterized by the existence of a zero eigenvalue (at a static bifurcation point) or a pair of purely imaginary eigenvalues (at a Hopf bifurcation point). At a static bifurcation point, there is a change in the number of steady-state solutions when system parameters are varied. At a Hopf bifurcation point, a periodic solution is born in a close vicinity of the steady-state solution [47]. The type of Hopf bifurcation point is identified by the stability of periodic solution that arises. The Hopf point is said to be supercritical whenever the periodic solution is stable, and subcritical whenever it is unstable [47]. The system behavior in the neighborhood of the two types of Hopf bifurcation points, supercritical and subcritical, differs distinctly. As the parameter is changed from a stable equilibrium to an unstable equilibrium point across a supercritical Hopf bifurcation point, a small-amplitude stable periodic solution emerges. Both the amplitude and period of the periodic solutions increase as the system parameter is increased. When the parameter change is reversed, the amplitude of the periodic solution gradually decreases until the periodic solution ceases to exist at the Hopf point, and the steady state becomes stable. On the other hand, changing the parameter from a stable equilibrium to an unstable equilibrium across a subcritical Hopf bifurcation point results in the sudden appearance of a large-amplitude stable periodic solution. On reversing the parameter change, stable periodic solutions persist beyond the Hopf point and coexist with unstable periodic solutions, which are born at the subcritical Hopf point [47].

Since there are experimentally measured maps embedded into the model for which bifurcation analysis (and subsequent control design) is being performed, it is imperative that these maps be smooth enough to be several times differentiable and accurate enough to give good interpolated estimates between measured data points. These represent conflicting objectives in this rig where there is a reasonable amount of scatter in data due to the low signal-to-noise ratio. In order to smooth the map data, we use the smoothing spline algorithm described in [48]. The amount of smoothing done is determined by the smoothing parameter, S, which is an input to the algorithm. This parameter is an upper bound on the error between experimental data points and smoothed data points. The algorithm fits the map with the cubic spline, which minimizes the second derivative of the map subject to the error constraint given by S. To do the smoothing, a variance of 2.5 percent was allowed in Mach number measurements and 2.3 percent in total pressure measurements. These values are based on the accuracy of the measurement sensors as specified by the sensor manufacturers [44]. The smoothed maps are obtained by first smoothing maps of the Mach number measurements and total pressure measurements individually as a function of the known throttle parameter A_9. The resulting smoothed maps are then combined to form the map used in the model. To choose an appropriate value of S, the following condition is used: Since the stability of an equilibrium point is determined by the slope (and hence, the degree of smoothness) of the maps of the model evaluated at that equilibrium point, the value of S is selected to ensure that the stability regions predicted by the model, using the smoothed maps, correspond to those observed experimentally. A more detailed procedure for smoothing (not employed here) would involve matching not only regions of instability but also regions and amplitudes of periodic solutions exhibited by the model to those seen in experiment.

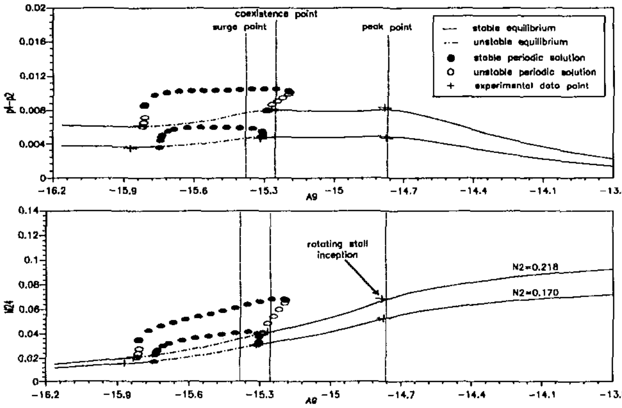

Fig. 12 Bifurcation diagram

To apply the bifurcation theory outlined in the foregoing discussion to the compression system model, we use the numerical software program AUTO [49]. This software is based on the pseudo-arc length continuation algorithm and is capable of continuing both static and dynamic steady-state solution branches as system parameters are varied. The dimensionless nozzle area, A_9, is regarded as the principal system parameter, while the dimensionless speed, N_2, is considered as an auxiliary parameter in generating the bifurcation diagrams. The bifurcation diagram for $N_2 = 0.218$ and $N_2 = 0.170$ are given in Fig. 12. In this diagram, the loci of stable equilibrium points are denoted by solid lines, and the loci of unstable equilibrium points are denoted by dash-dotted lines. The Hopf bifurcation points are marked with an ×. Additionally, the local maximum values of M_{24} and $p_4 - p_2$ on the periodic solutions corresponding to different values of parameter, A_9, are represented by circles on the same plot. The solid circles depict stable periodic solutions, while the open circles depict unstable periodic solutions. As can be seen, the model does not have any static bifurcation points at either speed, but it does have two subcritical Hopf bifurcation points for $N_2 = 0.218$ and two supercritical Hopf bifurcation points for $N_2 = 0.170$.

The existence and location of the Hopf bifurcation points are determined experimentally by tracing out the bifurcation diagram in Fig. 12. This is accomplished by very slowly varying the nozzle area. Due to this quasi-static variation of the nozzle area, the system operates approximately at steady-state conditions at all values of the nozzle area. Hence the points at which periodic solutions appear are clearly identified as the Hopf bifurcation points. The experimentally measured Hopf points are indicated in Fig. 12 by a +, and the match with that predicted by the model is good (the experimental points can hardly be seen as they are covered by the model Hopf points). This is, of course, expected because the smoothing of the maps embedded in the model was done to ensure that the regions of instability of the model were matched. The type of each Hopf bifurcation point can be determined experimentally by finding out where the periodic solutions disappear when moving the nozzle area back toward the value corresponding to the Hopf point. If the periodic solutions disappear at the Hopf point, then it is a supercritical Hopf bifurcation. However, if the periodic solutions disappear beyond the Hopf point, then it is a subcritical Hopf bifurcation. In the experiment, it was found that both Hopf bifurcation points were subcritical for $N_2 = 0.218$ and that both Hopf bifurcation points were supercritical for $N_2 = 0.170$ validating the behavior predicted by the model. Similar agreement was obtained for the location and types of Hopf bifurcation points for other speeds [45].

In the region near a subcritical Hopf bifurcation point, the coexistence of a stable equilibrium point, an unstable periodic solution, and a stable periodic solution divides the phase plane into three regions as shown in Fig. 13. The unstable periodic solution (depicted as dashed lines in Fig. 13) serves as the separatix for the regions of attraction of the stable equilibrium and the stable periodic solution. The unstable periodic solution was obtained by using the trajectory reversing technique discussed in [50]. The uncontrolled system response with initial conditions in region (*a*) of Fig. 13 traces out a trajectory that asymptotically approaches the stable equilibrium, while initial conditions in regions (*b*) or (*c*) trace out trajectories in the phase plane that asympotically approach the stable periodic solution. The coexistence of a stable equilibrium and a stable periodic solution in both the model and experimental data is the behavior described earlier in Fig. 11.

5 Closed-Loop Model Validation

In this discussion we demonstrate the control of surge via feedback compensation using the nozzle as the actuator. These controllers are designed directly from the model and implemented in experiment, with no a posteriori tuning of controller parameters, in order to validate the model for use in model based control design.

The analytical linear model obtained for this system [45] was used to generate eigenvalues for the system at each of the following operating conditions, which are marked in Fig. 12 for $N_2 = 0.218$:

	Surge	Peak	Coexistent
1	$-4.9161e+02+1.3377e+03i$	$-8.4670e+02+1.2260e+03i$	$-5.2286e+02+1.3369e+03i$
2	$-4.9161e+02-1.3377e+03i$	$-8.4670e+02-1.2260e+03i$	$-5.2286e+02-1.3369e+03i$
3	$-1.5472e+01+2.8477e+02i$	$-3.7123e+01+4.1699e+02i$	$-1.6418e+01+2.9800e+02i$
4	$-1.5472e+01-2.8447e+02i$	$-3.7123e+01-4.1699e+02i$	$-1.6418e+01-2.9800e+02i$
5	$-9.5749e+00$	$-2.5081e+01$	$-1.0713e+01$
6	$5.4883e-01+4.7300e+00i$	$-6.3747e-01+5.2776e+00i$	$-1.3369e-01+5.0062e+00i$
7	$5.4883e-01-4.7300e+00i$	$-6.3747e-01-5.2776e+00i$	$-1.3369e-01-5.0062e+00i$
8	$-3.0696e+00$	$-5.8211e+00$	$-3.3125e+00$
9	$-1.6999e-02$	$-2.9223e-02$	$-1.8089e-02$

where the surge point refers to a point where a surge limit cycle is the only stable condition, the peak point refers to the stable equilibrium point at the peak of the $p_4 - p_2$ curve of Fig. 12 that is near the rotating stall inception point, and the coexistent point refers to a point where either a stable equilibrium point or a surge limit cycle is a possible stable condition.

As can be seen, there is a complex conjugate pair of eigenvalues that has positive real parts (sixth and seventh) at the surge point (this instability leads to the surge limit cycle) and has negative real parts for the peak and coexistent point. The modes corresponding to these eigenvalues can be deduced from a transformation matrix obtained from the inverse of the eigenvector matrix in real modal form. For this unstable complex conjugate pair, it was found that the mode is predominantly made up of the states M_{25} and p_4 [45]. This analysis seems to give insight toward what are the best sensed variables to consider for control design, namely M_{25} and p_4. Of course, the ability to obtain these measurements must also be taken into account when control configurations are being considered. Now, M_{25} is not an easily measured quantity, but p_{s4}, which is essentially equal to p_4, is an easily measured quantity. Three controllers are designed, therefore, using A_9 as the actuator and p_{s4} as the sensed variable, as shown in the block diagram given in Fig. 14. As can be seen in this diagram, the variable p_{s4} is sensed and its nominal value $p_{s4,\text{nom}}$ is subtracted from it. This signal goes into the surge controller, which computes the signal $\delta A_{9,\text{surge}}$. This value is then added to the nominal value $A_{9,\text{nom}}$ to obtain the signal $A_{9,\text{cont}}$. An additional signal $A_{9,\text{dist}}$ is shown, which can be added to create disturbances in the closed-loop system. The resulting signal $A_{9,\text{demand}}$ is then used to drive the actuator for the nozzle area. One controller was designed for each of three operating conditions shown in Fig. 12 for $N_2 = 0.218$: the surge point, the peak point, and the coexistent point.

The controllers were designed by first forming an aug-

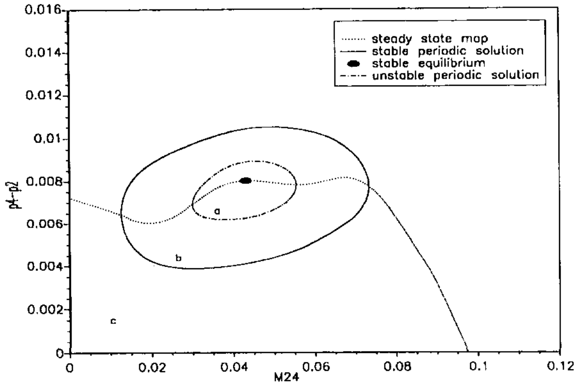

Fig. 13 Coexistence stable / unstable periodic solutions and stable equilibrium point

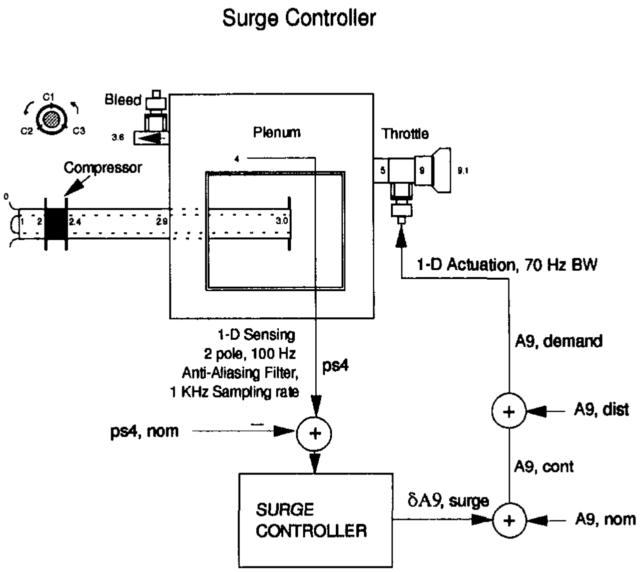

Fig. 14 Controller block diagram

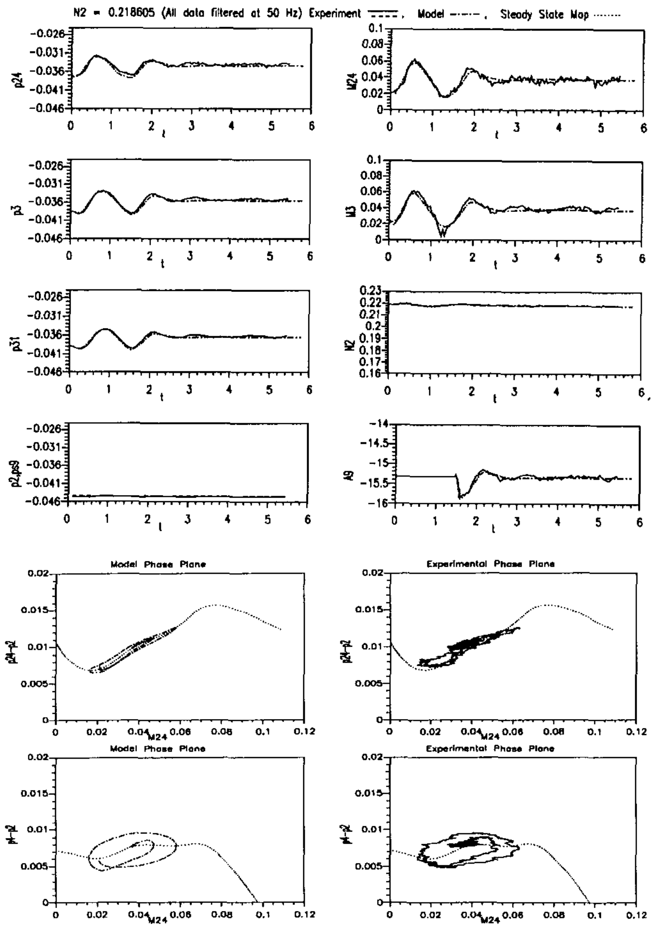

Fig. 15 Control at surge point

Table 5 Comparison of model and experiment gain and time delay margins

Point	Model Gain Margins (dB)	Exp. Gain Margins (dB)	Model Time Delay (sec)	Exp. Time Delay (sec)
Surge	+8.17, −11.2	+6.85, −5.51	.0753	.025
Coexistent	+12.2, −∞	+11.1, −∞	.1113	.042
Peak	+14.9, −∞	+11.4, −∞	.1305	.057

mented linear plant which was obtained by: (1) reducing the transfer function model order by truncating states in the balanced realization with small Hankel singular values [51] using the Matlab [52] m-file **schmr**, (2) appending experimentally determined actuator dynamics to the plant; the transfer function for these dynamics is given as follows:

$$\left(\frac{1}{9.9341 \times 10^{-5} s^2 + 0.010575 s + 1}\right)\left(\frac{1}{0.0077530 s + 1}\right), \tag{27}$$

and (3) appending the 100 Hz Butterworth anti-aliasing low-pass filter, which is on p_{s4}, to the plant along with another 50 Hz Butterworth low-pass filter to reduce signal noise seen by the controller. Once this augmented plant was obtained, control design was performed and the controller combined with the 50 Hz Butterworth filter became the controller that was implemented.

For the surge operating condition, the linear dynamics about the equilibrium point were unstable. The controller was designed to achieve optimally robust stabilization in the presence of stable additive perturbations to the normalized left coprime factorization of the plant using the algorithm described in [53]. The resulting controller was reduced in order using the same technique used for reducing the plant. The reduced order controller was then used to form the closed-loop plant, and closed-loop damping, gain margins, and phase margin were checked. It was found that the closed-loop damping was not very high ($\zeta = 0.11$), but that the gain margins (−13 dB, −5.1 dB) and phase margin (±46 deg) were quite good. Therefore, the upper gain margin was partially sacrificed to obtain increased damping by increasing the gain of the controller. The final fourth-order controller was obtained by doubling the gain of the original controller. The final closed-loop damping ($\zeta = 0.51$), gain margins (+8.2 dB, −11 dB), and phase margin (±53 deg) were all quite good. For brevity, the parameters for this controller are not listed here; however, they can be found in [45]. A comparison between the model and experiment of the controlled system is given in Fig. 15. In these plots, the system starts out in surge with the controller turned off. Then, at time $t \approx 1.4$ the controller is switched on, and the system is stabilized. As can be seen, these plots show good agreement between model and experiment and validates the model for use in model-based control designs. It was found, however, that although surge has been eliminated, rotating stall still exists in the controlled system, as expected [45]. Experimentally measured gain and time delay margins (phase margins cannot be measured) were obtained and are shown in Table 5 to compare reasonably well to those predicted by the model. As an additional comparison between the model and experiment under control, a closed-loop bifurcation diagram was generated for the system with the controller designed at the surge point. In the closed-loop bifurcation diagrams, the parameters of the linear controller designed at a particular point are used for a linear controller about the uncontrolled equilibrium point for each value of the parameter A_9. The closed-loop bifurcation diagram for the controller designed at the surge point is given in Fig. 18. As can be seen, the system has been stabilized at the design point, and the entire region of instability of the system has been eliminated. Experimentally measured equilibrium points of the controlled system are also indicated on the diagram with a +, and there is some discrepancy between the model and experiment. We believe, however, that the discrepancy in this diagram and in the margin comparisons is due to the fact that in the experiment, the controllers are implemented as quantized (or digital) discrete time systems, while in the model they are simulated as continuous systems. Further investigation of this point will be carried out in future work.

It is worthwhile to state here that the prospect of stabilizing surge with proportional feedback control from A_9 to p_{s4} was also investigated. However, it was found by looking at root locus plots that the system is not stabilizable at all operating conditions under such a fixed proportional control.

For both the peak and co-existent points, the controller was designed differently than for the surge point. For these points, the linearized dynamics were already stable and the objective was to increase the damping of the system. For this objective, it was sufficient to use a constant gain combined with the 50 Hz Butterworth filter. The design criterion was to give damping of $\zeta = 0.7$ while retaining acceptable gain and phase margins. For the peak point, the constant gain multiplying the 50 Hz Butterworth filter was −109, and the resulting closed-loop damping ($\zeta = 0.7$), gain margins (+15 dB, −∞ dB), and phase margin (±95 deg) were all quite good. For brevity, the parameters for this controller are also not listed here; however, they can be found in [45]. A comparison between the model and experiment of the controlled system is given in Fig. 16. In these plots, the controller is always on; however, for a short period of time a

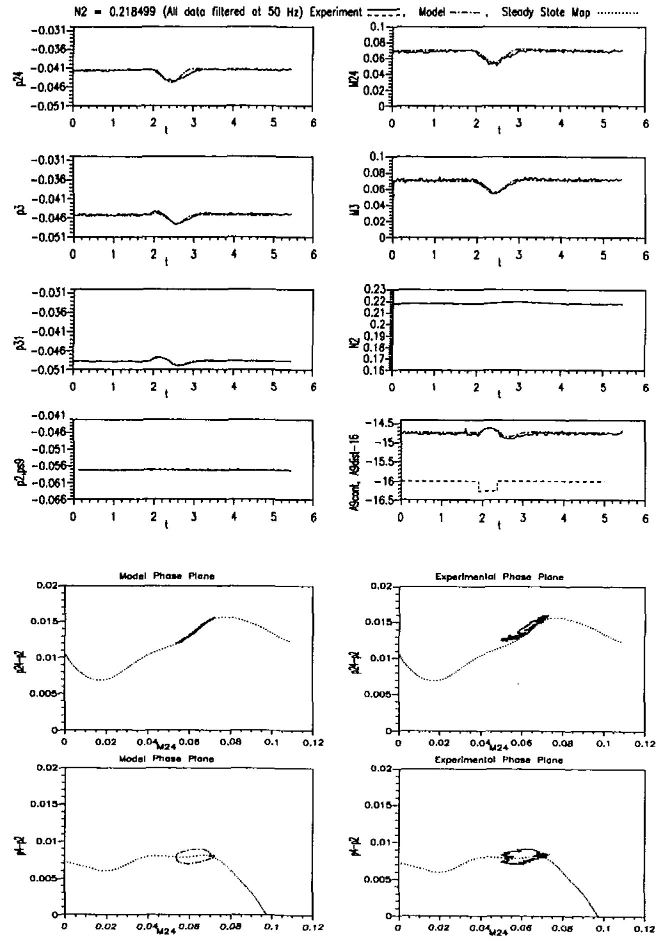

Fig. 16 Control at peak point

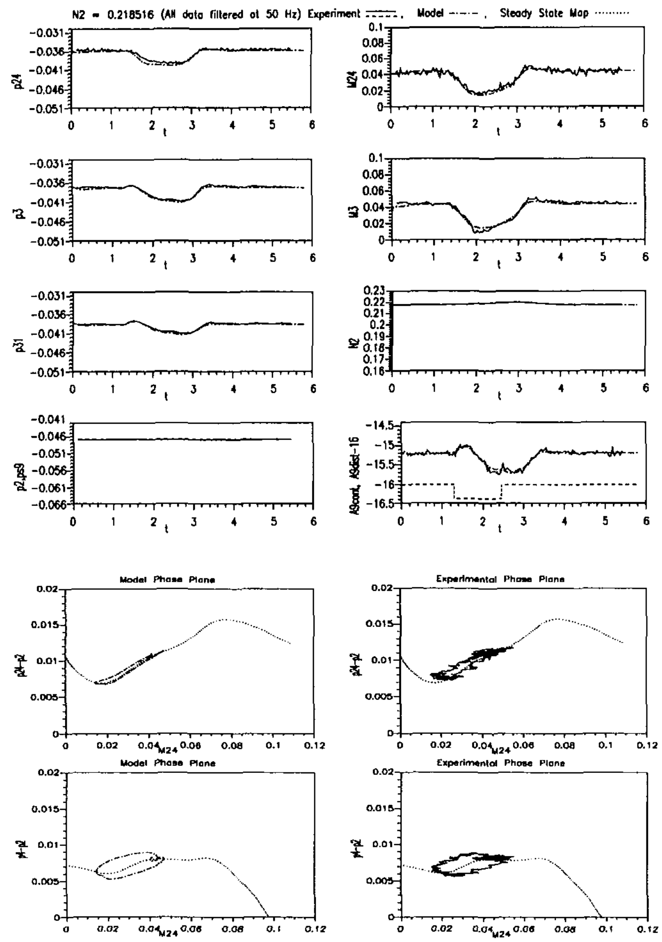

Fig. 17 Control at coexistent point

disturbance, $A_{9,\text{dist}}$, is added to perturb the system away from equilibrium. The same disturbance was introduced in Fig. 10 for the uncontrolled system. The controller output, $A_{9,\text{cont}}$, is shown in Fig. 16 along with the disturbance $A_{9,\text{dist}}$ seen by the system. As can be seen, these plots show good agreement between model and experiment and that the damping of the system has definitely been increased as indicated by the reduced or eliminated overshoot in various time traces (for example M_{24}) when compared to Fig. 10. A comparison of experimentally measured gain and time delay margins for this controller to those predicted by the model is given in Table 5, and they are shown to compare reasonably well. The closed-loop bifurcation diagram based on the peak controller is given in Fig. 19. In this diagram, it is seen that the controller designed at the peak also had some effect at points other than the design point. In fact, the region of instability has been significantly reduced as is evident by the decreased interval between the two Hopf bifurcation points. The experimentally measured equilibrium points are indicated on this diagram with a +, and once again there is some discrepancy between model and experiment, which we again attribute to the digital controller implementation.

For the coexistent point, the constant gain multiplying the 50 Hz Butterworth filter was -192, and the resulting closed-loop damping ($\zeta = 0.7$), gain margins ($+12$ dB, $-\infty$ dB), and phase margin (± 78 deg) were all quite good as well. The parameters for this controller can be found in [45]. A comparison between the model and experiment of the controlled system is given in Fig. 17. In these plots once again, the controller is always on, and for a short period of time a disturbance, $A_{9,\text{dist}}$, is added to perturb the system away from equilibrium. The same disturbance was introduced in Fig. 11 for the uncontrolled system. The controller output, $A_{9,\text{cont}}$, is shown in Fig. 17 along with the disturbance $A_{9,\text{dist}}$ seen by the system. As can be seen, these plots show good agreement between model and experiment and indicate that by increasing the damping at this point, the coexisting surge limit cycle has been eliminated, and only a stable equilibrium point remains. A comparison of experimentally measured gain and time delay margins for this controller to those predicted by the model is given in Table 5, and they are shown to compare reasonably well. The closed-loop bifurcation diagram for the controller at the coexistent point is given in Fig. 20. This diagram verifies that the coexisting periodic solutions are no longer present in the system. In fact, it shows that no periodic solutions are present in the system. The controller has

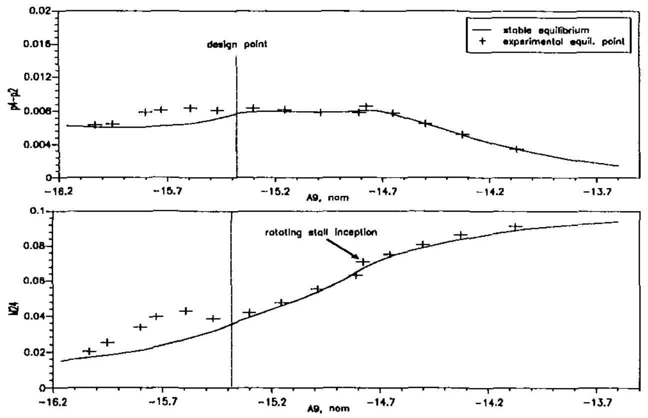

Fig. 18 Closed-loop bifurcation diagram for control at surge point

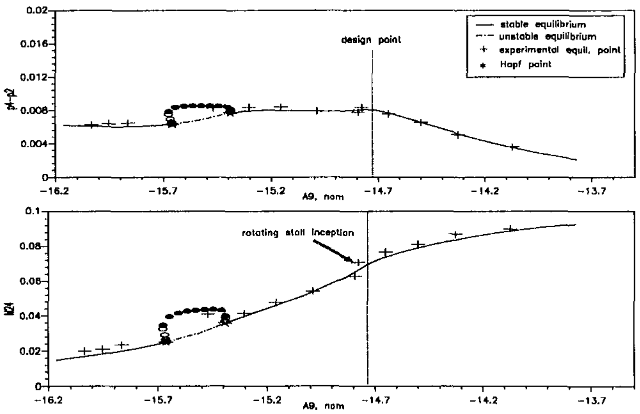

Fig. 19 Closed-loop bifurcation diagram for control at peak point

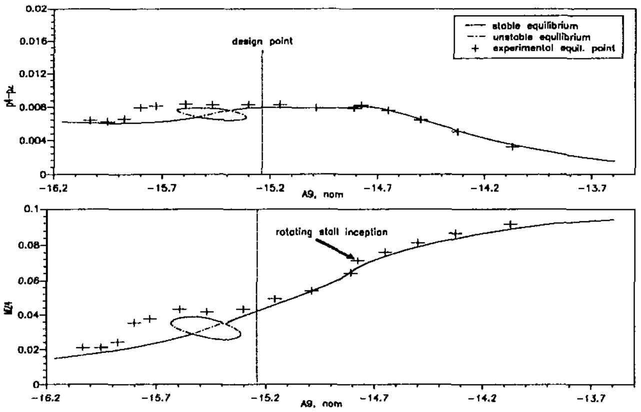

Fig. 20 Closed-loop bifurcation diagram for control at coexistent point

introduced a static bifurcation in the diagram. For all parameter values at least one stable equilibrium exists, and for some parameter values there are two stable equilibria coexisting with an unstable equilibrium. Although some of the original equilibria were not stabilized, the new equilibria at those parameter values are at higher Mach number and pressure rise, thus the new equilibria would be preferable. Experimentally measured equilibrium points of the controlled system are also indicated on the diagram with a +, and there is some discrepancy between the model and experiment, again attributable to the digital implementation of the controller.

In general, agreement between model and experiment is worse in closed-loop than in open-loop, owing perhaps to the fact that controller was implemented as a quantized (or digital) discrete time system in experiment and as a continuous time system in simulations. In other words, the discrepancy might be due to a poor controller model, as opposed to the compression system model.

6 Conclusions and Future Work

In this paper, the generic compression system model presented in [3] was applied to the LICCHUS multistage axial compressor rig [4], configured for single-stage operation, to obtain a one-dimensional unsteady compressible viscous flow model of this rig. The model and experimental data were compared with respect to both open-loop uncontrolled and closed-loop controlled behaviors. These comparisons focused on forced transients and global nonlinear dynamics and bifurcations, and in all cases the comparison between the model and experimental data was excellent. The model, which does not include any hysteretic maps, was able to predict experimentally observed hysteresis with respect to the onset and cessation of surge. Controllers used for closed-loop comparisons were designed directly from the model with no a posteriori tuning of controller parameters. The excellent closed-loop comparisons between the model and experimental data provide strong evidence in support of the validity of the model for use in model-based controller design. The excellent agreement between the model and experimental data summarized above was attributed in large part to the use of effective lengths within the model as prescribed by the modeling technique. The overall success of this model is believed to provide partial validation of the approach to control-oriented high-frequency turbomachinery modeling being developed by the authors.

Future work with the model given in this paper will focus primarily on the design and implementation of integrated surge control/rotating stall avoidance schemes for this axial compression system. In addition, one-dimensional unsteady compressible viscous flow models will be obtained for the same rig operating in a multistage configuration, and the LICCHUS turbojet engine experimental rig [4]. Finally, extensions of the one-dimensional model presented in this paper to a two-dimensional model will be undertaken, using a parallel compressor concept, so that rotating stall control schemes can be investigated.

Acknowledgments

This work was supported by ONR and NSF. The work of the third author on this paper was also supported by the Air Force Laboratory Graduate Fellowship Program.

References

1 Badmus, O. O., Eveker, K. M., and Nett, C. N., "Control-Oriented High-Frequency Turbomachinery Modeling, Part 1: Theoretical Foundations," in: *Proceedings of the 1992 AIAA Joint Propulsion Conference*, July 1992, AIAA Paper No. 92-3314.

2 Badmus, O. O., Eveker, K. M., and Nett, C. N., "Control-Oriented High-Frequency Turbomachinery Modeling: Theoretical Foundations," submitted for publication to the ASME JOURNAL OF TURBOMACHINERY, 1993.

3 Badmus, O. O., Eveker, K. M., and Nett, C. N., "Control-Oriented High-Frequency Turbomachinery Modeling: General 1D Model Development," ASME Paper No. 93-GT-385, 1993; accepted for publication in the JOURNAL OF TURBOMACHINERY.

4 Nett, C. N., "LICCHUS Experimental Facilities Summary: September 1992 (Months 1–18)," Oct. 1991; Videotape presentation, available from School of Aerospace Engineering, Georgia Tech, 120 min.

5 Mees, A. I., "A Plain Man's Guide to Bifurcations," *IEEE Transactions on Circuits and Systems*, Vol. CAS-30, No. 8, 1983, pp. 512–517.

6 Greitzer, E. M., "Surge and Rotating Stall in Axial Flow Compressors, Part 1: Theoretical Compression System Model," ASME *Journal of Engineering for Power*, Vol. 98, 1976, pp. 190–198.

7 Davis, M. W., and O'Brien, W. F., "A Stage-by-Stage Post-Stall Compression System Modeling Technique," AIAA Paper No. 87-2088, 1987.

8 Ffowcs-Williams, J. E., and Huang, X. Y., "Active Stabilization of Compressor Surge," *J. Fluid Mech.*, Vol. 204, 1989, pp. 245–262.

9 Sugiyama, Y., Tabakoff, W., and Hamed, A., "J85 Surge Transient Simulation," *J. Propulsion and Power*, Vol. 5, 1989, pp. 375–381.

10 Tang, G. C., "Basic Features of Speed Induced Transient Behaviour of Axial Flow Compressors," ASME Paper No. 90-GT-211, 1990.

11 Davis, M., "Parametric Investigation Into the Combined Effects of Pressure and Temperature Distortion on Compression System Stability," in: *AIAA/SAE/ASME/ASEE Joint Propulsion Conference*, June 1991, Paper No. AIAA-91-1895.

12 Greitzer, E. M., "Surge and Rotating Stall in Axial Flow Compressors, Part 2: Experimental Results and Comparison with Theory," ASME *Journal of Engineering for Gas Turbines and Power*, Vol. 98, 1976, pp. 199–217.

13 Stenning, A. H., "Rotating Stall and Surge," ASME *Journal of Fluids Engineering*, Vol. 102, 1980, pp. 14–21.

14 Fasol, K. H., "Recent Experiences with Modelling and Simulation of Some Industrial Plants," *Israel J. Technology*, Vol. 17, 1979, pp. 207–216.

15 Macdougal, I., and Elder, R. L., "Simulation of Centrifugal Com-

pressor Transient Performance for Process Plant Applications," ASME *Journal of Engineering for Gas Turbines and Power*, Vol. 105, 1983, pp. 885-890.

16 Wenzel, L. M., and Bruton, W. M., "Analytical Investigation of Nonrecoverable Stall," Technical Memorandum 82792, NASA, Feb. 1982.

17 Hosny, W. M., Bitter, S. J., and Steenken, W. G., "Turbofan Engine Nonrecoverable Stall Computer-Simulation Development and Validation," AIAA Paper No. 85-1432, 1985.

18 Chung, K., Leamy, K. R., and Collins, T. P., "A Turbine Engine Aerodynamic Model for In-Stall Transient Simulation," in: *21st Joint Propulsion Conference*, July 1985, AIAA Paper No. 85-1429.

19 Steenken, W. G., "Turbofan Engine Post-Instability Behavior: Computer Simulations, Test Validation, and Application of Simulations," in: *Engine Response to Distorted Inlet Flow Conditions*, AGARD-CP-400, 1987.

20 Epstein, A. H., Ffowcs-Williams, J. E., and Greitzer, E. M., "Active Suppression of Aerodynamic Instabilities of Turbomachines," *J. Propulsion and Power*, Vol. 5, 1989, pp. 204-211.

21 Ffowcs-Williams, J. E., and Graham, W. R., "Engine Demonstration of Active Surge Control," in: *Proceedings of the 1990 ASME International Gas Turbine and Aeroengine Congress and Exposition*, 1990.

22 Gysling, D. L., Dugundji, J., Epstein, A. H., and Greitzer, E. M., "Dynamic Control of Centrifugal Compressor Surge Using Tailored Structures," in: *Proceedings of the 1990 ASME Gas Turbine Conference*, 1990.

23 Pinsley, J. E., Guenette, G. R., Epstein, A. H., and Greitzer, E. M., "Active Stabilization of Centrifugal Compressor Surge," in: *Proceedings of the 1990 ASME Gas Turbine Conference*, 1990.

24 Hosny, W. M., Leventhal, L., and Steenken, W. G., "Active Stabilization of Multistage Axial-Compressor Aerodynamic System Instabilities," ASME Paper No. 91-GT-403, 1991.

25 Badmus, O. O., Nett, C. N., and Schork, F. J., "An Integrated Full-Range Surge Control/Rotating Stall Avoidance Compressor Control System," in: *Proceedings of the 1991 American Control Conference*, 1991.

26 Day, I. J., "Active Suppression of Rotating Stall and Surge in Axial Compressors," ASME Paper No. 91-GT-87, 1991.

27 Moore, F. K., "A Theory of Rotating Stall of Multistage Compressors, Parts I-III," ASME *Journal of Engineering for Gas Turbines and Power*, Vol. 106, 1984, pp. 313-336.

28 Moore, F. K., and Greitzer, E. M., "A Theory of Post-Stall Transients in Axial Compression Systems: Part 1, Development of Equations and Part 2, Application," ASME JOURNAL OF TURBOMACHINERY, Vol. 108, 1986, pp. 68-76, 231-239.

29 Moore, F. K., "Stall Transients of Axial Compression Systems With Inlet Distortion," *J. Propulsion and Power*, Vol. 2, 1986, pp. 552-561.

30 Paduano, J., Valavani, L., Epstein, A. H., Greitzer, E. M., and Guenette, G., "Modeling for Control of Rotating Stall," *Proceedings 29th IEEE Conference on Decision and Control*, 1991.

31 Paduano, J., "Active Control of Rotating Stall in Axial Compressor," PhD thesis, Massachusetts Institute of Technology, 1991.

32 Bonnaure, L., "Modelling High Speed Multistage Compressor Stability," Master's thesis, Department of Aeronautics and Astronautics, Massachusetts Institute of Technology, 1991.

33 Dugundji, J., Garnier, V. H., Epstein, A. H., Greitzer, E. M., Guenette, G., Paduano, J., Silkowski, P., Simon, J., and Valavani, L., "A Progress Report on Active Control of Flow Instabilities: Rotating Stall Stabilization in Axial Compressors," in: *Proceedings of the 1989 AIAA 2nd Shear Flow Conference*, Mar. 1989, AIAA Paper No. 89-1008.

34 Simon, J. S., and Valavani, L., "A Lyapunov Based Nonlinear Control Scheme for Stabilizing a Basic Compression System Using a Close-Coupled Valve," in: *Proceedings of the 1991 American Control Conference*, 1991.

35 Liaw, D. C., and Abed, E. H., "Stability Analysis and Control of Rotating Stall," in: *Proceedings of the 2nd IFAC Nonlinear Control Systems Design Symposium*, June 1992.

36 Greitzer, E. M., "Review—Axial Compressor Stall Phenomena," ASME *Journal of Fluids Engineering*, Vol. 102, 1980, pp. 134-151.

37 McCaughan, F. E., "Application of Bifurcation Theory to Axial Flow Compressor Instability," ASME JOURNAL OF TURBOMACHINERY, Vol. 111, 1989, pp. 426-433.

38 McCaughan, F. E., "Numerical Results for Axial Flow Compressor Instability," ASME JOURNAL OF TURBOMACHINERY, Vol. 111, 1989, pp. 434-441.

39 Abed, E. H., Houpt, P. K., and Hosny, W. M., "Bifurcation Analysis of Surge and Rotating Stall in Axial Flow Compressors," in: *Proceedings of the 1990 American Control Conference*, May 1990.

40 McCaughan, F. E., "Bifurcation Analysis of Axial Flow Compressor Stability," *SIAM Journal of Applied Math.*, Vol. 50, 1990, pp. 1232-1253.

41 Liaw, D. C., Adomaitis, R. A., and Abed, E. H., "Two-Parameter Bifurcation Analysis of Axial Flow Compressor Dynamics," *Proceedings of the American Control Conference*, pp. 2955-2960, 1991, IEEE Cat. No. 91CH2939-7.

42 Oliva, S. M., and Nett, C. N., "A General Nonlinear Dynamic Analysis of Second-Order, One-Dimensional, Theoretical Compression System Model," in: *Proceedings of the 1991 American Control Conference*, 1991.

43 Abed, E. H., and Liaw, D., "Two-Parameter Bifurcation Analysis of Axial Flow Compressor Dynamics," in *Proceedings of the 1991 American Control Conference*, 1991.

44 Thompson, J. W., and Abernathy, R. B., "Handbook of Uncertainty in Gas Turbine Measurements," Tech. Rep., AEDC, Feb. 1973, AEDC-TR-73-5.

45 Badmus, O. O., Chowdhury, S., Davis, E. J., Eveker, K. M., and Nett, C. N., "Single-Stage Compression System 1D Model," 1993, LIC-CHUS Internal Report No. 93-001.

46 Hindmarsh, A. C., "ODEPACK, A Systematized Collection of ODE Solvers," in: *Scientific Computing: Applications of Mathematics and Computing to the Physical Sciences*, R. S. Stepleman, ed., North-Holland, 1983, pp. 55-64.

47 Mees, A. I., *Dynamics of Feedback Systems*, John Wiley & Sons, 1981.

48 de Boor, C., *A Practical Guide to Splines*, Springer-Verlag, 1978.

49 Doedel, E., "AUTO: A Program for the Automatic Bifurcation Analysis of Autonomous Systems," *Cong. Num.*, Vol. 30, 1981, pp. 265-284.

50 Genesio, R., Tartaglia, M., and Vicino, A., "On the Estimation of Asymptotic Stability Regions: State of The Art and New Proposals," *IEEE Transactions of Automatic Control*, Vol. 30, 1985, pp. 747-755.

51 Maciejowski, J. M., *Multivariable Feedback Design*, Addison-Wesley, 1989.

52 The MathWorks, Inc., South Natick, MA, MATLAB Reference Manual, 1990.

53 Glover, K., Sefton, J., and Mcfarlane, D., "A Tutorial on Loop Shaping Using h-Infinity Robust Stabilization," *Robust Control*, 1990, pp. 117-126.

Prestall Behavior of Several High-Speed Compressors

M. Tryfonidis

O. Etchevers

J. D. Paduano

A. H. Epstein

Gas Turbine Laboratory,
Massachusetts Institute of Technology,
Cambridge, MA 02139

G. J. Hendricks

United Technologies Research Center,
East Hartford, CT 06108

High-speed compressor data immediately prior to rotating stall inception are analyzed and compared to stability theory. New techniques for the detection of small-amplitude rotating waves in the presence of noise are detailed, and experimental and signal processing pitfalls discussed. In all nine compressors examined, rotating stall precedes surge. Prior to rotating stall inception, all the machines support small-amplitude (<1 percent of fully developed stall) waves traveling about the circumference. Traveling wave strength and structure are shown to be a strong function of corrected speed. At low speeds, a ~ 0.5 times shaft speed wave is present for hundreds of rotor revolutions prior to stall initiation. At 100 percent speed, a shaft speed rotating wave dominates, growing as stall initiation is approached (fully developed rotating stall occurs at about 1/2 of shaft speed). A new, two-dimensional, compressible hydrodynamic stability analysis is applied to the geometry of two of the compressors and gives results in agreement with data. The calculations show that, at low corrected speeds, these compressors behave predominantly as incompressible machines. The wave that first goes unstable is the 1/2 shaft frequency mode predicted by the incompressible Moore–Greitzer analysis and previously observed in low-speed compressors. Compressibility becomes important at high corrected speeds and adds axial structure to the rotating waves. At 100 percent corrected speed, one of these hitherto unrecognized compressible modes goes unstable first. The rotating frequency of this mode is constant and predicted to be approximately coincident with shaft speed at design. Thus, it is susceptible to excitation by geometric nonuniformities in the compressor. This new understanding of compressor dynamics is used to introduce the concept of traveling wave energy as a real time measure of compressor stability. Such a wave energy-based scheme is shown consistently to give an indication of low stability for significant periods (100–200 rotor revolutions) before stall initiation, even at 100 percent corrected speed.

Introduction

A recent focus of rotating stall research has been the inception process. Using both models and experimental data, researchers have attempted to develop an improved description of rotating stall inception, including the connection between small and large-amplitude disturbances, and between stall and surge. Such a description would be useful in several arenas, including compressor design, stall warning and avoidance, and stall control (both active and passive).

In past practice, experimental studies of stall inception used few sensors per stage, and concentrated on understanding local blade-row phenomena during stall inception. A more recent method for studying rotating stall inception, motivated by a hydrodynamic theory of compressor stability developed by Moore and Greitzer (1986), was first introduced by McDougall et al. (1990). This method uses a circumferential array of sensors at one or more axial locations, and attempts to detect circumferential waves of perturbation pressure or velocity. Hydrodynamic theory predicts that sinusoidal rotating waves will become underdamped near the stall inception point, and thus spatial sinusoids should be detectable at small amplitudes before stall inception occurs. This information about the *spatial structure* of the prestall disturbances provides a guideline for combining multiple measurements. The subsequent improvement in signal-to-noise ratio potentially allows detection of low amplitude prestall waves, which would otherwise be missed in the noisy compressor environment.

Two questions have been raised concerning this approach to stall warning. First, it is important to understand whether, and under what conditions, spatial waves exist in high-speed axial compressors prior to stall inception. Clearly one cannot take advantage of the predicted temporal and spatial structure if this structure does not exist. Second, if waves exist, what are the best methods to detect them and to transform detection into an incipient stall warning signal?

The question of wave existence has been studied by several researchers, including Garnier et al. (1991), Day (1993a), Day and Freeman (1993c), Gallops et al. (1993), Hoying (1993), Boyer et al. (1993), and Freeman and Wilson (1993). In this

---

Contributed by the International Gas Turbine Institute and presented at the 39th International Gas Turbine and Aeroengine Congress and Exposition, The Hague, The Netherlands, June 13–16, 1994. Manuscript received by the International Gas Turbine Institute March 9, 1994. Paper No. 94-GT-387. Associate Technical Editor: E. M. Greitzer.

paper, we will present data from several compressors, some of which were studied previously by other investigators. Our approach is to show characteristics that are similar across a variety of high-speed compressors using common analysis tools and to connect these experimental observations with hydrodynamic stability theory.

It is important at the outset to distinguish the terminology that we will use. *Fully developed rotating stall* refers to the large-amplitude (50 ~ 100 percent mass flow fluctuations) rotating stall, during which amplitude variations of the perturbations are insignificant. *Stall inception* is the transient from axisymmetric, small-perturbation flow conditions to rotating stall, and thus includes large disturbances whose amplitudes change with time. The short-wavelength disturbances reported by Day (1993a) fall into this category. *Prestall* refers to the period of time immediately prior to stall inception, during which compressor operation is steady but may exhibit small-amplitude (on the order of 1 percent) dynamics. Perturbations associated with these dynamics are small compared both to stall inception and to fully developed stall perturbations. These three regions—prestall, stall inception, and fully developed stall—are difficult to separate precisely; rather the terminology allows us to communicate the ideas presented in the paper in a more concise manner. (Examples of delineating data in this way are given in Fig. 3, to be discussed in a later section.)

The stable, prestall inception region is in many ways the most interesting since stable operation is the design goal, a goal that is lost once stall is initiated. Yet compressor dynamics in this region has been little studied. Therefore, our focus is on the prestall inception dynamics of high-speed compressors, attacked with theory and experiment.

In the following sections, we will present a new data reduction procedure that reveals the presence of small amplitude, prestall traveling waves in all of the compressors studied. This wave structure is shown to be a strong function of corrected speed. The results of a new, compressible, hydrodynamic stability model are given, and are in agreement with the data. The calculations indicate that the speed dependence of the wave structure is due to the effects of compressibility at the higher rotational speeds. This understanding of high-speed compressor wave structure adds a new perspective to real-time stall warning prospects. Promising results of a wave energy-based scheme are presented. We close by discussing the implications of compressible wave structure and dynamics for compressor design.

Data Reduction Procedures

Since one of our primary goals in this paper is to investigate the existence of prestall waves in high-speed compressors, our data reduction procedures are purposefully designed to avoid predisposition of the results. Thus, for instance, we do not narrow-band pass filter the data, as this can yield spurious traveling when very little actual wave energy exists. In fact, we do not in any way take advantage of the predicted (and, often, measured) *temporal* structure of the waves in our initial analysis; presumably doing so (for instance, by doing model-based filtering such as Kalman filtering) would improve at least the appearance of the results.

We do take advantage, in some of our data reduction, of the *spatial* structure of the predicted traveling waves, and this provides a way to detect traveling of spatially coherent structures. Following the theoretical development of Garnier et al. (1991), we assume that the pressure perturbations of interest take the following form at a given axial station:

$$\delta P_x(\theta, t) = \mathrm{Re}\left\{\sum_{k=0}^{\infty} a_k(t)\cdot e^{ik\theta}\right\} \tag{1}$$

where x indicates the axial station at which the measurements are taken, and $a_k(t)$ are the *spatial* Fourier coefficients of the perturbations. According to linearized hydrodynamic theory of compressor stability, the spatial Fourier coefficients evolve independently and thus constitute the fundamental states of the system. (In contrast, the pressure perturbation $\delta P_x(\theta_n, t)$ at a given circumferential position θ_n is correlated to that at any other position, and thus constitutes an amalgam of dynamic effects that must somehow be distinguished.)

We can derive an approximation for $a_k(t)$ from a set of N circumferential measurements of δP_x by using the spatial Fourier transform:

$$a_k(t) = \frac{1}{N}\sum_{n=1}^{N} \delta P(\theta_n, t)\cdot \exp(ik\theta_n) \tag{2}$$

where N must obey the Nyquist criterion for the mode k, that is, $N \geq 2k+1$. The sensor locations θ_n are often, but not necessarily, evenly spaced; even or nearly even spacing insures that harmonics *below* the Nyquist do not alias into the estimate of $a_k(t)$.

If our assumption about the independence of spatial harmonics is correct, then we have effectively diagonalized the system, and the states $a_k(t)$ can be treated as evolving according to independent dynamics. This data reduction procedure assumes very little about what these dynamics are, but since we are searching for such dynamics it is important at this point to describe the expected behavior. In the low-speed (Garnier et al., 1991) hydrodynamic model, a single eigenvalue usually dominates at a given operating point and thus a simple model of spatial Fourier coefficient evolution is expected (see, for instance, Garnier):

$$\frac{da_k}{dt} = (\sigma_k - i\omega_k)a_k + V(t) \tag{3}$$

where $V(t)$ represents random excitation of the system related to the unsteady aerodynamics of the compressor, inflow distortions, etc. Since the character of this noise is currently unknown in compressors and engines, we assume here white noise excitation. Figures 1 and 2 show the behavior of such a system, based on simulation of Eq. (3), in two different ways.

Figure 1 shows the time history of the magnitude and phase of the first spatial harmonic, $a_1(t)$ for various values of the damping ratio, $\zeta = \sigma_k/|\sigma_k + i\omega_k|$, which goes to zero as the compressor approaches the instability point. The magnitude is the wave strength, while the phase is the wave angular position in the compressor annulus. The linear dynamics of the modeled compressor exhibit a gradual trend toward coherent traveling as the damping ratio decreases. However, the damping ratio is quite small here before traveling is absolutely deterministic in appearance (i.e., before the phase history is a straight line, Fig. 1*c*), and the magnitude of the waves at this point is correspondingly large. These results assume that there is no corrupting measurement noise in the data, so we expect that the damping ratio must indeed be quite small in order for a coherent, deterministic wave to be detected in the presence of both process and measurement noise.

Figure 2 shows the spatial power spectra (PSD of a_1) averaged over a period corresponding to each of the damping ratios in Fig. 1. Note that $a_k(t)$ is a complex function of time, so the power spectrum is *not symmetric about zero spatial frequency*, $\omega = 0$. This lack of symmetry allows us to distinguish between standing waves oscillating in amplitude, and rotating waves with constant amplitude (see appendix); standing waves yield no difference between positive and negative frequencies, while traveling waves show asymmetric peaks, which we term "traveling wave energy" in the spectrum. This distinction can be quite useful. The integral difference between the positive and negative spectra (the shaded area in Fig. 2) is a quantitative measure of the traveling wave energy that exists in the compressor over a given interval of time. In a noisy environment, an *integral* measure of traveling wave energy can

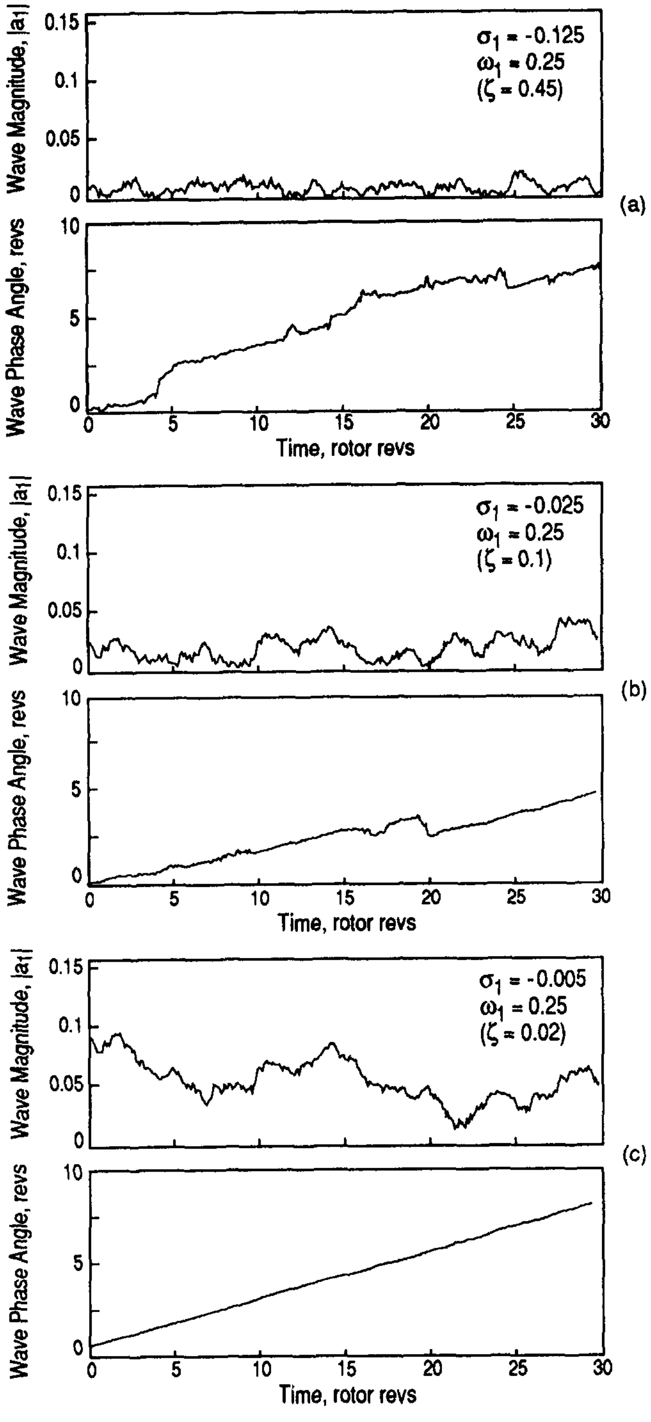

Fig. 1 Simulated compressor first Fourier harmonic wave amplitude and phase behavior, based on Eq. (3)

be a more sensitive detector of wave existence than *differential* schemes such as depending on straight line behavior of spatial phase plots. This is clearly illustrated by this simulation. At the higher damping ratios ($\xi = 0.45$ to 0.1), the evidence for traveling waves is ambiguous in the phase plots in Fig. 1, but traveling energy is readily apparent in the spatial power spectra of Fig. 2 at the same conditions (for more details see Etchevers, 1992).

The procedures outlined above can be compromised to various degrees by the existence in most data of relatively large amounts of traveling wave energy at multiples of the rotor frequency. This energy is due both to geometric excitation and the response of the compressor dynamics to that excitation. It may be desirable at times to eliminate this rotor frequency energy since its large amplitude can obscure other frequencies. In this case, a narrow-band notch filter of some type must be implemented. We utilize a feed-forward adaptive LMS approach (Widrow et al., 1975) to do this for two reasons: First, it allows slow variations in the rotor frequency to be automatically tracked (important for real-time implementations), and second, it allows wave energy, which is uncorrelated with the rotor passage, to pass through (this effect could be implemented with a nonadaptive scheme, but not without some difficulty).

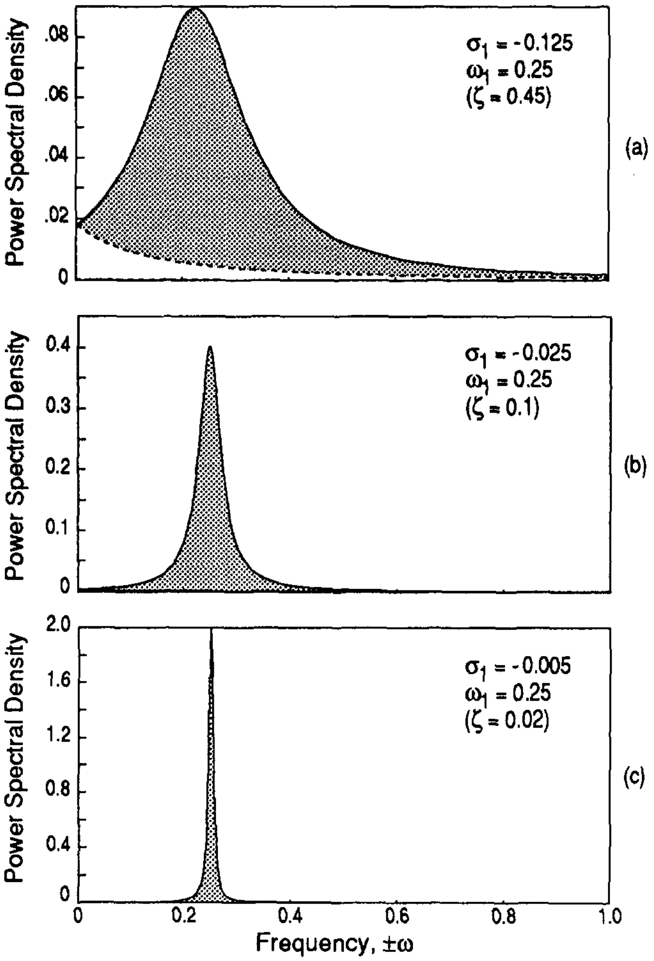

Fig. 2 Spatial spectra (PSD of a_1) of the simulations shown in Fig. 1. Solid line is the positive frequency spectrum, dotted line is the negative frequency (visible only in (*a*), close to zero in (*b*) and (*c*)). The shaded area difference between them is a measure of the traveling wave energy.

In this section, we have explained the motivation for several types of data reduction. Typically, one must examine the data from these various points of view to generate a complete picture of the behavior of the system. A typical set of data reduction steps is as follows:

1 Basic data preparation:
   (*a*) Examine raw data for outliers and anomalies;
   (*b*) Detrend the data to take out zero and very low frequency variations;
   (*c*) Normalize root mean square fluctuations (across the circumferential array) to take out effects of miscalibration and sensor positioning.
2 Calculate spatial Fourier coefficients [for example, 8 probes, which give spatial Fourier coefficients 1, 2, and 3 using Eq. (2)]; plot phase and magnitude as functions of time.

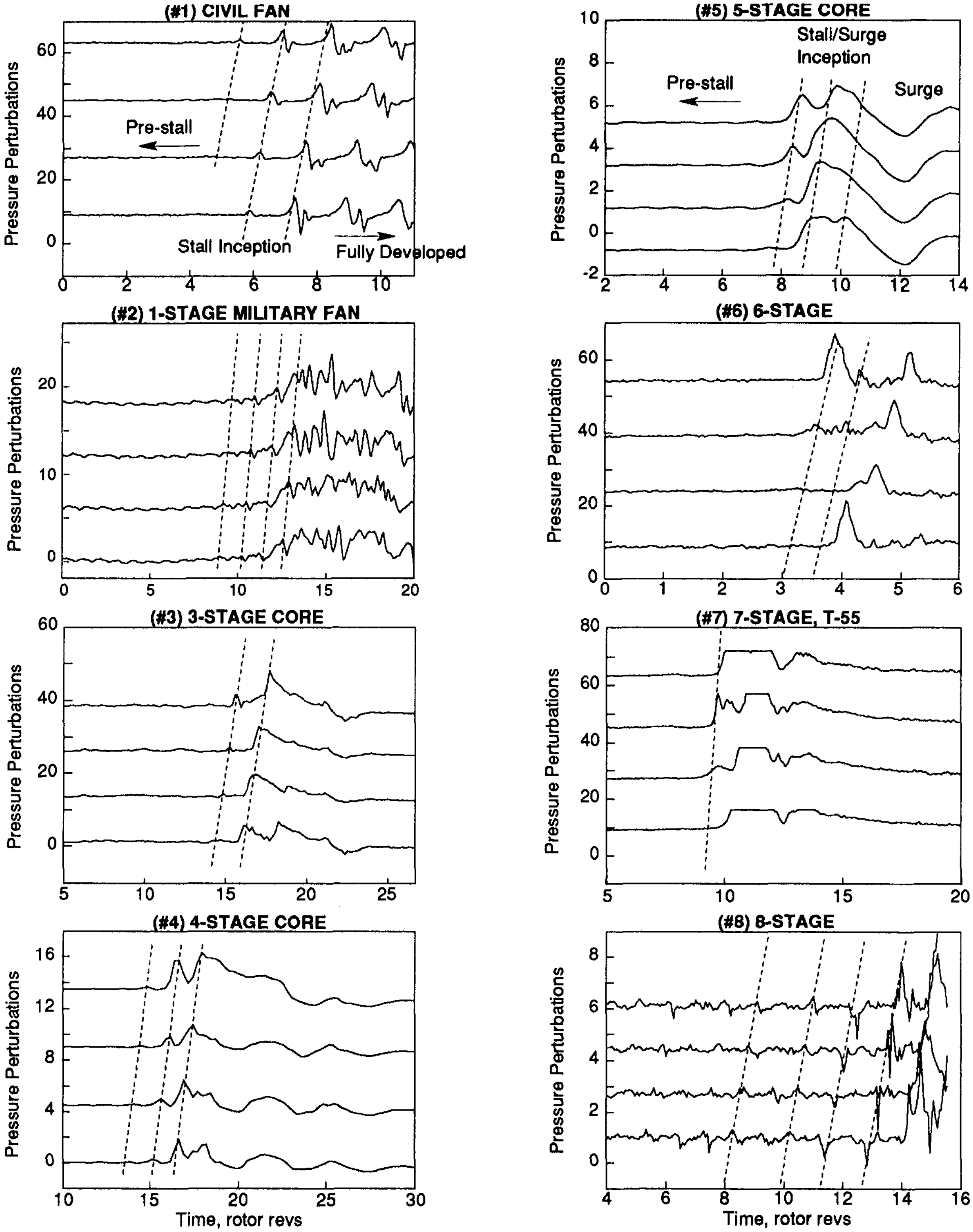

Fig. 3 Time traces of wall static pressure measured with four transducers equispaced about the compressor annulus during transients into stall/surge at 100 percent rotational speed. Data from eight different compressors are shown. Compressors 1 and 5 are labeled with the terminology discussed in the text.

3 When called for eliminate oscillations that are highly correlated with rotor rotation rate (feed-forward adaptive LMS algorithm), or local to a few sensors.
4 Calculate power spectra of the *prestall* data; plot and compare positive and negative frequencies.
5 Compute integrated area difference between positive- and negative-frequency spectra.

Clearly, to plot all of the results from this procedure for all of the compressors tested, for multiple trials, at their various operating condition, would fill a substantial volume. Here we will attempt to summarize the trends observed and characterize each compressor with respect to the current model of prestall compressor dynamics.

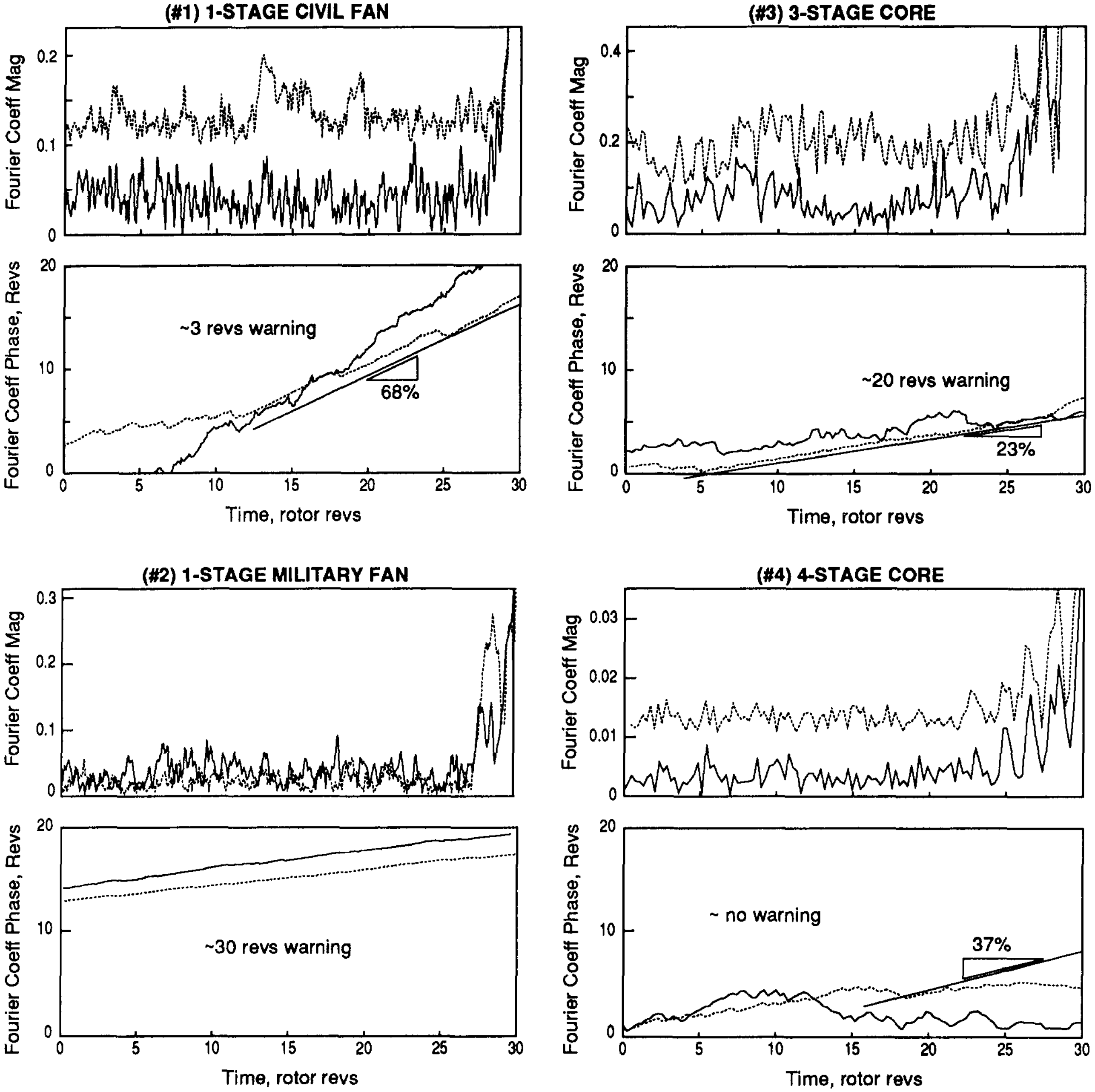

Fig. 4 First (solid line) and second (dotted line) spatial Fourier coefficients, a_1 and a_2, phase and magnitude immediately prior to stall/surge inception at 100 percent speed. The triangles indicate the speed at which the prestall wave travels about the compressor annulus (as a percent of rotor shaft speed).

Compressors Studied

The high-speed compressor data presented here were all taken by cooperating industrial and U.S. government organizations. The compressors studied cover over 30 years of design practice, ranging from older and current engine designs to advanced concepts. Some are fixed geometry, some have interstage bleeds, and some have variable IGVs and stators. In the latter machines, the geometry of the compressor varies with operating speed. In all cases, data are time resolved wall static pressure measurements, roughly equally spaced around the annulus at one or more axial stations. In cases where more than one axial station was instrumented, the station that gave the best results is shown here. All data were taken in compressor test rigs except for #9. The following designations will be used:

Compressor No.	Description
#1	1-stage civil fan, nacelle in wind tunnel
#2	1-stage high throughflow military fan (Boyer et al., 1993)
#3	3-stage core compressor (Garnier et al., 1991)
#4	4-stage core compressor (Hoying, 1993)
#5	5-stage core compressor
#6	6-stage
#7	7-stage axial, 1-centrifugal, T-55 data (Owen, 1993)
#8	8-stage
#9	8-stage, Viper engine data (Day and Freeman, 1993c)

All compressors used eight transducers about the circumference per station except #7, which had four transducers, and #9, which had five. Geometry and steady-state performance

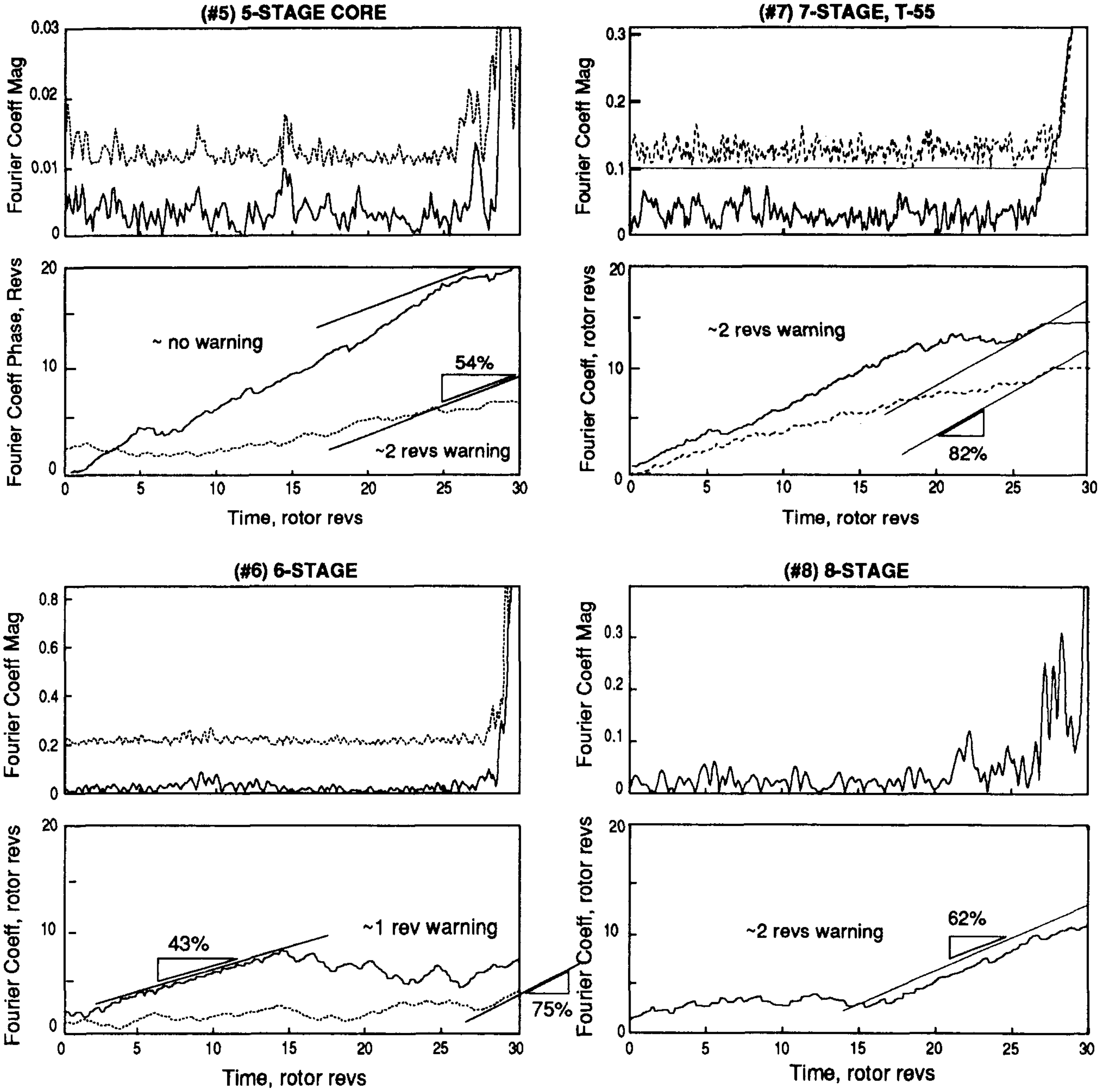

Fig. 4 (Continued)

data were provided for some of the compressors, facilitating comparison with theory; while for others, only normalized, unsteady, AC pressure traces were provided. For compressors with literature references, the data analyzed herein are not necessarily from that data set that appeared in previous publications.

Stall Inception Transients

The time-resolved transients into rotating stall are the rawest form of data we will present. Data for all eight rig compressors are presented in Fig. 3, formated primarily to indicate the similarities between the tests (for instance, the vertical axes are varied arbitrarily to achieve similar magnitudes of the perturbations). Data are presented for the highest rotational speeds for which we have data, which in most cases is 100 percent. The main point to note is that distinct, large-amplitude, rotating disturbances are seen in all of the compressors. We have generated over 100 such time histories for these and other compressors, at various operating conditions, and in all cases rotating perturbations exist prior to surge.

Note in Fig. 3 that most of the compressors tested (except #1 and #8) eventually exhibit planar, surge-type transients (which are sometimes followed by a transient due to opening of a downstream throttle, to prevent mechanical damage). Whether or not such surge instability occurs, however, all the compressors exhibit rotating disturbances first. Thus we conclude that rotating stall, and not surge, is the performance-limiting instability in axial compressors. Stated another way, if one were to stabilize or otherwise eliminate the surge mode of an engine, rotating stall would still occur, and no compressor range extension would be realized. This was demonstrated on a low-speed compression system by Greitzer et al. (1978).

Figure 3 also illustrates our delination of prestall, stall inception, and fully developed stall (see the traces from Com-

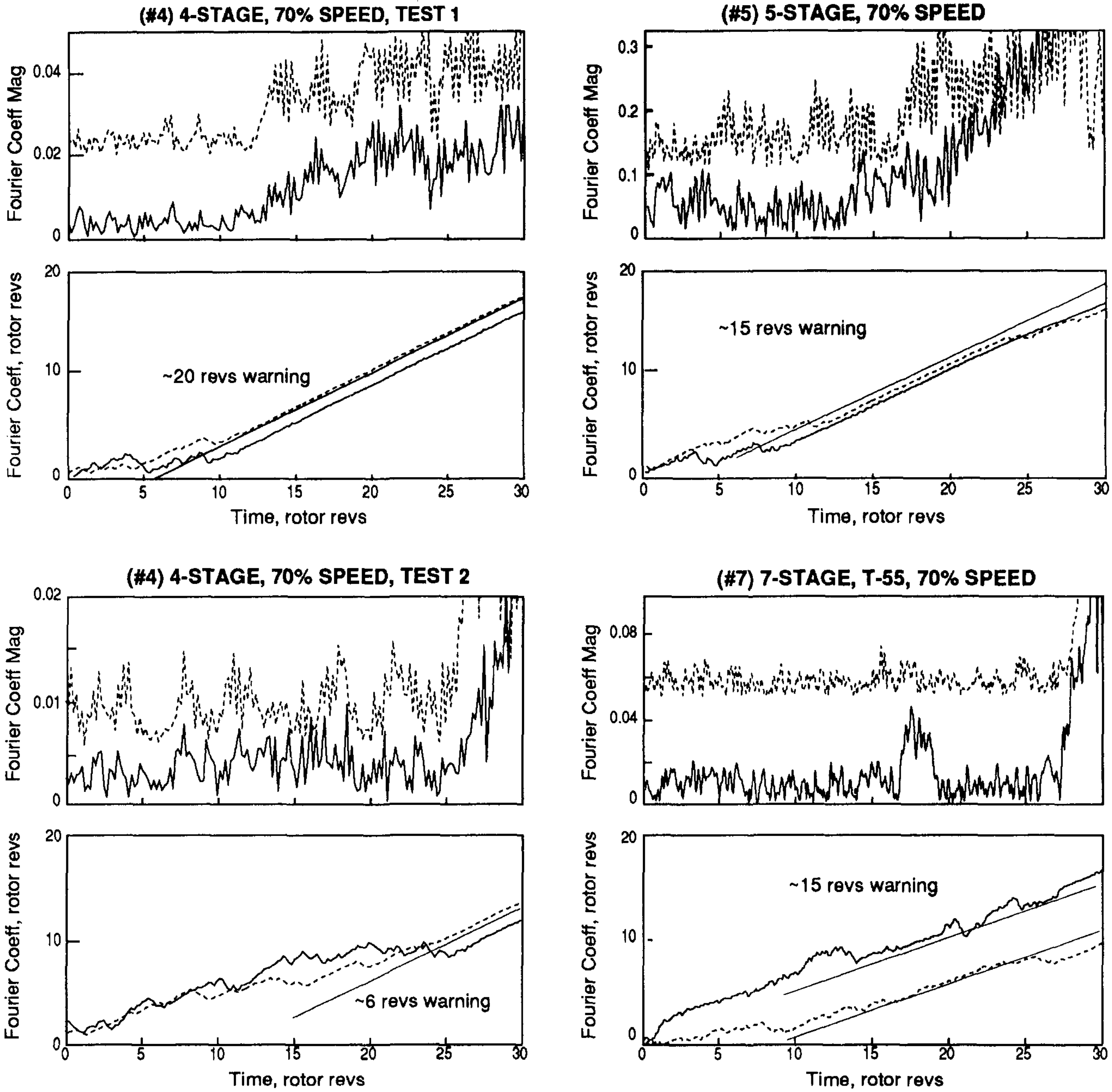

Fig. 5 Time history of first and second Fourier coefficients, as in Fig. 4 but at lower compressor rotational speeds

pressor 1 and Compressor 5). Most of the compressors tested begin to surge during stall inception. Thus coherent, fully developed stall is never reached, and in these compressors we use the delineation prestall, stall/surge inception, and surge.

Another view of stall inception is provided by plotting time histories of the spatial Fourier coefficients, $a_k(t)$ of Eq. (2), during stall inception. This approach highlights circumferentially traveling phenomena, allowing smaller amplitude perturbations to be detected prior to stall. These data are presented in Fig. 4 for the same 100 percent tests as in Fig. 3 (rotor frequency has been filtered out here). The main point is that all the compressors show some evidence of rotating waves prior to stall—as straight line traveling on the phase plots and as increased amplitude on the magnitude plots. Figure 5 shows data taken at 70 percent speed for some of the compressors. At part speed, the traveling waves are evident for a longer time than at 100 percent speed.

The data in Figs. 4 and 5 clearly indicate that coherent rotating waves exist prior to stall. In addition to using this information to elucidate the fluid mechanics of stall inception in high-speed compressors, it may be desirable to feed this "stall warning" information in real time to the engine fuel control for appropriate action to avoid stall (cutting back fuel, opening the nozzle or bleeds, repositioning the vanes, etc.). For stall avoidance based on rotating disturbance detection to be feasible, we must be capable of detecting disturbances sufficiently in advance of stall so as to permit the control system to take corrective action. Thus, there is motivation to optimize the analysis procedure so as to maximize the time over which waves can be detected.

Plots such as those in Figs. 4 and 5 can be used to determine a *very conservative* estimate of the period of time over which "small amplitude" rotating waves exist prior to stall. One such procedure, described by Garnier et al. (1991), is as follows: First, estimate the fully developed rotating stall amplitude. Next, assume that waves are small if they are one eighth of

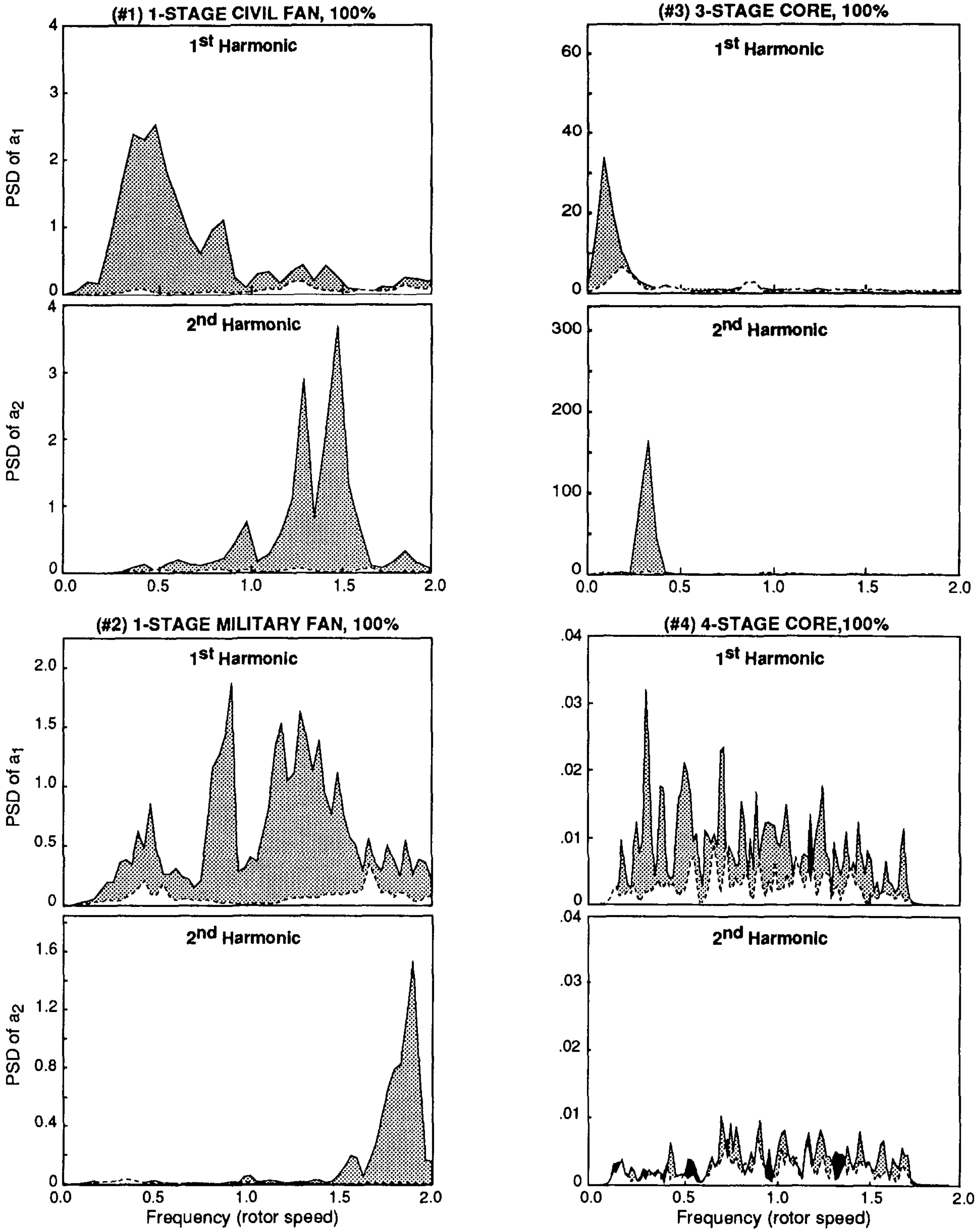

Fig. 6 Prestall spectra of first and second Fourier coefficients (PSD of a_1 and a_2), same data as Fig. 4. Solid line is positive frequency spectrum, dashed line is negative frequency spectrum. Gray areas: forward traveling wave energy; black areas: negative traveling wave energy; white areas: stationary wave energy.

this amplitude or smaller (this number is arbitrary but, again, conservative). Finally, determine the length of time for which the phase of the first or second Fourier harmonic exhibits straight-line (i.e., deterministic, coherent) motion prior to stall.

This is a very conservative approach for several reasons. In the simulation of Fig. 1, we showed that the wave damping must be quite low for coherent traveling to be *apparent* even in the ideal simulation environment; at this point, however, the corresponding wave amplitudes may be sufficiently large to trigger stall. Exacerbating this problem is the noisy test environment, which can mask the desired wave structure. This is particularly troublesome for multistage compressor data

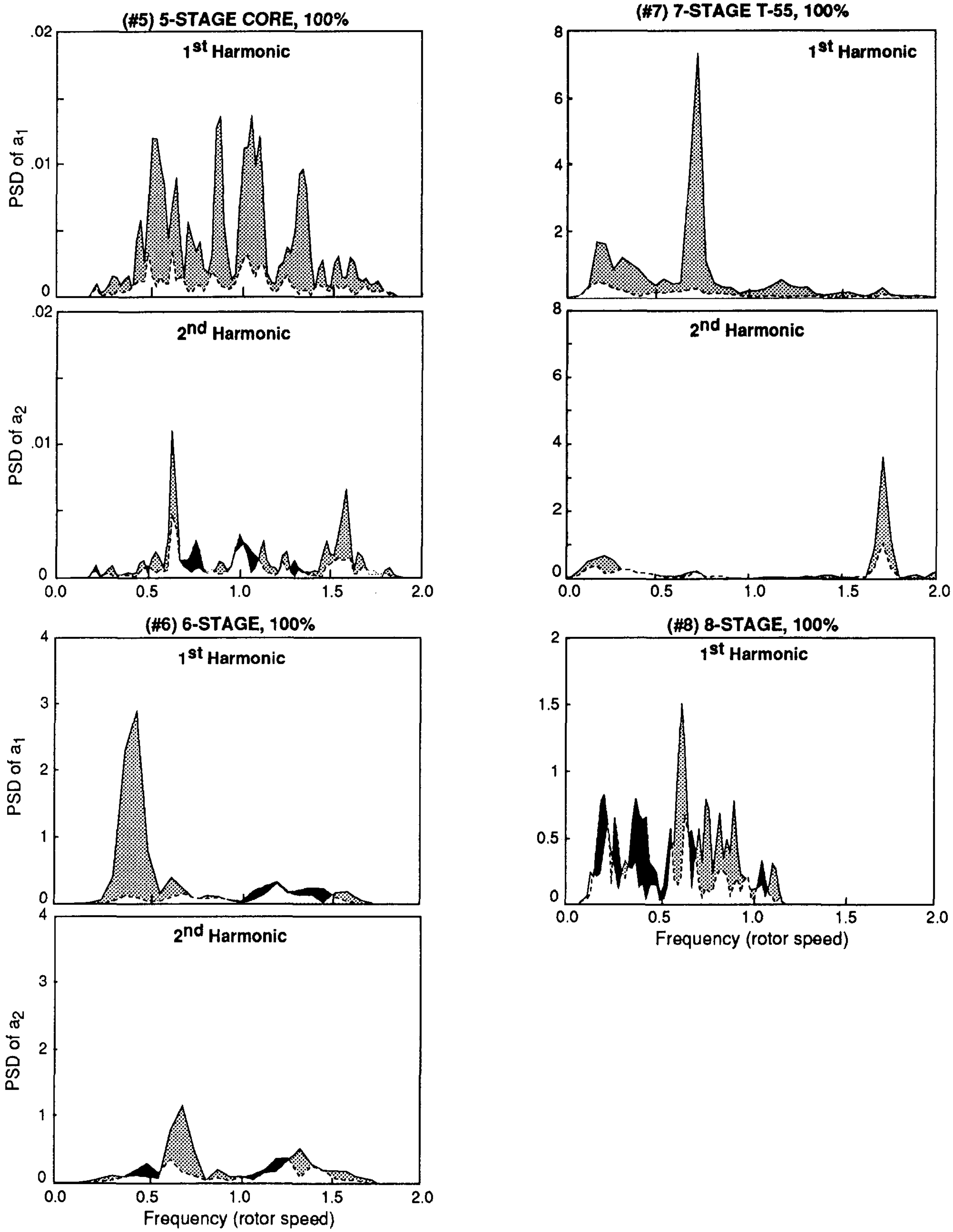

Fig. 6 (Continued)

taken with high-pressure, DC-coupled pressure transducers (as is the case for many of the compressors here), which may not have the sensitivity necessary to detect small amplitude waves when selected to survive surge in a high pressure compressor. (Some of these multistage data were taken with 50 or 100 psi full-scale pressure transducers; the prestall wave amplitudes detected here are only 0.05 psi.) It has also been shown (Mansoux et al., 1994) that nonlinear interaction between harmonics

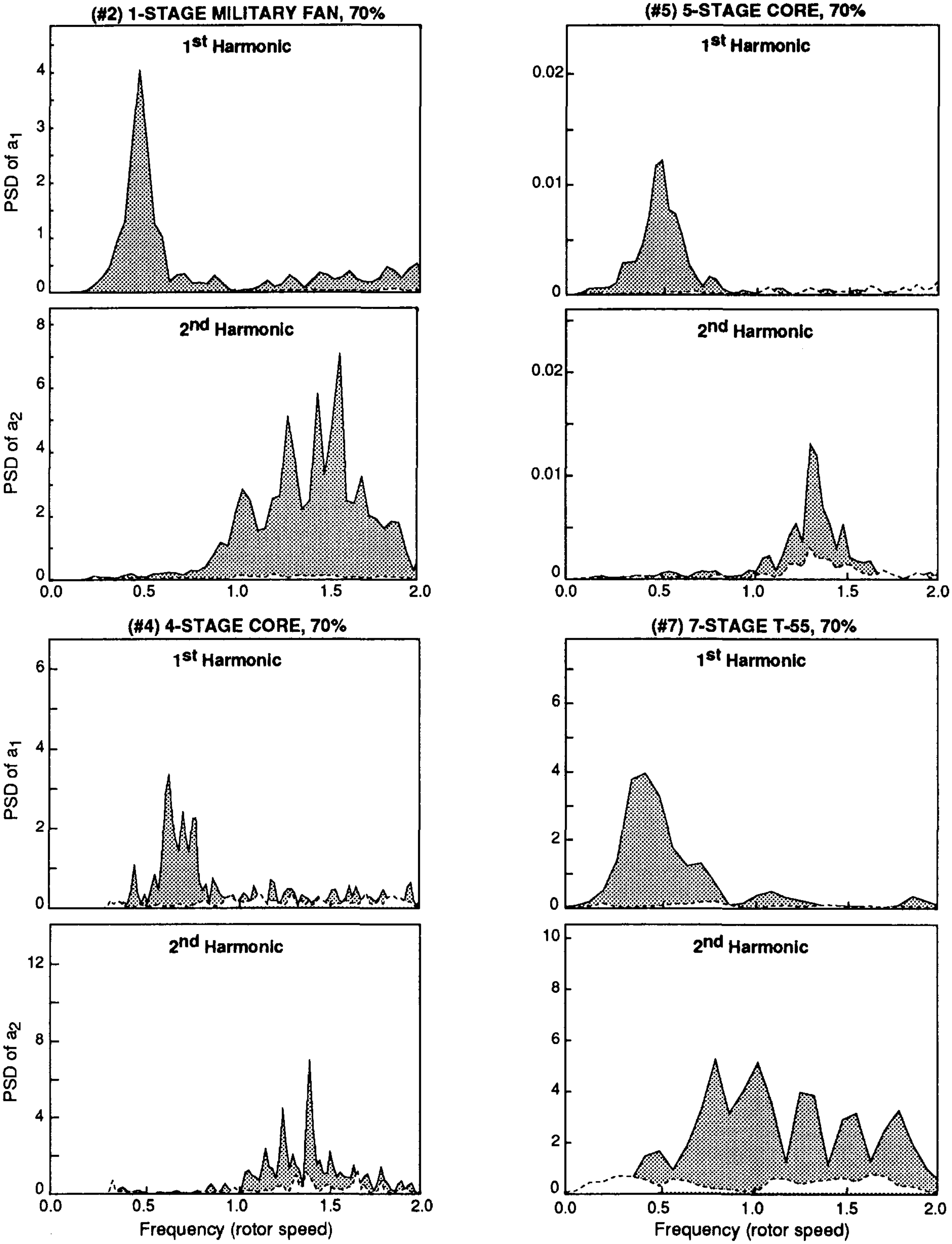

Fig. 7 Prestall spectra of first and second Fourier coefficients (PSD of a_1 and a_2), same data as Fig. 5. Solid line is positive frequency spectrum, dashed line is negative frequency spectrum. Gray areas: forward traveling wave energy; black areas: negative traveling wave energy; white areas: stationary wave energy.

during stall inception often produces a period during which wave energy is transferred between spatial harmonics. This behavior causes some wave amplitudes to shrink, while others grow. During the period that a given harmonic amplitude is small, its apparent phase can wander, both due to increased corruption by noise, and due to the nature of the nonlinear interaction. Thus, loss of apparent traveling during stall/surge inception is not evidence of the lack of existence of waves.

With these caveats in mind, "stall warning" estimates are indicated on Figs. 4 and 5. We have chosen as the relevant measure the length of time over which *either* the first or the second harmonic travels in a straight-line fashion. For instance,

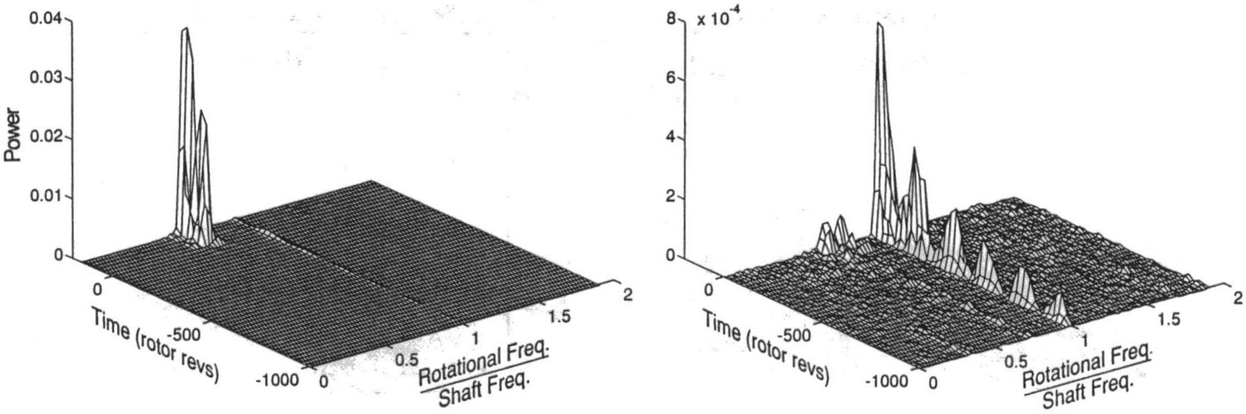

a) 4-Stage, In Stall **b) 4-Stage, Pre-Stall Region**

Fig. 8 Time evolution of the PSD of the first spatial Fourier coefficient, a_1, for the four-stage compressor at 70 percent corrected speed

in Fig. 4, compressors 1, 2, 3, and 7 exhibit distinct straight-line traveling of either the first or the second Fourier coefficient prior to stall. Thus in these cases it is unquestionable that prestall traveling waves exist. Stall warning times, however, are 2 or 3 revs in some cases because of occasional periods of wandering phase. Compressors 4 and 5, on the other hand, show less distinct straight-line traveling, and this is reflected in the lack of any "warning" time by this simple measure. Both of these plots show tendency to travel, but the results from the phase plots must be considered inconclusive.

Compressors 6 and 8 show clear periods of traveling. This traveling is not straight-line in nature, but rather occurs in a "stair-step" fashion. Compressor 4 exhibits similar stair-step behavior, as well as some traveling in the negative direction (against rotor rotation). Simulations have shown that this behavior is typical of compressors that are operating in distorted flow (Boussios, 1993). Note particularly the magnitude plots for compressors 6 and 8, which exhibit cyclic amplitude behavior, with the period of the cycle being approximately twice per revolution of the waves. This behavior is also typical of distorted flow operation, because the wave amplitude varies as it travels around the annulus due to the nonuniform flow conditions.

Data taken at lower corrected speed (Fig. 5) show a different picture of stall inception. In all cases, prestall traveling waves are both large in amplitude (note the prestall jumps in wave amplitude that occur in compressors 4 and 5, which are noticeable, but still much smaller than the jumps that occur at stall inception) and coherent (periods of straight-line traveling of 10 revolutions or more appear in all of the runs). Stall warning times are also longer. As can be seen in the two separate runs of compressor 4, the warning times are not repeatable using this simple straight-line phase plot technique.

Prestall Power Spectra

We have delineated and demonstrated the pitfalls of using spatial Fourier coefficient phase for investigating the existence of prestall waves. "Stall warning" times as computed in the previous section do not appear to be attractive for most applications. Much of this may rest with the fact that, although useful in many cases, phase plots can yield misleading and hard-to-interpret results because they are not robust to noise in the system. However, many of the problems encountered in temporal phase plots can be overcome by using the power spectra of the spatial Fourier coefficients, a measure of the wave energy, instead of the wave time history. Power spectra allow behavior over some time window to be computed, and thus show the existence of *stochastic* traveling waves, rather than relying on the appearance of deterministic waves. Specifically, we use the area difference between the positive-frequency and negative-frequency spectra (the shaded area in Fig. 2) as a clear indication of the amount of spectral energy traveling relative to that which is stationary—we term this area difference the "traveling wave energy" (see appendix). When this traveling wave energy is in the frequency range important to rotating stall, then sufficient information may be available for a prestall warning scheme.

Figures 6 and 7 show the spectra computed from the data in Figs. 4 and 5 in a stationary window approximately 100 rotor periods long ending just before stall inception (recall that the rotor frequency has been filtered from this data). Since these plots contain only the data *prior* to stall inception, no wave energy associated with stall inception or fully developed stall is included. Any traveling is purely due to prestall waves. We have again chosen arbitrary scales for the ordinate to facilitate comparison among the plots.

All of the compressors represented in Figs. 6 and 7 show small-amplitude traveling wave energy prior to stall or stall/surge inception at both 100 and 70 percent speed. Thus modeling small-amplitude wave behavior is a potentially useful method for describing prestall compressor behavior. A physical interpretation of such a spectrum is that a shaded peak indicates a wave rotating about the compressor at the designated speed. The wavelength of the disturbance is the compressor circumference divided by the spatial harmonic number (k). Some of the compressor data for a single harmonic agrees quite closely with the very simple model of Eq. (3) that is illustrated in Fig. 2. For example, the seven-stage compressor in Fig. 6 has (1) a first spatial harmonic wave (wavelength = compressor circumference) rotating at 0.7 times the shaft speed, and (2) a second harmonic wave (wavelength = 1/2 circumference) rotating at 1.7 times shaft speed. Other compressors show multiple peaks at a single spatial harmonic, as is the case for the five-stage machine in Fig. 6. Overall, it is clear in Figs. 6 and 7 that traveling wave energy is often much more broad-band and complex than would be expected if only a single harmonic mode (eigenvalue) were involved in the stall inception processes as the wave damping approached zero (as Eq. (3) and Fig. 2 assume). Note particularly in Fig. 6 that compressors 4, 5, and 8 exhibit extremely broad-band traveling behavior, and this accounts for the lack of distinct traveling in the phase plots for these compressors in Fig. 4. Even when a single peak is evident in the plots, it is often much wider than one would expect if the damping ratio of a single mode were close to zero (compressor 1 in Fig. 6, and all of the 70 percent cases).

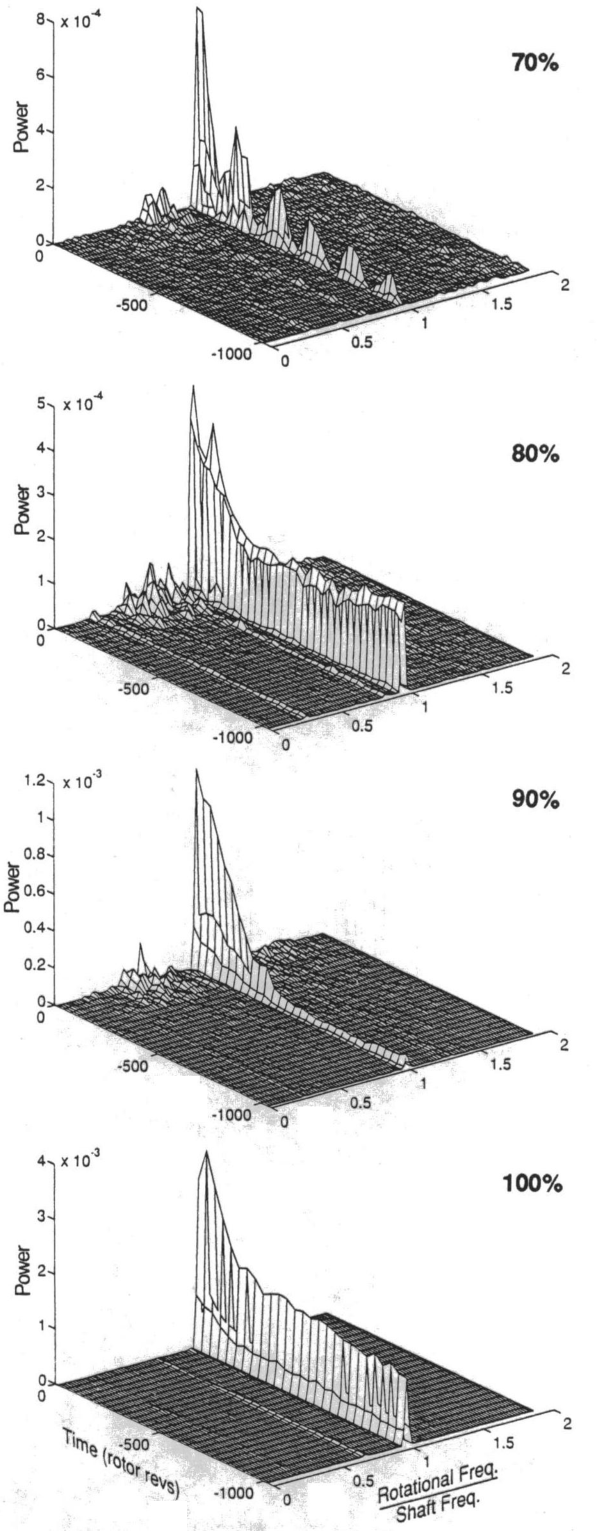

Fig. 9 Influence of corrected speed on the time evolution of first spatial harmonic of four-stage compressor. Note the change in vertical scales.

Rotating Wave Energy and Compressor Stability

For some of the compressors discussed here, we have data taken continuously during throttle traverses from full open to surge/stall along a constant speedline. A convenient way to examine this information is in the form of a three-dimensional "waterfall" spectral plot. Here, the power spectrum of a spatial harmonic is calculated over a window of fixed period (50 rotor revolutions in this case) and plotted as in Figs. 6 and 7. The window is then marched forward in time by a period of a few rotor revolutions and the process repeated. The result is a presentation of the variation of the rotating spatial wave spectral distribution over time and therefore (in this case) as a function of throttle or speedline position. Shaft frequency is not filtered out.

Figure 8(*a*) illustrates such a speedline traverse from wide open throttle through rotating stall for the four-stage compressor at 70 percent corrected speed. The large peak at 0.7 times shaft rotation frequency is readily identifiable as rotating stall in this machine. Little rotating wave energy is evident in this figure prior to stall. However, when the prestall period is replotted at an amplitude scale expanded by a factor of 50 (Fig. 8*b*), rotating waves are readily apparent for the entire time. Rotating wave energy is seen at both 0.7 and 1.0 times shaft frequency, even far away from stall (1000 revs) with the 100 percent wave being the strongest. As stall is approached, the energy at both frequencies rises sharply and energy appears at 0.5 times shaft frequency as well. (Note also that there may be some nonlinear intermode coupling in that the 0.7 and 1.0 frequencies appear to beat against each other.) Once the stall initiation process starts, it is the 0.7 frequency wave that evolves into rotating stall.

The prestall behavior of this four-stage compressor is a strong function of corrected rotor speed. Figure 9 shows the circumferential traveling wave spectral time histories during throttle traverses at four corrected speeds. At all speeds, waves traveling at both 0.7 and 1.0 times shaft speed are present throughout and rise sharply just before stall initiation. However, the strength of the 1.0 relative to the 0.7 frequency wave is much larger at 100 percent corrected speed than at lower speeds (200:1 compared to 6:1). Repeated test runs of this compressor confirm that this wave structure is consistent. (In some tests, the 0.7 wave rises just prior to stall by a factor of 5 ~ 10 times that shown in Fig. 9.)

How general is this behavior? Data from throttle traverses of four compressors are shown in Fig. 10. The single-stage (#2) and five-stage (#5) compressors show behavior similar to that of the four-stage machine. At 70 percent speed, the single-stage compressor data (Fig. 10*a*) show waves rotating at 0.5 and 1.0 of shaft speed. The 0.5 frequency wave grows as the throttle is closed until it develops into rotating stall. At 100 percent corrected speed, the 1.0 shaft frequency wave completely dominates the spectrum, growing in amplitude as stall is approached. (The stall speed is 0.5 times rotor frequency at both corrected speeds.) The five-stage compressor (Fig. 10*b*) differs only in that the 1.0 shaft frequency wave is barely detectable at 70 percent corrected speed. The 0.7 frequency wave dominates, growing in strength as the throttle is closed to rotating stall. As with the one-stage and four-stage compressors, the 1.0 shaft frequency wave dominates the spectrum at 100 percent corrected speed, growing in amplitude as stall is approached.

The seven-stage, T-55 data (Fig. 10*c*) looks somewhat different in that 1.0 frequency wave is always much stronger than the lower frequency disturbance (0.5). At 70 percent corrected speed, the 0.5 frequency wave is only discernible for a few hundred rotor revolutions before stall. At 100 percent speed, the growth of the 1.0 frequency wave with throttle closure is less pronounced than in the other three compressors. Note that a 0.7 frequency wave is still there, but cannot be readily discerned on the scale of Fig. 10. When the shaft frequency is filtered out as in Fig. 6, the lower amplitude wave is apparent. Lower frequency disturbances grow just before stall initiation and also there is a clearly discernible wave traveling at 1.6 times the shaft speed. Reasons for the apparent differences in dynamic behavior between this and the other three compressors may lie in geometry (this is a mixed flow—seven-stage axial, one-stage centrifugal—compressor, the others are just axials)

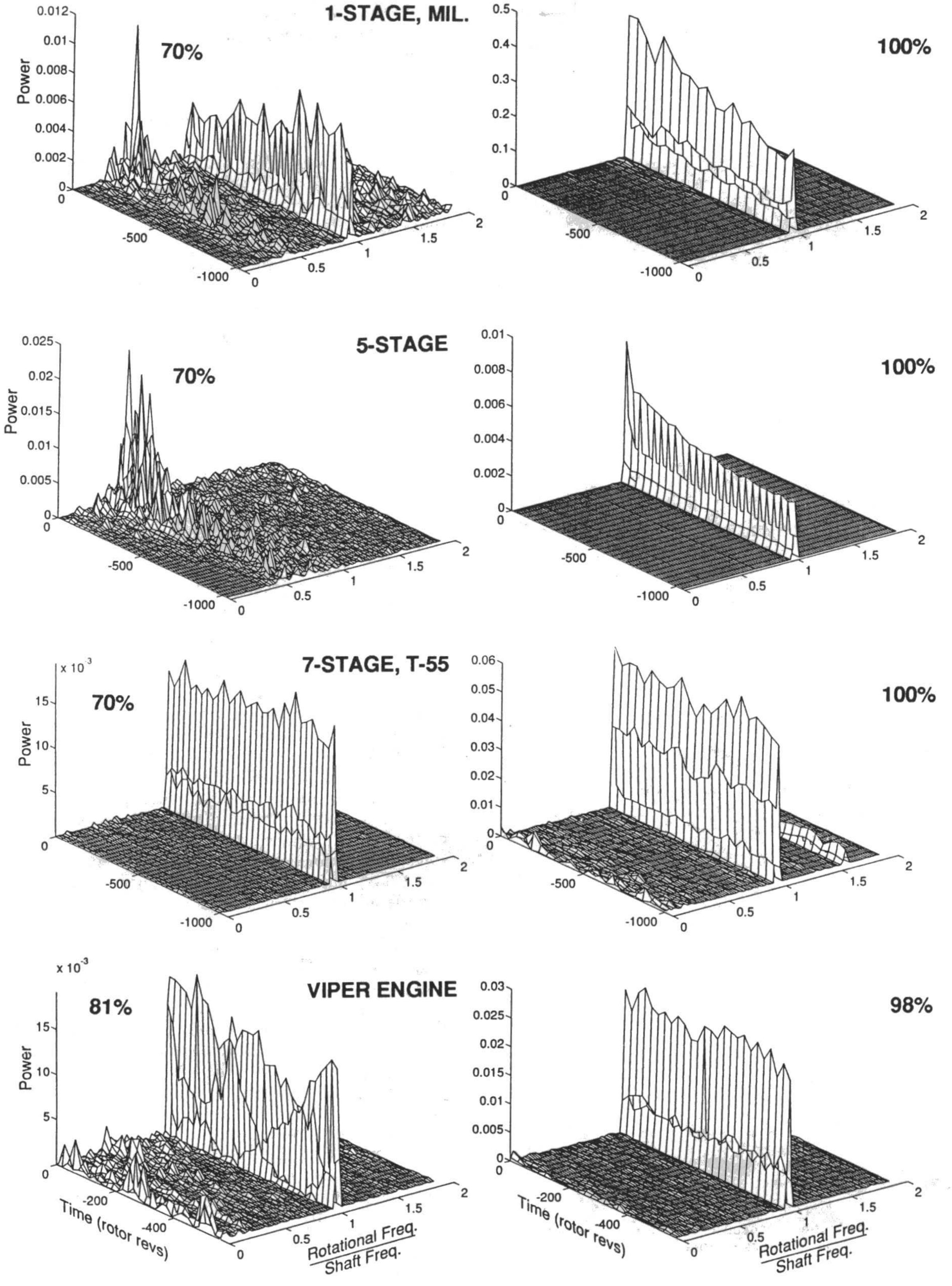

Fig. 10 First spatial harmonic spectra of four compressors at low and high corrected speeds

and/or in sensor placement. These data are from stage 3 sensors—the furthest back data available—while data from other compressors have shown that part-speed waves are best detected toward the rear of the compressor, especially at 100 percent speed.)

Viper engine data (Fig. 10*d*) is similar to that of the T-55. Here, part-speed waves appear along with the 1.0 per rev at low corrected speed (81 percent), but at high speed (98 percent), the 1.0 rotor frequency wave dominates. As with the T-55, the rise in energy in the 1.0/rev wave is gradual as stall is approached. Day and Freeman (1993c) reported that this compressor exhibits short (relative to the compressor circumference)

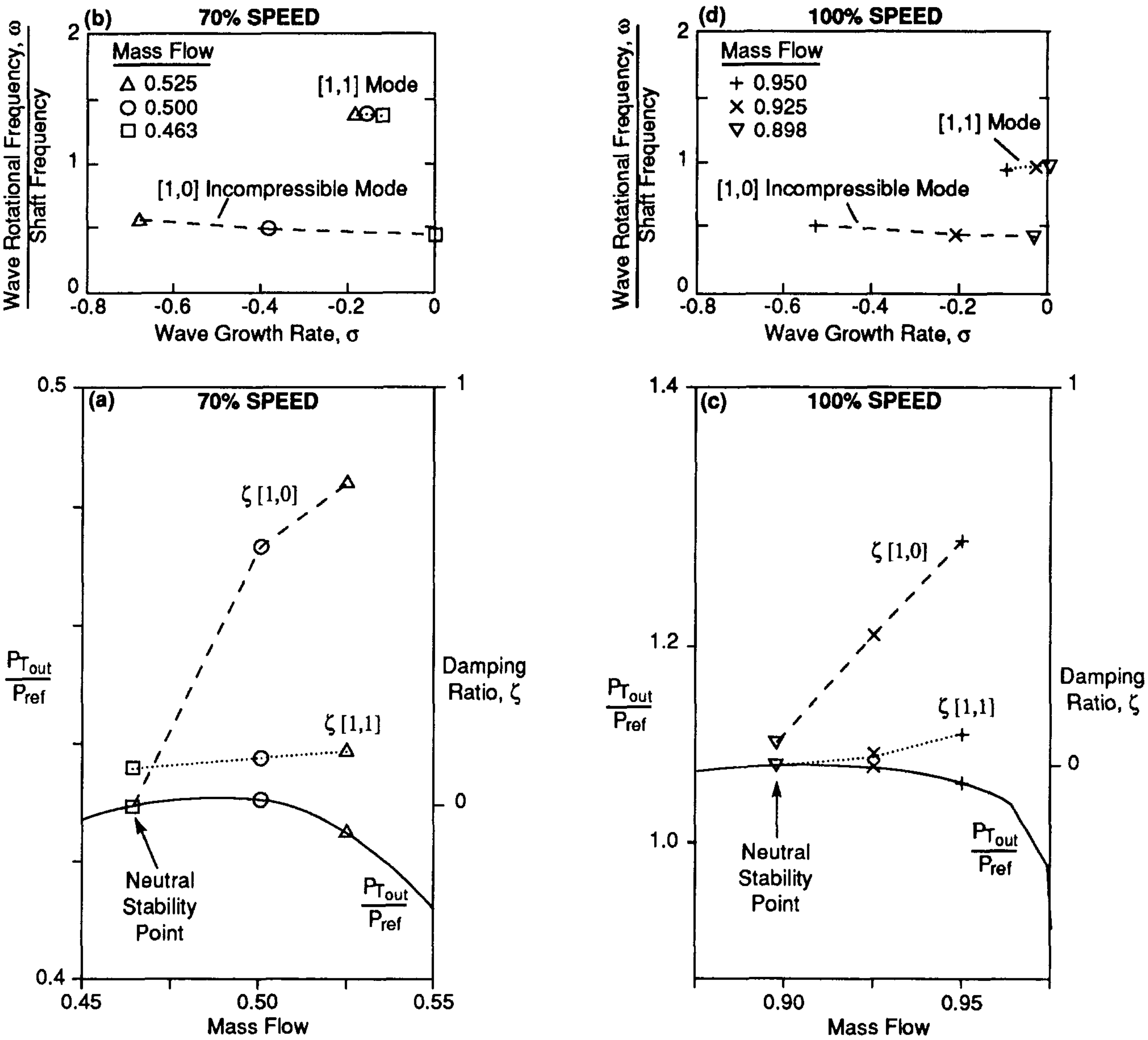

Fig. 11 Calculated influence of corrected speed on the first spatial harmonic mode structure of the four-stage compressor

wavelength rotating disturbances prior to stall, which are not readily seen with this type of analysis since the short wave energy is spread over several spatial harmonics.

Relating Theory to Experiment

How can the measured dynamic behavior exhibited in Figs. 8-10 be explained? Are the features in the data that are common among compressors more important than those that are different? Of what use is this type of data representation? In particular, what is the significance of the disturbances at shaft frequency? (One explanation would dismiss the engine order waves as disturbances resulting from geometric nonuniformities in the rotor. The change in amplitude of this 1/rev wave as the throttle is closed would be a reflection of the aerodynamics changing along a speedline.) We believe that a useful approach is to compare these measurements with a theoretical model of compressor stability.

Hendricks et al. (1993) have developed a compressible version of the two-dimensional, linearized hydrodynamic stability model of Moore and Greitzer (1986). This approach treats the compressor as a series of actuator disks (one per blade row) separated by interblade row volumes, with suitable boundary conditions at the compressor inlet and exit. The two-dimensional stability of the coupled rows is calculated. Required inputs are the meanline compressor geometry (blade lengths and angles, duct lengths, etc.) and the pressure rise characteristic for each blade row. The results of the calculation include the circumferential *and axial* shape of each spatial harmonic wave, the wave rotational frequency, and the wave growth rate. The calculation is linear so that the dynamics of each spatial harmonic are assumed to evolve independently. Since we are concerned here with the prestall region, in which the wave amplitudes are two orders of magnitude below that of rotating stall, the assumption should not pose a problem (Bonnaure, 1991).

We have applied this theory to the geometry of the four-stage compressor. The individual blade row characteristics have been estimated by a meanline flow calculation (and may thus be subject to some uncertainty). In contrast to the incompressible case, there are an infinite number of natural oscillatory (eigen) modes (as there are by analogy for a duct acoustic calculation). Physical reasoning or intuition must be applied to identify those (hopefully) few modes that control the dy-

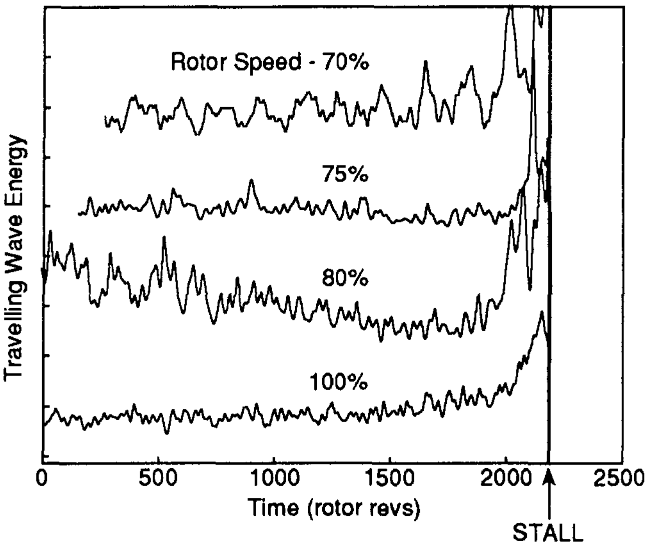

Fig. 12 First spatial harmonic traveling wave energy during slow throttle traverse into stall for a four-stage compressor

namics of interest. The lowest frequency mode (which we will designate [1, 0] by analogy with duct acoustics) has a circumferential wavelength equal to the compressor perimeter and is uniform in structure along the compressor axis. This is the mode familiar from the Moore-Greitzer analysis. It is the only type of mode that exists in an incompressible machine. (The second incompressible spatial harmonic would be the [2, 0] mode, etc.) The addition of compressibility now permits axial structure in the wave form. The next lowest mode is therefore [1, 1] with a circumferential wavelength equal to the compressor perimeter and an axial wavelength set by the compressor length (taking into account the inlet and outlet ducts). We will confine ourselves only to these two modes at present since damping tends to increase with mode number and therefore the lower modes are usually the most important.

Figure 11 presents in two ways the results of these calculations of the stability of the first spatial harmonic in the four-stage compressor. The variation in wave damping ratio (ζ) with compressor mass flow at 70 percent corrected speed is shown in Fig. 11(*a*). The compressible [1, 1] mode is lightly damped even at high mass flows, and its damping ratio decreases as the flow in the compressor is reduced. The incompressible [1, 0] mode is highly damped away from stall, but its damping ratio drops more rapidly than that of the [1, 1] mode as the compressor is throttled. The result is that the incompressible [1, 0] mode goes unstable first at 70 percent corrected speed. The companion root locus plot of Fig. 11(*b*) shows how the wave growth rate and rotation rate vary with compressor mass flow. The incompressible [1, 0] mode is predicted to rotate at about 0.5 times shaft frequency, decreasing by about 20 percent as the compressor is throttled. The compressible [1, 1] mode rotates at about 1.4 times shaft frequency and changes little with compressor mass flow. This picture alters as the compressor speed increases. The compressible [1, 1] mode is less stable at 100 percent corrected speed than it is at lower speeds, and drops more sharply as the compressor mass flow is reduced (Fig. 11*c*). Thus, the compressible mode goes unstable first at high corrected speed in contrast to the incompressible mode dominating at lower speeds. In addition, the nondimensional rotational frequency of the compressible [1, 1] mode drops as compressor speed is increased so that the natural frequency of this mode is the same as the shaft speed at 100 percent corrected speed (Fig. 11*d*).

The experimental data and theoretical calculations form a consistent picture of the dynamics of this machine. The compressor behaves as a multimode system excited by forcing with both wide and narrow band components. In this case, a primary forcing is at shaft frequency and is presumably the result of geometric nonuniformities in the flow path. The measured unsteady compressor flow at this frequency reflects both this forcing and the resultant dynamic response of the compressor.

The new result here is that compressible modes can exist in a high-speed compressor and dominate the stability at high corrected speeds. Furthermore, different modes appear to be stability-limiting at different speeds. It is also important to note that the compressible mode of interest here behaves differently than the incompressible mode familiar from the Moore-Greitzer analysis and low-speed compressor experiments. Specifically, the rotational rate of the compressible mode is fixed while that of the incompressible mode scales with shaft speed ($0.5x$). The numerical value of the compressible wave speed is approximately coincident with shaft frequency at design speed for this compressor, implying that this mode is very susceptible to forcing due to geometric imperfections in the rotor or eccentricity in the flow path.

We have learned many lessons from the study of this compressor. There are many more modes in a high-speed compressor compared to a low-speed machine. Which mode dominates the stall inception processes can be a function of compressor speed because of the dependence of the compressor system dynamics—mode frequency, system forcing, and mode damping—on the compressor operating point. In addition, calculations suggest that the upstream and downstream ducting can play a role in the modal dynamics. This implies that the same compressor may exhibit differing stability depending upon the installation, engine versus rig for example, or even different rigs. (This is well known for zero order surge instabilities but less widely recognized for rotating stall and stall initiation.) A major question is the generality of these findings. Are compressible modes the stability limit at high speeds for all, most, or some compressors? Is the coincidence of mode and shaft frequency at design speed peculiar to the compressors studied or is it more general due to design space limitations? The analytical model predicts that the compressible mode frequencies (ω) vary inversely with compressor length-to-diameter ratio (L/D). The rotational Mach number of the mode ($\omega r/a$) is a constant, independent of rotor speed (U). Thus, as the tangential Mach number of the rotor is reduced toward zero, the normalized mode rotational frequencies ($\omega r/U$) move toward infinity, so that the compressible modes do not participate in the dynamics of low speed (i.e., incompressible) machines. The four-stage compressor modeled here has an L/D of about 0.5 and a tangential Mach number of 1. Since these values are typical of many high-speed, multistage compressors, the approximate coincidence of shaft and compressible mode frequencies observed here may be widespread among such machines. The one-stage and five-stage compressors in Fig. 10 show the same behavior as the four-stage machine. (We have analyzed the five-stage compressor with the stability model, which predicts dynamics similar to those in the four-stage machine.)

The Viper compressor behavior shown in Fig. 10 is also similar in that it exhibits a prestall response at 0.4 and 1.0 of shaft frequency. At high speed, no energy is evident below shaft frequency, although response can be clearly seen at higher frequencies. (Viper spectra show narrow band response at discrete frequencies up to 10 times the shaft speed. Also, the second spatial harmonic spectrum is very rich with waves growing as stall inception is approached.) Since we do not have the geometry of this compressor, we have not been able to identify particular modes. At low corrected speed, the T-55 shows weak response at 0.4 times shaft frequency prior to stall initiation. At high speed, no energy is evident below shaft frequency, but response appears at 1.6 times the shaft speed. We are in the process of modeling this compressor to explore this behavior

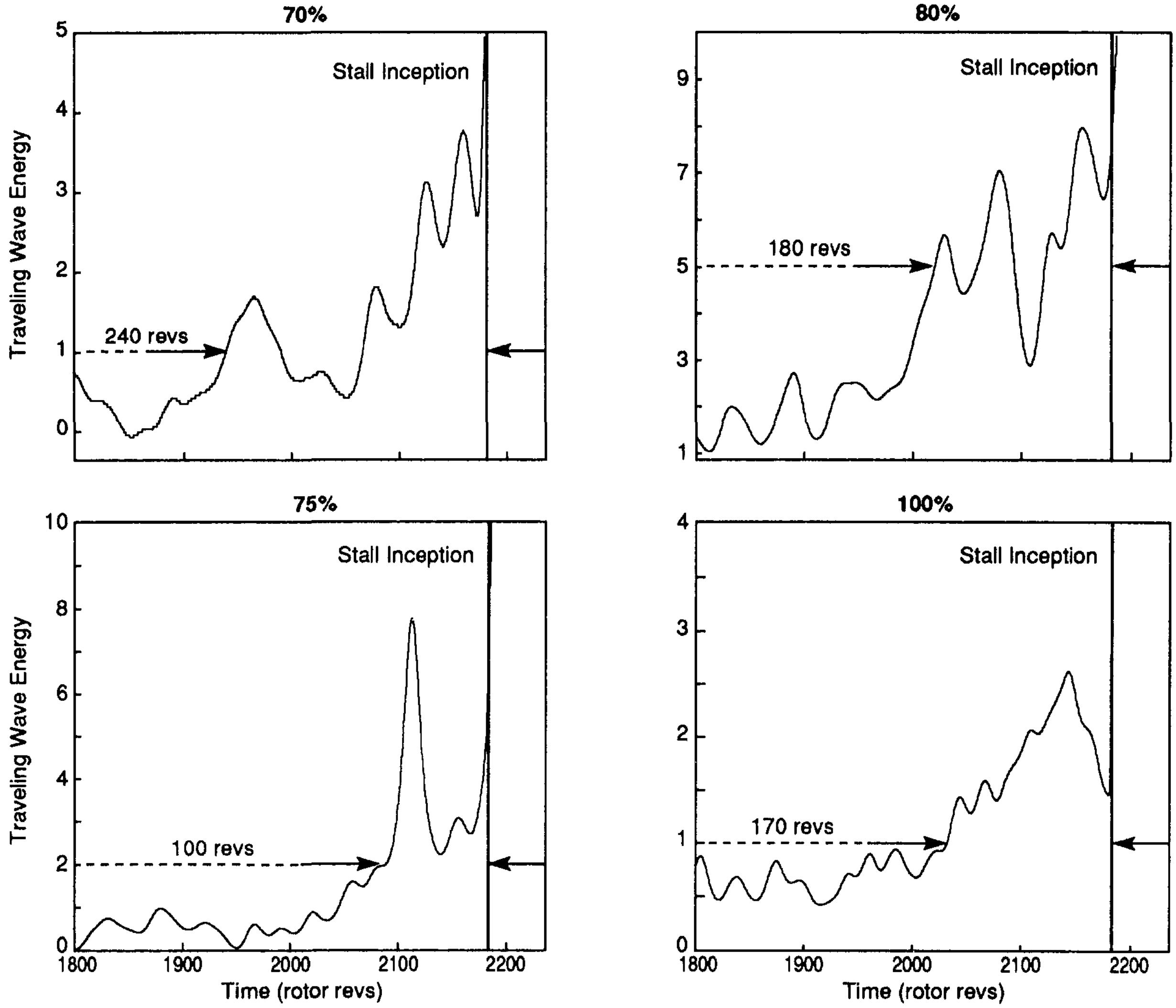

Fig. 13 Data of Fig. 12 replotted on an expanded scale illustrating stall warning times prior to stall inception

further. Also, the T-55 data shown in Fig. 10 were taken with relatively little throttle motion, near the stall point, and thus do not represent as wide a sweep along the speedline as is the case for the one-, four-, and five-stage compressors. More work needs to be done here.

Overall, these multistage, high-speed, axial compressors are rich in modes (eigenvalues), most of which do not exist in low-speed compressors. Detailed analysis is needed on each geometry to elucidate the physical significance of each mode and its importance to instability inception at any particular speed. It is clear, however, that modal response is exhibited by all of the machines studied.

Using "Wave Energy" as a Stall Warning

We have seen that prior to stall, significant traveling wave energy exists in all of the compressors studied and that this energy changes with operating point. The question is: Can this traveling energy be used as a stall warning indicator? One straightforward approach is simply to calculate the traveling wave energy as a function of time and then threshold this level at some appropriate value. This was done for a fixed-length time window in which the spectrum of the desired spatial Fourier coefficient was estimated (only data prior to the time sample were used so that the filter was causal). The integrated traveling wave energy for frequencies between 25 and 125 percent of the rotor frequency was then calculated from the spectrum (the positive area minus the negative area in Fig. 6) and assigned to that point. The window was then marched forward in time by one point and the process repeated. Since the raw compressor data are noisy, the length of the spectral window influences the variance of the wave energy estimate. The longer the window, the less the variance. Too long a window, however, will smooth out the transients of interest. Although we have not made a quantitative analysis of this tradeoff, we have found a 50 rotor rev window to be a workable compromise between reducing the noise and losing the detail of the prestall transient.

The time history of the traveling wave energy in the first spatial harmonic was so calculated for data taken during slow throttle traverses from full open to stall for the four-stage compressor. Figure 12 shows such a time history of the integrated wave energy at four corrected speeds. In all cases, the wave energy rises steeply at 100–200 rotor revolutions prior to stall. At 70 and 75 percent corrected speeds, the mean DC level is approximately constant during the throttle closure until the abrupt prestall rise. At 80 percent speed, the DC level drops for 1000 revs prior to stall (this is the only data set we have that behaves in this manner). At 100 percent speed, the DC level rises slowly as the throttle is closed until the more abrupt prestall rise. For some cases, we have multiple data sets at similar conditions. These can show a factor of two or so variation in the length of the prestall period of increased wave energy. (The shortest periods are illustrated here.)

To use this integrated wave energy concept as a stall warning indicator, we must set a threshold level in some manner. This requires some care as the wave energy time trace is noisy. Figure 13 shows the data from Fig. 12 replotted on an expanded scale. Here the very simple approach of adopting a level just higher than the highest peak observed before 200 revs prior to stall is used. This yields warning times on the order of 100 to 200 revolutions prior to stall initiation, even at 100 percent speed. For conditions at which we have multiple test runs, these results represent the shortest warning period. We believe that these are conservative values and that more sophisticated signal processing (removing the high frequency spikes, incorporating the low frequency DC level changes, for example) should yield considerably longer warning times for data such as those analyzed here.

Since the throttle closure rate was constant during any single test run and the pressure rise and mass flow were measured, the operating point along the speedline at the time corresponding to the stall warning period could be determined. At 100 percent speed, the warning period was equivalent to about a 0.2 percent change in mass flow. Data were analyzed for 100 percent speed tests in which the throttle rate varied by a factor of thirty (the rate was constant during any single test). The data from all tests behaved similarly in that the DC level of the integrated wave energy rose slowly until a more abrupt rise immediately preceding stall initiation. The level correlated with operating point on the speedline so that amplitude of the wave energy was found to be high for proportionately longer at low throttle rates than at higher ones. For this compressor, at least, the level of wave energy is clearly a function of the position along the speedline.

Overall, these results are very encouraging. They show that traveling wave energy can be used to identify prestall waves in high-speed compressors, even at the highest rotational speeds and throttle rates—conditions at which examination of time traces and Fourier coefficient histories have proven unreliable. Furthermore, increased wave energy is discernible for a significant time (at least 100–200 rotor revolutions) before stall in all cases. More work needs to be done in the signal processing of these somewhat noisy signals before they could be considered a reliable stall warning. The signal-to-noise ratio can be improved through judicious selection of the spatial harmonics and modes included in the wave energy calculation for any given compressor. Also, more sophisticated signal processing could be applied.

Discussion

The coherent picture that has emerged from these experimental and analytical studies is that the compressors examined behave like multimode, oscillatory, dynamic systems in the small amplitude prestall region. We would now like to discuss the implications and limitations of this physical model on compressor design and stall warning.

The specific mathematics used here are derived from the linearization of the approach of Moore and Greitzer so that they only apply to the small signal regime preceding stall inception. The stall inception process, as the waves grow to large-amplitude, fully developed rotating stall, is not described by this model. (It would also be inappropriate for describing the dynamics of the part-span rotating stall found in some compressors prior to surge or large amplitude stall.) In particular, the assumption that the dynamics of each spatial harmonic and each mode evolve independently is no longer true as the wave amplitude grows. This is readily seen in the data in which prestall energy at shaft speed evolves into 0.5 times shaft speed rotating stall through nonlinear mode coupling. A second assumption, that the flow can be described by a two-dimensional model, can also be limiting, especially in low hub-to-tip ratio compressors. The addition of a third spatial dimension enables additional resonant modes, and we have seen some evidence of such modes in the data from fans. Although it appears that a two-dimensional mode first goes unstable in the machines examined here, it is certainly conceivable that a three-dimensional mode might be the most critical in other compressors.

Historically, attention has been focused on fully developed rotating stall and surge or, more recently, on the stall inception processes. But in a very real sense, it is the prestall region that is the most interesting since the design intent for a compressor is to avoid instability—at whatever penalty in performance, weight, or cost that must be incurred. In many ways, the prestall fluid dynamic stability of the compressor can be viewed in a fashion analogous to its structural dynamic stability. In both cases, the compressor is a system rich in closely spaced, orthogonal modes operating in the presence of strong forcing. The point is not that the particular mode structure described in Fig. 11 is universal (which it surely is not), but that (1) many modes can exist simultaneously, and (2) which mode limits stability is a function of operating point and performance details.

In our two-dimensional representation, the mode structure and damping are set by the compressor mean line geometry and the blade row speedlines. As can be seen in Fig. 11, two or more modes may have very low damping simultaneously. The stability of the compressor may thus be set by the influence of the external forcing on the modes, which is beyond the scope of linear theory. In addition, precise prediction of mode damping is difficult since blade row speedline slopes cannot now be accurately estimated near the stall line. However, the influence of geometry changes on the relative compressor stability is often useful in design and this can now be assessed. For example, the modeling indicates that the modal damping is sensitive to axial loading distribution. Also, reduction of losses, blockages, and deviation all help to increase the speedline slope and therefore increase stability.

The aerodynamic forcing of the compressor modal dynamics is an important consideration in establishing the overall system stability. Dynamic systems as described here can be driven unstable when in a normally stable operating regime by external forcing of sufficient amplitude. With the exception of inlet distortion, the perturbation structure in compressors has not been studied in the context of compressor stability. Thus, it is currently difficult to characterize a particular machine as being weakly or strongly forced for this purpose. We do know, however, that compressors are very noisy and perturbations of several percent of the mean flow are not uncommon, especially at harmonics of shaft frequency. Manufacturing uniformity and uniformity of tip clearance may influence this forcing and therefore affect compressor stability.

The system dynamic response to forcing can be studied analytically. Even at damping ratios greater than zero, wave magnitudes can become large enough that they elicit a *nonlinear* response of the system. In this case the linear stability of the system is intact, but the nonlinear stability, or resistance to perturbations of finite magnitude, is very delicate. Mansoux et al. (1994) have studied this possibility by developing a Lyapunov stability analysis of the Moore–Greitzer model. When the so-called "domain of attraction" of the operating point becomes very small, perturbations that might be considered "linear" in magnitude can actually be unstable due to nonlinear effects. Thus it is not the damping ratio alone, but the increased perturbation level associated with low damping ratios *combined* with degradation of the nonlinear resistance to such perturbations, which determines the rotating stall inception point.

Much of the analysis to date has concentrated on the modal structure of the first spatial harmonic. For many compressors, rotating stall consists of two or more stall cells so that high order spatial harmonics can also be important. Second spatial harmonic waves are readily apparent in the data, in both the spectra in Fig. 6 (compressors 1, 3, 5, 6 and 7 for example) and even in the phase time history plots in Figs. 4 and 5 (compressors 3, 6, and 7). The higher harmonic waves travel at the same rotational speed as the first harmonic and are thus susceptible to the same forcing. Another concern is the short length scale disturbances during stall inception, reported in the Viper engine by Day and Freeman, and by Day in low-speed compressors, which may also play a role. These may be either a three-dimensional response of the system or represent system forcing, which triggers stall. These disturbances seem more properly a part of stall inception rather than prestall as they appear in the last few rotor revolutions before stall and have amplitudes relatively large compared to the prestall waves. As mentioned earlier, the data analysis techniques applied here are not well suited to the detection of short length disturbances since their energy would be spread across many spatial harmonics. Issues such as these deserve further study and time constraints prevented their inclusion herein.

Conclusions and Summary

In this paper, we have examined prestall data from nine, high-speed compressors, representing fans, core, and engine compressors from four different manufacturers, and encompassing many variations in design philosophy, number of stages, hub-to-tip ratio, and loading. While these differences do affect many of the details of the data, significant similarity exists, and these similarities are the focus of this paper. In particular, our focus has been on the steady, prestall dynamics of these compressors.

First of all, we have shown that stall precedes surge in all of the compressors tested. This is a conclusion that many researchers have reached based on their own experience, and it is useful to demonstrate that this observation is consistent among many different machines.

We have reviewed several techniques for the detection of small-amplitude rotating waves and explained their limitations. A new technique is introduced based on spectral analysis of the spatial Fourier harmonics of measured data. Using this approach, we have shown that:

1 Low-amplitude traveling waves are found in all of the compressors prior to stall.
2 The traveling wave structure is different at low and high corrected speeds. Specifically, a wave rotating at 1/2 of shaft frequency grows strongly at low speeds, while a shaft frequency disturbance dominates at 100 percent speed.
3 At constant speed, the wave structure is a function of the position on the compressor speedline.

A newly developed, two-dimensional, linearized, compressible, hydrodynamic stability model was used to analyze the geometry of two of the compressors. The analysis results are consistent with the experimental data. Several new findings have emerged, specifically:

1 Additional oscillatory modes exist in high-speed compressors compared to the same geometry with incompressible flow.
2 The dependence of mode damping and frequency on operating point is different for different modes.
3 At low corrected speeds, the incompressible mode predicted by the Moore-Greitzer analysis and observed in low-speed compressors sets the high-speed compressor stability limit.
4 At high corrected speeds, a hitherto unrecognized compressible mode is stability limiting.
5 The compressible mode differs from the incompressible mode in that its frequency is fixed (i.e., doesn't scale with shaft speed) and is approximately coincident with shaft frequency at 100 percent speed for many compressors.
6 The above implies that the stability of this mode and therefore that of the compressor can be strongly affected by external forcing due to sources such as geometric nonuniformities in the compressor.

Based on the ideas developed through this analysis and data reduction, we have introduced the concept of "integrated traveling wave energy" as a measure of compressor stability. The wave energy is shown to be a function of the position of the operating point on the speedline. Applying this wave energy technique to high-speed compressor data consistently gives at least 100-200 rotor revs warning prior to the inception of rotating stall for the data sets tested. When suitably developed, this approach may yield a usable stall warning scheme.

Finally, the data and analysis give a consistent picture of prestall initiation compressor stability dynamics behaving as a multimode dynamic system. We believe that this representation is of use for compressor design, data analysis, stall warning, and compressor control. Much work remains to be done in more thoroughly testing these concepts and understanding their ramifications.

Acknowledgments

This paper could not have been completed without the active assistance of many people and organizations in contributing data and time. We thank S. Baghdadi, J. E. Garberoglio, and D. Hobbs of Pratt & Whitney; W. Copenhaver, D. A. Hoying, and D. Rabe of the Wright Laboratory USAF; A. Sehra and S. Etter of Textron Lycoming; C. Freeman and A. Wilson of Rolls-Royce plc; and K. Owen of the US Army. D. Park thoughtfully prepared the manuscript and figures. This work was supported by the US Air Force Office of Scientific Research, Major D. Fant, program monitor; Pratt & Whitney; and NASA Lewis Research Center.

References

Boussios, C. I., 1993, "Rotating Stall Inception: Nonlinear Simulation, and Detection with Inlet Distortion," M.S. Thesis, MIT Dept. of Mechanical Engineering, Feb.

Bonnaure, L. P., 1991, "Modelling High Speed Multistage Compressor Stability," M.S. Thesis, MIT Dept. of Aeronautics and Astronautics, Sept.

Boyer, K. M., King, P. I., and Copenhaver, W. W., 1993, "Stall Inception in Single Stage, High-Speed Compressors With Straight and Swept Leading Edges," AIAA Paper No. 93-1870.

Day, I. J., 1993a, "Stall Inception in Axial Flow Compressors," ASME JOURNAL OF TURBOMACHINERY, Vol. 115, pp. 1-9.

Day, I. J., 1993b, "Active Suppression of Rotating Stall and Surge in Axial Compressors," ASME JOURNAL OF TURBOMACHINERY, Vol. 115, pp. 40-47.

Day, I. J., and Freeman, C., 1993c, "The Unstable Behaviour of Low and High Speed Compressors," ASME Paper No. 93-GT-26.

Etchevers, O., 1992, "Evaluation of Rotating Stall Warning Schemes for Axial Compressors," M.S. Thesis, MIT Dept. of Aeronautics and Astronautics, Aug.

Freeman, C., and Wilson, A. G., 1993, "Stall Inception and Post Stall Transients in an Aero Engine Axial Flow Compressor," presented at I. Mech E.

Gallops, G. W., Roadinger, T. J., and French, J. V., 1993, "Stall Testing and Analysis of Two Mixed Flow Turbofans," ASME Paper No. 93-GT-62.

Garnier, V. H., Epstein, A. H., and Greitzer, E. M., 1991, "Rotating Waves as a Stall Inception Indication in Axial Compressors," ASME JOURNAL OF TURBOMACHINERY, Vol. 113, pp. 290-302.

Greitzer, E. M., Fulkerson, D. A., and Mazzawy, R. S., 1978, "Flow Field Coupling Between Compression System Components in Asymmetric Flow," ASME *Journal of Engineering for Power*, Vol. 100, pp. 66-72.

Hendricks, G. J., et al., 1993, "Analysis of Rotating Stall Onset in High-Speed Axial Flow Compressors," AIAA Paper No. 93-2233.

Hoying, D. A., 1993, "Stall Inception in a Multistage High Speed Axial Compressor," AIAA Paper No. 93-2386.

Mansoux, C., Gysling, D. L., and Paduano, J. D., 1994, "Distributed Nonlinear Modeling and Stability Analysis of Axial Compressor Stall and Surge," to appear *Proc. of 1994 American Control Conference*, Baltimore, June.

McDougall, N. M., Cumpsty, N. A., and Hynes, T. P., 1990, "Stall Inception in Axial Compressors," ASME JOURNAL OF TURBOMACHINERY, Vol. 112, pp. 116-125.

Moore, F. K., and Greitzer, E. M., 1986, "A Theory of Post-stall Transients in Axial Compression Systems, Part I—Development of Equations; Part II—Application," ASME *Journal of Engineering for Gas Turbines and Power*, Vol. 108, pp. 68-97.

Owen, A. K., 1993, "Analysis of Rig Test Data for an Axial/Centrifugal

Compressor in the 12 kg/sec Class," presented at AGARD 82nd PEP, Montreal, Canada, Oct.

Paduano, J. D., 1992, "Active Control of Rotating Stall in Axial Compressors," Ph.D. Thesis, MIT Dept. of Aeronautics and Astronautics, Feb.

Widrow, B., et al., 1975, "Adaptive Noise Cancelling: Principles and Applications," *Proc. IEEE*, Vol. 63, pp. 1692-1716.

APPENDIX A

Power Spectra of Spatial Fourier Coefficients

Spectra analysis of the spatial Fourier coefficients offers a way to discern the nature of the stochastic signals that often occur in axial compressor data. The procedure is to plot the power spectral density (PSD) of each spatial Fourier coefficient during a period prior to stall. The stall event itself is *not* included in the analysis, so the spectra show resonant behavior, which exists in the small amplitude behavior of the system rather than the nonlinear limit cycle behavior. Analyzing the spatial Fourier coefficients in this way helps to determine whether waves in the compressor tend to rotate in the way predicted by the linearized theory of compressor dynamics.

Because the spatial Fourier coefficients are *complex* functions of time, the PSDs are not symmetric with respect to zero frequency, as is usually the case. This is true because, for a complex signal, the sign of the frequency has a very specific meaning. In the context of rotating stall, the sign of the frequency indicates the *direction of rotation of the wave.* To see this, consider a *k*th-mode spatial Fourier coefficient whose spectrum is a delta function at some frequency $-\omega_d$ *alone*, that is, there is no peak at $+\omega_d$. The time domain signal corresponding to this spectrum is

$$a_k(t) = e^{-j\omega_d t}$$

The signal is complex because the spectrum we started with was not symmetric about $\omega = 0$. Converting this spatial Fourier coefficient back into the spatial domain gives the spatial wave which produced the signal:

$$\delta P_x(\theta,\ t) = \mathrm{Re}\{a_k(t) \cdot e^{jk\theta}\} = \cos(k\theta - \omega_d t)$$

which corresponds to a rotating wave, *whose direction of rotating depends on the sign of* ω_d. A power spectrum which is symmetric, on the other hand, indicates a standing wave with oscillating amplitude. For instance, if we take a spectrum that is a delta function at *both* $+\ \omega_d$ *and* $-\omega_d$ then the corresponding time signal is

$$a_k(t) = e^{j\omega_d t} + e^{-j\omega_d t}$$

which in turn corresponds to the following wave in the space domain:

$$\delta P_x(\theta,\ t) = \mathrm{Re}\{2 \cdot \cos\ (\omega_d t) \cdot e^{jk\theta}\} = 2 \cdot \cos(\omega_d t)\ \cos\ (k\theta)$$

Here we see that ω_d is the rate at which the standing wave *magnitude* changes with time, rather than the rotation rate of the wave.

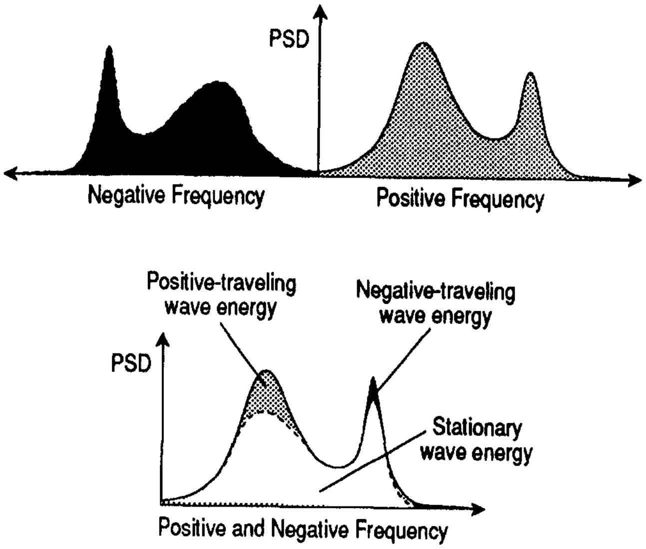

Fig. A.1 A sample nonaxisymmetric spectrum and its division into positive, negative, and stationary wave energy parts. Note that a peak in the spectrum may indicate resonance, which is primarily stationary. In this case, the frequency indicates the rate at which the spatially stationary wave oscillates in magnitude, rather than the wave rotation rate.

With this explanation we see that when we plot a spatial Fourier coefficient spectrum, we must plot both the negative and the positive frequencies, preferably flipping the negative frequency plot to overlay with the positive frequency plot. Then, only the peaks that do not exist at both negative and positive frequencies indicate waves that rotate. A given spectral frequency, then, consists of standing wave energy plus some traveling wave energy: The former is measured by the spectral energy that appears in both the positive and the negative spectra, while the latter appears in one but not the other—that is, it is the difference between the two spectra at that frequency. This difference can either be positive or negative, and the sign determines the direction of the traveling wave energy.

Figure A.1 gives an example of dividing the spectrum into its constituent elements. Note that there is a change in sign between the direction of the wave traveling and the frequency of the spectral line; this is due to the fact that cos $(k\theta\ -\ \omega_d t)$ represents a wave traveling in the positive direction at a rate ω_d. To avoid unnecessary confusion due to this sign change, we use a slightly different definition of the discrete Fourier transform in our computation of spatial Fourier coefficients, so that both the direction of traveling of the phase in a phase plot and the position of the peak in a spectrum correspond to the intuitively appealing convention that positive traveling waves travel with rotor rotation, and negatively traveling waves travel against rotor rotation. Consistency in definition and application of the Fourier transforms is, of course, the key to interpretation of the results in a physically accurate manner.

Monitoring of Aerodynamic Load and Detection of Stall in Multistage Axial Compressors

H. Hönen

H. E. Gallus

Institut für Strahlantriebe und
Turboarbeitsmaschinen,
Rheinisch-Westfälische Technische
Hochschule Aachen,
Aachen, Federal Republic of Germany

The unsteady flow in a single-stage axial flow compressor at different operating conditions has been investigated with hot-wire and hot-film probes to find out the influence of the aerodynamic compressor load on the periodic fluctuations. These results are compared with measurements in the last stages of a multistage high-pressure compressor of a gas turbine for normal operation and under stall conditions. From the patterns of the frequency spectra of the measuring signals a parameter for the detection of the approach to the stability line of a compressor is derived. A method for the on-line monitoring of the aerodynamic load is presented. Based on these results a monitoring system has been developed. First experiences with this system, applied to two multistage compressors, are reported.

Introduction

The trend to higher power densities and the wish for increasing efficiencies in turbomachines requires an operation with decreasing distance to the stability line of a compressor. Therefore the knowledge of this limit is the basis for an optimal operation.

With the progress in the application of measuring techniques for unsteady flows, various investigations on the topic of detection and prediction of rotating stall have been made. Most of them were carried out in research compressors with laboratory techniques. These investigations give a basis for the understanding of the flow effects near the stability line of a compressor.

Detailed measurements in axial compressors with arrays of hot-wire sensors illustrate the phenomena at the inception of rotating stall (Day, 1993; Poensgen, 1991). The changes in unsteady flow field are evident and point to a possibility to use these effects for the prediction of compressor stability line.

Paduano et al. (1993) presented a system for the active control of rotating stall. With an array of hot-wire sensors the unsteady flow field was measured over the circumference. The detection of rotating waves of axial velocity indicated the inception of rotating stall. Rotating waves of velocities and static wall pressure were also observed by Garnier et al. (1991) as an indicator for stall inception.

Gallus and Hönen (1986) showed that in regions of separated flow all periodic fluctuations are damped and covered by increased noise caused by random fluctuations. Inoue et al. (1991) investigated the flow in two isolated axial flow compressor rotors near stall. He showed that the collapse of the periodic fluctuations caused by a large stall region is an indicator for the approach to the stability line of a compressor.

All these investigations demonstrate the success in detection of stall in axial compressors. Nevertheless, the prediction of the stability limit, especially in multistage compressors is still an urgent problem that has to be solved.

Measurements in a Single-Stage Research Compressor Stator

Fundamental investigations were provided in a one-stage subsonic axial flow compressor with a hub-to-tip ratio of 0.38. The rotor speed was variable and the flow rate could be changed by a throttling valve system at the compressor outlet. Further constructional details of the compressor can be found from Gallus et al. (1979).

The experiments at different aerodynamic blade loads were carried out with hot-wire probes and hot-film glue-on probes. The hot-wire probes were traversed inside the stator between two stator blades from the hub to the casing. For a highly loaded operating point of the compressor the position and extension of the corner stall derived from measurements with different measuring techniques (Gallus and Hönen, 1986) is shown in Fig. 1. A hot-wire probe traversed near the suction side trailing edge of the vanes measures undisturbed flow in the upper part of the blade channel. In the lower part the probe is positioned inside the separation zone.

The distributions of the real time signals for these two regions and the corresponding frequency spectra show the influence of separated flows onto the periodic fluctuations (Fig. 2). In the frequency spectrum for undisturbed flow the peaks for the rotor blade frequency and the first harmonic causes by the rotor wakes passing the stator can be detected. For the measurements in the separated region the signal shows only strong random fluctuations. In the frequency spectrum for this case only a high noise level without periodic parts can be observed.

In the midspan of one stator blade on the suction side a hot-film glue-on probe with 11 sensors was mounted (Fig. 3). For two different operating points ($\varphi = 0.73$ and $\varphi = 0.63$) of

---

Contributed by the International Gas Turbine Institute and presented at the 38th International Gas Turbine and Aeroengine Congress and Exposition, Cincinnati, Ohio, May 24–27, 1993. Manuscript received at ASME Headquarters February 12, 1993. Paper No. 93-GT-20. Associate Technical Editor: H. Lukas.

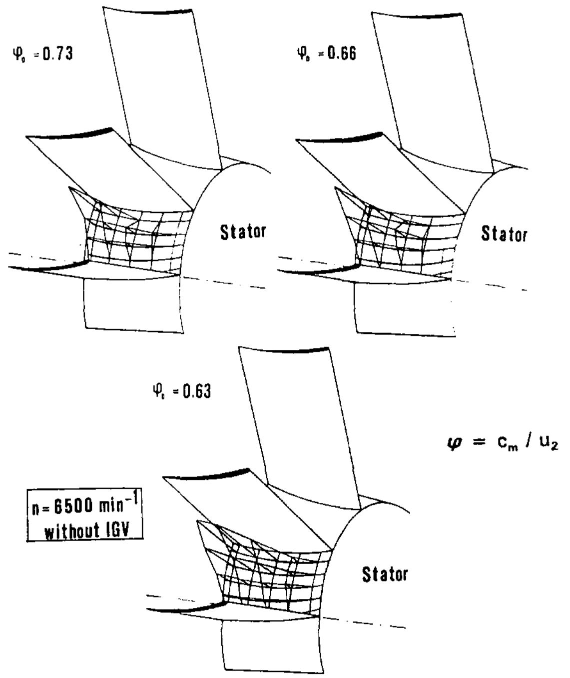

Fig. 1 Corner stall region in the single-stage axial compressor

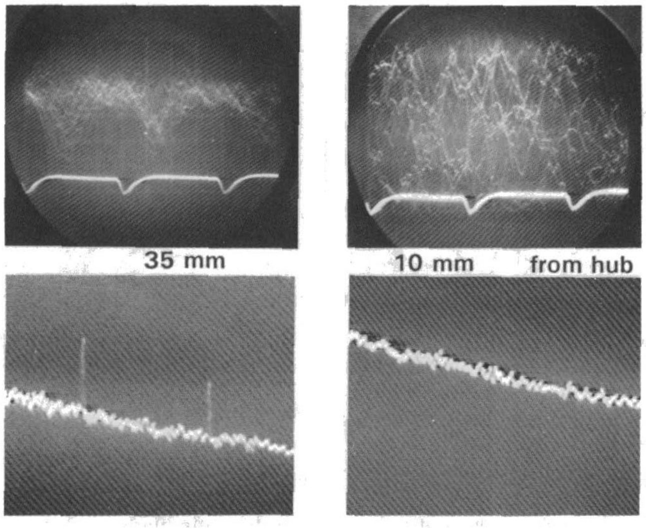

Fig. 2 Measuring results from a hot-wire probe for different radii

the compressor the separation lines on the surface are drawn. In the case of a flow rate of $\varphi = 0.63$ all sensors besides two are located inside the separation region. In the other case the measuring radius of the sensors is above the separation zone.

The real time measuring signals and the corresponding frequency spectra are presented in Fig. 4. With this measuring

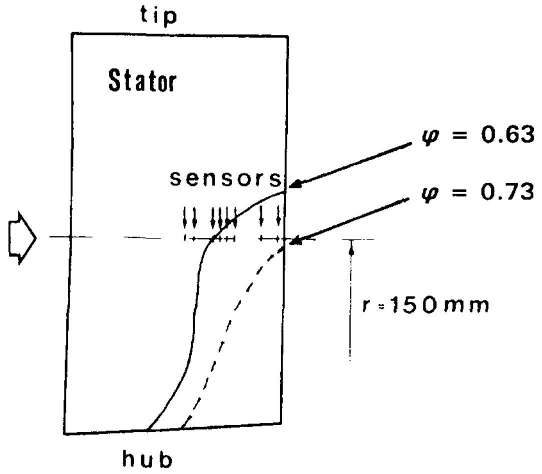

Fig. 3 Measuring blade with hot-film glue-on probes

technique the same effects can be observed as in the measurements with hot-wire probes. All sensors outside the separation region detect the periodic fluctuations from the rotor wakes. The sensors inside the separated regions only detect high random fluctuations. This is also visible in the frequency spectra. For the operating point $\varphi = 0.73$ the peak for rotor blade frequency occurs at all sensors, whereas for the highly loaded operating point of the compressor ($\varphi = 0.63$) only the first two sensors (outside the separation region) show periodic fluctuations with rotor blade frequency.

These results demonstrate that the concentration of low-energy material, as it occurs in a separation region, damps the periodic information from the undisturbed flow regions caused by the random fluctuations in cross and back flow direction. Furthermore, these fluctuations increase the noise level in the frequency spectra so that here small peaks from remaining periodic information are superposed. Therefore, measurements with dynamic sensors are an easy way to detect regions with low-energy material in turbomachines.

Measurements in a Multistage Compressor

Measurements in a multistage axial compressor of a LM5000 gas turbine validate and utilize this phenomenon. For a long-term investigation of the unsteady pressure distribution in eight stages of the 14-stage high-pressure compressor piezoelectric pressure transducers were mounted in the casing between rotor and stator. The transducers were connected to a FFT-analyzer via a multiplexer (MUX) and to a multichannel magnetic tape recorder (Fig. 5).

The measuring equipment was automatically controlled by a PC computer, which also picked up the measuring data from the FFT analyzer. Within an endless loop the computer switched the transducer signals to the FFT analyzer one after the other and started the FFT calculation. The frequency spectra were downloaded from the analyzer to the computer. For the definition of the operating point the thermodynamic data from

Nomenclature

a = weighting coefficient
ADC = analog-to-digital converter
c = velocity
c = chord length
f = frequency
HPC = high-pressure compressor
n = rotational speed
p = pressure
pfre = frequency amplitude of pressure fluctuations
$\overline{\text{pfre}}$ = mean value of frequency spectrum
PS = pressure side
pval = calculated fluctuating coefficient
r = radius
SL = stall level
SP = signal processor
SS = suction side
t = time
u = circumferential velocity
VSV = variable stator vanes
x = coordinate in chord direction
φ = flow rate

Subscripts

amp = amplitude
m = meridional
1 = compressor inlet
2 = compressor outlet
11 = 11th stage
12 = 12th stage
13 = 13th stage

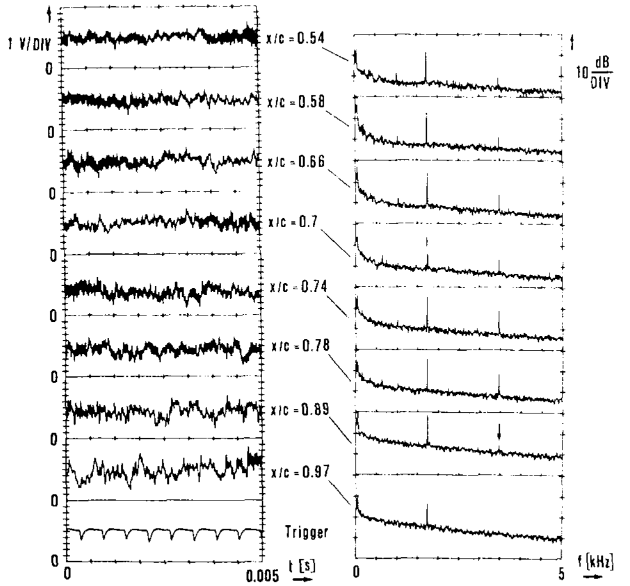

Fig. 4(*a*) Real time signals and frequency spectra for a moderately loaded operating point (φ = 0.73)

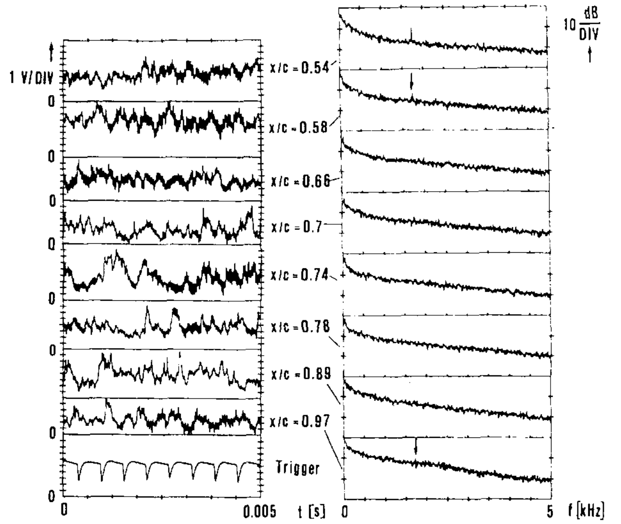

Fig. 4(*b*) Real time signals and frequency spectra for a highly loaded operating point (φ = 0.63)

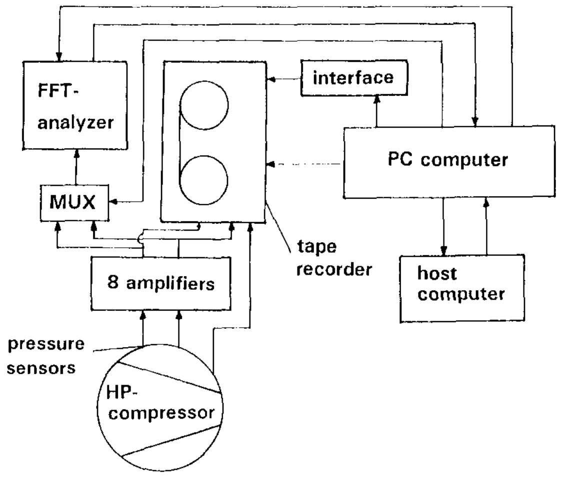

Fig. 5 Experimental setup for long-term measurements

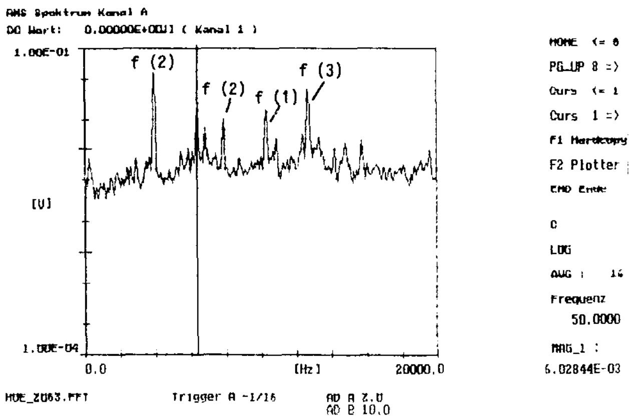

Fig. 6 Frequency spectrum in the third stage for compressor operation near design point

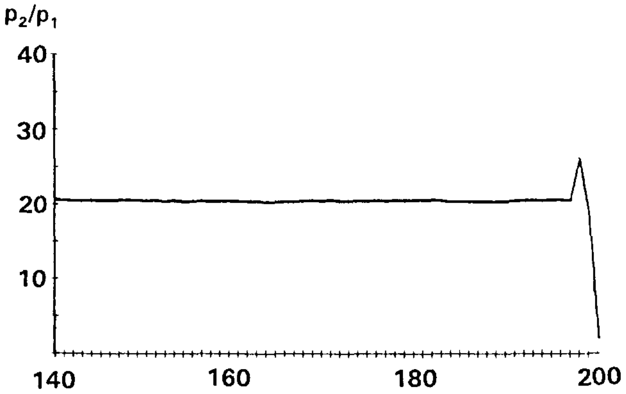

Fig. 7 Pressure ratio of the HPC for a period of three days before turbine shut down

the controlling computer of the gas turbine (host computer) were received.

Changing operating conditions of the compressor influence the unsteady flow field in a blading that can be detected by the casing-mounted dynamic pressure sensors. The frequency spectra of these measured real time signals show different patterns. This effect was used for the automatic long-term investigation of this compressor.

After the start of the gas turbine, the first frequency spectra of each sensor signal were stored as a reference pattern. When during operation differences occurred that exceeded a defined range, the magnetic tape was started by the computer and picked up the real time signals of all sensors. At the same time the current frequency spectra were stored as new reference patterns. By this procedure all changes in the unsteady flow field in the stages could be observed and saved.

For normal compressor operation the frequency spectrum of each stage sensor shows the peak for rotor blade frequency of this stage (Fig. 6). But also the characteristic frequencies of the neighboring stages are visible (marked with numbers for the several stages). The decrease of the fluctuating amplitudes at higher frequencies is caused by the damping of the adapters in which the pressure sensors were mounted.

The investigations were carried out over a time period of about four months at nearly constant operating conditions of the gas turbine. Figure 7 shows the pressure ratio of the compressor for a period of three days just around the occurrence of stall. The X axis shows the absolute number of measurement and the Y axis the pressure ratio of the whole compressure (p_2 = outlet pressure, p_1 = inlet pressure). At the end of this period a strong increase caused by a fault of the controlling system occurred. At the maximum pressure the surge control of the compressor became active and the gas turbine was shut down.

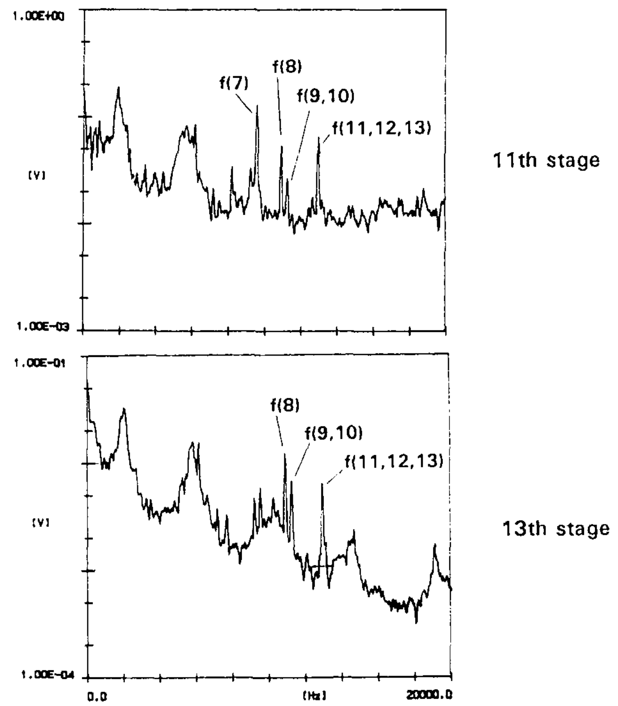

Fig. 8(*a*) **Frequency spectra of the 11th and 13th stages for normal compressor operation**

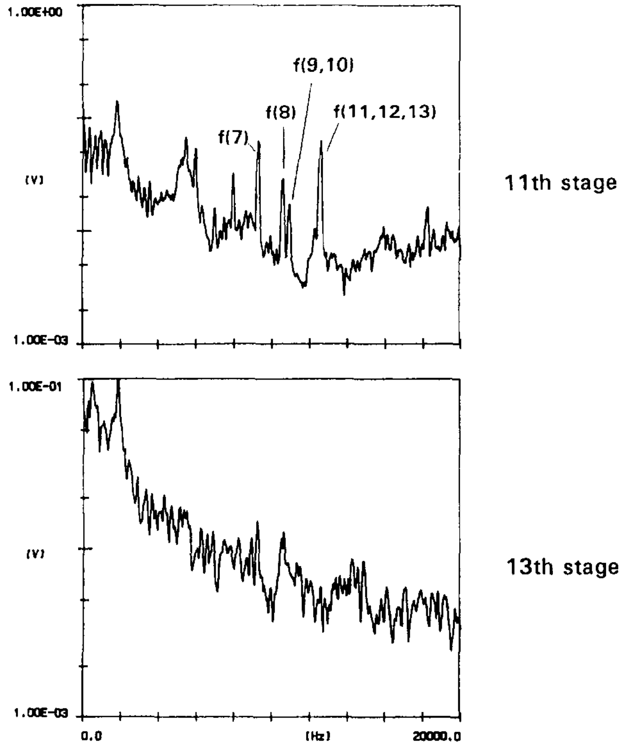

Fig. 8(*b*) **Frequency spectra of the 11th and 13th stages for compressor operation near the stability limit**

Figures 8(*a*–*c*) show the frequency spectra of the 11th and 13th stage sensors for three different points of time around the shut down point. The patterns for normal operating conditions are demonstrated in Fig. 8(*a*). The peaks for the rotor blade frequency of the 11th to 13th stage with 76 rotor blades each are clearly visible. Also the 9th and 10th stage peaks (60 rotor blades each) stand out of the noise in the spectrum.

Hereafter, the fault in the control system occurred and the operating point of the compressor drifted slowly toward the stability line. The spectra during these operating conditions show different patterns in the 11th and 13th stages (Fig. 8*b*). Whereas the periodic fluctuations in the 13th stage disappeared, in the 11th stage an increase of the characteristic frequency peak can be observed due to increased profile loads and wakes.

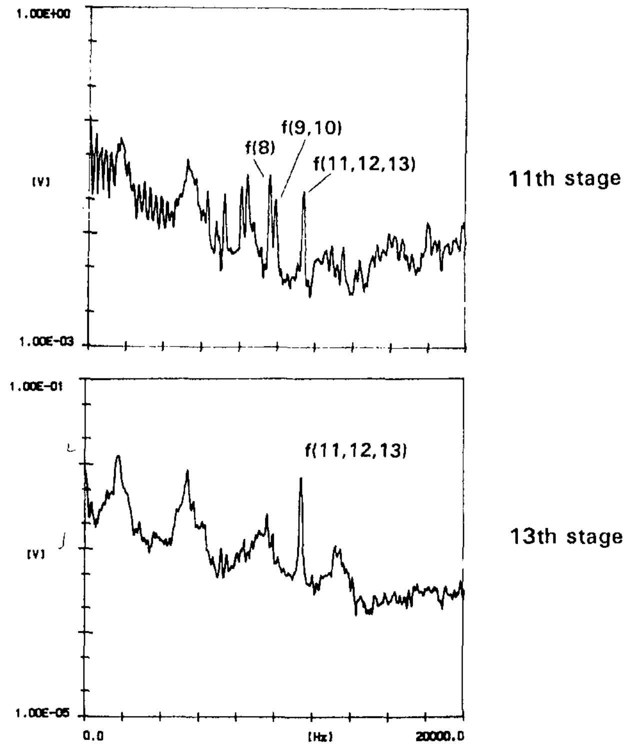

Fig. 8(*c*) **Frequency spectra of the 11th and 13th stages just after gas turbine shutdown**

Caused by the high pressure ratio of the compressor, the aerodynamic load of the 13th stage becomes so high, that low-energy material from increased wakes or even separated profile boundary layers (approaching stall) is centrifugated from the rotor blades. It accumulates near the casing behind the rotor and forms here a casing stall region, which reduces the pressure rise in this stage. The pressure sensor mounted in the gap between rotor and stator is covered by this low-momentum material so that the information from the undisturbed flow outside of the stall is extinguished at the measuring position due to increased turbulence and noise.

Due to the high aerodynamic load of the compressor and the reduced pressure rise in the last stages, the load of the upstream stages is increased. This causes a growth of the rotor wakes in these stages so that here the characteristic frequency peaks increase (see Fig. 8(*b*), 11th stage). The multistage compressor runs under stable conditions although in the 13th stage the limit for stall as it was defined for a single stage (Inoue et al., 1991) is exceeded.

After about a further 30 minutes the compressor load entered such a high level that surge occurred and the surge control system shut down the gas turbine. As the automatic measuring system had a cycle time of about 20 seconds from the start of the FFT analysis from the first to the last sensor the exact point of compressor surge was not recorded on the magnetic tape. The signals taken during this operation phase started the recorder a few moments after this event.

Just after the shutdown the compressor load diminishes and the frequency information of several stages can be detected again in the 13th stage (Fig. 8*c*). Due to the deceleration of rotor speed, the characteristic frequencies occur at lower values.

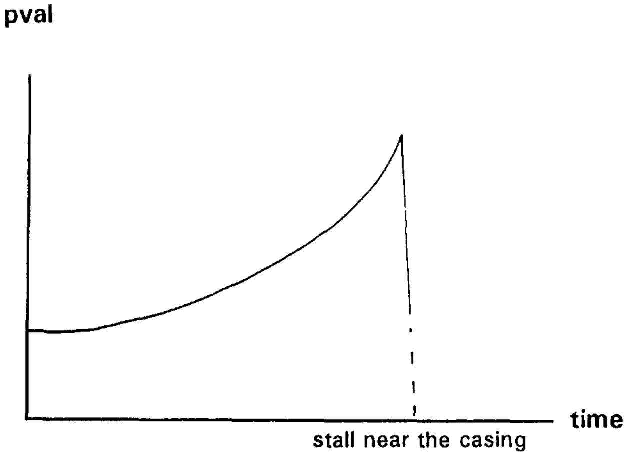

Fig. 9 Change of amplitudes at characteristic frequencies with increasing blade load

Design of an On-Line Monitoring System

Based on these results, a monitoring system for detecting the approach of the stability line in a multistage compressor has been developed. The measurements showed that the peak level at the characteristic frequency of a stage is an indicator for the aerodynamic load. Up to the point of the collapse of the periodic fluctuations, the peak amplitude grows out of the normal noise level, which also rises with increasing aerodynamic load (Fig. 9).

This behavior can be described in the following form:

$$\mathrm{pval}_{\mathrm{stage}} = \frac{\mathrm{pfre}_{\mathrm{stage}} - \overline{\mathrm{pfre}}}{\overline{\mathrm{pfre}}} \tag{1}$$

As the measuring results from the multistage compressor demonstrated, the collapse of the periodic information at the 13th stage sensor is not the limit for the stable compressor operation. Therefore, additional information must be used to define another parameter for the observation.

Measurements of unsteady wall pressures in three neighboring stages provide information on the stall development from the last to the upstream stages. Therefore, dynamic pressure transducers are located in the axial gaps between rotor and stator of the 11th, 12th, and 13th stages.

In order to get an informative value for the operator or an operating and control system from the measuring results in each stage, a new parameter was defined for the monitoring of the compressor load. This value (called stall level *SL*) takes into account the amplitudes of the frequency peaks in the three observed stages and the information about flow separation.

Since with increasing compressor load the amplitudes in the stages grow, this parameter can be defined in the following form:

$$SL = a_{13}\,\mathrm{pval}_{13} + a_{12}\,\mathrm{pval}_{12} + a_{11}\,\mathrm{pval}_{11} \tag{2}$$

wherein a_{11}, a_{12}, and a_{13} are weighting coefficients for the influence of the stages on the stability limit of the compressor. The optimal choice of these coefficients depends upon the compressor operating conditions and geometry. They are still the subject of further investigation and are proprietary.

As previously mentioned (see Fig. 8) for the shutdown of the compressor, the 11th stage was not yet separated at the casing measuring position. Therefore, for this compressor, terms of peak values (pval) from further upstream stages were not included. For other part-load operating points the station of measurements and the terms of the stages to be included in the stall level value (*SL*) must be selected correspondingly.

When casing stall in the 13th stage occurs the periodic fluctuations at the sensor are damped so that the observed characteristic peak in the frequency spectrum disappears or becomes very small compared to the increased noise level. Due to the lower pressure rise in this stage the loads of the upstream stages increase. Thus the amplitudes of the characteristic frequency peaks are enlarged.

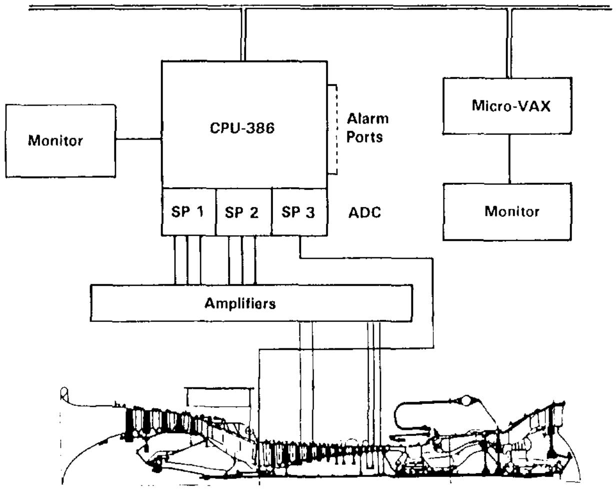

Fig. 10 Hardware setup for the on-line monitoring system

After the collapse of the observed frequency peak, the value of pval will decrease. Thus, although the compressor load is higher, a lower value for the stall level SL would be calculated with Eq. (2). In order to obtain an increasing trend with higher compressor load, the calculation of this parameter has to be switched. When in the 13th stage casing stall occurs, the maximum value of pval_{13} just before the collapse of the frequency amplitude is stored and used for the further stall level calculations. The same procedure will be applied if also in the next upstream stage casing stall damps the periodic information at the sensor. When the operating conditions change back to unseparated flow caused by lower aerodynamic loads, the calculation switches back to the former way (Eq. (2)).

This algorithm was applied to the unsteady pressure measurements of the long-term investigation (Fig. 8). It is mentioned that in this case the stall level was only calculated with the measuring results of the 11th and 13th stages. For the last measurements just before the shutdown (see Fig. 7) with increasing pressure ratio of the compressor, the stall level exceeds a value of 15. During the whole investigation period of four months at normal compressor operation, values up to 10 were calculated for the stall level.

This procedure of calculating a monitoring parameter for the compressor load described above was the foundation for the design of an on-line monitoring system on the basis of a PC computer with 80386-CPU and signal processor boards for parallel signal acquisition and enhancement (Fig. 10). The unsteady pressure signals are Fourier analyzed by the signal processors. The CPU coordinates the tasks of the processors, calculates the stall level from the frequency spectra, and sends the results to a host computer where the data are displayed on a monitor and stored for a trend analysis.

Experiences With the Monitoring System in Operation

This system was applied to the high-pressure compressors of two gas turbines of the type *LM5000*. In order to get an impression of the reliability of the monitoring system, the stall level is compared with the operating parameters of the compressor measured by the normal control system of the gas turbines. The trends of the speed of the high-pressure rotor and the pressure ratio of the HPC show a satisfying relation to the observed stall level (Figs. 11*a* and *b*).

With increasing pressure ratio, the stall level also grows up to values of about 7. After a while it decreases slowly although the pressure ratio keeps constant. The comparison with the

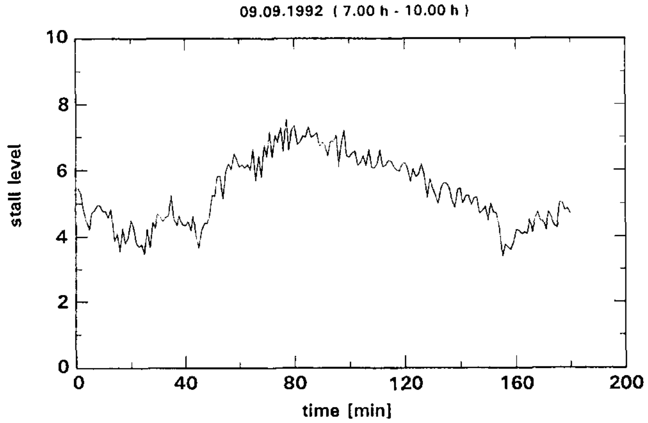

Fig. 11(*a*) Stall level over a time period of three hours

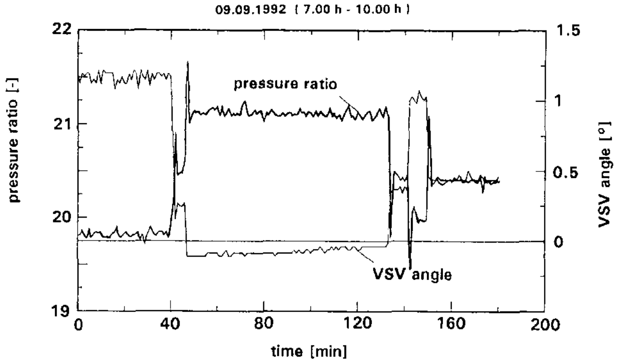

Fig. 11(*b*) HPC pressure ratio and VSV angle over a time priod of three hours

VSV angle (Fig. 11*b*) shows the reason for this behavior. At the same time when the stall level decreases, the VSV angle moves from an open position toward 0 deg so that the air flow through the compressor decreases. This lower aerodynamic load causes the decrease in stall level.

In order to get information about the vicinity to the stability line of the compressor, a limit value for the stall level has to be defined. The results from the long-term investigation and the experience with the monitoring system until now allow an estimation of this limit. The measurements and trends have shown that the 13th stage of the investigated compressor can operate stably with casing stall without the compressor exceeding the stability line. The stall region covers only a part of the blade height so that stable compressor operation is still possible. Assuming that with occurrence of casing stall also in the 12th stage the stall region in the 13th stage covers a large part of the span, this point would be the limit of stable compressor operation. Thus, if the maximum of $pval_{12}$ is known, the limit value of stall level can be calculated with Eq. (2). As the three observed stages have the same blade numbers and geometries in each rotor and each stator row, the patterns of periodic fluctuations should look quite similar. So, the maximum value of $pval_{12}$ will be in the same range as the maximum of $pval_{13}$ just before occurrence of casing stall in the 13th stage. By inserting these values into Eq. (2) the stall limit is calculated.

The value of the stall limit is influenced by many geometric parameters of the bladings. One important factor is the tip clearance of the rotor (Adamczyk et al., 1993; Inoue et al., 1991). The mixing of tip leakage vortex with low-momentum material centrifuged from the rotor blades play a nonnegligible role in the development of casing stall.

This causes different limit values of stall level with changing geometries and operating conditions. After longer operation time of the monitoring system more measuring data for different operating conditions of the compressor will be available. With these experiences the model for the definition of the limit value can take into account more influence parameters.

Summary and Conclusions

Based on experimental results of unsteady flow in a single and a multistage compressor a monitoring system for stable compressor operation has been developed. By detection of aerodynamic load and casing stall in three neighboring end stages of a multistage high-pressure compressor, the approach to the stability line can be observed.

Experiences with the monitoring system at two compressors demonstrate the reliability of the method. Changes in compressor load cause differences in calculated stall level. Additional measuring results from system operation will allow a more exact definition of various influence parameters.

By the detection of casing stall in the end stages only a stall monitoring near-design speed of the compressor can be realized at the present state. The system will be able to obtain monitoring data for lower speeds if measurements also will be taken in the front stages. Furthermore, additional measurements in different compressors can help to obtain further information about the influence of various geometries and loads.

Acknowledgments

The authors wish to acknowledge the DOW Stade GmbH for the financing of the investigations leading to this research work. Especially, we wish to thank Mr. H. Walter and Mr. E. Mizera for their support in preparing the experiments and the helpful comments concerning the application of the monitoring system. The discussions about the measuring results during the test phase are gratefully acknowledged. A patent application that relates to the technology covered by this work has been filed by DOW Deutschland Inc.

References

Adamczyk, J. J., Celestina, M. L., and Greitzer, E. M., 1993, "The Role of Tip Clearance in High-Speed Fan Stall," ASME JOURNAL OF TURBOMACHINERY, Vol. 115, pp. 28-39.

Day, I. J., 1993, "Stall Inception in Axial Flow Compressors," ASME JOURNAL OF TURBOMACHINERY, Vol. 115, pp. 1-9.

Gallus, H. E., Lambertz, J., and Wallmann, Th., 1979, "Blade-Row Interaction in an Axial-Flow Subsonic Compressor Stage," ASME Paper No. 79-GT-92.

Gallus, H. E., and Hönen, H., 1986, "Experimental Investigations of Airfoil- and Endwall Boundary Layers in a Subsonic Compressor Stage," ASME Paper No. 86-GT-143.

Garnier, V. H., Epstein, A. H., and Greitzer, E. M., 1991, "Rotating Waves as a Stall Inception Indication in Axial Compressors," ASME JOURNAL OF TURBOMACHINERY, Vol. 113, pp. 290-302.

Inoue, M., Kuroumaru, M., Iwamoto, T., and Ando, Y., 1991, "Detection of a Rotating Stall Precursor in Isolated Axial Flow Compressor Rotors," ASME JOURNAL OF TURBOMACHINERY, Vol. 113, pp. 281-289.

Paduano, J. D., Epstein, A. H., Valavani, L., Longley, J. P., Greitzer, E. M., and Guenette, G. R., 1993, "Active Control of Rotating Stall in a Low-Speed Axial Compressor," ASME JOURNAL OF TURBOMACHINERY, Vol. 115, pp. 48-56.

Poensgen, Ch., 1991, "Experimentelle Untersuchung der Strömung in einer Unterschall-Axialverdichterstufe bei hoher Drosselung und im Rotating Stall," Dissertation, RWTH Aachen, Federal Republic of Germany.

Rotating Stall Acoustic Signature in a Low-Speed Centrifugal Compressor: Part 1—Vaneless Diffuser

P. B. Lawless

S. Fleeter

School of Mechanical Engineering,
Purdue University,
West Lafayette, IN 47907

An experimental study is performed to identify spatially coherent pressure waves, which would serve as precursors to the development of an instability in the Purdue Low-Speed Centrifugal Research Compressor when configured with a vaneless diffuser. To achieve this, sensitive electret microphones were uniformly distributed around the circumference in the inlet and diffuser sections of the compressor. Fourier analysis of simultaneously sampled data from these microphone arrays was employed to identify the development of dominant spatial modes in the pressure field in the compressor. The transition to stall was observed to be a gradual process, with the growth of the pressure waves into those corresponding to a large-scale stall condition occurring over a time span of 26 impeller revolutions. The excitation of the pressure waves, as indicated by spatial Fourier analysis, occurred 14 impeller revolutions before small changes were evident in the microphone signals, and 26 revolutions before the stall condition could be considered fully developed.

Introduction

The operating range of a compressor is limited by the surge and choke lines on the system performance map. The surge line is of particular interest due to its proximity to the maximum efficiency point of the compressor. Current generation turbomachines must allow for a safety margin that places the operating point in a region far enough removed from the surge line so as to prevent the onset of instability.

The surge line refers to a barrier, typically represented on a constant-speed operating characteristic, where the compressor would exhibit unstable behavior if the machine were throttled to a lower mass throughflow. The term "surge line" is somewhat misleading since surge is only one of the possible phenomena that result when this boundary is reached. In turbomachinery, the types of instabilities found can be categorized as rotating stall or surge. Surge refers to a global oscillation of the mass flow through the compression system, often with complete flow reversal occurring. Surge is regarded as a phenomenon of the entire compression system, consisting of the compressor and the system into which it discharges. Rotating stall, in contrast, is an instability local to the compressor itself, and is characterized by a circumferentially nonuniform mass deficit that propagates around the compressor annulus at a fraction of wheel speed.

The disadvantages of bringing a compressor into a stall or surge condition are twofold. First, compressor performance falls drastically when instability is encountered. On flight-rated turbine engines, such a performance degradation and resulting loss of thrust can be catastrophic. Second, as discussed by Haupt et al. (1986), and Jin et al. (1992a, 1992b), rotating stall and surge can represent dangerous unsteady aerodynamic excitations to impeller and diffuser vanes. For these reasons, attempts to increase the stable operating range of compressors have long been an area of vigorous research activity.

Attempts to increase the stable operating range of compressors take the form of passive methods and, more recently, active control methods. Examples of the former range from conventional technologies such as close-coupled resistances and inlet prewhirl to more exotic solutions such as casing treatment. A discussion of such methods is given by Greitzer (1981). In general, all such methods appear to carry some performance penalty along with the sought-after increase in operating range.

Due to the promise of achieving increased stall margin while avoiding the performance penalties of passive methods, active control schemes have recently become an area of increased research activity. Definitive success has been achieved in the suppression of surge in centrifugal compressors, as reported by researchers such as Pinsley et al. (1991) and Ffowcs Williams and Graham (1990). Equally promising results have been demonstrated for rotating stall in low-speed axial compressors by both Day (1991a) and Paduano (1993).

Although exhibiting the same fundamental type of instabilities, centrifugal compressors are characterized by a much

---

Contributed by the International Gas Turbine Institute and presented at the 38th International Gas Turbine and Aeroengine Congress and Exposition, Cincinnati, Ohio, May 24–27, 1993. Manuscript received at ASME Headquarters March 10, 1993. Paper No. 93-GT-297. Associate Technical Editor: H. Lukas.

broader spectrum of unstable behavior than their axial counterpart. The wide variety of geometries that have been tested to date have resulted in an equally large variety of instability pathologies. The wide variety of instability behavior, along with the inherently complicated flow in such a machine, are primary reasons that rotating stall and surge in centrifugal compressors are less well understood than similar phenomenon in axial compressors.

An active control scheme to control rotating stall in a centrifugal compressor in a manner similar to that which has been applied to axial machines was theoretically investigated by Lawless and Fleeter (1991). A basic assumption in that analysis was that, in its early stages, rotating stall is well represented as a weak, linear disturbance, which grows into a finite disturbance in a region of preferential amplification on the performance map. Such a phenomenon has been observed in axial compressor stall initiation by Garnier et al. (1991). This concept of a "pre-stall" or "modal" wave type of stall initiation is in contrast to a different, and perhaps more traditional view that rotating stall is the result of the propagation of a finite separation zone on a rotor airfoil due to blockage effects, as described by Emmons (1955). The appearance of a finite stall cell, rather that the growth of a weak sinusoidal wave, is reported to be the primary mechanism of stall initiation in axial compressor investigations carried out by Day (1993b). Nevertheless, Day was able to achieve significant results with a control system designed to alleviate the stall condition by injecting air into the region near the developing stall cell (1993a).

From the investigations into axial compressor rotating stall, both mechanisms noted above appear to be important for stall initiation. In both cases, however, active control schemes based on detection of an early precursor to stall have proven successful. To date, similar results have not been reported for the problem of centrifugal compressor rotating stall. An obvious step in this direction is the investigation into rotating stall initiation in centrifugal compressors.

The work presented here is directed at providing a picture of stall and surge initiation in a low-speed centrifugal compressor when viewed with a tool that has proven useful in the investigations of axial stall initiation–Fourier analysis in the circumferential spatial domain. Compressor instability as a system phenomenon is considered, with the goal being to characterize the early stages of performance-limiting instabilities better and identify possible weak pressure, or acoustic, waves, which could serve as a precursor to centrifugal compressor stall and form the basis of an active control system. To this end, arrays of pressure transducers are circumferentially distributed in the inlet and diffuser sections of the Purdue Low Speed Centrifugal Research Compressor. The microphone arrays are sampled while bringing the compressor into an instability condition by slowly closing a throttle plate after the compressor has been allowed to reach a steady operating condition. Data acquisition is terminated when the trigger level from a single inlet microphone reaches a previously determined level and the proper number of posttrigger samples has been acquired.

In this paper, a detailed description of the data acquisition and reduction techniques employed to detect compressor instability precursors is introduced. These techniques are then applied in the analysis of the stalling behavior of the Purdue Low-Speed Centrifugal Research Compressor configured with a vaneless diffuser. The behavior of this compressor with three different vaned diffuser configurations is addressed in an accompanying paper.

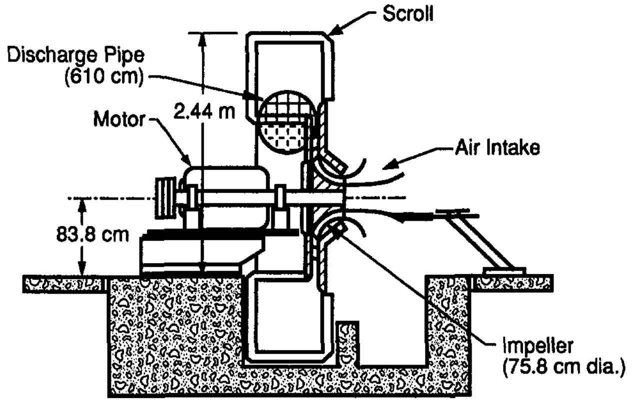

Fig. 1 Cutaway view of the Purdue low-speed centrifugal compressor facility

Experimental Facility and Instrumentation

Purdue Low-Speed Centrifugal Research Compressor. The experiments discussed herein were conducted in the Purdue Low-Speed Centrifugal Research Compressor (PLCRC). This compressor is shown schematically in Fig. 1. The compressor features a shrouded, mixed flow impeller with 23 backswept blades, and a diffuser that may be configured with up to 30 cambered vanes. Optionally, the diffuser vanes may be removed and the compressor operated with a parallel walled vaneless diffuser. The compressor is driven by a 29.8 kW (40 hp) induction motor. The nominal operating speed for the impeller is 1790 rpm, giving an impeller pass frequency of 29.8 Hz and a blade pass frequency of 686.2 Hz.

Flow enters the compressor impeller axially, passes through the impeller, enters into a curved vaneless space and then exits into a parallel walled vaned radial diffuser, as shown in Fig. 2. The diffuser empties into a scroll of square cross section. Flow is evacuated from the scroll through a discharge pipe, with a butterfly valve driven by a gear motor located at the termination of this discharge pipe serving to throttle the compressor.

When employed, the vanes are mounted using 30 eccentric cams imbedded in the endwall of the diffuser. By independent rotation of the cam and the vane, both the vane stagger angle and leading edge radius are modified. In the PLCRC facility, the configuration of the diffuser controls the type of instability behavior encountered. Rotating stall conditions exhibiting a variety of cell patterns as well as surge are observed when the compressor diffuser configuration is varied. In this investigation, the diffuser vanes were removed and the compressor operated with a parallel walled vaneless diffuser. A steady-state characteristic curve for this configuration is given in Fig. 3.

Instrumentation. The instrumentation used in this investigation was required to detect weak, low-frequency, spatially coherent waves in the compressor. To this end, researchers such as McDougall et al. (1990), Day (1993b), and Garnier et

Nomenclature

f_t = frequency measured by a single transducer
N = number of transducers in spatial array
n = mode number
p_e = exit static pressure
p_{ti} = inlet total pressure
t = time
U = wheel speed at mean inlet radius
V_p = phase angular velocity
V_z = axial velocity at inlet
α = mode phase angle
ρ = density

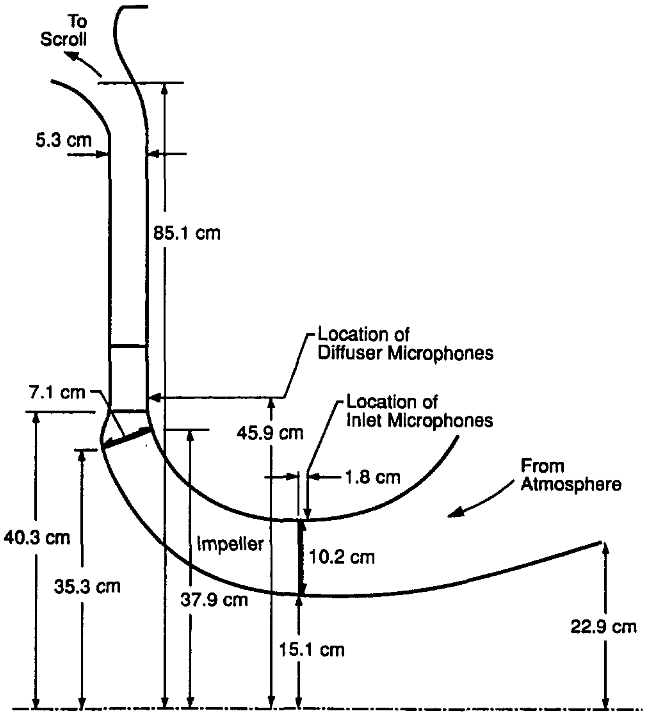

Fig. 2 Compressor flow path

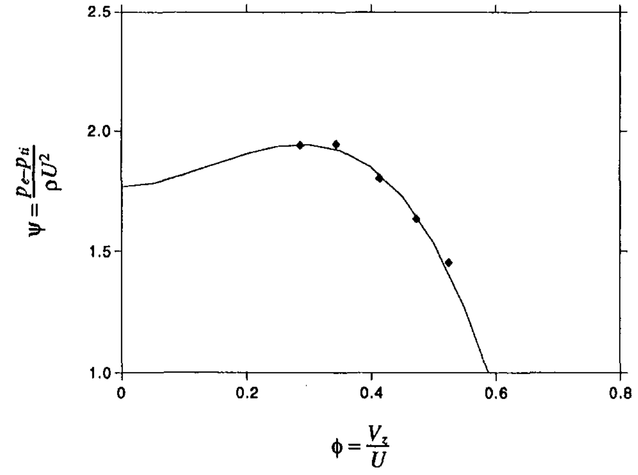

Fig. 3 Compressor characteristic curve

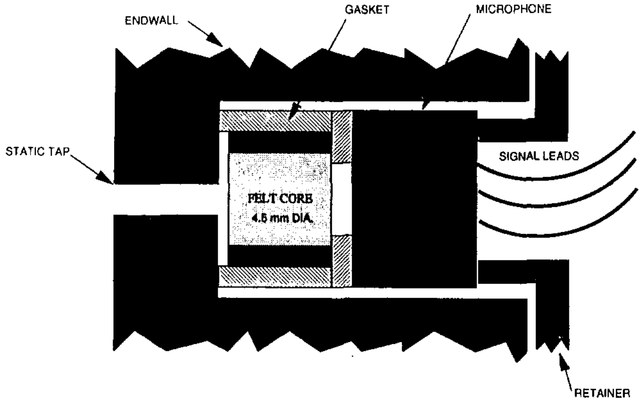

Fig. 4 Attenuator tube and microphone mounting schematic

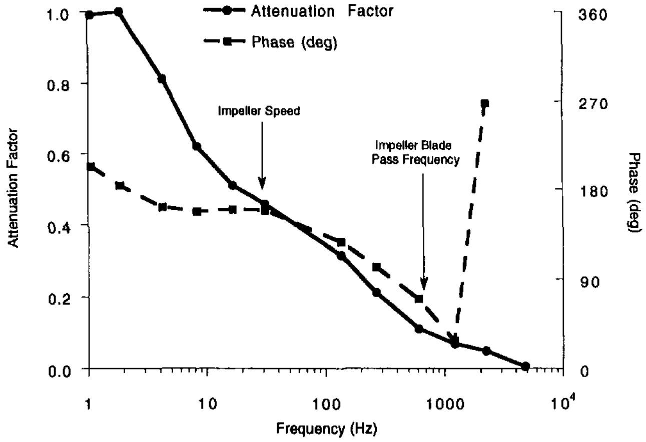

Fig. 5 Ratio of microphone gain to maximum microphone gain and the phase response of typical electret microphone and attenuator tube

al. (1991) have employed Fourier analysis of the signals from circumferentially distributed hot-wire probes. Although this type of instrumentation has proven successful, the high cost of the large number of sensors required (up to 15 sensors were eventually employed in this experiment) and the desire to avoid the introduction of intrusive probes into the diffuser section near the vaneless space discouraged their use in this application.

Recently, researchers such as Kendall (1990) and Johnston and Sullivan (1992) have put inexpensive audio electret microphone elements in service as dynamic pressure transducers. Because of their high sensitivity and low cost, these devices, with slight modifications, were chosen for use in the current study. Although the microphones show some nonlinearity in the frequency domain, they exhibit excellent amplitude linearity over a limited frequency band and also demonstrate excellent low-frequency response.

The microphones are connected to the flow by means of static pressure taps located on the O.D. endwall of the inlet and diffuser sections of the compressor. In the inlet, eight microphones are distributed uniformly around the inlet circumference 1.8 cm in front of the tip of the impeller leading edge. Fifteen microphones are placed, again with uniform circumferential spacing, in the diffuser mounting cams, allowing the static ports to be relocated when vanes are introduced and thus prevent their obstruction.

The PLCRC features a window in the diffuser case that allows optical access. To accommodate this window, three of the thirty mounting cams are located on the I.D. endwall and, therefore, one of the fifteen microphones was also mounted on the I.D. endwall. Since the disturbances of interest are representative of the core flow of the compressor rather than isolated to a particular boundary layer, this modification is considered an acceptable compromise.

To prevent the high-frequency signals from rotor blade passage and flow noise from dominating the low-frequency signals of interest, a short attenuator tube is installed between the microphones and the static taps in the compressor endwall, as shown in Fig. 4. The attenuator, consisting of a stainless steel tube of 4.5 mm diameter filled with a 5-mm-long porous felt core, serves as a pneumatic low-pass filter. Each microphone with its specific attenuator tube is dynamically calibrated against an Entran EPIL-6B-2 dynamic pressure transducer. Typical results from this calibration are given in Fig. 5. This figure presents the microphone gain magnitude relative to its maximum value, showing that signals at blade pass frequency are attenuated by a factor of 2.5 with respect to impeller speed, while a frequency of 5000 Hz marks the beginning of the stop band of the filter. With the addition of the attenuator tubes a highly nonlinear phase response is encountered, also shown in Fig. 5. Note that the unaltered microphones produce a negative voltage for an increasing pressure, which manifests itself as a response that is 180 deg out of phase with the pressure signal. Although the nonlinearity of the frequency response precludes direct conversion of the microphone voltage output to pressure, the approach taken in processing the signals, as discussed below, minimizes this difficulty. In addition, the device linearity is not a critical requirement for this application since the overall goal of the microphone arrays is to serve as spatial wave detectors rather than fine resolution pressure transducers. To obtain the best possible results from the spatial Fourier analysis, the microphones in the inlet and diffuser section were selected from a larger lot of 60 microphones for similar phase and magnitude response.

The static pressure rise in the compressor scroll is measured from a tap placed on the opposite side of the scroll from the discharge pipe. This pressure is monitored with a Scanivalve Model J pressure multiplexer and transducer.

Experimental Technique

Data Acquisition. Acquisition and digitization of the microphone signals is accomplished using four National Instruments NB-A2000 analog-to-digital conversion boards installed in an Apple Macintosh IIfx computer. This system allows 16 channels of simultaneously acquired data to be recorded. Data acquisition is initiated by an analog trigger signal supplied by one of the inlet microphones. The boards are operated in a pretrigger mode, where samples before the trigger occurred are recorded along with posttrigger data.

To bring the compressor into an instability condition, the throttle plate is slowly closed from the fully open position after the compressor has been allowed to reach a steady operating condition. Data acquisition is terminated when the trigger level from the inlet microphone reaches a previously determined level and the proper number of posttrigger samples have been acquired. Continuous motion of the throttle plate is employed throughout the acquisition sequence.

The frequencies at which periodic structures in the flow field erupted are first identified with a joint time-frequency analysis performed on the signal from a single microphone. Signals from a single inlet microphone and a single diffuser microphone are recorded as the compressor throttle is slowly closed. The rate of closure of the throttle was chosen to allow a complete record of significant phenomena occurring in the compressor to be digitized and retained. To increase resolution in the time and frequency domains, a sampling frequency of 1250 Hz is employed. Although this frequency results in an aliasing of the impeller blade pass signals, it was chosen so that the aliased frequency was still well above the expected rotating stall values.

After the stalling behavior is characterized with the time-frequency analysis, the detection of circumferential pressure waves in the compressor is undertaken. Data from the microphone arrays in the inlet and diffuser are acquired at a sampling frequency of 5000 Hz. Typically, 5 seconds of data is recorded with 92 percent of the retained samples taken before the trigger occurred. Data from the eight inlet microphones and five of the diffuser microphones, or all 15 of the diffuser microphones could be acquired simultaneously. The throttle closure rate used for these experiments is identical to that employed in acquiring the data for the joint time-frequency analysis.

Data Analysis Techniques. Two data analysis techniques are applied to the data acquired from the microphones. A joint time-frequency analysis of the signal from a single microphone is first performed to identify the frequency bands where instability was encountered. A spatial Fourier analysis of the simultaneously sampled microphone arrays is then made to provide a detailed picture of the stalling behavior.

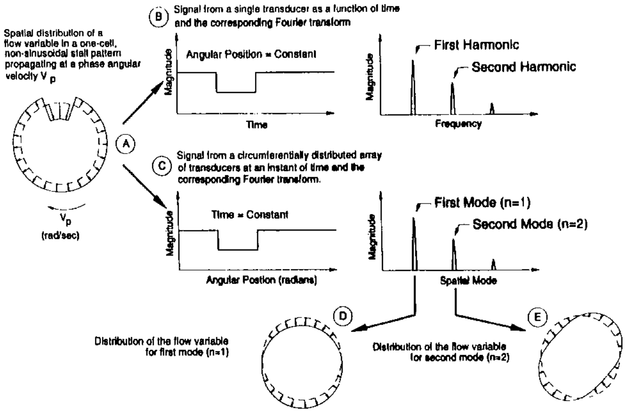

Fig. 6 Waveforms in the spatial and temporal domains, and their representation in the Fourier domain

Joint Time-Frequency Analysis. The joint time-frequency analysis consists of performing a Fourier transform on a fraction of the data, or window, and then repeating the process by advancing the window by a short time period. The resultant spectra at each step, when plotted together, form a picture of the transient frequency content of the signal under scrutiny. Because of the aforementioned nonlinearity of the microphone signals, data scaling for these results is performed in the frequency domain.

Spatial Domain Analysis: Signals in the Spatial Domain. As mentioned previously, Fourier analysis of signals from an array of circumferentially distributed sensors has proven effective in the detection of the early stages of spatially coherent events such as rotating stall. In such a technique, the Fourier transform is performed in the spatial domain on signals acquired at the same instant in time, with the resultant harmonics representing the wave number (n) or mode of the spatial pattern.

For illustrative purposes, Fig. 6 presents the representations in the frequency and spatial mode domains of an assumed stall pattern. The spatial distribution of a flow variable (e.g., velocity or pressure) about the compressor circumference is represented as a square wave. If at a given instant of time the phase angle of the stall pattern is given by α, the rate of propagation of the stall pattern around the annulus is given by time rate of change of α, here defined as the phase angular velocity V_p:

$$V_p = \frac{d\alpha}{dt} \qquad (1)$$

Although the customary units for an angular velocity are expressed as radians per unit time (e.g., rad/s), the relationship between the phase angular velocity of a modal pattern and the frequency of the stall phenomena make a phase velocity reported in Hertz the most useful quantity for this investigation. Specifically,

$$|V_p| = \frac{f_t}{n} \qquad (2)$$

where f_t is the frequency of the stall phenomenon that would be recorded by a single sensor at a fixed circumferential position.

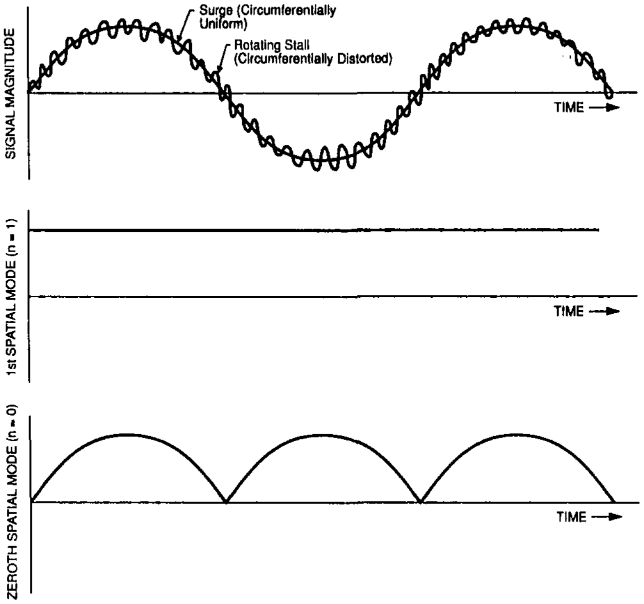

Fig. 7 Representation of a surge condition in the modal domain

As used in this application, the phase angular velocity in Hertz is a signed quantity where the sign represents the direction of propagation around the compressor annulus. By convention, the positive direction will be taken with impeller rotation.

When viewed as a time history of the signal from a single transducer at a fixed circumferential location, the stall cell would be represented by a square wave as shown in Fig. 6(*b*). After Fourier decomposition, the frequency domain representation of this signal is characterized by temporal harmonic components of decreasing magnitude.

In a spatial domain analysis of the stall pattern, a number of circumferentially distributed transducers are sampled simultaneously. If the flow variable is plotted against angular position at a given instant in time, as in Fig. 6(*c*), the signal again takes the form of a square wave. Fourier decomposition of the signal results in the representation of the signal in the modal domain. The spatial wave number or mode (n) reflects the number of peaks around the circumference for the particular component, as shown in Figs. 6(*d*, *e*). As in a frequency domain transform, the relative magnitudes of the fundamental and higher modes provides an indication of the nature of the waveform. A dominant fundamental mode indicates a wave that is sinusoidally distributed around the circumference. As the higher modes grow in magnitude, the wave takes on a more impulsive distribution.

It is important to note that the temporal harmonics and spatial modes are not independent phenomena. For the square wave shown in Fig. 6 the second temporal harmonic is represented in the spatial domain by the second mode, and vice versa. If the stall condition had been characterized by a two-cell pattern around the machine circumference, then the fundamental temporal harmonic would have corresponded to the second spatial mode ($n = 2$), and the second temporal harmonic would be represented in the spatial domain as the fourth mode ($n = 4$).

In the spatial domain, as in the time domain, the zeroth mode ($n = 0$) of the Fourier coefficients represents the mean level of the signal. When concerned with signals from an AC coupled device such as a microphone, confusion may result from the appearance of a time history of the $n = 0$ mode. To clarify results to be presented later, Fig. 7 shows a simplified representation of the signal from a single microphone when a compressor is simultaneously experiencing both surge and one-cell rotating stall, here represented by a low and high-frequency waveform, respectively. Since the low-frequency signal (surge) represents a change that occurs in a circumferentially uniform manner, the magnitude of this wave is represented by a cycloidal trace of the $n = 0$ mode from the spatial transform. The higher frequency rotating stall is a circumferentially nonuniform phenomenon, and hence appears as a line in a trace of the $n = 1$ mode.

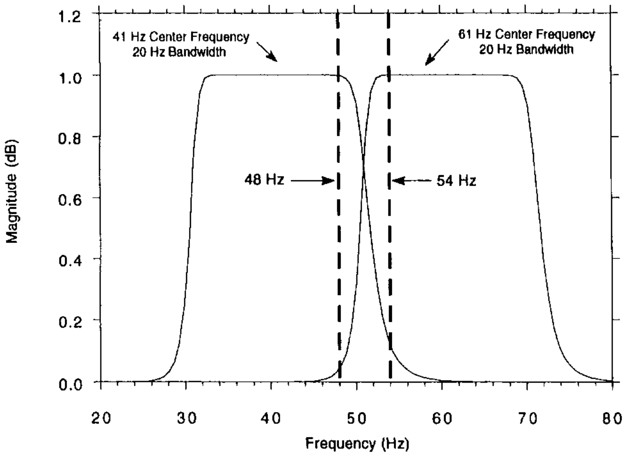

Fig. 8 Passbands of two 10th-order Butterworth filters used to separate signals with frequency content of 48 Hz and 54 Hz

Data Reduction. Data from the microphones are numerically band-pass filtered using Butterworth filtering algorithms. Although this was initially performed to reduce noise and allow the signals to be scaled by a representative gain value, initial results from the experiments provided additional motivation for this procedure. Early analysis of the stalling behavior of the compressor revealed that often, for a given spatial mode, both a fundamental and second temporal harmonic were in evidence within a narrow frequency band. To extract an accurate representation of the behavior of the compressor, high-order filters (order 10) of bandwidths as narrow as 15 Hz are employed around the frequency f_t identified in the joint time-frequency analysis. This "limited band" spatial Fourier analysis also aids in the prevention of signal aliasing, discussed below, by restricting the information used in the spatial transform to a single disturbance.

A typical example of the method used to isolate signals closely spaced in the frequency domain is given in Fig. 8. Here, the pass-bands of two 10th-order Butterworth filtering algorithms are shown. In this case, the filters are used to separate phenomena occurring at 48 Hz and 54 Hz, shown by the dashed lines. The filter cut-off frequencies have been selected to limit the interchange of information between the two frequencies of interest by attenuating one heavily while keeping the other inside the pass-band of the filter. It should be noted that phase distortion is introduced by such techniques. However, since the same filter is applied to the signals from each microphone in the simultaneously sampled array, these phase shifts did not adversely affect the analysis in the spatial domain.

The numerical filtering techniques discussed above introduce two significant difficulties into the interpretation of the results thus produced. First, numerical filters exhibit a starting transient proportional to filter order as the filter coefficients adjust from their initial values. This problem is easily disposed of by recording enough data to allow the transient to decay before the signals of interest are encountered. The second, and more significant, problem concerns the response of a filter to a transient event. As a signal changes character

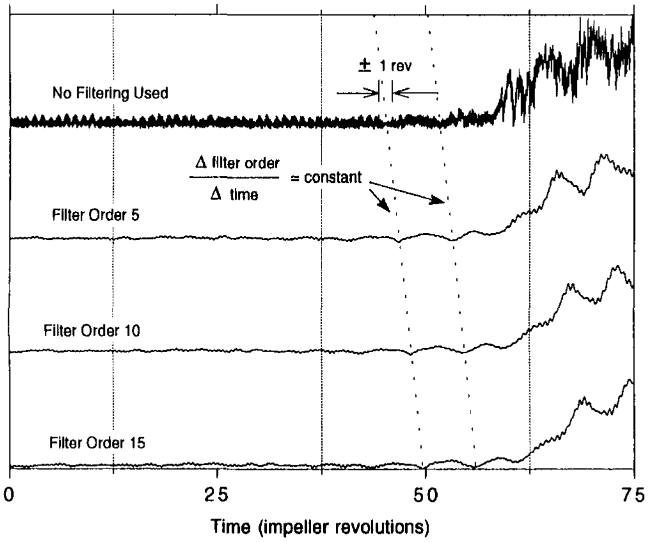

Fig. 9 Illustration of the relationship between filter order and time lag for a typical mode magnitude signal

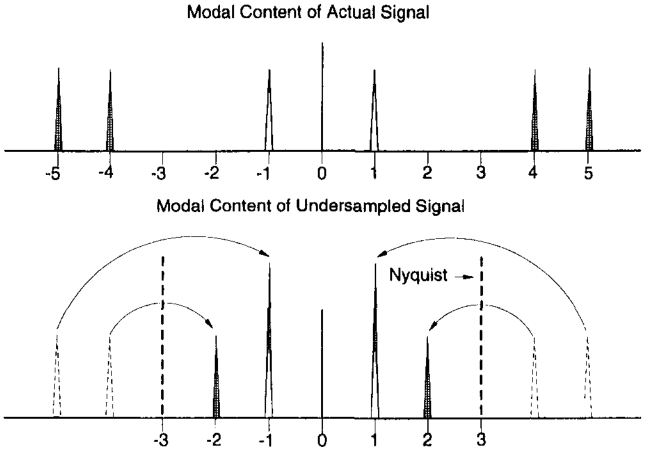

Fig. 10 Aliasing of an undersampled signal in the modal domain. Modes outside the Nyquist ($N = 3$) are erroneously aliased into lower order modes.

in time, a lag is introduced into the filtered signal as the coefficients adjust to the change. As in the case of the starting transient, this lag is proportional to filter order and also a function of the width of the filter pass-band.

The high-order, narrow-band filters used in this analysis introduced a time lag in the filtered signals of as much as three impeller revolutions. To adjust for this effect, the proportionality between the filter order and time lag is utilized to shift the filtered data in time. In this manner signals with a common temporal reference were generated to allow accurate comparison of transient events. An illustration of the technique is given in Fig. 9, where results of the rise of the magnitude of a spatial mode are shown. The figure shows four traces, each corresponding to results from signals processed with a different filter order. To determine the time lag introduced by the filtering, a singular feature in the signal traces is identified, and the time of this event at each trace noted. Fortunately, such unique structures were prevalent in the signals recorded in the current investigation. Two such occurrences are indicated by the dotted lines in Fig. 9, with the slope of these lines defining the relationship between filter order and introduced time lag. Once this slope is determined, the filtered data are shifted back in time to a common, unfiltered time reference. With careful application of this technique, temporal resolutions of ±1 revolution have been achieved in the data sets to be presented.

After filtering, the signals for each microphone are scaled by the appropriate gain value and then processed with the spatial Fourier transform. A finite difference estimate of the first derivative is used to calculate the phase propagation velocity of the spatial pattern V_p from the phase angle of the Fourier coefficients.

Because of the limited number of transducers that could be practically employed in the microphone arrays, the prospect of signal aliasing was of concern. Aliasing of a digitally acquired signal occurs when the sampling frequency is insufficient to allow reconstruction of the analog signal from the discrete digital data. A mathematical theorem, the sampling theorem, states that if an analog signal is sampled at a rate greater than twice the highest frequency contained in that signal, then the original signal can be exactly recovered from its sample values. This condition on the sampling frequency is known as the Nyquist criterion, and the value of one half the sampling rate is referred to as the Nyquist frequency. Violation of the Nyquist criterion by undersampling a waveform results in information from harmonic components of frequencies greater than the Nyquist frequency being spuriously represented in the frequency range below the Nyquist.

In a spatial domain sampling of a waveform, the number of transducers employed defines the sampling period and hence the effective "sampling frequency." Waves of harmonic number greater than the Nyquist (number of transducers divided by two) will be aliased into a different harmonic, possibly creating confusion as to the actual mode shape. This phenomenon is shown figuratively in Fig. 10, where the folding of an undersampled signal about the Nyquist wave number (or frequency) is shown. In this case, information from the $n = 4$ and $n = 5$ modes in the physical variable have been aliased into the $n = 1$ and $n = 2$ modes of the results from a spatial Fourier analysis of a six-transducer array. Such aliasing effects are reduced by the use of the numerical filtering techniques discussed above. However, the aliasing effect can be employed in the positive identification of the actual mode shape if two arrays of transducers, each with a different number of sensors sharing no common factor, are employed. For example, if an $n = 10$ wave was detected by an array of eight sensors, the information would be aliased into the $n = 2$ harmonic. The same $n = 10$ pattern would excite the $n = 5$ spatial mode of results from a fifteen sensor array. This knowledge was used with the inlet and diffuser microphone arrays to confirm the nature of the excited mode shapes in the compressor. The Nyquist folding diagrams for the inlet, full diffuser, and partial diffuser arrays are presented in Fig. 11.

Results

Stalling Behavior With Vaneless Diffuser. A series of experiments was performed with the diffuser vanes of the PLCRC removed. In this configuration the compressor enters a one-cell rotating stall condition. The development of this stall condition in the compressor is first characterized by a joint time-frequency analysis of the signal from a single transducer. This information is then used to extract detailed information on stall initiation by a limited band spatial Fourier analysis of the signals from the inlet and diffuser microphone arrays.

Joint Time-Frequency Analysis. Figure 12 shows the pressure trace from the scroll-mounted pressure transducer, the signal from an inlet microphone, and the signal from a diffuser microphone as the throttle of the compressor is

Nyquist Folding Diagram for 8 Microphone Inlet Array					
		•••	*13*	*12*	*Aliased Modes* *(Nyquist Mode =4)*
8	*9*	*10*	*11*	*12*	
8	*7*	*6*	*5*	*4*	
0	1	2	3	**4** (N/2)	Modes Represented in Fourier Transform Results

Nyquist Folding Diagram for 15 Microphone Diffuser Array									
		•••	*27*	*26*	*25*	*24*	*23*	*22.5*	*Aliased Modes* *(Nyquist Mode =7.5)*
15	*16*	*17*	*18*	*19*	*20*	*21*	*22*	*22.5*	
15	*14*	*13*	*12*	*11*	*10*	*9*	*8*	*7.5*	
0	1	2	3	4	5	6	7	**7.5** (N/2)	Modes Represented in Fourier Transform Results

Nyquist Folding Diagram for 5 Microphone Diffuser Array				
		•••	*7.5*	*Aliased Modes* *(Nyquist Mode =2.5)*
5	*6*	*7*	*7.5*	
5	*4*	*3*	*2.5*	
0	1	2	**2.5** (N/2)	Modes Represented in Fourier Transform Results

Fig. 11 Nyquist folding diagram for the inlet and diffuser microphone arrays, showing where aliased modes will appear in Fourier transform results

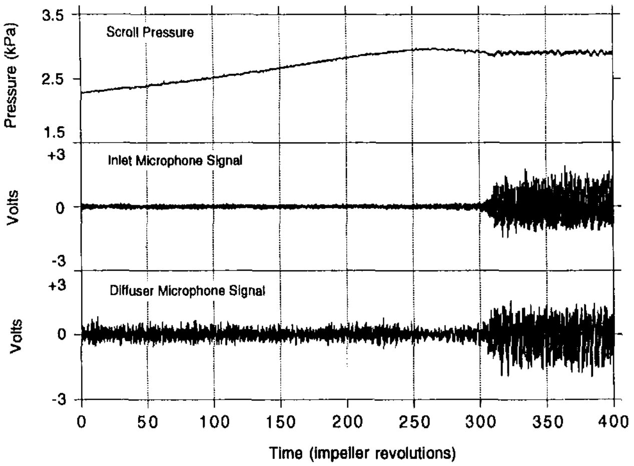

Fig. 12 Initiation of rotating stall for the centrifugal compressor with vaneless diffuser. Comparison of compressor scroll pressure, the signal from an inlet microphone, and the signal from a diffuser microphone as the throttle is closed.

slowly closed. Note that the time units have been scaled with impeller pass period, and thus is reported in impeller revolutions. To remove the effects of the extreme low-frequency sensitivity of the attenuated microphones, the signal traces have been high-pass filtered to eliminate frequency content below 3 Hz. Peak pressure rise in the compressor scroll occurs at $t = 275$ impeller revolutions. Shortly after this condition is achieved, at $t = 310$ revolutions, the inlet and diffuser microphones record a simultaneous increase in signal magnitude as the compressor enters rotating stall.

A joint time-frequency analysis was performed on the signals from the inlet and diffuser microphones shown in the previous figure, with results presented in Figs. 13 and 14, respectively. As described previously, these figures are created by plotting the spectra from a series of small-sample Fourier transforms. For these data, a sampling window of 24 revolutions in length was employed, and this window was progressed through the data set at an increment of three revolutions.

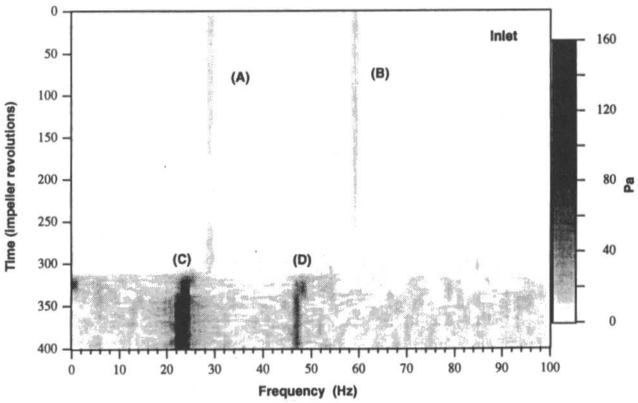

Fig. 13 Joint time-frequency analysis of the inlet microphone signal of Fig. 9. Development of a 24 Hz one-cell pattern and the second harmonic of this signal is shown.

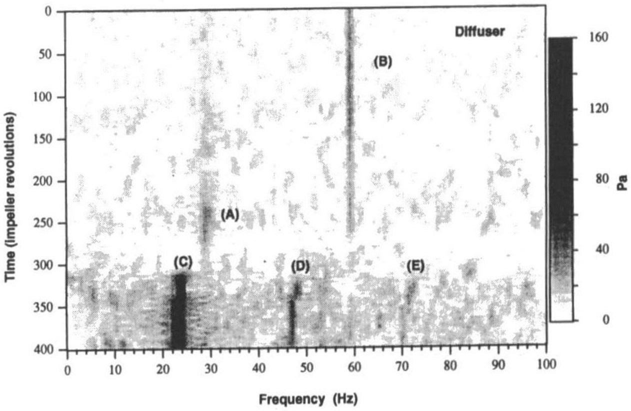

***Fig. 14* Joint time-frequency analysis of the diffuser microphone signal of Fig. 9. Evolution of a 24 Hz one-cell stall pattern and the second harmonic of this signal are shown.**

As the throttle is closed from the fully open position, excitations of frequencies corresponding closely to integral orders of impeller speed are evident near points A and B on the figure. For the current case of a compressor with a vaneless diffuser, the frequency corresponding to twice the impeller speed (59.6 Hz) showed the greatest excitation, here most clearly shown from the diffuser analysis of Fig. 14. Both the inlet and diffuser results show that these excitations are greatest at higher flow rates, and their magnitude is reduced significantly as the compressor approaches peak pressure rise just before instability is encountered.

At approximately $t = 300$ impeller revolutions (point C) a rotating stall condition appears in both the inlet and diffuser at a frequency of 24 Hz, with an apparent second harmonic of this signal evident at 48 Hz near point D.

To verify that these signals correspond to pressure signals rather than due to vibrational excitation of the microphone diaphragm or electrical noise, the experiment was repeated with the microphone static pressure ports sealed. Data from this experiment indicated that vibration and/or electrical noise measurements were two orders of magnitude less than the observed pressure readings. It is therefore concluded that the signals shown correspond to an actual pressure disturbance in the compressor.

Stall Initiation in the Spatial Domain. A more detailed picture of the stall initiation process in the compressor is provided by the spatial Fourier analysis of the signals from the inlet and diffuser microphone arrays. For this purpose, data from the arrays were acquired while the compressor throttle plate was closed at the same speed used for the time-frequency analysis above.

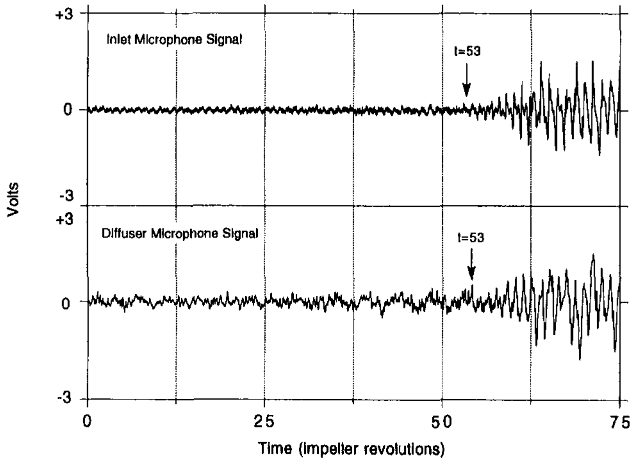

Fig. 15 Time history of a single inlet and a single diffuser microphone signal taken during simultaneous sampling of the inlet and diffuser microphone arrays. These signals correspond to the spatial domain analyses presented in Figs. 13–16.

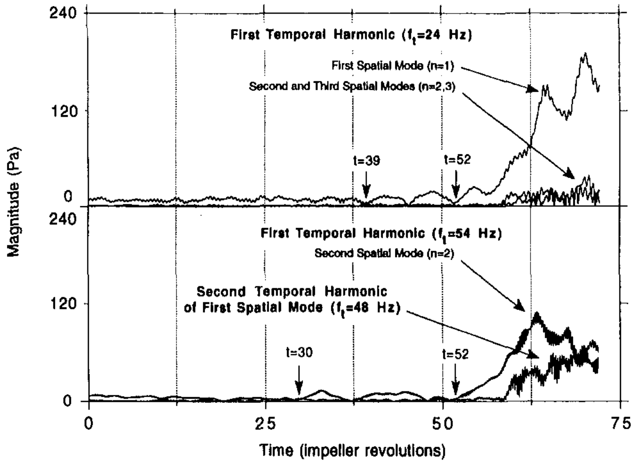

Fig. 16 Rise of the first and second temporal harmonics of $N = 1$ and $N = 2$ spatial modes. These data were obtained from the inlet microphone array.

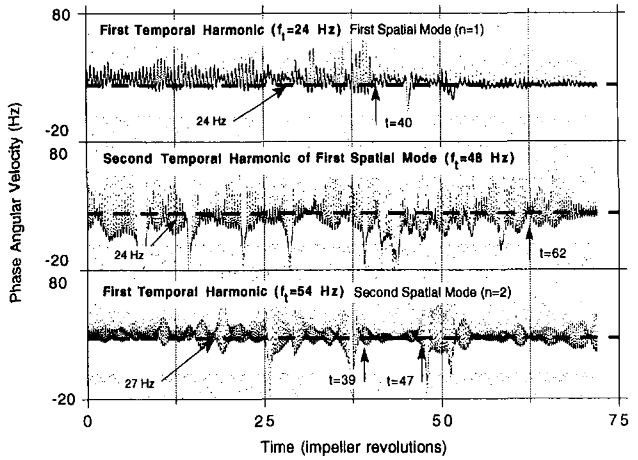

Fig. 17 Phase angular velocities for the spatial modes represented in Fig. 13

A sampling of the inlet and diffuser microphone arrays over a 2.5 second period during the throttle closure is represented by the signal traces of one microphone in each array given in Fig. 15. For this case, the eight inlet microphones and five of the diffuser microphones were simultaneously sampled during stall initiation. The first signs of a change in compressor behavior can be detected in both the inlet and diffuser traces at $t = 53$ revolutions, with the stall condition reaching its ultimate amplitude by $t = 65$ revolutions.

The spatial Fourier analysis was performed on the inlet and diffuser arrays and the resulting magnitude and phase angular velocity plotted as a function of time. Figure 16 presents the results for the rise of the magnitude of the first and second temporal harmonics of spatial modes with one and two peaks around the circumference (modes $n = 1$ and $n = 2$) for the inlet. As discussed previously, all data were numerically band-pass filtered around the frequency of interest (f_t) in order to distinguish fundamental and second harmonics of a given stall pattern.

The top frame of Fig. 16 shows that at $t = 39$ revolutions a change can be discerned in the behavior of the compressor. In the first temporal harmonic band ($f_t = 24$ Hz), the magnitude of the first spatial mode ($n = 1$) appears to exhibit a region where the magnitude of the mode oscillates at a frequency of approximately 7 Hz. This oscillation remains at a relatively constant magnitude until $t = 52$ revolutions, when the $n = 1$ mode begins uninterrupted growth, eventually achieving a peak magnitude of 185 Pa. The second and third spatial mode magnitudes in the first temporal band are included in the top frame of Fig. 16 to demonstrate the relative difference in the levels of excited and background spatial modes.

The 7 Hz oscillation frequency is interesting in that it corresponds roughly to the 6 Hz difference in frequency between a one cell wave traveling at impeller speed and the eventual stalling frequency of 24 Hz. This apparent "beating" phenomenon may be evidence of an impeller-speed order forcing function exciting an instability mode of the compressor, or may simply be the manifestation of the transducer detecting two independent pressure waves. The significance of this interaction in the signals will take further experimentation to describe accurately.

The bottom frame of Fig. 16 shows an event that was not entirely predicted on first examination of the joint time-frequency analysis of Figs. 13 and 14. Although the second temporal harmonic ($f_t = 48$ Hz, $n = 2$) of the fundamental $n = 1$ spatial mode appears to rise steadily after approximately 60 impeller revolutions, a second $n = 2$ spatial pattern arises at a frequency of approximately $f_t = 54$ Hz. This corresponds to a separate fundamental temporal harmonic of mode $n = 2$. Excitations of this mode appear as early as $t = 30$ revolutions and exhibit oscillatory behavior until the signal disappears at $t = 48$ revolutions. The final evolution of the pattern begins at $t = 52$ revolutions, achieving a peak of 110 Pa before beginning a rapid decay. Careful re-examination of the joint time-frequency results shows a weak magnitude rise in this region. However, the duration of this mode in that sampling may have been too short to effectively be detected by this type of analysis.

Figure 17 shows the phase angular velocity $V_p = f_t/n$ of the spatial modes presented in Fig. 16. These results were made from a finite difference estimation of the first derivative applied to the phase angle information returned from the spatial Fourier transform at each instant of time. Although V_p is an angular velocity, the units have been represented as Hertz rather than rad/s to allow comparisons between the mode propagation rate and the eventual stall frequency determined by the joint time-frequency analysis to be drawn. Note that positive values of V_p refer to propagation in the direction of rotor rotation with respect to the fixed reference frame.

For the first 40 impeller revolutions, the top frame of Fig. 17 shows the phase angular velocity of the $n = 1$ mode to be

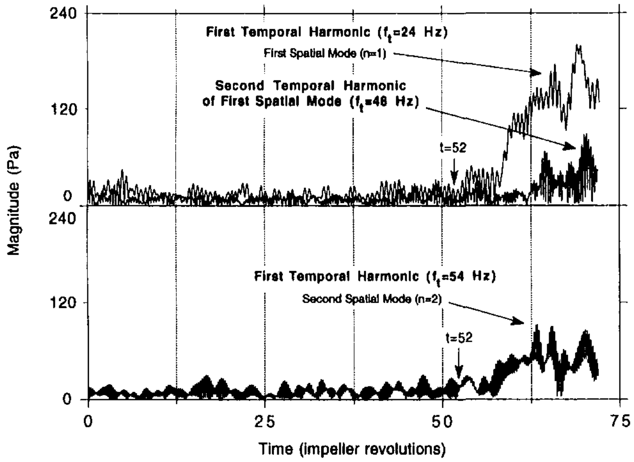

Fig. 18 Rise of the first and second temporal harmonics of $N = 1$ and $N = 2$ spatial modes. These data were obtained from five microphones in the diffuser array.

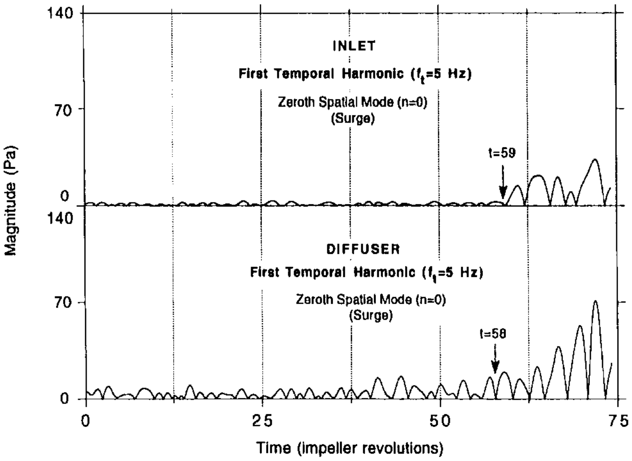

Fig. 19 Rise of the zeroth, or surge spatial mode ($N = 0$) in the inlet and diffuser

tracking a signal at impeller speed (29.8 Hz), corresponding to the weak pressure wave that was indicated by the joint time-frequency analysis. At $t = 40$ revolutions, the phase velocity becomes more clearly defined, with this point corresponding to the beginning of the oscillation that was observed in the magnitude of the $n = 1$ mode. During the next 10 revolutions, the $n = 1$ wave decelerates to the ultimate rotating stall frequency of 24 Hz.

The second panel of Fig. 17 shows the phase angular velocity for the second temporal harmonic of the $n = 1$ fundamental mode. All but the last 10 revolutions here show results that are typical for a spatial mode with poor phase correlation. Recall that all the data for these figures was band-pass filtered around the frequency of interest. Hence the approximate tracking of the signal at the center-band frequency is not unexpected. However, the dispersion of the data and the periodic drop to negative velocity values was found to be typical for a signal that was not related to a detectable spatial mode. The eventual adjustment of the phase velocity to a 24 Hz value beginning at $t = 62$ revolutions corresponds to the rise in the magnitude of the second harmonic indicated in Fig. 16.

The bottom frame of Fig. 17 presents the phase angular velocity for the fundamental $n = 2$ mode that briefly appears in the magnitude plot. Here, for the first 37 revolutions a weak $n = 2$ pattern is propagating at impeller speed (V_p = 29.8 Hz), corresponding to the weak two-per-revolution signal seen in the joint time-frequency analysis. At $t = 37$ revolutions, the phase velocity signal breaks up, re-emerging at $t = 39$ revolutions at the 27 Hz value of the $n = 2$ fundamental mode. This signal again loses coherence at $t = 47$ revolutions, corresponding to a drop in the magnitude of this mode as shown in the previous figure. The signal reappears at the 27 Hz value seven revolutions later, as the magnitude of the $n = 2$ pattern rises again.

Figure 18 shows the rise of the fundamental $n = 1$ and $n = 2$ modes obtained from the diffuser microphone array. The beginning of the growth of both the first and second spatial modes appears to correspond with the results obtained from the simultaneous sampling of the inlet, the $n = 1$ mode beginning a rise at $t = 52$ revolutions and the $n = 2$ mode also rising at $t = 52$ revolutions. Both the $n = 1$ and $n = 2$ fundamental harmonics achieve similar magnitudes in both the inlet and diffuser sections (185 Pa versus 196 Pa for $n = 1$, 110 versus 90 Pa for $n = 2$). The oscillatory behavior of the $n = 1$ mode magnitude seen in the inlet is not evident in the diffuser results. This is in part attributable to the difficulty in identifying weak pressure waves in the diffuser section due to a lower signal to noise ratio than in the inlet data.

Figure 19 shows the magnitude of the zeroth spatial mode ($n = 0$) from the inlet and diffuser analyses. This information was extracted from a 15 Hz band around a frequency of 5 Hz, this value being the surge frequency observed in this compressor with other diffuser configurations. Excitation of this mode occurs seven revolutions after the rise of the rotating stall harmonic was observed. Maximum level of the surgelike oscillation reaches 70 Pa in the diffuser section. However, results from the time-frequency analysis indicate that this phenomenon does not eventually grow into a finite surge condition in this configuration.

Significance for Control Applications. The stalling behavior portrayed above shows that the first signs of the developing stall condition in the modal domain were detected 14 impeller revolutions before the first traces were seen on the microphone signals and 26 revolutions prior to where the stall condition could be considered fully developed.

The detection of the stall precursors required substantial postprocessing of the data. For implementation in an active control system, such postprocessing would be impractical. The implementation of analog bandpass filters and short-sample averaging schemes will be required before the pressure signals can be used as an effective stall precursor for a control system, and this problem is currently being investigated by the authors.

The presence of two separate fundamental spatial modes ($n = 1$ and $n = 2$) suggests that a control system for a compressor exhibiting behavior similar to that seen here will have to address several spatial modes simultaneously. This would require a control system capable of introducing multiple control waves of near sinusoidal character, lest the higher harmonics of one of the control waves interfere with another mode. High-solidity arrays of oscillating inlet guide vanes are one possibility for the implementation of such a control scheme.

Summary and Conclusions

The goal of this investigation was to identify spatially coherent pressure waves, which would serve as precursors to the development of an instability in the Purdue Low-Speed Centrifugal Research Compressor when configured with a vaneless diffuser. To achieve this, sensitive electret microphones were uniformly distributed around the circumference in the inlet and diffuser sections of the compressor. Fourier analysis of simultaneously sampled data from these microphone arrays was employed to identify the development of dominant spatial modes in the pressure field in the compressor. Results from this analysis achieved the goal set for the investigation. The transition to stall was observed to be a gradual process, with the growth of the pressure waves into those corresponding to a large-scale stall condition occurring over a time span of 26 impeller revolutions. The behavior was typified by one or more weak, circumferentially distorted pressure waves adjusting to the ultimate phase propagation velocity of the finite stall pattern shortly after arising from the background noise of unexcited spatial modes. The waves would then grow into a finite stall condition, or dissipate as another, stronger mode gained dominance over the flow field. The growth of these waves often demonstrated a quite oscillatory nature. The excitation of the pressure waves, as indicated by spatial Fourier analysis, occurred 14 impeller revolutions before small changes were evident in the microphone signals, and 26 revolutions before the stall condition could be considered fully developed. Thus, it is concluded that such techniques are viable in the detection of stall precursors in the compressor under study.

Acknowledgments

Support of this research by the army Aviation Systems Command, NASA Lewis Research Center, Lawrence F. Schumann technical monitor, is most gratefully acknowledged.

References

Day, I. J., 1993a, "Active Suppression of Rotating Stall and Surge in Axial Compressors," ASME JOURNAL OF TURBOMACHINERY, Vol. 115, pp. 40–47.

Day, I. J., 1993b, "Stall Inception in Axial Flow Compressors," ASME JOURNAL OF TURBOMACHINERY, Vol. 115, pp. 1–9.

Emmons, H. W., Pearson, C. E., and Grant, H. P., 1955, "Compressor Surge and Stall Propagation," *Transactions of the ASME*, Vol. 79, pp. 455–469.

Ffowcs Williams, J. E., and Graham, W. R., 1990, "An Engine Demonstration of Active Surge Control," ASME Paper No. 90-GT-224.

Garnier, V. H., Epstein, A. H., and Greitzer, E. M., 1991, "Rotating Waves as a Stall Inception Indication in Axial Compressors," ASME JOURNAL OF TURBOMACHINERY, Vol. 113, pp. 290–302.

Greitzer, E. M., 1981, "The Stability of Pumping Systems," ASME *Journal of Fluids Engineering*, Vol. 103, pp. 193–242.

Haupt, U., Abdel-Hamid, A. N., Kaemmer, N., and Rautenberg, M., 1986, "Excitation of Blade Vibration by Flow Instability in Centrifugal Compressors," ASME Paper No. 86-GT-283.

Jin, D., Haupt, U., Hasemann, H., and Rautenberg, M., 1992a, "Excitation of Blade Vibration Due to Surge of Centrifugal Compressors," ASME Paper No. 92-GT-149.

Jin, D., Haupt, U., Hasemann, H., and Rautenberg, M., 1992b, "Blade Excitation by Circumferentially Asymmetric Rotating Stall in Centrifugal Compressors," ASME Paper No. 92-GT-148.

Johnston, R. T., and Sullivan, J. P., 1992, "Unsteady Wing Surface Pressures in the Wake of a Propeller," AIAA Paper No. 92-0277.

Kendall, J., 1990, "Microphone Detects Waves in Laminar Boundary-Layer Flow," *NASA Tech Briefs*, Vol. 14, No. 11.

Lawless, P. B., and Fleeter, S., 1991, "Active Unsteady Aerodynamic Suppression of Rotating Stall in an Incompressible Flow Centrifugal Compressor With Vaned Diffuser," AIAA Paper No. 91-8198.

McDougall, N. M., Cumpsty, N. A., and Hynes, T. P., 1990, "Stall Inception in Axial Compressors," ASME JOURNAL OF TURBOMACHINERY, Vol. 112, pp. 116–125.

Paduano, J. D., Epstein, A. H., Valavani, L., Longley, J. P., Greitzer, E. M., and Guenette, G. R., 1993, "Active Control of Rotating Stall in a Low-Speed Axial Compressor," ASME JOURNAL OF TURBOMACHINERY, Vol. 115, pp. 48–56.

Pinsley, J. E., Guenette, G. R., Epstein, A. H., and Greitzer, E. M., 1991, "Active Stabilization of Centrifugal Compressor Surge," ASME JOURNAL OF TURBOMACHINERY, Vol. 113, pp. 723–732.

Control of the Unsteady Flow in a Stator Blade Row Interacting With Upstream Moving Wakes

T. Valkov

C. S. Tan

Gas Turbine Laboratory,
Massachusetts Institute of Technology,
Cambridge, MA 02139

A computational approach, based on a spectral-element Navier–Stokes solver, has been applied to the study of the unsteady flow arising from wake–stator interaction. Direct, as well as turbulence-model calculations, provide insight into the mechanics of the unsteady flow and demonstrate the potential for controlling its effects. The results show that the interaction between the wakes and the stator blades produces a characteristic pattern of vortical disturbances, which have been correlated to the pressure fluctuations. Within the stator passage, the wakes migrate toward the pressure surface where they evolve into counterrotating vortices. These vortices are the dominant source of disturbances over the pressure surface of the stator blade. Over the suction surface of the stator blade, the disturbances are due to the distortion and detachment of boundary layer fluid. They can be reduced by tailoring the blade loading or by applying nonuniform suction.

1.0 Introduction

Turbomachinery flowfields are characterized by the presence of circumferential nonuniformities due to the wake and to the potential field of individual blades in each blade row. These nonuniformities interact periodically with the blades on adjacent blade rows in relative motion, resulting in the production of unsteady flow. The unsteady flow leads to significant fluctuations of the blade loading, and influences heat transfer, separation, and boundary layer characteristics. Turbomachinery designs could benefit from controlling the undesirable aspects of the unsteady flow in order to enhance a reliable and quiet operation.

In the last twenty years, several experimental as well as theoretical/computational studies of flow associated with blade row interaction in turbomachinery have been carried out (Kerrebrock and Mikolajczak, 1970; Adachi et al., 1974; Erdos et al., 1977; Gallus, 1979; Dring et al., 1982; Hodson, 1985; Rai, 1987; Capece and Fleeter, 1989; Giles, 1991). These works have yielded useful and significant results that aid the understanding of such flows.

This paper presents the results from a computational investigation, the purpose of which is: (1) to understand the mechanisms for production of unsteady flow as a stator blade row interacts with upstream wakes; and (2) to demonstrate the possibility for reducing the pressure fluctuations.

Many key aspects of the unsteady flow resulting from wake interaction can be dealt with in a two-dimensional context. Furthermore, our study is directed at turbomachines that operate in the incompressible and subsonic flow regimes. For this reason, we have used an incompressible two-dimensional flow model to obtain the results presented herein.

The stator blade row used in the simulation is characterized by a stagger angle of 12 deg, by a spacing-to-chord ratio of 0.4, and by an inlet swirl angle of 25 deg. The design Reynolds number of the flow is 1,000,000 based on the stator chord and U_∞. The tangential velocity of the upstream rotor blade is $2.0U_\infty$. The velocity defect of the incoming wakes at the axial station corresponding to the inlet boundary of the computational domain is 75 percent of the free-stream velocity in the rotating frame. This large value is due to the closeness of the inlet boundary to the rotor blade trailing edge. It is to be noted that in the stator frame, the wake has a tangential velocity *excess* in the direction of rotor rotation.

The present investigation is focused on the unsteady phenomena taking place when a wake interacts with a blade in the blade row. These phenomena are local and have a characteristic size, which is considerably smaller than that of the circumferentially rotating waves arising in turbomachines with nonunitary blade ratios. The interaction of these two types of unsteady flow of difference scale does not have, in our belief, a qualitative effect on their nature. For this reason, a rotor–stator blade ratio of 1:1 is used here to limit the computations to a single stator passage.

2.0 Computational Procedure

2.1 Governing Equations. The unsteady flow in the stator passage is governed by the Navier–Stokes equations, made nondimensional by using the stator blade chord as a reference length and the dynamic pressure and axial velocity far upstream of the stator as reference pressure and velocity:

Contributed by the International Gas Turbine Institute and presented at the 38th International Gas Turbine and Aeroengine Congress and Exposition, Cincinnati, Ohio, May 24–27, 1993. Manuscript received at ASME Headquarters February 12, 1993. Paper No. 93-GT-23. Associate Technical Editor: H. Lukas.

$$\nabla \cdot \mathbf{u} = 0 \tag{1}$$

$$\frac{\partial \mathbf{u}}{\partial t} + \mathbf{u} \cdot \nabla \mathbf{u} = -\nabla p + \nabla \left\{ \left(\frac{1}{\mathrm{Re}} + \nu_t \right) \nabla \mathbf{u} \right\} \tag{2}$$

In order to represent the moving wakes from the upstream rotor, unsteady Dirichlet boundary conditions are imposed on the velocity at the inflow boundary of the computational domain:

$$\begin{Bmatrix} u(y,t) \\ v(y,t) \end{Bmatrix} = \begin{Bmatrix} 1 - Af(y - Vt) \\ (1 - Af(y - Vt)) \tan \theta + Af(y - Vt)V \end{Bmatrix} \tag{3}$$

where the function $f(y)$ specifies the wake velocity profile in the rotor frame; in the work presented here $f(y)$ is taken to be a Gaussian distribution. In order to simulate the effect of control strategies involving fluid suction or injection, Dirichlet boundary conditions are imposed on the blade surface too:

$$\mathbf{u}(x_s, y_s, t) = \pm \sigma(x_s, y_s, t) \mathbf{e}_n \tag{4}$$

Simple extrapolation boundary conditions, which assume that the flow does not evolve further in the streamwise direction, are imposed at the outflow boundary of the computational domain.

2.2 Time Discretization. A fractional time-splitting scheme (Orszag and Kells, 1980) is used to advance the Navier–Stokes equations in time. The scheme updates the flowfield $\mathbf{u}$ at each time increment in three fractional steps:

1 *Convective step*, which extrapolates the change in velocity from time t to time $t + \Delta t$ due to convective effects only (Eq. (5)). A fourth-order Runge–Kutta scheme is used to implement the convective step:

$$\hat{\mathbf{u}}^{n+1} = \mathbf{u}^n - \int_t^{t+\Delta t} \mathbf{u} \cdot \nabla \mathbf{u} dt \tag{5}$$

2 *Pressure step*, correcting $\hat{\mathbf{u}}^{n+1}$ to give a velocity field that satisfies the continuity condition. This is accomplished by using a backward Euler scheme:

$$\frac{\hat{\hat{\mathbf{u}}}^{n+1} - \hat{\mathbf{u}}^{n+1}}{\Delta t} = -\nabla p^{n+1} \tag{6}$$

and by computing the pressure field from the following Poisson equation, with Neumann conditions on all prescribed-velocity boundaries (Tan, 1989):

$$\nabla^2 p^{n+1} = \frac{1}{\Delta t} \nabla \cdot \hat{\mathbf{u}}^{n+1} \tag{7}$$

3 *Viscous step*, which corrects the velocity update from the pressure step $\hat{\hat{\mathbf{u}}}$ to take into account dissipation effects. This step is based on an implicit Crank–Nicholson scheme:

$$\left[\nabla(D\nabla) - \frac{2}{\Delta t} \right] \mathbf{u}^{n+1} = -\nabla(D\nabla \mathbf{u}^n) - \frac{2}{\Delta t} \hat{\hat{\mathbf{u}}}^{n+1} \tag{8}$$

subject to Dirichlet boundary conditions at the inflow and blade surface boundaries. Homogeneous Neumann boundary conditions are imposed at the outflow boundary.

2.3 Spatial Discretization. The spatial discretization of Eqs. (5)–(8) is performed by dividing the computational domain into a number of *spectral elements*. Inside each element, the flow variables are expanded in series of local Lagrangian interpolants h_j (Patera, 1984; Korczak and Patera, 1986):

$$\begin{Bmatrix} \mathbf{u} \\ p \end{Bmatrix} = \sum_{j=0}^{j=N} \sum_{k=0}^{k=N} \begin{Bmatrix} \mathbf{u}_{jk} \\ p_{jk} \end{Bmatrix} h_j(\zeta) h_k(\eta) \tag{9}$$

where (ζ, η) is a set of natural coordinates local to each element. The periodic boundary conditions are implemented during the spatial discretization by using the same index $(\,)_{i,jk}$ for nodes on the periodic boundaries. The discretized form of Eq. (5) and Eqs. (6)–(7) in terms of pointwise velocity and pressure can be found from Tan (1989).

Due to the presence of a time-varying eddy-viscosity coefficient, the discretized form of the viscous step (Eq. (8)) is however different from that in Tan's paper. The new discretized form is

$$\sum^{i} \sum_{l} \sum_{m} \left[A_{jklm} + \frac{2}{\Delta t} B^{+}_{jklm} \right] \mathbf{u}^{n+1}_{lm,i} = \sum^{i} \lambda^{i}_{jk} \tag{10}$$

Using $\tilde{\nabla}_{jklm}$ and B_{jklm} as standard notation for the discretized Nabla and integral operators (Korczak and Patera, 1986; Tan, 1989), the viscous matrix A_{lmjk} is computed as follows:

Nomenclature

A = velocity defect of the wake in the rotor frame

A_{lmjk} = viscous step matrix

B = wake thickness parameter $= 4\delta_w^{-2} \ln 100A$

B^{+}_{lmjk} = surface integral operator (Tan, 1989)

$(C_{p,\max})^{+}_{LE}$ = peak positive pressure coefficient at leading edge

D = effective viscosity $= \nu_t + 1/\mathrm{Re}$

$\mathbf{e}_n$ = unitary vector normal to the blade surface

h_j = local Lagrangian interpolant

N = degree of the expansion in series (herein $N = 7$)

p = nondimensional static pressure

R_a = artificial viscosity parameter

Re = Reynolds number based on c_x and U_∞

t = nondimensional time

t_0 = instant of wake interception by leading edge

T = nondimensional wake passing period

$\mathbf{u} = u\mathbf{i} + v\mathbf{j}$ = nondimensional velocity in the stator frame

U_∞ = axial velocity component upstream of the stator

$\overline{\mathbf{U}}$ = base (steady) flow velocity field

V = upstream rotor blade tangential velocity

δ_w = nondimensional 99 percent wake thickness

Δt = nondimensional time increment

θ = flow turning angle at the inlet of the passage

λ_v = source term in the viscous step (Tan, 1989)

ν_t = nondimensional eddy viscosity coefficient

σ = nondimensional suction (blowing) rate

ω = vorticity

$(\,)_{jk,i}$ = discretized value at point (η_j, ζ_k) on element i

$(\,)^n$ = referring to the flowfield at time step n

$(\tilde{\,})$ = referring to the disturbance flow

$(\bar{\,})$ = referring to the steady flow

$(\hat{\,})$ = referring to the update from the viscous step

$(\hat{\hat{\,}})$ = referring to the update from the pressure step

$$A_{lmjk} = \sum_p \sum_q \sum_r \sum_s D_{pq} \tilde{\nabla}_{pqlm} B^{-}_{pqrs} \tilde{\nabla}_{rsjk} \qquad (11)$$

The fractional-stepping spectral-element discretization is an accurate and virtually nondissipative approach to solving the Navier–Stokes equations. Because of this, spectral methods are normally used for direct flow simulation at moderately high Reynolds numbers. By setting the eddy viscosity coefficient ν_t to zero in Eq. (2), we have carried out direct simulations of wake–stator interaction for Reynolds numbers of up to 50,000. Direct simulations have also been used to validate our solver against known analytical solutions of the Navier–Stokes equations (e.g., flow in a rectangular channel).

2.4 Turbulence Model. A variation of the Baldwin and Lomax (1978) turbulence model is used to compute the unsteady flow at high Reynolds numbers (Re ~ 10^6). Two reasons make the model formulated in the original 1978 paper unsuitable for wake-driven unsteady flow. First, the presence of free wake vortical disturbances far above the blade surface biases the calculation of $y_{\max}$ and $F_{\max}$ (the original notation of Baldwin and Lomax is employed herein) and results in excessive viscosity in the outer region. Second, to compute the values of the wake and Klebanoff factors F_W and F_K in the region of flow dominated by wake vorticity, it is necessary to continuously monitor the location of the wake centerlines, from which the y coordinate is measured.

To overcome the first problem, we have redefined $y_{\max}$ as the smallest distance at which $dF/dy = 0$. To overcome the second problem, the original form of the Baldwin–Lomax model is used only inside the boundary layer. In those regions of the flowfield dominated by wake vortical disturbances, the eddy viscosity is given by an implicit function of the local vorticity:

$$\nu_t = \frac{eKC_{CP}\sqrt{V_r^2 + 1}}{8C\sqrt{B}} \left(1 + 5.5C_{\mathrm{KLEB}}^6 B^3 r^6\right)^{-1} \qquad (12)$$

where r is the largest root of the following equation

$$re^{-Br^2} = \frac{|\omega|}{2ABC} \quad \text{with} \quad C = 1 + V^2 - \frac{V \tan\theta}{\sqrt{V^2 + 1}} \qquad (13)$$

This equation is derived by applying the Baldwin–Lomax model to a straight moving wake (Valkov, 1992). In view of the objective of this study, such a simplified procedure for computing the eddy viscosity is justified. While using another, more sophisticated turbulence model may improve the computed results quantitatively, we believe it will not affect the fundamental features of the computed flowfield.

3.0 Results from the Navier–Stokes Simulation

The flowfield in the absence of moving wakes at the design Reynolds number of 1,000,000 is shown in Fig. 1. This flowfield will be subtracted from the computed unsteady flow in order to visualize the unsteady effects due to the interaction of the wakes with the stator. The resultant difference shall be referred to as *disturbance flow*. The unsteady flow is computed at a Reynolds number of 1,000,000 too.

Figures 2–7 show detail snapshots of the disturbance vorticity, disturbance velocity, and static pressure in leading edge region, at the instant of wake interception and in between two wakes. The disturbance vorticity and velocity distribution within the entire stator passage are shown in Figs. 8–11 for the same time instants.

On Fig. 6, the incoming wake appears as a high-momentum stream directed toward the pressure surface of the stator blades. Once within the passage, the wake fluid migrates away from the suction surface toward the pressure surface, where it evolves into two counterrotating vortices referred to as *wake vortices*. As the results in Figs. 8–11 show, these vortices dominate the disturbance flow near the pressure surface. Each group of vortices seen on this figure corresponds to a rotor wake at a distinct stage of its evolution, and is convected downstream with the free-stream velocity.

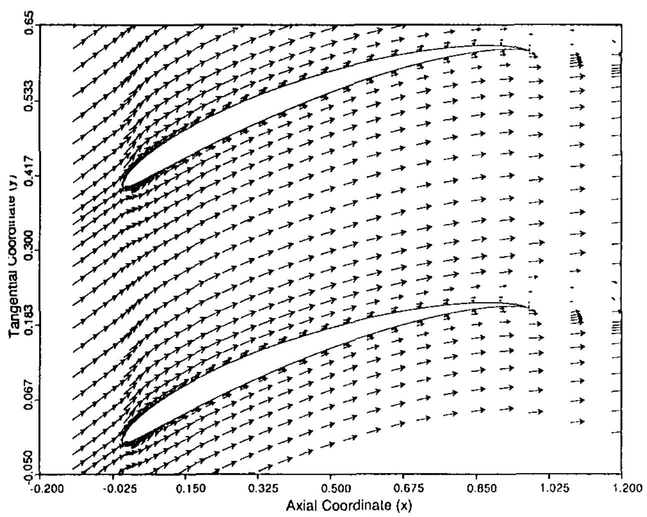

Fig. 1 Velocity vectors in the absence of rotor wakes

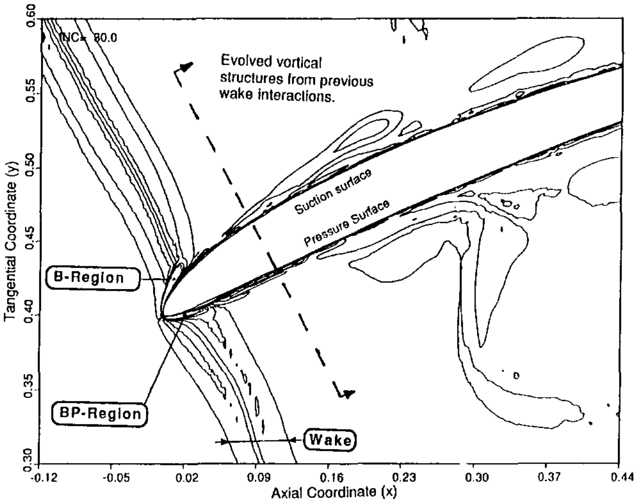

Fig. 2 Disturbance flow vorticity contours, time $t_0 + 0.1T$

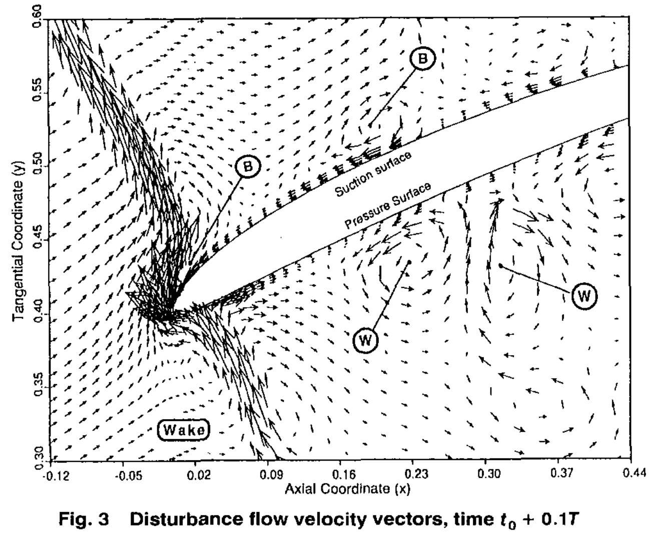

Fig. 3 Disturbance flow velocity vectors, time $t_0 + 0.1T$

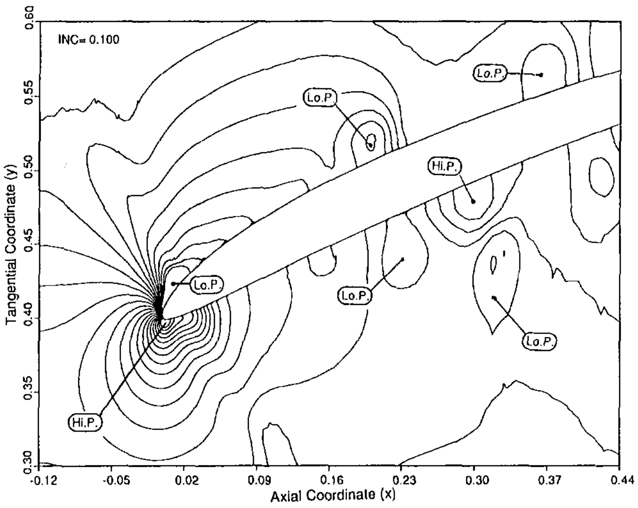

Fig. 4 Static pressure field, time $t_0 + 0.1T$

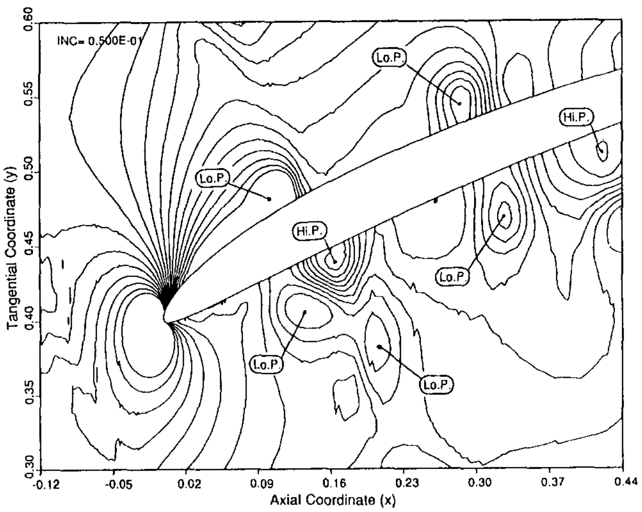

Fig. 7 Static pressure field, time $t_0 + 0.6T$

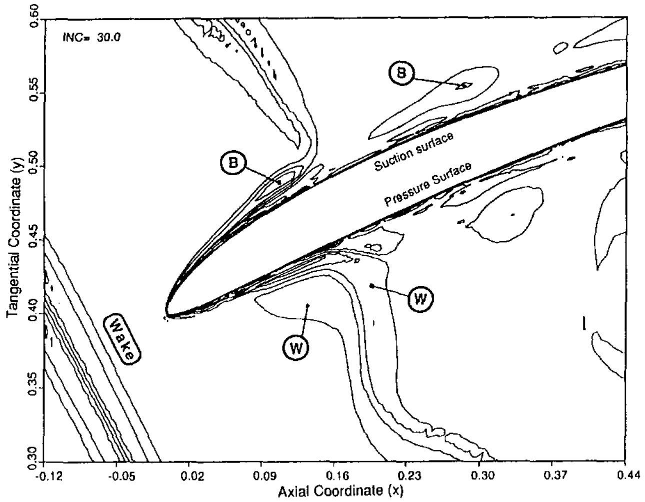

Fig. 5 Disturbance flow vorticity contours, time $t_0 + 0.6T$

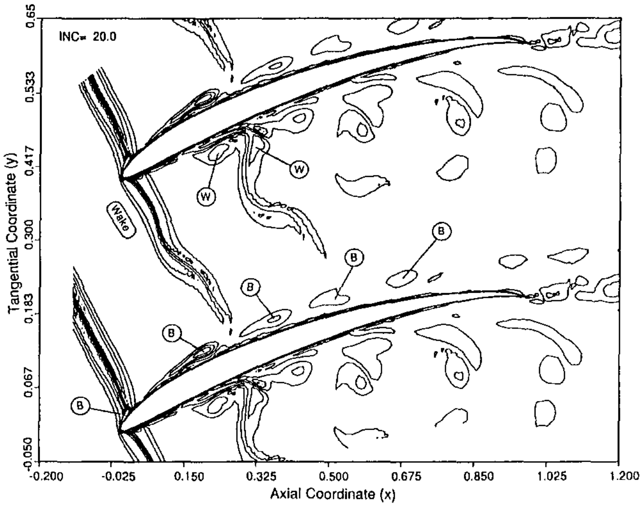

Fig. 8 Disturbance flow vorticity contours at time $t_0 + 0.1T$ within an entire stator passage

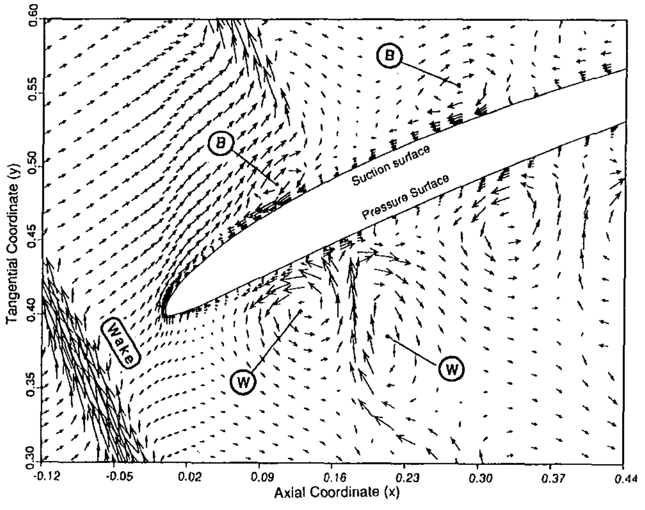

Fig. 6 Disturbance flow velocity vectors, time $t_0 + 0.6T$

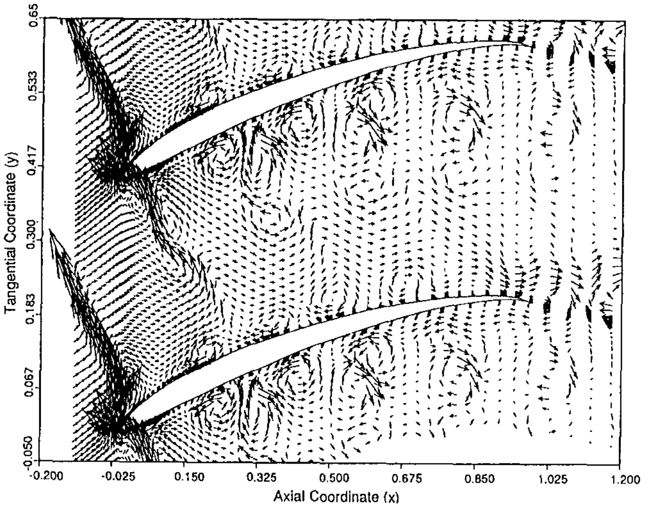

Fig. 9 Disturbance flow velocity vectors at time $t_0 + 0.1T$ within an entire stator passage

This wake migration can be explained by the excess of tangential velocity in the wake (Kerrebrock, 1970). The wake does not seem to penetrate into the pressure surface boundary layer. For this reason, the distance between the surface and the wake vortices scales as the local boundary layer thickness.

From the computed results, it appears that the unsteady flow over the suction surface of the stator blade is substantially different in nature from the flow over the pressure surface. As shown in Fig. 2, a distinct vortical region is

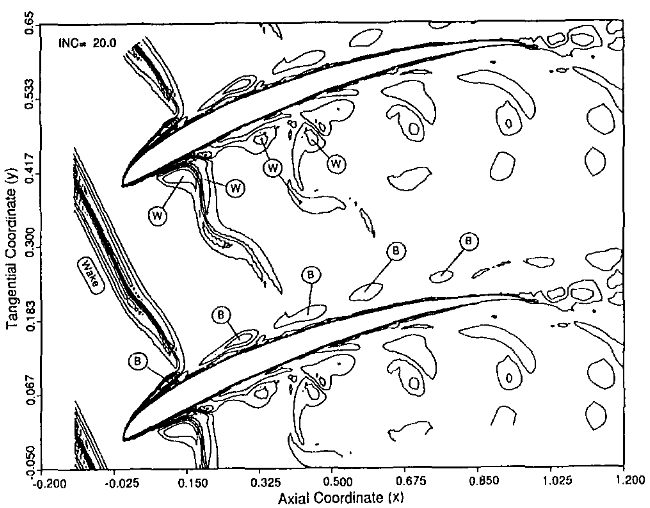

Fig. 10 Disturbance flow vorticity contours at time $t_0 + 0.6T$ within an entire stator passage

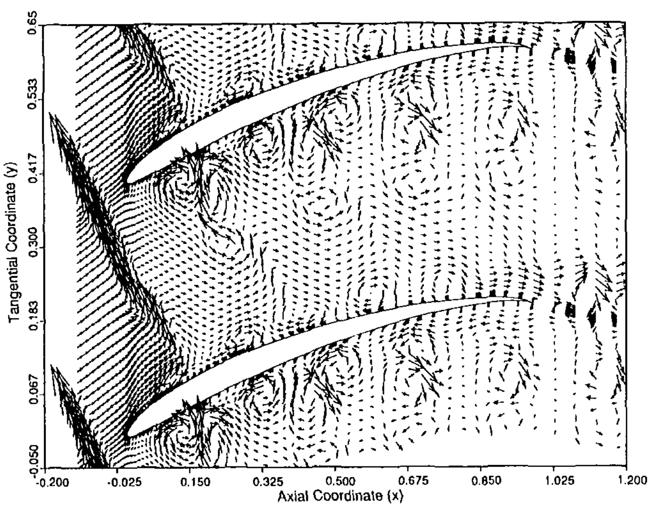

Fig. 11 Disturbance flow velocity vectors at time $t_0 + 0.6T$ within an entire stator passage

produced on each side of the leading edge upon interception of the wake. Both regions contain negative-sign (clockwise) vorticity, and will be referred to as *B-region* (on the suction side) and as *BP-region* (on the pressure side).

The unsteady effects associated with the BP-region are negligible when compared to those of the wake vortices, furthermore, this region does not evolve significantly as it is convected downstream. On the other hand, the B-region is lifted away from the blade surface and evolves into one *B-vortex*; this is shown in Fig. 5. As a consequence, the unsteady flow over the suction surface is characterized by a row of corotating B-vortices, each one corresponding to the interception of a rotor wake by the blade. It can be seen from Figs. 8 and 11 that these vortices dominate the unsteady flow over the suction surface.

From Figs. 8 and 10 it can be seen that at any particular instant, the number of B-vortices within the stator passage is larger than the number of wakes. This is a consequence of the production of B-vortices taking place in the boundary layer, where the convection velocity is smaller than the free-stream velocity.

The pressure fluctuations on the blade surface exhibit a characteristic pattern, which directly correlates with the forementioned vortical disturbances. The pattern, shown in Figs. 12 and 13, consists of:

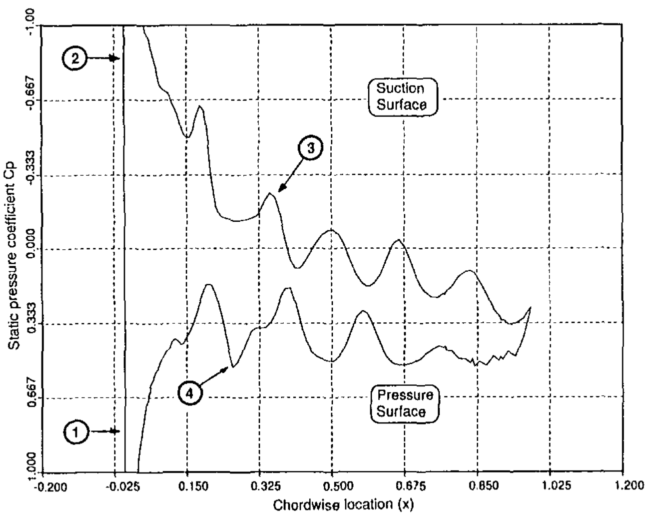

Fig. 12 Static pressure distribution on the blade surface at time $t_0 + 0.1T$

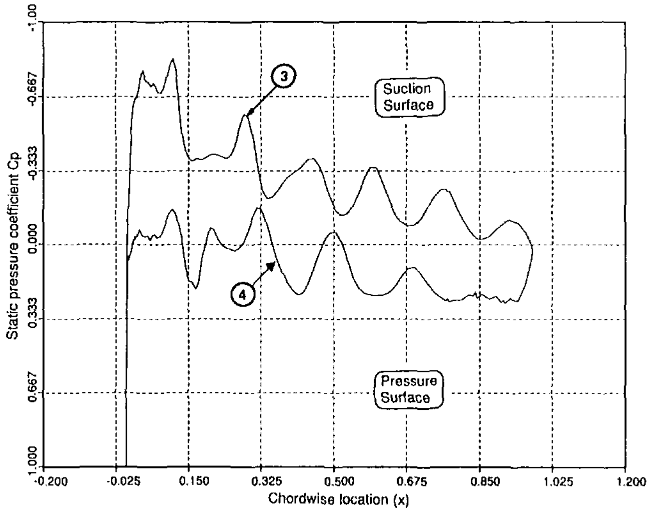

Fig. 13 Static pressure distribution on the blade surface at time $t_0 + 0.6T$

1 An intense high-pressure pulse on the pressure side of the stator blade leading edge, produced upon wake interception. This pulse is associated with the higher total pressure fluid in the rotor wake. Its peak value can be estimated using the following formula (Valkov, 1992):

$$C^{+}_{p,\max} = (1 - A)^2 \cos^{-2}\theta + 2A(1 - A)V\tan\theta + A^2V^2 \tag{14}$$

2 An intense low-pressure pulse on the suction side of the leading edge; produced upon wake interception. This pulse appears to be associated with the increase in local angle of attack when the wake is encountered.

3 A sequence of low-pressure peaks (depressions) moving downstream along the suction surface of the blade. As shown by correlating the pressure contours in Figs. 4 and 7 to the disturbance velocity field in Figs. 3 and 6, each depression is the reflection of a low static pressure region in the core of a nearby B-vortex.

4 A sequence of moving disturbances on the pressure surface. Each disturbance consists of low-pressure regions associated with the cores of the two wake vortices, interleaved with a high-pressure region where the disturbance flow is directed against the blade surface (Fig. 7 versus Fig. 6).

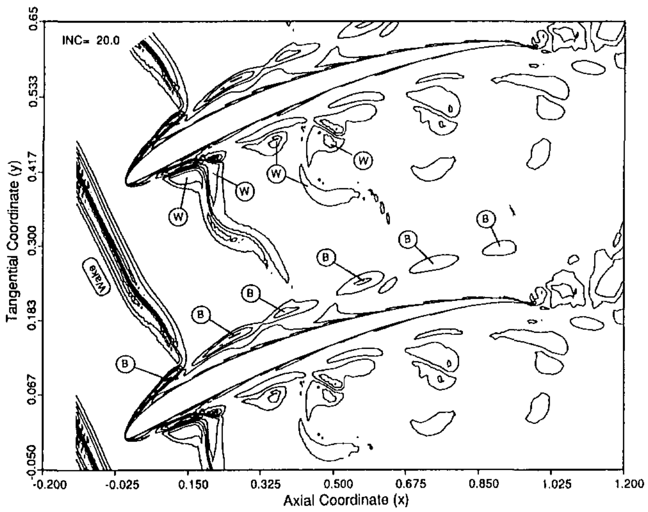

Fig. 14 Disturbance flow vorticity contours at time $t_0 + 0.6T$ within an entire stator passage. Result from a direct Navier–Stokes calculation at Re = 10,000

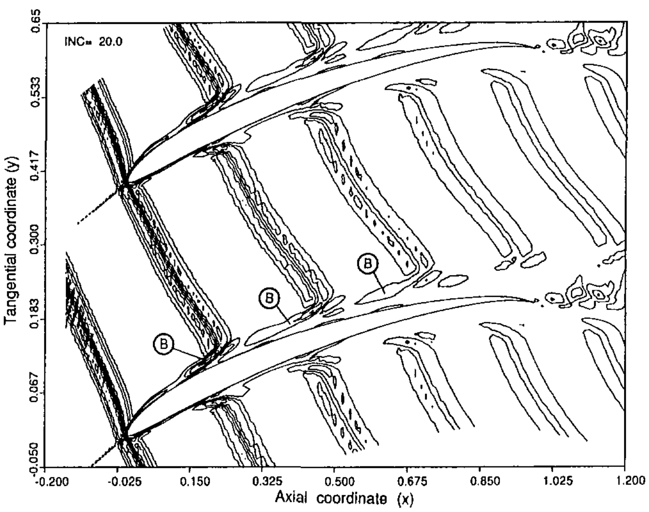

Fig. 15 Disturbance flow vorticity contours at time $t_0 + 0.0T$ from a linearized calculation with a viscous base flow (base flow Re = 1,000,000)

All the foregoing unsteady flow features have also been observed in direct Navier–Stokes simulations with various combinations of loading and wake parameters for Reynolds numbers ranging from 5000 to 50,000 (Valkov, 1992). This is illustrated in Fig. 14, which shows the instantaneous disturbance vorticity contours in the passage from a direct simulation at a Reynolds number of 10,000. The similarity between the results in Figs. 10 and 14 suggests that the wake vortices, the B-vortices, and the characteristic pressure fluctuation are *generic* features of wake-driven unsteady flows.

4.0 Origin of the Unsteady Flow Features

4.1 Method of Investigation. To provide insight into the origin of the unsteady flow features discussed above, we have compared the Navier–Stokes results to those from linearized and inviscid calculations. For this purpose, the unsteady flow in the stator is split in two parts:

$$U(x, y, t) = \overline{\mathbf{U}}(x, y) + \tilde{\mathbf{u}}(x, y, t) \qquad (15)$$

The first part, $\overline{\mathbf{U}}$, is the steady-state viscous flowfield that would exist in absence of wakes. This flowfield, shown in Fig. 1, will be referred to as *base flow*. The second part, $\tilde{\mathbf{u}}$, is the disturbance flowfield containing the unsteady effects. This allows one to re-formulate the Navier–Stokes equations in terms of disturbance flow with each term representing a specific unsteady process as follows:

$$\frac{\partial \tilde{\mathbf{u}}}{\partial t} + \underbrace{\overline{\mathbf{U}} \cdot \nabla \tilde{\mathbf{u}}}_{\text{I}} + \underbrace{\tilde{\mathbf{u}} \cdot \nabla \overline{\mathbf{U}}}_{\text{II}} + \underbrace{\tilde{\mathbf{u}} \cdot \nabla \tilde{\mathbf{u}}}_{\text{III}} = -\nabla \tilde{\mathbf{p}} + \underbrace{\nabla (D \nabla \tilde{\mathbf{u}})}_{\text{IV}} \qquad (16)$$

Term	Represents
I	Convection of the wake disturbances by the base flow.
II	Distortion of the base flow vorticity by the unsteady disturbance flow.
III	Self-advection of the disturbance flow.
IV	Dissipation of the disturbance under the effect of steady and turbulent shear stresses

Instead of solving the full Navier–Stokes equations and subtracting the base flow, we could have obtained the results in Figs. 2–14 by solving Eq. (16). However, this approach does not provide much insight into the mechanisms involved in the production of the unsteady flow features such as wake vortices and B-vortices. For this purpose, we have solved a simplified form of Eq. (16), referred to as *linearized perturbation equation*:

$$\frac{\partial \tilde{\mathbf{u}}}{\partial t} + \underbrace{\overline{\mathbf{U}} \cdot \nabla \tilde{\mathbf{u}}}_{\text{I}} + \underbrace{\tilde{\mathbf{u}} \cdot \nabla \overline{\mathbf{U}}}_{\text{II}} = -\nabla \tilde{p} + \frac{1}{R_a} \nabla^2 \tilde{\mathbf{u}} \qquad (17)$$

from which the nonlinear and viscous term have been dropped, and compared the results to those from the Navier–Stokes code.

The linearized equation is solved numerically by using a spectral element technique, which is very similar to that used in the Navier–Stokes solver. Since this technique is nondissipative, an artificial viscosity term is present in Eq. (17) in order to prevent numerical instability. The inviscid nature of the perturbation flow is however partly reproduced by using free-slip boundary conditions in the viscous step, and by keeping the artificial viscosity parameter R_a as high as possible.

4.2 Unsteady Flow Near the Suction Surface. The Navier–Stokes calculations show that the unsteady flow near the suction surface of the stator blade is dominated by the moving row of B-vortices. A linearized calculation using the viscous base flow from Fig. 1 reproduces this quite well. As shown by a comparison between Figs. 15 and 8, all major disturbance flow features (B-regions and subsequent B-vortices) over the suction surface are faithfully represented by the linearized calculation.

The linearized solver treats the disturbances as inviscid. This suggests that the origin of B-vorticity lies in the viscous base flow. One may postulate that the B-vorticity is associated with the distortion term $\tilde{\mathbf{u}} \cdot \nabla \overline{\mathbf{U}}$, which is common to both Eqs. (16) and (17). Under this hypothesis, the production of vortical B-region in the leading edge region can be described as a distortion of boundary layer fluid by the convective effect of the wake velocity field. This is illustrated in Fig. 16, where part of the boundary layer is lifted off from the surface by a passing wake. The resulting vortical B-region is subsequently detached from the boundary layer by the convective action of the wake. Once in the free stream, the B-region evolves into a B-vortex. Such a mechanism can explain why all B-vortices are of the same sign—they contain negative vorticity from the suction surface boundary layer.

To confirm that the B-vortices are produced from the boundary layer, a linearized calculation with inviscid base

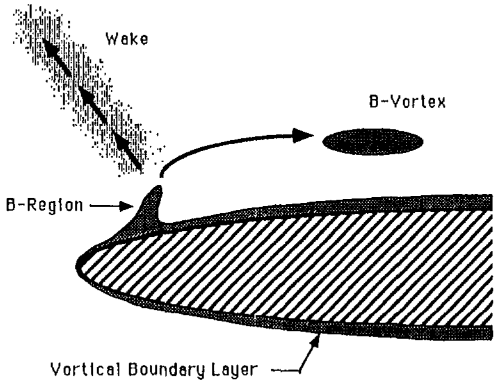

Fig. 16 Postulated mechanism for the production of B-vortices from the boundary layer

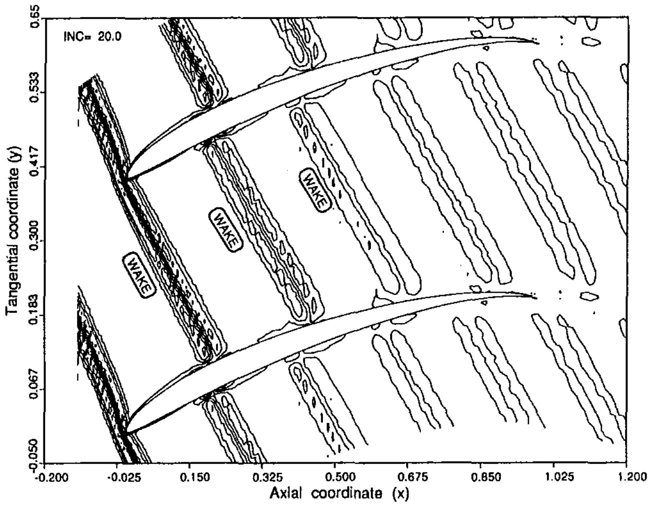

Fig. 17 Disturbance flow vorticity contours at time $t_0 + 0.0T$ from a linearized calculation with an inviscid base flow

flow has been carried out. This is equivalent to performing a linearized Euler calculation of the wake interaction. The inviscid base flow about the stator geometry used here has been generated using the PCPANNEL code by McFarland (1984).

Linearized calculations with the inviscid base flow are devoid of B-vortices, thereby confirming the above hypothesis. As shown in Fig. 17, the incoming wakes are simply cut by the stator blades without any other kind of interaction. The relative slip of the wakes as they move downstream in the stator passage is due to the circulation about the blade.

The linearized *inviscid-base-flow* calculations cannot thereby account for the moving row of pressure fluctuations on the suction surface, produced by the B-vortices (cf. Chap. 3.0). In our case, these fluctuations make up a significant part of the unsteady pressure on the suction surface. The only pressure fluctuations observed in the linear calculation with *inviscid* base flow are the leading edge pressure pulses, which constitute a potential flow effect. However, the linearized calculation with *viscous* base flow gives an unsteady pressure distribution on the suction surface that is virtually identical to that from the Navier–Stokes code.

4.3 Importance of the Nonlinear Effects. An examination of the disturbance flowfield in Figs. 15 and 17 shows that the linearized calculations cannot represent the phenomenon of wake migration toward the pressure surface and its subsequent piling up and evolution to counterrotating vortices.

This phenomenon is an exclusively self-advective process, represented by the nonlinear term $\tilde{\mathbf{u}} \cdot \nabla \tilde{\mathbf{u}}$ in the disturbance Navier–Stokes equation (Eq. (16)). The linearized calculations cannot represent migration of the wake because of the absence of this nonlinear convective term. For this reason, they exhibit persistent and straight wake segments.

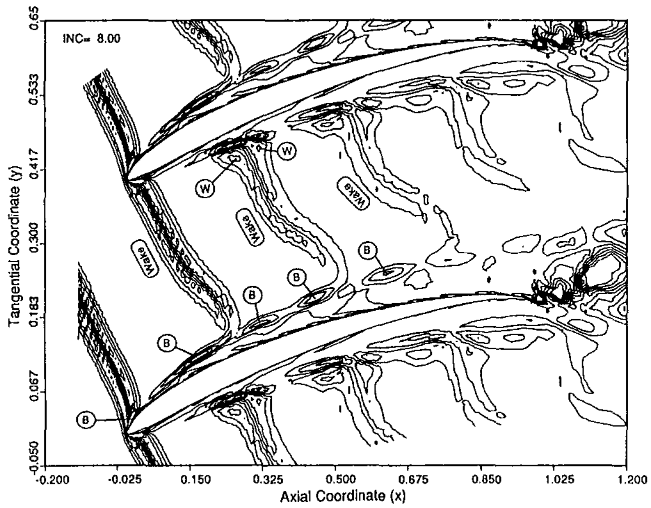

Fig. 18 Disturbance flow vorticity contours at time $t_0 + 0.1T$ from a Navier–Stokes calculation with a wake velocity defect equal to 30 percent of the free-stream velocity in the rotor frame

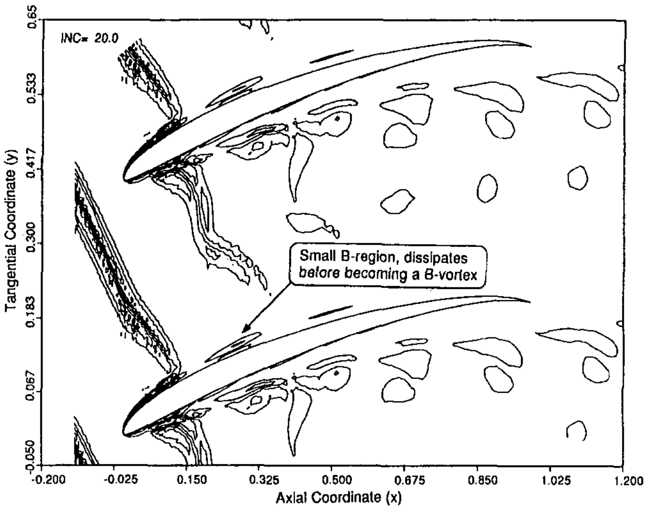

Fig. 19 Disturbance flow vorticity contours at time $t_0 + 0.6T$ from a Navier–Stokes calculation with nonuniform suction applied over the suction surface

The degree of disagreement between the Navier–Stokes and the linearized calculations depends on the strength of the wakes. The wake strength is directly related to the excess of tangential velocity in the wake in the stationary frame. The wake strength is thus proportional to the wake velocity defect in the rotor frame and to the rotor blade tangential velocity.

With strong wakes, such as those used in the above-mentioned runs, the nonlinear self-advective effects are large when compared to the convective action of the free stream. In this case, the time in which the wake fluid migrates toward the pressure surface is small when compared to the through-flow time. This gives an impression that the wake disappears while still within the stator passage. What actually happens is that the initially straight wake segments have evolved into pairs of counterrotating vorticity "clumps" (wake vortices).

With weaker wakes, the free-stream convective effect will dominate the self-advective effect. Figure 18 shows a Navier–Stokes disturbance vorticity field corresponding to a wake velocity defect of 30 percent. This solution is character-

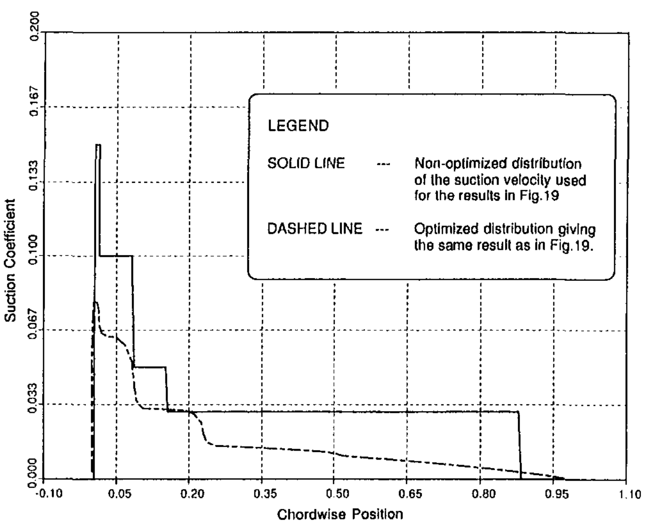

Fig. 20 Suction velocity distribution for the computational experiment shown in Fig. 19

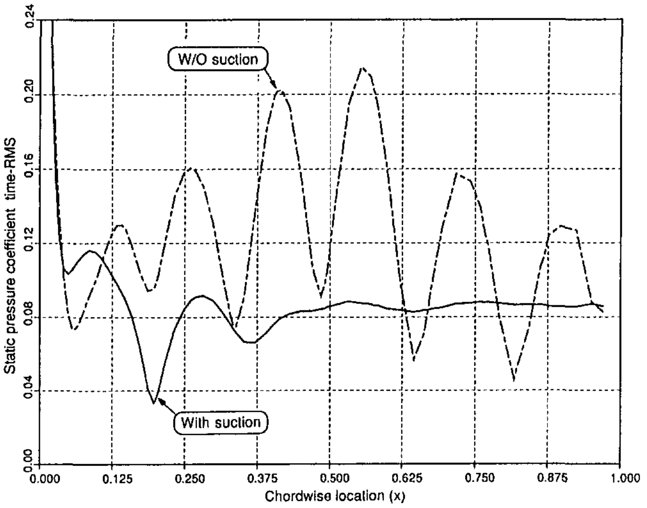

Fig. 21 *Chordwise distribution of the time-rms of the unsteady static pressure coefficient*

ized by more persistent wake segments and weaker vortices than in Fig. 8. In this case, the linearized results will appear closer to those from the Navier–Stokes solver.

These considerations lead to the conclusion that one cannot linearize the unsteady part of the flow in all circumstances. A linearized solution is valid for engineering purposes only when the self-advective term in Eq. (16) is small in comparison to the base flow convective term. This is not the case for the rotor–stator configuration used herein. As the wake vortices contribute to the fluctuating component of the static pressure loading, it is important to make linearized flow assumptions carefully.

5.0 Control of the Unsteady Flow

The purpose of the flow control strategies discussed herein is to reduce the blade loading fluctuations only. Unsteady flow control over the suction surface is based on preventing local distortion and detachment of the boundary layer by the wakes. Since the distorting effect of the wakes is rapidly attenuated by their migration toward the pressure surface control efforts need to be focused only over the foremost part of the stator blade.

Computational experiments carried out by Valkov (1992) show that a favorable local pressure gradient can decrease the strength of the B-vortices, thereby quadratically reducing the associated pressure fluctuations. Designning the stator blade with a less adverse or a favorable pressure gradient over the foremost part of the suction surface could be thus effective for reducing the unsteadiness there.

Active control strategies can be also used to remove the boundary layer or to increase its resistance to wakes. Active control offers the possibility to act directly on the unsteady flow in a manner that can be controlled by the user or by computer logic. Figure 19 shows the computed disturbance flowfield resulting from the application of suction that is nonuniformly distributed on the suction surface. The flowfield over the suction surface is virtually unsteadiness-free, and there is no production of B-vortices.

It is to be noted that this result is from a direct Navier–Stokes simulation at a Reynolds number of 10,000. We have not carried out active control simulations at a Reynolds number of 1,000,000 because the turbulence model used does not apply to boundary layer flows with fluid suction. However, we expect these results to carry over in the turbulent flow regime, as the unsteady flow features are qualitatively the same for both laminar and turbulent flows (cf. Chap. 3.0). This is so because the fundamental mechanisms responsible for these features operate in both the laminar and turbulent flow regimes.

Because the simulation of suction-based active control is carried out at a Reynolds number of 10,000, relatively large values of suction velocity are required in the leading edge region (Fig. 20). Since the suction surface boundary layer is thinner at Re = 1,000,000 than at Re = 10,000; we expect that much smaller suction velocities will be necessary to prevent the formation of B-vortices at Reynolds numbers of engineering interest.

A technique for minimizing the mass fraction of removed fluid has been devised by Valkov (1992). The nonoptimized suction distribution in Fig. 20 is equivalent to removing 7 percent of the total mass flow through the stator. After optimization, a similar low level of unsteadiness can be achieved by removing 3 percent of the mass flow. The optimized suction distribution is also shown in Fig. 20.

The unsteady flow due to the migration of wake fluid is somewhat difficult to influence from the blade surface. So far, *fluid injection from the pressure surface* appears able to reduce the loading fluctuations there. This strategy appears to operate by moving the wake vortices further away from the pressure surface, and thereby reducing the associated loading fluctuations. This requires, however, an injection velocity in excess of $0.1U_\infty$ from over most of the pressure surface. This amount of fluid injection appears too large for practical applications.

To quantify the effectiveness of different flow control strategies we can compare the time-rms distributions of the unsteady static pressure coefficient on the blade surface. In the absence of suction, the rms distribution (Fig. 21) is characterized by a peak in the leading edge region, due to the strong pressure pulses arising from wake interception. Aft of the leading edge, the rms distribution exhibits a series of "peaks" and "troughs," the presence of which can be explained by splitting the unsteady static pressure coefficient into two parts:

$$C_p(x,t) = \mathcal{P}(x)\sin\left(\frac{2\pi t}{T}\right) + \mathcal{V}(x)\sin\left(\frac{2\pi t}{T} + \frac{N\pi x}{U_\infty}\right) \tag{18}$$

The first term in the above equation represents an instantaneous change of loading resulting from the wake impinging on the leading edge. The second term represents a moving-wave-like fluctuation due to the moving row of vortices. It can be readily shown that the time-rms of functions of this form is similar to that in Fig. 21.

The rms levels of static pressure on the suction surface are significantly reduced aft of the leading edge in the presence of fluid removal. This reduction is associated with the suppression of the B-vortices. Fluid removal does not seem to affect the leading edge peaks, which are a result of unsteady potential flow effects. The control of these effects has not been addressed in our study.

6.0 Conclusions

Computational Fluid Mechanics (CFD) have been used herein to examine the mechanics of fluid flow associated with wake–stator interaction. The results have been used to design control strategies for reducing the blade loading fluctuations.

During their transport through the stator passage, the wakes migrate toward the pressure surface of the stator blades, where they evolve into pairs of counterrotating vortices. These vortices are the dominant form of unsteady flow over the pressure surface. Strong fluid injection from the pressure surface reduces, though not effectively, the blade loading fluctuations associated with the wake vortices. Calculations where the unsteady part of the flow is linearized about a steady mean flow cannot adequately represent the flow associated with wake migration.

The unsteady flow over the suction surface of the stator blades is characterized by a moving row of vortical disturbances (B-vortices) produced at the leading edge upon wake interception. The B-vortices consist of boundary layer fluid, which is distorted and lifted off the suction surface by the convective action of the wakes. The strength of the B-vortices and the associated pressure fluctuations can be reduced by tailoring the pressure gradient over the foremost part of the suction surface. The B-vortices can be virtually eliminated by removing boundary layer fluid from the foremost part of the suction surface by using nonuniform suction.

Acknowledgments

Support for this work was provided by the Applied Research Laboratory, under contract No. N00039-88-C-0051 and supervision of Dr. W. Zierke. Support for the preparation of this manuscript was provided by the NASA-Lewis Research Center, under grant No. NAG-3-660 and supervision of Dr. J. Adamczyk. The authors would like to thank also Dr. Adamczyk for making available the computational resources at NAS and NASA-Lewis.

These acknowledgments are extended to Dr. W. McFarland for making available the PCPANNEL computer program used to obtain irrotational flow solutions. Credit for the development of PCPANNEL is given to the Internal Fluid Mechanics Division of the NASA-Lewis Research Center.

References

Adachi, T., et al., 1974, "Study of the Interference Between Moving and Stationary Blade Rows in an Axial Flow Blower," *Bulletin of the JSME*, Vol. 17(109), pp. 904–911.

Baldwin, B., and Lomax, H., 1978, "Thin Layer Approximation and Algebraic Model for Separated Turbulent Flows," AIAA Paper No. 78-257.

Capece, V. R., and Fleeter, S., 1989, "Experimental Investigation of Multistage Interaction Gust Aerodynamics," ASME JOURNAL OF TURBOMACHINERY, Vol. 111, No. 4, pp. 409–417.

Dring, R. P., Joslyn, H. D., Hardin, L. W., and Wagner, J. H., 1982, "Turbine Rotor-Stator Interaction," ASME *Journal of Engineering for Power*, Vol. 104, No. 4, pp. 729–742.

Erdos, J. I., Alzner, E., and McNally, W., 1977, "Numerical Solution of Periodic Transonic Flow Through a Fan Stage," *AIAA Journal*, Vol. 15, No. 11, pp. 1559–1568.

Gallus, H. E., 1979, "Unsteady Flow in Turbomachines," *VKI Lecture Series LS-1979-3*, Vol. 2, Von Karman Institute.

Giles, M., 1991, "UNSFLO: A Numerical Method for the Calculation of Unsteady Flow in Turbomachinery," GTL Report No. 205, Massachusetts Institute of Technology.

Hodson, H. P., 1985, "An Inviscid Blade-to-Blade Prediction of a Wake-Generated Unsteady Flow," ASME *Journal of Engineering for Gas Turbines and Power*, Vol. 107, pp. 337–344.

Kerrebrock, J. L., and Mikolajczak, A. A., 1970, "Intra-stator Transport of Rotor Wakes and Its Effect on Compressor Performance," ASME Paper No. 70-GT-39.

Korczak, K. Z., and Patera, A. T., 1986, "An Isoparametric Spectral Element Method for Solution of the Navier–Stokes Equations," *Journal of Computational Physics*, Vol. 62, p. 361.

McFarland, E. R., 1984, "A Rapid Blade-to-Blade Solution for Use in Turbomachinery Design," ASME *Journal of Engineering for Gas Turbines and Power*, Vol. 106, No. 2, pp. 376–382.

Orszag, S. A., and Kells, L., 1980, "Transition in Plane Poiseuille and Plane Couette Flow," *Journal of Fluid Mechanics*, Vol. 96.

Patera, A. T., 1984, "A Spectral Element Method for Fluid Dynamics: Laminar Flow in a Channel Expansion," *Journal of Computational Physics*, Vol. 54, No. 3, pp. 98–108.

Rai, M. M., 1987, AIAA Paper No. 87-2058.

Tan, C. S., 1989, "A Multi-Domain Spectral Computation of Three-Dimensional Laminar Horseshoe Vortex Flow Using Incompressible Navier–Stokes Equations," *Journal of Computational Physics*, Vol. 85, No. 1.

Valkov, T. V., 1992, "Control of the Unsteady Flow in a Stator Blade Row Interacting With Upstream Moving Wakes," M.S. Thesis, Massachusetts Institute of Technology.

Experimental and Numerical Study of the Time-Dependent Pressure Response of a Shock Wave Oscillating in a Nozzle

P. Ott

A. Bölcs

T. H. Fransson[1]

Laboratoire de Thermique Appliquée,
et de Turbomachines (LTT),
Swiss Federal Institute of Technology,
Lausanne, Switzerland

Investigations of flutter in transonic turbine cascades have shown that the movement of unsteady normal shocks has an important effect on the excitation of blades. In order to predict this phenomenon correctly, detailed studies concerning the response of unsteady blade pressures versus different parameters of an oscillating shock wave should be performed, if possible isolated from other flow effects in cascades. In the present investigation the correlation between an oscillating normal shock wave and the response of wall-mounted time-dependent pressure transducers was studied experimentally in a nozzle with fluctuating back pressure. Excitation frequencies between 0 Hz and 180 Hz were investigated. For the measurements, various measuring techniques were employed. The determination of the unsteady shock position was made by a line scan camera using the Schlieren flow visualization technique. This allowed the simultaneous use of unsteady pressure transducers to evaluate the behavior of the pressure under the moving shock. A numerical code, based on the fully unsteady Euler equations in conservative form, was developed to simulate the behavior of the shock and the pressures. The main results of this work were: (1) The boundary layer over an unsteady pressure transducer has a quasi-steady behavior with respect to the phase lag. The pressure amplitude depends on the frequency of the back pressure. (2) For the geometry investigated the shock amplitude decreased with increasing excitation frequency. (3) The pressure transducer sensed the arriving shock before the shock had reached the position of the pressure transducer. (4) The computed unsteady phenomena agree well with the results of the measurements.

Introduction

Unsteady flow effects in turbomachines can be the source of various excitations that can lead to different vibrations, such as forced vibration and flutter. Turbomachine blade vibrations are known to appear over a large flight envelope for compressors in jet engines and on the last stages of industrial turbines. Main vibration problems appear in the transonic flow domain (Bölcs et al., 1989b; Ezzat et al., 1989; Usab and Verdon, 1991; Verdon, 1989; Araki et al., 1981; Széchényi et al., 1984, Széchényi, 1985; Buffum and Fleeter, 1989, 1990, 1993; Hanamura and Yamaguchi, 1988; Fransson, 1992; to mention just a few) and it has been noted both theoretically and experimentally that oscillating normal shock waves can introduce large unsteady local loads on the vibrating blades (Verdon, 1989; Bölcs et al., 1991). Because of the small blade dimensions usually employed for cascade experiments in the transonic flow domain, it is extremely difficult to obtain accurate information about the exact position of the shock wave, how much it fluctuates, its harmonic and nonharmonic content, as well as the correlation between the "free-stream" (outside the boundary layer) shock position and the time-dependent pressure responses on the blades.

Numerical predictions are presently performed for both the forced vibration and the flutter problem. In these, emphasis is sometimes put on the sharp shock capture (Carstens, 1991) or shock fitting (Verdon, 1989), whereas other results indicate that less sharp shock capture gives smaller local unsteady loads but over a more spread out region (Whitehead and Newton, 1985; Whitehead, 1990; Gerolymos, 1993a, b), and that the total chordwise load agrees with global experimental data.

For the correct interpretation of both experimental data and numerical predictions of the unsteady transonic flow around vibrating cascaded airfoils it is important to determine the correlation between the oscillating shock wave and fluctuating blade pressures, and the experimental and numerical results.

Previous numerical two-dimensional investigations in a nozzle (Bölcs et al., 1989a; Liang et al., 1992) indicated that both

---

[1] Present address: Division of Heat and Power Technology, Royal Institute of Technology, Stockholm, Sweden.

Contributed by the International Gas Turbine Institute and presented at the International Gas Turbine and Aeroengine Congress and Exposition, Cincinnati, Ohio, May 24-27, 1993. Manuscript received at ASME Headquarters March 1, 1993. Paper No. 93-GT-139. Associate Technical Editor: H. Lukas.

the amplitude and frequency of an imposed fluctuating back pressure are important parameters for the location of the unsteady shock. This study also indicated that the pressure jump over the shock, as well as the unsteady post-shock pressure, is different for identical shock positions during the cycle of fluctuation.

Similar measurements as here presented were made by Edwards (1987). The conditions were slightly different. The flow investigated was on a flat surface with a flow separation behind the shock. The boundary layers were thinner and especially the resolution of the device to find the shock position was smaller. This and some supplementary questions to answer made it necessary to re-investigate the problem.

The objectives of the present work are to obtain fundamental data for the correlation between an oscillating shock wave and the time-dependent pressures measured on a nozzle wall, in the presence of a thick boundary layer, further to validate an improved version of the numerical model previously presented against experimental data on oscillating shock waves in a nozzle.

Measuring Equipment

Test Facility. A Laval nozzle with a width of 40 mm was modified for the purpose of the present study. The facility was equipped with nozzle liners giving a converging–diverging section with a continuous first derivative of the area (Fig. 1 and Appendix 1). The inlet and outlet height of the test section is 80 mm and the throat height is 71 mm. A window is situated in the aft part of the convergent–divergent section and gives access to nonintrusive measurement techniques.

A four-stage radial, continuously running turbocompressor (pressure ratio 4, 10 kg/s mass flow) is used as the air source.

On the nozzle liners the boundary layer is cut off before the throat (Fig. 1). No suction of this mass flow is performed, and the air is blown by the flow behind the nozzle liners and again mixed with the main stream at the exit of the nozzle. The boundary layers at the side walls are not modified, which creates the fairly thick boundary layer used in the study.

Oscillating Shock. A normal shock is created in the test section of the nozzle by regulating the exit pressure of the nozzle.

At the exit section of the nozzle formed by the liners a cylindrical rod with elliptical cross section (Fig. 1 (*b*)) is rotated by a hydraulic motor. This rod is situated 480 mm downstream of the throat. The losses created by the wake of the rod are varied in time and in this way the outlet pressure of the nozzle is changed periodically. By this variation the normal shock is excited to oscillation frequencies between 0 and 180 Hz. For the present tests the shock is always oscillating in the divergent section of the nozzle. Upstream of the shock, depending on its position, Mach numbers between 1.2 and 1.4 are reached.

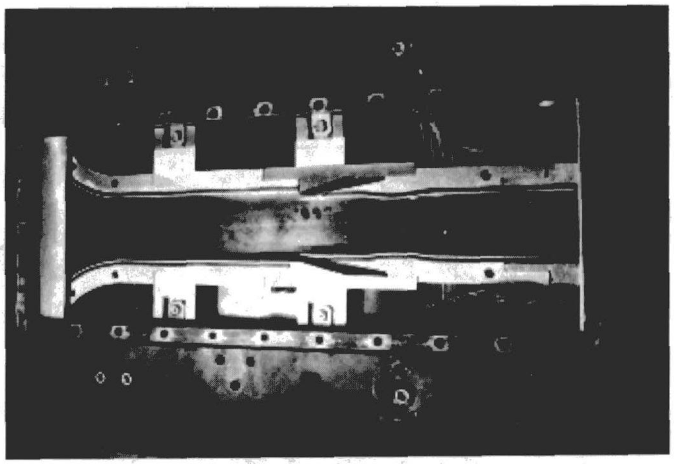

Fig. 1(*a*) Photo of the nozzle

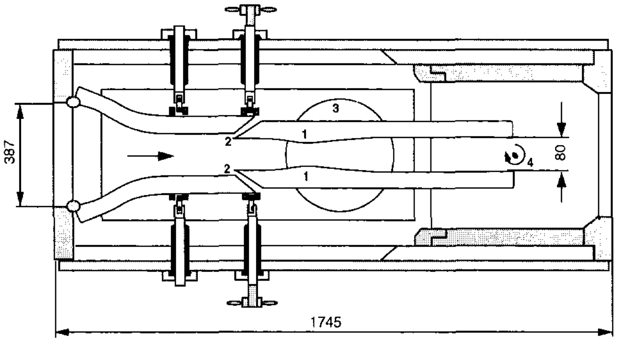

Fig. 1(*b*) Schematic view of the nozzle used: (1) nozzle liner; (2) boundary layer bleed; (3) Schlieren window; (4) rotating exciter

Instrumentation. On the nozzle liners and on the side walls steady-state pressure taps exist and give the steady-state pressure distribution through the nozzle.

For pressure measurements the mirror plate of the double-pass Schlieren system ("3" in Fig. 1(*b*)) is equipped with 80 pressure taps where either small tubes for static pressure measurements or tubes containing a high-frequency response pressure transducer[2] can be screwed in. Eight tubes containing pressure transducers were used for the present test series. The

---

[2] Pressure transducer ENDEVCO, model PS 8514-50, range: 0–3.4 bar, accuracy: 0.5 percent full scale.

Nomenclature

a = velocity of sound, m/s
$\mathbf{F}$ = flux vector
D = Jacobian determinant
e_c = total energy/unit mass, m^2/s^2
f = frequency, Hz
$\mathbf{G}$ = flux vector
h_c = total enthalpy/unit mass, m^2/s^2
M = Mach number
p = pressure, mbar
$\tilde{p}$ = pressure (unsteady perturbation), mbar
p_{tot} = total pressure, mbar
q = velocity, m/s
R = gas constant (≈ 287 for air), $m^2/(s^2K)$
Re = Reynolds number
t = time, s
T = temperature, K
u = velocity component in x direction, m/s
v = velocity component in y direction, m/s
$\mathbf{W}$ = flux vector
x = coordinate direction, mm
y = coordinate direction, mm
η = coordinate direction
κ = ratio of specific heats
ξ = coordinate direction
ρ = density, kg/m^3
τ = time
ω = circular frequency, rad/s

Subscripts and Superscripts

1 = inlet condition
c = stagnation value
n = pressure transducer number ($n = 1, \ldots, 8$)
ref = reference value
x = in x direction
y = in y direction
ξ = in ξ direction
η = in η direction

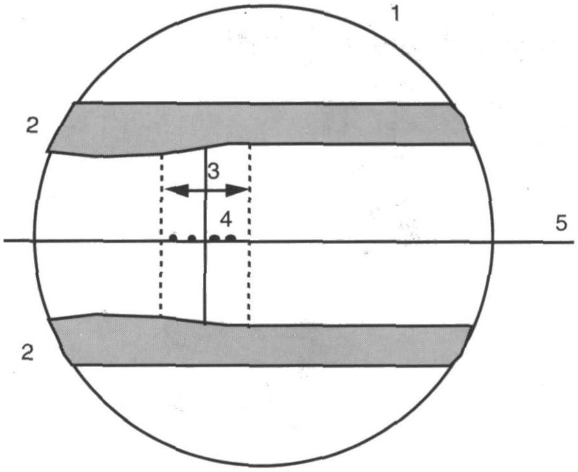

Fig. 2 Position of observed line and pressure transducers: (1) Schlieren window; (2) nozzle liner; (3) moving shock; (4) unst. press. transducer (mounted in mirror plate); (5) line observed with line scan camera

mounting was performed in a way that the pressure transducers were sitting just behind the surface of the mirror plate with a dead volume that is negligible. The transducers were calibrated for steady state and dynamic pressure, including the whole measuring chain (dead volume, cables, amplifiers, filters, etc.), while they were mounted in their corresponding measuring positions.

The shock form and position is observed by a reflecting Schlieren system using a video camera and a stroboscopic flash synchronized with this camera. Furthermore, the shock position, its form, the boundary layers and the flow velocities up- and downstream of the shock, are also determined with a Laser-2-Focus system, both for "steady-state" and time-dependent operating conditions at different frequencies. Finally, holographic interferometry was used to get some supplementary information about the boundary layers on the nozzle liners close to the shock for the steady state flow.

For the time-dependent measurements the flash is replaced by a continuous light source. The shock position is found by a line scan camera[3] which observes one line of the Schlieren picture normal to the shock (Fig. 2). A mask with well-known position is fixed on the window for determination of the geometric location of the shock in the channel. The distance left free by the mask was 40 mm for these tests. The Schlieren image is projected on the sensitive line of the camera composed by 1024 photodiodes (pixels). Under consideration of about 800 pixels within the range of the distance left free by the mask, a spatial resolution of 0.05 mm is reached. Figure 3(*a*) shows a schematic view of the flow field and a theoretical resulting signal of the line scan camera. Figure 3(*b*) shows a real signal. The shock position found this way is integrated over the nozzle height. Simultaneously to the camera signal the unsteady pressure distribution is measured by the time-dependent pressure transducers fixed in the mirror plate at the side wall.

The signals of the camera and the pressure transducers are recorded, together with a triggering signal of the exciter, on an analog data recorder[4] and digitized off-line. The digitized signals of the line scan camera can give the position of the shock in the moment when the line scan camera "froze" the instantaneous picture before writing out the voltage of all diodes (Fig. 3(*b*)).

After elimination of the time shift between the different

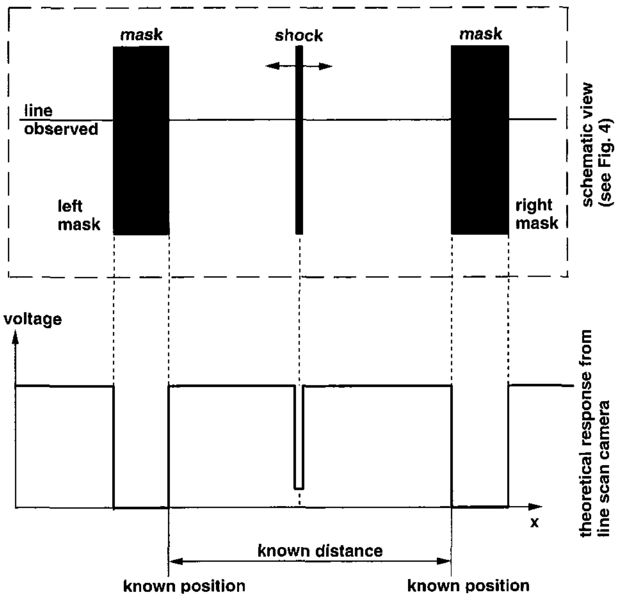

Fig. 3(*a*) Schematic illustration of Schlieren visualization and a line scan camera signal

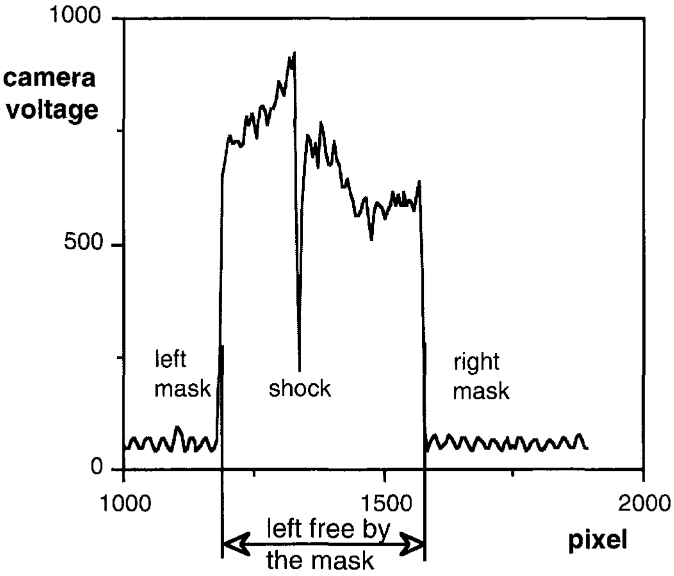

Fig. 3(*b*) Untreated signal of line scan camera with shock

signals due to the multiplexer used during the digitalization, a signal averaging for one excitation period is made for the pressure signals and the shock positions. The results can be presented in a form as shown by Fig. 7.

The trigger signal allows to locate the moment when the picture was taken inside one excitation period. As the phenomenon studied is periodic, a signal averaging for the pressure transducer signals and for the shock positions can be made. All results are then presented within one excitation period.

Figure 4 shows the positions of the unsteady pressure transducers for the measurements here presented. The pressure transducers were positioned such that some are located slightly outside of the shock oscillation range, and others where the shock always would be present. One transducer was mounted as far downstream from the shock as possible to measure the pressure oscillation at the outlet (pressure transducer p_8 in Fig. 4).

More details of the measuring equipment have been given by Ott et al. (1992).

---

[3] Line scan camera Reticon, model LC-1901.

[4] Tape recorder KYOWA, model RTP-802A.

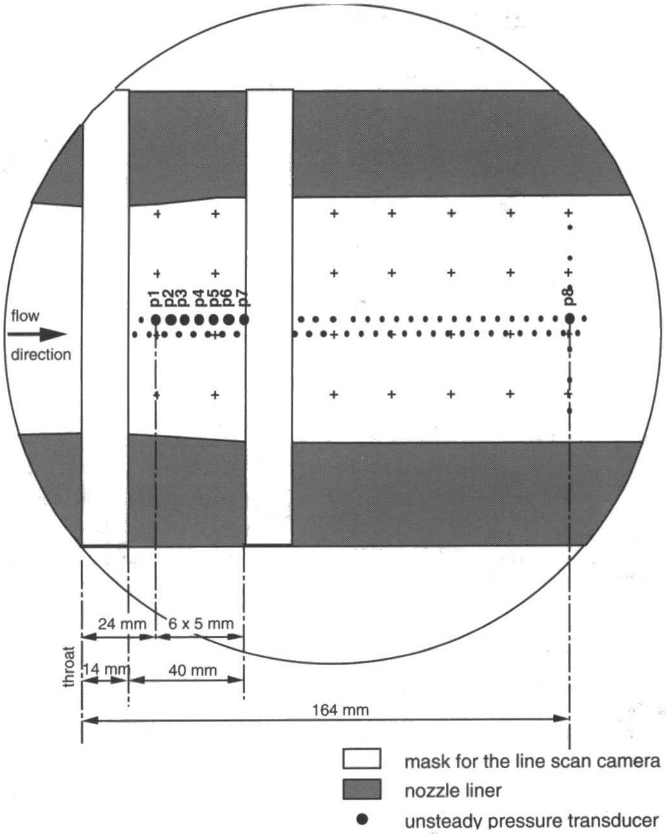

Fig. 4 **Positions of the unsteady pressure transducers during the tests**

Governing Equations and Numerical Method of Solution

Governing Equations. The computational method used here is an explicit, inviscid two-dimensional model of second-order accuracy, based on the Euler equations in conservative form. The model has been extended from a previous work (Bölcs et al., 1989a), and only a brief explanation of the model is thus given here.

The equations of continuity, momentum, and energy, which form the basis for the formulation, can be expressed in vector form:

$$\mathbf{W}_t+\mathbf{F}_x+\mathbf{G}_y=0 \tag{1}$$

The vectors can be expressed as:

$$\mathbf{W}=\begin{pmatrix}\rho\\ \rho u\\ \rho v\\ \rho e_c\end{pmatrix};\quad \mathbf{F}=\begin{pmatrix}\rho u\\ \rho u^2+p\\ \rho uv\\ \rho uh_c\end{pmatrix};\quad \mathbf{G}=\begin{pmatrix}\rho v\\ \rho uv\\ \rho v^2+p\\ \rho vh_c\end{pmatrix} \tag{2}$$

The equation of state for a perfect gas is used to find the relations between pressure, density, and temperature.

All variables presented in these equations have been made dimensionless by use of the reference values p_{ref}, $x_{\mathrm{ref}}=y_{\mathrm{ref}}$, T_{ref}, as well as:

$$\rho_{\mathrm{ref}}=\frac{p_{\mathrm{ref}}}{R\bullet T_{\mathrm{ref}}}\qquad q_{\mathrm{ref}}=\sqrt{R\bullet T_{\mathrm{ref}}}=a/\sqrt{\kappa}$$

$$t_{\mathrm{ref}}=\frac{x_{\mathrm{ref}}}{q_{\mathrm{ref}}}\qquad e_{\mathrm{ref}}=h_{\mathrm{ref}}=q_{\mathrm{ref}}^2 \tag{3}$$

The equation system (1) is mapped from the physical plane (x, y, t) to the computational plane (ξ, η, τ) with a general transformation:

$$\xi=\xi(x, y, t)$$
$$\eta=\eta(x, y, t)$$
$$\tau=t \tag{4}$$

Equation (1) becomes after this transformation:

$$\mathbf{W}'_t+\mathbf{F}'_\xi+\mathbf{G}'_\eta=0 \tag{5}$$

with the vectors:

$$\mathbf{W}'=D^{-1}\bullet\mathbf{W}$$
$$\mathbf{F}'=D^{-1}\bullet\{\xi_t\bullet\mathbf{W}+\xi_x\bullet\mathbf{F}+\xi_y\bullet\mathbf{G}\}$$
$$\mathbf{G}'=D^{-1}\bullet\{\eta_t\bullet\mathbf{W}+\eta_x\bullet\mathbf{F}+\eta_y\bullet\mathbf{G}\} \tag{6}$$

where D is the Jacobian determinant of the transformation (5) in the center of a computational cell and corresponds physically to the inverse of the cell area.

The solution follows with an upwinding model, in which the flux vectors are split in positive and negative fluxes:

$$\mathbf{F}=\mathbf{F}^{+}+\mathbf{F}^{-}$$
$$\mathbf{G}=\mathbf{G}^{+}+\mathbf{G}^{-} \tag{7}$$

The positive and negative fluxes are determined with respect to the physical domain of influence by the flux-vector splitting method of van Leer (Anderson et al., 1987). For a supersonic flow in x direction, for example, the negative part of the flux becomes zero; all flow information comes from upstream.

Numerical Grid. For the computations here presented an *H*-mesh was used with 81 mesh points in the streamwise direction (x) and 15 mesh points normal to this direction (y). The first row of points is situated half a mesh distance from the walls of the nozzle.

Spatial Differencing. The numerical model uses the approach of "Monotone Upwind Schemes for Conservation Laws (MUSCL)" proposed by van Leer (Anderson et al., 1985). In this approach the data are first prepared and eventually limited before the numerical differences are performed. The spatial derivatives are approximated as centered differences with values at half points.

A flux limiter is used at the location of the shock to reduce the accuracy of the computation to the first order.

Integration in Time. For the advance in time a two-step predictor-corrector method after MacCormack was used.

Boundary Conditions. The boundary treatment used at the inlet for the computations here presented is the so-called "capacitive boundary condition." It represents an inlet with constant total pressure, temperature, and imposed flow direction. A perturbation impinging on this border is reflected back into the flow field. The flow variables on this border are determined by the method of characteristics.

The boundary treatment used at the outlet corresponds in its quality to that chosen for the inlet. Here, the static pressure is imposed as a function of time.

Results and Discussion

Steady-State Flow. Two different steady-state flows were realized: With the exciter in its horizontal position the most downstream shock position is obtained; with the exciter in its vertical position the most upstream shock position is reached. In this way, the maximum and minimum outlet pressures are obtained for the inlet flow conditions under consideration here (M_1 = 0.70, p_1 = 1215 mbar, $p_{\mathrm{tot}\,1}$ = 1680 mbar). The Reynolds number during these tests was 1.0×10^6, based on the inlet flow and the throat height.

Figure 5 shows the steady-state pressure distribution on the side wall of the nozzle for both extreme positions for meas-

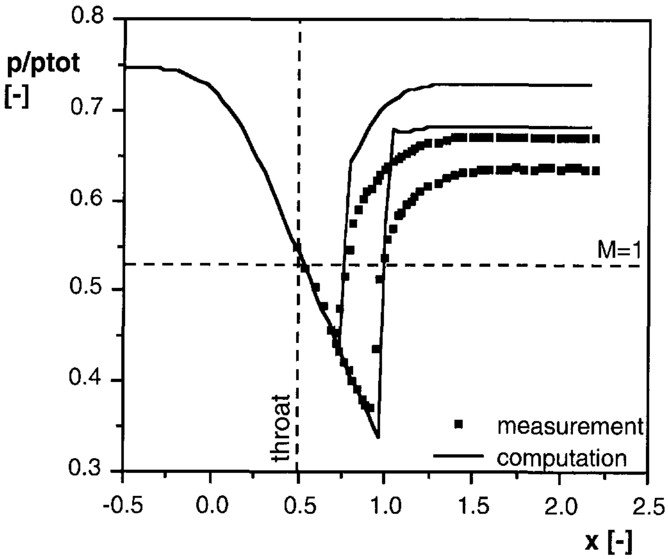

Fig. 5 Steady state pressure distribution (extreme values) on nozzle side wall together with numerical results (1 mesh size $\triangleq$ x = 0.0333 [−])

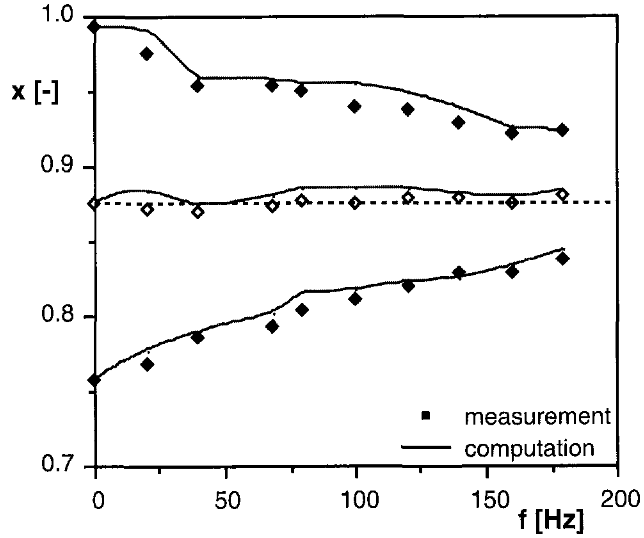

Fig. 6 Extreme shock positions for different excitation frequencies (measurement and numerical results)

urement and computation. The pressure jump measured at the side wall is not as sharp as expected. The reason is the interaction between the shock and the boundary layer at the side wall. In the middle of the channel the pressure behaves much more similar to the inviscid computations.

By using the static pressures measured in the aft of the nozzle for both extreme positions of the shock as input for the computation, it was observed that the shock positions found by the computation did not correspond with the shock positions measured. This was expected because of the presence of large boundary layers on the side walls. The losses due to the boundary layers mean an acceleration of the flow speed and a shock position more upstream than in an inviscid flow.

An inviscid computation cannot reproduce the effects of these boundary layers. For the later discussion of unsteady results, a correlation was made with the program by changing the back pressure until the computed shock position corresponds with the measured one. This was made for both extreme shock positions.

An estimation of the increasing displacement thicknesses of the boundary layers after the shock measured with a L2F velocimeter shows that the order of magnitude for the acceleration of the flow speed due to the smaller section corresponds to the difference of static pressure found by the above-mentioned iteration.

By different means, including Laser-2-Focus velocimeter and Pitot probes, large boundary layers on the side walls, up to 12 mm behind the shock, were observed. These large boundary layers lead to a flow information transport from the subsonic region downstream to the supersonic region upstream. The pressure transducers respond to the presence of the shock in a larger region than it is expected in a flow with smaller boundary layers.

Unsteady Flow Effects. Once the shock positions have been found for the two extreme "steady-state" operating conditions, the exciter is put into rotation. Figure 6 shows the extreme values of the shock positions measured with the line scan camera for different excitation frequencies. It is clearly seen that the amplitude of the shock decreases with increasing frequency. The mean shock position remains, for the present geometric and flow configuration, in the same location. The same observations can be made for the numerical results, which are presented in the same diagram.

The exit pressure did not show a constant amplitude for all excitation frequencies during the measurements. The amplitude decreased with increasing excitation frequency. This is normal since there must be a limit condition at very high frequencies where the pressure will be stable and the shock will not move any longer. The pressure amplitude at the outlet for the computation as it was found by the abovementioned iteration for 0 Hz excitation frequency was thus changed in the same scale as measured by the pressure transducer p_8 (Fig. 4). Appendix 2 shows the mean exit pressure and the pressure amplitudes used for the unsteady computations here presented.

The results of the computations fit very well the extreme shock positions measured. The agreement is given by both mean shock position and shock amplitude.

The evolution of the unsteady pressures measured by the different transducers on the side wall together with the shock positions as determined by the line scan camera are shown in Fig. 7 for three different excitation frequencies (f = 20, 80, 180 Hz). All results are presented within one excitation period. The positions of the pressure transducers are marked in the diagram with the shock position, i.e., the lower diagram. The presentation chosen allows us to correlate the signal of a pressure transducer with the motion of the shock wave with the aid of the vertical lines relating the upper and lower diagrams in each figure. This correlation shows clearly that the pressure transducers respond by a change in the pressure before the shock reaches the corresponding geometric locations. For small excitation frequencies the upstream influence distance corresponds to expected steady-state values (Inger, 1981). For higher frequencies the upstream influence distance increases for a shock moving downstream while it remains in the same order of magnitude as for small frequencies for the shock moving upstream, as can be seen from Fig. 7. For the highest excitation frequencies examined there no longer exists a domain of constant pressure while the shock is far away from the location of the pressure transducer.

It is clearly noted that the average shock movement is harmonic, whereas the pressure transducer response obviously is nonharmonic for the pressure transducers, which are directly under the influence of the moving shock. Nevertheless, it is also observed that the pressures have their minimum or maximum values at the same instant as the shock is in one of its extreme positions. The boundary layer increases the zone of influence of the shock, but there is no phase lag between the shock movement, as measured with the line scan camera and the Schlieren system, and the unsteady pressure evolution. This conclusion is valid for all frequencies up to 180 Hz.

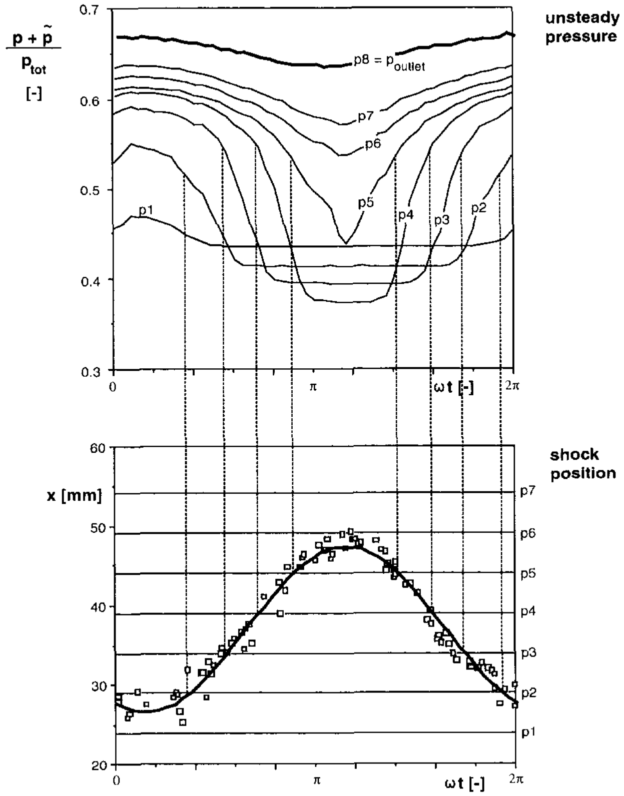

Fig. 7(*a*) Unsteady pressure evolution together with shock position (excitation frequency 20 Hz)

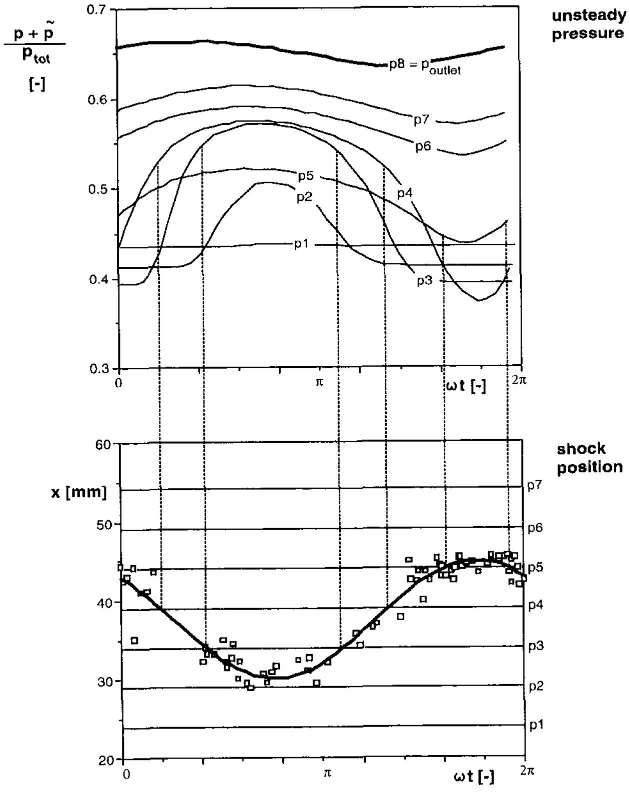

Fig. 7(*b*) Unsteady pressure evolution together with shock position (excitation frequency 80 Hz)

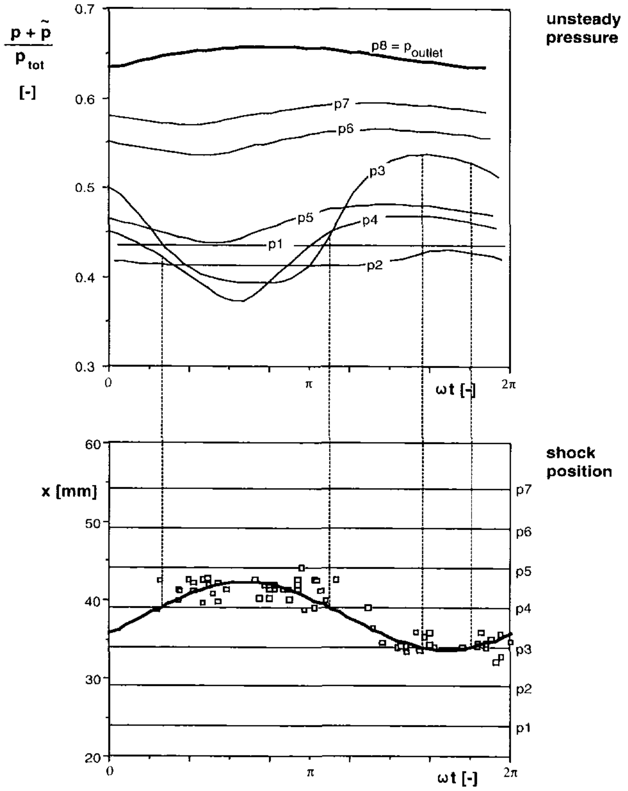

Fig. 7(*c*) Unsteady pressure evolution together with shock position (excitation frequency 180 Hz)

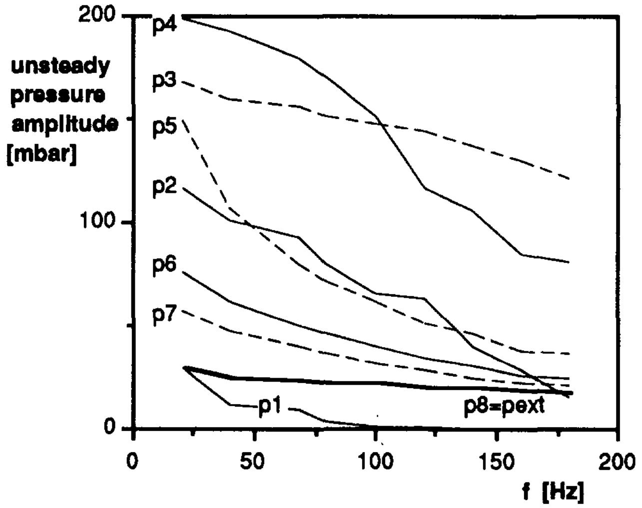

Fig. 8 Behavior of the pressure amplitude at the side wall for different excitation frequencies

It is seen from Fig. 7 that the pressure amplitude at a certain location decreases with increasing frequency. Figure 8 shows the evolution of the pressure amplitude on the side wall for the different pressure transducer locations. The pressure transducer p_1 is never situated under the moving shock: For small excitation frequencies it feels a small pressure perturbation, which comes through the boundary layer. For higher frequencies there is no signal at all, since this pressure transducer is always situated in the supersonic region and the distance to the extreme shock position is increasing with increasing fre-

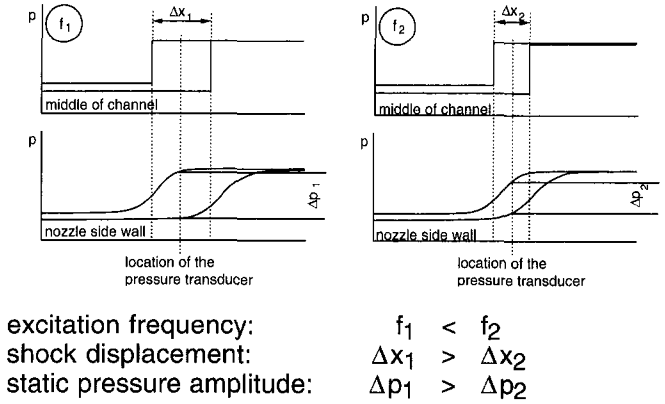

Fig. 9 Schematic comparison of the static pressure evolution in the middle of the channel and at the side wall for two different excitation frequencies

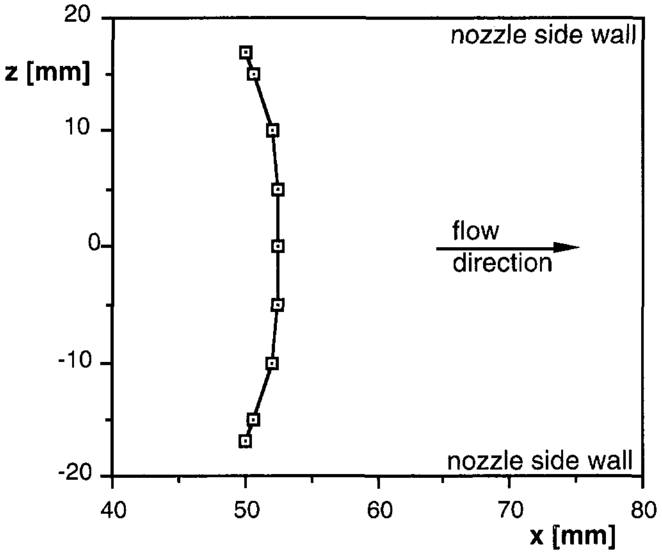

Fig. 10 Shock form over the channel width (measured with L2F velocimeter)

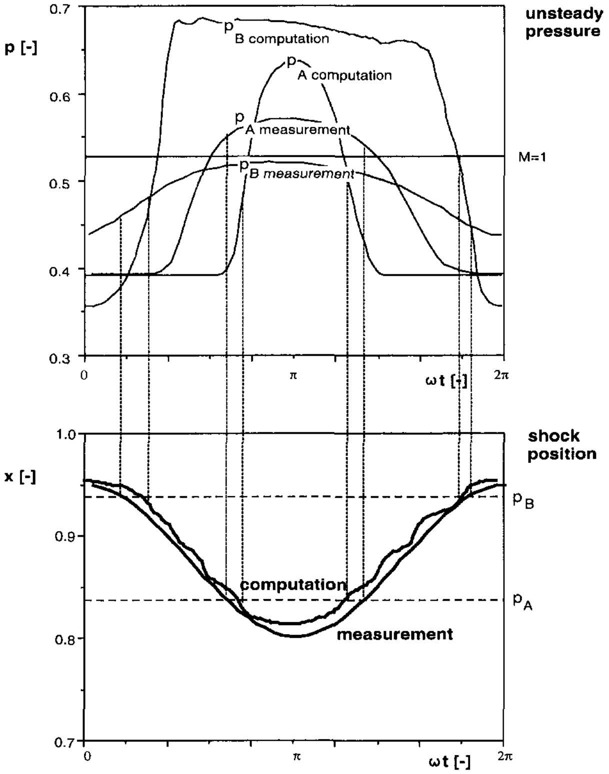

Fig. 11 Unsteady pressure evolution together with shock position (excitation frequency 80 Hz) (measurement and computation)

quency. The pressure transducers p_6 and p_7 are also never influenced directly by the shock. But since they are always located in the subsonic region, they show for high excitation frequencies, the same behavior as the pressure transducer p_8 which is situated far downstream of the shock; obviously with a certain phase lag corresponding to the time taken by the disturbances to travel from p_8 to p_7, p_6. The signals of pressure transducers, which are situated for all excitation frequencies under the moving shock, are more difficult to understand. The shock strength at this location is expected to be independent of the frequency. The flow speed before the shock is given by the shape of the nozzle. The shock velocity can be neglected compared to the flow velocity for the consideration of the strength of the shock. The reason for the diminution of the signal of the pressure transducers is the presence of the boundary layers. The pressure transducers measure at the side walls under a thick boundary layer of up to 12 mm. In Fig. 9 the evolution of the pressure under the shock is shown for the middle of the channel and for the side wall. For an increased excitation frequency the pressure variation at the location of the pressure transducer at the side wall is smaller even if the pressure variation in the middle of the channel remains unchanged.

From the curves in Fig. 8 it is seen that the amplitude of pressure transducer p_4 decreases faster than the signal of pressure transducer p_3. In Figs. 6 and 9 it can be seen that the mean shock position is closer to p_4 than to p_3. The pressure transducers p_3 and p_4 should thus behave opposite to what is seen in Fig. 8. Their behavior becomes more comprehensive by looking at the shape of the shock over the channel width (Fig. 10). The shock positions marked so far are the positions in the middle of the channel. At the side walls the shock is situated more upstream than in the middle of the channel. The mean shock position at the side walls is closer to p_3 than to p_4. This is also indicated by the behavior of the pressure transducers.

Figure 11 shows a comparison of the measured and the computed pressure distributions together with the shock position for the excitation frequencies of 80 Hz. The shock position for the computation shows waviness in its evolution. The shock position is found by an interpolation algorithm outgoing from the flow variables at the different mesh points to find the location where the flow speed corresponds to the sonic velocity. The small undulations that can be seen in the trace of the shock drawn in Fig. 11 probably appear because of an irregularity of the shock motion when the shock passes over a grid point. It can be seen that the magnitude of the measured pressures is lower than the computed pressures. This is also due to the influence of the viscous flow effects, which accelerate the flow, and which cannot be reproduced by the inviscid computation. The influence distance of the shock due to the presence of the boundary layers can clearly be seen by the comparison with the inviscid computations. The boundary layer transports the pressure information of the arriving shock in its subsonic part. In inviscid computations no boundary layer exists and what seems to be the influence distance corresponds simply to the distance between two points of the computational mesh. As soon as the shock passes the neighbor point the pressure begins to change. For the inviscid computations the influence distance seen in Fig. 11 has no physical meaning. The difference between measurement and computation shows the magnitude of the influence of the viscous flow effects.

Nevertheless, both measurement and computation, show the extreme values of the pressure evolution at the same moment as the shock reaches one of its extreme positions. There is no phase lag between shock movement and the pressure response.

Further information about the steady-state and unsteady results can be found from Ott (1992).

Conclusions

Experimental and numerical investigations on the behavior of an oscillating normal shock and the effects of this shock to the response of unsteady pressure transducers have been executed. The observations and conclusions made during this study are supposed to help for the interpretation and judgment of measurements and observations made in oscillating turbine or compressor cascades in the transonic flow domain. The numerical studies should help for the development of a numerical model for unsteady cascade computations. The observations and conclusions are as follows:

- For the reduced frequencies studied here ($k = 0->0.18$) it is permissible to consider the time-dependent pressure response on a wall as quasi-steady concerning the phase lag. No phase shift could be found between the oscillating shock wave and the side wall pressure response.
- The influence of the shock wave is noticed, due to the presence of the boundary layer, in the pressure response upstream of the shock position. This influence distance comports for low excitation frequencies as expected. For higher frequencies the upstream influence distance is larger for a shock moving forward in streamwise direction than for a shock moving backward.
- The amplitude of the shock oscillation decreases with increasing excitation frequency.
- The evolution of the unsteady pressure at the side wall under the normal shock passing the location of the transducer has a big nonharmonic behavior.
- Even if the viscous effects are important, an inviscid computational method can correctly reproduce the shock position and the shock amplitude.
- The comparison between measurement and computation of the pressure evolution shows differences due to viscous effects. Nevertheless for both measurement and computation, there is no phase shift between pressure response and shock movement found.

Acknowledgments

The present investigation was carried out as part of a research project funded by ASEA Brown Boveri, Baden, Switzerland (under the supervision of Dr. K. Vogeler) with financial support of the Swiss government. This support and the authorization to publish the results are kindly acknowledged.

References

Adamson, T. C., and Liou, M. S., 1977, "Unsteady Motion of Shock Waves in Two Dimensional Transonic Channel Flows," Report No. UM-014534-F, Department of Aerospace Engineering, University of Michigan, Ann Arbor, MI.

Adamson, T. C., and Liou, M. S., 1978, "Unsteady Motion of Shock Waves in Two Dimensional Transonic Channel Flows," Report No. UM-015411-F, Department of Aerospace Engineering, University of Michigan, Ann Arbor, MI.

Anderson, W. K., Thomas, J. L., and Rumsey, C. L., 1985, "Extension of Applications of Flux-Vector Splitting to Unsteady Calculations on Dynamic Meshes," AIAA Paper No. 85-0122.

Anderson, W. K., Thomas, J. L., and van Leer, B., 1987, "A Comparison of Finite Volume Flow With Shock Waves," AIAA Paper No. 87-1152.

Araki, T., Okamoto, Y., Ohtomo, F., and Arinobu, M., 1981, "Self-Excited Flow Oscillation in the Low Pressure Steam Turbine Cascade," *Communication de L'ITA/EPFL*, No. 10, pp. 171-186.

Bölcs, A., Fransson, T. H., and Platzer, M. F., 1989a, "Numerical Simulation of Inviscid Transonic Flow Through Nozzles With Fluctuating Back Pressure," ASME JOURNAL OF TURBOMACHINERY, Vol. 111, pp. 169-190.

Bölcs, A., Fransson, T. H., and Schläfli, D., 1989b, "Time-Dependent Measurements on Vibrating Annular Turbine Cascades Under Various Steady-State Conditions," *Unsteady Aerodynamic Phenomena in Turbomachines*, AGARD Conference Proceedings No. 468, pp. 19.1-19.14, Luxembourg, Aug. 28-30.

Bölcs, A., Fransson, T. H., and Körbächer, H., 1991, "Time-Dependent Pressure Fluctuations on an Oscillating Turbine Cascade at Transonic Off-Design Flow Conditions," *Proceedings of the 6th International Conference on Aeroelasticity in Turbomachines*, Sept. 10-15, Notre Dame, IN.

Buffum, D. H., and Fleeter, S., 1989, "Experimental Investigation of Transonic Oscillating Cascade Aerodynamics," AIAA Paper No. 89-0321.

Buffum, D. H., and Fleeter, S., 1990, "Oscillating Cascade Aerodynamics by an Experimental Influence Coefficient Technique," *Journal of Propulsion*, Vol. 6, No. 5, pp. 612-620.

Buffum, D. H., and Fleeter, S., 1993, "Wind Tunnel Wall Effects in a Linear Oscillating Cascade," ASME JOURNAL OF TURBOMACHINERY, Vol. 115, pp. 147-156.

Carstens, V., 1991, "Transonic Unsteady Aerodynamics and Aeroelasticity," presented at the 73rd Meeting of the AGARD Structures and Materials Panel, San Diego, CA, Oct. 7-11.

Edwards, J. A., 1987, "Surface Pressure Distributions in an Unsteady Shock/Boundary Layer Interaction," Thesis, Wolfson College, Cambridge, United Kingdom.

Ezzat, A., Fransson, T. H., and Jolles, F., 1989, "Self-started Blade Vibrations in an Annular Turbine Cascade Operating at Transonic and Supersonic Mach Numbers," ASME IGTI-Vol. 4, G. K. Serovy, T. H. Fransson, and J. Fabri, eds.

Fransson, T. H., 1992, "Analysis of Experimental Time-Dependent Blade Surface Pressures From an Oscillating Turbine Cascade Using the Influence-Coefficient Technique," *Journal of Physics III, France*, Apr., pp. 575-594.

Gerolymos, G. A., 1993a, "Advances in the Numerical Integration of the 3-D Euler Equations in Vibrating Cascades," ASME JOURNAL OF TURBOMACHINERY, Vol. 115, pp. 781-790.

Gerolymos, G. A., 1993b, "Coupled 3-D Aeroelastic Stability Analysis of Bladed Disks," ASME JOURNAL OF TURBOMACHINERY, Vol. 115, pp. 791-799.

Hanamura, Y., and Yamaguchi, K., 1988, "An Experimental Investigation on the Flutter of the Cascade of Turbomachinery in the Transonic Flow," *Journal of the Faculty of Engineering*, The University of Tokyo (B), Vol. XXXIX, No. 3, pp. 311-338.

Inger, G. R., 1981, "Application of a Shock-Turbulent Boundary-Layer Interaction Theory in Transonic Flowfield Analysis," in: *Transonic Aerodynamics*, Vol. 81, D. Nixon, ed., AIAA, ISBN 0-915928-65-5.

Liang, S. M., Tsai, C. J., and Ho, C. K., 1992, "Numerical Investigation of Unsteady Transonic Nozzle Flows," *AIAA Journal*, Vol. 30, No. 2, pp. 566-568.

Ott, P., 1992, "Oszillierender senkrechter Verdichtungsstoß in einer ebenen Düse," *Communication du Laboratoire de Thermique Appliquée et de Turbomachines*, No. 18, EPF-Lausanne.

Ott, P., Bölcs, A., and Fransson, T. H., 1992, "Experimental Study of an Oscillating Normal Shock Wave in a Nozzle," *Proceedings of the 11th Symposium on Measuring Techniques in Transonic and Supersonic Flows in Cascades and Turbomachines*, Sept. 14-15, München, Federal Republic of Germany.

Széchényi, E., Cafarelli, I., Notin, C., and Girault, J. P., 1984, "A Straight Cascade Wind-Tunnel Study of Fan Blade Flutter in Started Supersonic Flow," *Proceedings of the Third International Symposium on Unsteady Aerodynamics of Turbomachines and Propellers*, Cambridge, United Kingdom, Sept., pp. 447-458.

Széchényi, E., 1985, "Fan Blade-Single Blade Instability or Blade to Blade Coupling?" ASME Paper No. 85-GT-216.

Usab, W. J., and Verdon, J. M., 1991, "Advances in the Numerical Analysis of Linearized Unsteady Cascade Flows," ASME JOURNAL OF TURBOMACHINERY, Vol. 113, pp. 633-643.

Verdon, J. M., 1989, "The Unsteady Aerodynamic Response to Arbitrary Modes of Blade Motion," *Journal of Fluids and Structures*, No. 3, pp. 255-274.

Whitehead, D. S., and Newton, S. G., 1985, "A Finite Element Method for the Solution of Two-Dimensional Transonic Flows in Cascades," *International Journal for Numerical Methods in Fluids*, Vol. 5, pp. 115-132.

Whitehead, D. S., 1990, "A Finite Element Solution of Unsteady Two-Dimensional Flow in Cascades," *International Journal for Numerical Methods in Fluids*, Vol. 10, pp. 10-34.

APPENDIX 1

Nozzle Form

The shape of the nozzle is a modified derivation of that used by Adamson and Liou (1977, 1978). The height of the nozzle is computed by the following formula:

$$H(x) = H_{\text{Entry}} + \frac{1}{1+3\cdot\epsilon^2}\cdot\epsilon^2\cdot(f(x)-3) \qquad \text{(A1.1)}$$

with

$$f(x) = \begin{cases} 3 & -0.5 \le x \le -\frac{1}{6} \\ \frac{27}{13}\,[3(x-0.5)+2]^4 - \frac{48}{13}\,[3(x-0.5)+2]^3 + 3 & -\frac{1}{6} \le x \le \frac{1}{6} \\ \frac{18}{13}\,[3(x-0.5)]^2 & \frac{1}{6} \le x \le \frac{5}{6} \\ \frac{27}{13}\,[3(x-0.5)-2]^4 + \frac{48}{13}\,[3(x-0.5)-2]^3 + 3 & \frac{5}{6} \le x \le \frac{7}{6} \\ 3 & \frac{7}{6} \le x \le 1.5 \end{cases} \qquad \text{(A1.2)}$$

This places the throat of the nozzle at $x = 0$. The value ϵ was chosen as follows:

$$\epsilon = 0.181568259 \qquad \text{(A1.3)}$$

For the entry height of 80 mm we have

$$H_{\text{entry}} = 0.8[-] \qquad \text{(A1.4)}$$

The values for H and for x then are multiplied by 100 to obtain the coordinates in mm for the executed nozzle form in the chosen scale.

APPENDIX 2

Exit Pressures

The exit pressures found by an iteration with the objective to obtain the same extreme shock positions as measured were 0.68300 [–] and 0.73028 [–]. The mean exit pressure for the unsteady computations was thus set to p = 0.70664 [–] and the exit pressure amplitude for steady state to 0.02364. With the pressure amplitudes measured for increasing excitation frequency, a factor was determined using the pressure difference for steady-state pressure as reference. The pressure amplitudes for the computations for different excitation frequencies were found by applying this factor to the steady-state pressure difference found by the iteration. The pressure amplitudes used during the computations are presented in Table 1.

Table 1 Exit pressure amplitudes for different excitation frequencies

Frequency [Hz]	Exit pressure amplitudes measurement [mbar]	computation [-]
0	32.5	0.02364
20	31.0	0.02255
40	26.5	0.01927
68	25.5	0.01856
80	24.0	0.01745
100	24.0	0.01745
120	22.0	0.01600
140	22.0	0.01600
160	20.5	0.01492
180	19.5	0.01418

Leading Edge Separation Bubbles on Turbomachine Blades

R. E. Walraevens[1]

N. A. Cumpsty

Department of Engineering,
Whittle Laboratory,
Cambridge University,
Cambridge, United Kingdom

Results are presented for separation bubbles of the type that can form near the leading edges of thin compressor or turbine blades. These often occur when the incidence is such that the stagnation point is not on the nose of the aerofoil. Tests were carried out at low speed on a single aerofoil to simulate the range of conditions found on compressor blades. Both circular and elliptic shapes of leading edge were tested. Results are presented for a range of incidence, Reynolds number, and turbulence intensity and scale. The principal quantitative measurements presented are the pressure distributions in the leading edge and bubble region, as well as the boundary layer properties at a fixed distance downstream, where most of the flows had reattached. Reynolds number was found to have a comparatively small influence, but a raised level of free-stream turbulence has a striking effect, shortening or eliminating the bubble and increasing the magnitude of the suction spike. Increased free-stream turbulence also reduces the boundary layer thickness and shape parameter after the bubble. Some explanations of the processes are outlined.

Introduction

It has now become standard practice to use CFD in the design of all types of turbomachine. In some cases the agreement between predicted and measured pressure ratio and efficiency is excellent, but it is not uncommon for the efficiency to be in error by perhaps 1 or 2 percent. This discrepancy, though small, is enough to render the calculation process unable to replace expensive experimental testing. The principal cause of these occasional inaccuracies is believed to lie with the empirical inputs that are still necessary to represent the turbulent nature of the flow; among the most significant source of inaccuracy in these is the criterion for laminar-turbulent transition. Transition in turbomachines is still a subject of very active research and discussion, for example, Mayle (1991) and Walker (1993). Transition is therefore not sufficiently well developed that a sound and plausible model may be incorporated into a Navier-Stokes solver designed for the solution of flows in complicated turbomachinery geometries.

There are special problems associated with transition in turbomachinery: the high levels of free-stream turbulence and disturbance, the strong nondimensional pressure gradients and Reynolds numbers based on chord, which are typically one or two orders of magnitude less than aircraft wings. Of particular relevance to this paper is the sharpness of the leading edge region for most compressor blades and many low-pressure turbine blades. For example, a typical NACA 65 compressor blade, with a maximum thickness equal to 5 percent of chord, has a leading edge radius of only 0.4 percent of chord[2]; for double circular arc blades, such as are commonly used for transonic applications, the leading edge is much finer than this. With these sharp leading edges it is common to get leading edge separation bubbles and transition is therefore completed in the first few percent of chord.

The majority of three-dimensional calculation methods assume that transition occurs at the leading edge and empirical coefficients are adjusted to give reasonable agreement with measured loss at some conditions, typically near where minimum loss occurs. At other conditions the loss will not be well predicted and may be seriously underestimated. Figure 1 illustrates this, comparing two-dimensional measurements of loss obtained in a cascade with a two-dimensional calculation carried out by Calvert (1989) incorporating a well-tested boundary layer method. The calculated and measured losses agree closely near their minimum, but the calculation does not adequately predict the rise in loss with incidence. This is because the calculation does not take proper account of the comparatively thick turbulent boundary layer that exists after the flow reattaches downstream of the leading edge separation bubble. In Fig. 1 it can be seen that setting the boundary layer Reynolds number based on momentum thickness to be 500 at the leading edge gives some improvement; this is not only arbitrary but it does not give agreement at the highest incidence shown.

---

[1] Permanent affiliation: Institut für Strahlantriebe und Turboarbeitsmaschinen, RWTH Aachen, Federal Republic of Germany.

Contributed by the International Gas Turbine Institute and presented at the 38th International Gas Turbine and Aeroengine Congress and Exposition, Cincinnati, Ohio, May 24-27, 1993. Manuscript received at ASME Headquarters February 19, 1993. Paper No. 93-GT-91. Associate Technical Editor: H. Lukas.

[2] The NACA-65 aerofoil is normally defined with maximum thickness equal to 10 percent of chord and for this the leading edge radius is specified to be 0.687 percent of chord. Leading edge radius for an elliptic shape, such as the forward part of a NACA-65 aerofoil, is proportional to the square of the fineness ratio, and should therefore vary as the square of the thickness-chord ratio. In fact it is common to specify a leading edge radius proportional to thickness but, because of the difficulty of manufacture, it is not clear how often the specified values are achieved.

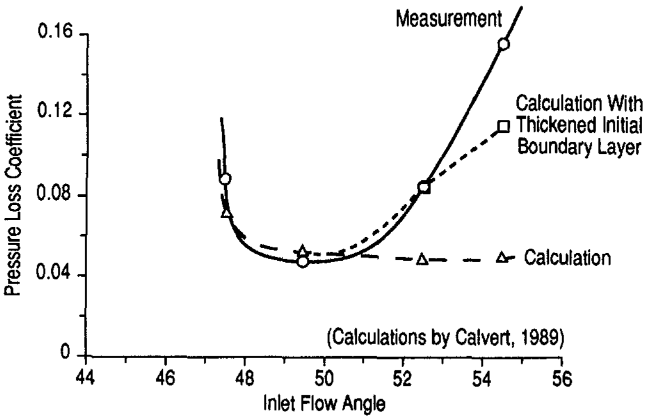

Fig. 1 Calculation and measured loss at trailing edge for two-dimensional cascade of blades

Separation bubbles have been studied for many years: Gaster (1967), Horton (1969), Roberts (1975), and Arena and Mueller (1980) are a few of the more recent papers. The basic structure is easily described. A strong adverse pressure gradient can cause a laminar boundary layer to separate, but once separated the shear layer is highly unstable and the flow can rapidly undergo transition. The turbulent flow entrains more fluid than the laminar flow, and as a result, the turbulent shear layer bends toward the solid wall, causing the flow to reattach as a turbulent boundary layer. A small plateau of almost uniform static pressure is normally observed, corresponding to the region where the flow is separated in the bubble and no pressure gradient can be supported. For so-called short bubbles, it has normally been assumed that the bubble has a small effect on the local static pressure on the aerofoil, whereas with long bubbles the reattachment takes place so far from separation that the overall pressure distribution is very different.

A special feature of the leading edge separation bubbles, which are the subject of this paper, is their closeness to the leading edge, so reattachment will normally occur within less than 5 percent of chord from the leading edge. Moreover, the leading edge bubble brings about an enormous alteration in the local static pressure distribution. An inviscid calculation of the flow around blades predicts a very large suction "spike" near the leading edge on the suction surface at all incidences significantly greater than that which puts the stagnation point on the leading edge (see Fig. 4.24 of Cumpsty, 1989). The suction spike is predicted because, according to the inviscid calculation, the flow leaving the stagnation point is accelerated very rapidly and is made to follow a curved path of small radius, the leading edge radius. The very steep deceleration on the downstream side of the spike would be more than sufficient in most cases to cause separation of the laminar boundary layer. Separation of the flow does take place and, if the incidence is not too large, the flow reattaches a short distance downstream to form a separation bubble. A sketch of the flow around a leading edge is shown in Fig. 2. Because the bubble effectively increases the radius of curvature followed by the flow in the leading edge region, it has a pronounced effect on the local pressure field, and the suction spike is greatly reduced compared with that predicted by inviscid methods.

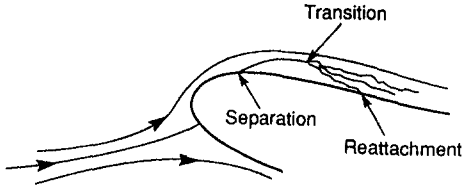

Fig. 2 Schematic of leading edge separation bubble

Leading edge bubbles can originate in a different way to that discussed in the previous paragraph. Many aerofoil sections for compressors and turbines were, and often still are, designed with a discontinuity in curvature in the leading edge region. A common design is a circular leading edge drawn in to meet the two surfaces; compared to the radius of the leading edge the suction and pressure surfaces are then almost flat. This rather crude design is understandable in view of the small size of many blades, for which a better shape might be difficult or impossible to produce economically. Furthermore the effect of manufacturing deficiencies or in-service damage may be to make the blade section worse that the design shape. It is perhaps useful to make the small size more concrete with an illustration of a typical blade, a NACA-65 blade of 5 percent thickness-chord ratio and 25 mm (1 in.) chord. For such a blade the leading edge radius is specified to be only 0.09 mm (0.0034 in.), a very small radius to make accurately. For blades with a discontinuity in surface curvature in the leading edge region the flow can separate at the point of discontinuity, forming a bubble downstream. This case is demonstrated very clearly by Arena and Mueller (1980). Aerofoils with either a circular or an elliptic leading edge joined onto flat suction and pressure surfaces are the subject of this paper.

In discussing the formation of separation bubbles, care must be taken to refer to incidence relative to that at which the stagnation point is on the nose of the aerofoil. For lifting blades this is *not* in general the condition of zero incidence, $i = 0$, when the direction of the camberline at the leading edge coincides with the direction of the incoming flow measured some considerable way upstream. The effect of the pressure

Nomenclature

c_p = static pressure coefficient $= (p - p_\infty)/(p_{01} - p_1)$
H_{12} = boundary layer form or shape parameter $= \delta^*/\theta$
i = incidence (angle between inlet flow direction and camberline at leading edge)
i_{eff} = effective incidence, see Fig. 3
L_{turb} = turbulence length scale at inlet derived from autocorrelation
M = Mach number
p = local static pressure
p_∞ = static pressure well away from the aerofoil leading edge
p_1 = inlet static pressure
p_{01} = inlet stagnation pressure
r = leading edge radius ($r = t/2$ for circular leading edge)
Re_t = Reynolds number based on inlet velocity and leading edge half-thickness $= t/2$
Re_θ = Reynolds number based on local free-stream velocity and θ
s = distance around surface from nose of leading edge
t = thickness of leading; for present tests thickness of plate forming aerofoil
Tu = inlet turbulence intensity
u = velocity inside boundary layer
U = velocity at boundary layer edge
U_1 = inlet velocity
y = distance normal to surface
δ^* = boundary layer displacement thickness
η = nondimensional distance from surface (used for Blasius laminar profile)
θ = boundary layer momentum thickness
ν = kinematic viscosity

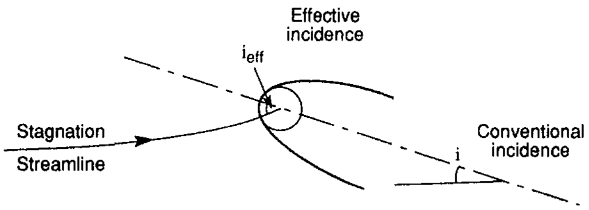

Fig. 3 Definition of effective incidence angle

field surrounding the aerofoil is to curve the incoming streamlines, including the stagnation streamline. (This is discussed by Cumpsty, 1989, in connection with Fig. 4.23.) In the immediate vicinity of the leading edge the crucial flow variable of the free stream is the position of the stagnation point relative to the nose. The stagnation streamline is normal to the surface where it collides with the surface. For a circular leading edge, or one for which it may be approximated by a circle very close to the leading edge, this may be characterized by the effective incidence, i_{eff}, shown in Fig. 3.

The principal quantities that were measured, and that form the body of this paper, are the distribution of static pressure coefficient c_p and the boundary layer integral properties (displacement thickness δ^* and momentum thickness θ). Each is a function of distance around the surface from the nose of the aerofoil, s. The boundary layer thicknesses and s may be made nondimensional by the leading edge half-thickness, $t/2$, which is equal to the leading edge radius for the circular leading edge aerofoils used here.

The range of variables that determine c_p for a compressor or turbine blade row are the incidence, the Mach number, the Reynolds number of the blade, the incoming turbulence level and turbulence scale, and the blade row geometry. To define the blade row geometry in two dimensions for conventional blading requires the camber, stagger, and solidity to be given. In planning a test program to examine the behavior of leading edge separation bubbles, it might therefore be imagined that a series of cascades (different camber, stagger, and solidity) should be tested at a range of incidences, Mach numbers, Reynolds numbers, and turbulence levels. All the current work was carried out for flows that are effectively incompressible, and the dependence on Mach number is therefore dropped. The program is greatly simplified once it is recognized that the flow in the immediate vicinity of the leading edge is determined only by the effective incidence i_{eff} defined above. For a particular geometry of leading edge tests are required over a range of effective incidence and then, by interpolation, these can be related to the effective incidence on the blade being designed or being calculated. In using effective incidence all the influence of camber, stagger, solidity, and conventional incidence is included, but the connection between these and effective incidence is predominantly inviscid and therefore easy to calculate. For any particular geometry there is a relation between i_{eff} and the conventional incidence i; in the present paper all tests are referred to in terms of the conventional incidence for the aerofoil.

The formal dependence for the pressure coefficient can then be written

$$c_p(2s/t) = f(i_{\text{eff}}, \text{Re}, Tu, L_{\text{turb}})$$

and similar expressions would be written for any of the boundary layer properties. Tu is the conventional turbulence intensity for the inlet free-stream flow and L_{turb} is its integral length scale. The Reynolds number that characterizes the flow about the leading edge must be based on a relevant dimension of the leading edge and the undisturbed inlet velocity. For circular leading edges the leading edge radius would provide the natural length scale, but for consistency with noncircular leading edges it is convenient to base Reynolds number on the half thickness of the leading edge, giving $\text{Re}_t = U_1 t/2\nu$, and this is used everywhere for consistency. As noted above the half-thickness of the circular leading edge is equal to the leading edge radius.

It has been widely recognized for some time that to represent flows inside turbomachines realistically the turbulence level needs to be much higher than is normal in wind tunnels. There has, however, been very little attempt to find the turbulence levels and scales inside machines. Some recent measurements have been made in multistage low-speed compressors with blading of current design (Camp, 1992). In these tests great care has been taken to remove the periodic unsteadiness from the overall so as to leave true turbulence. These show that at inlet to a blade row the level of turbulence is about 6 percent and the length scale is about 3 percent of blade chord. For a NACA 65 blade of 5 percent thickness-chord ratio the leading edge radius is specified at 0.34 percent of chord, so the length scale is about eight times leading edge radius. For a 5 percent thick C4 blade, which has a leading edge radius of 0.6 percent chord, the corresponding scale should be about five times leading edge radius. Some double circular arc blades have much thinner leading edges, while it is common with so-called supercritical blades to have fairly thick leading edges. It would seem that a range of turbulence scales of between, say, one and eight times the leading edge radius would cover most of the relevant range and allow the sensitivity to scale to be gaged.

Experimental Facilities and Technique

Each of the three aerofoils used had a chord of 460 mm and was mounted in the middle of the test section, height 680 mm, width 460 mm, and length 1000 mm. The aerofoil was pivoted not far from the leading edge to allow incidence to be adjusted and tests were carried out in the range ±5 deg. The tunnel could be operated at speeds up to 35 m/s at Mach number not exceeding 0.1. Three aerofoils were tested, two with circular leading edges and one with an elliptic leading edge. One of the aerofoils with circular leading edge had a half-thickness (which is the leading edge radius) of 3.0 mm, the other had a half-thickness of 6.3 mm. The elliptic leading edge aerofoil half-thickness was 6.6 mm thick (equal to the minor axis) and the major axis was 12.5 mm, a ratio of 1.89. This fineness ratio was chosen on the basis of Davis (1974) to be just sufficient to avoid laminar separation at zero incidence. With this combination the radius of curvature in the immediate vicinity of the elliptic leading edge was 3.5 mm, very similar to the value for the thinner aerofoil with a circular leading edge.

With no turbulence generating grid installed the turbulence level inside the working section was less than 0.5 percent. To raise the incoming turbulence a biplanar grid was inserted upstream of the working section. A total of eight different grids were used for which the intensities varied between 1.9 and 10 percent. Most of the tests were carried out with a particular grid installed 290 mm ahead of the leading edge, which gave an intensity of 5 percent and a length scale of 6 mm at the leading edge plane. (The turbulence quantities were measured at the position of the leading edge, but with the aerofoil removed, and integral length scale was estimated from autocorrelations.)

The circular leading edge aerofoils had static pressure tappings set into the surface around the curved part of the leading edge and the flat part downstream. For the elliptic leading edge, a technique used successfully by Bindon (1987) was adopted. In this nine longitudinal narrow, shallow slots were machined around the leading edge region and some way downstream on the flat part of the aerofoil. Each slot had a separate tube leading to a Scanivalve port and thence to a manometer. During tests the slots were covered with thin self-adhesive tape. To make a pressure measurement the tape was pricked with a sharp needle and in this way pressure measurements could be obtained at nine positions (i.e., one for each slot). Nine, however, was a much smaller number than the total needed to get

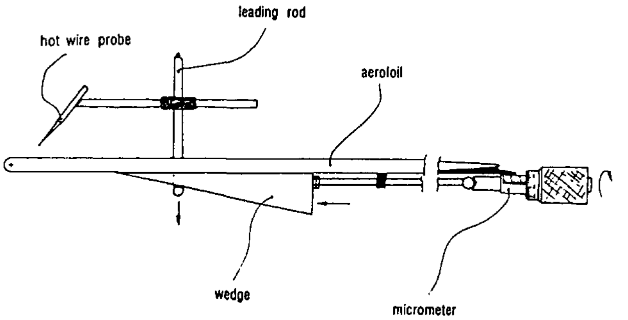

Fig. 4 **Manually driven traverse gear attached to aerofoil. Leading rod held under tension by a wire attached to a spring outside the tunnel.**

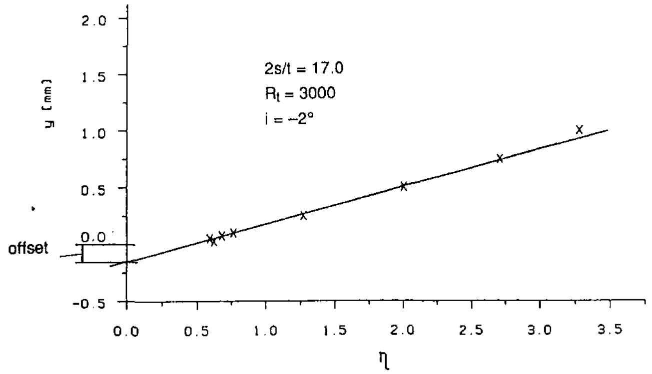

Fig. 5 **Position correction using laminar profile in zero pressure gradient: *y* from micrometer scale plotted against η derived from *u/U* for Blasius profile**

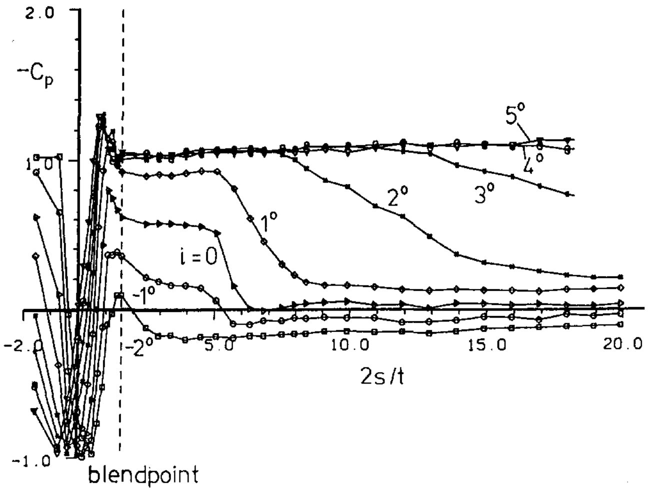

Fig. 6 **Distribution of c_p about circular leading edge for a range of incidence: Re_t = 3000; *Tu* < 0.5 percent**

adequate definition of the pressure field. For efficiency the pressures would be measured at all the combinations of Reynolds number and incidence required before replacing the tape and pricking another set of holes at different positions.

Velocity profiles were measured with a subminiature hot wire; the wire length was about 1 mm and the wire diameter about 5 μm. The wire was calibrated *in situ* in the free stream and compensation for variation in free stream temperature was obtained using the Bearman (1971) expression. A manually operated traverse gear, shown in Fig. 4, was mounted on the aerofoil for maximum rigidity and the avoidance of vibration problems. The wedge was driven with a micrometer head and, combined with the slant of the wedge, this provided resolution in position of about 3 μm.

Although the movement of the hot wire was known very precisely, the effective position of the wire relative to the surface was more difficult to obtain, and without some special provision the accuracy of the profile measurements would have been seriously compromised. To find the true effective wire position, advantage was taken of the ability to adjust the incidence of the aerofoil without moving or altering the setting of the traverse gear (except by turning the micrometer head). When the aerofoil was set at a negative incidence of 2 deg the pressure was very nearly uniform on its upper surface and the boundary layer was laminar. The boundary layer was therefore expected to approximate a Blasius profile closely, for which the form $u/U = u/U(\eta)$ is well established and the results tabulated. The nondimensional variable $\eta = y(Ux/\nu)^{1/2}$ is proportional to the distance from the surface y. The procedure for determining the effective hot-wire position is to traverse the hot wire toward the surface and measure the ratio of local to free-stream velocity, u/U. From the measured u/U the value of η corresponding to a Blasius profile can be found from the accurate tabulation of the profile. The values of η are then plotted versus the scale readings from the micrometer and, if the assumption of a Blasius profile is correct, a straight line should result. Figure 5 shows an example of this, from which it is easy to find the offset needed to the scale readings. In the example shown in Fig. 5 the offset is about 0.2 mm. The typical accuracy of the technique was about 0.025 mm. The only remaining inaccuracy with this technique is associated with differences in wall effect between laminar and turbulent boundary layers.

All pressure and hot-wire data were digitized and stored on a personal computer. In the case of the hot-wire data several seconds worth of raw data were recorded at each condition to enable a subjective impression of the condition of the flow to be obtained and to allow detailed analysis at a later data.

Results

Static Pressure Measurements. The pressure coefficient for the circular leading edge aerofoil are shown in Fig. 6 for a range of incidences from -2 to $+5$ deg. (Note that in all the plots of experimental pressure coefficient $-c_p$ is shown, so the suction peaks appear positive.) These were for a Reynolds number based on plate half thickness, Re_t, of 3000 and for a low-turbulence inlet flow. At zero incidences the flow can be seen to separate close to the blend point, the position where the circular leading edge meets the flat surfaces. This is evident from the uniform pressure plateau immediately downstream of the separation. As the flow reattaches to the surface, the bubble is formed and the pressure increases. At higher incidence the separation appears to occur at a similar position, but the bubble becomes longer and the level of uniform pressure in the plateau becomes lower. At $i = 3$ deg the flow shows a trend to reattach a long way downstream, but for higher incidence the flow appears fully separated. Although it is difficult to see in the figure, the suction peak remained virtually constant for incidences of 2 deg and upward, implying that the shape of the shear layer very close to the leading edge was similar in all cases.

Figure 7 shows the effect of Re_t in the range 1000 to 5000 at $i = 1$ deg for the circular leading edge with low free-stream turbulence. The bubble does shorten and the pressure in the bubble is lowered as the Reynolds number increases, but the effect is comparatively small. A separate series of tests were run at lower Reynolds of 250, 500, and 750 with the same aerofoil and low inlet turbulence. Although not presented here, these showed that at very low Reynolds numbers the plateau region associated with the separation bubble could be absent, and instead a more or less smooth and continuous increase in static pressure could occur downstream of the minimum in what is assumed to be laminar reattachment. This was evident

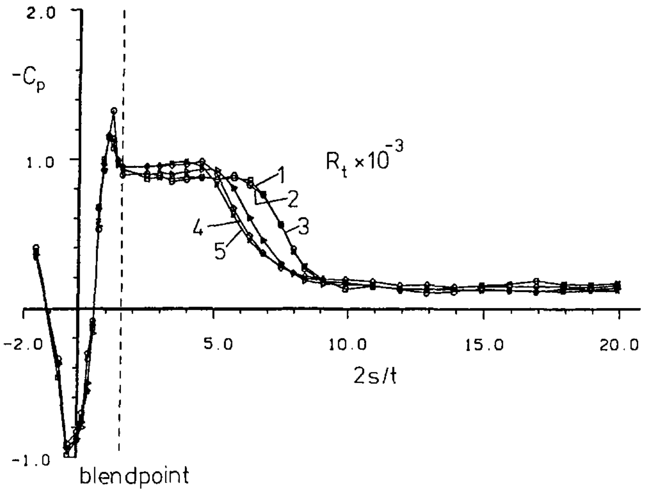

Fig. 7 Distribution of c_p about *circular* leading edge for range of Reynolds number: Incidence = 1 deg; *Tu* < 0.5 percent

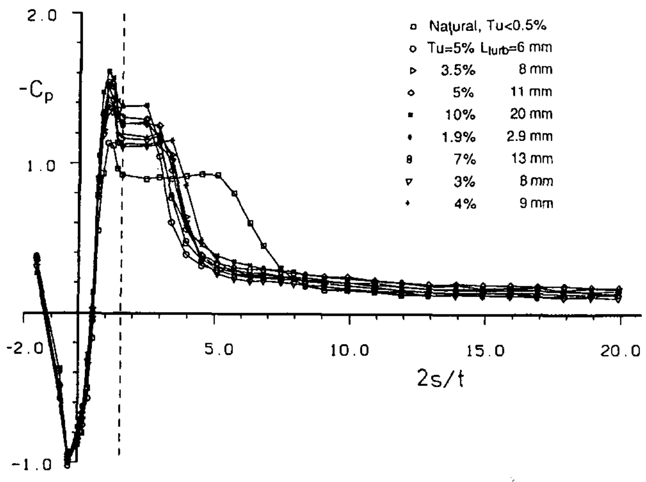

Fig. 9 Distribution of c_p about circular leading edge for a range free-stream turbulence level: Incidence = 1 deg; Re_t = 3000

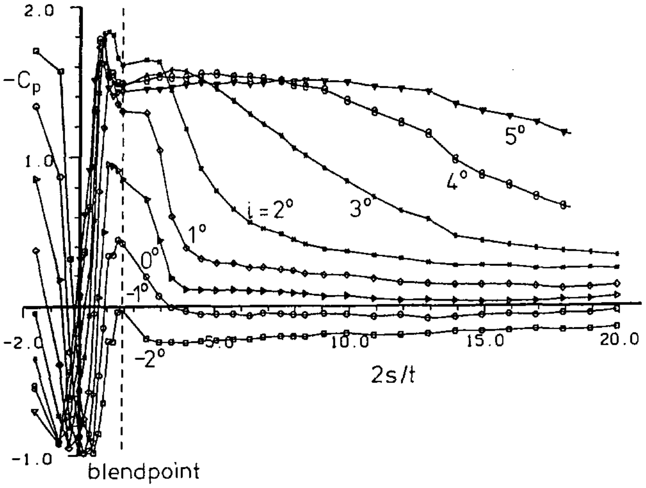

Fig. 8 Distribution of c_p about circular leading edge for a range of incidence: Re_t = 3000; turbulent free stream, *Tu* = 5 percent, L_{turb} = 6 mm

for $i = 0$ at $Re_t = 750$ and for $i = 1$ deg at $Re_t = 250$. The length needed for the reattachment process to occur was substantially longer, perhaps 50 percent longer, when a clear bubble with a plateau did not occur.

Figure 8 is the counterpart to Fig. 6 when the free-stream turbulence was increased to about 5 percent with a length scale of about 6 mm. The bubbles are only about half the length of the corresponding ones with low free-stream turbulence, the suction peak is up to about 50 percent greater, and the static pressure of the plateau is lower. The shorter bubble and the lower pressure in the bubble are related because a shorter (and smaller) bubble will force the flow around the leading edge to follow a tighter radius of curvature. The greater suction peak with the turbulent free stream, particularly clear for $i = 2$ deg incidence, indicates that the bubble exerts a strong influence on the local free-stream flow upstream of the point of separation; in other words the blockage of the bubble is enough to affect the local streamline radius of curvature. It may also be noted that, as a result of the higher free-stream turbulence, reattachment takes place up to higher incidence: At $i = 3$ deg reattachment is complete at about $2s/t \approx 17$, reattachment is going to occur for $i = 4$ deg and may also happen a long way downstream for $i = 5$ deg. In Fig. 8 it is also apparent that at zero incidence there is no clear plateau region and transition of the shear layer presumably takes place more or less immediately.

Figure 9 shows the pressure distribution measured around the circular leading edge when eight different turbulence-generating grids were used, together with results for low free-stream turbulence. The highest level of turbulence from the grids was 10 percent with a scale of 20 mm (nearly seven times the leading edge radius) while the lowest level was about 2 percent with a scale of 2.9 mm (comparable to the leading edge radius). The individual traces are hard to see in Fig. 9 but the two main features are clear. The first is that the pressure distributions for the cases with elevated free-stream turbulence all have a similar bubble length, which is much less than the length with low free-stream turbulence. The second, and related, observation is that the suction peak is greater and the bubble plateau pressure is at lower level when the free-stream turbulence is high. More careful scrutiny shows that the scale of the turbulence seems to have little effect, but the level of turbulence is significant and the greatest suction peak occurs at the highest turbulence level tested. The shortest bubble in Fig. 9 was obtained with the grid used for most other tests (e.g., Figs. 8 and 12), which produced a level of 5 percent and a scale of 6 mm. Tests at higher incidence, not presented here, showed that the variation in suction peak, plateau level, and length of bubble were somewhat more dependent on the turbulence level than at $i = 1$ deg. The biggest single difference was nevertheless between natural levels of unsteadiness in the tunnel (*Tu* < 0.5 percent) and the lowest level of turbulence introduced, *Tu* = 1.9 percent.

The pressure distributions with the 6.3 mm circular leading edge were sufficiently similar to those with the 3 mm leading edge that they have been omitted here in the interests of brevity. The pressure distributions were very similar at zero incidence, and in reasonable agreement at 1 deg incidence. At higher incidences a discrepancy was evident and with the thicker aerofoil a shorter bubble was formed. In fact a higher incidence was needed to achieve the same effective incidence: The thicker aerofoil needed an incidence of about 2.5 deg to match the effective incidence of the thinner one at 2 deg. (Separate calculations by Mr. W. J. Calvert recently showed that the most important scaling parameter was the ratio of leading edge thickness to pitch, for a cascade, or to tunnel height for these tests.) The results from the thicker circular leading edge should have been used to compare with the elliptic leading edge, which is of similar thickness. Nevertheless checks have shown that appropriate conclusions can be drawn from the 3 mm circular leading edge and the 6.6 mm elliptic leading edge by using the data on the effective incidence.

Figure 10 shows the pressure distribution about the elliptic leading edge for $Re_t = 3000$ and for low free-stream turbulence. In this case the zero incidence flow does not separate,

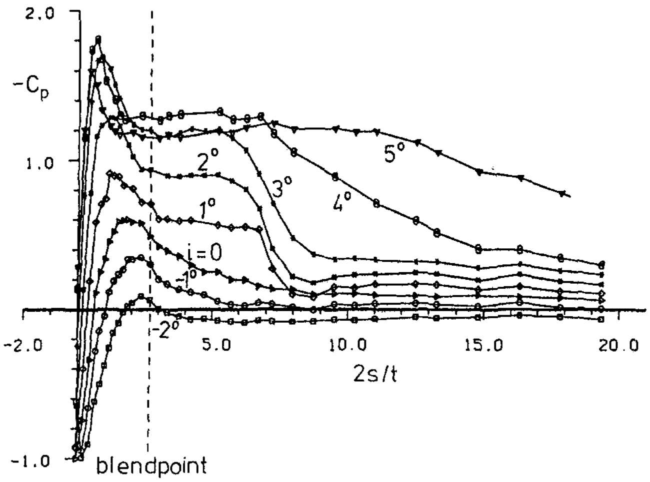

Fig. 10 Distribution of c_p about *elliptic* leading edge for a range of incidence: Re_t = 3000; *Tu* < 0.5 percent

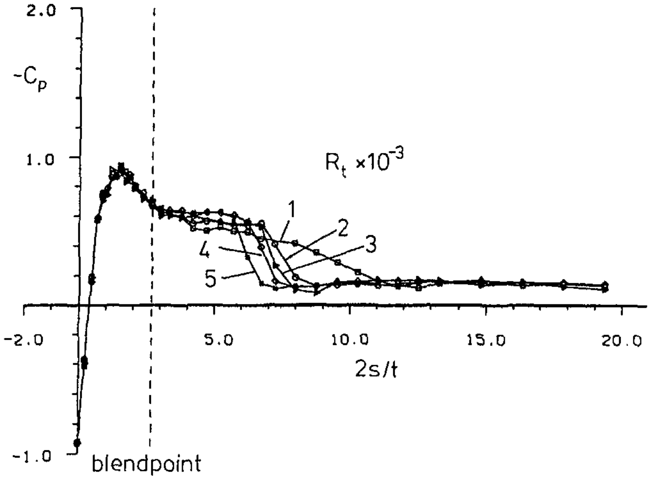

Fig. 11 Distribution of c_p about elliptic leading edge for a range of Reynolds number: incidence = 1 deg; *Tu* < 0.5 percent

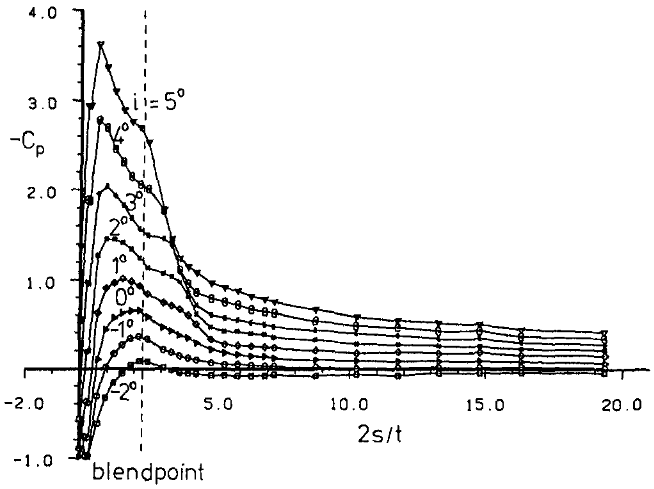

Fig. 12 Distribution of c_p about elliptic leading edge for a range of incidence: Re_t = 3000; turbulent free stream, *Tu* = 5 percent, L_{turb} = 6 mm

as had been the design intent. For this leading edge much higher incidence can be tolerated without the breakdown of the bubble structure, $i = 4$ deg compared to only $i = 2$ deg for the circular leading edge. Even at $i = 5$ deg reattachment ultimately seems to be going to occur some way downstream. Comparing Fig. 10 with Fig. 6 for the circular leading edge, it is clear that the suction peak reaches much greater values with the elliptic leading edge at the higher incidences and the plateau corresponds to a lower value of static pressure. The highest incidence at which the classical bubble form (with a clearly defined plateau) occurs for the circular leading edge is $i = 1$ deg, when the plateau is at about $c_p = -0.9$. For the elliptic leading edge the corresponding highest incidence is 3 deg, when the plateau is at about $c_p = -1.2$. The actual pressure rise during reattachment is, however, very similar in each because the pressure asymptotes to a lower value in the case of the elliptic blade at $i = 3$ deg. The maximum rise in c_p during reattachment is about 0.8 for the circular leading edge at $i = 1$ deg and 0.9 for the elliptic one at $i = 3$ deg, values remarkably similar since the comparison is for results at incidence in arbitrary whole numbers of degrees.

Figure 11 shows the pressures for the elliptic leading edge aerofoil at $i = 1$ deg with low free-stream turbulence at a range of Reynolds numbers and is the counterpart of Fig. 7 for the circular leading edge. Because the entrainment rate is lower for laminar than turbulent flow, laminar reattachment in the case at $Re_t = 10^3$ occurred farther downstream.

The pressure coefficients for the elliptic leading edge at a range in incidences with an inlet turbulence level of 5 percent and a length scale of 6 mm are shown in Fig. 12 for Re_t = 3000. These should be compared with Fig. 10 for the same case with low free-stream turbulence. The effect of the turbulence is even more marked in this case than it was for the circular leading edge. With the elliptic leading edge, reattachment is rapid even at $i = 5$ deg, with a very large suction peak. Unlike other cases shown, the results for the elliptic leading edge with a turbulent inlet flow do not show any plateau, but rather there is a continuous deceleration. Transition must be so rapid that turbulent reattachment is immediate (or else separation is totally suppressed) and the following deceleration of the turbulent boundary layer without separation must be made possible by the high free-stream turbulence. The very much higher suction peaks in Fig. 12 with the turbulent inlet flow compared to those without indicates that the free-stream flow in the leading edge region is being forced to follow a much tighter radius of curvature and confirms that the separation bubble has been removed or greatly reduced.

Results (not presented in this paper) for the elliptic leading edge at Re_t = 1000 with the same raised turbulence level and scale as Fig. 12 did show a separation bubble with a plateau for incidences of 2 deg and upward. At this lower Reynolds number a length of separated shear layer must be required for the shear layer to be made turbulent by the free stream, whereas at Re_t = 2000 and upward the shear layer can be made turbulent without separation being perceptible in the pressure distribution.

Pressure distributions around the elliptic leading edge were measured with a range of different turbulence grids upstream and the effects of the different scales and levels were similar for most of the conditions tested, just as for the circular leading edge. The biggest difference was again between the flow without artificially raised turbulence and those with. At $i = 4$ and 5 deg, however, the effect of turbulence level was pronounced, so that at $i = 5$ deg the suction peak was almost twice as great for the turbulence level of 10 percent, scale 20 mm, as for a level of 1.9 percent, scale 2.9 mm.

The lowest Reynolds number tested for the elliptic leading edge was Re_t = 500. With low free-stream turbulence a long reattachment without a plateau was found at incidences up to 4 deg, presumably laminar reattachment. At the same Reynolds number the effect of a free-stream turbulence level of 5 percent was to produce a separation bubble with a plateau at $i = 3$, 4, and 5 deg, with relatively rapid reattachment, indicating turbulent flow. At lower incidences no separation or bubble were evident for this Reynolds number.

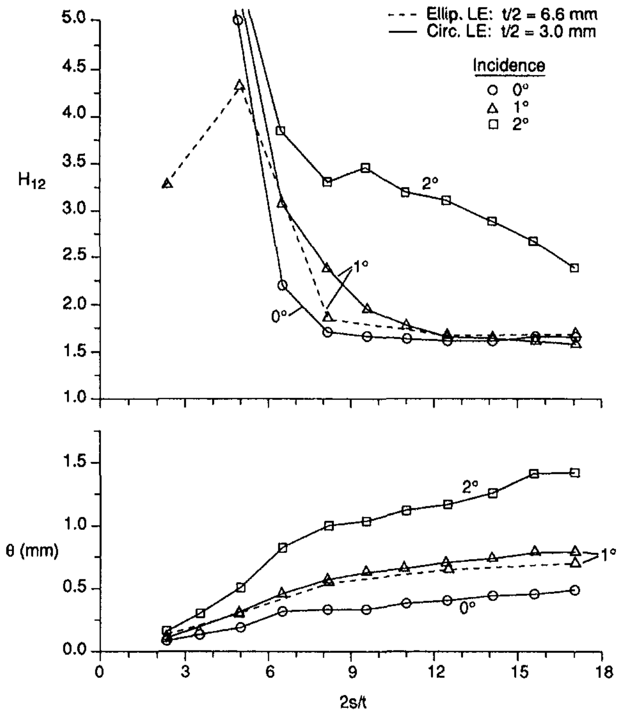

Fig. 13 Boundary layer momentum thickness and form factor along aerofoils: Re_t = 2700; low free-stream turbulence

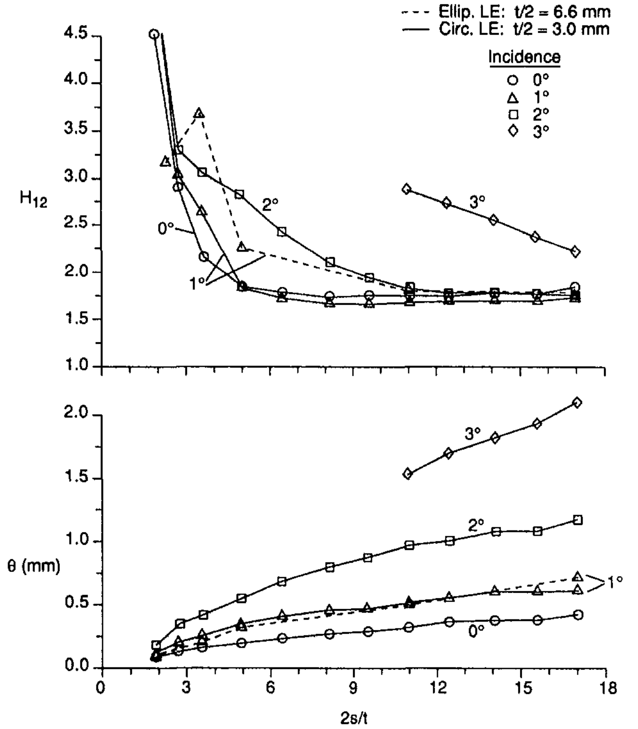

Fig. 14 Boundary layer momentum thickness and form factor along aerofoils: Re_t = 2700; free-stream turbulence, Tu = 5 percent, L_{turb} = 6 mm

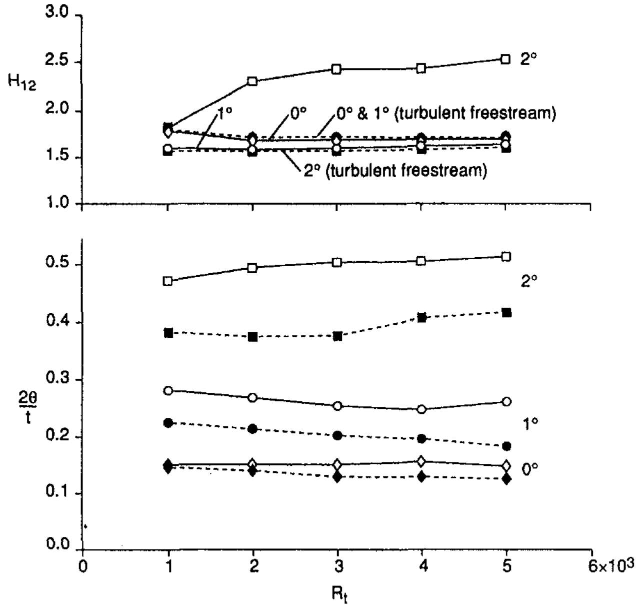

Fig. 15 Boundary layer momentum thickness and form factor at $2s/t$ = 17 for circular leading edge at various incidences (key on Fig. 16)

Boundary Layer Measurements. Figure 13 presents measurements of the boundary layer momentum thickness θ and form parameter $H_{12} = \delta^*/\theta$ at a range of positions along the surface of the aerofoils, all for Re_t = 2700 and for low inlet turbulence. For the circular leading edge aerofoil the results are given for incidences of 0, 1, and 2 deg, whereas for clarity the elliptic leading edge results are presented only for i = 1 deg. The rapid drop in form parameter shows the reattachment taking place at around $2s/t \approx 6$. At $2s/t \approx 17$, where it was decided to standardize the taking and presentation of boundary layer measurements, it can be sen that most of the curves have steadied out and only the form parameter for i = 2 deg is still varying significantly. The strong influence of incidence is apparent, because at i = 1 deg the form parameter at $2s/t \approx 17$ is similar to that for a turbulent boundary layer in zero pressure gradient, H_{12} = 1.6, whereas at i = 2 deg H_{12} = 2.3, a value comparable with that normally associated with separation or reattachment. Likewise the momentum thickness at i = 2 deg is approximately twice as big as at i = 1 deg. The magnitude of the momentum thickness shown in Fig. 13 for i = 1 deg is comparable for the circular and the elliptic leading edges, but this is highly misleading. The thickness of the elliptic leading edge is 2.2 times that of the circular leading edge and in appropriate nondimensional terms the boundary layer is more than twice as thick on the circular aerofoil.

The measurements of momentum thickness and form parameter with the free-stream turbulence level raised to 5 percent are shown in Fig. 14. The trends are in most cases similar to those in Fig. 13 obtained with low turbulence. One difference is that reattachment is much farther upstream with the raised turbulence; another difference is that the form parameter drops sharply at $2s/t \approx 3$, well upstream of the low free-stream turbulence case. The magnitudes of the momentum thickness are about 20 percent lower than the corresponding low free-stream turbulence cases and the form parameter for i = 2 deg is now similar to that for lower incidence, $H_{12} \approx 1.7$.

For the circular leading edge aerofoil the variations in momentum thickness and form parameter H_{12} are shown in Fig. 15 versus Re_t for incidences of 0, 1, and 2 deg for both low and raised free-stream turbulence levels. All these measurements were obtained at $2s/t$ = 17. The most obvious trends are the weak dependence on Re_t and strong dependence on incidence, particularly for θ. As noted above, raising the free-stream turbulence reduces the momentum thickness by about 20 percent. Most of the form parameter values are between 1.6 and 1.7, the exception being i = 2 deg with low turbulence, which shows a most surprising result. At Re_t = 1000 H_{12} = 1.8 but this rises to H_{12} = 2.3 at Re_t = 2000, above which it stays almost constant. This is counterintuitive, since form parameter normally decreases as Reynolds number is raised. Quite independent measurements of the static pressure at i = 2 deg

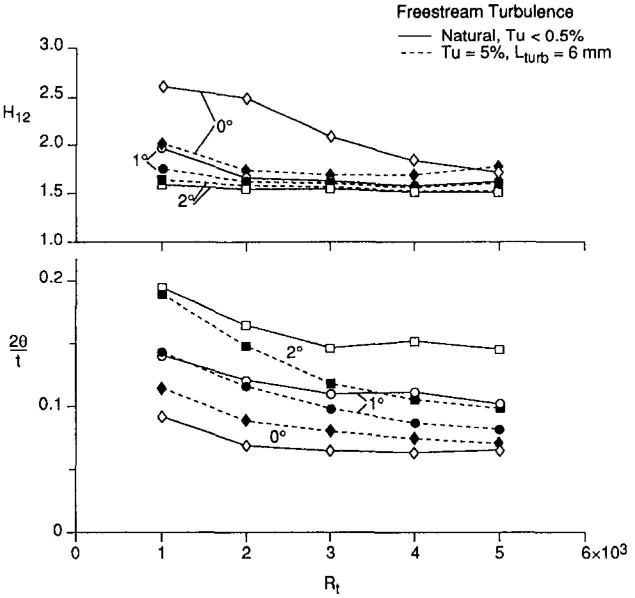

Fig. 16 Boundary layer momentum thickness and form factor at $2s/t = 17$ for elliptic leading edge at various incidences

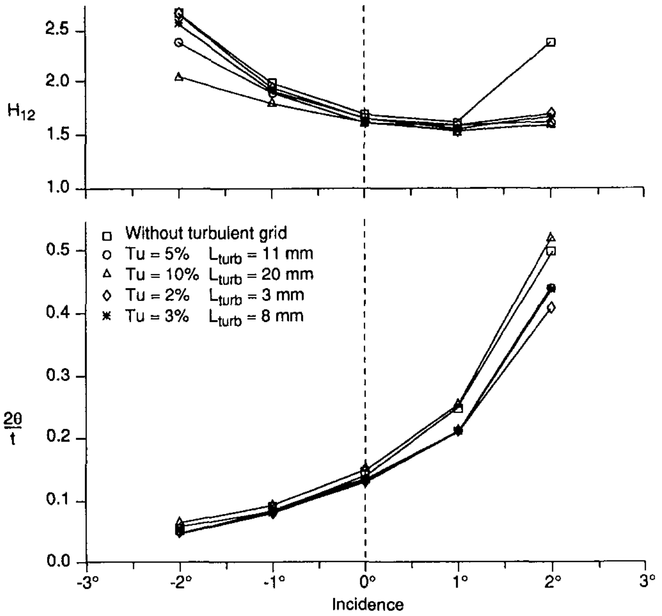

Fig. 17 Boundary layer momentum thickness and form factor at $2s/t = 17$ at various turbulence levels for circular leading edge: $\mathrm{Re}_t = 3000$

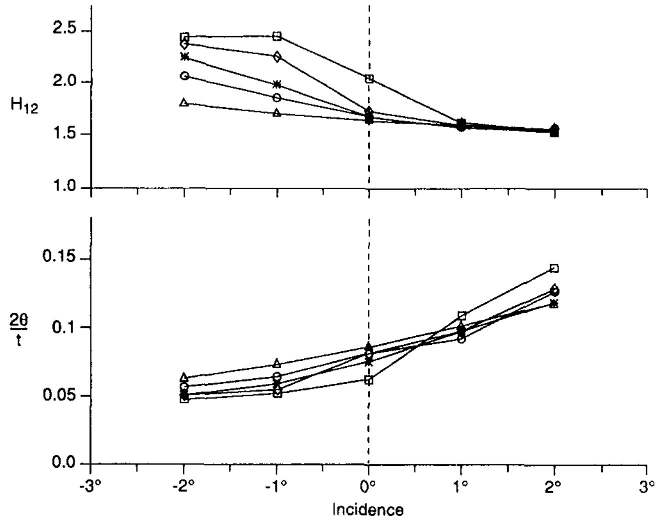

Fig. 18 Boundary layer momentum thickness and form factor at $2s/t = 17$ at various turbulence levels for elliptic leading edge: $\mathrm{Re}_t = 3000$ (key on Fig. 17)

supported the unusual trend in H_{12}, since the bubble was shorter and the plateau at lower pressure for $\mathrm{Re}_t = 1000$ than $\mathrm{Re}_t \geq 2000$. No explanation can be offered for this.

Figure 16 presents results for the elliptic leading edge corresponding to those for the circular leading edge in Fig. 15. It will be seen that the nondimensional momentum thicknesses $2\theta/t$ are on the order of one third those for the circular leading edge. The effect of free-stream turbulence is more complicated for the elliptical leading edge at $i = 1$ and 2 deg; evidently if transition can be accomplished far enough upstream the momentum thickness is up to about 20 percent less, but this demands the presence of high free-stream turbulence and a sufficiently high Reynolds number. The high values of H_{12} for low Re_t at zero incidence with low free-stream turbulence are evidence that the boundary layer is still laminar at $2s/t = 17$.

Figures 17 and 18 show the momentum thickness and form parameter versus incidence angle for the circular and elliptic leading edge aerofoils respectively at $2s/t = 17$. All the measurements are for $\mathrm{Re}_t = 3000$. The parameter varied in each case is the free-stream turbulence level and scale; the squares in each are the measured values with no turbulence grid installed. At negative incidence there is no separation bubble and at low free-stream turbulence the flow is in some cases still laminar at the $2s/t = 17$ station. At positive incidence the effect of turbulence is generally small, except for the circular leading edge at $i = 2$ deg, for which H_{12} is much greater in the low turbulence case. At positive incidence the momentum thickness is generally higher for low free-stream turbulence, the one exception being for the circular leading edge with the highest level of turbulence, 10 percent, and a scale equal to 20 mm.

Discussion

Separation bubbles have been shown to occur on the suction surface very near the leading edge of thin aerofoils when the incidence is greater than needed to put the stagnation point on the nose of the aerofoil, in other words when the effective incidence is positive. For aerofoils with a marked discontinuity in surface curvature, such as those formed with a circular leading edge, the discontinuity can cause a separation bubble even when the effective incidence is zero. Even at higher incidence the separation appears to occur very close to the position where the discontinuity in curvature occurs.

For any particular leading edge geometry the length of the separation bubble depends on the Reynolds number Re_t and incidence. The length of the bubble generally reduces as Re_t is increased, and this effect was found to be more pronounced with the elliptic leading edge than the circular one. As the bubble is shortened the static pressure of the spike and in the plateau region decreases, reflecting the tighter radius of curvature the flow outside the shear layer is made to follow.

At higher incidence (2 deg in the case of the circular leading edge and 4 deg for the elliptic one) and with low free-stream turbulence, the character of the flow alters and reattachment occurs much more slowly. The alteration in the flow that accompanies this is not understood at the present time. At still higher incidence the flow was found not to reattach at all.

Free-stream turbulence has a far greater effect on the behavior of the bubble than had been expected. Increasing free-stream turbulence for the circular leading edge at all positive incidences produced a noticeably shorter bubble, with a higher suction peak and lower pressure at the plateau. Increased free-stream turbulence also allowed bubbles to persist to higher incidences (2 deg for the circular arc leading edge with elevated turbulence, compared to 1 deg without, for a conventional bubble with a well-defined plateau region). A leading edge region flow without a clear bubble was also possible at substantially higher incidence with free-stream turbulence.

The effect of free-stream turbulence was even more pronounced for the elliptic leading edge than the circular one; in this case the plateau region was effectively removed so that an almost continuous rapid deceleration took place from a high value of the suction peak. In these cases the readjustment in pressure from the peak near the leading edge to the level well back on the aerofoil was virtually complete by $2s/t \approx 5$ (the leading edge blend point occurring at $2s/t \approx 2.2$). This was much sooner than for the elliptic leading edge without the high free-stream turbulence, for which adjustment was more typically completed at $2s/t \approx 10$. At a lower Reynolds number, $\mathrm{Re}_t = 1000$, the turbulence did not bring about this marked alteration to the pressure distribution around the elliptic leading edge and the conventional bubble with a plateau was formed. It therefore seems that for $\mathrm{Re}_t \geq 2000$ the effect of free-stream turbulence was to suppress the separation, or make it imperceptible, by bringing about transition almost immediately. The largest suction peak was $c_p = -4.6$ and was found for the elliptic leading edge at 5 deg incidence with elevated turbulence. In this case the free-stream velocity was virtually halved between the peak and, say, $2s/t \approx 10$, a very steep gradient.

It is often thought that with a well-shaped leading edge, such as the elliptic leading edge used here, the boundary layer will be in better shape because the suction peak can be avoided. The results here show that the suction peak is not reduced, except for small incidence, and that larger suction peaks were found on the elliptic leading edge than the circular one. This can be seen by comparing the measurements for $i = 3$ deg in Figs. 8 and 12; with the circular leading edge the peak is $c_p \approx -1.85$, whereas for the elliptic leading edge it is $c_p \approx -2.05$. A different reason must explain why the boundary layers are so much thinner for the elliptic blade at the same incidence. It is possible that the rapidity with which reattachment takes place, and the corresponding thinness of the shear layer, is related to the shape of the leading edge as distinct from the pressure distribution set up by the leading edge. If the shear layer separates from the surface inclined at a large angle from the direction of surface downstream of where it may reattach, a longer bubble with a lot of entrainment will be necessary. If, on the other hand, the shear layer leaves in a direction more nearly parallel to the surface, a shorter bubble is likely to be formed. It seems very likely that the elliptic leading edge favors this latter case.

At low Reynolds numbers and for low free-stream turbulence it appears possible for reattachment to occur without transition taking place. This can be seen for the elliptic leading edge in Fig. 11 at $\mathrm{Re}_t = 1000$, and it was also observed for the circular leading edge at Re_t between 250 and 750, depending on incidence. In these cases the behavior is very different, since the flow reattaches without the formation of a plateau, giving what is assumed to be a wholly laminar bubble. In the case of the elliptic leading edge the inlet velocity is about half that for the circular leading edge aerofoil for the same Re_t, because the aerofoil was approximately twice as thick. Furthermore the shear layers were substantially thinner in the case of the elliptic leading edge, as shown by the smaller values of θ measured. The resulting Reynolds numbers based on shear layer thickness for the elliptic leading edge were therefore lower for the same Reynolds number based on leading edge half thickness, Re_t. As a result the Reynolds number based on the shear layer was low enough at $\mathrm{Re}_t = 1000$ and $i = 1$ deg that transition could not take place and a laminar reattachment occurred for the elliptic leading edge, but a turbulent reattachment for the circular one.

Boundary layer momentum thickness grows smoothly along the suction surface, including through the region in which the bubble occurs. The form parameter drops precipitously in the region where reattachment occurs, and downstream of this it can relax back to the value appropriate for the overall pressure gradient. Increasing the turbulence level leads to a reduction in momentum thickness of about 20 percent, compared to that for low free-stream turbulence, for the cases in which the flow has reattached in the low turbulence case. In low free-stream turbulence flows for which reattachment does not occur, the decrease in momentum thickness brought about by the higher level of turbulence can be much greater than 20 percent. Similarly, if the boundary layer form parameter with a low free-stream turbulence level is high, free-stream turbulence can reduce the boundary layer form parameter very sharply.

Reynolds number based on the leading edge thickness, Re_t, has only a weak influence on pressure distribution and boundary layer properties in the range investigated, 1000 to 5000, and the variable of primary importance is the incidence. The boundary layer properties are more nearly independent of Reynolds number for the circular leading edge, for which $2\theta/t$ is very nearly a function of incidence alone. Downstream of the reattachment region Re_θ can therefore vary substantially and in some cases very low values of Re_θ for a turbulent boundary layer were measured at $2s/t = 17$. For the circular leading edge at $\mathrm{Re}_t = 1000$ and $i = 1$ deg measurements gave $\mathrm{Re}_\theta = 309$ and $H_{12} = 1.59$ for the case without turbulence and $\mathrm{Re}_\theta = 245$ and $H_{12} = 1.62$ for the case with 5 percent free-stream turbulence at a scale of 6 mm. The comparatively low value of the form parameter indicates that these are turbulent profiles. With the elliptic leading edge the values of Re_θ were even lower at $\mathrm{Re}_t = 1000$ and $i = 1$ deg: $\mathrm{Re}_\theta = 148$ and $H_{12} = 1.98$ without high free-stream turbulence and $\mathrm{Re}_\theta = 147$ and $H_{12} = 1.79$ with. For these latter cases, however, the boundary layer would appear to be transitional. In every case, since θ is almost independent of Re_t, the value of Re_θ rises almost in proportion to Re_t.

It was noted earlier that the thicker aerofoil with a circular leading edge produced a smaller effective incidence for the same geometric incidence, mainly because the height of the wind tunnel was not increased in proportion to the thickness. The boundary layers for the elliptic and circular leading edges should have been compared for aerofoils of the same thickness; in other words the thicker circular leading edge (6.3 mm half-thickness) should have been used to compare with the elliptic aerofoil of similar thickness (6.6 mm). Unfortunately this was not realized when the measurements of the boundary layer for the circular leading edge were made, all with the 3 mm half-thickness aerofoil. It is nevertheless possible to obtain a clear indication of the comparative boundary layer thicknesses by matching the effective incidences. For 2 deg incidence onto the thinner circular leading edge aerofoil, the effective incidence is approximately equal to that on the thicker circular leading edge aerofoil at about 2.5 deg. From Fig. 18 for the elliptic leading edge it is easy to extrapolate the trend to 2.5 deg incidence to get a value of $2\theta/t \approx 0.15$. The corresponding value of $2\theta/t$ for the circular leading edge results shown in Fig. 17 at 2 deg incidence is about 0.45. The values of momentum thickness normalized by the leading edge half thickness, $2\theta/t$, are therefore between two and three times greater for the circular leading edge than the elliptic one, the exact value depending on the incidence and on the level of free-stream turbulence.

For a compressor blade suction surface, the pressure distribution downstream of the reattachment may be adverse and strong for most of the chord; if this is the case the contribution of the skin friction is negligible and the momentum integral equation reduces to

$$U d\theta/ds = -\theta(2+H_{12})dU/ds.$$

The growth rate of momentum thickness is therefore proportional to the local value of momentum thickness and the value of θ at the trailing edge would be proportional to the value just downstream of the reattachment near the leading edge if H_{12} remained constant as the boundary layer developed. In fact H_{12} is likely to increase more rapidly if the boundary layer is thicker, increasing further the growth rate of θ. The propensity for the boundary layer to separate also depends on the nondimensional velocity gradient, so an increase in θ near the leading edge can precipitate another separation farther downstream.

It was remarked in the introduction that the leading edge of a compressor blade is normally so thin that accurate and consistent manufacture is difficult to achieve. A blade with a smooth transition from the leading edge radius to that over the suction surface may therefore have a thin boundary layer at the suction surface trailing edge, a thin wake, and relatively low loss, whereas a blade in the same row that has a less smooth shape in the leading edge region may cause much more loss. It seems probable that some of the blade-to-blade variation in wake thickness frequently observed is caused by leading edge variations. Whereas the benefits of an elliptic leading edge over other cruder shapes is apparent, it must be realized from the measurements presented here that the penalty for failing to meet the very tight requirements may be high and mechanical damage to the leading edge region of a carefully designed blade could lead to serious degradation in performance.

The results have confirmed that for proper modeling of flow inside compressors or turbines it is essential to include a level of free-stream turbulence substantially higher than was found naturally in the tunnel used ($Tu < 0.5$ percent). It seems, however, that the behavior is relatively insensitive to the level of turbulence or its scale, and this makes it possible to carry out representative tests without giving particular attention to the precise conditions inside the compressor or turbine or to the precise nature of the turbulence used in the wind tunnel. Some evidence points to the lowest level of turbulence used, 1.9 percent, being too low to give an accurate modeling of flow inside a compressor, and the highest level, 10 percent, being too high. The level used here for most of the tests, 5 percent, seems about right and in line with that measured inside multistage compressors. The flow does not seem very sensitive to the scale of the turbulence.

This paper, which is already long, has concentrated on presenting results that may be directly incorporated into calculation methods for the flow about compressor or turbine blade rows. The explanation for many of the observations lies with the process or processes of transition in the separated shear layer. To elucidate this it is necessary to look at the instantaneous ("raw") velocity traces and this will form the subject of another paper.

Conclusions

1 Leading edge shape has a very large effect on the boundary layer immediately downstream of the leading edge and therefore on the development of the boundary layer over the remainder of the aerofoil. There is clearly a practical problem in manufacturing the leading edge accurately enough to minimize the loss as well as in determining the leading edge precisely enough to allow accurate calculations to be performed.

2 With a circular leading edge a separation bubble can form in low-turbulence flow even with a small negative incidence. With raised free-stream turbulence the bubble is barely detectable at zero incidence.

3 With an elliptic leading edge a separation bubble may be absent at zero incidence because separation is avoided. When bubbles form they are shorter than with a circular leading edge and, furthermore, can reattach at higher incidence.

4 At low Reynolds numbers and zero or small incidence, it is possible for the flow to reattach without forming a bubble with a detectable pressure plateau, though the process takes longer. This is believed to be laminar reattachment.

5 The bubble length, pressure distribution, and the boundary layer conditions downstream are strong functions of incidence. Incidence matters in that it positions the stagnation point relative to the nose of the aerofoil (i.e., fixes the effective incidence). The same quantities are weak functions of Reynolds number based on leading edge half thickness.

6 Raising the inlet free-stream turbulence to around 5 percent has a marked effect on the bubble, roughly halving the length and raising the peak suction level by up to 50 percent for the circular leading edge. A raised free-stream turbulence has an even more pronounced effect on the pressure distributions about the elliptic leading edge; at most of the Reynolds numbers tested the plateau region associated with the normal bubble structure is missing and the deceleration from the peak is rapid and monotonic, suggesting that transition appears to take place before or, more likely, immediately after separation. At low Reynolds numbers the normal bubble pressure distribution reappears for the elliptic leading edge even with high free-stream turbulence.

7 The effect of free-stream turbulence can be achieved by a wide range of levels and length scales, the effect of scale being even weaker than level.

8 At about 17 leading edge half-thicknesses downstream from the nose of the aerofoil, the boundary layer has settled to a comparatively slowly changing state and this provided a useful condition for comparing results. It would also provide a convenient starting position for the calculation of boundary layers farther downstream.

9 The boundary layer thickness is significantly greater for the circular leading edge when nondimensionalized by the leading edge half-thickness. For example, for the circular leading edge at 2 deg incidence $2\theta/t \approx 0.45$ at $2s/t = 17$, but for the elliptic leading edge at the same condition $2\theta/t \approx 0.15$. A circular leading edge is by no means the worst shape that can be created and it is to be expected that badly made or damaged leading edges will result in even greater values of $2\theta/t$ and therefore of loss.

10 Form parameter, H_{12}, varies considerably with incidence, being high if the boundary layer is laminar (at negative incidence, especially with low free-stream turbulence) and high for substantial positive incidence when the turbulent boundary layer is near to separation. The range of values of H_{12} is greatly reduced by the presence of high free-stream turbulence.

11 The values of boundary layer parameters such as Re_θ and H_{12} can vary widely at the same position on the aerofoil as incidence, Reynolds number Re_t, and free-stream turbulence condition are altered. With high levels of free-stream turbulence a turbulent boundary layer was measured for which $\mathrm{Re}_\theta = 245$, a value much lower than is normally assumed the minimum.

12 The tests performed have been at very low Mach numbers, $M < 0.1$. It is to be expected that very different behavior occurs at high subsonic Mach numbers when an expansion around the bubble could lead to a supersonic patch terminated by a shock.

Acknowledgments

This project was suggested by Mr. W. J. Calvert and the authors are pleased to express their appreciation of his support and assistance throughout the course of the project. The work was supported by the Ministry of Defence, now the Defence Research Agency, whose permission to publish this is acknowledged. The insights of Reviewer Number 1 in highlighting the effect of thickness are gratefully recorded.

The experimental work was made possible through the assistance of Mr. D. Barlow and Mr. P. Hunt. The paper was

written while NAC was Jerome C. Hunsaker Visiting Professor in the Department of Aeronautics and Astronautics of MIT and the help of Ms. D. Parks in the MIT Gas Turbine Laboratory in preparing the diagrams is gratefully recorded.

References

Arena, A. V., and Mueller, T. J., 1980, "Laminar Separation, Transition, and Turbulent Reattachment Near the Leading Edge of Airfoils," *AIAA Journal*, Vol. 18, No. 7, pp. 747-753.

Bearman, P. W., 1971, "Corrections for the Effect of Ambient Temperature Drift on Hot-Wire Measurements in Incompressible Flow," *DISA Inf. Den.*, Vol. 11, pp. 25-30.

Bindon, J. P., 1987, "Pressure Distributions in the Tip Clearance Region of an Unshrouded Axial Turbine as Affecting the Problem of Tip Burn Out," ASME Paper No. 87-GT-230.

Calvert, W. J., 1989, private communication.

Camp, T. R., 1992, private communication.

Cumpsty, N. A., 1989, *Compressor Aerodynamics*, Longman, United Kingdom.

Davis, M. R., 1974, "Design of Flat Plate Leading Edges to Avoid Flow Separation," *AIAA Journal*, Vol. 18, No. 5, pp. 598-599.

Gaster, M., 1967, "The Structure and Behaviour of Laminar Separation Bubbles," Aeronautical Research Council, R&M 3595.

Horton, H. P., 1969, "A Semi-empirical Theory for the Growth and Bursting of Laminar Separation Bubbles," Aeronautical Research Council, CP1073.

Mayle, R. E., 1991, "The Role of Laminar-Turbulent Transition in Gas Turbine Engines," ASME JOURNAL OF TURBOMACHINERY, Vol. 113, pp. 509-537.

Roberts, W. B., 1975, "The Effect of Reynolds Number and Laminar Separation on Axial Cascade Performance," ASME *Journal of Engineering for Power*, Vol. 97, pp. 261-274.

Roberts, W. B., 1980, "Calculation of Laminar Separation Bubbles and Their Effects on Airfoil Performance," *AIAA Journal*, Vol. 18, pp. 25-31.

Walker, G. J., 1993, "The Role of Laminar-Turbulent Transition in Gas Turbine Engines: A Discussion," ASME JOURNAL OF TURBOMACHINERY, Vol. 115, pp. 207-217.

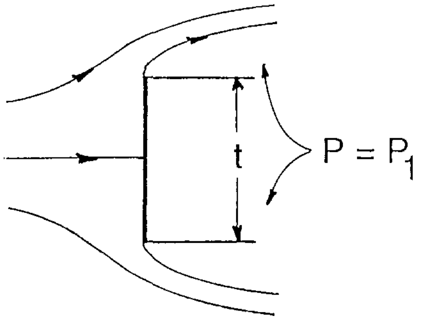

Fig. 19 Free streamline flow around a lamina

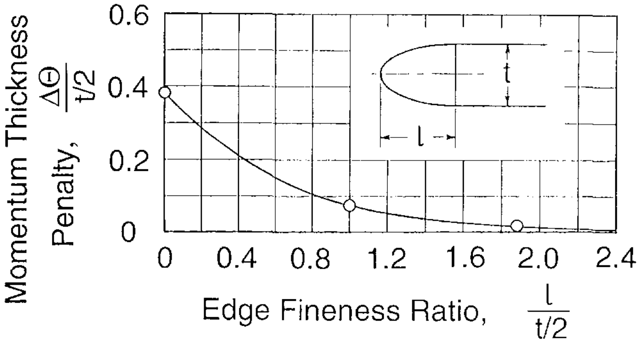

Fig. 20 Penalty for blunt leading edges

DISCUSSION

L. H. Smith, Jr.[3]

This paper adds to the literature some important data that can be used to help estimate the effects of leading edge contour on turbomachine performance. Although it provides guidance to designers who specify edge shapes, a more important use of these data will be in the assessment of the consequences of manufacturing imperfections and imperfections that result from injudicious rework of edges that have been damaged in service.

The authors show that the bluntness of a circular edge is harmful compared to that of a 1.89:1 ellipse, but in practice edges considerably blunter than circular may be encountered. Test results for such edges would be useful, but lacking these this discusser offers below a means to estimate them.

The extreme of bluntness is a square edge. It is reasonable to assume that the pressure distribution over such an edge, at subsonic Mach numbers, is nearly the same as that given by the Kirchhoff free streamline analysis of the flow around a lamina placed normal to the stream; see Fig. 19. Since the pressure behind the lamina is ambient, the force on the lamina is equal to the integral of the pressure over the upstream face, and it is given by Lamb (1932) to be

$$F=0.440\rho U_1^2$$

A control volume analysis over the forward part of our square-edged plate (back to $s = 17(t/2)$) yields, if we assume that the net shear stress on the sides of the plate is negligible in that region,

$$\rho U_1^2\theta=F/2$$

yielding

$$\frac{2\theta}{t}=0.440$$

for the square-edged case. This can be compared with 0.133 for the circular edge and 0.078 for the elliptic edge, obtained from Figs. 17 and 18 at zero incidence.

It is of interest to know what the loss *penalty* is for not having a "perfect" edge. An aerodynamically perfect edge would be one shaped such that there would be very little excess velocity at or near where the edge blends into the plate. Inspection of Fig. 12 suggests that, for the present test series, this condition is approached when the elliptic-edged plate is placed at an incidence between −1 and −2 deg, and in this range Fig. 18 gives approximately 0.06 for $2\theta/t$. Accepting this as the "perfect edge" value, we then subtract it from the values given above for the three edges considered to obtain their $\Delta\theta$ penalty values. The results are plotted in Fig. 20, where engineering judgment has been used to interpolate and extrapolate around the three data points. It is hoped that this will be useful when estimating the performance penalties associated with different degrees of bluntness.

References

Lamb, Sir Horace, 1932, *Hydrodynamics*, 6th ed., Dover, New York, Art. 76, pp. 99-102.

Authors' Closure

The authors would like to thank Dr. Smith for his interesting and illuminating discussion. They were aware of the significance of damaged or imperfect blades, but had not appreciated how the Kirchhoff free-surface theory could be used to provide a solution for the extreme case of the flat leading edge.

The authors would also like to thank Dr. Smith for his earlier help, in the anonymous role of reviewer, in improving the paper and correcting some errors.

---

[3] GE Aircraft Engines, Cincinnati, OH 43215.

written while NAC was Jerome C. Hunsaker Visiting Professor in the Department of Aeronautics and Astronautics of MIT and the help of Ms. D. Parks in the MIT Gas Turbine Laboratory in preparing the diagrams is gratefully recorded.

References

Arena, A. V., and Mueller, T. J., 1980, "Laminar Separation, Transition, and Turbulent Reattachment Near the Leading Edge of Airfoils," *AIAA Journal*, Vol. 18, No. 7, pp. 747-753.

Bearman, P. W., 1971, "Corrections for the Effect of Ambient Temperature Drift on Hot-Wire Measurements in Incompressible Flow," *DISA Inf. Den.*, Vol. 11, pp. 25-30.

Bindon, J. P., 1987, "Pressure Distributions in the Tip Clearance Region of an Unshrouded Axial Turbine as Affecting the Problem of Tip Burn Out," ASME Paper No. 87-GT-230.

Calvert, W. J., 1989, private communication.

Camp, T. R., 1992, private communication.

Cumpsty, N. A., 1989, *Compressor Aerodynamics*, Longman, United Kingdom.

Davis, M. R., 1974, "Design of Flat Plate Leading Edges to Avoid Flow Separation," *AIAA Journal*, Vol. 18, No. 5, pp. 598-599.

Gaster, M., 1967, "The Structure and Behaviour of Laminar Separation Bubbles," Aeronautical Research Council, R&M 3595.

Horton, H. P., 1969, "A Semi-empirical Theory for the Growth and Bursting of Laminar Separation Bubbles," Aeronautical Research Council, CP1073.

Mayle, R. E., 1991, "The Role of Laminar-Turbulent Transition in Gas Turbine Engines," ASME JOURNAL OF TURBOMACHINERY, Vol. 113, pp. 509-537.

Roberts, W. B., 1975, "The Effect of Reynolds Number and Laminar Separation on Axial Cascade Performance," ASME *Journal of Engineering for Power*, Vol. 97, pp. 261-274.

Roberts, W. B., 1980, "Calculation of Laminar Separation Bubbles and Their Effects on Airfoil Performance," *AIAA Journal*, Vol. 18, pp. 25-31.

Walker, G. J., 1993, "The Role of Laminar-Turbulent Transition in Gas Turbine Engines: A Discussion," ASME JOURNAL OF TURBOMACHINERY, Vol. 115, pp. 207-217.

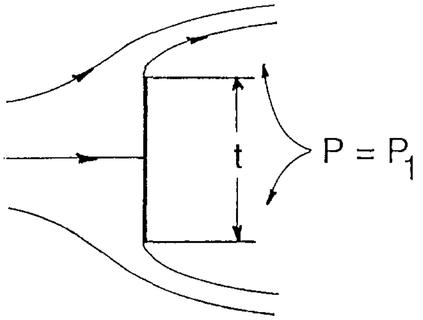

Fig. 19 Free streamline flow around a lamina

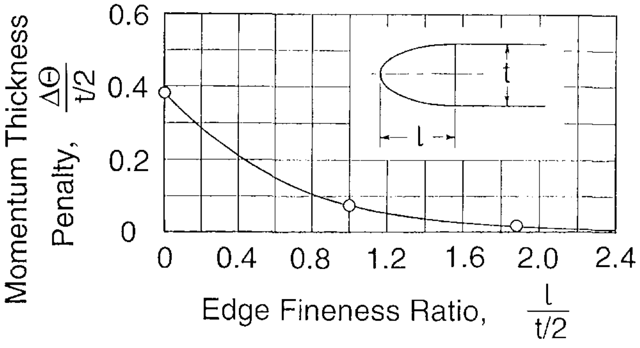

Fig. 20 Penalty for blunt leading edges

DISCUSSION

L. H. Smith, Jr.[3]

This paper adds to the literature some important data that can be used to help estimate the effects of leading edge contour on turbomachine performance. Although it provides guidance to designers who specify edge shapes, a more important use of these data will be in the assessment of the consequences of manufacturing imperfections and imperfections that result from injudicious rework of edges that have been damaged in service.

The authors show that the bluntness of a circular edge is harmful compared to that of a 1.89:1 ellipse, but in practice edges considerably blunter than circular may be encountered. Test results for such edges would be useful, but lacking these this discusser offers below a means to estimate them.

The extreme of bluntness is a square edge. It is reasonable to assume that the pressure distribution over such an edge, at subsonic Mach numbers, is nearly the same as that given by the Kirchhoff free streamline analysis of the flow around a lamina placed normal to the stream; see Fig. 19. Since the pressure behind the lamina is ambient, the force on the lamina is equal to the integral of the pressure over the upstream face, and it is given by Lamb (1932) to be

$$F = 0.440 \rho U_1^2$$

A control volume analysis over the forward part of our square-edged plate (back to $s = 17(t/2)$) yields, if we assume that the net shear stress on the sides of the plate is negligible in that region,

$$\rho U_1^2 \theta = F/2$$

yielding

$$\frac{2\theta}{t} = 0.440$$

for the square-edged case. This can be compared with 0.133 for the circular edge and 0.078 for the elliptic edge, obtained from Figs. 17 and 18 at zero incidence.

It is of interest to know what the loss *penalty* is for not having a "perfect" edge. An aerodynamically perfect edge would be one shaped such that there would be very little excess velocity at or near where the edge blends into the plate. Inspection of Fig. 12 suggests that, for the present test series, this condition is approached when the elliptic-edged plate is placed at an incidence between −1 and −2 deg, and in this range Fig. 18 gives approximately 0.06 for $2\theta/t$. Accepting this as the "perfect edge" value, we then subtract it from the values given above for the three edges considered to obtain their $\Delta\theta$ penalty values. The results are plotted in Fig. 20, where engineering judgment has been used to interpolate and extrapolate around the three data points. It is hoped that this will be useful when estimating the performance penalties associated with different degrees of bluntness.

References

Lamb, Sir Horace, 1932, *Hydrodynamics*, 6th ed., Dover, New York, Art. 76, pp. 99-102.

Authors' Closure

The authors would like to thank Dr. Smith for his interesting and illuminating discussion. They were aware of the significance of damaged or imperfect blades, but had not appreciated how the Kirchhoff free-surface theory could be used to provide a solution for the extreme case of the flat leading edge.

The authors would also like to thank Dr. Smith for his earlier help, in the anonymous role of reviewer, in improving the paper and correcting some errors.

---

[3] GE Aircraft Engines, Cincinnati, OH 43215.

G. Perrin

F. Leboeuf

Laboratoire de Mécanique
des Fluides et d'acoustique,
Ecole Centrale de Lyon,
Ecully, France

Investigation of Throughflow Hypothesis in a Turbine Cascade Using a Three-Dimensional Navier–Stokes Computation

The results of a computation, performed with a three-dimensional Navier–Stokes computation at ONERA, have been averaged in the blade-to-blade direction; the spatial fluctuations around the averaged flow variables have also been determined. It has then been possible to estimate all terms in the average components of the momentum equations. The comparison of the two-dimensional balances of these three equations shows that the shear stress plays a minor role in the momentum balance, except on the dissipation of the passage vortex kinetic energy downstream of the blade trailing edges. The kinetic energy of the spanwise component of the velocity spatial fluctuations has a very strong influence on the radial pressure gradient; it introduces a convection effect. This is a key effect for all these balances.

Introduction

The computation of the flow in blade passages of compressors and turbines may be performed with efficient three-dimensional Navier–Stokes codes, which give access to very fine local flow structures in only a few hours on a vector computer (Escande and Cambier, 1991; Dawes, 1987). The practical treatment of the large amount of flow data is, however, a severe limitation for the use of such tools, particularly if some global information is looked for during the design process for example. Simpler tools are then needed, such as the throughflow computation. This model solves the flow equation in a two-dimensional form, and can also handle a whole multistage machine in a single pass. Consistent throughflow models with three-dimensional Navier–Stokes solutions are also needed. They may be based on various averages in the blade-to-blade direction, the most useful and coherent of which seems to be the mass-averaging procedure (Hirsch and Dring, 1987). A whole set of mass-averaged Navier–Stokes equations have been given by Hirsch (1990).

The main limitation of throughflow computation is its apparent inability to reproduce three-dimensional effects, of which there are three types: convection, diffusion due to shear stress and heat flux, and blade pressure and friction forces. Some phenomena may however be simulated, provided special models are employed. For instance, the passage vortex is linked to the action of the blade pressure force on the end-wall shear layer. If the pressure field is not too distorted by the vortex, then a boundary layer hypothesis may be used for the end-wall layer computation. Similarly, in an inviscid flow, the information about the pressure force may be replaced by the flow deviation. The secondary flow deviation, which is an aspect of the three-dimensional convection effect, may then be easily computed with the help of a vorticity transport equation. In this equation, the explicit influence of the pressure is naturally weak, and appears implicitly through the inviscid flow deviation. Leboeuf and Brochet (1985) have obtained some good results inside blade compressor passages. However, because this type of method does not take into account three-dimensional convection or diffusion, it forces the secondary vorticity and also the losses, to be confined to the end-walls. This behavior is a severe limitation for the computation of multistage machines.

Supplementary models have been derived that may account for a so-called "radial mixing" process. Two basic approaches have been followed. Adkins and Smith (1982) assume a model, based on "the convection of fluid properties by the secondary flow field" with various contributions of the passage vortex, the leakage clearance effects, the centrifugal effect on the blade boundary layer and wake. On the contrary, Gallimore and Cumpsty (1986) assume a diffusion model for the radial mixing process. In practice, both models introduce diffusion terms in the throughflow equation. A mixing diffusion coefficient has to be adjusted to fit the experimental data. Dring (1993) has shown that, even for very high values of the mixing coefficient, neither of the previous radial mixing models were able to correct the discrepancy between the measured blade pressure force and the measured momentum changes across the blade row for his two-stage axial flow compressor. More important, according

---

Contributed by the International Gas Turbine Institute and presented at the 38th International Gas Turbine and Aeroengine Congress and Exposition, Cincinnati, Ohio, May 24–27, 1993. Manuscript received at ASME Headquarters February 1993. Paper No. 93-GT-21. Associate Technical Editor: H. Lukas.

to this author, the impact of these models "is small, and it is not in general driving it toward the measured results." In his conclusion, Dring suggests the possible strong influence of corner stall on his test case.

Leylek and Wisler (1991) have performed a three-dimensional Navier–Stokes computation in axial-flow compressors. In their answers to the written discussion of the paper, they remark that "there is general agreement ... that both secondary flow (three-dimensional convection effects) and turbulent diffusion can play important roles in the mixing process."

The objective of this paper is to estimate the relative importance of the various terms that occur after an azimuthal average is applied on the Navier–Stokes equations. For that purpose, we have performed a numerical experiment with a three-dimensional Navier–Stokes code. The results of a computation, performed with a three-dimensional Navier–Stokes computation at ONERA, have been used. For the test case, we use a turbine profile with a high deviation capability; this enables a strong three-dimensional distortion of the flow. However, a cascade with straight blades was chosen, to focus on the main flow features related to viscous and turbulent effects. The results of the Navier–Stokes computation have been averaged in the blade-to-blade direction. The various terms of the throughflow momentum equations have been computed. Our purpose is to show how three-dimensional effects will disturb the averaged blade-to-blade quantities, with particular emphasis on convection, pressure, and shear-driven phenomena.

The Test Case and the Navier–Stokes Computation

We have used the test turbine proposed by Denton et al. (1990). This is a cascade of turbine blades with a profile typical of the root section of a low-pressure aircraft gas turbine. It has been tested in the variable density cascade tunnel at the Whittle Laboratory in Cambridge (United Kingdom). The experimental conditions are: overall deviation of the flow 92.4 deg, inlet Mach number 0.5, isentropic exit Mach number 0.71, inlet Reynolds number 2.3×10^5.

The computation has been performed by ONERA with the code CANARI. This method has been developed by different authors at ONERA (Cambier et al., 1988). The numerical method is characterized by an explicit centered finite difference scheme of Lax–Wendroff type, with two steps, associated with a multigrid accelerator. Artificial viscosity of second and fourth order is added to the equation, to ensure numerical stability. Boundary conditions as well as connections between subdomains are treated with compatibility relationships.

The code is used here with a fine mesh, which allows an accurate description of the wall geometry. The splitting of the domain in an O-type mesh around the blade and two H-type subdomains upstream and downstream allows an accurate description of the rounded trailing and leading edges. The subdomains have respectively 28,875, 262,605, and 42,875 meshes, from upstream to downstream, on the half-blade span. The location of the mesh points in the laminar sublayer enables the capture of very small vortex structures. The turbulence model is the mixing length model of Michel et al. (1969), corrected for three-dimensional geometries by the model from Buleev (1962). Although it is a very simple turbulence model, it produces a good qualitative picture of the flow behavior. All the flow quantities, and the terms in the equations presented in this paper, have been nondimensionalized by reference quantities: temperature $T_{\text{ref}} = 293$ K, density $\rho_{\text{ref}} = 1293$ kg/s, velocity $u_{\text{ref}} = 341.1$ m/s, length $L_{\text{ref}} = 0.05253$ m. The fluid is air.

This code has been validated on various fundamental and turbomachine cases, including turbines with similar meshes (Cambier et al., 1988; Escande and Cambier, 1991). The predictions appear to be of good quality. As it is not our purpose to check the accuracy of the predictions against experimental results, we shall assume that these numerical data produce a good qualitative simulation of the local flow structures.

The Blade-to-Blade Average

The results of the computation have been mass averaged in the blade-to-blade direction z, which stands for the circumferential direction θ in a cylindrical frame of reference. As the turbine blades are arranged in a straight fixed cascade, we use a Cartesian frame where x is the axial direction and y is a direction parallel to the blade span.

The mass-averaging process is described by the following formulas. If $A(x, y, z)$ is a flow variable, $\bar{A}$ is the related mass-weighted spatial average and A' is the spatial fluctuation of A in the z direction:

$$A(x, y, z) = \bar{A}(x, y) + A'(x, y, z) \tag{1}$$

$$\overline{\rho A} = \tilde{\rho}\bar{A} = \frac{1}{b}\int_0^b \rho A d(z/g) \tag{2}$$

where g is the blade pitch and b is the fraction of space free of blades. The variable A stands for any flow variables, except for the density ρ, the pressure P, and the shear stress for which Eq. (2) is replaced by a simple area average. In that case, the following notation is used:

$$\rho(x, y, z) = \tilde{\rho}(x, y) + \rho''(x, y, z)$$

$$P(x, y, z) = \tilde{P}(x, y) + P''(x, y, z)$$

Using this averaging process on the gradient operator, we get:

$$\overline{\boldsymbol{\nabla}} A = \frac{1}{b}\overline{\boldsymbol{\nabla}}(b\bar{A}) + \frac{1}{b}\Delta[A\,\mathbf{n}]_{ps}^{ss} \tag{3}$$

where $\overline{\boldsymbol{\nabla}}$ is the gradient operator in the (x, y) plane, and Δ is the difference operator. The last term of Eq. (3) stands for a blade effect; it is the origin of the blade pressure and shear force in the momentum equations.

The average of the nonlinear terms in the transport equa-

Nomenclature

b = blade blockage in the z direction
g = distance between two consecutive blades, in the z direction, outside the blade passage
K = kinetic energy of the spatial fluctuation in the z direction
P = static pressure
Re = Reynolds number
T = temperature
u = velocity
x, y, z = axial, spanwise, and blade-to-blade directions
ρ = static density
τ = shear stress
n = unit vector in z direction

Superscripts

$\bar{}$ = mass average in the z direction (see Eq. (2))
$'$ = fluctuation in the z direction around the mass average (see Eq. (3))
$\tilde{}$ = area average in the z direction
$''$ = fluctuation in the z direction around the area average

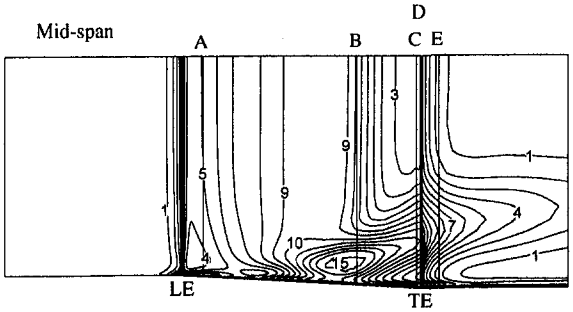

Fig. 1 Averaged kinetic energy $\overline{K}$ of the spatial fluctuation in the (x, y) surface (*LE* and *TE* stand for leading edge and trailing edge, respectively)

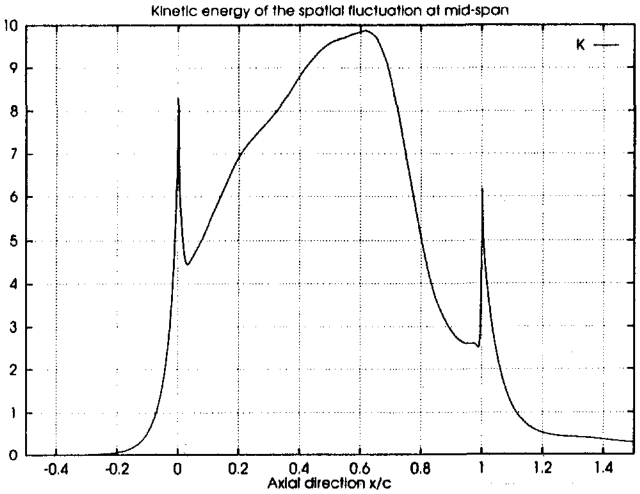

Fig. 2 Axial evolution of the averaged kinetic energy $\overline{K}$ at midspan

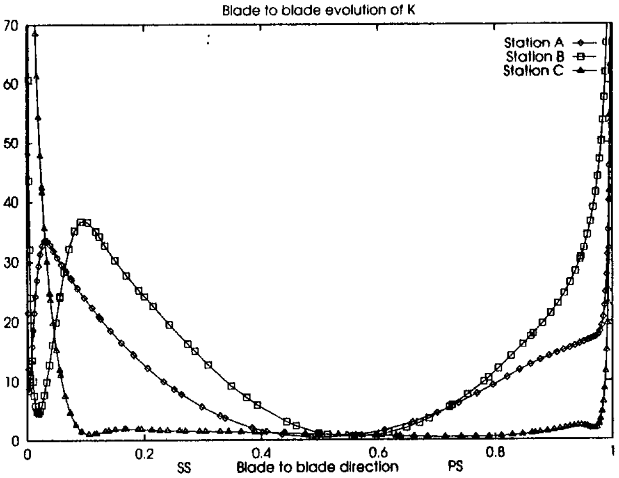

Fig. 3 Blade-to-blade evolution of K for the station A to C defined in Fig. 1

tion will introduce some new unknowns, from the point of view of the averaged quantities:

$$\overline{\rho AB} = \tilde{\rho}\overline{A}\,\overline{B} + \overline{\rho A'B'} = \tilde{\rho}\overline{A}\,\overline{B} + \tilde{\rho}\overline{A'B'} \qquad (4)$$

The last term in Eq. (4) is derived according to Eq. (2); it accounts for the nonuniformity of the flow in the blade-to-blade direction, which is influenced by the three-dimensional nature of the flow.

This averaging process is then applied to the three components of the momentum equation. It is described in the following paragraphs.

The Kinetic Energy of the Spatial Fluctuation

The local value of the spatial fluctuation kinetic energy K is defined as:

$$K = K_x + K_y + K_z = \frac{1}{2}\left(u_x'^2 + u_y'^2 + u_z'^2\right)$$

and the averaged value:

$$\overline{K} = \overline{K_x} + \overline{K_y} + \overline{K_z} = \frac{1}{2}\left(\overline{u_x'^2} + \overline{u_y'^2} + \overline{u_z'^2}\right) \qquad (5)$$

Figure 1 displays the evolution of the averaged kinetic energy $\overline{K}$ in the (x, y) plane. Figures 4(a) to 4(e) give five representations of the local quantity K in (y, z) planes. The locations of these planes are given by the symbols A to E on Fig. 1, with the following axial locations x/c = 0.1, 0.75, 0.98, 1.0, 1.1.

We consider first the structure of the spatial fluctuation kinetic energy $\overline{K}$. At midspan, the flow is two dimensional (x, z), because it is a symmetric plane. Figure 2 gives the axial evolution of the averaged kinetic energy $\overline{K}$ at midspan. Upstream the leading edge $\overline{K}$ strongly increases until a maximum occurs at the leading edge, then it decreases. This phenomenon results from the blade surrounded by the flow. This is a potential effect. In Fig. 1, we notice that this effect is reinforced near the end-wall by the boundary layer separation that occurs in front of the leading edge. In the blade passage, $\overline{K}$ is maximum just after midchord and then strongly decreases. This has two origins: the boundary layer development on the blade walls, and the blade suction side acceleration that is a consequence of the curvature. The blade-to-blade evolution at midspan of the local spatial fluctuation kinetic energy is given in Fig. 3 for the stations A to C defined above. Clearly the suction side acceleration effect is dominant in stations A and B, while near the trailing edge (station C), where no wall curvature exists, there is only the blade wall boundary layer effect. Finally, at the trailing edge, the wake leads to an important discontinuity on K (Fig. 2). The peak of $\overline{K}$ is a consequence of a strong local flow reorganization. The strong dissipation of the wake may be seen on this figure. At midspan, we can remark on Fig. 1, that the previous observations are maintained up to 5 percent of the half-span from the end-wall at the leading edge, and 25 percent at the trailing edge. This shows that the flow is strictly two dimensional in this region.

We describe now, the three-dimensional effects on K: the leading edge vortex, the suction side corner effect, the blade passage, and the wake influences. On Fig. 4(a) located near the leading edge, the maximum of kinetic energy K, shown near the end-wall, indicates the leading edge vortex. Only the suction side leg may be seen on this figure; the pressure side one is already dissipated. On Fig. 4(b, c) located after midchord in the blade passage, the maxima of K are located near the blade walls, as a consequence of the wall boundary layer and of the passage vortex. A small area of high K value may also be observed in the pressure side corner; this is a consequence of the averaging process as there is a difference in direction between the blade walls and the average flow in the end-wall shear layer. On Fig. 4(c, d, e), two regions of maximum kinetic energy may be observed. First in the suction side corner, a strong dissipation and a strongly reduced velocity magnitude exists. Furthermore near the suction side, but displaced away from the end-wall along the blade, a maximum exists; this area is influenced by a strong passage vortex that interacts with the blade wall, with a corresponding strong increase in velocity magnitude near the wall. At the trailing edge, the averaged fluctuation kinetic energy suddenly increases all over the blade span (Figs. 1 and 2).

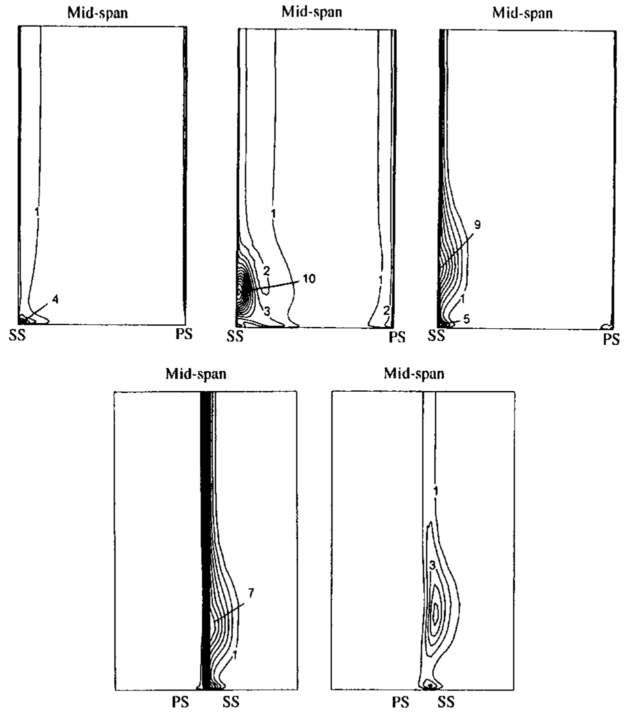

Fig. 4 Local kinetic energy *K* of the spatial fluctuation in four (*y*, *z*) surfaces (*a*), (*b*), (*c*), (*d*), and (*e*) whose axial locations are given on Fig. 1

The passage vortex effect and the suction side corner one are superposed on wake effect (Fig. 4(*d*)). As seen on Fig. 4(*d*, *e*), and on Fig. 1, the secondary kinetic energy *K* strongly decreases after the trailing edge, particularly in the wake, while the passage vortex is still detected 50 percent of chord downstream.

The Averaged *y* Component Equation: The "Radial Equilibrium" Equation

The averaged *y* component of the momentum equation is written as:

$$\frac{\partial}{\partial x}\left(b\bar{\rho}\overline{u_x u_y}\right) + \frac{\partial}{\partial y}\left(b\bar{\rho}\overline{u_y}^2\right) = -\frac{\partial}{\partial y}b\bar{P} - \frac{\partial}{\partial x}\left(b\bar{\rho}\overline{u'_x u'_y}\right) - \frac{\partial}{\partial y}\left(b\bar{\rho}\overline{u'^2_y}\right) + \frac{1}{R_e}\left\{\frac{\partial}{\partial x}\left(b\bar{\tau}_{xy}\right) + \frac{\partial}{\partial y}\left(b\bar{\tau}_{yy}\right)\right\} - \frac{1}{R_e}\left\{\Delta\left[\tau_{xy}\frac{\partial z}{\partial x}\right]_{ps}^{ss} + \Delta\left[\tau_{yy}\frac{\partial z}{\partial y}\right]_{ps}^{ss} - \Delta\left[\tau_{zy}\right]_{ps}^{ss}\right\} \quad (6)$$

The blades are not twisted, and so $\partial z/\partial y = 0$ on the blade surfaces. As the no-slip condition is used in the three-dimensional computation, the average of the convective transport terms does not introduce any contribution on the blade surfaces. The different terms of Eq. (6) are written as follows:

Convection terms

= Pressure terms + Fluctuation terms + Shear stress terms

Figure 6 gives the *y* momentum balance at station B defined in Fig. 1. Figures 5(*a*) to 5(*c*) give the contributions of the individual terms to the balance of Eq. (6). We have not presented the shear stress terms, because their contributions are significant only near the end-wall as we can see in Fig. 6.

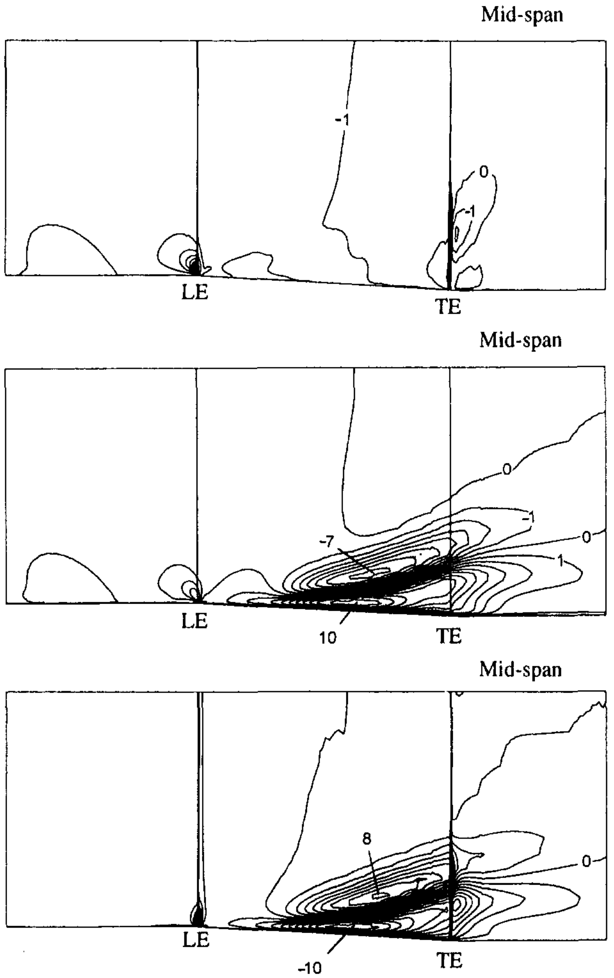

Fig. 5 Contributions of the most important terms in the *y* component of the momentum Eq. (6): (*a*) convection term, (*b*) pressure term, (*c*) spatial fluctuation term

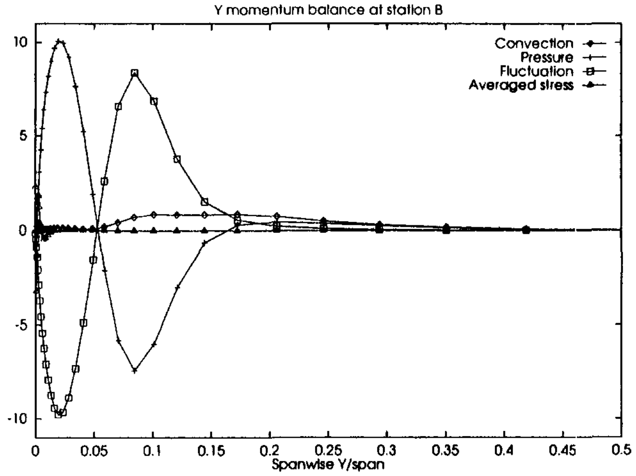

Fig. 6 *Y* momentum balance at station *B* along *y* direction

We have found from the numerical computations that the following terms are negligible compared to the others:

$$\frac{\partial}{\partial y}\left(b\bar{\rho}\overline{u_y}^2\right) \approx 0, \quad \frac{\partial}{\partial x}\left(b\bar{\rho}\overline{u'_x u'_y}\right) \approx 0,$$

$$\left\{\Delta\left[\tau_{xy}\frac{\partial z}{\partial x}\right]_{ps}^{ss} + \Delta\left[\tau_{yy}\frac{\partial z}{\partial y}\right]_{ps}^{ss} - \Delta\left[\tau_{zy}\right]_{ps}^{ss}\right\} \approx 0 \quad (7)$$

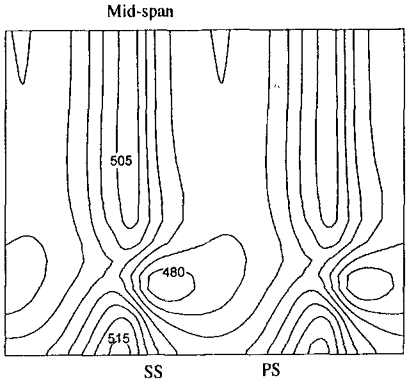

Fig. 7 Static pressure contours at station *E*

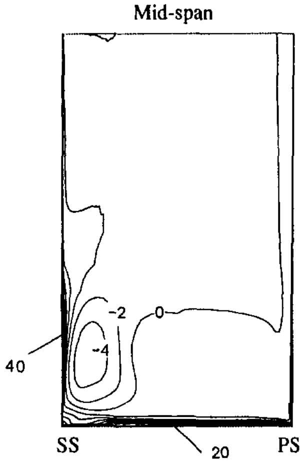

Fig. 8 Local shear stress component τ_{xy} at station C

From Fig. 5, we may conclude that the convective terms (*a*) are negligible compared to the pressure (*b*) and fluctuation terms (*c*). The pressure term (*b*) is then only influenced by the fluctuation terms (*c*); this is a consequence of the passage vortex. This can be understood by considering the static pressure contour station *E* (Fig. 7). We observe a strong distortion of static pressure.

Figure 8 gives the local shear stress component τ_{xy} in station *C*. As mentioned above, the averaged shear stress is significant only near the endwall. Nevertheless, Fig. 8 shows that even though the shear term is negligible in Eq. (6), the local shear stress effect may be important.

From this analysis, we conclude that the influence of the three-dimensional flow structures on the *y* momentum balance (the "radial equilibrium" equation) is very strong, as can be seen on the pressure gradient variations (Fig. 5(*b*)). The pressure varies along *y* mainly under the influences of the gradient along *y* of the fluctuation kinetic energy K_y. A second important conclusion from these computations is the negligible role of the shear stress terms in the *y* momentum balance except near the endwall.

These remarks may suggest some guidelines for throughflow modeling. First, the importance and the convective nature of the spatial fluctuation effect, described in Fig. 5(*c*), should question the exclusive use of diffusive models for the so-called "radial mixing" effects. Second, the present results show clearly that shear stress terms are negligible almost everywhere in the *y*-averaged momentum balance. Finally, trailing edge phenomena are dominated by three-dimensional convection terms and their dissipation. We conclude that shear stress effects mainly occur through the dissipation of the spatial fluctuations.

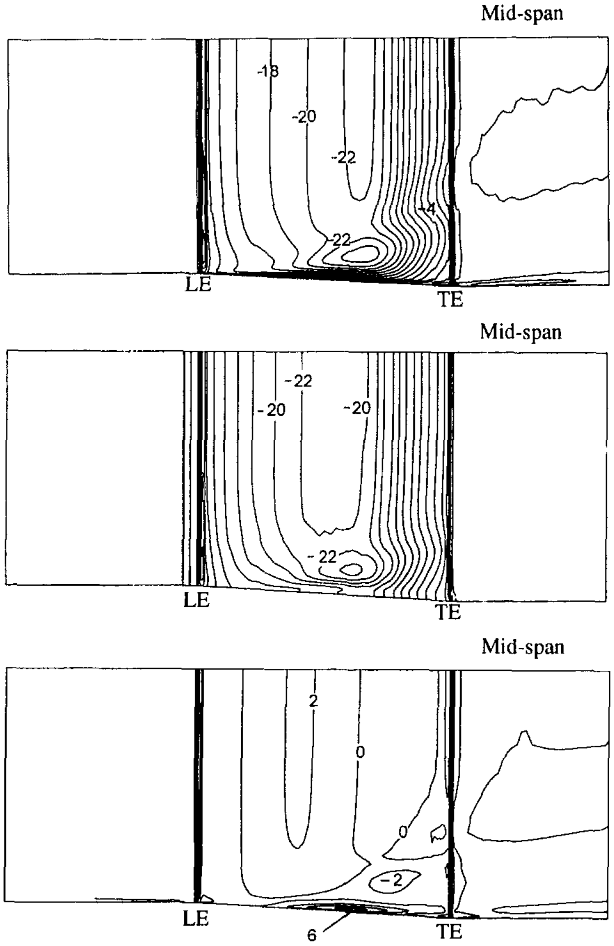

Fig. 9 Contributions of the most important terms in the z component of the momentum Eq. (8): (*a*) convection term, (*b*) blade pressure term, (*c*) spatial fluctuation term

The Averaged *z* Component Equation: The "Blade-to-Blade" Equation

The *z* component of the average momentum equation is given below:

$$\frac{\partial}{\partial x}\left(b\tilde{\rho}\overline{u_x u_z}\right)+\frac{\partial}{\partial y}\left(b\tilde{\rho}\overline{u_y u_z}\right)$$
$$=-\Delta[P]_{ps}^{ss}-\frac{\partial}{\partial x}\left(b\tilde{\rho}\overline{u'_x u'_z}\right)-\frac{\partial}{\partial y}\left(b\tilde{\rho}\overline{u'_y u'_z}\right)$$
$$+\frac{1}{R_e}\left\{\frac{\partial}{\partial x}\left(b\tilde{\tau}_{xz}\right)+\frac{\partial}{\partial y}\left(b\tilde{\tau}_{yz}\right)\right\}$$
$$-\frac{1}{R_e}\left\{\Delta\left[\tau_{xz}\frac{\partial z}{\partial x}\right]_{ps}^{ss}+\Delta\left[\tau_{yz}\frac{\partial z}{\partial y}\right]_{ps}^{ss}-\Delta[\tau_{zz}]_{ps}^{ss}\right\}\quad(8)$$

We have found from our numerical computations that the gradient along *y* of the momentum is negligible compared to the *x* one. As in the previous paragraph, the blade shear stress terms are negligible too. Figure 10 presents the *z* momentum balance at station *B* and Figs. 9(*a*) to 9(*c*) the evolution of the individual terms in the *z*-momentum equation in the (*x*, *y*) plane. The blade pressure force (Fig. 9(*b*)) is maximum and midchord. Figure 10 shows that the blade pressure term has a strong counterpart in the gradient along *x* of the momentum. This momentum gradient is also influenced by the shear stress terms near the end-wall and by the spatial fluctuation terms everywhere (about 10 percent). The evolution of the fluctuation terms (Fig. 9(*c*)) has three ori-

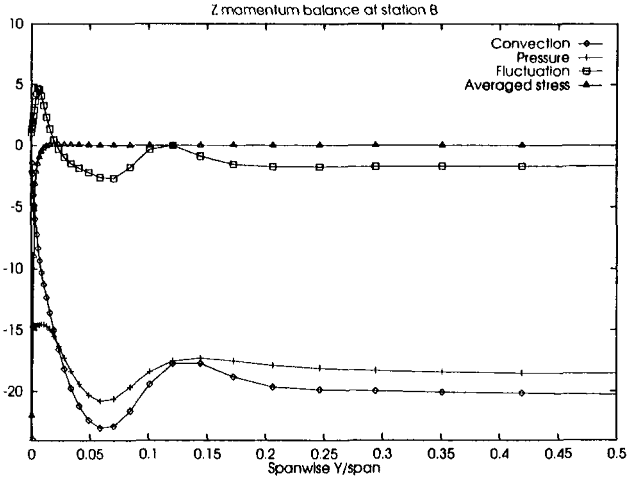

Fig. 10 The *z* momentum balance at station *B* along *y* direction

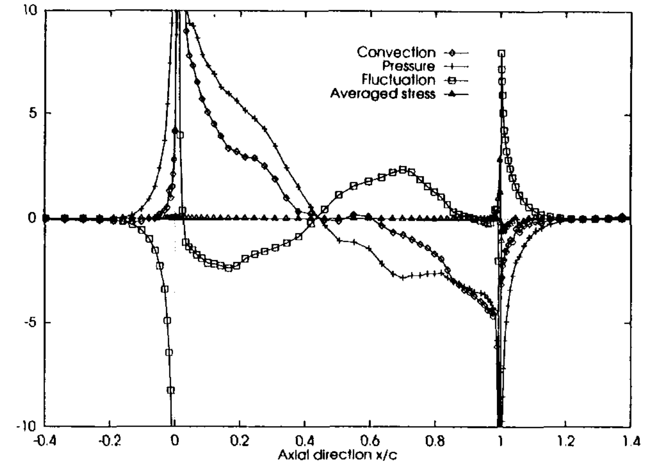

Fig. 11 Axial evolution of the *x*-momentum balance at midspan along *x* direction

gins: a two-dimensional effect described above (Fig. 2), an important contribution of the suction side corner effect, and a slight influence of the passage vortex.

The local components of the shear stress tensor are not presented in detail here, for lack of space; however, their overall behaviors are very well represented by the τ_{xy} value in Fig. 8.

We conclude that the spatial fluctuation terms have a small but not negligible influence on the balance of the z-momentum equation. However, the three-dimensional effects have a stronger indirect control on this equation. They modify the pressure gradient in the y equation (Fig. 5(*b*)). This has some consequence on the blade pressure force, particularly near the end-wall (Fig. 9(*b*)); in particular, the location of the passage vortex core very near the blade suction side (Fig. 7) is responsible for the high variation of the blade force. The shear stresses have a negligible direct effect on the z-momentum balance except near the endwall.

The Averaged Axial x Component Equation

The x component of the average momentum equation is given below:

$$\frac{\partial}{\partial x}\left(b\tilde{\rho}\overline{u_x^2}\right) + \frac{\partial}{\partial y}\left(b\tilde{\rho}\overline{u_x u_y}\right) =$$
$$-\frac{\partial}{\partial x}(b\tilde{P}) + \Delta\left[P\frac{\partial z}{\partial x}\right]_{ps}^{ss} - \frac{\partial}{\partial x}\left(b\tilde{\rho}\overline{u'_x u'_x}\right) - \frac{\partial}{\partial y}\left(b\tilde{\rho}\overline{u'_x u'_y}\right)$$
$$+\frac{1}{R_e}\left\{\frac{\partial}{\partial x}(b\tilde{\tau}_{xx}) + \frac{\partial}{\partial y}(b\tilde{\tau}_{xy})\right\}$$
$$-\frac{1}{R_e}\left\{\Delta\left[\tau_{xx}\frac{\partial z}{\partial x}\right]_{ps}^{ss} + \Delta\left[\tau_{xy}\frac{\partial z}{\partial y}\right]_{ps}^{ss} - \Delta[\tau_{xz}]_{ps}^{ss}\right\} \quad (9)$$

Figures 12(*a*) to 12(*c*) give the contributions of the most important terms in the x components of the momentum Eq. (9): (*a*) convection term, (*b*) axial pressure gradient and pressure blade force, (*c*) the fluctuation terms.

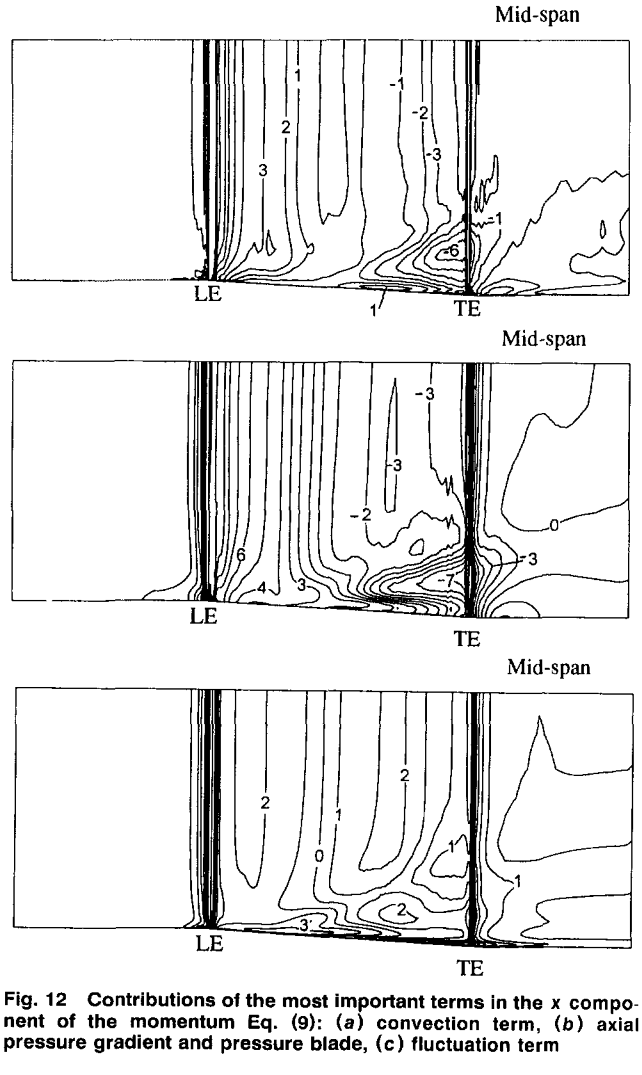

Fig. 12 Contributions of the most important terms in the *x* component of the momentum Eq. (9): (*a*) convection term, (*b*) axial pressure gradient and pressure blade, (*c*) fluctuation term

As previously, the blade shear stress terms are negligible, and the axial averaged shear stress gradient is significant only near the end-wall. On the whole, there exists an approximate balance between the pressure term (*b*) and the convection term (*a*). We can notice that the axial pressure gradient and the pressure blade forces have the same order of magnitude in the pressure term (*b*), although their contributions are not shown here. Moreover the three-dimensional influence is more important on the pressure blade force than on the axial pressure gradient. Figure 11 presents the axial evolution of the momentum balance at midspan. It shows that, in the blade passage, the fluctuation terms are of the order of 10 to 20 percent of the other terms, with strong peaks at the leading and trailing edges. Their origins are linked to the suction side acceleration described in the paragraph on the spatial fluctuation kinetic energy (Fig. 2).

Conclusion: Some Comments About Axisymmetric Flow Computation

From the previous momentum balance analysis, we may suggest some guidelines for axisymmetric flow modeling.

First we show that the spatial fluctuation influences are important in the x, y, and z components of the momentum equation. They have two origins: the three-dimensional flow structures and a two-dimensional effect. The latter is a consequence of the blade curvature and of the boundary layers on the blade walls. This is a major contribution in the x and z components of the momentum equation. We have shown that the radial kinetic energy K_y is modified by the passage vortex. It is responsible for the strong variations of the averaged static pressure along y, as observed inside the blade passage (Eq. (6)). This three-dimensional effect is transferred into the other components of the momentum equation, with the averaged pressure variations along y. A blade pressure force variation along the span will modify the balance in the blade-to-blade (z) and axial (x) directions. The most important contribution to the three-dimensional convection effect is then clearly K_y and the distribution role of the pressure. Note that the blade pressure force is strongly influenced by fluctuation terms and namely the three-dimensional effects. This fact is generally ignored in the through-flow computations.

Furthermore, we have found from the numerical computation that the blade shear stress terms as well as the averaged shear stress terms are negligible almost everywhere except in the endwall region, although τ may reach high local values. The shear stresses have then an indirect effect on the momentum balance through the dissipation of the fluctuation terms. This is particularly obvious after the trailing edge, although this effect should occur all over the blade passage.

Acknowledgments

The authors like to thank Mr. G. Meauze and G. Billonnet from ONERA, Chatillon, for having performed this three-dimensional Navier–Stokes computation. Their help and interest throughout this work have been strongly appreciated.

We would also thank EDF, SEP, SNECMA, and TURBOMECA, which as partners of a Firtech organization, have provided part of the financial support for the grant of G. Perrin.

References

Adkins, G. G., and Smith, L. H., Jr., 1982, "Spanwise Mixing in Axial-Flow Turbomachines," ASME *Journal of Engineering for Power*, Vol. 104, pp. 97–110.

Buleev, N. I., 1962, "Theoretical Model of the Mechanism of Turbulent Exchange in Fluid Flows," *Teploperedacha*, Moscow, USSR, pp. 64–98; AERE translation 957, Atomic Energy Research Establishment, Harwell, United Kingdom, 1963.

Cambier, L., Couaillier, V., and Veuillot, J. P., 1988, "Résolution numérique des équations de Navier–Stokes à l'aide d'une méthode multigrille," *La Recherche Aérospatiale*, No. 1988-2, pp. 23–42.

Dawes, W. N., 1987, "A Numerical Analysis of the Three-Dimensional Viscous Flow in a Transonic Compressor Rotor and Comparison With Experiment," ASME JOURNAL OF TURBOMACHINERY, Vol. 109, pp. 83–90.

Denton, J. D., Hodson, H. P., and Dominy, R. G., 1990, "Test Case E/CA-7: Subsonic Turbine Cascade LA," in: "Test Cases for Computation of Internal Flows in Aero-engine Components," AGARD-AR-275, Fottner, ed., pp. 124–138.

Dring, R. P., 1993, "Radial Transport and Momentum Exchange in an Axial Compressor, " ASME JOURNAL OF TURBOMACHINERY, Vol. 115, pp. 477–486.

De Ruyck, J., and Hirsch, C., 1988, "A Radial Mixing Computation Method," ASME Paper No. 88-GT-68.

Escande, B., and Cambier, L., 1991, "Validation du Code CANARI par le Calcul de l'Ecoulement Tridimensionnel Turbulent dans un Distributeur de Turbine," AGARD CP 510, San Antonio, TX.

Gallimore, S. J., and Cumpsty, N. A., 1986, "Spanwise Mixing in Multistage Axial Flow Compressors: Part I—Experimental Investigations; Part II—Through Flow Calculations Including Mixing," ASME JOURNAL OF TURBOMACHINERY, Vol. 108, pp. 2–16.

Hirsch, C., and Dring, R. P., 1987, "Through-Flow Models for Mass and Momentum-Averaged Variables," ASME JOURNAL OF TURBOMACHINERY, Vol. 109, pp. 362–370.

Hirsch, C., 1990, *Numerical Computation of Internal and External Flows*, Wiley.

Leboeuf, F., and Brochet, J., 1985, "The Use of a Secondary Flow Computation in the Compressor Design Process," *Three Dimensional Flow Phenomena in Fluid Machinery*, Hamed, Herring, and Povinelli, eds., ASME FED-Vol. 32.

Leylek, J. H., and Wisler, D. C., 1991, "Mixing in Axial-Flow Compressors: Conclusions Drawn From Three-Dimensional Navier–Stokes Analyses and Experiments," ASME JOURNAL OF TURBOMACHINERY, Vol. 113, pp. 139–160.

Michel, R., Quemard, C., and Durant, R., 1969, "Application d'un schéma de longueur de mélange à l'étude des couches limites turbulentes d'équilbres," ONERA NT No. 154.

The Influence of Load Distribution on Secondary Flow in Straight Turbine Cascades

A. P. Weiss

L. Fottner

Institut für Strahlantriebe,
Universität der Bundeswehr München,
8014 Neubiberg, Federal Republic of
Germany

This paper describes an experimental study of the three-dimensional flow within two highly loaded turbine cascades subjected to the same overall load but different load distributions. Data were obtained using pneumatic probes, pressure tappings, and a surface flow visualization technique. It is found that the general nature of the flow is similar for both cascades. In the exit plane the cascades show different spanwise loss distributions. However, the averaged secondary loss is quite similar in this plane. Examining the measurements farther downstream and also by comparing the calculated mixed-out values, it becomes clear that a higher magnitude of secondary loss is generated by the front-loaded cascade.

Introduction

Modern axial turbines operate with a high level of efficiency. In order to achieve a further improvement the design engineer has to aim at a reduction of the profile losses as well as of the secondary losses, e.g., by endwall contouring or three-dimensional design of the airfoils. The design of turbines with reduced secondary losses requires a detailed knowledge of the various secondary flow phenomena and the attributable losses. Therefore in recent years detailed studies of flow have been carried out with the objective to evaluate the influence of various parameters like Mach number (Perdichizzi, 1990), Reynolds number (Hodson and Dominy, 1987a, b), blade-loading (Yamamoto and Nouse, 1988), aspect ratio (Watzlawick, 1992), and inlet boundary layer thickness (Chen and Dixon, 1986) on the nature of secondary flow and the mechanism of loss production. Another important parameter that has not been studied sufficiently yet is the load distribution. Only a few publications, e.g., Marchal (1980) have been published dealing with cascades of the same deflection but different profiles. Marchal investigated two turbine cascades of the same aerodynamic loading but different load distributions. He did not find an effect on the secondary losses. He explains this unexpected result by means of a quality factor Q, which describes the influence of different load distributions. For the investigated cascades this quality factor was equal. Therefore no influence could be determined.

If it is possible to reduce the magnitude of secondary losses by an optimized load distribution, that will be a relative simple optimization process in contrast to a three-dimensional design of the airfoils. However, the design engineer needs some criteria to choose the profile velocity distribution with respect to low secondary losses. The main goal of the research project in the scope of which the presented investigations have been performed is to acquire these criteria.

In order to answer the following questions, two highly loaded turbine cascades subjected to the same overall load but different load distributions have been studied:

1 Are the overall secondary losses affected by the load distribution?
2 How does the development of the secondary flow field behave when subjected to different load distributions?
3 Which significant loss mechanisms can be found?
4 How are the spanwise loss and angle distributions influenced by the load distribution?

Experimental Details

The experiments described in this report were conducted in the High-Speed Cascade Wind Tunnel of the German Armed Forces University/Munich. It consists of an open-loop test facility with an open test section. The whole wind tunnel is installed in a cylindrical pressure tank. By evacuating the tank partly, Mach number and Reynolds number of the flow can be varied independently (see Sturm and Fottner, 1985).

To investigate the influence of profile pressure distribution on secondary flows, two highly loaded low-pressure turbine cascades were selected, which were designed for the same overall load but different load distributions. The objective of the design of T104 was to obtain a profile pressure distribution that prevents any deceleration region (see Hoheisel et al., 1987). It could be achieved by a strong acceleration in the front part of the suction side incorporating a small amount of deceleration in the rear part. Thus, the velocity distribution along the pressure side is a result of the required aerodynamic loading. According to this specification a front-loaded cascade was designed. The requirement for the T106 was to maintain the laminar boundary layer on the suction side as far downstream as possible by a long acceleration part. Therefore the T106

Contributed by the International Gas Turbine Institute and presented at the 38th International Gas Turbine and Aeroengine Congress and Exposition, Cincinnati, Ohio, May 24-27, 1993. Manuscript received at ASME Headquarters February 19, 1993. Paper No. 93-GT-86. Associate Technical Editor: H. Lukas.

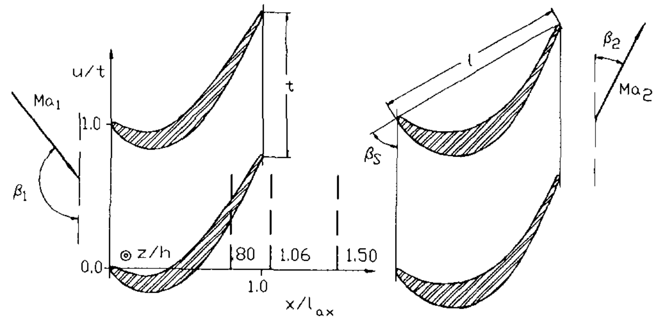

T104
t/l = 0.758
β_S = 52.50°

T106
t/l = 0.799
β_S = 59.28°

Design Conditions: $Ma_{2th} = 0.59$, $Re_{2th} = 5*10^5$, $\beta_1 = 127.7°$, $\beta_2 = 26.8°$

Fig. 1 Cascade geometries and measuring planes

cascade is aft-loaded. The associated profile shapes and cascade geometries are shown in Fig. 1. The radii of the leading edges and the trailing edges of both cascades are identical.

Cascades consisting of seven blades were taken for the respective tests. The large aspect ratio of 3.0 (l = 100 mm, h = 300 mm) ensured that there was no direct interference between the secondary flow fields of the two ends of a blade. The cascades were instrumented with static pressure tappings along the midspan section of the blade profiles (51 tappings) and with 108 tappings at the endwall. The static pressure at the inlet of the cascades and the upstream boundary layer profile were measured about one axial chord length upstream of the leading edge plane. A conventional pitot probe was placed 500 mm upstream of the cascade inlet plane, close to the channel center line. The total temperature was measured using resistance thermometers in the settling chamber. With the assumption of an adiabatic flow, this temperature corresponded to the total temperature in the test section.

For the flow field traverses a five-hole spherical probe was used (head diameter 2.6 mm). A flattened pitot (0.6 mm × 1.2 mm, overall) was used to traverse the upstream boundary layer.

The facility is equipped with a computer-controlled data acquisition system. Probe movement can be achieved using three linear and one angular traverse mechanisms. The pressures of the five-hole probe are measured by differential pressure transducers of different ranges. A Scanivalve system is available for pressure distribution measurements.

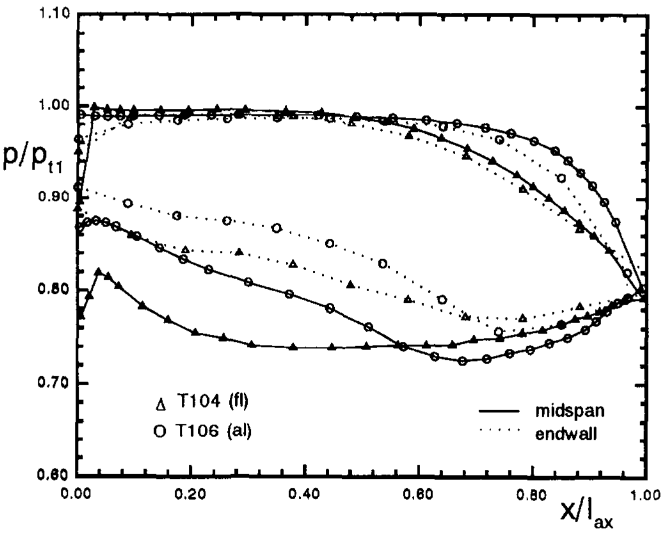

Fig. 2 Profile pressure distributions

Oil-and-dye surface flow pattern were obtained using a mixture of oil, turpentine, and a fluorescent powder, which was photographed under the illumination of ultraviolet light. Because of the wide range of wall shear stresses that occurred within the cascades it was quite difficult to find the optimal mixture in order to show all flow patterns.

All of the tests described in this report were conducted at the design conditions of the both cascades, i.e., an exit Mach number of $M_{2th} = 0.59$ and an exit Reynolds number of $Re_{2th} = 5*10^5$. For these values the degree of turbulence at the cascade inlet plane was about 4 percent (Römer, 1990) simulated by a turbulence grid, which was installed in front of the nozzle of the wind tunnel.

Results and Discussion

Profile Pressure Distribution. The measured midspan profile pressure distributions of the two turbine cascades are presented in Fig. 2.

Nomenclature

al = aft-loaded
fl = front-loaded
H_{12} = shape factor = δ^*/δ^{**}
h = blade height, m
l = blade chord, m
M = Mach number
PS = pressure side
p = static pressure, Pa
p_t = total pressure, Pa
Re = Reynolds number
q = dynamic pressure, Pa
s = distance across blade passage, m
SS = suction side
$S1, S2, S3, S4$ = separation lines
SKE = Secondary Kinetic Energy = $(\rho_g/2*w_{S,g}**2)/q_{2th}$
T_t = total temperature, K
t = blade pitch, m
x, u, z = axial, circumferential, and spanwise coordinate, m
w = flow velocity, m/s
β = circumferential flow angle, deg
β_S = stagger angle, deg
$\Delta\beta$ = deviation from midspan flow angle = $\beta_{m,MS} - \beta$, deg
γ = radial flow angle, deg
Δ = interval of contour plots
δ = boundary layer thickness
δ^* = displacement thickness
δ^{**} = momentum thickness
ζ = loss coefficient = $(p_{t1} - p_t)/q_{2th}$
ρ = density, kg/m^3

Subscripts

ax = axial
fs = free stream
g = total value; mass-averaged in circumferential and spanwise direction
MS = midspan
m = pitchwise mass-averaged
P = profile
S = secondary
t = total
th = isentropic
1 = inlet value
2 = downstream mixed-out value
∞ = mean value (between inlet and outlet)

Table 1 Quality factor Q

	T104	T106
$(\Delta p_{max}/q_{\infty}*l_{ax}/s)$	5.97	5.86
$(1 - x_{min}/l_{ax})$	0.55	0.32
Q	5.13	2.92

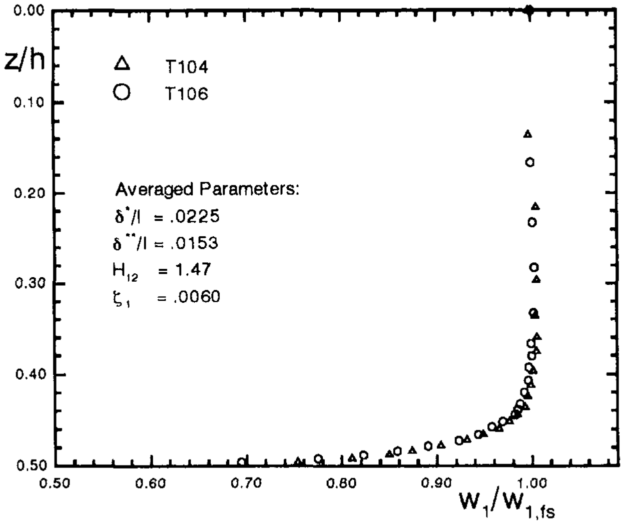

Fig. 3 Inlet boundary layers

As mentioned above the characteristic of the T104 is front-loaded (*fl*) compared with that of the T106, which is aft-loaded (*al*). The T104 reaches the minimum value of p/p_{t1} already at $x/l_{ax} = 0.45$ followed by a slight deceleration to the exit value. For the T106 cascade the minimum suction side pressure doesn't occur until $x/l_{ax} = 0.68$. The following deceleration is stronger. Due to the higher positive pressure gradient on the rear part of the suction surface, there is a weak separation bubble hardly visible in the pressure distribution but in the suction surface visualization.

As mentioned in the introduction Marchal (1980) proposed a quality factor Q, which allows a qualitative evaluation of the effect of blade design on secondary losses:

$$Q = (\Delta p_{\max}/q_{\infty} * l_{ax}/s)^{1.25} * (1 - x_{\min}/l_{ax})$$

The first term takes into account the maximum pressure difference across the blade passage, divided by the corresponding distance between pressure and suction sides nondimensionalized by the mean kinetic energy (q_{∞}) of the main flow. The second term assesses the axial load distribution evaluated by the distance ($x_{\min}$) of the minimum suction side pressure from the leading edge plane. The interesting values of the investigated cascades are given in Table 1.

The maximum pressure gradients are almost equal. Due to the position of the minimum suction side pressure at $x/l_{ax} = 0.45$ the front-loaded cascade T104 shows a higher value of Q. Therefore higher secondary losses are expected.

Inlet Boundary Layer. Figure 3 shows two almost identical velocity profiles of the incoming boundary layers for the turbine cascades at design condition. This agreement is not surprising because the inlet conditions of both cascades are identical and the traverses were carried out about one chord length upstream of the cascades where the potential influence of the cascades is negligible. All boundary layer parameters have been determined using the incompressible form of the appropriate expressions. This is sufficient with respect to the low inlet Mach number $M_1 < 0.3$. The shape factor H_{12} shows that the boundary layers are turbulent. The displacement thickness-chord ratio (δ^*/l) of 0.025 is somewhat high because the natural boundary layer of the wind tunnel was used. However, this value is still close to results from a model turbine (Hunter, 1982).

Surface Flow Visualization. Oil-and-dye pictures are a useful tool in order to obtain a lot of information about the flow characteristics. But it must be taken into account that these flow patterns only provide information about the near surface flow. Therefore, regarding the main body of the flow, the conclusions drawn have to be supported by other measurements (flow field traverses, pressure distributions).

The endwall flow visualizations combined with the measured endwall pressure distributions are shown in Fig. 4. In order to support the discussion of the flow patterns, a schematic interpretation of those is drawn into the endwall pressure distributions (dashed). For both cascades the characteristics of a significant secondary vortex system are visible (see Sieverding, 1985). The "liftoff" line of the upstream boundary layer ahead of the horseshoe vortex with its two legs *S1p* and *S1s* is clearly recognizable as well as the two branches of the separation line of the horseshoe vortex *S2p* and *S2s*. The axial extent of the front yard limited by the separation line *S1* in the case of the front-loaded cascade T104 is larger than that of the T106 (*al*). The suction side legs of the separation lines (*S1s*, *S2s*) join each other before they intersect the suction side at $x/l_{ax} = 0.21$ (T104). For the T106 (*al*) the separation line *S2s* doesn't intersect the suction surface until $x/l_{ax} = 0.24$. The stagnant separation bubble between the separation lines *S1p* and *S2p* is wider on the T104 (*fl*). The streamlines in this region as well as downstream of the separation line *S2p* are generally perpendicular to the isobars. Because of the strong deflection in the T104 cascade just downstream of the leading edge plane, combined with a concentration of the axial circulation distribution in this region, the upstream potential influence of the T104 cascade is stronger. Therefore the separation of the endwall boundary layer occurs farther upstream. Also the evolution of the suction separation lines *S1s* and *S2s* is dictated by the stronger transverse pressure gradient downstream of the leading edge plane especially near the suction side. This causes the earlier intersection of the separation lines with the suction side. The aforementioned separation bubble between the line *S1p* and *S2p* affects the endwall pressure distribution, too. The pressure gradient in the mean flow direction in this region is almost zero. Behind the separation line *S2p* a break occurs in the slope of the isobars. Downstream of the intersection point of the *S1p* with suction surface (T104: $x/l_{ax} = 0.28$; T106: $x/l_{ax} = 0.35$) the formation of a separation line *S3* indicates the development of a suction corner vortex. The striking feature of the endwall pressure distributions is that the pressure minimum appears in the region of the throat ($x/l_{ax} \approx 0.65$) for both cascades. That is remarkable because the midspan profile pressure distributions (see Fig. 2) show that the T104 is quite front-loaded in contrast to the T106. This difference seems to be weaker at the endwall. In order to check this the endwall pressure tappings closest to the profiles were used to determine the endwall profile pressure distributions. In addition to the values at midspan, these endwall distributions are plotted in Fig. 2. Obviously both cascades become unloaded up to $x/l_{ax} = 0.6$ caused by the endwall flow as mentioned by Langston et al. (1976), too. The pressure side distributions are hardly changed. However, the most important aspect is that the distribution of the T104 loses its front-loaded character. At the endwall the maximum pressure difference across the blade passage doesn't occur until $x/l_{ax} = 0.6$.

On the suction surface (see Fig. 5) the separation line of the suction side leg of the horseshoe vortex migrates beside the

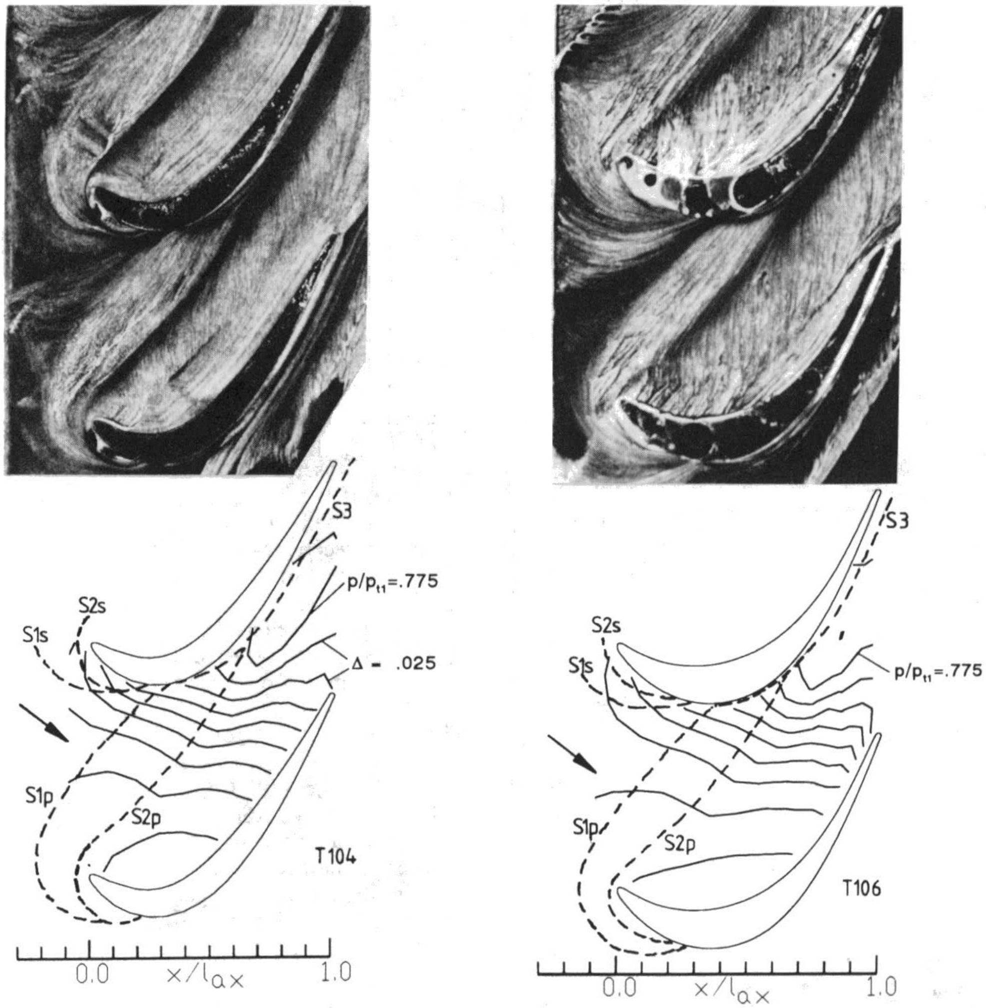

Fig. 4 Endwall flow visualizations compared with endwall pressure distribution measurements

separation line of the passage vortex *S*4 to the exit plane. An important feature to note is the larger depth of penetration into the mean flow of the limiting streamlines for the front-loaded T104 (T104: *S*4 $z/h = 0.385$, *S2s* $z/h = 0.34$; T106: *S*4 $z/h = 0.4$, *S2s* $z/h = 0.36$). This larger depth of penetration indicates a stronger passage vortex (see Sharma and Graziani, 1983). Between the separation line *S2s* and *S*4 less dye is removed. That is an indication for a high-loss core. As mentioned above a weak separation bubble is visible on the suction surface of the T106. It seems that this bubble has no significant effect on the evolution of the three-dimensional flow.

Traverse Results. The results of the five-hole probe traverses in the first measuring plane at $x/l_{ax} = 0.8$ are plotted in Fig. 6, in the form of loss coefficient contours (ζ), secondary velocity vectors, and isoclinics for the circumferential flow angle β and the radial flow angle γ. Applying the isoclinal method of Binder and Romey (1983) the location of the secondary vortices can be identified by means of the flow angles β and γ. In the present analysis for straight cascades, secondary flow is defined as the deviation from flow at midspan. Therefore the pitchwise local flow directions at midspan were used to determine the secondary flow vectors at other spans; secondary flow vectors were calculated in the following: flows at other spans were projected onto a plane normal to the flow direction at midspan, which is located at the same pitchwise location as the calculated points (see Marchal and Sieverding, 1977). Due to the minimal distance from the walls of about 5 mm, which is necessary with respect to the five-hole probe, it was not possible to determine the profile boundary layers and the new endwall boundary layer. The locations of the limiting streamlines (Fig. 5) are marked in the loss contours. The nondimensional coordinate $z/h = 0.0$ corresponds with midspan; $z/h = 0.5$ corresponds with the endwall. The measuring planes were parallel to the cascade exit planes (see Fig. 1).

At $x/l_{ax} = 0.8$ the inlet boundary layer has already rolled up and has been transported into the suction side endwall corner. In addition, the high loss fluid in the pressure side endwall corner has been replaced by fluid from the free stream. That is why a low loss region develops there. Both cascades show two loss cores in this plane. The first, located between the separation lines *S2s* and *S*4 close to the suction surface, belongs to a three-dimensional separation. This separation is a result of the interaction of the passage vortex and the suction side leg of the horseshoe vortex. The second peak is separated from the suction side and the endwall and is more clearly developed in the T104 (*fl*) cascade. Also the radial extent of the endwall loss region is larger for the T104 cascade.

These layers of the upstream boundary layer, which are closest to the endwall and which contain the highest losses, roll up into the horseshoe vortex. The suction side leg is deflected by the traverse pressure gradient to the suction surface (see Figs. 4 and 5) and migrates beside the passage vortex along the suction surface toward the trailing edge. Therefore, there is a loss core between *S2s* and *S*4 on the suction surface. The pressure side leg of the horseshoe vortex transports a part of the low-momentum fluid across the blade passage into the core of the developing passage vortex and initiates the second loss core.

The secondary velocity field is dominated by the passage

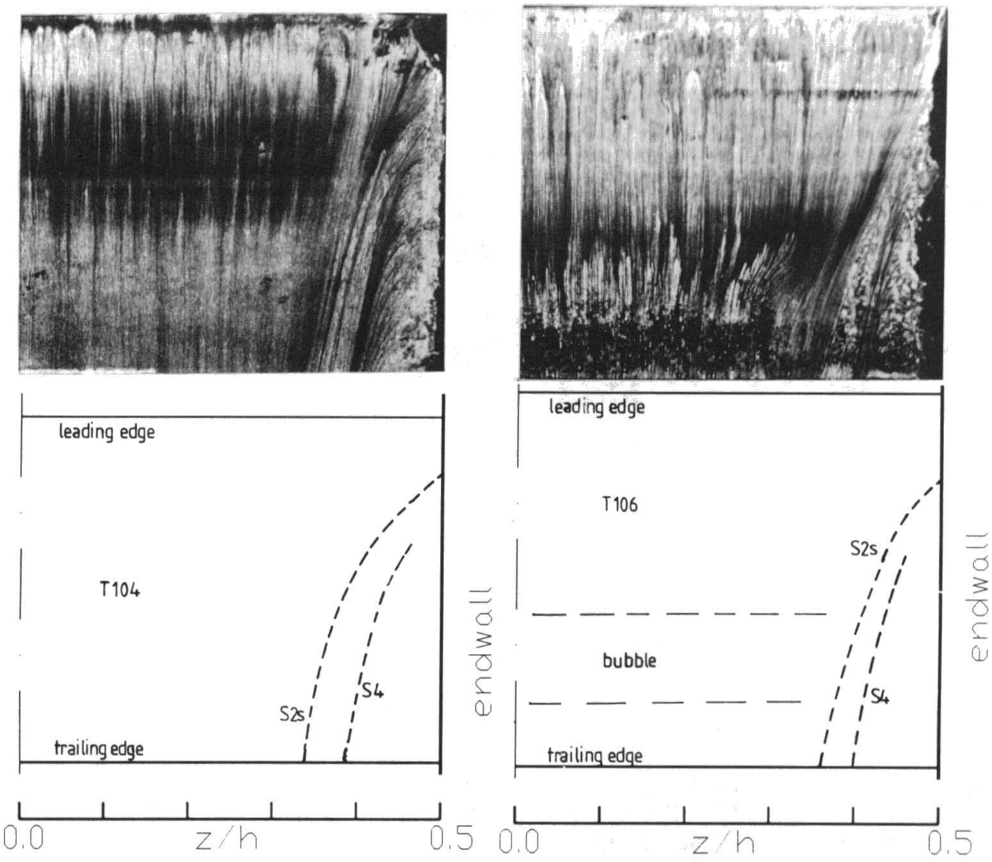

Fig. 5 Suction surface flow visualizations

T104(fl)

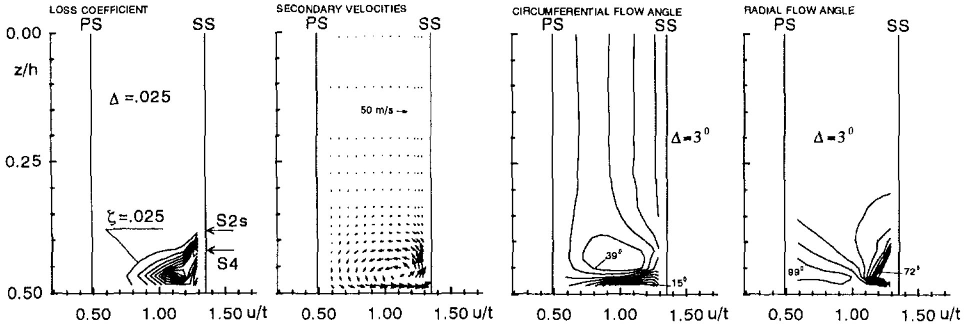

T106(al)

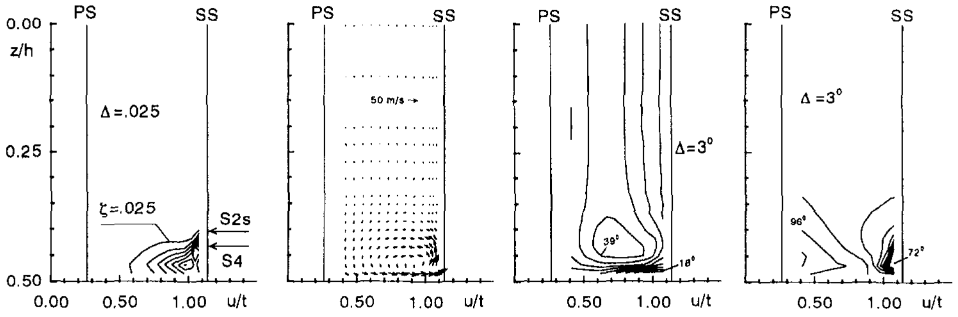

Fig. 6 Traverse results at x/l_{ax} = 0.80

vortex. Also, the isoclinics do not show any other vortex. However, as a result of a simple experiment with a filament probe, it is known that the suction leg of the horseshoe vortex follows the suction surface beside the passage vortex as observed by Hodson and Dominy (1987a, b) and Marchal and Sieverding (1977). Due to its small spatial extent it was impossible to detect it by the five-hole probe. For the T104 (*fl*) cascade the core of the passage vortex (z/h = 0.45; u/t =

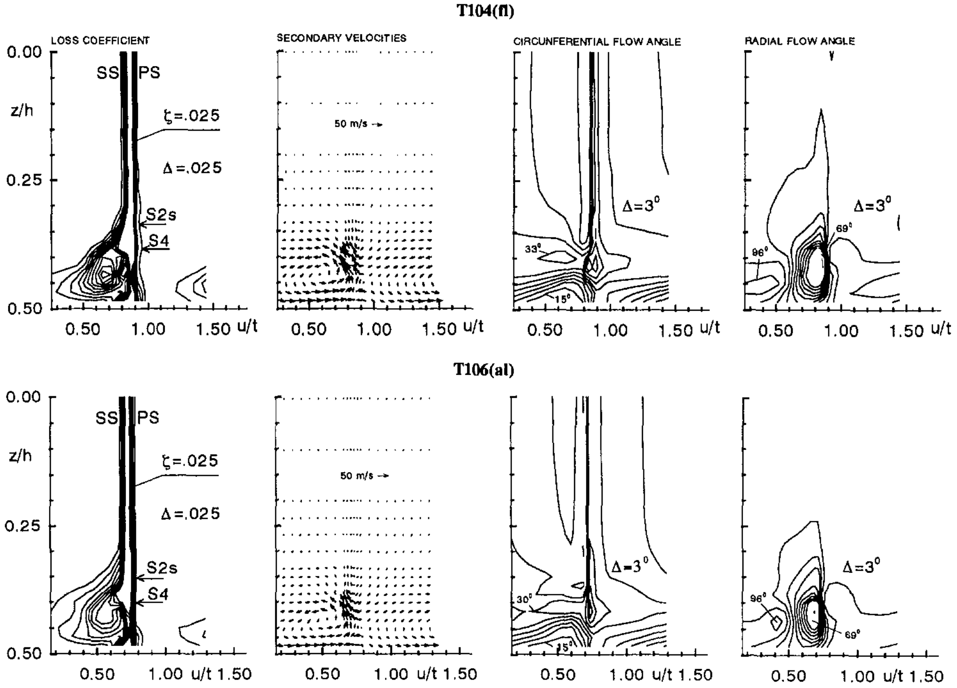

Fig. 7 Traverse results at x/l_{ax} = 1.06

0.16) coincides with the second loss peak. That is not true for the T106 (*al*) (vortex core: z/h = 0.45; u/t = 0.16). Comparing the secondary velocity distributions and the isoclinic distributions, it is obvious that the passage vortex is stronger within the front-loaded T104 cascade. Up to z/h = 0.35 the flow is two-dimensional for both cascades in this measuring plane.

The spanwise extent of the endwall loss region has increased in the second measuring plane, just downstream of the trailing edge (x/l_{ax} = 1.06, see Fig. 7). Again a high loss region between the separation lines *S2s* and *S4* is visible. For the T104(*fl*) this region shows a further penetration into the bulk flow than in the case of the T106 (*al*). This is an effect of the stronger passage vortex. A second loss core is exhibited by the T104, which coincides with the core of the passage vortex in contrast to the T106 (*al*). In the suction side endwall corner a third loss core appears that belongs to the corner vortex. The separation line *S3* has already been mentioned during the discussion of the endwall flow visualizations (Fig. 4). Again this loss core is more significant for the front-loaded cascade T104 (*fl*). Probably, the starting point of the corner vortex further upstream (T104) is the reason for the different sizes of these loss cores. The old endwall boundary layer has been totally rolled up and has been engulfed by the passage vortex in the cascade exit plane. Again, due to this evolution the losses decrease, close to the endwall. As an effect of the flow toward the endwall near the pressure side, which is induced by the vortical motion of the passage vortex, the pressure side profile boundary layer has been thickened in the corner. The secondary velocity field is dominated by the passage vortex. The suction side leg of the horseshoe vortex cannot be identified. The examination of the secondary vector distributions and the isoclinics distributions yields again a stronger passage vortex for the front-loaded T104 cascade. The core of the passage vortex has moved away from the endwall. It is transported by its own induced flow field toward midspan. The highest values of secondary velocities occur in the region of the separation line *S4*. For the T104 (*fl*) these velocities reach 35 percent of the magnitude of the midspan exit velocity compared to 25 percent just beyond the exit plane of the T106 (*al*). Maybe these high secondary velocities are a indication for the interaction of the passage vortex and the counterrotating suction side leg of the horseshoe vortex. The isoclinics of the circumferential flow angle show a typical distribution of a RANKINE vortex (see Niehuis et al., 1989).

The last measuring plane (x/l_{ax} = 1.5; Fig. 8) shows a typical "bone shape" for the loss contours, which can be generally observed downstream of highly loaded turbine cascades. The wake has decayed and becomes distorted by the vortical motion. Up to z/h = 0.28 the wake is two dimensional. Thus the endwall losses have been transported farther toward midspan. For the loss distribution of the T104 (*fl*) a "double-peak" occurs. The core of the passage vortex coincides with the weaker one. The T106 (*al*) again shows only one peak. The accumulation of low-momentum fluid close to the endwall belonging to the loss core in the suction side endwall corner is more significant for the T104 (*fl*). The secondary velocity fields are almost similar in this measuring plane. The passage vortex is the main feature for both cascades. Its core is located at z/h = 0.42. Supported by the isoclinic distributions a second, counterrotating vortex can be detected close to the passage vortex at z/h = 0.38. Very probably, it is the trailing shed vorticity, which has rolled up to a discrete vortex. The rolling up is initiated by the suction side leg of the horseshoe vortex, which has the same sense of rotation. Resulting from the interaction of these two vortices, secondary vorticities are induced with about 25 percent of the magnitude of the free-stream exit velocity. Examining the circumferential isoclinics, it is conspicuous that on the one hand the values of overturning decrease, and on the other hand the values of underturning increase. The rise of the underturning is caused by the rolling up of the trailing shed vorticity to a discrete vortex, which enhances the underturning effect of the passage vortex. Wall friction and the action of the counterrotating corner vortex are responsible for the decrease of overturning close to the endwall.

Pitchwise Mass-Averaged Results. The variations across the span of the pitchwise mass-averaged loss coefficient ζ_m and the mass-averaged circumferential flow angle β_m are plotted in Figs. 9 and 10. At x/l_{ax} = 0.80 the inlet boundary has already rolled up for both cascades. Therefore there is a loss peak separated from the endwall at z/h = 0.46. This loss peak

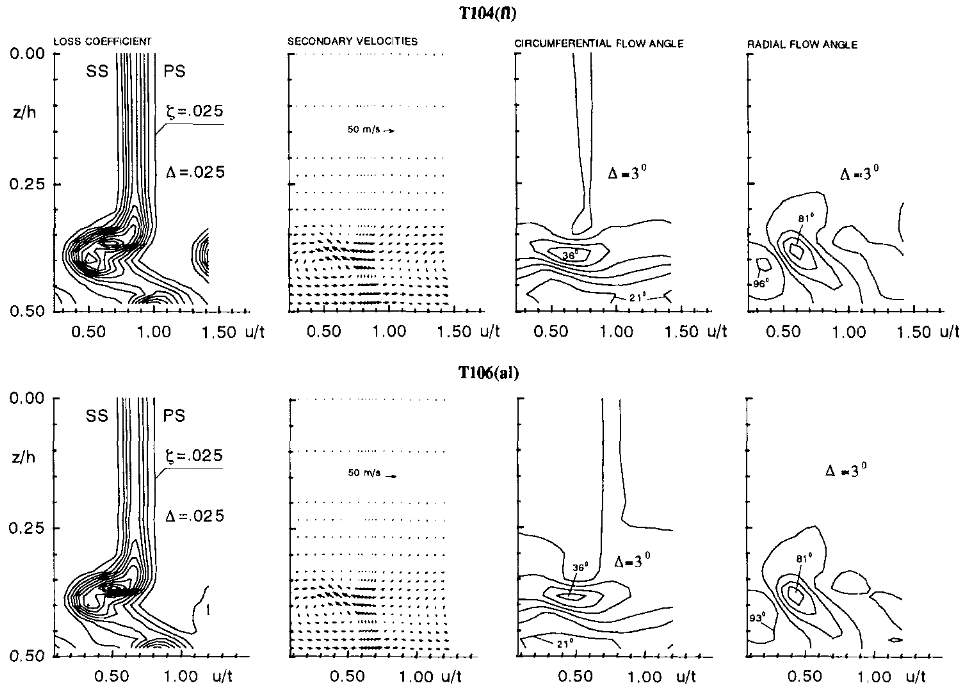

Fig. 8 Traverse results at x/l_{ax} = 1.50

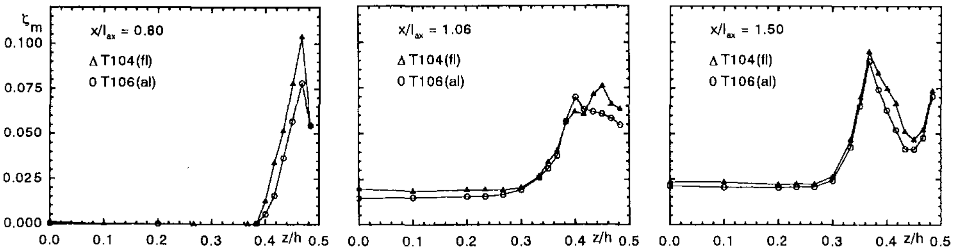

Fig. 9 Spanwise loss distribution

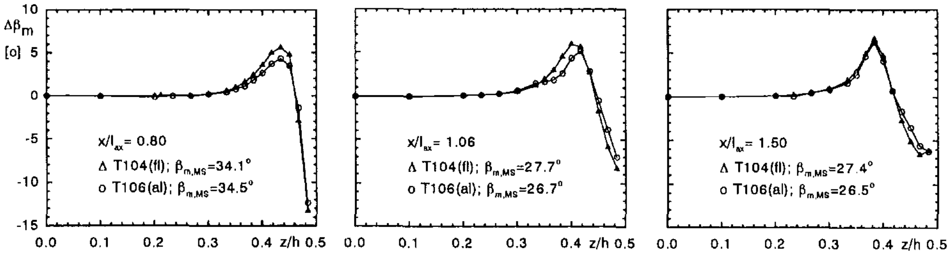

Fig. 10 Spanwise angle distribution

belongs to the high loss core in the region of the passage vortex in Fig. 6. The rise of the endwall losses starts at z/h = 0.38. This position corresponds with the beginning of the loss accumulation between $S2s$ and $S4$ (Fig. 6). Just beyond the trailing edge x/l_{ax} = 1.06 the front-loaded cascade T104 shows a higher profile loss than the T106 (*al*) as mentioned earlier by Hoheisel et al. (1987). The rise of the endwall losses starts at z/h = 0.30. The spanwise extent has increased. In this measuring plane there is a qualitative difference in the spanwise loss distributions of the two investigated cascades. For the T106 (*al*) an absolute maximum appears at z/h = 0.4. It is formed by the low-momentum fluid between $S2s$ and $S4$ (Fig. 7). From this peak the losses drop continuously up to the endwall. The new endwall boundary layer is still very thin and could not be determined. For the T104 (*fl*) only a loss plateau has been generated at z/h = 0.4. The absolute loss maximum occurs closer to the endwall at z/h = 0.45. It belongs to the loss peak in the core of the passage vortex (Fig. 7). As mentioned above, it is thought that the horseshoe vortex plays an important role with respect to the distribution of the low-momentum fluid of the inlet boundary layer within the blade passage. Maybe, these different distributions of this low-energy material between suction side legs and pressure side legs of the horseshoe vortices between the two cascades are responsible for the different spanwise loss distributions in this plane. The suction side front yard of the T104 cascade is less developed (see Fig. 4). The separation lines $S1s$ and $S2s$ intersect earlier with suction surface than for the T106 (*al*). The pressure field of the T104 (*fl*) deflects the main part of the upstream boundary layer fluid toward the pressure side. It is engulfed by the pressure side leg of the horseshoe vortex. This material is transported in the core of the passage vortex. Therefore already at x/l_{ax} = 0.8 a significant loss core exists for the T104 (Fig. 6). In the case of the T106 (*al*) a bigger part of the low-momentum fluid is shifted to the suction surface. That is why the suction side leg of the horseshoe vortex is stronger and the pressure side leg weaker within the T106 cascade. Farther downstream at $x/l_{ax} = 1.50$ these differences have mixed out. Again the spanwise loss distributions are similar. To a great extent the distribution of the T104 (*fl*) is just moved up by the difference of the profile losses. That is not true between the loss peak at $z/h = 0.36$ and the local minimum at $z/h = 0.44$. The decrease of the losses is less significant for the T104. The value of the local minimum is higher than for the T106 (*al*). This is a result of the higher losses of the stronger passage vortex within the front-loaded cascade. Close to the endwall the losses grow again because of the low-momentum fluid coming out of the suction side endwall corner and the increasing new endwall boundary layer.

Figure 10 shows the deviation of the circumferential flow angle as an result of the vortical motion. At $x/l_{ax} = 0.8$ both cascades have already done the same deflection. Nevertheless, a stronger passage vortex is indicated by the higher magnitudes of overturning ($\Delta\beta < 0$) and underturning ($\Delta\beta > 0$) for the T104 (*fl*) cascade. Farther downstream the overturning has dropped due to the wall friction and the influence of the corner vortex. The underturning shows a slight increase. It is remarkable that at $x/l_{ax} = 1.06$ the angle distributions show a qualitative difference, too. In the distribution of the T106 (*al*) a second point of inflection appears at $z/h = 0.38$. Probably, this difference is caused by a stronger suction side leg of the horseshoe vortex as mentioned above. At $x/l_{ax} = 1.50$ almost identical angle distributions occur for both cascades. Near the endwall, the separated minimum of $\Delta\beta$ indicates a stronger corner vortex for the T104. The underturning has increased significantly for both cascades. That is a result of the rolling up of the trailing shed vorticity. For the T106 (*al*) the stronger suction side leg of the horseshoe vortex has caused a more significant increase of the underturning downstream of the cascade.

Overall Pressure Loss. Figure 11 presents the evolution of the overall total pressure losses and secondary losses. Subtracting the profile loss and the loss of the upstream boundary layer from the total loss, the secondary loss can be obtained. Due to the large aspect ratio of 3.0 it can be assumed that the evolution of the profile boundary layers at midspan is not influenced by the endwall flow. Employing the conservation equations for mass, momentum, and energy (see Scholz, 1955) mixed-out values have been calculated for the last measuring plane (Table 1). It has to be taken into account that not all values include the endwall boundary layer, so these results represent what is happening to the bulk flow, rather than giving the true loss at each plane.

From $x/l_{ax} = 0.80$ to $x/l_{ax} = 1.06$ the total loss rises sharply. At the second measuring plane, just downstream of the trailing edge, the losses of the profile boundary layer could be collected including the trailing edge losses (wake). Some caution should be exercised for the values of this plane because the data points were not sufficiently close within the blade wake to give a good definition. Therefore in this plane there is still some uncertainty with respect to the magnitude of the profile losses, which affects the calculated secondary losses, too. Nevertheless, it is conspicuous that the secondary loss in the case of the T104 (*fl*) cascade grows continuously whereas there is a sharp increase for the T106 (*al*). Probably this differing evolution depends on the long acceleration within the blade passage of the aft-loaded cascade T106 in contrast to the T104. Langston et al. (1976) and Marchal and Sieverding (1977) have mentioned earlier for a highly loaded turbine cascade that a significant rise of the secondary losses appears not until the throat. The steeper increase of the total losses and the secondary losses downstream of the cascade T104 (*fl*) is a result of the decay of the stronger passage vortex. The dissipation of this stronger passage vortex results in a secondary loss coefficient (mixed-out), which is 25 percent higher than that of the T106 (*al*). This statement is confirmed by the higher magnitude of the Secondary Kinetic Energy, which drops remarkably downstream of the exit plane of the T104.

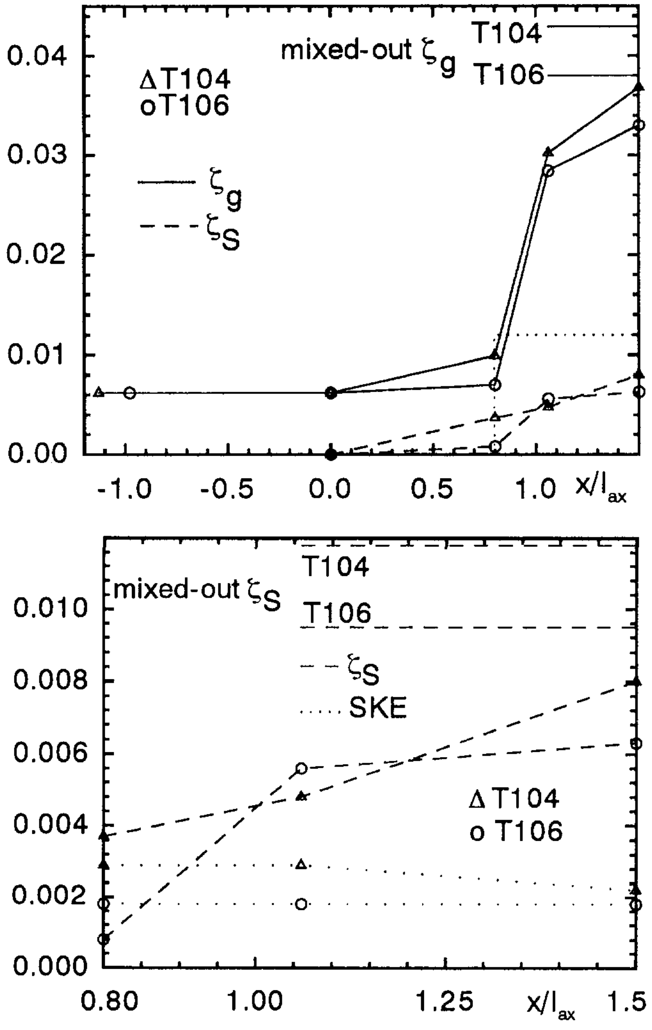

Fig. 11 Overall losses and secondary kinetic energy

The difference between the mixed-out value of the secondary loss and the mass-averaged value at $x/l_{ax} = 1.50$ makes clear that the mixing loss attributable to the three dimensionality of the flow is generated essentially by the dissipation of SKE. Although the mixing loss of the blade wake ($\zeta_{P,2} - \zeta_P$) has a similar magnitude as the mixing loss of the secondary flow ($\zeta_{S,2} - \zeta_S$) the mixing losses related to the averaged values at $x/l_{ax} = 1.50$ (Table 2) show that the mixing process plays a more important role for the magnitude of the secondary loss than for the profile loss.

Conclusion

The development of the secondary flow field in two highly loaded turbine cascades has been investigated with a focus on the influence of the different load distributions. Detailed measurements were carried out using various measurement techniques. It is shown that the general nature of the flow is very similar for both cascades. The following results should be pointed out:

1 In both cascades the passage vortex dominates the secondary flow field. In addition a corner vortex occurs and a more or less developed suction side leg of the horseshoe vortex is detectable.

Table 2 Mixed-out values

x/l_{ax} = 1.50	T104 (fl)	T106 (al)
$\zeta_{g,2}-\zeta_g$	.0063	.0050
$\zeta_{P,2}-\zeta_P$	.0027	.0020
$\zeta_{S,2}-\zeta_S$	.0036	.0030
SKE	.0027	.0020
$(\zeta_{P,2}-\zeta_P)/\zeta_P$	.19	.10
$(\zeta_{S,2}-\zeta_S)/\zeta_S$	.45	.48

2 Close to the endwall, both cascades become strongly unloaded as a result of the secondary flows. That leads to a remarkable change of the character of the endwall profile pressure distribution within the T104 (*fl*) cascade. At the endwall the pressure distribution becomes more rear-loaded.

3 Just beyond the cascade exit plane the spanwise distributions of loss coefficient and circumferential flow angle show different features for the two cascades. However, the overall secondary loss coefficient is nearly equal. Further downstream the differences in spanwise distribution disappear due to mixing processes.

4 The front-loaded T104 cascade exhibits the stronger passage vortex. The dissipation of the kinetic energy accumulated in the vortical motion of this stronger vortex is responsible for the higher magnitude of the secondary loss in the case of the T104.

The strong flow deflection, which starts just downstream of the cascade inlet plane of the T104 (*fl*), generates strong transverse pressure gradients. These pressure gradients react on a relatively undisturbed thick boundary layer with high velocity gradients. In the blade passage of the aft-loaded cascade T106 the peak pressure gradient does not occur until the throat, where it reacts on a very thin new boundary layer. That is why the T104 generates a stronger vortex combined with higher losses.

Acknowledgments

The research project in the scope of which the reported work was performed is part of a national research cooperation "AG TURBO Arbeitsgemeinschaft Hochtemperatur Gasturbine." The project has been supported by the German Ministry of Science and Technology and the Motoren- und Turbinen Union München. The permission for publication is gratefully acknowledged.

References

Binder, A., and Romey, R., 1983, "Secondary Flow Effects and Mixing of the Wake Behind a Turbine Stator," ASME *Journal of Engineering for Power*, Vol. 105, pp. 40-46.

Chen, L. D., and Dixon, S. L., 1986, "Growth of Secondary Flow Losses Downstream of a Turbine Blade Cascade," ASME *Journal of Engineering for Gas Turbines and Power*, Vol. 108, pp. 270-276.

Hodson, H. P., and Dominy, R. G., 1987a, "Three-Dimensional Flow in a Low-Pressure Turbine Cascade at Its Design Condition," ASME JOURNAL OF TURBOMACHINERY, Vol. 109, pp. 177-185.

Hodson, H. P., and Dominy, R. G., 1987b, "The Off-Design Performance of a Low-Pressure Turbine Cascade," ASME JOURNAL OF TURBOMACHINERY, Vol. 109, pp. 201-209.

Hoheisel, H., Kiock, R., Lichtfuss, H. J., and Fottner, L., 1987, "Influence of Free-Stream Turbulence and Blade Pressure Gradient on Boundary Layer and Loss Behavior of Turbine Cascades," ASME JOURNAL OF TURBOMACHINERY, Vol. 109, pp. 210-219.

Hunter, I. H., 1982, "Endwall Boundary Layer Flows and Losses in an Axial Turbine Stage," ASME *Journal of Engineering for Power*, Vol. 104, pp. 184-193.

Langston, L. S., Nice, M. L., and Hooper, R. M., 1976, "Three-Dimensional Flow Within a Turbine Cascade Passage," ASME *Journal of Engineering for Power*, Vol. 99, pp. 21-28.

Marchal, P., and Sieverding, C. H., 1977, "Secondary Flows Within Turbomachinery Bladings," AGARD-CP-469.

Marchal, P., 1980, "Etude des ecoulements secondaires en grille d'aubes de detent," Ph.D. Thesis, U. Libre de Bruxelles, Belgium.

Niehuis, R., Lücking, P., and Stubert, B., 1989, "Experimental an Numerical Study on Basic Phenomena of Secondary Flows in Turbines," AGARD-CP-469.

Perdichizzi, A., 1990, "Mach Number Effects on Secondary Flow Development Downstream of a Turbine Cascade," ASME JOURNAL OF TURBOMACHINERY, Vol. 112, pp. 643-651.

Römer, N., 1990, "Untersuchungen zum Umschlagverhalten der Profilgrenzschicht an Verdichter und Turbinengittern," Dissertation, Universität der Bundeswehr München, Federal Republic of Germany.

Scholz, N., 1955, "Systematische Untersuchungen über Sekundärverluste in Schaufelgittern, Teil III," Bericht 55/19, Institut für Strömungsmechanik, TH Braunschweig, Federal Republic of Germany.

Sharma, O. P., and Graziani, R. A., 1983, "Influence of Endwall Flow on Airfoil Suction Surface Midheight Boundary Layer Development in a Turbine Cascade," ASME *Journal of Engineering for Power*, Vol. 105, pp. 147-155.

Sieverding, C. H., 1985, "Recent Progress in the Understanding of Basic Aspects of Secondary Flows in Turbine Blade Passages," ASME *Journal of Engineering for Gas Turbines and Power*, Vol. 107, pp. 248-257.

Sturm, W., and Fottner, L., 1985, "The High-Speed Cascade Wind Tunnel of the German Armed Forces University Munich," *Proceedings of the 8th Symposium on Measuring Techniques for Transonic and Supersonic Flows in Cascades and Turbomachines*, Oct. 24-25, Genoa, Italy.

Yamamoto, A., and Nouse, H., 1988, "Effects of Incidence on Three-Dimensional Flows in a Linear Turbine Cascade," ASME JOURNAL OF TURBOMACHINERY, Vol. 110, pp. 486-496.

Watzlawick, R., 1992, "Bestimmung der wesentlichen Einflussgrössen in der Korrelation der Sekundärströmungsverluste bei Veränderung des Schaufelseitenverhältnisses," *MTZ Motortechnische Zeitschrift*, Vol. 53.

Osborne Reynolds: Energy Methods in Transition and Loss Production: A Centennial Perspective

J. Moore

J. G. Moore

Department of Mechanical Engineering,
Virginia Polytechnic Institute
and State University,
Blacksburg, VA 24061

Osborne Reynolds' developments of the concepts of Reynolds averaging, turbulence stresses, and equations for mean kinetic energy and turbulence energy are viewed in the light of 100 years of subsequent flow research. Attempts to use the Reynolds energy-balance method to calculate the lower critical Reynolds number for pipe and channel flows are reviewed. The modern use of turbulence-energy methods for boundary layer transition modeling is discussed, and a current European Working Group effort to evaluate and develop such methods is described. The possibility of applying these methods to calculate transition in pipe, channel, and sink flows is demonstrated using a one-equation, q-L, turbulence model. Recent work using the equation for the kinetic energy of mean motion to gain understanding of loss production mechanisms in three-dimensional turbulent flows is also discussed.

Introduction

This year we celebrate the centenary of Osborne Reynolds' presentation of the first paper on turbulence stresses and turbulence energy (1894/95). Reynolds had earlier shown that the critical Reynolds number for transition from laminar to turbulent flow in pipes of circular section was between 1900 and 2000 (1883). His object then was to show that this transition criterion follows from the equations of motion. In his attempt he established the foundations of modern turbulence modeling. He effectively showed the modelers which equations to develop and solve, and the experimentalists which flow properties to measure. For example, he focused on the turbulence-energy equation in a manner similar to that of many current transition studies; and he modeled the exchange of energy between mean motion and turbulent motion and the dissipation of turbulent fluctuations in ways that are currently used in the study of loss production in turbulent flows. Choosing these examples from the many possible, this paper intends to illustrate the extent of Reynolds' influence on flow research.

Reynolds' Equations

Reynolds considered incompressible turbulent flow with density, ρ. Writing the velocity components in terms of mean and fluctuating velocities,

$$u = \bar{u} + u', \quad v = \bar{v} + v', \quad \text{and} \quad w = \bar{w} + w',$$

he performed Reynolds averaging of the momentum equations and showed that these contained additional Reynolds stresses of the form $-\rho\overline{u'u'}$, $-\rho\overline{u'v'}$, $-\rho\overline{u'w'}$, etc., etc. He then derived equations for the kinetic energy of the mean motion, $\bar{E} = p(\bar{u}^2 + \bar{v}^2 + \bar{w}^2)/2$, and the kinetic energy of the turbulence, $\overline{E'} = \rho(\overline{u'^2} + \overline{v'^2} + \overline{w'^2})/2$. These are shown in Figs. 1 and 2 in the form Reynolds used, but corrected for "typographical" errors. The terms $\bar{p}_{xx}$, p'_{xx}, etc., are the mean and fluctuating stresses due to pressure and viscosity.

Reynolds noticed that the last terms on the right of each of the equations, in Figs. 1 and 2, were identical in form and opposite in sign. He concluded that they represent the total exchange of energy between the kinetic energy of the mean motion and the kinetic energy of the turbulence. We now recognize these terms as the turbulence production terms, $-\rho\overline{u_i u_j}\partial U_i/\partial x_j$, and we speak of them as representing the work of deformation of the mean motion by the turbulence, or Reynolds, stresses (Hinze, 1975).

Reynolds' Energy Method for Transition Modeling. To explain transition in pipe or channel flow, Reynolds' approach was then to determine the condition under which turbulence energy could be sustained. Using the turbulence-energy equation, Fig. 2, he considered a control volume for which the turbulent diffusion of turbulence energy, represented by the first term on the right-hand side, would integrate to zero. His criterion for transition was then that, integrating over the pipe or channel volume, turbulence production equaled turbulence dissipation, as shown in Fig. 3.

Contributed by the International Gas Turbine Institute and presented at the 39th International Gas Turbine and Aeroengine Congress and Exposition, The Hague, The Netherlands, June 13–16, 1994. Manuscript received at the International Gas Turbine Institute February 25, 1994. Paper No. 94-GT-225. Associate Technical Editor: E. M. Greitzer.

$$\left(\frac{d}{dt}+\bar{u}\frac{d}{dx}+\bar{v}\frac{d}{dy}+\bar{w}\frac{d}{dz}\right)\bar{E}=$$

$$-\left\{\begin{array}{l}\frac{d}{dx}\left[\bar{u}\left(\bar{p}_{xx}+\rho\overline{u'u'}\right)\right]+\frac{d}{dy}\left[\bar{u}\left(\bar{p}_{yx}+\rho\overline{u'v'}\right)\right]+\frac{d}{dz}\left[\bar{u}\left(\bar{p}_{zx}+\rho\overline{u'w'}\right)\right]\\+\frac{d}{dx}\left[\bar{v}\left(\bar{p}_{xy}+\rho\overline{v'u'}\right)\right]+\frac{d}{dy}\left[\bar{v}\left(\bar{p}_{yy}+\rho\overline{v'v'}\right)\right]+\frac{d}{dz}\left[\bar{v}\left(\bar{p}_{zy}+\rho\overline{v'w'}\right)\right]\\+\frac{d}{dx}\left[\bar{w}\left(\bar{p}_{xz}+\rho\overline{w'u'}\right)\right]+\frac{d}{dy}\left[\bar{w}\left(\bar{p}_{yz}+\rho\overline{w'v'}\right)\right]+\frac{d}{dz}\left[\bar{w}\left(\bar{p}_{zz}+\rho\overline{w'w'}\right)\right]\end{array}\right\}$$

$$+\left\{\begin{array}{l}\overline{p_{xx}}\frac{d\bar{u}}{dx}+\overline{p_{yx}}\frac{d\bar{u}}{dy}+\overline{p_{zx}}\frac{d\bar{u}}{dz}\\+\overline{p_{xy}}\frac{d\bar{v}}{dx}+\overline{p_{yy}}\frac{d\bar{v}}{dy}+\overline{p_{zy}}\frac{d\bar{v}}{dz}\\+\overline{p_{xz}}\frac{d\bar{w}}{dx}+\overline{p_{yz}}\frac{d\bar{w}}{dy}+\overline{p_{zz}}\frac{d\bar{w}}{dz}\end{array}\right\}+\left\{\begin{array}{l}\rho\overline{u'u'}\frac{d\bar{u}}{dx}+\rho\overline{u'v'}\frac{d\bar{u}}{dy}+\rho\overline{u'w'}\frac{d\bar{u}}{dz}\\+\rho\overline{v'u'}\frac{d\bar{v}}{dx}+\rho\overline{v'v'}\frac{d\bar{v}}{dy}+\rho\overline{v'w'}\frac{d\bar{v}}{dz}\\+\rho\overline{w'u'}\frac{d\bar{w}}{dx}+\rho\overline{w'v'}\frac{d\bar{w}}{dy}+\rho\overline{w'w'}\frac{d\bar{w}}{dz}\end{array}\right\}$$

Fig. 1 The "equation of energy of mean-mean-motion," Reynolds (1895)

Reynolds considered flow driven by a pressure gradient between parallel walls, a distance h apart. He choose an analytical function for a small disturbance superimposed on a laminar viscous flow and evaluated the two terms on the right-hand side of the equation in Fig. 3. The result was a critical Reynolds number, $\rho U_m h/\rho = 517$. This is appreciably lower than the experimental values of approximately 1300 obtained later by Davies and White (1928) and Patel and Head (1969).

Reynolds' result is similar to that obtained soon afterward by Lorentz (1897/1907) using the same energy-balance method. Lorentz considered Couette flow and calculated a critical value for $U_o h/\nu = 288$, which is considerably lower than the value of 1900 measured by Couette (1890).

Discussions of the Energy-Balance Method. The energy-balance method is the subject of excellent discussions by Horace Lamb (1932) a former student of Reynolds, Prandtl (1934), and Hinze (1975). The main criticism is that the assumed disturbances of Reynolds and Lorentz were only made to satisfy the continuity equation. The question of whether the disturbances were solutions of the Navier–Stokes equations and were hydrodynamically possible was not considered.

Also, a fundamental question is whether it is correct to start from the integrated form of the energy equation, Fig. 3. If the study of transition should start with local flow instabilities such as Tollmien–Schlichting waves (Schlichting, 1979) and proceed through the modeling of turbulent spots (Em-

Nomenclature

A = area of measuring plane, area of integration
c = blade axial chord
c_f = skin friction coefficient
C_{Pt} = total pressure loss coefficient = $(P_{to}-P_t)\Big/\left(\frac{1}{2}\rho U_o^2\right)$
$\bar{E}, \bar{E}'$ = (Reynolds) kinetic energy of the mean motion and turbulence
F_{tu} = turbulent viscosity reduction factor for transitional flow
h = channel height
H = shape factor
k = turbulence kinetic energy = $\overline{u_i u_i}/2$
K = acceleration parameter
L = mixing length
L_{fre} = free-stream mixing length
N = normalization constant in Eq. (3) = $c\Big/\left(\bar{V}_n A \frac{1}{2}\rho U_o^2\right)$
P, p = mean and fluctuating static pressure
$\bar{p}_{xx}, p'_{xx}$ = (Reynolds) mean and fluctuating stresses due to pressure and viscosity
P_t = total pressure
q = magnitude of the fluctuating velocity, $q^2 = u_i u_i$; in q-L turbulence model, $q = k^{1/2}$
Re = Reynolds number
R_{tu} = turbulent viscosity Reynolds number, Eq. (a14)
t = time
$\overline{Tu}$ = mean turbulence intensity

u, v, w, or u_i = (Reynolds: u', v', w') = Cartesian components of the fluctuating velocity; see Fig. 7 for cascade flow
U, V, W, or U_i = (Reynolds: $\bar{u}, \bar{v}, \bar{w}$) = Cartesian components of the mean velocity; see Fig. 7 for cascade flow
U_o = cascade upstream free-stream velocity
$\bar{V}_n$ = area-averaged velocity normal to measuring plane
x, y, z, or x_i = Cartesian coordinates; see Fig. 7 for cascade
X, Y, Z = cascade coordinates, Fig. 7
y = distance normal to the wall
δ = boundary layer thickness
μ, μ_1 = laminar viscosity
μ_t = turbulent viscosity
ν = kinematic viscosity
ρ = density

Overbars

$\bar{\ }$ = time average
$\bar{\bar{\ }}$ = mass average

Subscripts

d = pipe diameter
h = channel height
o = upstream of cascade in free stream
s = start of transition
t = total, stagnation
x = distance along plate
θ = momentum thickness

$$\left(\frac{d}{dt}+\bar{u}\frac{d}{dx}+\bar{v}\frac{d}{dy}+\bar{w}\frac{d}{dz}\right)\overline{E'} =$$

$$-\left\{\begin{array}{l}
\frac{d}{dx}\left[u'\left(p'_{xx}+\rho\frac{u'u'}{2}\right)\right]+\frac{d}{dy}\left[u'\left(p'_{yx}+\rho\frac{u'v'}{2}\right)\right]+\frac{d}{dz}\left[u'\left(p'_{zx}+\rho\frac{u'w'}{2}\right)\right] \\
+\frac{d}{dx}\left[v'\left(p'_{xy}+\rho\frac{v'u'}{2}\right)\right]+\frac{d}{dy}\left[v'\left(p'_{yy}+\rho\frac{v'v'}{2}\right)\right]+\frac{d}{dz}\left[v'\left(p'_{zy}+\rho\frac{v'w'}{2}\right)\right] \\
+\frac{d}{dx}\left[w'\left(p'_{xz}+\rho\frac{w'u'}{2}\right)\right]+\frac{d}{dy}\left[w'\left(p'_{yz}+\rho\frac{w'v'}{2}\right)\right]+\frac{d}{dz}\left[w'\left(p'_{zz}+\rho\frac{w'w'}{2}\right)\right]
\end{array}\right\}$$

$$+\left\{\begin{array}{l}
p'_{xx}\frac{du'}{dx}+p'_{yx}\frac{du'}{dy}+p'_{zx}\frac{du'}{dz} \\
+p'_{xy}\frac{dv'}{dx}+p'_{yy}\frac{dv'}{dy}+p'_{zy}\frac{dv'}{dz} \\
+p'_{xz}\frac{dw'}{dx}+p'_{yz}\frac{dw'}{dy}+p'_{zz}\frac{dw'}{dz}
\end{array}\right\}
-\left\{\begin{array}{l}
\rho\overline{u'u'}\frac{d\bar{u}}{dx}+\rho\overline{u'v'}\frac{d\bar{u}}{dy}+\rho\overline{u'w'}\frac{d\bar{u}}{dz} \\
+\rho\overline{v'u'}\frac{d\bar{v}}{dx}+\rho\overline{v'v'}\frac{d\bar{v}}{dy}+\rho\overline{v'w'}\frac{d\bar{v}}{dz} \\
+\rho\overline{w'u'}\frac{d\bar{w}}{dx}+\rho\overline{w'v'}\frac{d\bar{w}}{dy}+\rho\overline{w'w'}\frac{d\bar{w}}{dz}
\end{array}\right\}$$

Fig. 2 **"The equation for the mean rate of change in the energy of relative-mean-motion," Reynolds (1895)**

... we have, if the energy of relative-mean-motion is maintained, neither increasing or diminishing,

$$-\rho\iiint\left\{\begin{array}{l}
\overline{u'u'}\frac{d\bar{u}}{dx}+\overline{u'v'}\frac{d\bar{u}}{dy}+\overline{u'w'}\frac{d\bar{u}}{dz} \\
+\overline{v'u'}\frac{d\bar{v}}{dx}+\overline{v'v'}\frac{d\bar{v}}{dy}+\overline{v'w'}\frac{d\bar{v}}{dz} \\
+\overline{w'u'}\frac{d\bar{w}}{dx}+\overline{w'v'}\frac{d\bar{w}}{dy}+\overline{w'w'}\frac{d\bar{w}}{dz}
\end{array}\right\}dx\,dy\,dz$$

$$-\mu\iiint\left\{\begin{array}{c}
2\left[\left(\frac{du'}{dx}\right)^2+\left(\frac{dv'}{dy}\right)^2+\left(\frac{dw'}{dz}\right)^2\right] \\
+\left(\frac{dw'}{dy}+\frac{dv'}{dz}\right)^2+\left(\frac{du'}{dz}+\frac{dw'}{dx}\right)^2 \\
+\left(\frac{dv'}{dx}+\frac{du'}{dy}\right)^2
\end{array}\right\}dx\,dy\,dz = 0$$

which is a discriminating equation as to the conditions under which relative-mean-motion can be sustained.

Fig. 3 **Turbulence production equated to turbulence dissipation, Reynolds (1895)**

mons, 1951), or turbulence slugs (Lindgren, 1957) then the starting point should be the continuity and momentum equations, supplemented by the general turbulence-energy equation, Fig. 2.

In his book on boundary layer theory, Schlichting discusses the modeling of such local phenomena. Further he comments "the energy method ... did not prove successful; we shall, therefore, refrain from considering it in detail" (1979, p. 457). Consistent with this, the main body of the book does not present the turbulence-energy equation, Fig. 2. But in Chapter XIX, Section f, he introduces a modeled form of the turbulence energy equation due to Prandtl (1945), and notes the work of Glushko (1965) and Beckwith and Bushnell (1968) using similar equations. Their calculations of boundary layer development on a flat plate included transition from laminar to turbulent flow and heralded renewed interest and research in energy methods.

Modern Applications of the Turbulence-Energy Equation

The starting point for modeling the kinetic energy of turbulence in incompressible flows is a development of the equation given in Fig. 2. The equation is given by Hinze (1975) in the form

$$\underbrace{\frac{D}{Dt}\left(\overline{\frac{q^2}{2}}\right)}_{\substack{\text{Substantial}\\ \text{derivative}}} = \underbrace{-\frac{\partial}{\partial x_i}\overline{u_i\left(\frac{p}{\rho}+\frac{q^2}{2}\right)}}_{\text{Diffusive transport}} \underbrace{-\overline{u_iu_j}\frac{\partial U_j}{\partial x_i}}_{\text{Production}}$$

$$+\underbrace{\nu\frac{\partial}{\partial x_i}\overline{u_j\left(\frac{\partial u_i}{\partial x_j}+\frac{\partial u_j}{\partial x_i}\right)}}_{\substack{\text{Work by turbulent}\\ \text{viscous stresses}}} \underbrace{-\nu\overline{\left(\frac{\partial u_i}{\partial x_j}+\frac{\partial u_j}{\partial x_i}\right)\frac{\partial u_j}{\partial x_i}}}_{\text{Viscous dissipation}} \qquad (1)$$

where

$$\frac{\overline{q^2}}{2} = \frac{\overline{u_iu_i}}{2} = k$$

is the kinetic energy of turbulence per unit mass.

This equation forms the basis of one-equation and two-equation turbulence models used extensively in computational fluid dynamics. All the terms on the right-hand side are then modeled or manipulated as discussed, for example, by Arnal (1984); and much attention is given to the accurate modeling of near-wall and low Reynolds number flows as discussed by Patel et al. (1985). Throughout this development process, empirical data and correlations are used to establish the constants and functional forms needed in the models.

The result of these developments is then a large number of similar but different versions of the turbulence-energy equation and other supporting equations that need testing and verification. This requires cooperation and effort on a national and international scale. One such effort is being organized for the European Community by ERCOFTAC, a European Research Community on Flow, Turbulence and Combustion (Hirsch, 1993). A Special Interest Group on Transition/Re-transition has a project on Transition Modeling for Turbomachinery. This Working Group is considering a class of flows for which these turbulence-energy models seem appropriate. They are transitional boundary layers with high free-stream turbulence levels and pressure gradient effects such as commonly found in turbomachinery (Mayle, 1991).

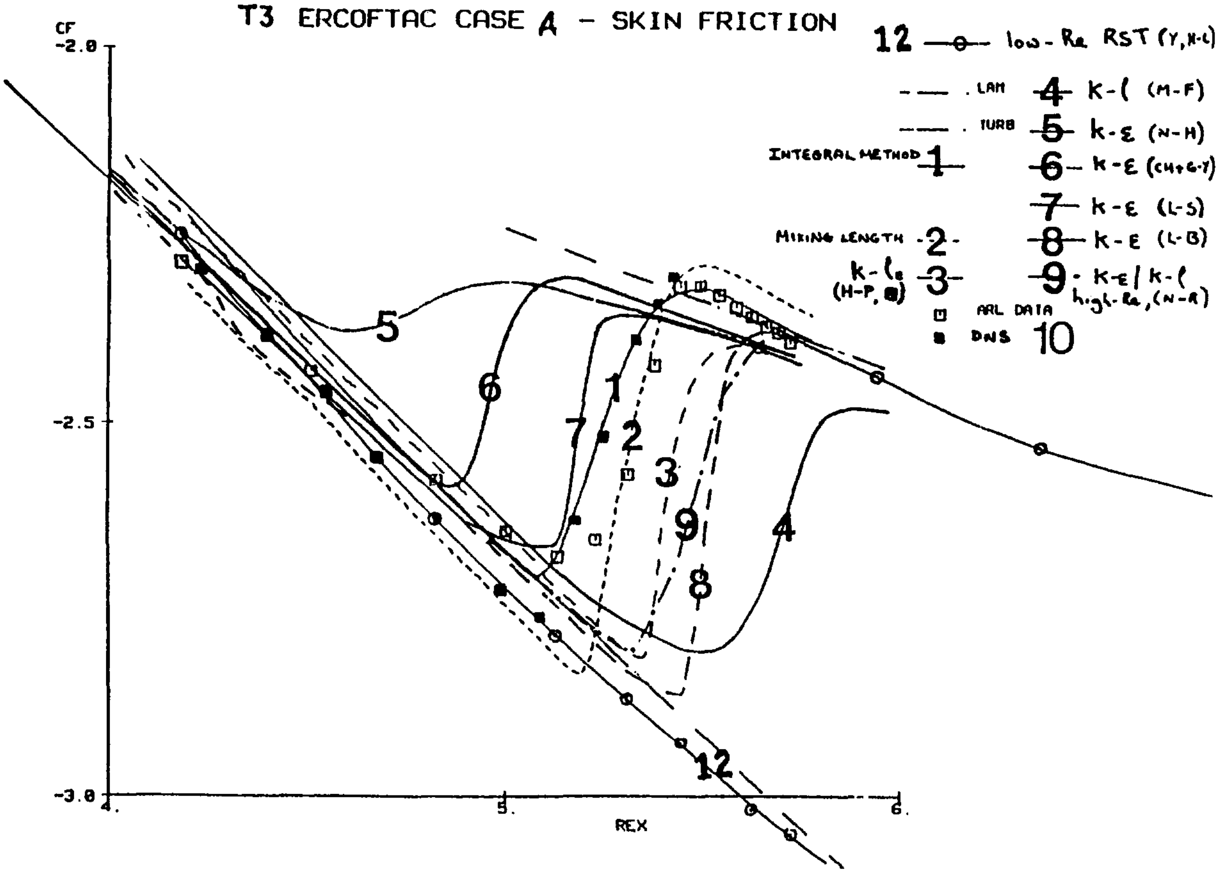

Fig. 4 **ERCOFTAC results for zero-pressure-gradient boundary layer transition with 3 percent free-stream turbulence, Savill (1992). □ Rolls-Royce data; ■ direct numerical simulation; 1–12 calculations.**

With high free-stream turbulence levels, the initial stages of the natural transition process involving Tollmien-Schlichting waves are effectively bypassed, hence the term "bypass" transition (Morkovin, 1969). Apparently then, turbulence in the free stream triggers the production of turbulent spots within the boundary layer, and the transition process involves production, growth and convection of these spots (Mayle, 1991). It is this process that the low Reynolds number turbulence-energy models are attempting to simulate, albeit in an average sense. As Arnal states, it appears that "the transport equations can provide fairly good results in such situations" (1984).

The ERCOFTAC Working Group was formed in 1991 and at the end of 1992 Savill reported on its progress (1992). Results were presented for six test cases with free-stream turbulence levels ranging from 1 percent to 6 percent, mostly with zero pressure gradient but with one pressure gradient representative of an aft-loaded turbine blade. The models being evaluated include modified correlation/integral methods, one-equation q-L or k-L models, single or multiscale two-equation low-Re k–ϵ models, several Reynolds stress transport closure schemes, as well as various subgrid scale model large eddy simulations. This largely unfunded effort includes contributions from 33 participants, 20 from 9 different European countries and the rest from the U.S.A., Asia, and Australia.

Typical results for ERCOFTAC test case T3A are presented in Fig. 4. This is a zero pressure gradient, 3 percent free-stream turbulence flow. The plot shows skin friction coefficient as a function of Reynolds number based on distance along the plate. The Rolls-Royce data are plotted as unfilled squares, and superimposed on this are the results of eleven calculations, as well as correlations for laminar and fully turbulent flow. Most of the predictions use the turbulence-energy equation and there appears to be a wide diversity of results. Of these turbulence-energy methods, the best prediction for this first test case was provided by the Launder–Sharma k–ϵ model (1974). But this is just a preliminary conclusion and we await with interest the final conclusions when all the results are compared for the proposed 21 transition test cases.

Testing Turbulence Models on Pipe, Channel, and Sink Flows. A question now arises, are these turbulence models also able to solve the problem of calculating the transition from fully laminar to fully turbulent pipe or channel flow? To indicate how this might be accomplished, the present authors have undertaken such an exercise. In the appendix a one-equation q–L turbulence model is described, which was developed to calculate transition in pipes, channels, and laminarescent sink flows, as well as transition in flat plate boundary layers. This model is similar to those described by Arnal (1984) and Patel et al. (1985), but it uses a correlation of a turbulence reduction factor, F_{tu}, as a function of a layer-averaged turbulent viscosity Reynolds number, R_{tu}, which is similar to that used by McDonald and Fish (1973).

The exercise is quite straightforward. First, determine functions $F_{tu}(R_{tu})$ which allow fully developed flow calculations to match the skin friction versus Reynolds number plots for pipe and channel flows given by Patel and Head (1969). Then use these functions to calculate laminarescent sink flow boundary layers[1] and compare with the data compiled by

---

[1] Sink flow is the flow that develops in a convergent channel between intersecting planes. Even though the flow is accelerating, similar boundary layers develop with dimensionless properties that are invariant with distance along the channel.

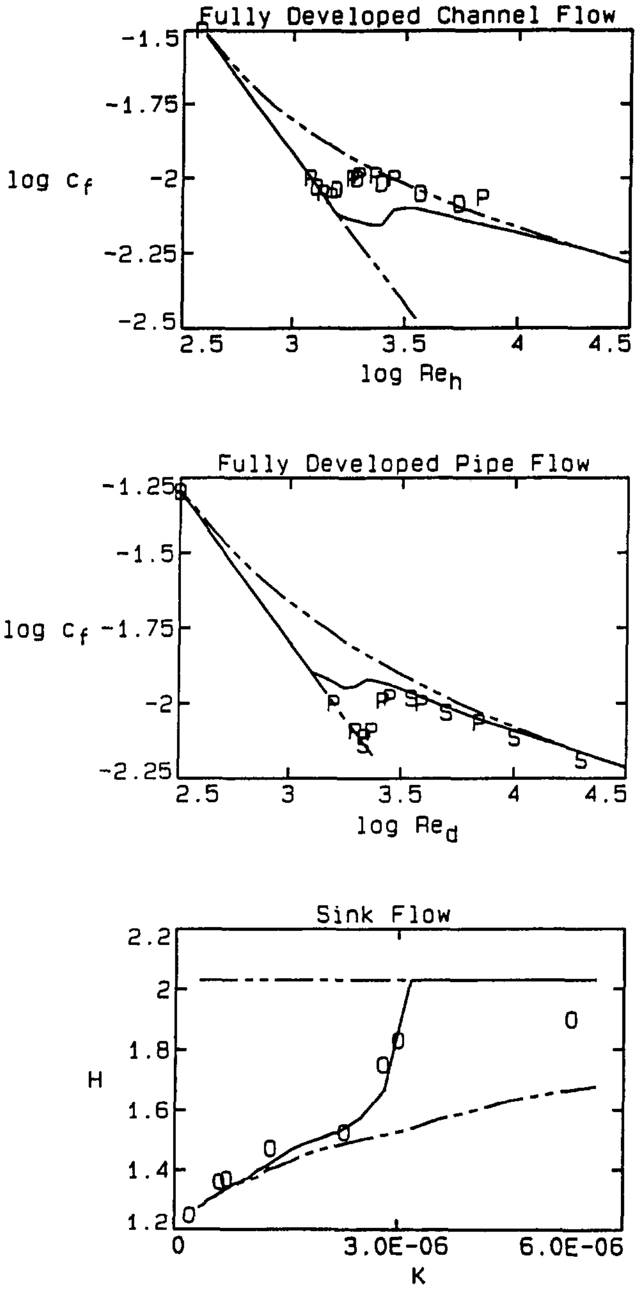

Fig. 5 Transition in nondeveloping flows. Data: P—Patel and Head (1969); D—Davies and White (1928); S—from Schlichting (1979); O—from Launder and Jones (1969). ——— fully laminar and fully turbulent calculations; ——— calculation with *q-L* turbulence model.

Launder and Jones (1969). Next, choose a function that gives reasonable results for all three types of flow. Finally, adjust the functional relation at low turbulence Reynolds numbers to reproduce the effect of free-stream turbulence on transition Reynolds number for zero-pressure-gradient boundary layer flows. McDonald and Fish (1973) and later Wang et al. (1985) have presented a plot of measured displacement thickness Reynolds number at transition with varying free-stream turbulence levels from a wide range of experiments, suitable for use in this last step.

This procedure was followed in developing the model described in the appendix. In that case, when the pipe flow and channel flow models were compared with the sink flow data, both models lay within the scatter of the data for momentum thickness Reynolds number as a function of acceleration parameter, K. But the shape factor data appeared more consistent, and the pipe flow model gave "transition" at too low a value of K, while the channel model gave "transition" at too high a value. Overall the sink flows were best modeled by a function in between the pipe and channel flow models. This function, after modification at low turbulence Reynolds numbers, $R_{tu} < 6$, is shown in Fig. A3. It gave the channel, pipe, and sink flow results shown in Fig. 5.

In each of the figures in Fig. 5, there are three computed lines and a set of data points. One of the limiting lines is for fully laminar flow, $F_{tu} = 0$, while the other limiting line is for fully turbulent flow, $F_{tu} = 1$. In between these lines are the lines showing the calculated transition from fully laminar to fully turbulent pipe and channel flows, and the calculated sink flows. For the channel flow, the transitional flow results follow the laminar curve up to a Reynolds number, Re_h, of 1600. This value for the lower critical Reynolds number may be compared with the approximate value of 1300 measured by Patel and Head (1969). This agreement is quite good and the shape of the transition curve is also in reasonable agreement with the measurements. But the agreement with pipe data is not as good. The calculated lower critical Reynolds number, Re_d, is 1300 compared with the value of about 2000 quoted by Patel and Head, while the data show a steeper rise in skin friction than the calculations. The rise in the shape factor H, however, for the laminarescent sink flows at an acceleration parameter K of around 3.0×10^{-6}, is well modeled. So overall, for these three types of nondeveloping flow, one fairly simple one-equation turbulence model does reasonably well at modeling them all.

Tests on Boundary Layer Transition. Three test cases for transition in flat plate boundary layers were chosen from the data and correlations presented by Abu-Ghannam and Shaw (1980). These zero-pressure-gradient cases were selected to have low, medium, and high free-stream turbulence levels of 0.03, 1.25, and 4.8 percent, respectively. They provide the final tests for the exercise.

The data of Schubauer and Klebanoff (1955) give a case with very low free-stream turbulence, $\overline{Tu} = 0.03$ percent, well below the usual lower limit of about 1 percent considered by turbulence-energy equation modellers. At this low level, the free-stream turbulence is relatively unchanged along the plate. The transition Reynolds numbers are quite high, $\mathrm{Re}_{\theta,s} = 1230$ and $\mathrm{Re}_{x,s} = 2.4 \times 10^6$. The case with a turbulence intensity, $\overline{Tu} = 1.25$ percent, is typical of that found in many low-speed wind tunnels, and so the transition Reynolds number $\mathrm{Re}_{x,s} = 4.5 \times 10^5$ is also typical. The free-stream turbulence intensity actually varies between about 1.5 percent at the leading edge of the plate and 0.9 percent at the end of transition. There are no corresponding plots for a high-turbulence test case presented by Abu-Ghannam and Shaw. So we constructed a case using their data for the end of transition with $\overline{Tu} = 4.8$ percent and their correlation for the start of transition. Now, at this turbulence level, which may be found in multistage turbomachinery, the transition Reynolds numbers are quite low, $\mathrm{Re}_{\theta,s} = 170$ and $\mathrm{Re}_{x,s} = 6.7 \times 10^4$. The free-stream turbulence intensity varies from 5.0 percent at the leading edge to 4.1 percent at the end of transition.

The calculation results for all three test cases are shown in Fig. 6; and shown for comparison are data and correlation results for the start and end of transition. In their experiments, Abu-Ghannam and Shaw used the surface Pitot-tube method to determine the start and end of transition, the start being where the surface velocity showed a rapid rise and the end the peak value. Also shown for comparison on Fig. 6 are the skin friction variations for laminar and fully turbulent flat plate boundary layers. These are $0.664\ \mathrm{Re}_x^{-1/2}$ and $0.0592\ \mathrm{Re}_x^{-1/5}$, from Eqs. (7.32) and (21.11), respectively, of Schlichting (1979).

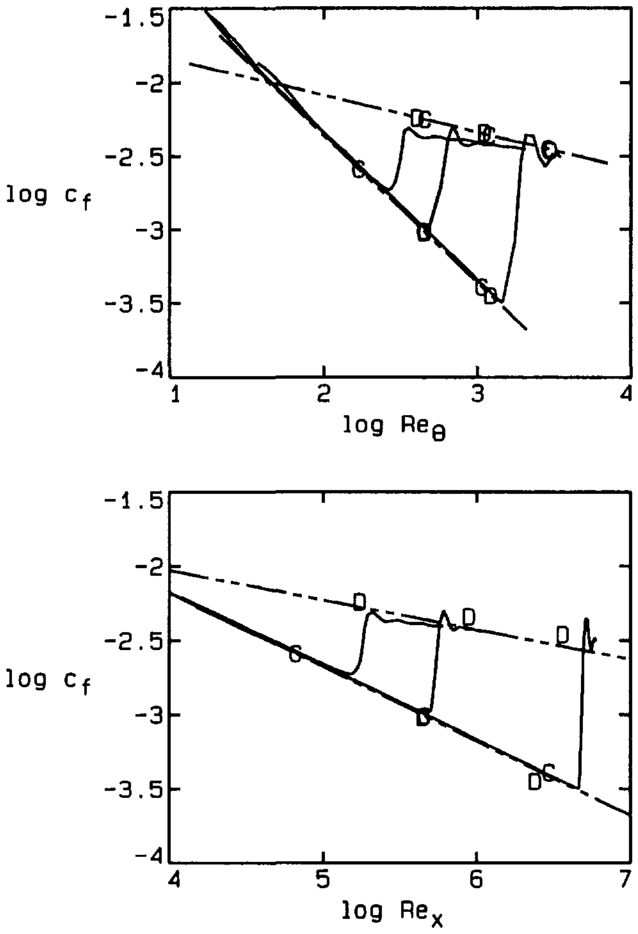

Fig. 6 Transition in developing flat plate boundary layers for free-stream turbulence intensities of 0.03, 1.25, and 4.8 percent. Data, D, and correlation, C, of Abu-Ghannam and Shaw (1980). ----- fully laminar and fully turbulent limits; ——— calculation with *q*-*L* turbulence model.

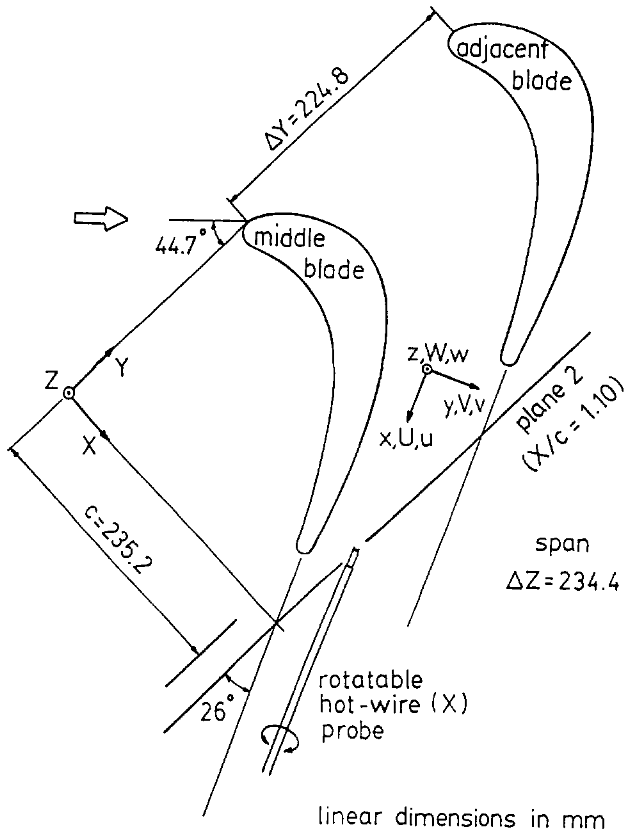

Fig. 7 Turbine cascade geometry with coordinate systems for the cascade (*X*, *Y*, *Z*) and for primary and secondary flow downstream (*x*, *y*, *z*), Moore et al. (1987).

Overall, the calculations reproduce the trends of the data and the correlations remarkably closely. It is perhaps surprising how well the low turbulence test case is modeled considering that the free-stream turbulence intensity is only 0.03 percent. But it is in quite close agreement especially in terms of momentum thickness Reynolds number. The medium turbulence test case is also well modeled, especially the start of transition. For the high turbulence test case, the start of transition is late, and in common with the other calculations the length of transition is appreciably shorter than that shown by the data.

In summary, this exercise in developing and testing a low Reynolds number turbulence-energy equation model has shown the potential for reconciling transitional behavior in pipes, channels, sink flows, and zero-pressure-gradient boundary layers. It can be a useful supplement to working group test programs and it offers an interesting project for fluid mechanics and computational fluid dynamics teaching. With further improvements in the quality of the agreement with flow measurements, it may be possible, eventually, to declare that an acceptable model has been found for the lower critical Reynolds number in pipe and channel flows. This work may also contribute to the goal of developing a model of acceptable precision to predict transition in industrial design.

Dissipation Mechanisms in Turbulent Flows

Just as the turbulence-energy equation has become a cornerstone of turbulence modeling in the last 25 years, so the equation for the kinetic energy of the mean motion, Fig. 1, has become a key factor in understanding loss production in three-dimensional flows, in the last ten years. Again, following Hinze (1975), we may write the equation for the kinetic energy of the mean motion of incompressible flow as

$$\underset{I}{\frac{1}{2}\frac{\partial}{\partial t}(\rho U_i U_i)} + \underset{II}{\frac{\partial}{\partial x_j}U_j\left(P+\frac{1}{2}\rho U_i U_i\right)} + \underset{III}{\frac{\partial}{\partial x_j}\rho\overline{u_i u_j}U_i}$$
$$- \underset{IV}{\frac{\partial}{\partial x_j}\mu U_i\left(\frac{\partial U_i}{\partial x_j}+\frac{\partial U_j}{\partial x_i}\right)}$$
$$= \underset{V}{\rho\overline{u_i u_j}\frac{\partial U_i}{\partial x_j}} - \underset{VI}{\mu\left(\frac{\partial U_i}{\partial x_j}+\frac{\partial U_j}{\partial x_i}\right)\frac{\partial U_i}{\partial x_j}} \qquad (2)$$

The terms in this equation represent:

(I) local rate of change of mean kinetic energy;
(II) change in convective transport of total pressure;
(III) the rate at which mean kinetic energy is diffused by turbulent fluctuations;
(IV) the rate at which viscous stresses do work on the control volume;
(V) work of deformation of the mean motion by the turbulence stresses per unit volume and time; this term represents the rate at which mean kinetic energy is converted to turbulence kinetic energy;
(VI) the rate at which energy of the mean flow is dissipated through the action of viscosity per unit volume and time.

Upon integration over an area *A*, downstream of a cascade of turbine blades, Moore et al. (1987) found that terms

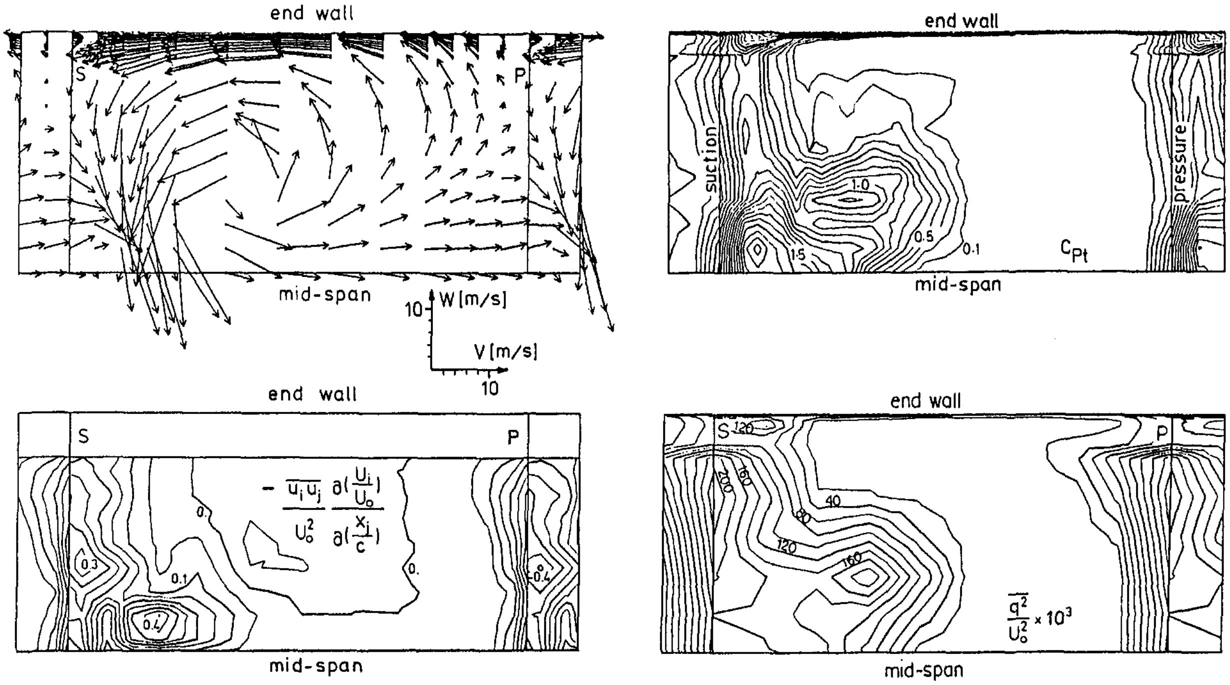

Fig. 8 Flow properties from measurements downstream of a linear turbine cascade at $X/c = 1.10$, Moore et al. (1987)

III and IV in Eq. (2) were of negligible significance. Omitting these terms, the equation for steady flow becomes

$$\frac{\partial}{\partial\left(\frac{X}{c}\right)}\left(\overline{\overline{C}}_{pt}\right) \cong N\int\int_A -\rho\overline{u_iu_j}\frac{\partial U_i}{\partial x_j}dA + N\int\int_A \mu\left(\frac{\partial U_i}{\partial x_j}+\frac{\partial U_j}{\partial x_i}\right)\frac{\partial U_i}{\partial x_j}dA \quad (3)$$

where $\overline{\overline{C}}_{pt}$ is the mass-averaged total pressure loss coefficient, X/c is the axial distance made dimensionless by the blade axial chord, and N is a nondimensionalization factor.

In Eq. (3), the left-hand side can be evaluated from total pressure and mean velocity data, and the last term on the right-hand side can be evaluated from measured velocity distributions. With additional measurements of Reynolds stresses over the area A, it is then possible to:

(*a*) evaluate the turbulent deformation work terms,
(*b*) balance Eq. (3), and
(*c*) discover the mechanism for the production of total pressure losses and for the dissipation of mean kinetic energy.

Dissipation Mechanism Downstream of a Turbine Cascade. Moore et al. (1987) measured the flow downstream of a linear turbine cascade, as shown in Fig. 7. Reynolds stress measurements were made with hot-wire anemometry at plane 2, 10 percent of an axial chord downstream of the blade trailing edges, i.e., at $X/c = 1.10$. Five-hole and three-hole pressure probe measurements were also available from Moore and Adhye (1985), at $X/c = 0.96$, 1.10, 1.25, and 1.40.

Figure 7 shows the primary velocity component, U, defined in the direction of the mean camber line at the blade trailing edges ($\beta_2 = 26$ deg). The secondary velocity components are then W, in the spanwise direction, and V, perpendicular to U and W.

The free-stream velocity at the cascade inlet was $U_o = 23.5$ (± 0.4) m/s and the exit velocity was about 37 m/s, giving an exit Reynolds number based on axial chord of 5.2×10^5. The endwall boundary layers at the inlet were thick with a ratio of displacement thickness to blade height of 0.023. With these conditions the flow downstream of the cascade was dominated by the decay of passage vortices and the dissipation of secondary kinetic energy.

The flow physics at plane 2 is summarized in Fig. 8, which shows the results for the top half of the passage, from 50 percent to 100 percent of height, in the symmetric flow. The figure shows the secondary velocity vectors (the resultant of the secondary velocities V and W), pictured in the measurement plane. The corresponding contours of total pressure loss coefficient, C_{pt}, and turbulence kinetic energy, $\overline{q^2}/U_o^2$, are also shown; and finally the distribution of the deformation work due to the Reynolds stresses (term V in Eq. (2)) is shown over the range of the full Reynolds stress measurements.

Of particular interest in this paper are the large spanwise velocities toward midspan in the blade wake, where W is of the order of -20 to -25 m/s, and the high rates of deformation work in this spanwise flow. Also of interest is the high turbulence energy, $\overline{q^2}/U_o^2 = 0.20$, directly downstream of the blade trailing edges at about 80 percent of span, where the total pressure loss is relatively low. The turbulence here is possibly associated with trailing edge vortex shedding.

Evaluating the terms in Eq. (3), Moore et al. obtained quite a good balance, as shown in Table 1. This was for the top half of the passage, as shown in Fig. 8. The contributions of the individual terms to the area integral of the deformation work on plane 2 were also evaluated and are presented in Table 2. This shows contributions in two regions of the flow, one from 90.6 to 100 percent height, near the top endwall, where single-wire measurements were made, and the other, down to midheight, from 90.6 to 50 percent of height, were two-wire measurements were made.

The rate of increase of total pressure loss at plane 2 was $\partial\overline{\overline{C}}_{pt}/\partial(X/c) = 0.25$, which was remarkably close to the value of 0.24 obtained from the deformation work integrals. Table 1 shows the turbulent stresses giving 94 percent of the

Table 1 Contributions to the rate of increase of total pressure loss at plane 2

$$\frac{\partial}{\partial\left(\frac{X}{c}\right)}(\overline{\overline{C}}_{Pt}) \cong N\iint_A -\rho\overline{u_i u_j}\frac{\partial U_i}{\partial x_j}dA + N\iint_A \mu\left(\frac{\partial U_i}{\partial x_j}+\frac{\partial U_j}{\partial x_i}\right)\frac{\partial U_i}{\partial x_j}dA$$

$\cong$	(0.226) *Turbulent contribution* (94%)	+	(0.014) *Laminar contribution* (6%)

$0.25^{(1)} \cong 0.240^{(2)}$

(1) From total pressure measurements

(2) From Reynolds stresses and velocity gradients.

Table 2 Contributions of individual terms to the area integral of the deformation work on plane 2

$$N\iint_A -\rho\overline{u_i u_j}\frac{\partial U_i}{\partial x_j}dA + N\iint_A \mu\left(\frac{\partial U_i}{\partial x_j}+\frac{\partial U_j}{\partial x_i}\right)\frac{\partial U_i}{\partial x_j}dA$$

range	(% height)	integral	
from	(50.-100.)	= 0.240	100%
$-\rho\overline{vw}\frac{\partial W}{\partial y}$	(50.-90.6)	= 0.075	31%
$-\rho\overline{uw}\frac{\partial U}{\partial z}$	(90.6-100.)	= 0.072	30%
$-\rho\overline{u^2}\frac{\partial U}{\partial x}$	(50.-90.6)	=-0.046	-19%
$-\rho\overline{w^2}\frac{\partial W}{\partial z}$	(50.-90.6)	= 0.040	17%
$-\rho\overline{v^2}\frac{\partial V}{\partial y}$	(50.-90.6)	= 0.036	15%
$-\rho\overline{uv}\frac{\partial U}{\partial y}$	(50.-90.6)	= 0.026	11%
$\mu\left(\frac{\partial U}{\partial z}\right)^2$	(90.6-100.)	= 0.013	5%
$-\rho\overline{v^2}\frac{\partial V}{\partial y}$	(90.6-100.)	= 0.010	4%
$-\rho\overline{vw}\frac{\partial V}{\partial z}$	(90.6-100.)	= 0.010	4%
Rest		$\leq \pm$ 2%	

loss production, with 6 percent from laminar shear near the endwall.

Table 2 then ranks the contributions in order of significance. Thus we see the largest single contribution, 0.075 or 31 percent of the total, from the term $-\rho\overline{vw}\partial W/\partial y$ between 50 and 90.6 percent of span. Other mechanisms for dissipation involve the terms $-\rho\overline{uw}\partial U/\partial z$ in the endwall region (30 percent), and $-\rho\overline{w^2}\partial W/\partial z$ (17 percent), $-\rho\overline{v^2}\partial V/\partial y$ (15 percent), and $-\rho\overline{uv}\partial U/\partial y$ (11 percent) between 50 and 90.6 percent of span. A contribution of the opposite sign comes from $-\rho\overline{u^2}\partial U/\partial x$ (−19 percent), which acts to produce mean kinetic energy from turbulence kinetic energy in the accelerating wake flow.

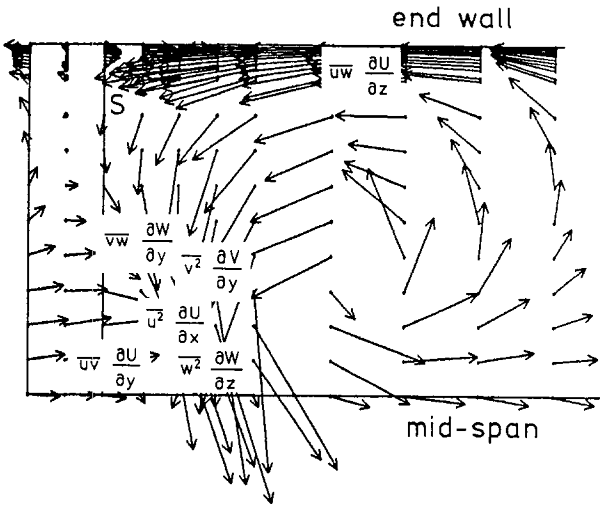

Fig. 9 Locations of the peak rates of the principal loss mechanisms at $X/c = 1.10$, superimposed on the secondary velocity vectors of Fig. 8

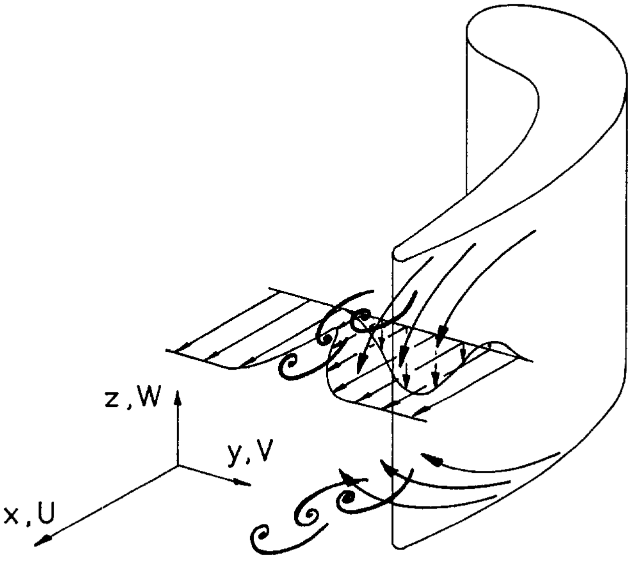

Fig. 10 Sketch of a possible mechanism for $-\rho\overline{vw}\partial W/\partial y$

The locations of the peak rates of these principal loss mechanisms are shown in Fig. 9 superimposed on the secondary velocity vectors in the suction side half of the flow at plane 2, as seen in Fig. 8. The largest contributions from the shear stresses occur where the flow shear is largest, on the pressure side of the blade wake, where the thin boundary layer from the blade pressure surface mixes with the thicker suction surface boundary layer and passage vortex flow, and in the thin endwall boundary layer. The normal stress contributions are largest where the secondary flows "stagnate" as the vortex flow convects back toward the blade wake and then down toward midspan, and also where the blade wake is accelerating, as discussed above.

Of the two major contributions, the endwall boundary layer shear term, $-\rho\overline{uw}\partial W/\partial z$, is easy to understand. However, the mechanism for the term $-\rho\overline{vw}\partial W/\partial y$ is less obvious. This is partly because the shear stress $-\rho\overline{vw}$ is not often encountered as a significant factor in flow development,

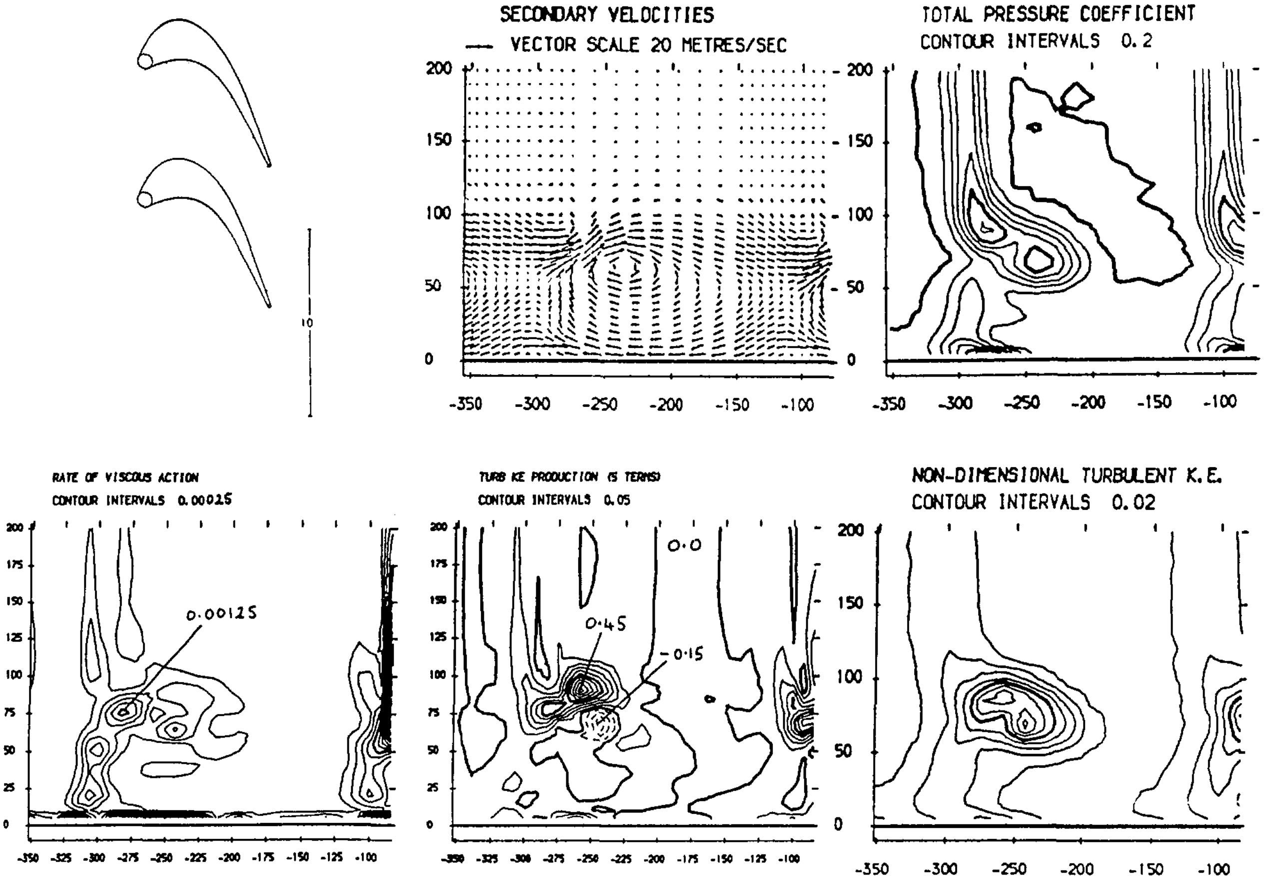

Fig. 11 Flow properties from measurements downstream of a linear turbine cascade at slot 10, Gregory-Smith and Cleak (1992)

although the shear of the spanwise flow, $\partial W/\partial y$, can be readily inferred from Fig. 8. So the mechanism sketched in Fig. 10 is offered as a possible explanation. Notice the spanwise downward flow in the blade wake, and the region of negative $\partial W/\partial y$. Note also the possibility of trailing edge vortex shedding from the blade. In this region, then, there are large fluctuations in the V and W velocity components and a correspondingly large negative shear stress $-\rho\overline{vw}$, in fact the largest shear stress values measured between 50 percent and 90.6 percent of span. The result is a large positive contribution to loss production in this flow from $-\rho\overline{vw}\partial W/\partial y$, centered at the location shown in Fig. 9.

Qualitative support for this mechanism was obtained by probing the flow field at plane 2 with a single-wire hot-wire anemometer and searching for natural frequencies. Over most of the passage vortex and blade wake, there was little indication of dominant frequencies. But at about 90 percent of span and 10 percent of blade-to-blade distance from the suction side (relative to the blade camber lines downstream of the trailing edges, shown in Fig. 8), a marked peak at approximately 800 Hz was found. This may be compared with a Strouhal frequency, based on blade trailing edge diameter and exit velocity, of about 500 Hz.

Overall, for the flow in Fig. 8, the deformation work of the primary flow, U, gives 27 percent of the loss production rate. The V velocity gives a similar contribution, 26 percent. The largest factor in loss production is the spanwise velocity, W, with 47 percent. Thus, the secondary flow components, V and W, combined account for 73 percent of the loss production at plane 2. This supports the earlier finding by Moore and Adhye (1985) that loss production downstream of this cascade was dominated by the dissipation of secondary kinetic energy. It also draws attention to the difficulty in axial flow turbomachinery of efficiently utilizing spanwise components of velocity.

Other Loss Production Studies for Three-Dimensional Flows. The study just described addresses problems discussed from ten to fifteen years ago by Langston (1980) and by Gostelow (1984). Langston noted that "An important problem that arises in the design of modern gas turbines and in the analysis of their performance, is the understanding and prediction of the nature and influence of secondary flows. Based on the current state of the art, a turbine designer might well define secondary flows as those three-dimensional flow effects in a turbine that he had not planned on." To this, we might add ... and which offer further possibilities for dissipating mean kinetic energy, for creating turbulence kinetic energy, and for creating mechanisms for further dissipation.

Gostelow (1984) in discussing secondary flow losses commented that "Having obtained a description of the flow field resulting from secondary vorticity it would be logical to suppose that this information could be used directly in a subsequent loss calculation. Unfortunately such a procedure has proved illusory." He proceeds to note that "Kinetic energy is lost from the main stream into the secondary vorticity and, knowing the secondary flow field, this loss may be calculated. ... However, the losses obtained by such inviscid approaches are many times less than observed secondary flow losses."

From these observations it is apparent that there is a need for more understanding of loss production rates themselves. More particularly, based on Eq. (3) and the results in Table 1, there is a need to study the deformation work terms

$$-\rho\overline{u_i u_j}\frac{\partial U_i}{\partial x_j} + \mu\left(\frac{\partial U_i}{\partial x_j} + \frac{\partial U_j}{\partial x_i}\right)\frac{\partial U_i}{\partial x_j}. \quad (4)$$

There have been many attempts to measure, or calculate the precursors of, $\partial U_i/\partial x_j$, but relatively few attempts to measure or calculate the Reynolds stresses, $-\rho\overline{u_i u_j}$, in three-dimensional flows. Fewer still are the attempts to extract information about loss production rates from either experimental or computational flow studies.

Gregory-Smith and Cleak (1982) are, to the authors' knowledge, the only other experimentalists to evaluate the terms in Eq. (4) for a three-dimensional flow field. In a study similar to that of Moore et al. (1987), they also measured the flow downstream of a linear turbine cascade, as shown in Fig. 11. They measured five of the six Reynolds stresses and were able to evaluate all the terms except $-\rho\overline{vw}(\partial V/\partial z + \partial W/\partial y)$ in Eq. (4). Without this term, their results show the deformation work by the viscous stresses to be only one percent of the deformation work (or rate of turbulence production) by the turbulence stresses. Of the turbulent deformation work, 55 percent was due to the shear stress $-\rho\overline{uv}$ and 35 percent was due to the normal stress $-\rho\overline{w^2}$; all the other contributions were less than 10 percent.

It is also possible to evaluate loss production rates from the results of three-dimensional turbulent flow calculations. Moore and Moore (1983a) present a procedure for obtaining the entropy production rate per unit volume, σ, from computed flow properties. For incompressible flow, the quantity $T\sigma$, where T is the temperature, gives the deformation work of Eq. (4). Moore and Moore were therefore able to study loss production in a rectangular elbow with 90 deg of turning (1983b) and in a centrifugal compressor impeller (Moore et al., 1984). While these papers did not present distributions of deformation work in the flow fields and did not discuss the contributions of individual terms or mechanisms, they did give insight into the loss production processes. Clearly much more detailed studies are possible, and these should aid in the development of more accurate calculation methods for loss production in three-dimensional flows.

Concluding Remarks

It is apparent from this brief review of Osborne Reynolds' ideas for energy modeling of turbulent flows that they are central to current turbulence research. His developments of the concepts of turbulence, or Reynolds, stresses, his recognition of the importance of the turbulence production terms in the exchange of energy between mean motion and turbulence, and his appreciation of the significance of turbulence dissipation are all part of the common currency of turbulence modeling. In essence, he conceived and modeled the idea of the energy cascade. One can take his equations for the kinetic energy of mean motion and for turbulence energy and with little modification derive the forms of the corresponding equations in common use today.

These energy equations are fundamental to research on turbulent flows and this paper has discussed just two examples of current work, transition from laminar to turbulent flow, and loss production in turbulent flow. In these areas one can see Reynolds' ideas in the essential physics and one can see that those ideas have not yet been fully exploited. For example, it is intriguing to ask whether new turbulence energy models for boundary layer transition will also be able to calculate the lower critical Reynolds number for pipe and channel flows. Surely, Reynolds would be delighted if they could. Again, imagine his surprise if computational fluid dynamics codes could calculate the distributions of Reynolds stresses in a three-dimensional flow and thereby complete the modeling of loss production rates. A measure of the value of Reynolds' contributions is that after one hundred years there are still challenges such as these following from his paper.

References

Abu-Ghannam, B. J., and Shaw, R., 1980, "Natural Transition of Boundary Layers—the Effects of Turbulence, Pressure Gradient and Flow History," *J. Mechanical Engineering Science*, Vol. 22, No. 5.

Arnal, D., 1984, "Description and Prediction of Transition in Two-Dimensional, Incompressible Flow," NATO AGARD Report No. 709, Special Course on Stability and Transition of Laminar Flow.

Beckwith, I. E., and Bushnell, D. M., 1968, "Detailed Description and Results of a Method for Computing Mean and Fluctuating Quantities in Turbulent Boundary Layers," NASA TN D-4815.

Couette, M., 1890, *Ann. Chim. Phys.*, Vol. 21, p. 433.

Davies, S. J., and White, C. M., 1928, "An Experimental Study of the Flow of Water in Pipes of Rectangular Section," *Proc. Roy. Soc. A*, Vol. 119, p. 92.

Emmons, H. W., 1951, "The Laminar-Turbulent Transition in Boundary Layer—Part I," *J. Aero. Sci.*, Vol. 18, pp. 490–498.

Glushko, G. S., 1965, "Turbulent Boundary Layer on a Flat Plate in an Incompressible Fluid," *Bull. Acad. Sci. USSR*, *Mech. Ser.*, No. 4, pp. 13–23; English trans. in NASA TTF 10, 080.

Gostelow, J. P., 1984, *Cascade Aerodynamics*, Pergamon Press, New York.

Gregory-Smith, D. G., and Cleak, W. J. E., 1992, "Secondary Flow Measurements in a Turbine Cascade With High Inlet Turbulence," ASME JOURNAL OF TURBOMACHINERY, Vol. 114, No. 1, pp. 173–183.

Hinze, J. O., 1975, *Turbulence*, 2nd ed., McGraw-Hill, New York, p. 72.

Hirsch, C., 1993, "ERCOFTAC: A European Research Network on Flow, Turbulence and Combustion," ASME Paper No. 93-GT-369.

Lamb, H., 1932, *Hydrodynamics*, Dover Publications, New York.

Langston, L. S., 1980, "Crossflow in a Turbine Cascade Passage," ASME *Journal of Engineering for Power*, Vol. 102, pp. 866—874.

Launder, B. E., and Jones, W. P., 1969, "Sink Flow Turbulent Boundary Layers," *J. Fluid Mech.*, Vol. 38, Part 4, pp. 817–831.

Launder, B. E., and Sharma, B. I., 1974, "Application of the Energy Dissipation Model of Turbulence to the Calculation of Flow Near a Spinning Disc," *Letters in Heat and Mass Transfer*, Vol. 1, pp. 131–138.

Lindgren, E. R., 1957, *Archiv für Fysik*, Vol. 12, p. 1.

Lorentz, H. A., 1907, "Uber die Entstehung turbulenter Flussigkeitsbewegungen und uber den Einfluss dieser Bewegungen bei der Stromung durch Rohren," *Abhandlungen uber theoretische Physik*, Vol. I, p. 43, Leipzig.

Mayle, R. E., 1991, "The Role of Laminar-Turbulent Transition in Gas Turbine Engines," ASME JOURNAL OF TURBOMACHINERY, Vol. 113, pp. 509–537.

McDonald, H., and Fish, R. W., 1973, "Practical Calculations of Transitional Boundary Layers," *Int. J. Heat and Mass Transfer*, Vol. 16, pp. 1729–1744.

Moore, J., and Adhye, R. Y., 1985, "Secondary Flows and Losses Downstream of a Turbine Cascade," ASME *Journal of Engineering for Gas Turbines and Power*, Vol. 107, pp. 961–968.

Moore, J., and Moore, J. G., 1983a, "Entropy Production Rates From Viscous Flow Calculations, Part I—A Turbulent Boundary Layer Flow," ASME Paper No. 83-GT-70.

Moore, J., and Moore, J. G., 1983b, "Entropy Production Rates From Viscous Flow Calculations, Part II—Flow in a Rectangular Elbow," ASME Paper No. 83-GT-71.

Moore, J., Moore, J. G., and Timmis, P. H., 1984, "Performance Evaluation of Centrifugal Compressor Impellers Using Three-Dimensional Viscous Flow Calculations," ASME *Journal of Engineering for Gas Turbines and Power*, Vol. 106, pp. 475–481.

Moore, J., Shaffer, D. M., and Moore, J. G., 1987, "Reynolds Stresses and Dissipation Mechanisms Downstream of a Turbine Cascade," ASME JOURNAL OF TURBOMACHINERY, Vol. 109, pp. 258–267.

Morkovin, M. V., 1969, "On the Many Faces of Turbulence," *Viscous Drag Reduction*, C. S. Wells, ed., Plenum Press, New York, pp. 1–31.

Patel, V. C., and Head, M. R., 1969, "Some Observations on Skin Friction and Velocity Profiles in Fully Developed Pipe and Channel Flows," *J. Fluid Mechanics*, Vol. 38, Part 1, pp. 181–204.

Patel, V. C., Rodi, W., and Scheuerer, G., 1985, "Turbulence Models for Near-Wall and Low Reynolds Number Flows: A Review," *AIAA Journal*, Vol. 23, No. 9, pp. 1308–1319.

Prandtl, L., 1934, "The Mechanics of Viscous Fluids," *Aerodynamic Theory*, W. F. Durand, ed., Vol. III, pp. 178–190.

Prandtl, L., 1945, "Uber ein neues Formelsystem der ausgebildeten Turbulenz," *Nachr. Akad. Wiss. Gottingen*, pp. 6–19; also *Coll. Works II*, pp. 874–888.

Reynolds, O., 1883, "An Experimental Investigation of the Circumstances Which Determine Whether the Motion of Water Shall be Direct of Sinuous, and of the Law of Resistance in Parallel Channels," *Phil. Trans. Roy. Soc. A*, Vol. 175, p. 935.

Reynolds, O., 1895, "On the Dynamical Theory of Incompressible Viscous Fluids and the Determination of the Criterion," *Phil. Trans. Roy. Soc. A*, Vol. 186, p. 123.

Savill, A. M., 1992, "Transition Modelling for Turbomachinery," *Proceedings of the ERCOFTAC Turbomachinery Special Interest Group Seminar and Workshop on 3D Turbomachinery Flow Prediction*, Part I.

Schlichting, H., 1979, *Boundary-Layer Theory*, McGraw-Hill, New York.

Schubauer, G. B., and Klebanoff, P. S., 1955, "Contribution to the Mechanism of Boundary-Layer Transition," NACA TN No. 3489.

Wang, T., Simon, T. W., and Buddhavarapu, J., 1985, "Heat Transfer and Fluid Mechanics Measurements in Transitional Boundary Layer Flows," ASME *Journal of Engineering for Gas Turbines and Power*, Vol. 107, pp. 1007–1015.

APPENDIX

A One-Equation Turbulence Model

The one-equation turbulence model used in the exercise described in the text is a q-L model. In this appendix, q is defined as $k^{1/2}$, i.e., the square root of the turbulence kinetic energy; and L is the mixing length of the turbulence. The Reynolds stresses are modeled using a turbulent viscosity. The model is described by the following equations:

$$\underbrace{\rho U_i \frac{\partial q}{\partial x_i}}_{\textit{Convection}} - \underbrace{\frac{\partial}{\partial x_i} \mu_{\text{eff}} \frac{\partial q}{\partial x_i}}_{\textit{Diffusion}} = \underbrace{P_q}_{\textit{Production}} \quad \underbrace{-D_q}_{\textit{Dissipation}} \qquad (a1)$$

$$P_q = \frac{1}{2q} \mu_t \left(\frac{\partial U_i}{\partial x_j} + \frac{\partial U_j}{\partial x_i} \right) \frac{\partial U_i}{\partial x_j} \qquad (a2)$$

$$D_q = \frac{C_\mu^2}{2} \frac{\mu_l}{F_{vd}^{1/2}} \frac{q}{L^2} \qquad (a3)$$

$$\mu_{\text{eff}} = \mu_l + \mu_t \qquad (a4)$$

$$\mu_t = C_\mu \rho q L F_{vd} F_{tu} \qquad (a5)$$

$$F_{vd} = 1 - \exp(-A_\mu \kappa y \rho q / \mu_l) \qquad (a6)$$

To obtain Eq. ($a1$), the equation for turbulence kinetic energy has been divided by $2q$. The convection and production terms come directly from the k equation. The diffusion and dissipation terms model the rest of the k equation. The form of the dissipation term was chosen to give the right near-wall behavior. The constants were determined from high Reynolds number fully developed pipe flow:

$$\kappa = 0.41, \quad A_d = 0.08, \quad A_\mu = 0.0295, \quad C_\mu = 0.548 \qquad (a7)$$

Mixing Length

In boundary layers, the mixing length is

$$L = \text{smaller of } \kappa y \text{ and } A_d \delta \qquad (a8)$$

For fully developed pipe and channel flows the boundary layer width, δ, is half the pipe diameter or half the channel height. For the sink flow and developing flat plate boundary layers δ is found by a search procedure. The search procedure uses Crocco's theorem, for steady inviscid incompressible flow with no body forces,

$$\mathbf{U} \times (\nabla \times \mathbf{U}) = \frac{1}{\rho} \nabla P_t \qquad (a9)$$

Boundary layers are then regions where

$$|(w/U^2)\mathbf{U} \times (\nabla \times \mathbf{U})| > 1$$

$$\text{with width } w = \text{smaller of } 2.5y(\rho y |\mathbf{U}|/\mu_l)^{0.2} \text{ or}$$
$$\text{a characteristic duct width} \qquad (a10)$$

Outside of boundary layers, the mixing length is taken as constant:

$$L = L_{\text{fre}} \qquad (a11)$$

For the fully developed pipe and channel flows, L_{fre} is not needed. For the sink flow, L_{fre} was taken as $A_d \delta$. For the developing flat plate boundary layers, L_{fre} was set to give a reasonable decay rate of free-stream turbulence.

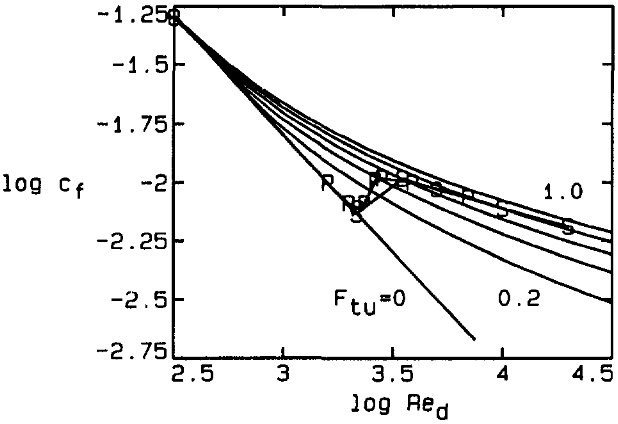

Fig. A1 Skin friction coefficient for fully developed pipe flow. Plot used to determine F_{tu} (R_{tu}). Data: P—Patel and Head (1969); S—from Schlichting (1979). ——— calculations with F_{tu} = 0.0, 0.2, 0.4, 0.6, 0.8, and 1.0.

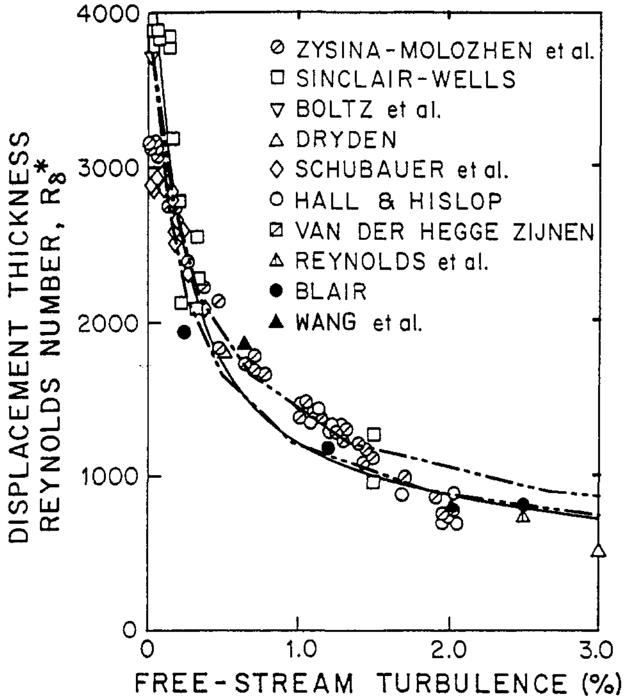

Fig. A2 $Re_{\delta*}$ and Tu at start of transition for developing flat plate flow. – – – – calculations using q-L model and free-stream mixing lengths, L_{fre} = 0.001 m and 0.005 m. ——— McDonald and Fish prediction (1973).

The discontinuity in L between the boundary layer and the free stream is smoothed by modifying the mixing length outside the layer so that the slope is less than κ:

$$|\partial L/\partial y| \le \kappa \qquad (a12)$$

Modification Factor for Transition

The turbulence reduction factor, F_{tu}, is assumed to depend on the mean turbulent viscosity Reynolds number, R_{tu}, which is evaluated by integrating across the boundary layer:

$$F_{tu} = f(R_{tu}) \qquad (a13)$$

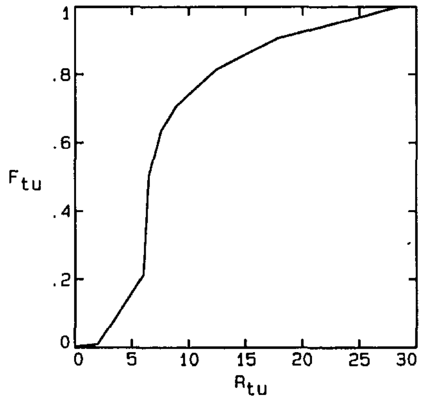

Fig. A3 Turbulence reduction factor for transition

$$R_{tu} = A_d C_\mu \int_0^\delta (\rho q/\mu_l) dy. \qquad (a14)$$

F_{tu} is applied in the boundary layer, and in free-stream regions $F_{tu} = 1$. Discontinuities at the edge of the boundary layer are prevented by decreasing F_{tu} where necessary so that

$$|\partial(LF_{tu})/\partial y| \leq \kappa \qquad (a15)$$

Determining $F_{tu} = f(R_{tu})$

The data for pipe flow are the most extensive and consistent. Therefore it was used as the empirical basis for the modeling of transitional flow. Figure A1 compares the calculated skin frictions, with measured values for the cases

$$F_{tu} = \text{constant} = 0, 0.2, 0.4, 0.6, 0.8, 1. \qquad (a16)$$

From this it can be seen that a relation between F_{tu} and Re_d can be found that fits the data, and correspondingly, by noting the R_{tu} values at the intersecting points, a relation between F_{tu} and R_{tu} which fits the data may be obtained. This procedure was followed to determine the basic shape of the function.

Then the R_{tu} scaling was adjusted to match the skin friction versus Reynolds number plot for fully developed channel flows. These two functions were used to calculate sink flows and a final R_{tu} scaling was chosen that gave reasonable results for all three types of flow. Finally, the F_{tu}–R_{tu} relation was modified, at the low turbulence end, until agreement was obtained with the displacement thickness Reynolds number versus free-stream turbulence intensity data for zero-pressure-gradient boundary layers, shown in Fig. A2. The resulting F_{tu}–R_{tu} relation is shown in Fig. A3.

The calculated flat plate results (Fig. A2) depend on the free-stream mixing length. This changes the decay rate of free-stream turbulence. Thus the mean turbulence intensity over the plate up to transition is changed as well as the free-stream turbulence intensity at transition. Reasonable high and low values for L_{fre}, 0.001 m and 0.005 m ($\mathrm{Re}_{L,\mathrm{fre}}$ = 1350 and 6750), a factor of five different, were used in the assessment. The dashed lines of Fig. A2 show the good agreement obtained between the calculated and measured displacement thickness Reynolds numbers at the start of transition. The lower of the two curves, which corresponds to $L_{\mathrm{fre}} = 0.001$ m, closely follows the McDonald and Fish prediction. The higher curve, corresponding to $L_{\mathrm{fre}} = 0.005$ m, goes through the bulk of the data between $Tu = 0.5$ percent and 1.5 percent.

Effects of Criterion Functions on Intermittency in Heated Transitional Boundary Layers With and Without Streamwise Acceleration

F. J. Keller

T. Wang
Department of Mechanical Engineering,
Clemson University,
Clemson, SC 29634-0921

Attempting to understand the mechanisms of momentum and thermal transports in transitional boundary layers has resulted in the use of conditional sampling to separate the flow into turbulent and nonturbulent portions. The choice of a proper criterion function to discriminate between the two flow conditions is critical. A detailed experimental investigation was performed to determine the effects of different criterion functions on the determination of intermittency for application in heated transitional boundary layers with and without streamwise acceleration. Nine separate criterion functions were investigated for the baseline case without pressure gradient and three cases with streamwise pressure gradient. Inherent differences were found to exist between each criterion function's turbulence recognition capabilities. The results indicate that using a criterion function based on Reynolds shear stress, $(\partial uv / \partial \tau)^2$, for turbulent / nonturbulent discrimination in a heated transitional boundary layer is superior to a single velocity or temperature scheme. Peak values in intermittency for the early to midtransitional region were found to occur away from the wall at approximately $y / \delta = 0.3$ for all cases. To match the universal intermittency distribution of Dhawan and Narasimha (1958), the minimum values of intermittency at $y / \delta \approx 0.1$ should be used as the representative "near-wall" values.

Introduction

Boundary layer transition from laminar to turbulent flow has been recognized as an important feature in the through-flow of a gas turbine (Graham, 1979, 1984; Mayle, 1991). Heat transfer in a turbulent boundary layer with a moderate Prandtl number is typically treated as a passive process controlled by the turbulent momentum transport. For a gas turbine blade, where as much as 50–80 percent of the turbine blade surface is covered with flow undergoing laminar-turbulent transition (Turner, 1971), this relation between momentum and thermal transport has not been verified. In addition, turbine blades are exposed to diverse pressure gradients that may compound these transport differences. Recognizing and understanding the fundamental mechanisms involved in transitional convective heat transfer are keys to improving the heat transfer modeling and enhancing the accuracy of thermal load predictions on gas turbine blades.

Attempting to understand the mechanisms in transitional momentum and thermal transports has resulted in the use of conditional sampling to separate the flow into turbulent and nonturbulent portions. Conditional sampling techniques used in turbulent boundary layer and shear flows are many; however, their application to heated transitional flow is not well developed. The choice of a proper criterion function to discriminate between the two flow conditions is critical. The use of temperature as a passive contaminant to discriminate between the turbulent and nonturbulent portions as done in turbulent boundary layer flows and shear flows is questionable in transitional boundary layers since discrepancies between the momentum and thermal transport in a transitional boundary layer exist. Blair (1982, 1992), Sharma (1987), and Volino and Simon (1991) determined that the length of transition for accelerating flows is longer for the thermal than for the momentum boundary layer. Sharma recommended the use of a separate intermittency factor for the thermal boundary layer under these conditions. In light of these observations, a need exists to determine the sensitivity of the intermittency factor in the heated transitional boundary layer to the choice of criterion function.

Emmons' (1951) statistical theory of transition introduced the concept of an intermittency factor for calculation in the

---

Contributed by the International Gas Turbine Institute and presented at the 38th International Gas Turbine and Aeroengine Congress and Exposition, Cincinnati, Ohio, May 24–27, 1993. Manuscript received at ASME Headquarters February 18, 1993. Paper No. 93-GT-67. Associate Technical Editor: H. Lukas.

transitional boundary layer. Emmons proposed that the turbulent patches could be treated as fully turbulent flow and the nonturbulent patches as laminar flow. The bulk flow properties could then be reconstructed as $X = (1 - \Gamma)X_{nt} + \Gamma X_t$. For example, the skin friction coefficient in the transitional region could be found from the intermittency factor and the appropriate combinations of the turbulent and laminar values; $C_f = (1 - \Gamma)C_{f_{nt}} + \Gamma C_{f_t}$. By knowing the intermittency factor at any streamwise location, the bulk properties of the transitional boundary layer could be determined. Treating the turbulent portion of transitional flow as a fully turbulent flow and the nonturbulent portion as a laminar flow is a widely used engineering practice (Arnal, 1984; Narasimha, 1985; Mayle, 1991). This practice has been recently questioned by Kuan and Wang (1990). Their concern was not on the concept of intermittency but on the adequacy of treating the turbulent portion as a fully turbulent flow and the nonturbulent portion as a laminar flow. They concluded that both turbulent and nonturbulent portions of the transitional flow are different from their counterparts in the fully turbulent and laminar flow.

The determination of the turbulent and nonturbulent portions of the transition region and their subsequent separation relies on the technique of conditional sampling. This technique was discussed in detail by Hedley and Keffer (1974) and Muck (1980). It is comprised of three main stages: selection of a criterion function, determination of a threshold level, and generation of an intermittency function.

Turbulent flow is a three-dimensional rotational flow characterized by the dissipation of mechanical energy into heat through a cascade of eddies of diminishing sizes. The criterion function should be ideally representative of this turbulence and offer a good contrast between the turbulent and nonturbulent portions. However, detection of an energy cascade requires spectral analysis and renders an instantaneous decision for or against turbulence difficult. Fluctuating vorticity was used by Corrsin and Kistler (1955), but this requires the use of a complex probe capable of spatial differentiation and is considered by most too difficult to implement, especially in a transitional boundary layer.

Chen and Blackwelder (1976), Muck (1980), and Antonia (1981) considered the use of a passive scalar such as temperature to be superior to velocity or vorticity as a criterion function. However, Muck (1980) pointed out that the question remains whether the thermal interface coincides with the turbulent (vorticity) interface. For a fully turbulent heated boundary layer, turbulent/nonturbulent discrimination occurs primarily in the outer boundary layer where the turbulent fluid is rotational and the nonturbulent fluid is irrotational. The temperature in the irrotational portion remains constant and is lower than the temperature in the turbulent regions. The classic temperature discrimination scheme uses the temperature directly and identifies "hot" fluid as turbulent and "cold" fluid as nonturbulent. The validity of this classic scheme needs to be re-examined in the transitional boundary layer where the vorticity dynamics are different. The dynamics of the vortices on the rotational/irrotational interface of the fully turbulent boundary are different than the vortex tubes on the boundary between the turbulent and nonturbulent portion in a transitional boundary layer. The temperature in the irrotational portion of the turbulent outer boundary layer maintains a constant lower temperature than the rotational portion. However, the temperature of the nonturbulent portion of the transitional boundary layer is not necessarily lower than the temperature in the turbulent portion. In the transitional boundary layer, the temperature profile, similar to the velocity profile, will alternate between a laminarlike profile and a turbulentlike profile. In addition, the "calming region" at the trailing edge of a turbulent patch imposes difficulty for discriminating the turbulent/nonturbulent portions since both fluctuating magnitudes and mean values are changing. No such calming region is observed in the interface between a turbulent boundary layer and free stream.

Difficulties also arise in using velocity fluctuations. Velocity fluctuations are not unique to the turbulent fluid and may be due to amplified oscillations of the free-stream disturbances or Tollmien–Schlichting waves. As a result, some procedure must be used to desensitize it. Also, spurious dropouts (short regions where the criterion function falls below the threshold level indicating nonturbulent flow) occur within a turbulent burst and some form of smoothing is required. Smoothing may take the form of a running average to eliminate the spurious dropouts or the use of a holding time where any excursions shorter than the holding time are still considered turbulent. Hedley and Keffer (1974) recommended $[(\partial^2 u/\partial\tau^2)^2 + (\partial^2 v/\partial\tau^2)^2]$ or $[(\partial u/\partial\tau)^2 + (\partial v/\partial\tau)^2]$ for use as the discrimination scheme stating that the Reynolds shear stress has a lack of definition at the interface leading edge. Antonia (1972) used $(\partial uv/\partial\tau)^2$ and reported a sharp drop in the Reynolds shear stress at the interface conflicting with the results of Hedley and Keffer.

Nomenclature

C_f = skin friction coefficient = $\tau_w/(\rho \bar{U}_\infty^2/2)$
C_p = pressure coefficient = $(P - P_{\text{ref}})/[(1/2)\rho \bar{U}_{\infty\text{ref}}^2]$
K = pressure gradient parameter = $(\nu/\bar{U}_\infty^2)(d\bar{U}_\infty/dx)$
P = static pressure
Re_x = Reynolds number = $\bar{U}_\infty x/\nu$
t = instantaneous fluctuation in temperature
t' = rms value of temperature fluctuation
T = instantaneous temperature
u, v, w = instantaneous velocity fluctuations in streamwise, cross-stream, and spanwise directions
u', v', w' = rms values of velocity fluctuations
u^* = friction velocity = $\sqrt{\tau_w/\rho}$
U, V = instantaneous velocities
$\bar{U}$ = mean velocity
U^+ = $\bar{U}/u^*$
$\overline{uv}$ = mean Reynolds shear stress
$\overline{ut}$ = mean Reynolds streamwise heat flux
$\overline{vt}$ = mean Reynolds cross-stream heat flux
x = coordinate in streamwise direction
y = coordinate normal to the surface
Y^+ = yu^*/ν
Γ = intermittency factor
δ = boundary layer thickness at $0.995\ U_\infty$
δ^* = displacement thickness
ϵ = turbulent dissipation rate
ν = kinematic viscosity
ξ = length in transition region = $x_{\Gamma=0.75} - x_{\Gamma=0.25}$
ρ = density
τ = time
τ_w = shear stress on the wall

Subscripts

∞ = free-stream value
nt = nonturbulent
ref = reference location at x = 20 cm
s = onset of transition
t = turbulent
w = at the wall

Muck (1980) investigated several discrimination schemes and concluded using $|\partial uv/\partial\tau|$ or $|\partial^2 uv/\partial\tau^2|$ worked best and was closest to the temperature scheme.

The threshold value is the minimum value of the criterion function set just above the background noise and nonturbulent fluctuations. Several different methods for choosing a threshold level have been proposed. Corrsin and Kistler (1955) plotted the cumulative distribution functions of the intermittency as a function of threshold value. The point of maximum curvature was then used to select the threshold value. This method worked well when the intermittency was low but was unreliable for high values of intermittency (Muck, 1980). Hedley and Keffer (1974) raised the threshold level and determined the average time duration of all the nonturbulent zones of the discrimination scheme until a constant value was reached. This process was repeated for all streamwise and cross-section locations. A similar threshold value was observed when the beginning of the constant time average duration was reached. This single value was used for all locations. However, this method is very sensitive to spurious dropouts and the smoothing procedure. Antonia (1972) set the threshold equal to a fraction (0.3) of the overall average of the function. With all these different schemes being tried what remains clear is that there is no rational method of choosing a threshold value. It is typically adjusted by trial and error until the results conform with the individual researchers expectations (Muck, 1980).

The above-mentioned investigations were performed in fully turbulent boundary layers. These same ideas are usually extended into transitional boundary layers but it remains to be verified because the flow and thermal structures in the transitional boundary layer are different from those in the turbulent boundary layer as explained previously. The work presented in this paper is a systematic investigation performed to determine the effects of different criterion functions on intermittency in a heated transitional boundary layer, to establish an adequate conditional sampling technique to separate the flow into the appropriate turbulent/nonturbulent portions, and to investigate specifically the difference between velocity and thermal intermittency if it exists. Experiments were first performed in a transitional boundary layer flow over a flat surface without a streamwise pressure gradient and followed by three cases of accelerated boundary layer at three different K values.

Experimental Program

Test Facility. The test facility used in this research program consisted of a two-dimensional, open circuit, blowing type wind tunnel. The maximum air speed was 35 m/s, uniform within 0.7 percent and steady within 1 percent over a 20-hour period. An inlet airflow filter box was covered with a layer of Rayon-viscous felt capable of filtering out particles larger than 5 μm. The free-stream air temperature was controlled by the heat exchanger and the air conditioning system in the laboratory and could be maintained within 0.5°C over a period of 20 hours and uniformly within 0.1°C. A suction fan and low-pressure plenum were installed at the leading edge to provide suction. A detailed description of the wind tunnel is provided by Kuan (1987) and Kuan and Wang (1990).

To provide the two-dimensional flow required in this investigation, the test section was designed with a large aspect ratio of 6. The test section was 0.15 m wide, 2.4 m long, and 0.92 m high consisting of a heated test wall, an outer observation wall, a top wall cover, and a bottom wall table. A composite construction was utilized for the rectangular 2.4 m × 0.92 m heated test wall. The back surface was covered with 25.4 cm of R30 fiberglass insulation to minimize backplane conduction losses. The heating pad consisted of a heater foil sandwiched between glass cloth and silicon rubber sheets. A 1.56-mm-thick aluminum sheet was vulcanized to the front surface of the heater pad to ensure uniformity of the heat flux. A 1.56 mm polycarbonate sheet was placed on the front surface to provide a smooth test surface on which the air flows and measurements were taken. One hundred eighty-five 3-mil E-type thermocouples were embedded beneath the test surface and were strategically placed along the test surface to capture the evolution of the wall heat transfer during the transitional flow process.

Fourteen measuring holes of 2.54 cm diameter were drilled along the centerline axis and eight measuring holes of equal diameter were drilled along the off-centerline in the cross-span direction. The first centerline measuring hole (station 1) is located 20 cm from the leading edge with the remaining measuring holes placed every 15 cm (labeled sequentially station 2 through station 14). Plexiglass plugs, flush with the inner surface, were used to plug the holes when measurements were not being taken. Slots cut into the table and the top wall provide for adjustment of the outer wall in order to vary the pressure gradient in the test section. A schematic of the thermocouple layout and the location of the profile measurement locations is shown in Fig. 1. The detailed description of the test section and heated test wall was documented by Wang et al. (1992) and Zhou (1993).

Geometry of the Test Section. For the baseline case, with no acceleration, the outer wall of the test section was adjusted to account for the growth of the boundary layer and to maintain a near-zero pressure distribution inside the test section with a variation of pressure coefficient, Cp, within 1 percent as shown in Fig. 2.

Three different favorable pressure gradients were utilized in this investigation. A constant pressure gradient parameter, K, was maintained during each case. One of the advantages of using a constant K over other pressure gradient parameters is that a constant K can be directly related to the geometry of the test section. By linearly decreasing the wall separation between the inlet and exit, a relatively constant K value can be obtained. For each acceleration case, the width of the test section inlet was maintained at 15.24 cm and the downstream width was arranged to decrease linearly to the exit plane. An exit width of 14.6 cm was used for the lowest acceleration case of $K = 0.07 \times 10^{-6}$ while an exit width of 8.9 cm was used for the highest acceleration case of $K = 0.25 \times 10^{-6}$. The free-stream velocity distribution and pressure coefficient for each case is shown in Fig. 2. It should be noted that a constant K flow is inherently different from a Falkner–Skan flow, which has a constant Λ [$\equiv (\delta^2/\nu)(dU_\infty/dx)$] value. For a bounded passage flow, as in the turbine, a use of K-value to characterize the flow acceleration is more appropriate than the use of Λ even for situa-

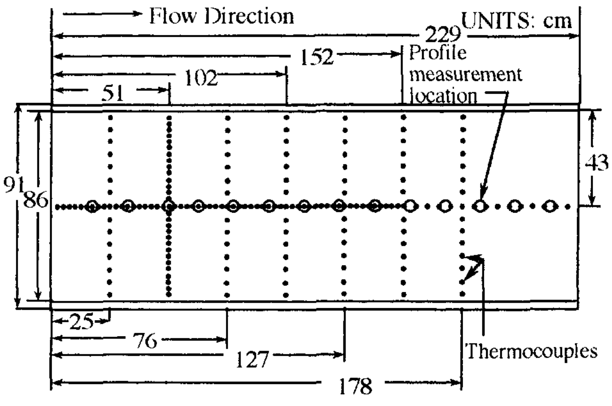

Fig. 1 Thermocouple layout on heated test wall

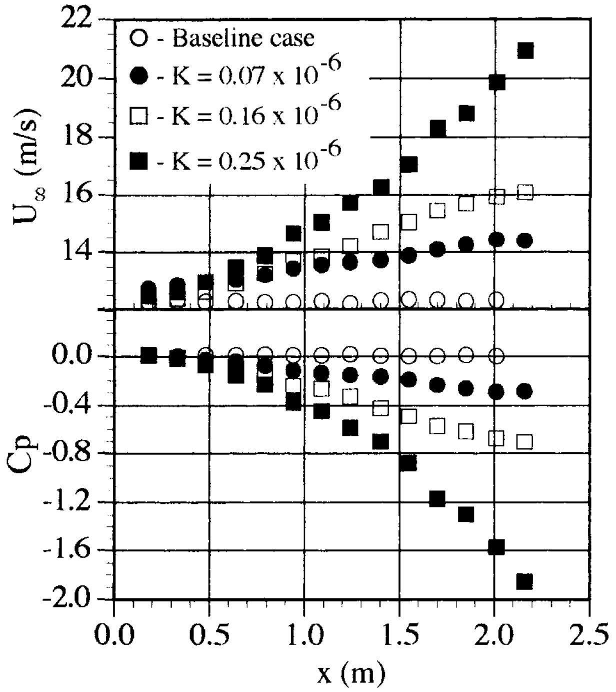

Fig. 2 Free-stream velocity and corresponding *Cp* values for each case

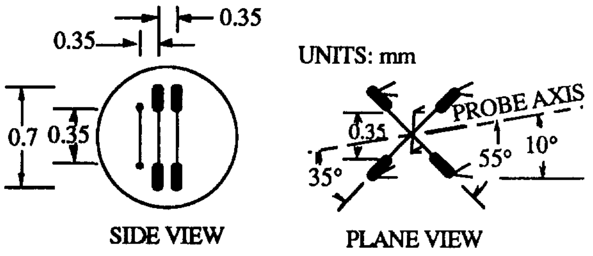

Fig. 3 Three-wire boundary layer sensor

tions with the boundary layer thickness much smaller in comparison with the passage width. Detailed explanations concerning the physical meaning of flow and thermal features of accelerated boundary layers with constant *K* values and the differences between a constant *K* and a constant Λ flow were made by Zhou and Wang (1992).

Three-Wire Sensor. A specially designed miniature three-wire probe was used to measure all the boundary layer velocity and temperature data. This sensor is similar to that used by Sohn et al. (1989). An **X** array, consisting of 1.0-mm-long and 2.5-μm-dia Wollaston-type platinum-coated tungsten wires, was utilized for the velocity sensors. An active sensing length of 0.5 mm was etched in the center. The **X** wires were placed orthogonal to each other with a spacing of 0.35 mm. The temperature sensor is a 0.35-mm-long unplated platinum wire 1.2 μm in diameter placed normal to the mean flow direction in a plane parallel to the plane of the cross wire and spaced 0.35 mm from the **X** array. This orientation for the temperature wire was chosen to eliminate any streamwise temperature gradients. Due to the difficulty in maintaining the accurate sensor arrangement during fabrication when bending the three pairs of prongs, as for a typical boundary-layer type probe, the prongs were kept straight; the probe stem was bent at an angle of 10 deg from the probe axis. This angle was chosen to ensure that both of the **X** wires touched the wall simultaneously without interference between the probe stem and the wall (see Fig. 3). A complete description of the probe design and qualification, specifically in a heated transitional boundary layer, can be found in Shome (1991).

Measurements and Instrumentation. The velocity-sensors were operated in a constant-temperature mode using a TSI model IFA 100 Intelligent Flow Analyzer. The IFA 100 allows simultaneous operation of up to four channels. A DISA M20 temperature bridge was used to operate the temperature sensor in the constant current mode. For future turbulent power and thermal power spectral analysis, TSI Model 157 signal conditioners were used to low pass filter signals from all three sensors. The **X**-wires of the three-wire sensor were operated at overheat ratios of 1.43 and 1.66. The 1.2 μm temperature sensor was operated with a very low overheat ratio. The probe current was set at 0.1 mA and an amplifier gain of 3500 was used. For convenience, the velocity wires are called hot wires and the temperature wire is called cold wire in this study. The TSI IFA 100 is also equipped with a square wave generator with a frequency range of 0.3–30 kHz and amplitude range of 0–4.5 V. The square wave generator was used to optimize the frequency response of each velocity wire prior to calibration to ensure minimum under or over damping of the wire response. The optimum frequency response found for each velocity wire was approximately 200 kHz. The frequency response of the temperature sensor was experimentally determined ranging from 4800–6400 Hz depending on the velocity using the DISA M20 constant current bridge (see Wang et al., 1992, for details). The data from all three sensors were subsequently sampled at 2 kHz for 20 seconds with the low pass filter set at 1 kHz.

The wind tunnel, the test wall power supply, and the cooling water supply were started at least 12 hours prior to the experimentation. A global measurement for wall temperature distribution was performed by scanning the temperature approximately every two hours. Each time an average of three different scans, which each scan made at a sample rate of 1 channel/second, was obtained. During the measurement of each boundary layer temperature profile, a check of the steadiness of the local wall temperature was performed before, midway, and at the end of each measurement. Both the global and local check served to monitor the steadiness of the wall and the free-stream temperature. For all thermocouple measurements a Metrabyte IEEE-488 general interface I/O expansion board was used. A Fluke 8842A 5½ digit digital multimeter and a Fluke 2205A 100-channel switch controller were interfaced with the IEEE-488 board. Special low voltage scanner modules (Model 2205A-600), each with silver-coated shields, were installed in the switch controller to provide a voltage resolution of 1 μV for thermocouple emf measurements. For each case a uniform heat flux of 335 W/m^2 was applied to the test wall and the free-stream temperature was maintained at approximately 15° C. The resulting wall temperatures ranged from 24° C to 41° C.

Conditional Sampling Technique. Conditional sampling consists of three primary stages: the choice of a criterion function, the determination of a threshold value, and the generation of an intermittency function. The determination of the threshold value and intermittency function are discussed below.

To determine the appropriate threshold value for each criteria function, a "dual-slope method" was used. This method is based on the cumulative distribution of probability density functions (PDF) used by Corrsin and Kistler (1955) and was extended by Kuan and Wang (1990). This method uses a graphic approach to find the threshold value at each location. A program was used to generate the cumulative distribution of intermittency as a function of threshold value. For each data reading, the criterion function was compared to the threshold value. If the value was greater than the

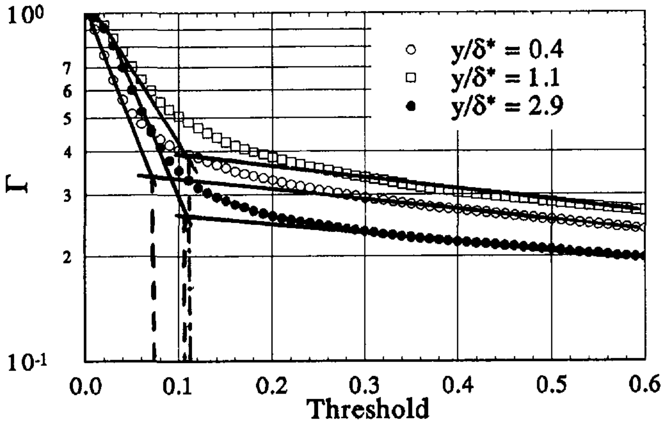

Fig. 4 Cumulative distribution of intermittency for varying threshold value ($Re_x = 7.43 \times 10^5$ with $d^2U/d\tau^2$)

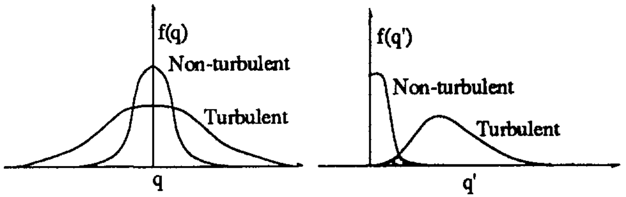

(a) (b)

Fig. 5 (*a*) Possible probability density function for the turbulent and nonturbulent fluid, and (*b*) final probability density function for the desensitized criterion function (Hedley and Keffer, 1974)

threshold, the reading was considered turbulent. If the value was less than the threshold and the next two readings also less than the threshold, the reading was considered nonturbulent. Once all the readings for a given location were categorized, the final intermittency for that threshold was determined. The threshold value was then increased and the process repeated. The resulting intermittency distribution function was then plotted as shown in Fig. 4. When presented in a semi-log coordinate, two straight lines of different slopes were apparent (therefore, named dual-slope method) and the threshold value at the intersection of these two lines was taken as the initial estimate. Further refinement was required to find an optimum value. The reasoning behind this method is as follows. The background noise and fluctuations in the nonturbulent portion are close to a Gaussian probability density, $f(q)$. The fluctuations in the turbulent portions also have a Gaussian probability density but with a larger standard deviation (Fig. 5*a*). By choosing the appropriate criterion function and desensitizing it, the intersecting region of these two curves is minimized (Fig. 5*b*). The area of intersecting regions depends on the actual flow behaviors. An inevitable overlap region will represent the probability of indeterminable discrimination of turbulence from nonturbulence. For each threshold value 32768 (2^{15}) data readings were processed.

After the sampled data were reduced, the intermittency function was obtained. The value of this function is 1 if the flow is turbulent and is 0 otherwise. Due to inherent spurious dropouts amidst turbulent signals, a holding time was introduced to smooth out these spurious dropouts. Hedley and Keffer (1974) suggested an optimum holding time based on the Kolmogorov length scale, $\eta = (\nu^3/\epsilon)^{1/4}$. The recommended holding time will be η divided by the convective velocity of the smallest eddies. However, the probe resolution and the digital sample rate must also be considered. The actual holding time is therefore suggested by Hedley and Keffer (1974) to be approximately 15–35 times this Kolmogorov scale. Hedley and Keffer used a value of 4 times the sampling time interval, which was 0.0004 seconds. Since the eddy size in transitional flow is larger than the eddy size in a fully turbulent flow, the holding time was assigned a larger interval for the transitional flow. For this investigation, with a sample rate of 2 kHz the holding time was set equal to three sampling time intervals, which corresponds to approximately 200 times the Kolmogorov scale for the fully turbulent boundary layer (baseline case).

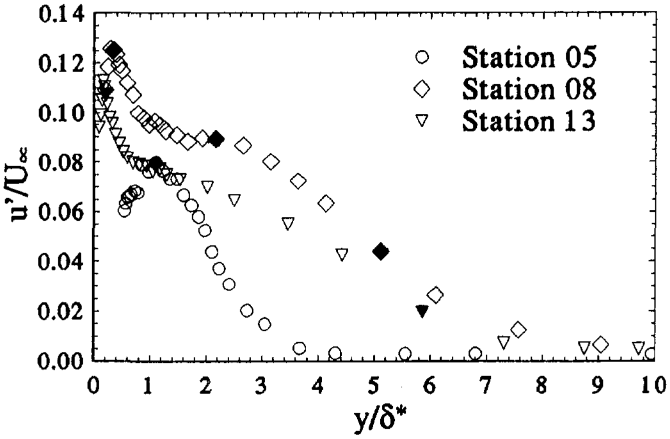

Fig. 6 Distribution of streamwise velocity fluctuations for zero-pressure gradient (shaded symbols represent points investigated)

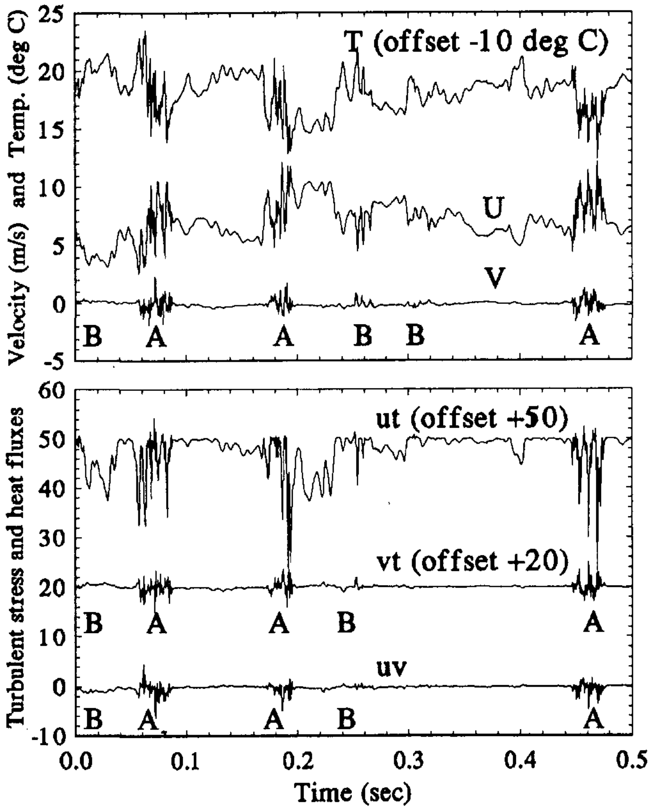

Fig. 7 Signals and correlations for Γ = 0.5, $y/\delta^* = 1.1$ (baseline case); *A*: clearly defined turbulent region; *B*: questionable region

Results and Discussion

Criterion Functions. All criterion functions were generated from the output signals of the three-wire sensor. The streamwise and cross-stream velocities (U and V), the temperature (T), and the corresponding correlations (ut, vt, and

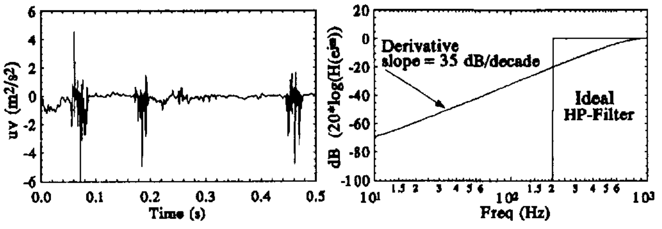

a) Input signal. b) Frequency response.

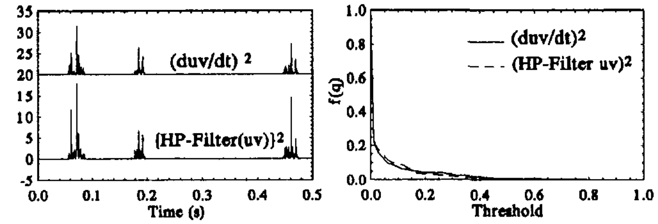

c) Filtered signal. d) Probability density.

Fig. 8 Comparison of first derivative to ideal digital high-pass filter

uv) were used. Sixteen locations were investigated for the zero-pressure gradient boundary layer (baseline case). Each cross-stream location was selected based on the distribution of streamwise velocity fluctuations (u'). Station 5 ($\mathrm{Re}_x = 6.13 \times 10^5$) was the first measuring location to indicate signs of transition in the form of turbulent bursts. A location of $y/\delta^* = 1.2$ corresponding to the maximum peak in u' was investigated for this station. For each remaining station in the transition region, stations 6 through 8 ($\mathrm{Re}_x = 7.43 \times 10^5$ through $\mathrm{Re}_x = 9.87 \times 10^5$), three cross-stream locations were selected corresponding to the maximum peak in u', the plateau region following this maximum peak, and a point near the edge of the boundary layer. For stations 9 through 13 ($\mathrm{Re}_x = 11.2 \times 10^5$ through $\mathrm{Re}_x = 16.2 \times 10^5$), a single location near the edge of the boundary layer was investigated. A near-wall point was also investigated for the fully turbulent boundary layer of station 13. Similar points were chosen for each pressure gradient case. Three representative u' distributions for stations 5, 8, and 13 of the baseline case and the corresponding locations of investigation are shown in Fig. 6. An example of the signals and correlations from the baseline case for station 6 with $\Gamma = 0.5$ are shown in Fig. 7. It is apparent that turbulent/nonturbulent discrimination from the direct use of *T*, *U*, or *ut* would be difficult. For *V*, *vt*, and *uv* the turbulent portions are most clearly defined (labeled *A* in Fig. 7) but several questionable regions still exist (labeled *B*). The raw signals shown in Fig. 7 are inappropriate for use as criterion functions especially with the presence of unsteady oscillations in the nonturbulent portion. A means of desensitizing the signal to the nonturbulent fluctuations must be implemented. The method most commonly used is to high-pass filter the signal or to differentiate the signal with respect to time and square it, thus emphasizing the high-frequency components.

A comparison of the effects of using an ideal digital high-pass filter and taking the derivative of an example signal is shown in Figs. 8(*a–d*). For all differentiation throughout the analysis, a second-order central-difference technique was utilized. A 0.5 second sample of the Reynolds shear stress sampled at 2 kHz with a 1 kHz analog filter is shown in Fig. 8(*a*). The frequency response of the first time derivative and the ideal digital high-pass filter with a 200 Hz cutoff frequency are shown in Fig. 8(*b*). The first time derivative behaves as a high-pass filter with a linear phase and a frequency response with a slope of 35 dB/decade. Applying both the time derivative and the ideal digital high-pass filter to the signal shown in Fig. 8(*a*) and squaring, results in the criterion functions shown in Fig. 8(*c*). The resulting probability distributions for each case are indicated in Fig. 8(*d*). For the transitional flow signal, no significant differences are observed between using the first time derivative filter and the ideal digital high-pass filter. These results are significant for several reasons. First, using a digital filter in post-acquisition allows more flexibility than using a high-pass analog filter during acquisition. This allows for post-acquisition filter adjustment for different signals and flow conditions. Second, using a low-order derivative is easier to implement and requires less computational time than a higher order digital filter. A higher order filter requires more terms to implement in the time domain than a low-order derivative, thus increasing computational time. Implementation of an ideal digital high-pass filter must be done in the frequency domain, which requires performing an FFT and IFFT, resulting in more than an order of magnitude increase in computational time.

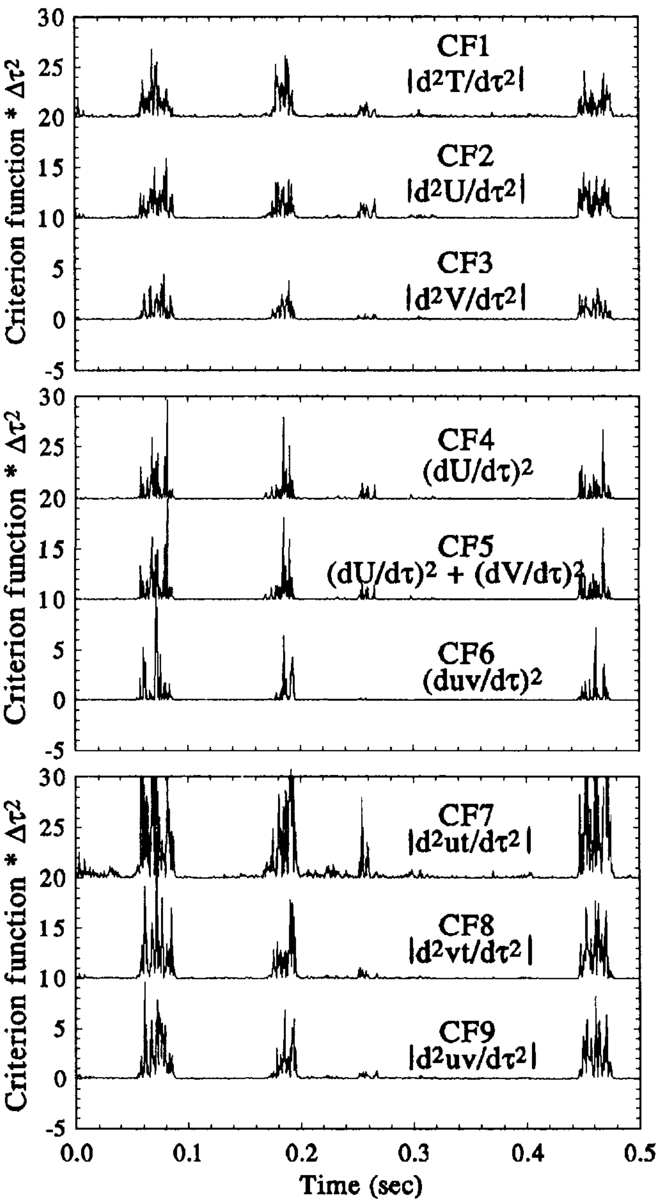

Fig. 9 Corresponding criterion functions for $\Gamma = 0.5$, $y/\delta^* = 1.1$ (baseline case)

Nine separate criterion functions were investigated for the baseline case and the three pressure gradient cases. An example of the criterion functions investigated corresponding

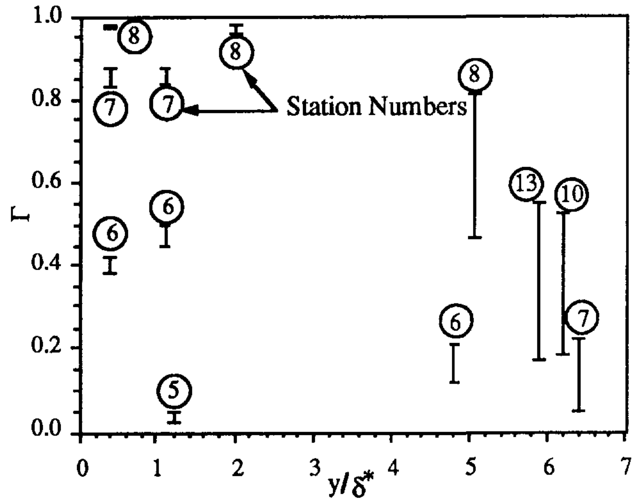

Fig. 10 Intermittency variation for different criterion functions (baseline case)

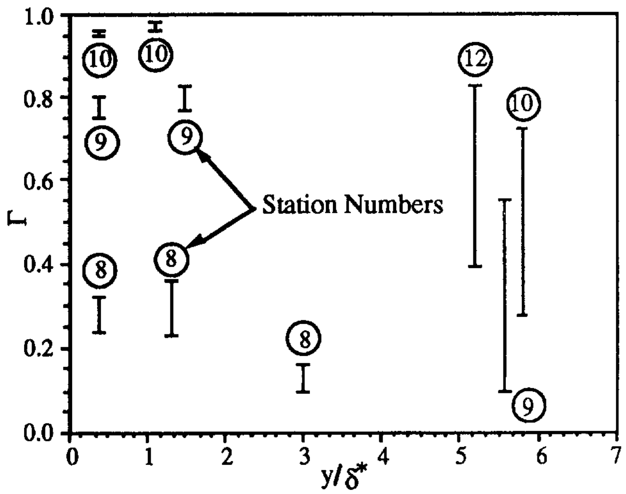

Fig. 11 Intermittency variation for different criterion functions ($K = 0.07 \times 10^{-6}$)

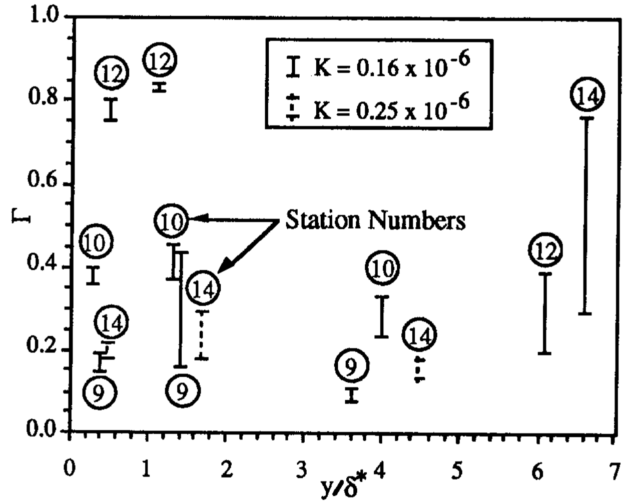

Fig. 12 Intermittency variation for different criterion functions ($K = 0.16 \times 10^{-6}$ and $K = 0.25 \times 10^{-6}$)

to the signals in Fig. 7 are shown in Fig. 9. Six criterion functions were based on the second derivative of the signals while three criterion functions were based on the square of the first derivative. In both these figures, 0.5 seconds of data (1000 data points) are shown from the 16.38 seconds (32768 point) record. The intermittency determined from the "dual-slope method" for each criterion function was compared to that obtained by direct observation (the eyeball method). In all cases the discrepancy between the two methods was within 5 percent. From Fig. 9 it is observed that differences in turbulence discrimination exist between the various criterion functions. A larger uncertainty is observed in using the second derivative of the streamwise Reynolds heat flux, $d^2ut/d\tau^2$ (CF7). The demarcation between the turbulent and nonturbulent portions for this criterion function is not as pronounced as the others. This correlation could not be desensitized to low-frequency unsteadiness, resulting in several false turbulence readings. This low-frequency unsteadiness was more apparent in several of the other signals (not shown in this paper). The intermittency values obtained using criterion functions based on temperature (CF1) or a single velocity signal (CF2 through CF5) were comparable within 5 percent throughout the transition region. No advantage was gained by combining velocity signals (CF5), as recommended by Hedley and Keffer (1974). Using criterion functions based on uv (CF6 and CF9) or vt (CF8) resulted in intermittency values 0.14 to 0.38 lower in the outer boundary layer region ($y/\delta > 4.0$) than the values found from the single-signal-based criterion functions. These discrepancies occurred in the late transitional and early turbulent regions (stations 8–13). The range of intermittency values determined for several locations of the baseline case are presented in Fig. 10. The large variation in the outer boundary layer is apparent. This same procedure was repeated for each pressure gradient case with similar results (Figs. 11 and 12). A complete listing of all the intermittency and threshold values for each criterion function was documented by Keller (1993). The intermittency determined for each criterion function from the "dual-slope method" was compared to the eyeball method for verification and was always within 5 percent. It is apparent from these results that near-wall intermittency values were similar regardless of the criterion function. Only in the outer boundary layer were significant differences observed. The results from using the temperature based scheme, CF1, were consistent with the results from the other single signal schemes (CF2 through CF5) for all cases investigated. *No differences were found using the temperature-based criterion function to support the use of separate thermal intermittency factor.*

From the results above the criterion functions were divided into two groups, the single signal schemes (CF1 through CF5) and the correlation schemes (CF6 through CF9). One criterion function from each group was selected for further investigation. CF2 was chosen from the first group and CF6 from the second. Each of these criterion functions showed the greatest demarcation between the turbulent and nonturbulent portion of the flow for their respective groups. In addition, these two criterion functions are the ones most commonly used by researchers.

Best Criterion Function. Several factors were considered for determining which criterion function is the best choice for use in the transitional boundary layer. These factors include: (1) a sharpness in demarcation between turbulent and nonturbulent portions of the flow, (2) a small variation of threshold value throughout the transition region, (3) a low uncertainty in determining the threshold value, and (4) a low sensitivity of the resulted intermittency to the uncertainty in choosing the threshold value. A single location in the mid-transition region was selected for detailed comparison of the two chosen criterion functions. A location from station 6 for $y/\delta^* = 1.1$ was selected. For this location, both criterion functions indicated an intermittency value of approximately 0.5.

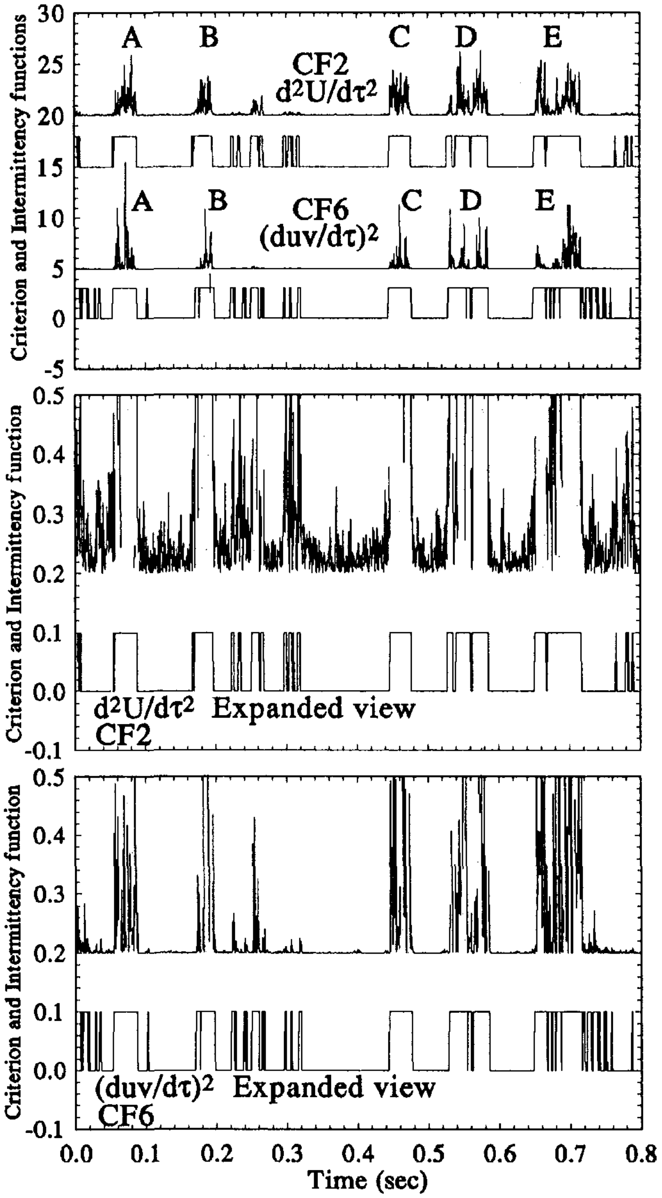

Fig. 13 Comparison of two criterion functions and corresponding intermittency functions, $\Gamma = 0.5$, $y/\delta^* = 1.1$ (baseline case)

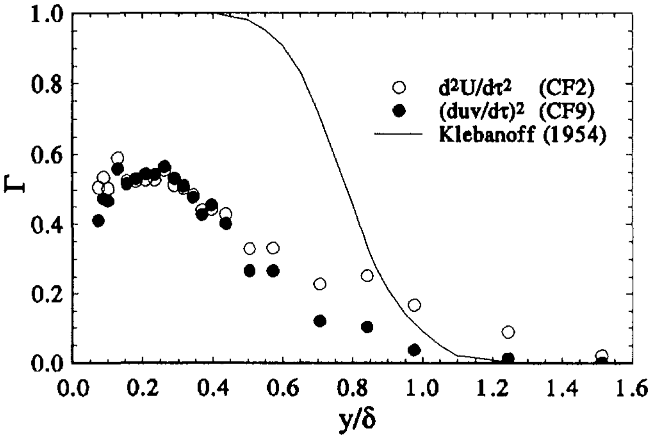

Fig. 14 Intermittency distribution through boundary layer for different criterion functions ($Re_x = 7.43 \times 10^5$, baseline case)

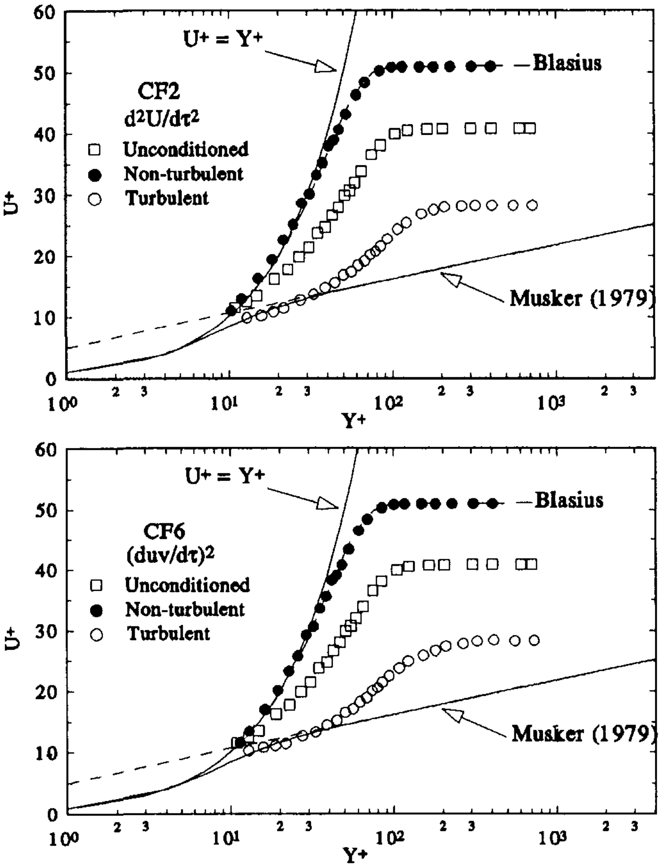

Fig. 15 Comparison of U^+ versus Y^+ for different criterion functions ($Re_x = 7.43 \times 10^5$, $\Gamma = 0.5$, baseline case)

A detailed view of the two criterion functions and the resultant intermittency function is shown in Fig. 13. The raw signals up to 0.5 seconds of Fig. 13 are previously shown in Fig. 7. Both criterion functions are of the same order of magnitude within the regions labeled *A–E* in Fig. 13. However, each criterion function weights different areas within each region differently. For example, for region *E*, CF6 indicates intense turbulent activity toward the end of the region with less turbulent activity toward the beginning of the region. CF2 indicates the turbulent activity at the beginning and end of region *E* is of the same order of intensity. The two different criterion functions do not recognize turbulence equivalently; inherent differences exist. It remains to determine which criterion function more accurately represents turbulence. Also shown in Fig. 13 is an expanded view of each criterion function in order to investigate the detailed structure between and within each region. While regions *A–E* are of the same order of magnitude, the expanded views show that the areas between these regions are not. CF6 has a much sharper demarcation between the turbulent and non-turbulent portions. This difference results in different variations of threshold value throughout the transition region for each criterion function. For CF2, large variations of the threshold value occur. Typically the threshold value is the smallest very close to the wall and increases nonlinearly, asymptotically approaching a constant value near the edge of the boundary layer. An increase of 500 percent is typical. No quantitative correlation is found to describe this trend. A similar observation was made by Kuan and Wang (1989, 1990) using the same criterion function (CF2). For CF6, negligible variation in the threshold value occur in this study. The results from the "dual-slope method" consistently indicate an almost constant threshold value regardless of location. This nature of a nearly constant threshold value is especially advantageous in the outer boundary layer in the

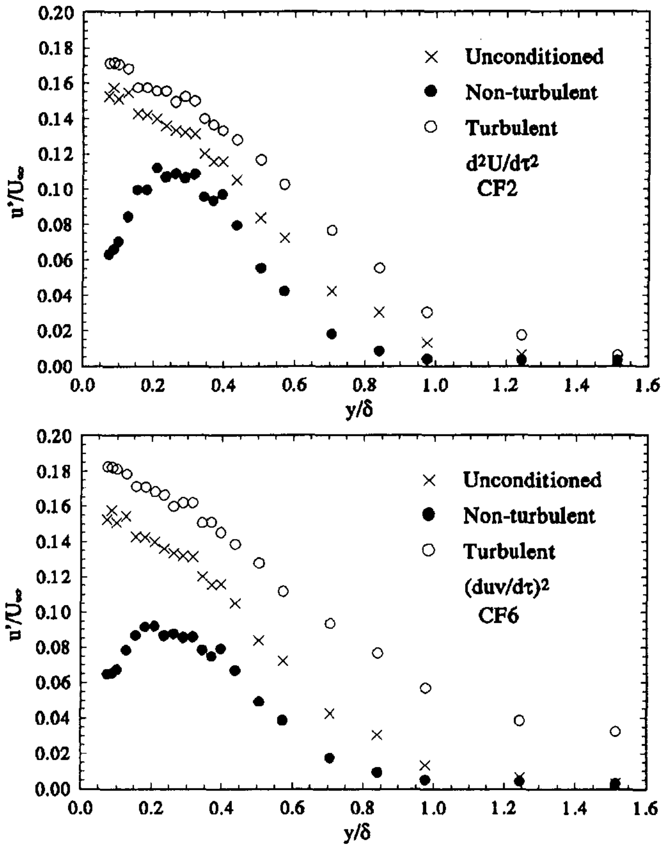

Fig. 16 Comparison of streamwise Reynolds normal stress for different criterion functions ($Re_x = 7.43 \times 10^5$, $\Gamma = 0.5$)

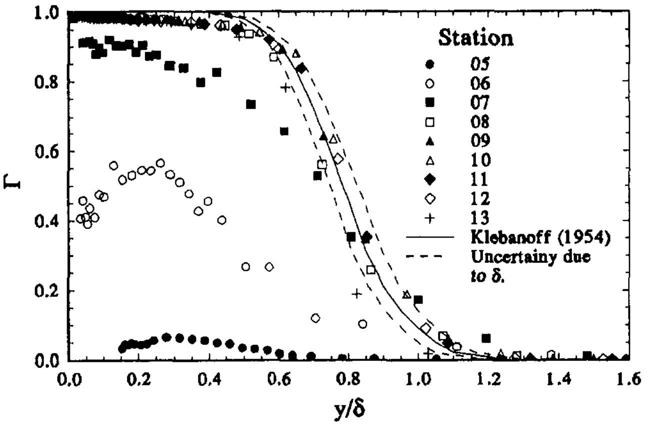

Fig. 17 Intermittency distribution through boundary layer using $(duv/d\tau)^2$, baseline case

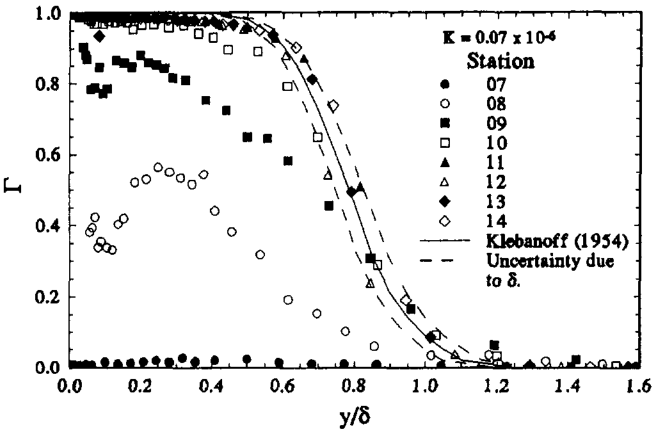

Fig. 18 Intermittency distribution through boundary layer using $(duv/d\tau)^2$, $K = 0.07 \times 10^{-6}$

late transitional and turbulent region because the linear slope representing the Gaussian probability density distribution of the nonturbulent portion in the dual-slope diagram (Fig. 4) in these regions becomes very short and vague. The four factors previously mentioned for determining the best threshold value are best satisfied using the Reynolds shear stress. This indicates that the Reynolds shear stress is easier to implement in transitional flow and more accurately indicates the turbulent regions.

While the intermittency factor for the overall record was approximately 0.5 for both criterion functions, the intermittency functions displayed in Fig. 13 indicate that regions identified as turbulent were not the same for each criterion function. For example, region E is identified as two turbulent bursts using CF2 but was identified as two large bursts with several smaller bursts using CF6. These smaller bursts are not picked up as the turbulent portion when CF2 is used. Sometimes, using the streamwise velocity may indicate the same overall intermittency factor as the Reynolds shear stress but analysis of the turbulent and nonturbulent portions will most likely not yield the same results.

To investigate these differences further, 30 points through the boundary layer at station 6 were conditionally sampled using both criterion functions. Figure 14 shows the distribution of intermittency through the boundary layer. The discrepancy in outer boundary layer intermittency is apparent for $y/\delta > 0.4$ with Γ from CF6 being consistently lower than Γ from CF2. For $y/\delta < 0.4$ the intermittency values from each criterion function are nearly identical. The conditionally sampled mean velocity profiles for each criterion function are presented in U^+ versus Y^+ coordinates and are shown in Fig. 15. Both criterion functions result in similar profiles. The nonturbulent portions matched the Blasius profile while the turbulent portions do not exhibit the logarithmic law-of-the-wall region. *No differences were discernible between the abilities of each criterion function to separate the mean velocity.* The conditionally sampled Reynolds normal stresses are shown in Fig. 16 where differences are seen between the results from the two criterion functions. For CF2, the peak intensity in the nonturbulent portion is 11 percent while the corresponding peak intensity for CF6 is 9 percent. Both peak intensities occur at approximately $y/\delta = 0.3$. The turbulent part from using CF6 indicates higher values in Reynolds normal stress than the results from using CF2. Similar results are observed for the Reynolds shear stress, $-\overline{uv}/u^{*2}$ (not shown here). The criterion function using streamwise mean velocity underevaluated the Reynolds stresses in the turbulent portion and overevaluated them in the nonturbulent portion.

Intermittency Distributions. Using CF6 as the best criterion function, the intermittency distribution through the transition region for each case was determined. The results are shown in Figs. 17–20. The results for a fully turbulent boundary layer obtained by Klebanoff (1954) are included for comparison. The dashed lines in each figure represent the uncertainty in determining the boundary layer thickness, δ. The uncertainty in the mean streamwise velocity for the three-wire sensor is approximately 3 percent, which corresponds to an uncertainty in δ of ± 5 percent. This variation in δ results in a large variation in Γ for the fully turbulent profile near the edge of the boundary layer. For the baseline case, the intermittency distributions for stations 8 through 13 are seen to match the fully turbulent profile (within the uncertainty band). Station 6 exhibits a peak in intermittency

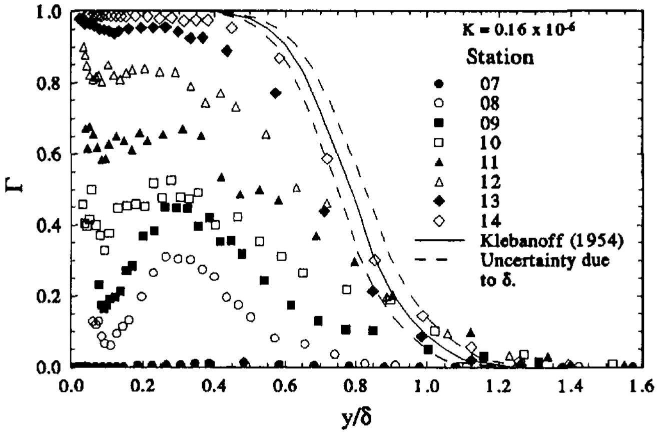

Fig. 19 Intermittency distribution through boundary layer using $(duv/d\tau)^2$, $K = 0.16 \times 10^{-6}$

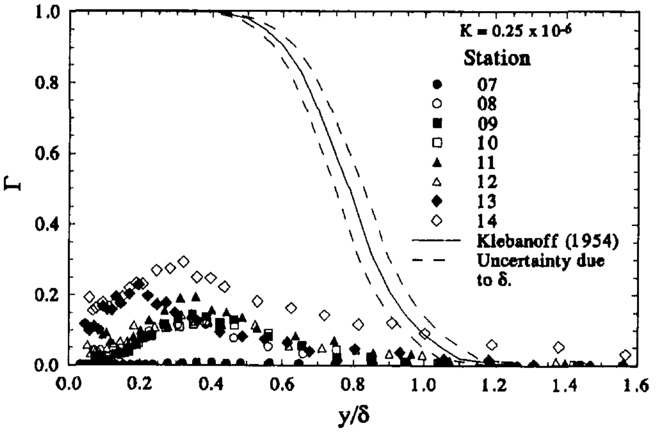

Fig. 20 Intermittency distribution through boundary layer using $(duv/d\tau)^2$, $K = 0.25 \times 10^{-6}$

away from the wall similar to that reported by Kuan and Wang (1989, 1990), Sohn et al. (1989), and Gostelow and Walker (1990). For the acceleration cases of $K = 0.07 \times 10^{-6}$ and $K = 0.16 \times 10^{-6}$ (Figs. 18 and 19, respectively), similar observations are made. In the late transitional and early turbulent regions intermittency distributions match the fully turbulent results of Klebanoff. Peak values in intermittency for the early to midtransitional regions occur away from the wall at approximately $y/\delta = 0.3$ for all three accelerating cases. As K increases, the length of transition increases, thus allowing more stations to be measured in the transition region. For $K = 0.16 \times 10^{-6}$ in Fig. 19, three profiles are observed to have intermittency peaks away from the wall. These peaks disappear approximately midway through the transition region. Visual inspection of the instantaneous correlation signals verifies that the frequency of breakdown increases to a maximum away from the wall then decreases toward zero in the free stream. A similar observation was made by Kuan and Wang (1990), who attributed these peaks to the overhang of a typical turbulent spot. Blair (1992) did not observe the peak in his experiment in a transitional boundary layer with a free-stream turbulent of 0.8 percent and $K = 0.2 \times 10^{-6}$. However, he reported observing a near-wall minimum and a peak at about $y/\delta = 0.3$ in the intermittency distribution in higher turbulence cases (1.9 and 2.5 percent). Mayle (1991) pointed out the controversy on the peak in intermittency distribution across the boundary layer and attributed it to the differences in the turbulent flow discrimination schemes used to determine intermittency. As early as 1958, Dhawan and Narasimha concluded that although the $\Gamma(y)$ variation is probably important to the detailed structure of the turbulent motion associated with the turbulent spots, the value near the wall is the characteristic property for the transition region. These authors believe the peak intermittency at about $y/\delta = 0.3$ in the early to middle transitional boundary layer is real and it reflects the stretching of a turbulent spot away from the wall. This vortex stretching is a very important part of the vortex dynamics during the early transitional process.

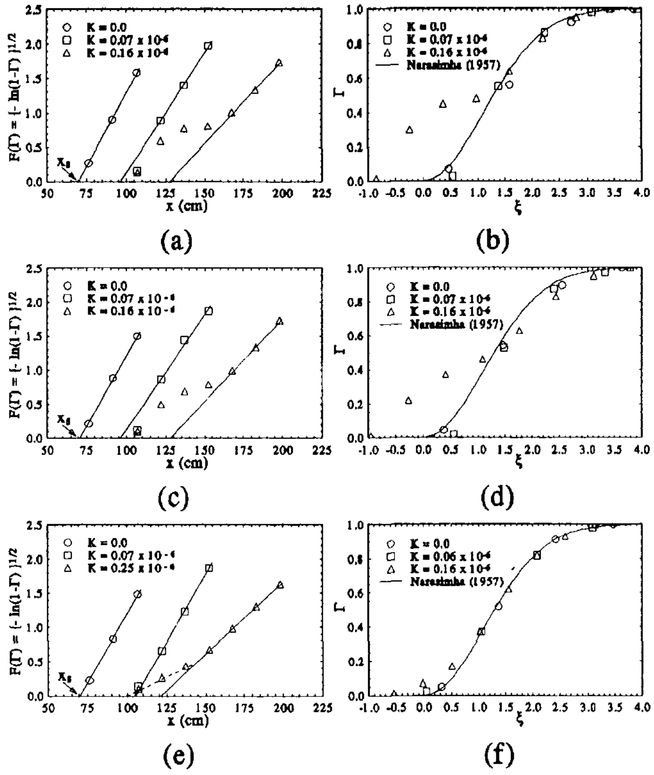

Fig. 21 Determination of x_s and corresponding representative near wall intermittency in Γ versus x coordinates using the value of Γ at different y/δ locations as the representative intermittency

The general appearance of the intermittency distribution across the boundary layer of an accelerated flow is very similar to that of a nonaccelerated flow; however, a distinctive near-wall minimum exists at about $y/\delta = 0.1$ for most of the stations even as late as $\Gamma = 0.9$ (Figs. 18 and 19). The intermittency value increases at a clear trend toward the wall from this minimum, which is not observed in the baseline case in Fig. 17. For the strongest accelerating case, $K = 0.25 \times 10^{-6}$, the intermittency distributions for stations 8 to 11 are almost identical (see Fig. 20). This implies a strong suppression of the growth of turbulent spots. The transition process for this case is not completed at the exit of the test section of the current facility.

To find the intermittency factor, $\Gamma(x)$, through the transition region, the method first developed by Dhawan and Narasimha (1958) was used. Dhawan and Narasimha proposed a "universal" intermittency distribution of the form

$$\Gamma(x) = 1 - \exp\left[-0.412(x - x_s)^2/\xi^2\right]$$

where

$$\xi = x_{\Gamma=0.75} - x_{\Gamma=0.25}.$$

The applicability of using this technique in boundary layer flows subjected to pressure gradients was discussed by Narasimha et al. (1984).

To determine the start of transition, x_s, the following procedure is taken following their recommendations. The function $\sqrt{-\ln(1-\Gamma(x))}$ is plotted versus x and a straight line fit to the data between $0.25 < \Gamma < 0.75$. The x intercept is x_s. An appropriate value of $\Gamma(x)$ to represent the intermittency at each x location must still be determined in light of the nonuniform distribution of intermittency across the boundary layer. Mayle (1991) stated that most researchers who use anemometers to determine the intermittency typically chose the near-wall value to be around $y/\delta = 0.2$. In order to look into this issue, three locations were chosen for the selection of the representative intermittency value, $\Gamma(x)$: the location of the intermittency peak (approximately $y/\delta = 0.3$), the value at $y/\delta = 0.2$ as suggested by Mayle, and the value at the local minimum near the wall ($y/\delta \approx 0.1$) for using the peak value of intermittency (note: since the flows for $K = 0.25 \times 10^{-6}$ never completed transition in the present facility they are excluded from further discussion). For $K = 0.16 \times 10^{-6}$, only the results for $\Gamma(x) > 0.6$ followed a linear relation when plotted in $F(\Gamma)$ versus x coordinates. The representative intermittency distribution obtained from these results are shown in Fig. 21(*b*). Too large a deviation from the universal distribution is observed for $K = 0.16 \times 10^{-6}$ to justify using the peak value in Γ. This procedure was repeated for the intermittency values obtained at $y/\delta = 0.2$ and the results are shown in Figs. 21(*c*) and 21(*d*). The representative intermittency distribution still shows a large variation from the correlation of Dhawan and Narasimha (1958). The results using the values of intermittency obtained from the minimum near the wall ($y/\delta \approx 0.1$) are shown in Figs. 21(*e*) and 21(*f*). For $K = 0.16 \times 10^{-6}$, two linear regions of different slopes are present in the $F(\Gamma)$ versus x coordinate similar to the results of Narasimha et al. (1984) and Blair (1992). Narasimha (1985) termed this sudden change in flow behavior "subtransition," indicating the flow changes from a subcritical to a supercritical state. The near-wall intermittency distribution is seen to match the "universal" distribution of Dhawan and Narasimha with slightly higher values for $K = 0.16 \times 10^{-6}$ in the early transition region. Acharya (1985) and Blair (1992) measured the streamwise distribution of boundary layer intermittency for flows with $K > 0$ and both reported a similar observation. The results of the near-wall intermittency distributions indicate that in order to match the correlation of Dhawan and Narasimha (1958), the near-wall value of intermittency at $y/\delta \approx 0.1$ should be used instead of at $y/\delta \approx 0.2$ suggested by Mayle (1991).

Conclusions

The effects of different criterion functions on the determination of intermittency were investigated for application in heated transitional boundary layers with and without streamwise acceleration. Nine separate criterion functions were investigated for the zero-pressure gradient baseline case and three constant K, accelerated cases. The criterion functions were classified into two general categories: single signal schemes, those based in U, V, and T, and correlation schemes, those based on uv, vt, or ut. For the baseline case, criterion functions based on the correlation schemes resulted in intermittency values 0.14 to 0.38 lower in the outer boundary layer region ($y/\delta^* > 4.0$) than the values found from the single signal schemes. Similar differences were found for the accelerated cases. No differences were found using the temperature based criterion function to support the use of a separate thermal intermittency factor in accelerated flows.

Inherent differences exist between each criterion function's turbulence recognition capabilities. Each criterion function weights different areas within a turbulent burst differently. No differences were discernible between the abilities of each criterion function to separate the mean velocity; however, the results of using single-signal schemes tended to underevaluate the Reynolds stresses in the turbulent portion and overevaluate them in the nonturbulent portion. A criterion function based on Reynolds stress, $(\partial uv/\partial\tau)^2$, resulted in the sharpest demarcation between turbulent and nonturbulent portions of the flow. This criterion function also had a negligible variation of threshold value throughout the transition region with the lowest uncertainty in determining the threshold value and the lowest sensitivity of the resultant intermittency to the variation of the threshold value. These results indicate that using the Reynolds shear stress for turbulent/nonturbulent discrimination in a heated transitional boundary layer is superior to a single velocity or temperature scheme. A criterion function based on the streamwise velocity, $(\partial U/\partial\tau)^2$, results in "near-wall" intermittency values within 5 percent of the values obtained from using $(\partial uv/\partial\tau)^2$ and may be easier to implement since only a single-wire probe is required. However, this criterion function has a higher uncertainty in determining the threshold value and has a higher sensitivity of the resultant intermittency to the variation of the threshold value. In addition, using the streamwise velocity may indicate the same overall intermittency factor as the Reynolds shear stress but analysis of the turbulent and nonturbulent portions would not always yield the same results.

Peak values in intermittency for the early to midtransitional regions were found to occur away from the wall at approximately $y/\delta = 0.3$ for the baseline case and three accelerated cases. A distinctive near-wall minimum in intermittency and a clear trend of increasing values of intermittency toward the wall from this minimum were observed for the accelerating flow cases. To match the universal intermittency distribution of Dhawan and Narasimha (1958), the values of intermittency at this near-wall minimum $y/\delta \approx 0.1$ should be used as the representative "near-wall" values.

Using a digital time derivative is considered superior for use as a criterion function to an ideal digital high-pass filter since no significant differences are observed between the two methods in determining the probability densities of a transitional flow and the derivative requires less computational time.

Acknowledgments

This program was sponsored by the Air Force Office of Scientific Research (Grant No. AFOSR-89-0324) and the Office of Naval Research (Grant No. N00014-89-J-3105). The program monitors are Major Dan Fant and Dr. Gabriel Roy, respectively.

References

Acharya, M., 1985, "Pressure-Gradient and Free-Stream Turbulence Effects on Boundary Layer Transition," Brown Boveri Report KLR 85-127 C.

Antonia, R. A., 1972, "Conditionally Sampled Measurements Near the Outer Edge of a Turbulent Boundary Layer," *J. Fluid Mech.*, Vol. 56, pp. 1–18.

Antonia, R. A., 1981, "Conditional Sampling in Turbulence Measurement," *Ann. Rev. Fluid Mech.*, pp. 131–156.

Arnal, D., 1984, "Description and Prediction of Transition in Two-Dimensional, Incompressible Flow," AGARD-R-709, 2-1.

Blair, M. F., 1982, "Influence of Free-Stream Turbulence on Boundary Layer Transition in Favorable Pressure Gradients," ASME *Journal of Engineering for Power*, Vol. 104, pp. 743–750.

Blair, M. F., 1992, "Boundary Layer Transition in Accelerating Flows With Intense Freestream Turbulence; Part 1—Disturbances Upstream of Transition Onset; Part 2—The Zone of Intermittent Turbulence," ASME *Journal of Fluids Engineering*, Vol. 114, pp. 313–332.

Chen, C. P., and Blackwelder, R. F., 1976, "Large-Scale Motion in a Turbulent Boundary Layer: A Study Using Temperature Contamination," *J. Fluid Mech.*, Vol. 89, part 1, pp. 1–31.

Corrsin, S., and Kistler, A. L., 1955, "Free-Stream Boundaries of Turbulent Flows," NACA Rept. 1244.

Dhawan, S., and Narasimha, R., 1958, "Some Properties of Boundary Layer Flow During the Transition From Laminar to Turbulent Motion," *J. Fluid Mech.*, Vol. 3, pp. 418–436.

Emmons, H. W., 1951, "The Laminar-Turbulent Transition in a Boundary Layer—Part I," *J. Aero. Sci.*, Vol. 18, pp. 490–498.

Gostelow, J. P., and Walker, G. J., 1990, "Similarity Behavior in Transitional Boundary Layers Over a Range of Adverse Pressure Gradients and Turbulence Levels," ASME JOURNAL OF TURBOMACHINERY, Vol. 113, pp. 617–625.

Graham, R. W., 1979, "Fundamental Mechanisms That Influence the Estimate of Heat Transfer to Gas Turbine Blades," ASME Paper No. 79-HT-43.

Graham, R. W., ed., 1984, *Transition in Turbines*, Symposium Proceedings, NASA TM-79128.

Hedley, T. B., and Keffer, J. F., 1974, "Turbulent/Nonturbulent Decisions in an Intermittent Flow," *J. Fluid Mech.*, Vol. 64, Part 4, pp. 625–644.

Keller, F. J., 1993, "Flow and Thermal Structures in Heated Transitional Boundary Layers With and Without Streamwise Acceleration," Ph.D. Dissertation, Dept. of Mech. Engr., Clemson University, Clemson, SC.

Klebanoff, P. S., 1954, "Characteristics of Turbulence in a Boundary Layer With Zero Pressure Gradient," NACA Technical Note #1247, supersedes NACA TN#3178.

Kuan, C. L., 1987, "An Experimental Investigation of Intermittent Behavior in the Transitional Boundary Layer," M.S. Thesis, Dept. of Mech. Engr., Clemson University, Clemson, SC.

Kuan, C. L., and Wang, T., 1989, "Some Intermittent Behavior of Transitional Boundary Layer," AIAA Paper No. 89-1890.

Kuan, C. L., and Wang, T., 1990, "Investigation of Intermittent Behavior of Transitional Boundary Layer Using a Conditional Averaging," *Exp. Thermal Fluid Sci.*, Vol. 3, pp. 157–170.

Mayle, R. E., 1991, "The Role of Laminar-Turbulent Transition in Gas Turbine Engines," ASME JOURNAL OF TURBOMACHINERY, Vol. 113, pp. 509–537.

Muck, K. C., 1980, "Comparison of Various Schemes for the Generation of the Turbulent Intermittency Function," IC AERO Report 80-03.

Musker, A. J., 1979, "Explicit Expression for the Smooth Wall Velocity Distribution in a Turbulent Boundary Layer," *AIAA Journal*, Vol. 17, No. 6, June, pp. 655–657.

Narasimha, R., 1957, "On the Distribution of Intermittency in the Transition Region of a Boundary Layer," *J. Aero. Sci.*, Vol. 24, pp. 711–712.

Narasimha, R., Devasia, K. J., Gururani, G., and Badri Narayanan, M. A., 1984, "Transitional Intermittency in Boundary Layers Subjected to Pressure Gradient," *Experiments in Fluids* 2, pp. 171–176.

Narasimha, R., 1985, "The Laminar-Turbulent Transition Zone in the Boundary Layer," *Prog. Aerospace Sci.*, Vol. 22, pp. 29–80.

Sharma, O. P., 1987, "Momentum and Thermal Boundary Layer Development on Turbine Airfoil Suction Surfaces," AIAA Paper No. 87-1918.

Shome, B., 1991, "Development of a Three-Wire Probe for the Measurement of Reynolds Stresses and Heat Fluxes in Transitional Boundary Layers," M.S. Thesis, Dept. of Mech. Engr., Clemson University, Clemson, SC.

Sohn, K. H., O'Brien, J. E., and Reshotko, E., 1989, "Some Characteristics of Bypass Transition in a Heated Boundary Layer," NASA TM 102126.

Turner, A. B., 1971, "Local Heat Transfer Measurements on a Gas Turbine Blade," *J. Mech. Engr. Sci.*, Vol. 13, No. 1, pp. 1–12.

Volino, R. J., and Simon, T. W., 1991, "A Review of Bypass Transition in Boundary Layers," NASA CR-187187.

Wang, T., Keller, F. J., and Zhou, D., 1992, "Experimental Investigation of Reynolds Shear Stresses and Heat Fluxes in a Transitional Boundary Layer," *Fundamental and Applied Heat Transfer Research for Gas Turbine Engines*, ASME HTD-Vol. 226, pp. 61–70.

Zhou, D., and Wang, T., 1992, "Laminar Boundary Layer Flow and Heat Transfer With Favorable Pressure Gradient at Constant K Values," ASME Paper No. 92-GT-246.

Zhou, D., 1993, "Flow and Thermal Structures in Heated Transitional Boundary Layers With Elevated Free-Stream Turbulence and Pressure Gradients," Ph.D. Dissertation, Dept. of Mech. Engr., Clemson University, Clemson, SC.

Bypass Transition in Boundary Layers Including Curvature and Favorable Pressure Gradient Effects

R. J. Volino

T. W. Simon

Department of Mechanical Engineering,
Heat Transfer Laboratory,
University of Minnesota,
Minneapolis, MN 55455

Recent experimental studies of two-dimensional boundary layers undergoing bypass transition have been reviewed to attempt to characterize the effects of free-stream turbulence level, acceleration, and wall curvature on bypass transition. Results from several studies were cast in terms of "local" boundary layer coordinates (momentum and enthalpy thickness Reynolds numbers) and compared. In unaccelerated flow on flat walls, skin friction coefficients were shown to match those from a laminar integral solution before transition and quickly adjusted to match those from a fully turbulent correlation after transition. Stanton number data also matched a correlation in the laminar region, but do not match correlation values so well in the turbulent region. The data showed that the relationship between skin friction coefficient and momentum thickness Reynolds number is unaffected by streamwise acceleration. Stanton numbers were strongly affected by acceleration, however, indicating a breakdown in Reynolds analogy. Concave curvature caused the formation of Görtler vortices, which strongly influenced the skin friction. Convex curvature had an opposite, and lesser effect. The location and length of the transition region generally followed the expected trends as free-stream turbulence level, curvature, and acceleration were varied; the onset location and the transition length were extended by acceleration and convex curvature and reduced by concave curvature and enhanced turbulence. When individual cases were compared, some inconsistencies were observed. These inconsistencies indicate a need to characterize the flows to be compared more completely. Better spectral and length scale measurements of the free-stream disturbance would help in this regard. Within the transition region, the intermittency data from all the cases on flat walls (no curvature) were consistent with an intermittency distribution from the literature. Turbulent spot production rates were shown to be mostly dependent on free-stream turbulence, with a noted increase in spot production rate due to concave curvature and little effect of convex curvature. The acceleration effect on spot production rate was small for the cases studied.

Introduction

Transition to turbulence is a complex phenomenon, which has been studied extensively but is still not well understood. A better understanding of transition is needed since the transition process is an important factor in determining the distribution of heat transfer rates from a surface. On a typical gas turbine blade, for example, the transition zone may cover a significant fraction of the blade surface, and the heat transfer rate will increase several fold through the transition zone. It is therefore important to know the location and length of the transition region as well as the behavior of the flow and heat transfer within the transition zone.

The first studies of transition dealt with flows that were subject to only small disturbances. Such flows can be studied using linear stability analysis. They undergo what is known as Tollmien–Schlichting (TS) transition, which involves the growth of small perturbations in the boundary layer into two-dimensional disturbances known as Tollmien–Schlichting waves. The TS waves eventually become three dimensional due to secondary instabilities as they move downstream. Such instabilities culminate as turbulent spots in the boundary layer flow.

Bypass transition occurs in flows disturbed by finite perturbations such as free-stream turbulence, surface roughness, or acoustic excitation. Under high free-stream turbulence conditions, turbulent eddies in the free-stream are believed to buffet the boundary layer, providing a nonlinear transition mechanism, which acts either in place of or in combination

---

Contributed by the Heat Transfer Committee and presented at the ASME Winter Annual Meeting, Anaheim, California, November 8–13, 1992. Manuscript received at ASME Headquarters March 18, 1994. Associate Technical Editor: M. G. Dunn.

with the linear growth of disturbances within the boundary layer (the operational mechanism when the disturbance level is low). During bypass transition, TS transition stages are not visible, however. Bypass transition is poorly understood in part because it thus far has not been amenable to analysis. It is the mode of transition believed to be operational in gas turbine engine internal flows. In such flows, turbulence intensities of 5 to 20 percent are common.

The conditions under which bypass transition occurs are not well defined. Narasimha (1985) identified the following three modes of transition: "disturbance limited" transition at $TI < 0.1$ percent, "turbulence driven" transition at 0.1 percent $< TI < 4$ percent, and "stability limited" transition at $TI > 4$ percent. The first mechanism is Tollmien–Schlichting transition and the third is clearly bypass transition. The intermediate *TI* cases exhibit some elements of both *TS* and bypass transition. Sohn and Reshotko (1991) present spectral measurements taken in boundary layers at six different free-stream turbulence levels. At the three lowest turbulence levels (nominal 0.45, 0.83, and 1.1 percent) evidence of TS waves appeared as broadband humps in the spectra at the unstable frequencies predicted by linear stability theory. In the 0.45 percent case the perturbations in the unstable range were amplified at the successive downstream stations, while the disturbances outside this frequency range were damped. This behavior is in agreement with linear stability theory and provides evidence of TS transition. At 0.83 and 1.1 percent, however, perturbations at frequencies both within the band that was predicted to be unstable by linear theory, and at higher frequencies, were amplified. These two cases could be considered bypass transition cases since they show deviations from linear theory, despite the evidence of TS-type disturbances at upstream stations. Morkovin (1978) defined bypass as "those roads to transition which cannot be identified as starting from a known linear instability." It is not clear whether the presence of TS waves constitutes sufficient evidence to conclude that the "road" or path that ultimately resulted in transition began as a linear instability. Either it begins as a linear growth, which is modified by the flow to produce a much higher growth rate, or it is surpassed by another instability, which grows more rapidly.

An attempt to define bypass transition more sharply beyond that given above may be futile since the demarcation between TS and bypass transition is rather fuzzy. A need is recognized for a better understanding of transition at both the intermediate and high *TI* ranges of disturbances.

The last few years have seen considerable activity in experimental documentation of bypass transition. This paper is an attempt to collect and compare this recent work and to extract additional useful information from the ensemble. This comparison is limited to, nominally, two-dimensional boundary layer flows that are known to undergo bypass transition. The separate and combined effects of variable free-stream turbulence intensity, wall streamwise curvature, and free-stream acceleration, as seen in the data, will be examined.

Comparison of Data Sets

Most data used in this study were taken from Kim and Simon (1991), Wang (1984), Sohn and Reshotko (1991), Blair and Werle (1980, 1981), Blair (1981a, 1981b), Blair and Anderson (1987), Kuan (1987), Kuan and Wang (1990), and Rued (1987). Some of the data are also available in shorter papers by Wang et al. (1985), Wang and Simon (1987), Kim et al. (1994), Kim et al. (1992), Sohn et al. (1989), Blair (1982, 1983) and Rued and Wittig (1985, 1986)). The strategy for comparing the various data sets is to concentrate on dimensionless and integral quantities such as Reynolds numbers based upon boundary layer thicknesses, skin friction coefficients, and Stanton numbers. A selection of results from this comparison is presented. Additional and more complete comparisons are available in Volino and Simon (1991).

The following section presents the dimensionless quantities employed in the comparison. The acceleration parameter $k = (\nu/U_\infty^2)(\partial U_\infty/\partial x)$ has been used to characterize the streamwise pressure gradient in most studies. The ratio θ/R at the start of transition will be used to characterize strength of curvature. The numerator, θ, is the momentum thickness and R is the radius of curvature, positive for convex curvature.

A consistent means of describing free-stream turbulence level, *TI*, is lacking in the data set. Some researchers have measured only streamwise velocity and present turbulence intensity as $TI = \sqrt{\overline{u'^2}}/U_\infty$ while others have measured all three components of velocity, presenting $\sqrt{\left(\overline{u'^2} + \overline{v'^2} + \overline{w'^2}\right)/3U_\infty^2}$. Grid-generated turbulence contains considerable anisotropy, especially at upstream locations; thus, the definitions above could lead to measurably different *TI* values for a given experiment. The free-stream turbulence, presented in terms of the streamwise velocity, $TI = \sqrt{\overline{u'^2}}/U_\infty$, is available from all the data sets and could be chosen to provide consistency between all studies, but u' does not provide as complete a description of the turbulence as does an expression with all three components. The total

Nomenclature

c_f = skin friction coefficient
$f(\gamma)$ = function of intermittency
k = acceleration = $\dfrac{\nu}{U_\infty^2}\dfrac{\partial U_\infty}{\partial x}$
n = turbulent spot production rate
$\hat{n}$ = dimensionless turbulent spot production rate = $\dfrac{n\nu^2}{U_s^3}$
R = radius of curvature
Re = Reynolds number
Re_x = length Reynolds number
Re_θ = momentum thickness Reynolds number
Re_{Δ_2} = enthalpy thickness Reynolds number
St = Stanton number
TI = free-stream turbulence intensity: (1D) TI based on streamwise velocity only = $\sqrt{\overline{u'^2}}/U_\infty$; (2D) TI based on two velocity components = $\sqrt{\left(\overline{u'^2} + 2\overline{v'^2}\right)/3U_\infty^2}$; (3D) TI based on all three velocity components = $\sqrt{\left(\overline{u'^2} + \overline{v'^2} + \overline{w'^2}\right)/3U_\infty^2}$
U = mean streamwise velocity
u' = fluctuating component of U
v' = fluctuating component of cross-stream velocity
w' = fluctuating component of spanwise velocity
x = streamwise coordinate
γ = intermittency
δ = boundary layer thickness
$\delta_{99.5}$ = 99.5 percent boundary layer thickness
δ^* = displacement thickness
Δ_2 = enthalpy thickness
θ = momentum thickness
ν = kinematic viscosity
σ = turbulent spot propagation parameter

Subscripts

e = end of transition
s = start of transition
∞ = free stream

free-stream turbulence $TI = \sqrt{\overline{u'^2} + \overline{v'^2} + \overline{w'^2}} \, / \, \sqrt{3}\, U_\infty$ is a better choice when data are available. Using only u' for consistency would result in casting out valuable data. Thus *TI* will be based on all three components when they are available. When only u' and v' are available, $v' \approx w'$ will be assumed and $TI = \sqrt{\left(\overline{u'^2} + 2\overline{v'^2}\right)/3U_\infty^2}$ will be computed. In cases where only u' is available, $TI = \sqrt{\overline{u'^2}} \, / U_\infty$ will be used for lack of a better alternative. To distinguish the basis for the *TI* values quoted in this paper, their numerical values will be followed by (1D) for cases based only on u', (2D) for cases based on u' and v', and (3D) for cases based on all three velocity components.

The frequency ranges over which reported turbulence intensities are measured varies from study to study. Some researchers give a value based on the entire spectrum, while others apparently filter at some unspecified frequency to separate the free-stream turbulence associated with eddy motion from low-frequency unsteadiness. Filtering at low frequencies can have a significant effect on the reported *TI*. Kim and Simon (1991), for example, reported a low *TI* case with nominal 0.6 percent (2D) free-stream turbulence. The u' component based on the entire spectrum was 0.61 percent. Spectral analysis shows that a high pass filter at 1 Hz reduces this value to 0.36 percent. A high pass filter at 10 Hz reduces the value further to 0.116 percent. Filtering out frequencies below 20 Hz, which probably still does not eliminate any frequencies associated with eddy motion, reduces the reported *TI* to 0.069 percent. The effect of filtering at higher turbulence intensities is not as severe as for the 0.61 percent case described above, but is still significant. Kim and Simon's nominal 8 percent (3D) *TI* case had a u' value of 7.509 percent based on the entire spectrum. With a high pass filter at 10 Hz this was reduced to 7.198 percent, and with a filter at 20 Hz it was reduced to 6.885 percent. It is not clear at this time what effect the low-frequency unsteadiness has on transition. If the low-frequency unsteadiness and the higher-frequency turbulent eddy motions have similar effects on transition, then there is no need to attempt to separate the *TI* into low- and high-frequency components. If the low frequencies do not play a role in transition, however, then they should not be included in the reported free-stream turbulence levels. If a cutoff frequency is used to separate the components, it must be chosen carefully, as is evident from the discussion of the sensitivity of *TI* to cutoff given above. Further work is needed on this question. Future studies should include complete documentation of the free-stream spectra to very low frequencies, such as 0.1 Hz.

The location at which *TI* is to be specified also must be consistent. Especially in high free-stream turbulence, the *TI* level decays significantly with streamwise distance and a single value may not be representative of values for the entire test section. In accordance with the practice of Abu-Ghannam and Shaw (1980), the published *TI* level in this report is based on the measured level midway between the transition start location and the leading edge. This results in slightly different values in this report than those presented with the various data sets upon which this study is based. Most authors chose to use values measured at the leading edge. When the end of transition is being discussed, the *TI* levels midway between the transition end and the leading edge are given.

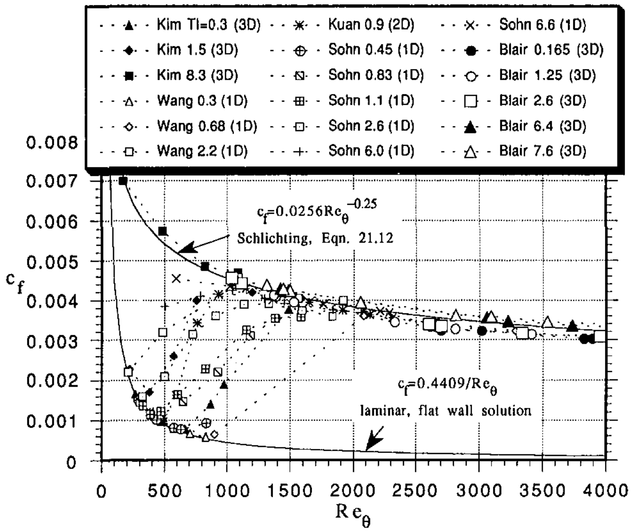

Fig. 1 c_f versus Re_θ, flat wall, unaccelerated cases

For complete documentation of a data set, the length scales and spectra associated with the free-stream turbulence should be specified. Though it is not yet clear how these scales affect the flow, the value of this documentation will surely emerge as more is learned. Spectral measurements have been presented in a few studies of the data sets used herein, but in the majority of cases, such measurements are lacking. Even in those studies where spectral measurements were made (e.g., Kim and Simon, 1991, and Sohn and Reshotko, 1991) spectra are usually only presented for streamwise velocity fluctuations, which provides only a partial description since the free-stream is somewhat anisotropic.

In previous studies, data are often presented in terms of the spatial position, x, or its dimensionless value, Re_x. This is convenient since the streamwise location of any measurement station is easily found. It would be more appropriate for the purpose of comparing cases, however, to present data in terms of "local" boundary layer coordinates, coordinates that describe the maturity of the flow, rather than merely the position of the measurement point. This is particularly true after transition, where the development of the flow changes, and, thus the position relative to the leading edge position loses significance. Several local coordinates for describing the fluid mechanics, including $\delta_{99.5}$, δ^*, and θ, are possible. The momentum thickness, θ, is chosen for all hydrodynamic comparisons. The enthalpy thickness, Δ_2, is used for heat transfer comparisons.

Skin Friction. The skin friction coefficient, c_f, is plotted versus Re_θ in Figs. 1–3. Figures 1[1] shows the results of flat-wall, zero-pressure-gradient cases. Before transition, c_f follows the laminar solution, and, after transition, it matches a fully turbulent correlation from Schlichting (1979, Eq. (21–12)). Within transition, most of the data appear reasonable, showing the expected trend toward earlier transition as *TI* is increased. There is, however, some unexpected behavior apparent in Fig. 1. The 0.68 percent (1D) *TI* case of Wang et al. undergoes transition after Kim and Simon's 0.3 percent (3D) case. Kuan and Wang's 0.9 percent (2D) case starts transition after Sohn and Reshotko's 0.83 percent (1D) and 1.1 percent (1D) cases, but then crosses these two cases and Sohn and Reshotko's 2.6 percent (1D) case in the transition region. Sohn and Reshotko's 2.6 percent (1D) case appears out of order with respect to Kim and Simon's 1.5 percent (3D) case and the 2.2 percent (1D) case of Wang et al. There appears to be some transition behavior that is not fully explained by the *TI* values given. There must be some other factors, possibly the effects of turbulence spectra or length scales, which could differ substantially between two cases with the same *TI* (1D) value. It is important to recognize that such variability exists among this array of carefully conducted experiments. The 0.68 percent (1D) case of Wang et al. and Kim and Simon's 0.3 percent (3D) case, for exam-

---

[1] For clarity, only first authors' names appear in the figure legends.

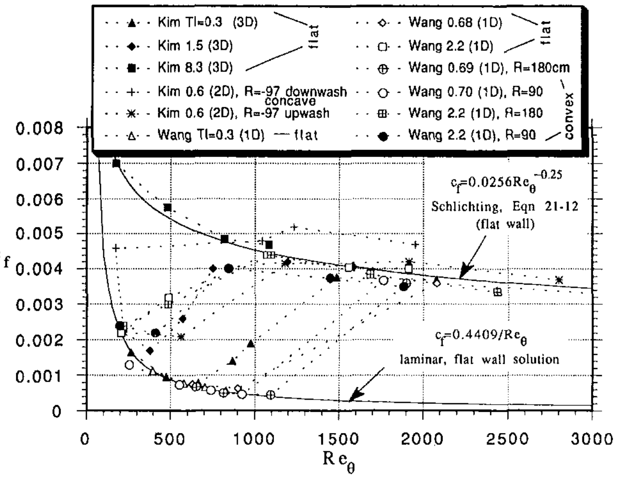

Fig. 2 c_f **versus** Re_θ**, curved wall cases**

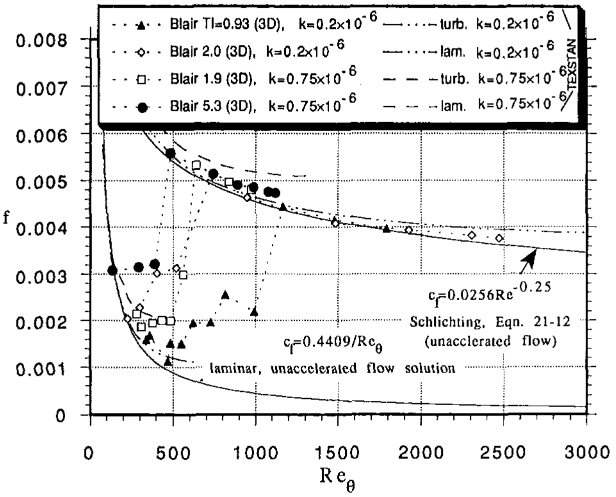

Fig. 3 c_f **versus** Re_θ**, accelerated cases with TEXSTAN solutions**

ple, were conducted in the same facility under approximately the same conditions. The facility was modified between these studies, however, to reduce vibration effects from the wind tunnel fan. This may have changed the nature of the free-stream turbulence in an unexpected manner, resulting in the observed behavior.

Figure 2 shows the effect of curvature on skin friction. In Wang and Simon's (1985) 0.68 percent (1D) *TI* cases, weak curvature ($R = 180$ cm, $\theta/R = 2.49 \times 10^{-4}$) delayed transition as expected, but stronger curvature ($R = 90$ cm, $\theta/R = 4.68 \times 10^{-4}$) caused transition to shift back upstream. The $R = 90$ cm case may have developed more secondary flow due to stronger curvature which, in turn, may have had the small effect on transition needed for the observed trend. At $TI = 2$ percent (1D) ($\theta/R = 1.96 \times 10^{-4}$ and $\theta/R = 4.45 \times 10^{-4}$) convex curvature had little effect on transition. The effect of concave curvature is obvious. At $TI = 0.6$ percent (2D) ($R = -97$ cm, $\theta/R = -1.84 \times 10^{-4}$) streamwise (Görtler) vortices developed in the laminar boundary layer and persisted through transition. The results at the upwash and downwash locations of these vortices were very different from one another and from the convex and flat-wall cases. At the downwash locations in particular, c_f was well above the fully turbulent correlation line even after transition was complete. The upwash data appear to more or less agree with the flat wall data. It may be that transition starts at the upwash in a similar manner to that on the flat wall, at least in terms of Re_θ. The flow in the downwashes may be prematurely, in terms of Re_θ, tripped to turbulence by another mechanism, possibly associated with instability at the upwash positions of the Görtler vortices.

Figure 3 shows the effects of acceleration on c_f using Blair's (1981b) data. The skin friction coefficient, c_f, in transition was calculated in this study from Blair's velocity profile data by estimating $\partial U/\partial y$ at the wall. After transition, Blair gives c_f obtained using the Clauser technique. There is considerable scatter in the transition region data due to the uncertainty involved in computing the wall velocity gradient $\partial U/\partial y$. Agreement with the empirical correlations for unaccelerated flow is good in both the laminar and fully turbulent regions. Crawford's TEXSTAN program (an updated version of Crawford and Kays' (1976) STAN5 program), which was used with a mixing length closure model, predicted higher c_f values in terms of Re_θ for accelerated cases in both laminar and fully turbulent flow. This is particularly apparent in Fig. 3 for the fully turbulent, $k = 0.75 \times 10^{-6}$ simulation. Blair's data tend to agree with the TEXSTAN predictions in the laminar region. The data fall above the unaccelerated flow correlation but below the TEXSTAN predictions in the fully turbulent region.

Heat Transfer. The effects of free-stream turbulence and acceleration on Stanton number are shown in Figs. 4 and 5. Figure 4 shows Stanton number plotted versus enthalpy thickness Reynolds number, Re_{Δ_2}, for the unaccelerated, flat wall cases. Also show are laminar and turbulent correlations obtained using a solution procedure from Ambrok as described by Kays and Crawford (1993, p. 286). Most of the experimental data were taken directly from the referenced studies, but Blair's (1981a) data do not include enthalpy thickness in the transition region. These values were calculated by integrating the Stanton number data provided. Before transition, the match to the laminar solution is good. After transition there is considerable deviation from the turbulent correlation. The higher *TI* cases match the correlation best. The behavior of the Stanton number is somewhat different than that of the skin friction coefficient (Fig. 1). The c_f data match the turbulent correlation relatively quickly after transition. A review of Blair's (1981a) data in Fig. 4 shows that St is lower in the turbulent flow for lower *TI* cases. The data of Wang et al. (1989) indicate unusually low St in the transition and fully turbulent region. Wang et al. presented an energy balance for this case based upon tunnel centerline values. It deviated somewhat from two-dimensional closure at downstream locations. Off-centerline Stanton number measurements from this case show steep spanwise gradients in the transition zone and Stanton numbers as much as 13 percent above the centerline values in the fully turbulent zone. There may have been significant cross-stream transport in the streaky transitional zone, which led to a deviation from two dimensionality. The deviations from an energy balance are large enough to explain the trajectory of Stanton number data after the onset of transition in Fig. 4.

Acceleration effects are shown in Fig. 5. Stanton number data are plotted versus Re_{Δ_2} for Blair's (1981b) accelerated flow cases. The data follow the laminar correlation (which was derived for unaccelerated flow) before transition. Also, TEXSTAN solutions show only a slight deviation of the accelerated solutions from the unaccelerated laminar solution. In and after transition, the effects of acceleration in the data are very apparent. At $TI \approx 2$ percent (3D), higher acceleration clearly delays transition. This delay is even more apparent when the data are plotted in St versus x coordinates (Blair and Werle, 1981). Downstream of transition, high-acceleration cases show a rapid drop in St with increasing Re_{Δ_2}. TEXSTAN simulations of fully turbulent cases at the two acceleration values are in good agreement with the trends of the experimental data.

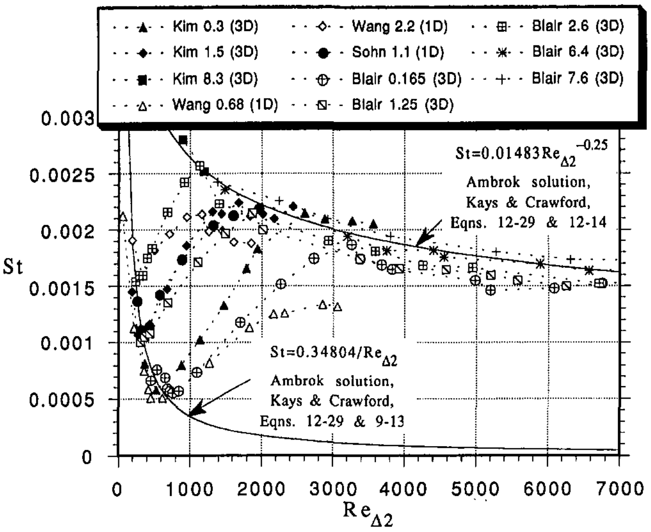

Fig. 4 St versus $Re_{\Delta 2}$, flat wall, unaccelerated cases

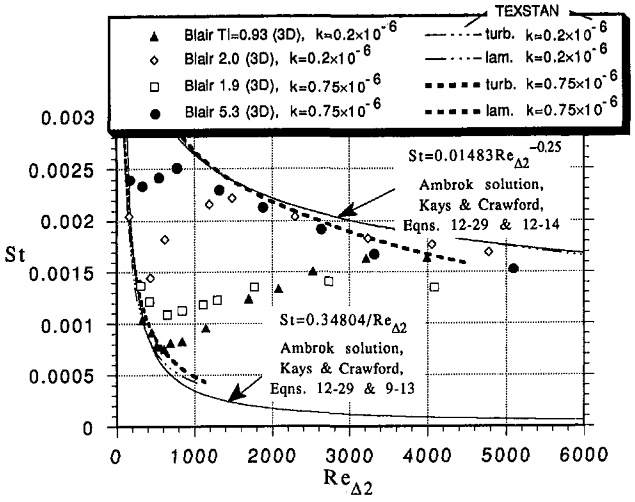

Fig. 5 St versus $Re_{\Delta 2}$, accelerated cases with TEXSTAN solutions

The Location of Transition. The location of the transition zone can be determined by a number of methods. Kuan and Wang (1990) list the following seven:

1 The origin of the turbulent boundary layer, obtained by extrapolating the turbulent boundary layer thickness back to zero.
2 The point of *minimum skin friction coefficient.*
3 The point at which the near-wall intermittency reaches a prescribed small value, for example, $\gamma(x, y \approx 0) = 0.1$.
4 The streamwise location of minimum dynamic pressure at a small, fixed distance from the wall.
5 The point at which the shape factor (δ^*/θ) deviates from the laminar flaw value of 2.6.
6 The first occurrence of a breakdown of TS transition as indicated by a complex waveform overriding the sinusoidal signal (applies more appropriately to low disturbance cases).
7 The first appearance of a turbulent streak or turbulent spot.

An additional criterion for heat transfer cases is the point of minimum heat transfer (minimum St). The data sets under consideration allow determination of the transition location by use of Stanton number data and intermittency profiles.

Table 1 Transition start and end based on Stanton number

Study		TI start	Re_{x_s} ×10^{-6}	Re_{θ_s}	TI end	Re_{x_e} ×10^{-6}	Re_{θ_e}	$\hat{n}\sigma$ ×10^{11}
Kim (1992)		0.3 (3D)	0.884	620	0.3 (3D)	1.379	–	1.88
		1.5 (3D)	0.264	322	1.5 (3D)	0.710	1017	2.32
	concave R=-97 cm downwash	0.6 (2D)	0.276	441	0.6 (2D)	0.491	832	9.97
	upwash	1.5 (1D)	0.217	–	1.5 (1D)	0.336	–	32.6
Wang (1984)		0.3 (1D)	1.15	760	–	–	–	–
		0.68 (1D)	1.05	750	0.68 (1D)	2.16	2100	0.374
		2.2 (1D)	0.195	336	2.2 (1D)	0.513	948	4.56
	convex R=180 cm	0.69 (1D)	1.72	981	0.69 (1D)	2.55	1864	0.669
	convex R=180 cm	2.2 (1D)	0.226	349	2.1 (1D)	0.578	1014	3.72
	convex R=90 cm	0.70 (1D)	1.65	882	0.73 (1D)	2.24	1610	1.32
	convex R=90 cm	2.2 (1D)	0.256	367	2.2 (1D)	0.605	1019	3.78
Sohn and Reshotko (1991)		0.45 (1D)	0.894	660	0.45 (1D)	1.67	–	0.766
		0.83 (1D)	0.423	448	0.83 (1D)	1.	1480	1.38
		1.1 (1D)	0.358	419	1.1 (1D)	0.90	1501	1.57
		2.6 (1D)	0.271	406	2.6 (1D)	0.571	1065	5.12
		6.0 (1D)	–	–	5.6 (1D)	0.380	885	–
		6.6 (1D)	–	–	6.5 (1D)	0.229	588	–
Blair and Werle (1981)	k= 0.2×10^{-6}	0.93 (3D)	0.86	480	0.82 (3D)	2.3	1500	0.499
	k= 0.2×10^{-6}	2.0 (3D)	0.29	365	1.9 (3D)	0.70	897	3.63
	k=0.75×10^{-6}	1.9 (3D)	0.58	390	1.4 (3D)	2.50	925	1.65
	k=0.75×10^{-6}	5.3 (3D)	0.0815	134	3.8 (3D)	0.336	487	9.86
Blair and Werle (1980)	k=0	0.165(3D)	1.275	750	0.165(3D)	1.772	2450	1.87
	k=0	1.25 (3D)	0.465	453	1.2 (3D)	1.057	1400	1.32
	k=0	2.6 (3D)	0.2658	342	2.5 (3D)	0.5303	850	6.59
Rued (1987)	k=0	1.3 (2D)	0.24	325	–	–	–	–
	k=0	2.1 (2D)	0.18	281	1.9 (2D)	0.50	1000	4.5
	k=0	3.5 (2D)	–	–	3.1 (2D)	0.20	460	–
	k=0	5.6 (2D)	–	–	5.6 (2D)	0.15	400	–
	k=0	8.7 (2D)	–	–	7.8 (2D)	0.11	250	–

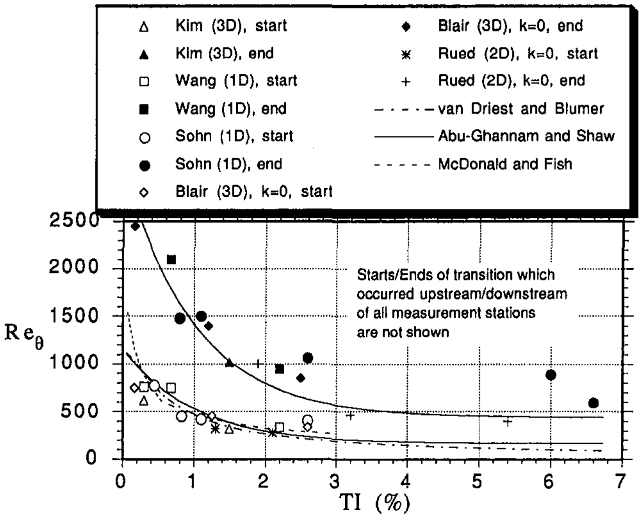

Fig. 6 Transition start and end based on St, flat wall, unaccelerated cases

Skin friction data were also available, but in most cases such data were too sparse for accurate determination of the transition location. From the Stanton number data, the beginning of transition was taken as the point of minimum Stanton number value. The end of transition was taken as the local maximum following this minimum. The corresponding Re_θ and *TI* were determined by interpolating or extrapolating the available data from the velocity profiles and free-stream turbulence measurements. The results, listed in Table 1, are plotted in Fig. 6. Also in the figure are the empirical curves of Abu-Ghannam and Shaw (1980). These curves are based on older studies, which determined the transition start and end locations on the minimum skin friction coefficient, the minimum dynamic pressure near the wall, and flow visualization. Also shown in Fig. 6 are onset correlations from Mc-

Table 2 Transition start and end based on γ

Study		TI start	Re_{x_s} $\times 10^{-6}$	Re_{θ_s}	TI end	Re_{x_e} $\times 10^{-6}$	Re_{θ_e}	$\hat{n}\sigma$ $\times 10^{11}$
Kim (1992)		0.3 (3D)	0.886	620	0.3 (3D)	1.94	1627	0.412
		1.5 (3D)	0.277	332	1.5 (3D)	0.757	1104	2.01
Sohn and Reshotko (1991)		1.1 (1D)	0.264	347	1.1 (1D)	0.822	1362	1.48
		2.6 (1D)	0.139	247	2.6 (1D)	0.527	954	3.06
Blair and Anderson (1987)	$k = 0.2\times10^{-6}$	0.93 (3D)	0.892	489	0.82 (3D)	2.19	1398	0.594
	$k = 0.2\times10^{-6}$	2.0 (3D)	0.174	262	1.9 (3D)	0.707	912	2.19
	$k = 0.75\times10^{-6}$	1.9 (3D)	0.401	325	1.6 (3D)	2.84	934	1.23
	$k = 0.75\times10^{-6}$	5.3 (3D)	0.019	90	4.2 (3D)	0.491	655	3.40
Kuan and Wang (1990)		0.9 (2D)	-0.094	–	0.9 (2D)	1.231	1591	0.262
Present study	concave R=-97 cm downwash	0.6 (2D)	0.350	361	0.6 (2D)	0.468	586	see* below
	mid-vortex		0.353	363		0.467	500	
	upwash		0.356	403		0.472	686	

*Turbulent Spot Propagation Rates for TI=0.6% (2D) Concave-Wall Case

	effective $\hat{n}\sigma \times 10^{11}$ at transition start	effective $\hat{n}\sigma \times 10^{11}$ at transition end	effective overall $\hat{n}\sigma \times 10^{11}$
upwash	5.87	91.7	33.0
mid-vortex	11.7	105.2	35.4
downwash	14.2	93.4	34.2

Donald and Fish (1973) and Van Driest and Blumer (1963), which are in reasonable agreement with the Abu-Ghannam and Shaw (1980) correlation. The correlations differ by as much as $Re_\theta = 100$, but this is small compared to the scatter in the experimental data. The agreement between the experimental data and the correlations for zero-pressure-gradient, flat wall cases in Fig. 6 is reasonable. Given the variability in specifying the *TI*, described above, no better fit could be expected. The following can be stated from the curved-wall and accelerated flow cases in Table 1: (1) In the curved wall cases, the limited amount of data makes it difficult to draw any clear conclusions. The expected trends of convex curvature delaying transition and concave curvature causing a shorter transition zone are supported, but more experimental evidence would be desirable. (2) Favorable pressure gradients on flat walls appear to have little effect on the transition location in terms of Re_θ. This agrees with the findings of Abu-Ghannam and Shaw (1980), who showed only a small acceleration effect on transition onset. Transition is delayed significantly in terms of x and Re_x, however.

A second method of determining transition location, basing it on intermittency, is next discussed. The method presented herein is based on Narasimha's (1984) theory, which is, in turn, derived from Emmons' (1951) theory of turbulent spots. The highest γ value in the γ versus y profile at each streamwise measuring station in a test was selected and used to calculate the function

$$f(\gamma) = (-\ln(1-\gamma))^{1/2} \tag{1}$$

versus x. In most of the flat-wall cases the data lie along a straight line, although some exceptions were seen at low γ (particularly in accelerated flow) in a region Narasimha (1984) referred to as "subtransition." To determine the start and end of transition, attention was focused on the data points downstream of any subtransition. A least-squares fit to these data points was extrapolated to $f = 0$ and $f = 2.146$, which correspond to $\gamma = 0$ and $\gamma = 0.99$, respectively. The corresponding x values at the two extrapolated points were taken as the locations of the start and end of transition, x_s and x_e, respectively. Re_θ, Re_x and *TI* at the indicated x_s and x_e were found using the original data sets. The results for several studies representing both unaccelerated and accelerated flows are presented in Table 2. The extrapolation technique could not be applied in a straightforward manner to new data taken by the authors along a concave wall (under the conditions of Kim and Simon's (1991) 0.6 percent (2D) *TI* concave-wall case, in which Görtler vortices were observed). This new data, when plotted as $f(\gamma)$ versus x, did not lie along a straight line. The trajectory of $f(\gamma)$ versus x changed slope in the middle of the transition region. Thus, x_s and x_e were determined in this case using two extrapolations. The data near the start of transition were extrapolated to $f(\gamma) = 0$ to determine x_s, and the high γ data were extrapolated to $f(\gamma) = 2.146$ to find x_e. This was done at three spanwise locations for this case, corresponding to the upwash, downwash, and midvortex locations of the Görtler vortices. Such data are given in Table 2. There is no reason to expect the intermittency-based transition start and end to correspond exactly with the point of minimum heat transfer, but agreement with the Stanton-number-based transition locations of Table 1 and Fig. 6 is reasonable. In the cases where the Stanton number and intermittency-based results do not agree (e.g., when $x_s < 0$ by the extrapolation technique) it must be remembered that the choice of extrapolating to $\gamma = 0$ and $\gamma = 0.99$ is somewhat arbitrary and that the intermittency based x_s and x_e are still acceptable and useful for further intermittency processing. The negative value of x_s is merely an artifact of the technique.

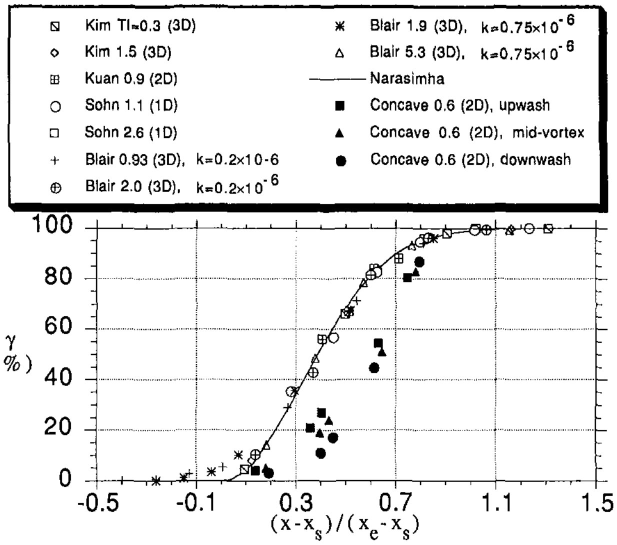

Fig. 7 Intermittency profiles

Intermittency. The intermittency within the transition zone is plotted as a function of the dimensionless streamwise coordinate $(x - x_s)/(x_e - x_s)$ in Fig. 7. The abscissa is a modified version of Dhawan and Narasimha's (1958) coordinate. Dhawan and Narasimha used $(x - x_s)/(x_e - x_s)$ where x_s is taken at $\gamma = 0.25$ and x_e is taken at $\gamma = 0.75$. Here, x_s is taken at the extrapolated $\gamma = 0$ location and x_e at the extrapolated $\gamma = 0.99$ location. The modification was done to give x estimates that are closer to the actual start and end of transition. The change was purely algebraic; the theory remains exactly as Dhawan and Narasimha presented it. Dhawan and Narasimha present a formula that, when modified to take the changed abscissa into account, is

$$\gamma = 1 - \exp\left(-4.6\left(\frac{x - x_s}{x_e - x_s}\right)^2\right) \tag{2}$$

This curve is plotted along with experimental data in Fig. 7. Unaccelerated and accelerated cases agree well with the analytical curve. Results presented by Gostelow and Walker (1991) show that the agreement is also good for adverse pressure gradient cases. New data taken by the authors along a concave wall indicate that the theory does not always hold when curvature effects are introduced. Although it is possible to force any two data points from an experimental case to fit the theoretical curve (through appropriate choice of x_s and x_e), it is impossible to fit all the concave-wall data to the theoretical curve. This behavior is believed to be due to a change in the transition mechanism associated with the Görtler vortices in the low-*TI*, concave-wall case. For the concave cases, transition occurs earlier than on the flat wall. From Fig. 7, we can also say that it tends to progress more slowly, in a relative sense, during early transition and more quickly during later stages of transition, compared to flat-wall behavior. High-*TI*, unaccelerated cases were not included here because intermittency values could not be measured for these cases.

Turbulent Spot Formation Rate. The production and growth of turbulent spots in the transition region can be predicted according to Dhawan and Narasimha's (1958) theory. As given by Mayle (1991),

$$\gamma = 1 - \exp\left[-\frac{n\sigma}{U_\infty}(x - x_s)^2\right] \tag{3}$$

where n is the turbulent spot production rate and σ is the turbulent spot propagation parameter. A dimensionless spot production rate, $\hat{n}$, is defined as $n\nu^2/U_s^3$. The velocity, U_s, is the free-stream velocity at the start of transition. The product $\hat{n}\sigma$ is directly related to the length of the transition zone. Given the location of the transition start and $\hat{n}\sigma$, it should be possible to calculate the location of the end of transition and the intermittency within the transition region. From the discussion above, one can show

$$\hat{n}\sigma = \frac{4.6}{(\mathrm{Re}_{x_e} - \mathrm{Re}_{x_s})^2} \tag{4}$$

in unaccelerated flow, where Re_{x_s} and Re_{x_e} are taken at $\gamma = 0$ and $\gamma = 0.99$. A single value of $\hat{n}\sigma$ is applied through transition. For accelerating flows, Mayle (1991) proposed a formulation based on the work of Chen and Thyson (1971). He replaced σ by the modified propagation parameter $\bar{\sigma}U_s/\bar{U}$, where $\bar{U}$ is an average free-stream velocity for the transition zone. This results in

$$\hat{n}\bar{\sigma} = \frac{4.6\bar{U}\nu^2}{(x_e - x_s)^2 U_s^3} \tag{5}$$

Using the Stanton-number-based data from Table 1, $\hat{n}\sigma$ were calculated and plotted verses *TI* in Fig. 8. Also shown is an empirical curve given by Mayle (1991), which is based on flat-wall, unaccelerated-flow data. This curve is recommended by Mayle for application to gas turbine flows. The unaccelerated data in Fig. 8 tend to agree with the trend of Mayle's curve. The two lowest *TI* cases do not follow Mayle's curve, but these are at a lower *TI* than is generally of interest for gas turbine work.

The accelerated flow cases shown in Fig. 8 deviate somewhat from the correlation. Acceleration causes a lower spot propagation rate, although the differences between the accelerated cases and the correlation are not excessive for the cases shown.

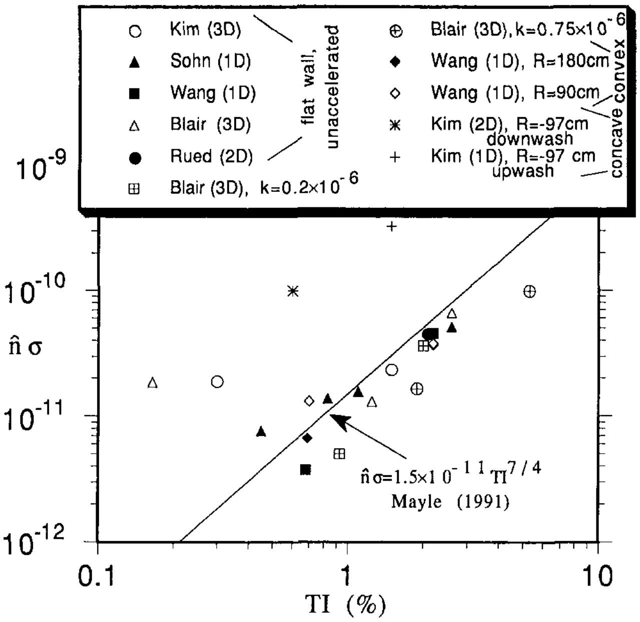

Fig. 8 Turbulent spot production rate based on St

Curved wall cases are also shown in Fig. 8. Convex curvature appears to have little effect on spot propagation. Wang and Simon's data are in reasonable agreement with the flat wall correlation. Concave curvature appears to have a significant effect on $\hat{n}\sigma$. Kim and Simon's 0.6–1.5 percent *TI* cases show $\hat{n}$ approximately 15 times higher than the flat wall correlation at the same *TI*. It is not clear what effect concave curvature would have at higher *TI*. One can speculate that the effects seen might persist, somewhat, to higher free-stream turbulence levels, but experimental evidence does not yet exist to support this speculation. Kim and Simon reported a concave-curved, high-*TI* case (*TI* = 8.3 percent), but because of the very early transition experienced in this case, no intermittency data during transition could be obtained.

Spot propagation data based upon intermittency are given in Table 2 and plotted in Fig. 9. They are consistent with the Stanton-number-based data discussed above. The agreement of the intermittency data with Narasimha's theory in Fig. 7 suggests that the choice of a single $\hat{n}\sigma$ for the entire transition region is appropriate for the flat wall cases. For the concave-wall case, however, the local effective $\hat{n}\sigma$ values increase as one moves downstream through transition. The first three γ values in each of the three concave-wall curves in Fig. 7 were used to determine an effective local $\hat{n}\sigma$ at the start of transition. Similarly, the last two γ values in each curve were used to determine an effective local $\hat{n}\sigma$ for the end of transition. These are presented in Table 2 for the upwash, downwash, and midvortex locations of this case. In Fig. 9, all the concave wall $\hat{n}\sigma$ values are seen to lie significantly above Mayle's correlation and the flat wall data, in agreement with Fig. 8. The effective $\hat{n}\sigma$ increases by an order of magnitude between the beginning and end of transition. An effective overall $\hat{n}\sigma$ is also presented, based on the extrapolated Re_{x_s} and Re_{x_e} given in Table 2.

Conclusions and Recommendations

Local coordinates (Re_{Δ_2} and Re_θ) used in the various comparisons were useful in reducing and comparing the data. Data in the laminar and fully turbulent regions of the flow matched the expected correlations well in these coordinates. An overshoot above the turbulent correlations after transition, seen in x or Re_x coordinates, was eliminated when using these local coordinates. In using local coordinates (Δ_2 and θ), the problem of a shift in virtual origin due to transition is eliminated.

The variation in the location of the transition region from case to case could not be completely explained by the *TI* level and other documented evidence alone. Other effects

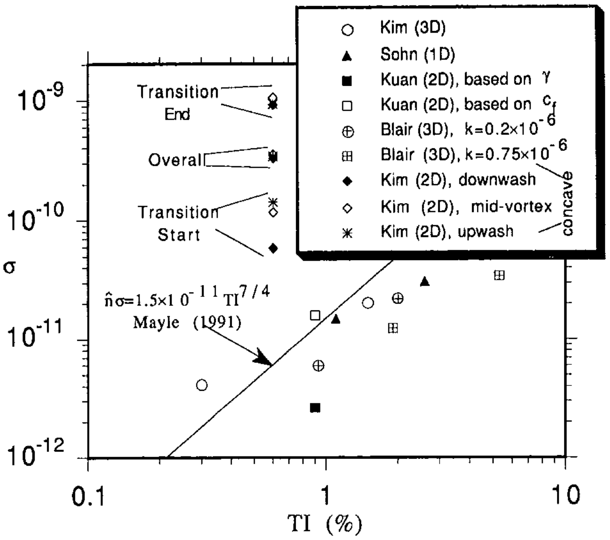

Fig. 9 Turbulent spot production rate based on γ

such as variability of the spectra and length scales of the free-stream turbulence or other uncontrolled variables must have played a role in the transition process and, thus, would have resulted in additional case to case variations. These factors should be investigated and free-stream turbulence documentation should be more complete in future experiments.

The practice of reporting a single value for the free-stream *TI* is insufficient. Future experiments should include documentation of the frequency ranges over which reported *TI* values are measured, presentation of spectral distributions of power, and computation of length scales. Some consensus should be reached regarding standardization of reported values.

The intermittency values in the transition region of the flat wall cases, including those with streamwise pressure gradients, closely follow the behavior predicted by Dhawan and Narasimha (1958). This was true even for those cases that show unexpected behavior in other comparisons. Recent experiments on concave walls show deviation from this behavior, however. The intermittency behavior in curved-wall cases should be studied further.

Curvature was seen to play a significant role in transition. Convex curvature tended to delay transition at lower *TI* values. Concave curvature shifted the transition zone upstream and, for low *TI* values, introduced three dimensionality in the form of Görtler vortices. Transition began at the Görtler vortex upwashes, proceeding along a path similar, in terms of Re_θ, to that seen in flat-wall cases. The behavior at the downwash locations was significantly different, however, showing transition at lower Re_θ values. Further investigation of curved-wall cases should proceed.

Acceleration has a pronounced effect both on transitional and turbulent flow behavior. Acceleration appears to enhance the breakdown in Reynolds analogy during transition. The transition onset position in terms of momentum thickness Reynolds number for the accelerated flow cases matches the flat wall cases, however. Further investigation of acceleration effects, including the combined effects of curvature and acceleration, should be made.

The turbulent spot formation rate was found to depend strongly on the free-stream turbulence level. Agreement with Mayle's (1991) empirical correlation was reasonable for the flat wall cases considered. Convex curvature had little effect on the spot formation rate, but concave curvature caused a significant increase in the spot formation rate in Kim and Simon's low-*TI* (0.6 percent (2D)) case. Acceleration appears to have a relatively small but still noticeable effect of decreasing the spot formation rate in the cases considered.

Acknowledgments

The preceding work was sponsored by the Lewis Research Center of NASA under grant NASA/NAG3-881. The authors thank the grant monitor, Fred Simon, for this guidance.

References

Abu-Ghannam, B. J., and Shaw, R., 1980, "Natural Transition of Boundary Layers—The Effects of Turbulence, Pressure Gradient, and Flow History," *J. Mechanical Engineering Science*, Vol. 22, No. 5, pp. 213–228.

Blair, M. F., and Werle, M. J., 1980, "The Influence of Free-Stream Turbulence on the Zero Pressure Gradient Fully Turbulent Boundary Layer," United Technologies Research Center report R80-914388-12.

Blair, M. F., 1981a, "Final Data Report—Vol. I—Velocity and Temperature Profile Data for Zero Pressure Gradient, Fully Turbulent Boundary Layers," United Technologies Research Center report R81-914388-15.

Blair, M. F., 1981b, "Final Data Report—Vol. II—Velocity and Temperature Profile Data for Accelerating, Transitional Boundary Layers," United Technologies Research Center report R81-914388-16.

Blair, M. F., and Werle, M. J., 1981, "Combined Influence of Free-Stream Turbulence and Favorable Pressure Gradients on Boundary Layer Transition and Heat Transfer," United Technologies Research Center report R81-914388-17.

Blair, M. F., 1982, "Influence of Free-Stream Turbulence on Boundary Layer Transition in Favorable Pressure Gradients," ASME *Journal of Engineering for Power*, Vol. 104, pp. 743–750.

Blair, M. F., 1983, "Influence of Free-Stream Turbulence on Turbulent Boundary Layer Heat Transfer and Mean Profile Development, Part I, Experimental Data," ASME *Journal of Heat Transfer*, Vol. 105, pp. 33–40.

Blair, M. F., and Anderson, O. L., 1987, "Study of the Structure of Turbulence in Accelerating Transitional Boundary Layers," United Technologies Research Center report R87-956900-1.

Chen, K. K., and Thyson, N. A., 1971, "Extension of Emmons' Spot Theory to Flows on Blunt Bodies," *AIAA Journal*, Vol. 9, pp. 821–825.

Crawford, M. E., and Kays, W. M., (1976), "STAN5—A Program for Numerical Computation of Two-Dimensional Internal and External Boundary Layer Flows," NASA CR-2742.

Dhawan, S., and Narasimha, R., 1958, "Some Properties of Boundary Layer Flow During the Transition From Laminar to Turbulent Motion," *J. Fluid Mech.*, Vol. 3, pp. 418–436.

Emmons, H. W., 1951, "The Laminar-Turbulent Transition in a Boundary Layer—Part I," *J. Aeronautical Science*, Vol. 18, pp. 490–498.

Gostelow, J. P., and Walker, G. J., 1991, "Similarity Behavior in Transitional Boundary Layers Over a Range of Adverse Pressure Gradients and Turbulence Levels," ASME JOURNAL OF TURBOMACHINERY, Vol. 113, pp. 617–625.

Kays, W. M., and Crawford, M. E., 1993, *Convective Heat and Mass Transfer*, McGraw-Hill, New York.

Kim, J., Simon, T. W., and Kestoras, M., 1994, "Fluid Mechanics and Heat Transfer Measurements in Transitional Boundary Layers Conditionally Sampled on Intermittency," ASME JOURNAL OF TURBOMACHINERY, Vol. 116, pp. 405–416.

Kim, J., Simon, T. W., and Russ, S., 1992, "Free-Stream Turbulence and Concave Curvature Effects on Heated Transitional Boundary Layers," ASME *Journal of Heat Transfer*, Vol. 114, pp. 338–347.

Kim, J., and Simon, T. W., 1991, "Free-Stream Turbulence and Concave Curvature Effects on Heated, Transitional Boundary Layers. Vol. I—Final Report," NASA CR 187150; "Vol. II—Program Listings and Tabulated Data," NASA CR 187151.

Kuan, C. L., 1987, "An Experimental Investigation of Intermittent Behavior in the Transitional Boundary Layer," M.S. Thesis, Clemson University, Clemson, SC.

Kuan, C. L., and Wang, T., 1990, "Investigation of the Intermittent Behavior of Transitional Boundary Layer Using a Conditional Averaging Technique," *Experimental Thermal and Fluid Science*, Vol. 3, pp. 157–173.

Mayle, R. E., 1991, "The Role of Laminar-Turbulent Transition in Gas Turbine Engines," ASME JOURNAL OF TURBOMACHINERY, Vol. 113, pp. 509–537.

McDonald, H., and Fish, R. W., 1973, "Practical Calculation of Transitional Boundary Layers," *Int. J. Heat Mass Transfer*, Vol. 16, pp. 1729–1744.

Morkovin, M. V., 1978, "Instability, Transition to Turbulence and Predictability," AGARD-AG-236.

Narasimha, R., 1984, "Subtransitions in the Transition Zone," *Proc. 2nd IUTAM Symposium on Laminar-Turbulent Transition*, Novosibirsk, pp. 141–151.

Narasimha, R., 1985, "The Laminar-Turbulent Transition Zone in the Boundary Layer," *Progress in Aerospace Science*, Vol. 22, No. 1, pp. 29–80.

Rued, K., and Wittig, S., 1985, "Free-Stream Turbulence and Pressure Gradient Effects on Heat Transfer and Boundary Layer Development on Highly Cooled Surfaces," ASME *Journal of Engineering for Gas Turbines and Power*, Vol. 107, pp. 54–59.

Rued, K., and Wittig, S., 1986, "Laminar and Transitional Boundary Layer Structures in Accelerating Flow with Heat Transfer," ASME JOURNAL OF TURBOMACHINERY, Vol. 108, pp. 116–123.

Rued, K., 1987, "Transitional Boundary Layers Under the Influence of High Free Stream Turbulence, Intensive Wall Cooling and High Pressure Gradients in Hot Gas Circulation," NASA TM-88524.

Schlichting, H., 1979, *Boundary Layer Theory*, 7th ed., McGraw-Hill, New York.

Sohn, K. H., O'Brien, J. E., and Reshotko, E., 1989, "Some Characteristics of Bypass Transition in a Heated Boundary Layer," NASA TM-102126.

Sohn, K. H., and Reshotko, E., 1991, "Experimental Study of Boundary Layer Transition With Elevated Freestream Turbulence on a Heated Flat Plate," NASA CR-187068.

Van Driest, E. R., and Blumer, C. B., 1963, "Boundary Layer Transition: Freestream Turbulence and Pressure Gradient Effects," *AIAA Journal*, Vol. 1, No. 6, pp. 1303–1306.

Volino, R. J., and Simon, T. W., 1991, "Bypass Transition in Boundary Layers Including Curvature and Favorable Pressure Gradient Effects," NASA CR-187187.

Wang, T., 1984, "An Experimental Investigation of Curvature and Freestream Turbulence Effects on Heat Transfer and Fluid Mechanics in Transitional Boundary Layer Flows," Ph.D. Thesis, Department of Mechanical Engineering, U. of Minnesota.

Wang, T., Simon, T. W., and Buddhavarapu, J., 1985, "Heat Transfer and Fluid Mechanics Measurements in Transitional Boundary Layer Flows," ASME *Journal of Engineering for Gas Turbines and Power*, Vol. 107, pp. 1007–1015.

Wang, T., and Simon, T. W., 1987, "Heat Transfer and Fluid Mechanics Measurements in a Boundary Layer Undergoing Transition on a Convex-Curved Wall," ASME JOURNAL OF TURBOMACHINERY, Vol. 109, No. 3, pp. 443–452.

Experimental and Theoretical Investigations of Heat Transfer in Closed Gas-Filled Rotating Annuli

D. Bohn

E. Deuker

R. Emunds

V. Gorzelitz

Institute of Steam and Gas Turbines,
Technical University of Aachen,
Aachen, Federal Republic of Germany

The prediction of the temperature distribution in a gas turbine rotor containing closed, gas-filled cavities, for example in between two disks, has to account for the heat transfer conditions encountered inside these cavities. In an entirely closed annulus, forced convection is not present, but a strong natural convection flow exists, induced by a nonuniform density distribution in the centrifugal force field. Experimental investigations have been made to analyze the convective heat transfer in closed, gas-filled annuli rotating around their horizontal axes. The experimental setup is designed to establish a pure centripetal heat flux inside these annular cavities (hot outer, and cold inner cylindrical wall, thermally insulated side walls). The experimental investigations have been carried out for several geometries varying the Rayleigh number in a range usually encountered in cavities of turbine rotors ($10^7 < Ra < 10^{12}$). The convective heat flux induced for $Ra = 10^{12}$ was found to be a hundred times larger compared to the only conductive heat flux. By inserting radial walls the annulus is divided into 45 deg sections and the heat transfer increases considerably. A computer program to simulate flow and heat transfer in closed rotating cavities has been developed and tested successfully for annuli with isothermal side walls with different temperatures giving an axial heat flux. For the centripetal heat flux configuration, three-dimensional steady-state calculations of the sectored annulus were found to be consistent with the experimental results. Nevertheless, analysis of unsteady calculations show that the flow can become unstable. This is analogous to the Bénard problem in the gravitational field.

Introduction

The development of gas turbines toward higher gas temperatures at the turbine inlet with a simultaneous increase of compressor pressure ratio is a promising trend to increase their thermal efficiency. In connection with this trend, attention is being paid to the mechanically and thermally stressed parts of the gas turbine. To estimate these stresses a proper evaluation of temperature distributions in units and components operating in the hottest zones is required. In such a zone temperature nonuniformities may lead to considerable supplementary stresses, the permissible value of which is also determined by the temperature level.

At present only an approximate estimation of the temperature distribution in a gas turbine rotor containing gas-filled enclosures (Fig. 1) is possible. In those cavities a strong, free convective flow is induced. This convection is caused by the buoyancy force corresponding to centrifugal acceleration and temperature differences of the cavity walls. Such a flow increases the heat transfer throughout the cavities considerably.

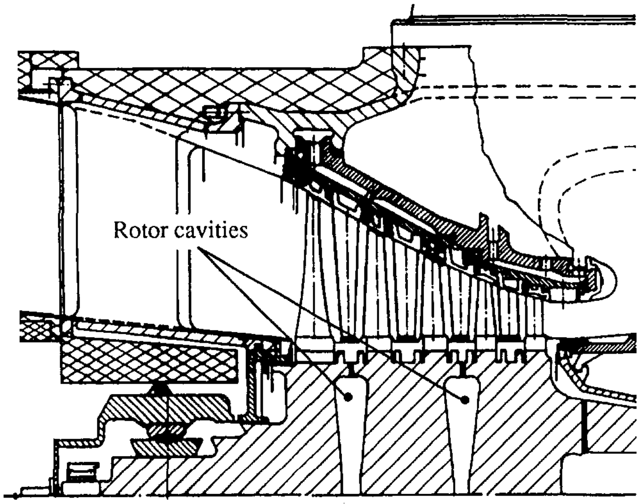

Fig. 1 Rotating enclosure in a turbine rotor

In the past many theoretical and experimental investigations have been carried out to study the heat transfer in rotating enclosures with a throughflow of cooling fluid, e.g., Ong and Owen (1991), Farthing et al. (1992), and Owen et al. (1985). For sealed cavities with a purely free convection flow, the known theoretical and experimental investigations pertain mainly to constant-temperature walls, and are limited to qualitative descriptions of the convective processes. These investigations differ with respect to the direction of the heat flux in the cavity (Fig. 2).

Contributed by the International Gas Turbine Institute and presented at the 38th International Gas Turbine and Aeroengine Congress and Exposition, Cincinnati, Ohio, May 24–27, 1993. Manuscript received at ASME Headquarters March 10, 1993. Paper No. 93-GT-292. Associate Technical Editor: H. Lukas.

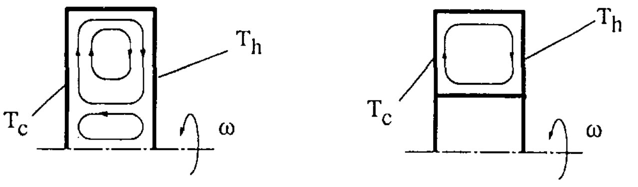

I: Cylindrical cavity
heat flux directed axially

II: Annular cavity
heat flux directed axially

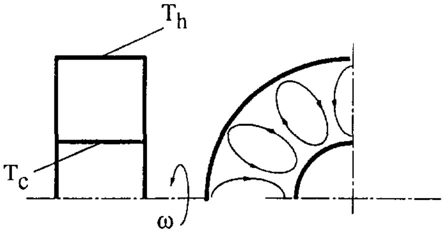

III: Annular cavity
heat flux directed radially

Fig. 2 Configurations of rotating enclosures

Most of the investigations have been done for an axially directed heat flux applied on a cylindrical rotating enclosure shown in Fig. 2(I). Kapinos et al. (1981) have performed experimental investigations on heat transfer in an enclosure as described above. They pointed out the influence of Coriolis forces on the fluid motion and compared their experimental results with numerical investigations given by Harada and Ozaki (1975). Abell and Hudson (1975) conducted experiments on an oil-filled rotating cylinder. They deduced a correlation between the Nusselt number and the temperature difference between the hot and cold wall of the cylindrical cavity and the rotational Reynolds number. Chew (1985) also did numerical investigations on heat transfer in these enclosures, producing computations consistent with the experimental results achieved by Abell and Hudson (1975).

Investigations on rotating annular cavities, as in Fig. 2(II), have been conducted by only a few authors. Most of these studies are not even performed under conditions encountered in turbomachinery. Müller and Burch (1985) obtained measurements of the transient natural convection in an axially heated rotating annular enclosure simulating geophysical conditions. Similar experimental studies are reported by Hignett et al. (1981).

Considering the heat transfer in a cavity such as that shown in Fig. 2(III), Lin and Preckshot (1979) calculated the temperature, velocity, and streamline distribution. Zysina-Molozhen and Salov (1977) analyzed experimentally the influence of rotational speed and various thermal conditions on heat transfer in a rotating annular enclosure. The heat flux applied on the test rig was directed centripetally and photographs were taken, showing the flow pattern inside the enclosure. They note the absence of any regular fluid circulation contours in the cavity.

However, there is still a lack of knowledge on rotating sealed cavities, bounded by an outer and an inner cylindrical wall and operating under conditions valid for gas turbines.

At the Institute of Steam and Gas Turbines at the Technical University Aachen experimental and theoretical investigations have been carried out studying the influence of heat flux direction and geometry on the convective heat transfer inside such enclosures. The development of a computer code to simulate free convection flow in rotating annuli is described in a previous paper (Bohn et al., 1994), and results are presented for the axial heat flux situation as given in Fig. 2(II).

In this paper experimental and numerical results of convective heat transfer in a rotating closed annulus with radial heat flux (Fig. 2(III)) are presented for conditions very close to turbomachinery operation.

Analyzing the basic conservation equations of mass, momentum, and energy (see below), it can be demonstrated that

$$\mathrm{Nu} = f(\mathrm{Ra}, \mathrm{Re}, \mathrm{Pr}, H/r_m, b/r_m) \qquad (1)$$

The Nusselt number (Nu) is defined as the ratio of the heat flux throughout the cavity to that flux that would occur in solid-body rotation without any motion relative to a corotating frame of reference; Nu is thus equal to one for no convection and is greater than one when convection takes place. The rotational Reynolds number (Re) has its origin in the Coriolis force terms in the momentum equations. The rotational Rayleigh number (Ra) is the product of the Grashof number and the Prandtl number and is related to the buoyancy term in the radial momentum equation. The Prandtl number is a combination of fluid properties and does not change significantly due to temperature variations.

Nomenclature

a = thermal diffusivity
b = distance between lateral side walls
c_p = specific heat at constant pressure
H = distance between outer and inner cylindrical walls
L = distance between hot and cold wall ($L = H$ for heat flux directed radially, $L = b$ for heat flux directed axially)
p = pressure
$\dot{q}$ = heat flux from the outer to the inner cylindrical wall
$\dot{q}_\lambda$ = heat transfer by conduction alone
r = radius
R = gas constant
T = temperature
ΔT = temperature difference between hot and cold cylindrical wall
(x, r, φ) = axial, radial, circumferential coordinates
(u, v, w) = relative velocity components in (x, r, φ) directions
α = section angle
λ = thermal conductivity
μ = dynamic viscosity
ρ = density
ω = angular velocity of the cavity
$\mathrm{Gr} = \dfrac{r_m \cdot \omega^2 \cdot \Delta T \cdot L^3 \cdot \rho^2}{T_m \cdot \mu^2}$ = Grashof number
$\mathrm{Pr} = \dfrac{\mu \cdot c_p}{\lambda} = \dfrac{\mu}{\rho \cdot a}$ = Prandtl number
$\mathrm{Ra} = \mathrm{Gr} \cdot \mathrm{Pr}$ = Rayleigh number
$\mathrm{Re} = \dfrac{\rho \cdot \omega \cdot r_m \cdot L}{\mu}$ = Reynolds number
$\mathrm{Nu} = \dfrac{\dot{q}}{\dot{q}_\lambda}$ = Nusselt number
$\mathrm{Ec} = \dfrac{(\omega \cdot r_m)^2}{2 \cdot c_p \cdot \Delta T}$ = Eckert number

Subscripts

c = cold
h = hot
i = inner
m = arithmetic mean
max = maximum
min = minimum
o = outer
red = reduced
SB = solid body
w = water
0 = reference

Superscripts

n = time level
ν = iteration level

Experiments

Apparatus. The experimental investigations of heat transfer in sealed rotating cavities were performed on three different geometric configurations *A*, *B*, and *C*. The test fluid contained in the enclosures is air. The dimensions of the enclosures are given in Fig. 3.

Test configurations *A* and *B* are closed annuli rotating around their horizontal axes. The radius of the inner cylindrical wall as well as the width of the annular cavity are the same for both configurations *A* and *B*. Only the radius of the outer cylindrical wall differs for these geometries. The geometric dimensions of the test cavity *C* are identical to *B*, but eight radial walls divide the annulus into 45 deg segments. The separation walls do affect the development of the flow in circumferential direction inside the enclosure. This is to study the influence of Coriolis forces on heat transfer.

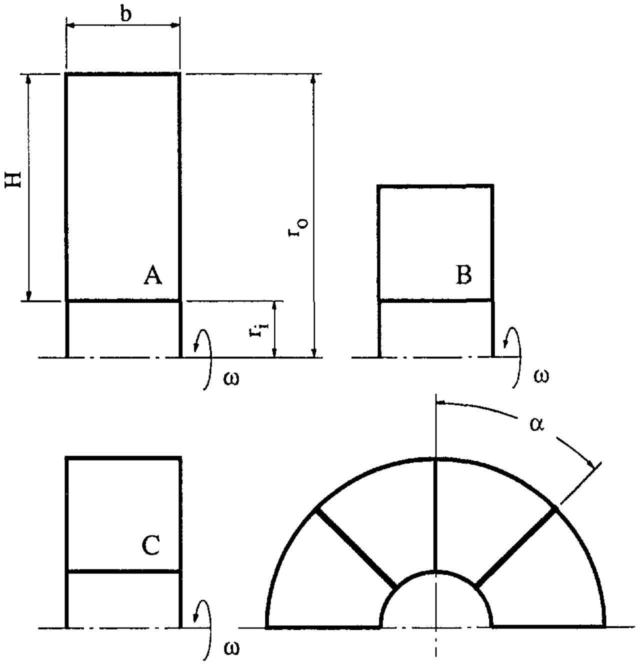

Cavity	r_i [mm]	r_o [mm]	H [mm]	b [mm]	α [-]
A	125	355	230	120	-
B	125	240	115	120	-
C	125	240	115	120	45°

Fig. 3 Dimensions of the annular cavities

The experimental investigations on all three configurations were performed at the test rig shown in Fig. 4. This cross section of the experimental apparatus shows the annular cavity of configuration *A*. The annulus is formed by two rotor disks with a cylindrical ring on the upper radius between them. The rotor shaft forms the inner cylindrical wall of the annulus. Heat input into the cavity is accomplished by an electrical heater placed at the outer radius of the annulus. To enable a homogeneous temperature distribution at the heater surface, the heater is made of a copper ring with a heating wire embedded into a helical groove. Power supply for the electrical heater is realized by a slipping brush assembly. Heat is removed out of the cavity by the water-cooled rotor shaft. The water enters the rotor shaft by a rotary transmission leadthrough, flows to the cooling bottom, and, concentric to the inflow, back out to a drain housing. Both lateral surfaces of the annulus are thermally insulated. The heat insulating panels are made of a bounded honeycomb sandwich construction. The honeycomb consists of an aramid-fiber paper treated with a heat-resistant phenolic resin. Both bounded face sheets consist of a phenolic resin prepreg. Using this sandwich construction, a thermal conductivity of the heat insulating panels is achieved, which is virtually as little as that of air. The cavity can be pressurized while running the rotor by using a labyrinth housing. The rotor shaft is driven by a DC motor using a belt drive. Measurements of the rotational speed are accomplished by mounting a perforated disk on the shaft and using a coil to produce a voltage spike when one of the perforations passes it. Double bearings are installed at the ends of the rotor shaft, enabling steady rotation.

Heat fluxes from the outer cylindrical wall to the working fluid and from the working fluid to the inner cylindrical wall are determined by measuring the temperature differences across a thermal resistance (Fig. 5).

The thermal resistance consists of an epoxy layer held

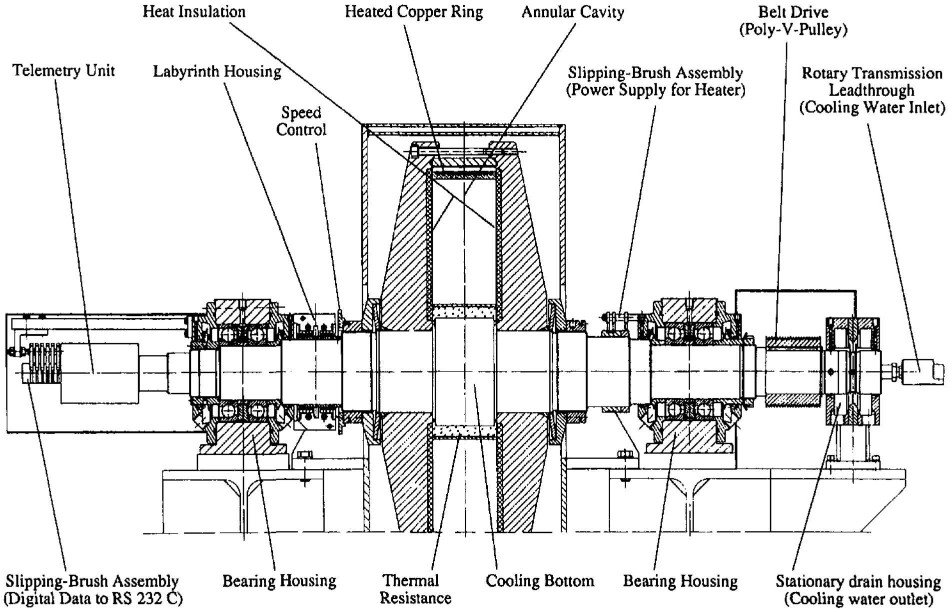

Fig. 4 Cross section of the experimental apparatus

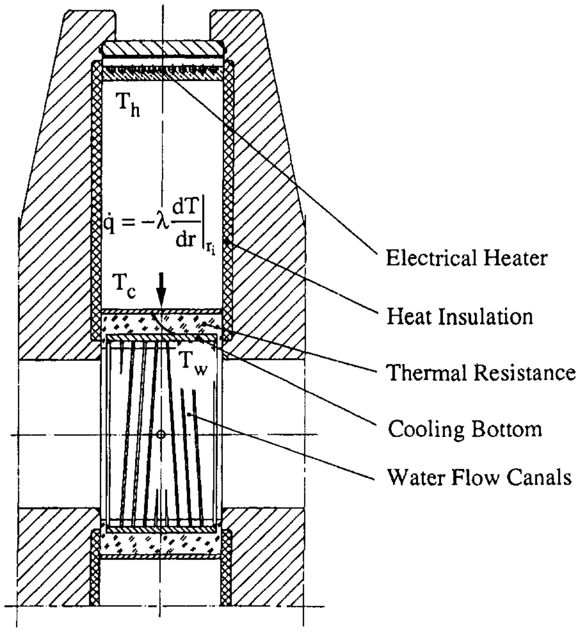

Fig. 5 Heat flux measuring device

between the rotor shaft and a steel tube concentric to it. The conductivity and thickness of the layer are chosen so that a sufficient temperature drop can be obtained due to the expected heat fluxes. Temperatures are measured using thin-film resistance thermometers of platinum (5 × 5 × 0.3 mm) installed prior to pouring the epoxy layer. Nine thermometers are located across the length of the thermal resistance on its outer and inner surface. The temperature distribution on the rotor surface inside as well as outside the enclosure, is recorded by an additional 18 thin-film thermometers. A telemetry unit, fixed on one end of the rotor shaft, registers the analogue signals of the resistance thermometers and converts them into digital. The digital data are transmitted out of the telemetry unit to an interface of a personal computer (RS 232 C) by a slipping-brush assembly. The digital circuit can measure the absolute temperature of a resistance thermometer to an accuracy of 0.01° C.

The dimensions of cavity configuration *B* on this experimental apparatus are realized only by mounting a smaller heated cylindrical ring between the two rotor disks. This also gives the basic dimensions of configuration *C*. In contrast to cavity *B*, cavity configuration *C* is not an annulus, but it is divided into 45 deg segments by eight heat insulating panels (thickness of 10 mm).

Procedure. During the experiments, the rotor speed, the cavity pressure, electric current to the heater, and the mass flow rate of cooling water were kept at constant levels. The maximum rotor speed is set up to 3500 rpm. The maximum cavity pressure is set up to 4 bar. The maximum temperature at the outer heated cylindrical wall is varied up to 100° C. The minimum temperature at the cooling bottom is fixed by the cooling water, which is taken from a water tap (about 15° C in summer and 8° C in winter).

Experimental test loops are continued until thermal conditions reach steady state. Data from all measuring points are recorded repeatedly at intervals of two minutes. To meet the criterion of steady-state conditions the relative rate of temperature changes should not exceed 1 percent for temperatures of about 10° C and 0.1 percent for temperatures of about 100° C during an observation period of ten minutes. The heat flux throughout the cavities is calculated from the measured temperature drop across the epoxy layer of known thermal conductivity.

Experimental Results. The governing equations (Eqs. (4) to (8), see below) make clear that the Nusselt number depends mainly on three dimensionless parameters, i.e., the Prandtl number, the rotational Rayleigh number Ra, and the rotational Reynolds number Re. The geometry is given by the two ratios H/r_m and b/r_m. (For configuration *C* the section angle occurs additionally.) In the present study the Prandtl number was not varied. Therefore, no information is obtained from the experiments regarding the dependence on Pr. Consequently, for a given fluid and a specified geometric configuration, i.e., for fixed H/r_m and b/r_m ratio, it might be expected that

$$\mathrm{Nu} = f(\mathrm{Ra}, \mathrm{Re}) \tag{2}$$

Since

$$\mathrm{Ra} = (\Delta T/T_m) \cdot (H/r_m) \cdot \mathrm{Re}^2 \cdot \mathrm{Pr}^2 \tag{3}$$

it is apparent that for a fixed value of $\Delta T/T_m$ the Re number cannot be treated as an independent variable. Due to the permissible temperature levels of the epoxy layer in the experimental setup, the ratio $\Delta T/T_m$ can only be varied in a small range. Furthermore, it was found that the values of $\Delta T/T_m$ that could be realized in experiment decrease continuously as the Ra number increases. Therefore, for all three cavity configurations *A*, *B*, and *C*, we only consider the Nusselt number's dependence on the rotational Rayleigh number and give a correlation equation for the corresponding Re number.

Values were obtained from the experiments for the temperature distribution at the cavity walls at different heat fluxes, rotational speeds, and cavity pressures. The surface temperatures of the heater and the thermal resistance were virtually isothermal. Only in a very narrow region at the lateral ends of the thermal resistance did the temperature differ from the mean surface temperatures, but by no more than 1.5 K and only for very large rotational speeds. However, the local heat flux along the length of the thermal resistance is virtually constant. Average surface temperatures were calculated and used throughout the analysis of the heat transfer results. Although this introduces some error into the results, it is not expected to have a significant influence on the Nusselt number.

The heat loss through the insulating lateral walls was estimated from the temperature drop across the walls of known thermal conductivity. The heat loss decreases with higher rotational speeds due to the friction on the outer rotor surface. For low rotational speeds of about 250 rpm the heat loss is about 20 percent of the total heat input. At high rotational speeds of about 3500 rpm this amounts to no more than 10 percent. In spite of varying rotor speed and cavity pressure at constant Ra and Re numbers, the Nu numbers were always reproducible in a maximum range of ±1 percent.

The influence of the radiative heat transfer on the heat flux throughout the cavity was calculated. For Nusselt numbers higher than 30, this amounts to no more than 2 percent of the total heat flux and, therefore, has not been taken into account.

In Figs. 6, 7, and 8 the Nusselt number is shown as a function of Ra for cavity configurations *A*, *B*, and *C*, respectively. The experimental points meet satisfactorily the straight line, which is calculated from the data by means of a least-squares fit. The figures show that the heat transfer depends strongly on the Rayleigh number.

In Fig. 9 results for configurations *A* and *B* are compared. With the reduction of the outer radius the distance *L* between hot and cold walls is reduced, which is a very sensitive parameter for natural convection flows. Note that $\mathrm{Ra} \sim L^3$ and $\mathrm{Re} \sim L$. The ratio H/r_m and the ratio b/r_m are also changed by the reduction of the outer radius. Thus, without

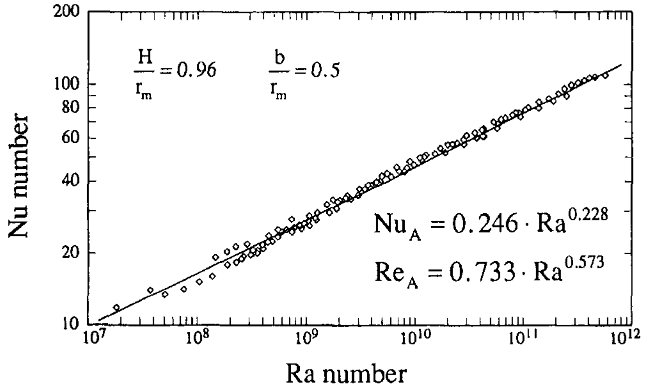

Fig. 6 **Heat transfer in cavity *A*, obtained at different rotational speeds and cavity pressures**

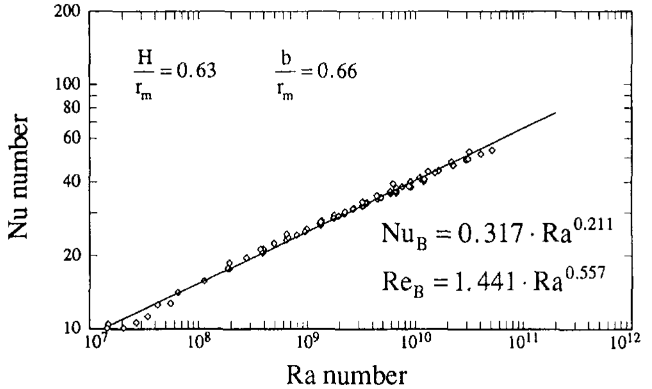

Fig. 7 **Heat transfer in cavity *B*, obtained at different rotational speeds and cavity pressures**

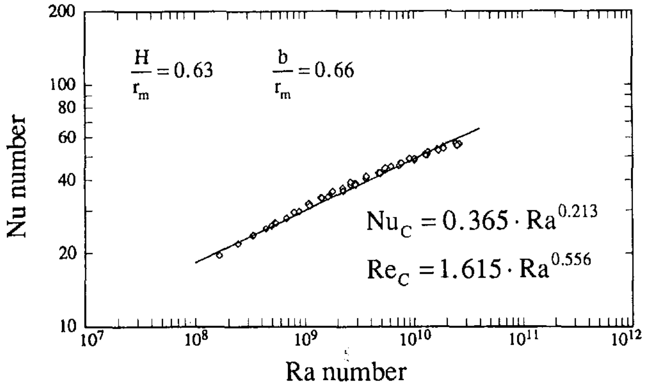

Fig. 8 **Heat transfer in cavity *C*, obtained at different rotational speeds and cavity pressures**

further information it is not possible to separate the influences of the parameters mentioned above on Nu. However, it is noteworthy that Nu does not change very much due to this geometry variation. Note that for the same Ra, Re in case *B* is nearly twice that in case *A*.

A numerical study has been performed to show the influence of the ratio b/r_m on heat transfer. Increasing b by a factor of 2 decreases Nu by about 4.7 percent, and, when increased by a factor of 3, Nu was found to be 7.6 percent smaller. Although these calculations have been done for configuration *C* at Ra = 10^9, similar results may be expected for cases *A* and *B*. Therefore, it is believed that the b/r_m ratio (which changes only by 34 percent from case *A* to case *B*) has only a weak influence on Nu.

In Fig. 10 configurations *B* and *C* are compared. The only difference between the two geometries is the insertion of radial separation walls in case *C*, but this does not affect the other dimensionless parameters given in Eq. (1).

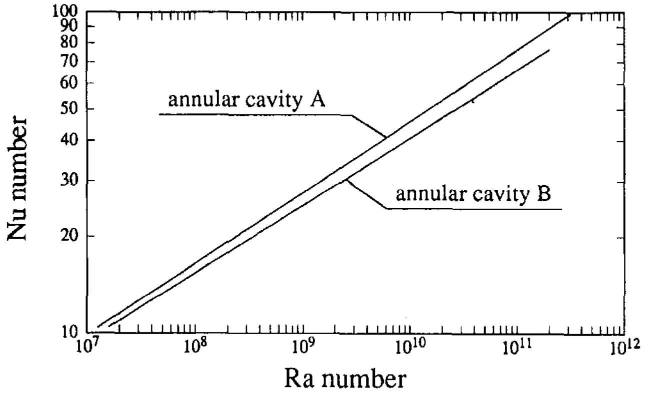

Fig. 9 **Comparison of cavity configurations *A* and *B***

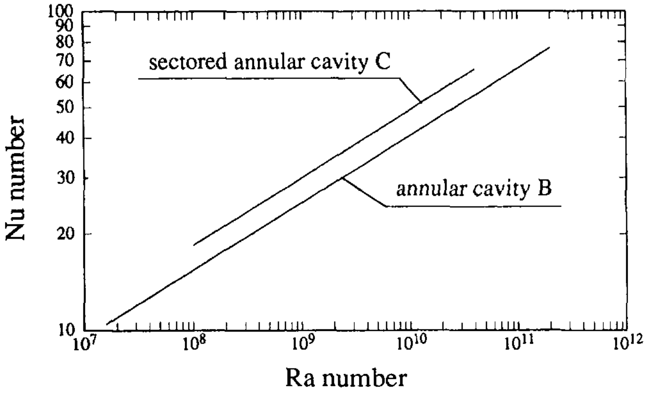

Fig. 10 **Comparison of cavity configurations *B* and *C***

The insertion of separation walls attenuates the relative circumferential velocity inside the cavity, resulting in a decrease of the radial component of the Coriolis force (see Eq. (6)). In the previous paper (Bohn et al., 1994) it was pointed out that Coriolis forces have a dampening effect on the flow. Thus, attenuating the Coriolis forces by inserting separation walls, the natural convection flow inside the cavity is strengthened so that the heat transfer increases. This is confirmed by the results shown in Fig. 10.

Numerical Investigation

Although the geometry of the cavities under consideration is quite simple, the flow is characterized by a complex interaction of convection, viscous forces, pressure forces, buoyancy effects, and Coriolis forces. In the previous paper (Bohn et al., 1994) flow structure and heat transfer have been analyzed for the axial heat flux situation, and special attention has been given to the buoyancy and Coriolis forces, which were found to be the most important terms to determine the heat transfer.

In the present case of a pure centripetal heat flux an additional difficulty occurs: The temperature gradient is in the opposite direction to the centrifugal force, and the flow in basically unstable.

A similar, well-known situation is found in the gravitational field: a fluid layer between two horizontal plates, where the temperature at the bottom surface is greater than the temperature at the top wall. In that case the temperature gradient is in the opposite direction to the gravitational force, and an unstable flow called Bénard convection occurs. It is known from literature that in this case the flow pattern also depends on the thermal boundary conditions of the side walls and the initial conditions (see, for example, Liang et al., 1969).

From our experiments, no information about the flow structure and only a little information about the thermal conditions at the side walls can be obtained. Therefore, for the time being we restrict our numerical analysis to the idealized case of adiabatic side walls and isothermal cylindrical walls. Although this is not a detailed investigation of the flow pattern inside our test cavity, it may highlight some basic features of this type of flow and can be considered as a basic case that is independent of special thermal conditions at the side walls.

Basic Modeling Assumptions. The radial heat flux was modeled assuming the temperatures at the cylindrical walls were different but uniformly distributed, while all other walls (the two side walls and the separation walls in radial direction) were assumed to be adiabatic.

The computer program solves the conservation equations for mass, momentum, and energy. All computations were carried out for air, the density is calculated by the ideal gas law, and all other properties are treated as functions of temperature. Some common assumptions for natural convection flows are made: In the viscous terms of the momentum equations the compressibility is neglected because the velocities at this type of flow are very small. In the energy equation the influence of the dissipation and pressure changes are assumed to be negligible too, due to very small Eckert numbers (Ec < 0.1). The flow is assumed to be laminar in the range of Gr numbers considered. The previously presented results verify this assumption for the axial heat flux situation; see Bohn et al. (1994) for a more detailed discussion.

Governing Equations. The steady-state governing equations are derived and declared comprehensively by Bohn et al. (1994). Now, the code has been extended to simulate unsteady flow. The dimensionless form of the equations reads:

$$\frac{\partial\bar{\rho}}{\partial\bar{t}} + \frac{1}{\bar{r}} \cdot \left(\frac{\partial\bar{\rho}\bar{u}\bar{r}}{\partial\bar{x}} + \frac{\partial\bar{\rho}\bar{v}\bar{r}}{\partial\bar{r}} + \frac{\partial\bar{\rho}\bar{w}}{\partial\varphi} \right) = 0 \qquad (4)$$

$$\frac{\partial\bar{\rho}\bar{u}}{\partial\bar{t}} + \frac{1}{\bar{r}}\left(\frac{\partial}{\partial\bar{x}}\bar{\rho}\overline{ruu} + \frac{\partial}{\partial\bar{r}}\bar{\rho}\overline{rvu} + \frac{\partial}{\partial\varphi}\bar{\rho}\overline{wu} \right)$$
$$- \frac{\mathrm{Pr}}{\bar{r}} \cdot \left(\frac{\partial}{\partial\bar{x}}\left(\bar{\mu}\bar{r}\frac{\partial\bar{u}}{\partial\bar{x}} \right) + \frac{\partial}{d\bar{r}}\left(\bar{\mu}\bar{r}\frac{\partial\bar{u}}{\partial\bar{r}} \right) + \frac{\partial}{\partial\varphi}\left(\frac{\bar{\mu}}{\bar{r}}\frac{\partial\bar{u}}{\partial\varphi} \right) \right)$$
$$= -\frac{\partial\bar{p}_{\mathrm{red}}}{\partial\bar{x}} \qquad (5)$$

$$\frac{\partial\bar{\rho}\bar{v}}{\partial\bar{t}} + \frac{1}{\bar{r}}\left(\frac{\partial}{\partial\bar{x}}\bar{\rho}\overline{ruv} + \frac{\partial}{\partial\bar{r}}\bar{\rho}\overline{rvv} + \frac{\partial}{\partial\varphi}\bar{\rho}\overline{wv} \right)$$
$$- \mathrm{Pr} \cdot \left(\frac{\partial}{\partial\bar{x}}\left(\bar{\mu}\bar{r}\frac{\partial\bar{v}}{\partial\bar{x}} \right) + \frac{\partial}{\partial\bar{r}}\left(\bar{\mu}\bar{r}\frac{\partial\bar{v}}{\partial\bar{r}} \right) + \frac{\partial}{\partial\varphi}\left(\frac{\bar{\mu}}{\bar{r}}\frac{\partial\bar{v}}{\partial\varphi} \right) \right)$$
$$= -\frac{\partial\bar{p}_{\mathrm{red}}}{\partial\bar{r}} - \mathrm{Pr}\frac{\bar{\mu}}{\bar{r}^2}\left(\bar{v} + 2\frac{\partial\bar{w}}{\partial\varphi} \right) - \bar{\rho}\frac{\bar{w}^2}{\bar{r}} + 2\bar{\rho}\bar{w}\frac{L}{r_m}\mathrm{Re} \cdot \mathrm{Pr}$$
$$-\bar{\rho}_{SB}\bar{r}\frac{T_m}{T}\frac{L}{r_m}\mathrm{Ra} \cdot \mathrm{Pr} \cdot \bar{T} \qquad (6)$$

$$\frac{\partial\bar{\rho}\bar{w}}{\partial\bar{t}} + \frac{1}{\bar{r}}\left(\frac{\partial}{\partial\bar{x}}\bar{\rho}\overline{ruw} + \frac{\partial}{\partial\bar{r}}\bar{\rho}\overline{rvw} + \frac{\partial}{\partial\varphi}\bar{\rho}\overline{ww} \right)$$
$$- \mathrm{Pr}\left(\frac{\partial}{\partial\bar{x}}\left(\bar{\mu}\bar{r}\frac{\partial\bar{w}}{\partial\bar{x}} \right) + \frac{\partial}{\partial\varphi}\left(\frac{\bar{\mu}}{\bar{r}}\frac{\partial\bar{w}}{\partial\varphi} \right) + \frac{\partial}{\partial\bar{r}}\left(\bar{\mu}\bar{r}\frac{\partial\bar{w}}{\partial\bar{r}} \right) \right)$$
$$= -\frac{1}{\bar{r}}\frac{\partial\bar{p}_{\mathrm{red}}}{\partial\varphi} - \mathrm{Pr}\frac{\bar{\mu}}{\bar{r}^2}\left(\bar{w} - 2\frac{\partial\bar{v}}{\partial\varphi} \right) - \bar{\rho}\frac{\bar{v}\bar{w}}{\bar{r}} - 2\bar{\rho}\bar{v}\frac{L}{r_m}$$
$$\cdot \mathrm{Re} \cdot \mathrm{Pr} \qquad (7)$$

$$\frac{\partial\bar{\rho}\bar{T}}{\partial\bar{t}} + \frac{1}{\bar{r}}\frac{\partial}{\partial\bar{x}}\left(\bar{\rho}\bar{r}\bar{u}\bar{T} - \frac{\bar{\lambda}\bar{r}}{\bar{c}_p}\frac{\partial\bar{T}}{\partial\bar{x}} \right) + \frac{1}{\bar{r}}\frac{\partial}{\partial\bar{r}}\left(\bar{\rho}\bar{r}\bar{v}\bar{T} - \frac{\bar{\lambda}\bar{r}}{\bar{c}_p}\frac{\partial\bar{T}}{\partial\bar{r}} \right)$$
$$+ \frac{1}{\bar{r}}\frac{\partial}{\partial\varphi}\left(\bar{\rho}\bar{w}\bar{T} - \frac{\bar{\lambda}}{\bar{r}\bar{c}_p}\frac{\partial\bar{T}}{\partial\varphi} \right) = 0 \qquad (8)$$

Herein the Re number occurs within the Coriolis terms, while the Ra number is related to the buoyancy term. The dimensionless variables marked with an overbar result from the following definitions:

$$u = \bar{u} \cdot \frac{a_0}{L}; \quad p = \bar{p} \cdot \frac{\rho_0 \cdot a_0^2}{L^2}; \quad \rho = \bar{\rho} \cdot \rho_0;$$
$$T = \bar{T} \cdot \Delta T + T_m; \quad \lambda = \bar{\lambda} \cdot \lambda_0; \quad \mu = \bar{\mu} \cdot \mu_0;$$
$$c_p = \bar{c}_p \cdot c_{p0}; \quad x = \bar{x} \cdot L; \quad r = \bar{r} \cdot L; \quad t = \bar{t} \cdot \frac{L^2}{a_0}$$

The fluid properties λ_0, a_0, ρ_0, μ_0, c_{p0} are evaluated for T_m as the reference temperature ($T_m = 0.5(T_h + T_c)$, see Fig. 2(III)). They have also been used to calculate the values of Re, Ra, and Pr. To obtain the reduced pressure defined by

$$p_{\mathrm{red}} = p - p_{SB}$$

the radial momentum equation for a rotating solid body at constant temperature is used:

$$-\frac{\partial p_{SB}}{\partial r} + \rho_{SB} \cdot \omega^2 \cdot r = 0$$

$$\rho_{SB} = \frac{p_{SB}}{R \cdot T_m}$$

Numerical Procedure. The system of coupled differential equations is solved numerically with a finite volume scheme. A nonuniform staggered grid is defined, with T and p being calculated at the main grid points and u, v, w being calculated at locations midway between the main grid points. In the employed "hybrid" differencing method upwind differencing is used for the convective terms when the cell Peclet number is greater than 2, otherwise central differencing is used for these terms.

The unsteady pressure correction is based on an iteration procedure defined by Patankar and Spalding (1972). From the momentum equations (not considering the source terms) for the time step n (Eq. (9)) and for the actual time iteration (Index ν, Eq. (10))

$$\frac{\rho \cdot \mathbf{v}^n - \rho \cdot \mathbf{v}^{n-1}}{\Delta t} = -\nabla p^n - (\mathbf{v}^n \cdot \nabla)\rho \cdot \mathbf{v}^n + \mu \cdot \nabla^2\mathbf{v}^n \qquad (9)$$

$$\frac{\rho \cdot \mathbf{v}^* - \rho \cdot \mathbf{v}^{n-1}}{\Delta t} = -\nabla p^\nu - (\mathbf{v}^* \cdot \nabla)\rho \cdot \mathbf{v}^* + \mu \cdot \Delta^2\mathbf{v}^* \qquad (10)$$

an equation for the unsteady pressure correction p' can be derived (by neglecting the convective and diffusive terms),

$$\nabla^2 p' = \frac{1}{\Delta t}(\nabla \cdot \rho\mathbf{v}^*) \quad \text{and} \quad p^\nu = p' + p^{\nu-1} \qquad (11)$$

where the continuity equation is used. Equation (11) has to be solved for the velocity field $\mathbf{v}^*$ resulting from Eq. (10). The iteration process has to be continued until p' is sufficiently small. At this time the velocity field $\mathbf{v}^*$ is the correct velocity field for the new time level $\mathbf{v}^n$ and the pressure p^ν is the correct pressure p^n.

Theoretical Results for the Closed Rotating Sectored Cavity (Steady-State Calculations). In the first instance we restricted ourselves to the sectored geometry (Configuration C) because the number of grid points required in circumferential direction is considerably smaller in that case. The calculations were carried out on a numerical grid containing about 36,000 grid points. Because the experiments gave steady-state results we started the numerical simulation with a steady algorithm keeping in mind that the flow might be unsteady. A more detailed discussion of the unsteady behavior of the flow is given below.

Figure 11 shows a comparison of the Nu numbers taken from experiment and from numerical (steady) simulation for a wide range of Ra numbers. Over the entire range the numerically calculated Nu numbers are slightly greater than those achieved by experiment. One reason for this deviation is the boundary condition of the side walls, which were treated as adiabatic for the numerical simulation. By adding the heat losses of the side walls to the heat transferred throughout the thermal resistance at the inner radius of the cavity the Nu numbers obtained from experiment increase by about 10 to 20 percent. Thus, the difference between experiment and numerical calculation becomes much smaller and the steady numerical algorithm was found to be a sufficient predictor of the heat transfer.

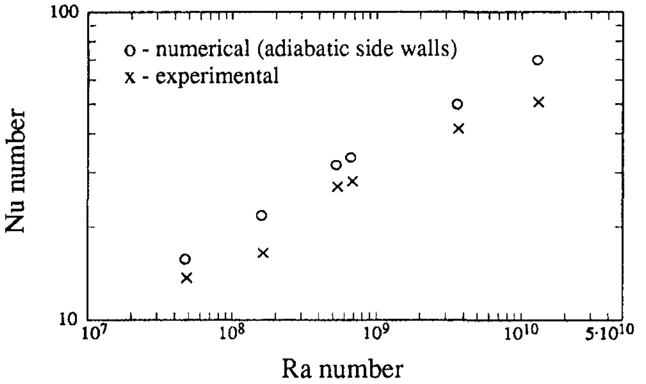

Fig. 11 Comparison of Nu obtained from experiment and from numerical simulation for various Ra

As a typical example, Fig. 12 shows the flow field in radial and circumferential direction for three axial positions and the temperature distribution for the medium axial position. The calculation was carried out for air for $T_m = 330.3$ K, which gives a Prandtl number of 0.70. In all three axial positions the fluid circulates in boundary layers, and nearly no motion occurs in the core region. The flow pattern does not change significantly in the axial direction.

In Table 1 the maxima and minima of the velocity components at the medium axial position are compared. The axial velocity component is significantly smaller than the radial and circumferential component. At other axial positions the results are similar. This makes it clear that the mean flow takes place in the $r-\varphi$ plane.

The direction of rotation of the flow can be explained with the Coriolis and buoyancy terms in the radial momentum equation (Eq. (6)). An estimation of the order of magnitude shows that the buoyancy term and the Coriolis term are much greater than the convective and diffusive terms ($V \ll \omega r_m$ and $\mu/\rho \ll \omega r_m^2$, respectively). At the hot wall T is

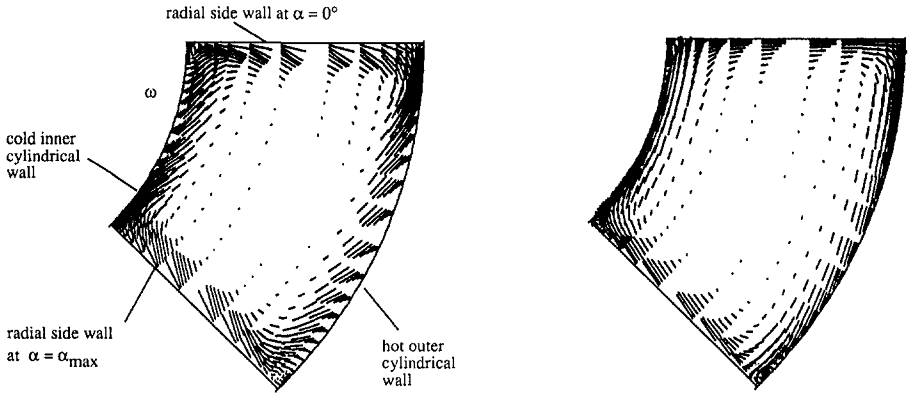
a) Flow field in the r - φ - plane at x / b = 0.001

b) Flow field in the r - φ - plane at x / b = 0.5

c) Flow field in the r - φ - plane at x / b = 0.999

d) Temperature distribution (x / b = 0.5)

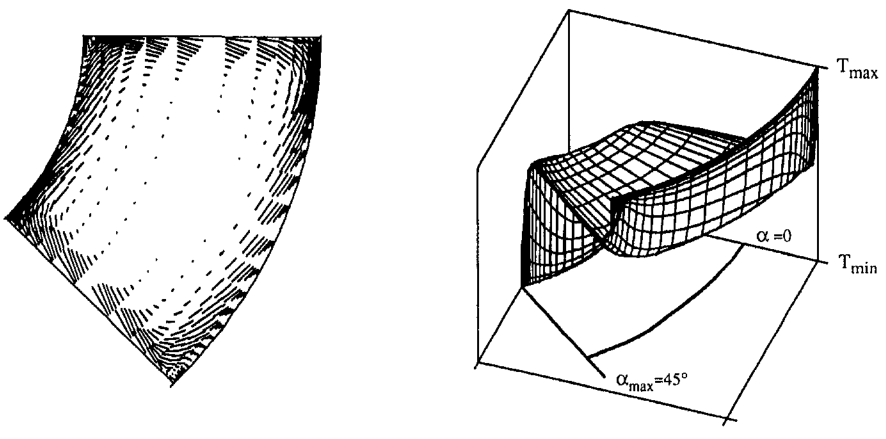

Fig. 12 Flow pattern at $x/b = (0.001, 0.5, 0.999)$, temperature distribution at $x/b = 0.5$ in a rotating cavity (Ra = 4.86×10^7, Re = 3.00×10^4)

Table 1 Comparison of the maxima and minima of the velocity components at medium axial position in the cavity ($Ra = 4.86 \times 10^7$, $Re = 3.00 \times 10^4$)

direction	max. size [m/s]	min. size [m/s]
axial	0,11	-0,071
radial	0,893	-0,821
circum-ferential	0,78	-0,70

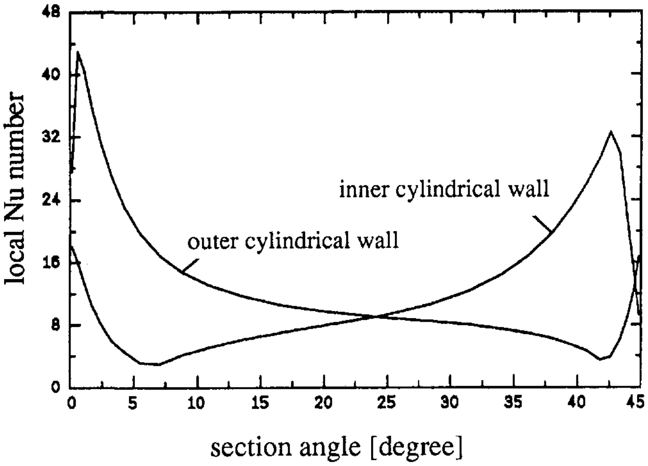

Fig. 13 Heat transfer at the hot and the cold cylindrical wall at a medium axial position ($Ra = 4.86 \times 10^7$, $Re = 3.00 \times 10^4$)

greater than zero, giving a negative buoyancy term. Therefore, the Coriolis term must be positive to balance the buoyancy term, which effects a positive circumferential velocity component at the hot wall. At the cold wall the buoyancy term is positive and, therefore, the Coriolis term and the velocity component in the circumferential direction have to be negative.

Moving from the cold wall to the hot wall along the radial separation wall at $\alpha = 0$, the fluid has a nearly constant temperature $T \approx 0.5$ ($T_{\max} + T_{\min}$) (Fig. 12*d*). A large positive temperature gradient occurs when the fluid reaches the hot wall. Similarly, near the cold wall at $\alpha = \alpha_{\max}$ a large negative temperature gradient occurs. In the core itself a nearly constant temperature is found, where heat is conducted neither in the radial direction nor in the circumferential direction. Thus, the heat transfer is strictly determined by convection in the boundary layers.

In Fig. 13 the distribution of the local Nu number at the hot outer and the cold inner cylindrical wall of the rotating annulus is plotted for a medium axial position. At the outer cylindrical wall most of the heat is transferred in the region where the cold fluid reaches this wall (great temperature gradients occur, see Fig. 12*d*). Moving along the hot wall the fluid is warmed up. Therefore, the heat transfer (represented by the local Nu) decreases. Due to the edge vortex in the corner of the hot wall and the radial wall at $\alpha = \alpha_{\max}$ (see Figs. 12*a*,*b*,*c*), fluid with a lower temperature is transported back to the hot wall. This effect leads to an increase of the local Nu number in this region. Similarly, at the cold inner cylindrical wall an analogous effect is found at $\alpha = 0$.

Results of Unsteady Calculations for a Rotating Closed Cavity. To identify some more basic features of this type of flow, unsteady calculations have been carried out for a special test geometry ($H/b = 1$, $r_m/b = 3$, section angle $\alpha = 45$ deg). This geometry is quite favorable for the comparison of the axial and radial heat flux situations because the characteristic length for the buoyancy effects, i.e., the distance L between the hot and cold walls, is the same in both cases. Thus, Re and Ra are the same for the two kinds of heat fluxes. Calculations are carried out for an axial and a radial heat flux (for $T_m = 575$ K, $Ra = 8 \times 10^5$, $Re = 6 \times 10^4$). Both calculations were started at $t = 0$ with a relative velocity field equal to zero and heat conduction as an initial condition for temperature field.

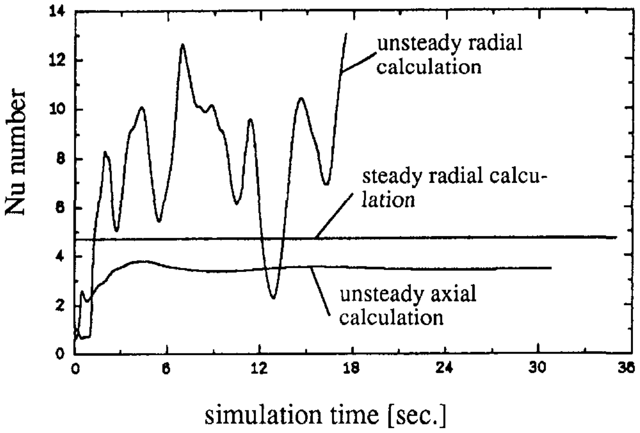

Fig. 14(*a*) Development of Nu for the axial and radial heat flux configurations

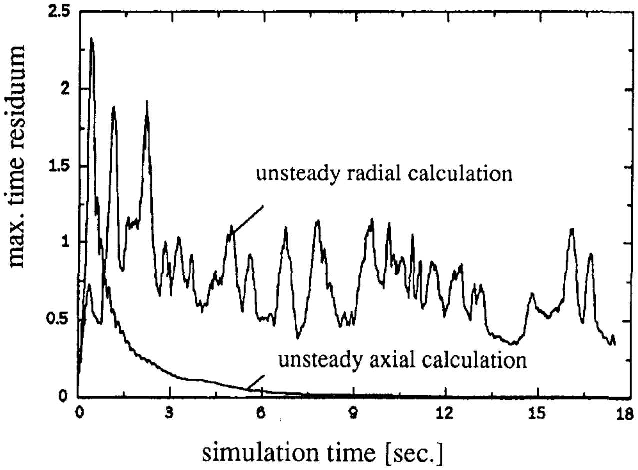

Fig. 14(*b*) Distribution of the maximum time residuum for the axial and radial heat flux configurations

To ensure time accuracy, the time step Δt was set very small. A CFL number defined by

$$CFL = u \cdot \Delta t / \Delta x$$

u = maximum relative velocity in the flow field
Δx = minimum distance of two grid points

may be used to characterize the unsteady conditions. This number was smaller than one for the unsteady calculations. The calculation of the radial heat flux configuration shown in Fig. 14 took more than 10,000 time steps.

In Fig. 14(*a*) the Nu number at the hot wall versus the time is plotted for the unsteady calculation of the axial heat flux configuration and the steady and unsteady simulation of the radial heat flux configuration.

In the axial case it can be seen that the unsteady calculation converges to steady state rather quickly. In Fig. 14(*b*) the distribution of the maximum time residuum from the conservation equations for each time step is plotted. In the axial case a strong increase of the residuum occurs at the beginning of the simulation followed by a continuous decrease.

The time-dependent distribution of Nu (Fig. 14*a*) for the radial heat flux configuration is irregular during the whole simulation time of 18 seconds. A more detailed flow simulation was not performed because of drastically increased CPU time requirement. The calculation was performed on an IBM 3090 Computer using the vector facilities and required more than 10 CPU hours. Additionally, Fig. 14(*a*) shows the value of Nu calculated with the steady state algorithm. For the unsteady calculation it is not possible at this time to deduce a tendency, i.e., whether the flow will converge to steady state or become periodic or even remain irregular.

An unsteady behavior of natural convection flow is well known from the Bénard convection. This type of flow can be approached by the rotating annulus with radial heat flux direction by setting a very large r_m/H ratio. The angular velocity ω must fit the condition that the centrifugal acceleration $\omega^2 r_m$ equals the gravity acceleration. The Coriolis forces are negligible for this extreme situation.

It is reported by many authors that the flow pattern of Bénard convection changes significantly several times with increasing Ra number. For Ra < 1700 no fluid motion at all is observed. At Ra numbers of about 10^4 a steady two-dimensional flow is established. With further increases of the Ra number the flow becomes periodically unsteady, then irregularly unsteady (thermals rising from the bottom and the top surface) and at last fully turbulent. (See Tritton, 1988, for details and further references.)

Summary and Conclusions

Investigations have been carried out on convective heat transfer in closed annuli rotating around their horizontal axes. A pure centripetal heat flux throughout the cavities was applied by heating the outer and cooling the inner cylindrical wall. Both lateral walls of the annular cavities were thermally insulated.

Measurements have been performed varying the Rayleigh number in a range usually encountered in the gas-filled cavities of gas turbine rotors ($10^7 < \mathrm{Ra} < 10^{12}$). Varying the ratio from $H/r_m = 0.96$ to $H/r_m = 0.63$ yields no significant influence on the Nu number. With the annulus divided into sections, by inserting radial separation walls, the influence of the Coriolis forces is reduced, resulting in an increase of heat transfer.

Theoretical investigations for the basic case of isothermal cylindrical walls and adiabatic side walls have been made for the sectored annular cavity. The calculations were carried out using a steady-state numerical algorithm. The results obtained for the convective heat transfer are consistent with the experiments.

In addition, unsteady calculations have been carried out for an axial and centripetal heat flux applied on the rotating annulus. For the axial heat flux steady-state conditions were reached rather quickly. For the centripetal heat flux, within 10 hours CPU time, no prediction can be made about whether the flow will become periodic, steady, or remain irregular.

The numerical results show that the flow inside the cavity may be affected by instability phenomena. From the experiments no information can be obtained about the flow structure. However, the heat losses through the side walls, which were inevitable during the experiment, could serve to stabilize the flow and to establish steady-state conditions. On the other hand, Zysina-Molozhen and Salov, who took photographs from the flow inside a rotating cavity with centripetal heat flux, note the absence of any regular fluid circulation contours.

Further experimental and theoretical investigations should work out the conditions for instability and show the influence of the thermal boundary conditions of the side walls on the flow and the heat transfer in the cavity.

Acknowledgments

The authors thank the Arbeitsgemeinschaft Hochtemperatur-Gasturbine (AG Turbo) for sponsoring the experimental research work. The AG Turbo is funded by German Gas Turbine Industry Companies and the Ministery of Research and Technology (BMFT).

References

Abell, S., and Hudson, J. L., 1975, "An Experimental Study of Centrifugally Driven Free Convection in a Rectangular Cavity," *Int. J. Heat Mass Transfer*, Vol. 18, pp.1415–1423.

Arkad'ev, B. A., 1965, "A Note on Free Convection in Turbine Cavities," *Journal of Engineering Physics*, Vol. 9, No. 1.

Bohn, D., Dibelius, G. H., Deuker, E., and Emunds, R., 1994, "Flow Pattern and Heat Transfer in a Closed Rotating Annulus," ASME Journal of Turbomachinery, Vol. 116, pp. 542–547.

Bohn, D., and Gorzelitz, V., 1992, "Experimental Investigations of Heat Transfer in a Gas-Filled Rotating Annulus," presented at the International Symposium on Heat Transfer in Turbomachinery, Athens, Greece; to be published by Hemisphere Publishing Corporation, New York.

Chew, J. W., 1985, "Computation of Convective Laminar Flow in Rotating Cavities," *J. Fluid Mech.*, Vol. 153, pp. 339–360.

Farthing, P. R., Long, C. A., Owen, J. M., and Pincombe, J. R., 1992, "Rotating Cavity With Axial Throughflow of Cooling Air: Heat Transfer," ASME Journal of Turbomachinery, Vol. 114, pp. 229–236.

Harada, I., and Ozaki, N., 1975, "A Numerical Study of the Thermal Spin-up of a Stratified Fluid in a Rapidly Rotating Cylinder," *Lecture Notes in Physics*, Vol. 35, pp. 197–203.

Hignett, P., Ibbetson, A., and Killworth, P. D., 1981, "On Rotating Thermal Convection Driven by Non-uniform Heating From Below," *J. Fluid Mech.*, Vol. 109, pp. 161–187.

Kapinos, V. M., Pustovalov, V. I., and Rudko, A. P., 1981, "Effect of Stabilization in Free Convection of a Cylindrical Rotating Enclosure," *Energeticeskoe masinostroenie*, No. 32, pp. 76–79 [in Russian].

Liang, S. F., Vidal, A., and Acrivos, A., 1969, "Buoyancy-Driven Convection in Cylindrical Geometries," *J. Fluid Mech.*, Vol. 36, Part 2, pp. 239–256.

Lin, T. Y., and Preckshot, G. W., 1979, "Steady-State Laminar Natural Convection in a Rotating Annulus," *Studies in Heat Transfer—A Festschrift for E.R.G. Eckert*, Hemisphere Publishing Corporation, Washington, DC, pp. 219–246.

Müller, M. R., and Burch, J. N., 1985, "An Experimental Study of the Behavior of Transient Isolated Convection in a Rigidly Rotating Fluid," *Experiments in Fluids*, Vol. 3, pp. 17–23.

Ong, C. L., and Owen, J. M., 1991, "Prediction of Heat Transfer in a Rotating Cavity With a Radial Outflow," ASME Journal of Turbomachinery, Vol. 113, pp. 115–122.

Owen, J. M., Pincombe, J. R., and Rogers, R. H., 1985, "Source-Sink Flow Inside a Rotating Cylindrical Cavity," *J. Fluid Mech.*, Vol. 155, pp. 233–265.

Patankar, S. V., and Spalding, D. B., 1972, "A Calculation Procedure for Heat, Mass and Momentum Transfer in Three-Dimensional Parabolic Flows," *Int. J. Heat Mass Transfer*, Vol. 15, pp. 1787–1806.

Tritton, D. J., 1988, *Physical Fluid Dynamics*, 2nd ed., Clarendon Press, Oxford, United Kingdom.

Zysina-Molozhen, L. M., and Salov, N. N., 1977, "Heat Exchange and Flow Regime of Liquids in a Closed Rotating Annular Cavity," *Soviet-Aeronautics*, Vol. 20, No. 1, pp. 39–43.

Z. Wang

P. T. Ireland

T. V. Jones

Department of Engineering Science,
University of Oxford,
Oxford, United Kingdom

An Advanced Method of Processing Liquid Crystal Video Signals From Transient Heat Transfer Experiments

A new method of processing the liquid crystal color change data obtained from transient heat transfer experiments is presented. The approach uses the full-intensity history recorded during an experiment to obtain an accurate measurement of the surface heat transfer coefficient at selected pixels. Results are presented for a model of a turbine blade cooling passage with combined ribs and film cooling holes. The implementation of the technique and the advantages to be gained from its application are discussed.

Introduction

Thermochromic liquid crystals exhibit wavelength-dependent reflectivity that changes with temperature. They are particularly suitable to the measurement of surface temperature over a complete area and have been used by many workers from different research groups to measure heat transfer coefficients. The crystals are supplied in a robust encapsulated form and are glued to the surface to form a layer between 10 and 20 μm thick. This temperature-sensitive coating is typically illuminated from a diffuse source and the reflected light monitored with a color CCD camera.

Two methods of measuring heat transfer coefficients are commonly used. The steady-state method, described by Baughn et al. (1989) and Hippensteele and Russell (1984), employs an electrical heater to provide a uniform heat flux boundary condition. The second method affects convective heat transfer by using a flow that is at a different temperature to the starting temperature of the test section (Ireland and Jones, 1986). The technique discussed here is based on the change in the optical signal from the temperature-sensitive coating during a transient heat transfer experiment.

Theory

Transient heat transfer measurements are made by exposing a model made from a thermal insulator to a flow at a different temperature. The surface temperature is analyzed under simplifying assumptions about the conduction process to yield the local heat transfer coefficient (Clifford et al., 1983). In the analysis, the conduction process is assumed to be one dimensional since, under experimental conditions, heat conducted in the direction parallel to the surface can be neglected compared to the heat flow normal to the surface. It is also reasonable to assume that the gas temperature change is accurately represented as a step function and that the thermal properties of the perspex do not change, as the model warms up, throughout the experiment. Liquid crystals are used to measure the surface temperature and the response of the crystal coating is recorded with a standard video system. The technique uses a video recording of the luminance signal to determine the surface temperature. The present work has concentrated on the automatic processing of video signals obtained from transient heat transfer experiments. The analysis method is unique in that it uses a record of the variation of the optical signal throughout a transient experiment. Other methods have processed image data from selected frames and used the surface color to calculate the temperature. Applications of the latter method have been reported by Camci et al. (1992) and Akino et al. (1988). Both methods are independent of the local strength of illumination, which usually varies over the surface of the model.

The intensity history was used by Davenport (1989) and Wang et al. (1990) to produce detailed distributions of local heat transfer coefficient. The intensity variation is shown at four selected locations in a model of a cooling passage in Fig. 1. The temperature-sensitive coating used by Wang (1991) consisted of a mixture of two encapsulated liquid crystals, which exhibited color play over two narrow temperature ranges. The redundancy introduced by the extra time measurement enabled the effect of the heat capacity of a coating of copper grains to be accounted for. The experimental times elapsed from the start of the test to the peak intensities were used in the analysis of video data at selected pixels. A similar double crystal approach was used by Vedula and Metzger (1991) to measure the heat transfer driving gas temperature as well as the local heat transfer coefficient downstream of a row of film cooling holes. The new method is an extension of this approach but is intrinsically more accurate. The improve-

---

Contributed by the International Gas Turbine Institute and presented at the 38th International Gas Turbine and Aeroengine Congress and Exposition, Cincinnati, Ohio, May 24–27, 1993. Manuscript received at ASME Headquarters March 10, 1993. Paper No. 93-GT-282. Associate Technical Editor: H. Lukas.

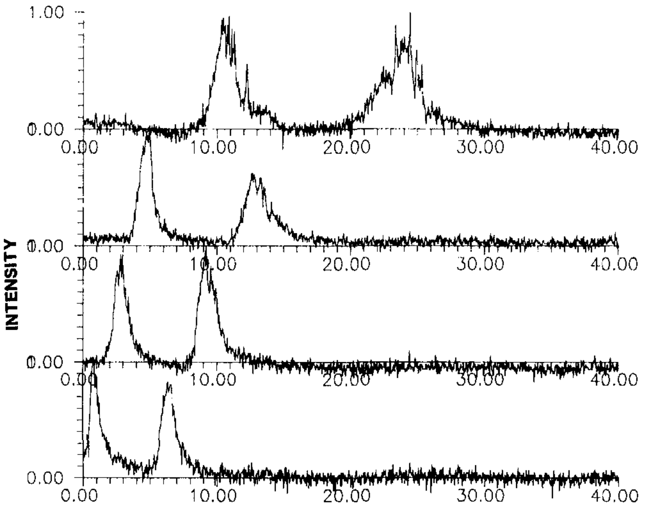

Fig. 1 Measured intensity histories at different locations employing two types of liquid crystal

ment in accuracy is achieved by using the full local intensity history to calculate the local heat transfer coefficients.

In order to explain the monochromatic processing technique used, a brief description of the tristimulus method of representing color is given in the following. The three signals from photosensitive detectors, which receive light through red, green, and blue filters are taken to be sufficient to represent color (Watt, 1989). The signals R, G, and B can be calculated from the illumination spectrum, $E(\lambda)$, and reflectance spectrum, $R(\lambda)$, by performing the following integrals:

$$R = \int_{-\infty}^{\infty} E(\lambda)R(\lambda)r(\lambda)d\lambda \quad (1)$$

$$G = \int_{-\infty}^{\infty} E(\lambda)R(\lambda)g(\lambda)d\lambda \quad (2)$$

$$B = \int_{-\infty}^{\infty} E(\lambda)R(\lambda)b(\lambda)d\lambda \quad (3)$$

where $r(\lambda)$, $g(\lambda)$, and $b(\lambda)$ are the filter transmissivities. In the case of the signal from a liquid crystal coated surface, the reflectance, $R(\lambda)$, is a function of temperature. To indicate this dependence, we will replace the surface reflectance with $R(\lambda, T)$ from this point.

Both the NTSC (American) and the PAL (European) broadcasting standards use three signals that are linearly related to R, G, and B. Only the Y signal, defined as

$$Y = 0.299R + 0.587G + 0.114B \quad (4)$$

is used when the video signal is processed in a monochrome sense. It should be noted that the current method uses the Y signal, although it could be used to process the other color variables such as hue.

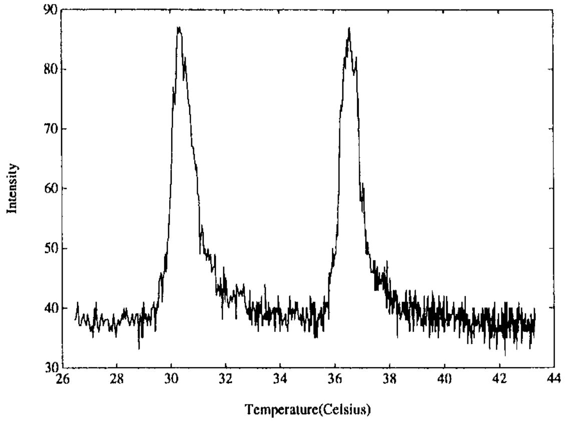

Fig. 2 Liquid crystal calibration

Equations (1)–(4) show that the intensity value Y is a function of the lighting $E(\lambda)$, the liquid crystal reflectance $R(\lambda, T)$, and the camera response. Assuming that the illumination at different locations on the surface varies only in total power and not in normalized spectral distribution ($e(\lambda)$, defined as $E(\lambda)/I$), Y can be rewritten

$$Y = I * \int_{-\infty}^{\infty} e(\lambda)R(\lambda, T)(0.299r(\lambda) + 0.587g(\lambda) + 0.114b(\lambda))d\lambda \quad (5)$$

which can be abbreviated

$$Y = I \times C[T] \quad (6)$$

Hence, the measured Y signal as the liquid crystal changes color is a function of the surface temperature and is proportional to the local lighting level. An example of a measured double crystal coating response is given in Fig. 2. Two liquid crystals are shown reaching their peak intensities at 30.5°C and 36.5°C. It is clear from the above that the absolute intensity level may vary with local lighting but the shape of the curve will be the same at all surface locations.

Earlier methods for processing monochrome signals from transient experiments have used one (or at most two) identifiable points on the intensity history to determine the surface temperature. For instance, Wang (1991) used the peak intensities from a double crystal coating in an automated image processing procedure. The basis of the new method is to utilize the entire calibration curve to process the data from transient heat transfer tests. During a transient heat transfer experiment, the surface temperature history is a function of the initial temperature, T_{initial}, the gas temperature, T_{gas}, the thermal product of the substrate, $\sqrt{\rho c k}$, and the local heat transfer coefficient h. The surface temperature, $T(t)$, can be expressed as

$$T(t) = T\left(t, h, T_{\text{gas}}, T_{\text{initial}}, \sqrt{\rho c k}\right) \quad (7)$$

Nomenclature

c = specific heat capacity
C = intensity function, Eq. (6)
$e(\lambda)$ = normalized illumination spectrum
$E(\lambda)$ = illumination intensity spectrum
h = heat transfer coefficient
I = local lighting intensity
k = conductivity
n = number of intensity samples
$r(\lambda), g(\lambda), b(\lambda)$ = red, green, and blue filter functions
$R(\lambda)$ = surface reflectance
R, G, B = red, green, and blue signals
t = time
T = surface temperature
Y = intensity (or luminance) signal
β = see Eq. (8)
λ = wavelength
ρ = density

Subscripts

gas = gas
initial = initial
1, 2 = measurement locations

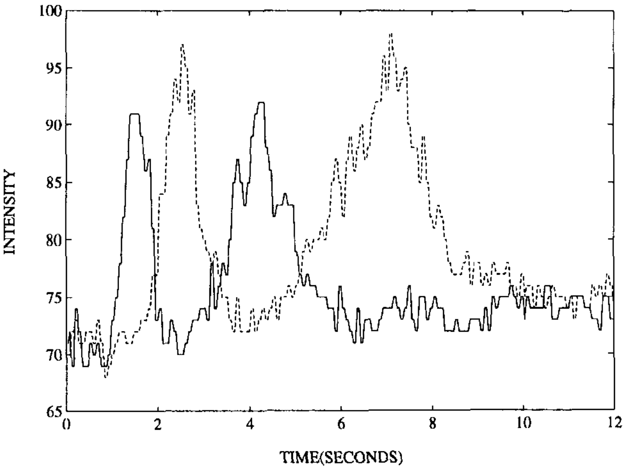

Fig. 3 Comparison of the intensity history at two locations

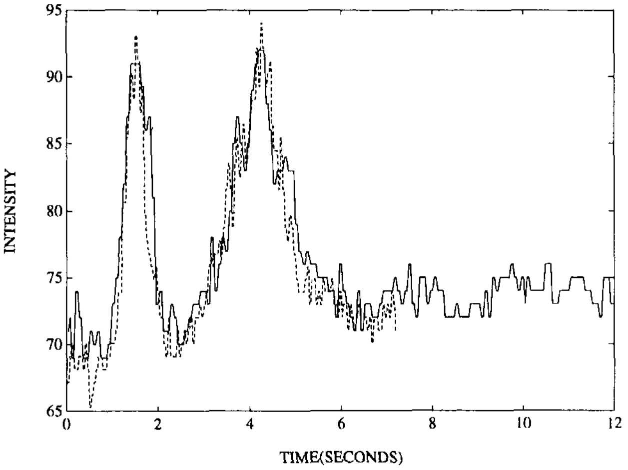

Fig. 4 Intensity data after scaling

where t represents time. When the expression for temperature from the equation above is used in Eq. (5), the intensity history $Y(t)$ is now a function of parameters I, h, T_{gas}, T_{initial}, and the properties of the substrate. It would be possible to use the spectral response of the camera and crystal together with the illumination spectrum to predict the functional form of Eq. (6). This predicted intensity history should match the intensity history measured during the test. When one (or more) of the parameters are unknown, their values can be determined by regression in which the discrepancy values between the measured and the predicted intensity histories are minimized. This intensity history matching method uses the complete profile of the measured data. It is therefore more accurate than techniques that use a single point to determine the surface temperature. It should also be noted that the method is equally applicable to processing any time varying parameter from a color signal. The calibration function, Eq. (5), would differ but regression could readily be used to determine the heat transfer coefficient ratio.

The method has been applied to the case most commonly encountered in transient liquid crystal heat transfer experiments. Specifically, this is a semi-infinite wall with known uniform initial temperature, which is subjected to a step change in fluid temperature. In this case the surface temperature is given by the following equation:

$$\frac{T(t) - T_{\text{initial}}}{T_{\text{gas}} - T_{\text{initial}}} = 1 - \exp(\beta^2)\operatorname{erf}c(\beta) \qquad (8)$$

where

$$\beta = \frac{h\sqrt{t}}{\sqrt{\rho c k}} \qquad (9)$$

Under these conditions, substitution for T in Eq. (5) yields

$$Y = I \times C\left[T\left(T_{\text{initial}}, (T_{\text{gas}} - T_{\text{initial}}), \frac{h\sqrt{t}}{\sqrt{\rho c k}}\right)\right] \qquad (10)$$

This equation shows that the intensity history at different locations for a particular experiment is only a function of local intensity, I, and dimensionless time $h\sqrt{t}/\sqrt{\rho c k}$. This means that the surface intensity histories as functions of dimensionless time, β, can be collapsed onto a single curve by multiplying by a factor that depends on I. In other words, if the local lighting intensity at one position was twice that at a second location, by multiplying the measured Y history for the former by one half we would be able to collapse the two signals as functions of dimensionless time.

Two intensity time signals for different model sites but for the same experiment are shown in Fig. 3. It can be seen that the local illumination intensity is greater for the data presented as the dashed line than for the continuous line measurements. Multiplying the dashed line intensity data by approximately 0.95 would drive the intensity levels for the peaks (and plateaux) to the same values. Under this operation, a new signal Y_2' is derived from Y_2:

$$Y_2' = \frac{I_1}{I_2} Y_2 \qquad (11)$$

Y_2', however, would still not match Y_1, the intensity history at model point one, since the heat transfer coefficients differ at the two sites. It is clear that, if the heat transfer coefficients were known, then it would be possible to calculate β in each case. Consideration of Eqs. (8)–(10) shows that Y_2' and Y_1 plotted as functions of β would then match exactly. This equation shows that β must be the same, for example, at the time of the first peak at both sites. Defining t_1 and t_2 to be the time for this event at the two locations, the ratio of the heat transfer coefficients could then be calculated from this condition

$$h_1\sqrt{t_1} = h_2\sqrt{t_2} \qquad (12)$$

since the thermal product is uniform. In other words, the h ratio follows from the time ratio

$$t_2 = \frac{h_1^2}{h_2^2} t_1 \qquad (13)$$

In practice, all of the measured intensity data and not just the first peak are used to determine the heat transfer coefficient ratio. it is numerically preferable to determine the factor, which, when multiplying the time measurements from the second point, produces the best match to the first intensity history. This process is illustrated graphically in Fig. 4 where the continuous line data from Fig. 3 have been replotted as a function of time. All of the time values for the dashed line (Fig. 3) data were multiplied by a chosen factor. The factor that produces the best agreement with the continuous line data has been applied to the dashed line time values and the data plotted as the crosses in Fig. 4. It follows from Eq. (12) that $(h_2/h_1)^2$ is equal to the chosen factor. If the heat transfer coefficient at the reference location is obtained by other means, the heat transfer coefficient distribution can be calculated from the heat transfer coefficient ratios over the full surface.

The determination of the time scaling factor is achieved by a least-squares regression. The objective of the regression is to minimize the difference between the two measured inten-

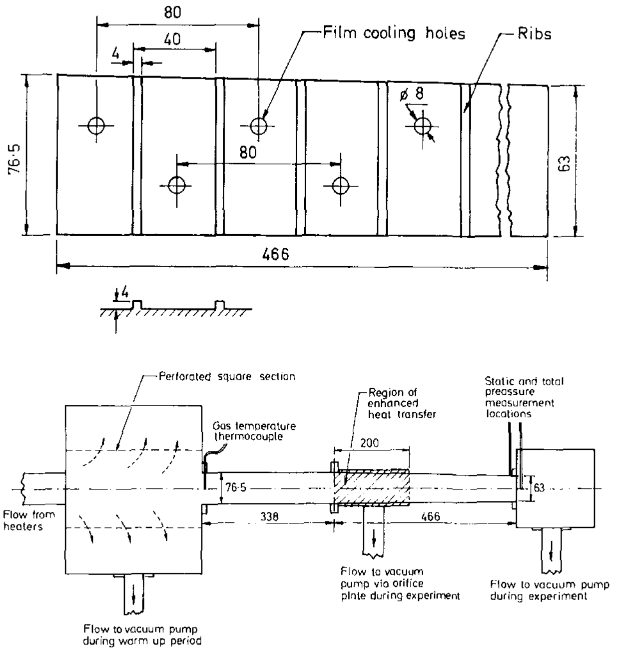

Fig. 5 Experimental apparatus

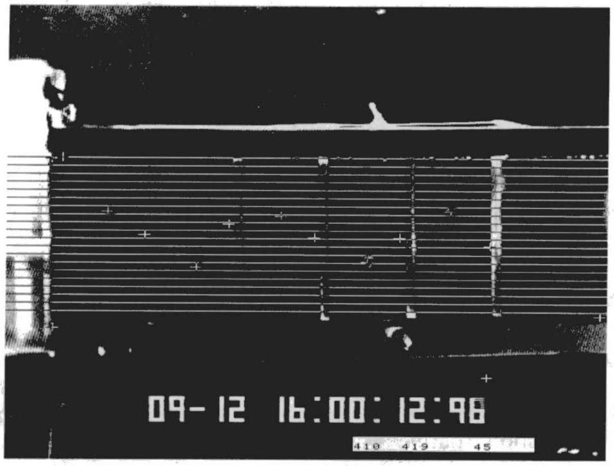

Fig. 6 Camera view of the experiment

sity histories. A target function is constructed as:

$$\Delta\left(\frac{h_1}{h_2},\frac{I_1}{I_2}\right)=\sum_{i=0}^{n}\left(Y_1(t_{1_t})-Y_2'(t_{2_i})\right)^2 * w_i \qquad (14)$$

in which n is the number of measurements, Y_2' is the sampled intensity history undergoing time axis scaling, and

$$w_i = 0.5 * \left(Y_1(t_{1_i}) + Y_2'(t_{2_i})\right) \qquad (15)$$

is included to increase the weighting of discrepancies at the liquid crystal peak locations. The target function would be zero if the intensity root time variations agreed exactly. The two ratios, h_1/h_2 and I_1/I_2, are obtained through regression by minimizing the target function. In this study, a commercially available subroutine, which uses the approach described in Gill and Murray (1972), was employed to accomplish the minimization. The application of the method developed is discussed in the following section.

Results

Figure 5 shows the model used in a transient liquid crystal heat transfer experiment. It simulates, at large scales, an internal passage of a turbine blade and has an entrance with uniform square cross-section followed by a converging square section. The flow from the heaters is drawn through the perforated square section in the left-hand box until the heaters have reached thermal equilibrium. The perspex model starts to be heated when fast-acting valves are actuated and the flow is rapidly switched through the test section. Heat transfer data were obtained over the region of the wall between the five ribs shown as the shaded area (detailed in the close-up). The liquid crystal surface was illuminated by two fluorescent strip lights aligned parallel to the flow section and placed above and below the transparent tunnel. It was demonstrated experimentally that the lights were sufficiently far from the wind tunnel to ensure that the illumination angle change over the surface did not affect the crystal calibration. The measurement of the enhancement in heat transfer coefficient in the presence of bleed to the film cooling holes was the subject of the experimental investigation. The test section wall is covered with a coating of two liquid crystals having the calibration shown in Fig. 2. The lines along which the liquid crystal color changes intensity histories are digitized are shown in Fig. 6. The digitized intensity history along one particular row of pixels is represented in Fig. 7. The vertical axis indicates time, which increases from the top downward. The crystal intensity at any pixel is indicated by the shade (grey level) of the figure. Pixel position along the digitized line corresponds to the horizontal position in the figure. Thus, the dark gray shade in the top left-hand corner shows that, at the start of the test, the liquid crystal was not undergoing color change at the upstream edge of the measurement zone. By moving down the left-hand edge, we can see that the crystal intensity, at this point in the tunnel, increased (the figure whitens) twice at approximately a quarter and three quarters of the way through the test. The distance of the middle of each white band from the top of the box is proportional to the time elapsed from test start to peak intensity (c.f. Fig. 2). The five bright vertical bands are at the locations of the ribs and are caused by the high reflectance of the rib tops. Figure 8 shows the intensity histories along the same line after scaling. In other words, the time axis has been multiplied by a (different) factor at each pixel, by choosing the heat transfer coefficient ratio that minimizes the target function, Eq. (14). After scaling, it can be seen that all of the intensity peaks occur at the same vertical location (scaled time). The heat transfer coefficient, normalized by that at the reference position, has thus been determined at each pixel.

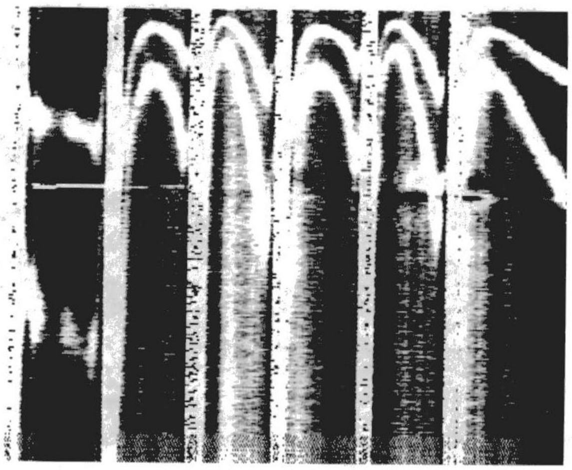

Fig. 7 Intensity history along one line of pixels

The heat transfer coefficients, normalized by that at the

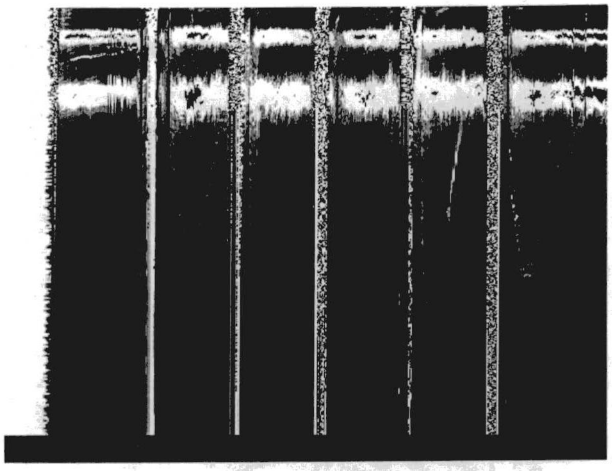

Fig. 8 Intensity history after scaling

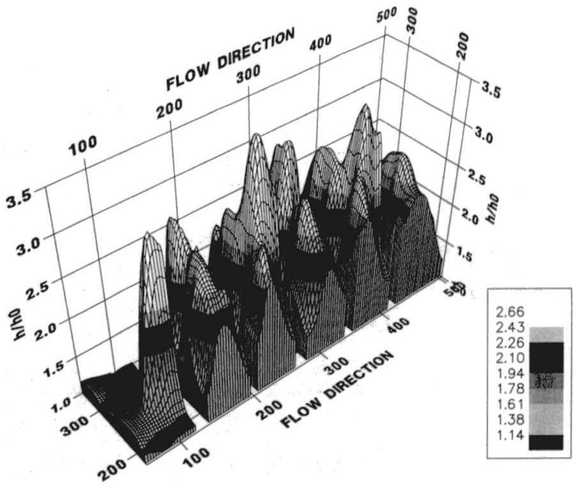

Fig. 10 Surface distribution of heat transfer coefficient ratio

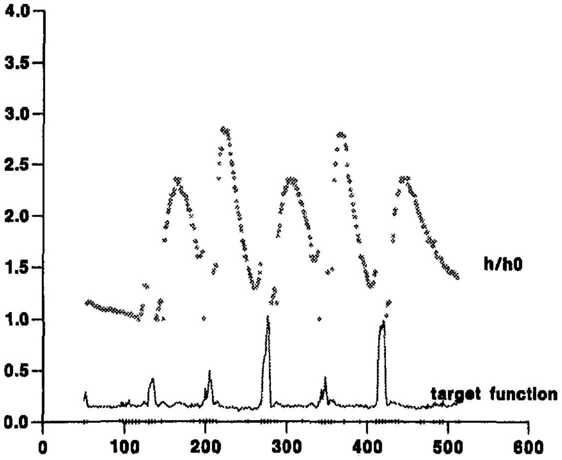

Fig. 9 Heat transfer coefficient ratio and the residual of the target function

reference position, are presented at the upper line in Fig. 9. At 510 points out of the 512 processed, the program gave the correct results without user interaction. The lower line shows the target function, Eq. (12), for the same line. The heat transfer enhancement over the complete surface was then obtained by interpolating between the results from 20 such lines. This surface distribution of heat transfer coefficient ratio is presented in Fig. 10. The results from this set of experiments are discussed by Shen et al. (1994).

Conclusions

A new method of processing video images from the transient liquid crystal heat transfer experiment has been described. The method has been implemented as a fully automated computer program, which does not require user interaction. Its use offers the following advantages over existing methods:

(*a*) A knowledge of the collapse of intensity variation on dimensionless time, β, has been applied to use all of the monochrome information available in the recorded video signal at the measurement locations. The accuracy of the method is thus better than transient methods, which determine the surface temperature by using only data at a limited number of specific calibrated reflectances.

(*b*) The method offers a unified processing method for any liquid crystal coating (i.e., any number of liquid crystals or any type of liquid crystal). The method is also suitable for color as well as the monochrome processing reported.

(*c*) It is possible to extend the type of transient heat transfer experiment that can be analyzed using the intensity history method. The above has considered the case of a uniform initial temperature and a known step change in gas temperature. If the calibration for intensity as a function temperature is determined, Eq. (6), then the regression analysis could be extended to determine other parameters such as the gas temperature or initial temperature.

A computationally economical procedure has been realized for the most common case in transient liquid crystal experiments. The test case shows that very detailed and accurate results have been obtained from the fully automated computer program.

Acknowledgments

This work has been carried out with the support of the UK Ministry of Defense and Rolls-Royce P.L.C. The technical assistance of Mr. P. J. Timms was also much appreciated. The liquid crystals were supplied by Hallcrest LCT and the minimization routine was from the Numerical Algorithms Group Ltd.

References

Akino, N., Kunugi, T., Ueda, M., and Kurosawa, X., 1988, "Liquid Crystal Thermometry Based on Automatic Color Evaluation and Applications to Measure Turbulent Heat Transfer," *Transport Phenomena in Turbulent Flows*, Hemisphere, Washington, DC, pp. 807–820.

Baughn, J. W., Ireland, P. T., Jones, T. V., and Saniei, N., 1989, "A Comparison of the Transient and Heated-Coating Methods for the Measurement of Local Heat Transfer Coefficients on a Pin Fin," ASME *Journal of Heat Transfer*, Vol. 111, pp. 877–881.

Camci, C., Kim, K., and Hippensteele, S. A., 1992, "A New Hue Capturing Technique for Quantitative Interpretation of Liquid Crystal Images Used in Convective Heat Transfer Studies," ASME JOURNAL OF TURBOMACHINERY, Vol. 114, pp. 765–775.

Clifford, R. J., Jones, T. V., and Dunne, S. T., 1983, "Techniques for Obtaining Detailed Heat Transfer Coefficient Measurements Within Gas Turbine Blade and Vane Cooling Passages," ASME Paper No. 83-GT-58.

Davenport, R., 1989, "Innovative Use of Thermochromic Liquid Crystals for Turbine Blade Internal Cooling Passage Flow Visualisation and Heat Transfer Measurements," *Proceedings of European Propulsion Forum, Modern Techniques and Developments in Engine and Component Testing*, Royal Aeronautical Society, 16.1–16.5

Gill, P. E., and Murray, W., 1972, "Quasi-Newton Methods for Unconstrained Optimization," *Journal of the Institute of Mathematics and Its Applications*, Vol. 9, pp. 91–108.

Hippensteele, S. A., and Russell, L. M., 1984, "Use of a Liquid-Crystal, Heater-Element Composite for Quantitative, High-Resolution Heat Transfer Coefficients on a Turbine Airfoil, Including Turbulence and Surface Roughness Effects," NASA TM 87355.

Ireland, P. T., and Jones, T. V., 1986, "Detailed Measurements of Heat Transfer on and Around a Pedestal in Fully Developed Passage Flow," *Proceedings of 8th International Heat Transfer Conference*, Hemisphere, Washington, DC, pp. 975–980.

Shen, J. R., Wang, Z., Ireland, P. T., and Jones, T. V., 1994, "Heat Transfer Enhancement Within a Turbine Blade Cooling Passage Using Ribs and Combinations of Ribs With Film Cooling Holes," ASME Paper No. 94-GT-232; to be published in the *Transactions of the ASME*.

Vedula, R. J., and Metzger, D. E., 1991, "A Method for the Simultaneous Determination of Local Effectiveness and Heat Transfer Distributions in Three-Temperature Convective Situations," ASME Paper No. 91-GT-345.

Wang, Z., Ireland, P. T., and Jones, T. V., 1990, "A Technique for Measuring Convective Heat Transfer at Rough Surfaces," ASME Paper No. 90-GT-300.

Wang, Z., 1991, "The Application of Thermochromic Liquid Crystals to Detailed Turbine Blade Cooling Measurements," D. Phil Thesis, Department of Engineering Science, University of Oxford, United Kingdom.

Watt, A., 1989, *Three Dimensional Computer Graphics*, Addison Wesley, Chap. 14.

A Numerical Simulation of a Brush Seal Section and Some Experimental Results

M. J. Braun

V. V. Kudriavtsev

Department of Mechanical Engineering,
The University of Akron,
Akron, OH 44325

The brush seal technology represents quite a promising advance in the effort of construction of more efficient, and possibly smaller size engines. Conclusions of recent workshops determined that while the brush seal works well, there is a need to improve its performance characteristics. The considerable amount of experimental work performed to date has indicated the importance of the local flow phenomena in the global sealing process performance of the brush (Braun et al., 1990a, 1991b, 1992; Hendricks et al., 1991a). The distributed flow and pressure fields are thus of vital importance for the prediction of the possible sudden failure of the brush seal under unexpected local "pressure hikes." It is in this context that the authors developed a numerical, two-dimensional time accurate dependent formulation of the Navier–Stokes equations with constant properties, and included the effects of inertia, viscous, and pressure terms. The algorithm is applied to a set of noncompliant multirow, multicolumn pin configurations that are similar to the ones found in an idealized brush seal configuration. While the numerical parametric investigation aims at establishing the occurrence of major flow patterns and associated pressure maps, the experimental portion of the paper is aimed at gaining further insight into the relevant flow structures, and thus guiding the development of the mathematical and numerical models.

I Introduction

Turbomachine seals control leakage, dynamics, and tolerance to boundaries, and manage lubricant flow. As all these functions affect engine performance, it is important to understand both their interdependence and fundamental aspects. From the many types of contacting or noncontacting seal that are used in turbomachinery applications, this paper will treat the subject of the brush seal. In particular, we shall present a numerical model for flow in a generic array of brushlike pins, and the experimental work conducted for guidance and qualitative validation of the numerical effort.

The reduced leakage and physical compliance of the brush body to external perturbing factors are features that stand out in turbomachinery applications where there are expected boundary variations due to mass flow, brush fibers' pressure compliance, temperature, and time-dependent eccentric shaft motion. All these features have made the brush configuration an especially interesting and worthy candidate. The geometric configuration of a simulated brush seal is shown in Fig. 1(A). Recently, among others, Chupp and Dowler (1993) and Braun et al. (1990a, 1991a, 1992) have published extensive experimental information concerning the nature of the flow and pressure drops in a brush, and formulated theoretical models that explain the physical concept of sealing, and the functionality of the brush seal (Braun et al., 1990b).

The initial concept of such a seal has been investigated by General Electric many years ago (1955) under the J-47 engine test program. In the 1980s, Rolls-Royce (RR) has successfully introduced a brush seal (manufactured by Cross Mgf. Ltd. (CML)) on a demonstrator engine, and tested it for several thousand hours (Fergusson, 1988). More recently EG & G Sealol, Technetics, and Detroit-Allison have implemented full programs of study of this type of seal. Unfortunately, a large amount of the data generated by industry is restricted.

Following experiments done by CML, Flower (1990) cited leakages that are approximately 5 to 10 percent of those found in finned labyrinth configurations. The brushes manufactured by CML have been eventually incorporated in the RR design of the IAE V2500. Detroit-Allison has also reported successful incorporation of brush seals in some of their engines. According to Holle and Krishman (1990), the T800 engine was tested with a brush seal located at the turbine discharge, while the T406 Plus engine contained 13 brush seals between the compressor interstages. Experiments performed at Teledyne CAE (Chupp et al., 1991) have also shown that the leakages are reduced by a factor of four to seven, and the leakage performance follows a hysteresis curve dependent on the shaft speed excursions. Gorelov et al. (1988) examined the effects of the brush seal's geometric

---

Contributed by the International Gas Turbine Institute and presented at the 38th International Gas Turbine and Aeroengine Congress and Exposition, Cincinnati, Ohio, May 24–27, 1993. Manuscript received at ASME Headquarters March 3, 1994. Paper No. 93-GT-398. Associate Technical Editor: H. Lukas.

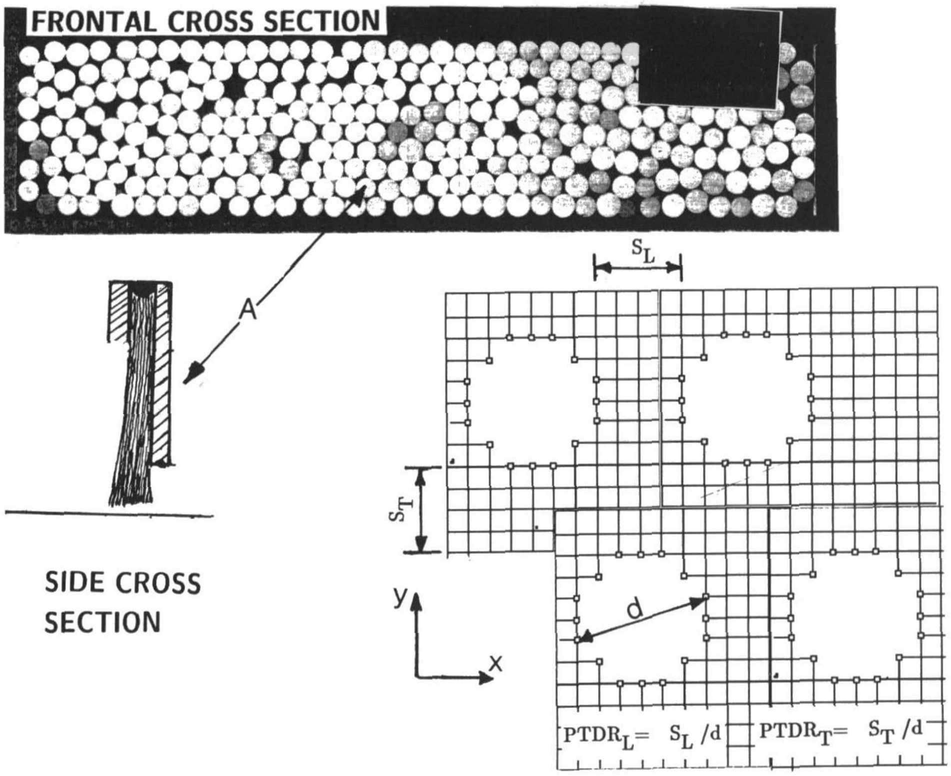

Fig. 1 Brush seal geometry: (A) physical configuration; (B) computational grid

parameters on the leakage flow rate of air, and compared them with data available from labyrinth seals. Braun et al. (1990a, 1991a, 1992) studied nonintrusively the fundamental flow patterns and reconstructed graphically the fluid velocities inside a cascade of brushes. The flow field was visualized by means of the Full Flow Field Tracking (FFFT) method, and revealed regions that are characterized by river jetting, and vortical or crossflow formations that exist upstream, downstream, or within the seal. These patterns are caused by variations in fiber void that are spatial and temporal, and affect changes in seal leakage and stability. The morphological deformation of the brushes was determined to be a function of upstream pressure and the magnitude of the mass flow leakage. The pressure measured during these experi-

Nomenclature

$\mathcal{C}_x(u)$, $\mathcal{C}_y(u)$, $\mathcal{C}_x(v)$, $\mathcal{C}_y(u)$ = first-order conservative upwind approximation for convective terms
d = pin diameter
Eu = $P_o/\rho U_o^2$; Euler number
h = channel height
p = pressure, Pa (lb/in.^{2})
$P = p/P_o$; $P_o = \rho U_0^2$, Eu = 1
$\text{PTDR}_L = S_L/d$; longitudinal pitch-to-diameter ratio
$\text{PTDR}_T = S_T/d$; transverse pitch-to-diameter ratio
$\mathcal{Q}_y(p)$, $\mathcal{Q}_x(p)$ = second-order central finite difference for the pressure terms
$\mathcal{Q}(u, v)^{n+1}$ = finite difference approximation of the source terms in the Poisson equation
$\text{Re}_h = U_o h\rho/\mu$; Reynolds number based on channel height
$\text{Re}_d = U_o d\rho/\mu$; Reynolds number based on pin diameter
S_L = longitudinal pitch
S_T = transverse pitch
t = time, s
u, v = fluid velocities, m/s (ft/sec)
$T_0 = h/U_o$; time scale
$T = t/T_o$; dimensionless time
$U = u/U_o$; dimensionless velocity in X direction
U_o = free-stream velocity, m/s (ft/sec)
$V = v/U_o$; dimensionless velocity in Y direction
$X = x/h$; dimensionless coordinate
$Y = y/h$; dimensionless coordinate
$\Lambda_{xx}(u)$, $\Lambda_{yy}(u)$ = second-order central finite difference for diffusion terms, u direction
$\Lambda_{xx}(v)$, $\Lambda_{yy}(v)$ = second-order central finite difference for the diffusion terms, v direction
$\Lambda_{xx}(p)$, $\Lambda_{yy}(p)$ = second-order central finite difference for pressure terms in the Poisson equation
μ = dynamic viscosity, N · s/m^2 (lb · s/ft^2)
ρ = fluid density, kg/m^3 (lb/ft^3)
σ = pseudo-time step, the pressure equation
$\Delta\tau$ = real time step

ments fell monotonically across the brush. Pressure inversions were observed due to peculiar flow patterns that form immediately downstream of the brush. Braun et al. (1991b) studied the effects of the brush morphology on the leakage path, and mapped the ensuing pressure drops. Through visual observation, the authors identified three major types of flow resistance networks that are instrumental to brush performance, and to its failure modes. It has been found that high brush resistance to throughflow can result in sudden catastrophic failure of the seal, while at lower brush resistance the failure is gradual. Hendricks et al. (1991a) reported experimental brush seal leakage rates in air for different cases of brush-rotor radial clearance. The authors found that leakages were greatly altered by bristle hysteresis, or inlet flow variations. It was generally concluded that configurations that contain series of brushes allow higher pressure drops, are more insensitive to shaft speed excursions, and significantly reduce the leakage level.

Presently, there is a strong ongoing numerical effort to simulate the hydraulic behavior and performance of the brush seal. Braun et al. (1990b) and Hendricks et al. (1991b) have developed a bulk flow model based on the porosity concept. Their analysis predicts the pressure and leakage performance as a function of bristle configuration, "porosity," deformation, interface loading, and type of brush interference with the rotating shaft. The authors identified five design similitude parameters: load per unit length, bristle tip pressure, Reynolds number, interface wear and heating, and fatigue life. The model indicated an abrupt upward change in leakage flow when the compliant interface of the brush changes from interference fit to hydrodynamic lubrication. Trend-wise, for the interference fit, these results compare favorably with experimental results reported by Flower (1990), even though the abrupt changes predicted by the model (due to change in the lubrication regime) do not appear in Flower's reported data. Another leakage flow model is reported by Chupp et al. (1991). While the basic premise of the model is similar to that advanced by Braun et al. (1990b) and Hendricks et al. (1991b), the only parameter considered is the effective brush thickness. Chupp et al. (1991) showed that the single-parameter model has the capability to predict pressure drops and temperature rises, when compared to experimental data generated by Teledyne CAE and Detroit-Allison.

II Scope of the Present Work

Conclusions of a recent brush seal workshop (Liang, 1991) indicate that there is a need to improve the performance characteristics of the brush seals. Such a goal can be achieved by using cascades of brushes, nonhomogeneous brush morphology, "nonconventional" brush structure design (Hendricks et al., 1992), and in general, a process of optimization of brush design parameters (Griner, 1991). The concept employed by the lumped bulk flow numerical models (Braun et al., 1990b; Hendricks et al., 1991b; Chupp et al., 1991) cannot predict local brush compliance, and the associated **local** flow and pressure patterns. Neither can the empirical formulas used for the calculation of the pressure drops in an array of tubes (Zukauskas, 1972). The importance of the **local** flow phenomena in the sealing process is paramount to the global performance of the brush (Braun et al., 1990a, 1991b, 1992; Hendricks et al., 1991a). The **distributed** velocity fields (u, v), and the associated pressure maps are of vital importance for the prediction of the **average** pressure drop, or the possible sudden failure of the brush seal under unexpected local "pressure hikes." The momentum carried by these velocities, or the upstream pressure, can force the brush deformation, and can create favorable conditions for the brush "opening," followed by seal failure (Braun et al., 1991b).

It is in this context that the development and validation of a numerical model with distributed primitive variables (u, v, p) becomes important. The **numerical parametric** investigation aims to simulate the occurrence of major flow patterns and associated pressure maps that characterize the geometry under study. The **experimental portion** of the paper is aimed at gaining further insight into the relevant flow structures, and guiding the development of the mathematical and numerical models.

III Development of the Analytical and Numerical Models

III.1 Mathematical Model. "Unexpected" local recirculation, reverse and lateral flows between the rows of the brush, or downstream of the brush zone, appear to play a major role in the sealing process. What's more, the compliance of the brush body generates an ever-changing geometry during operation and requires continuous prediction of the bristle position. It was shown that the operating environment of a brush seal will generate component flows that are mainly directed (i) normally to the brush surface (crossflow due to the pressure difference between the upstream and downstream of the brush), and (ii) circumferentially (due to the shaft rotation and its interaction with the stationary brush). While the rotation Reynolds number is rather high $\mathrm{Re}_{\mathrm{rot}} = 10^4\text{–}10^6$, the leakage Reynolds number associated with the crossflow is, by comparison, relatively low, $\mathrm{Re}_{\mathrm{leak}} = 10^2\text{–}10^3$. Such low velocities justify both the laminar and incompressible assumptions used in the numerical model.

If one considers a uniform flow with zero angle of incidence past an array of round cylinders (pins), Fig. 1, the two-dimensional Navier–Stokes equations for unsteady incompressible viscous flow in a Cartesian coordinate system can be written in dimensionless conservative form as

$$\frac{\partial U}{\partial T} + \frac{\partial (UU)}{\partial X} + \frac{\partial (UV)}{\partial Y} = -\mathrm{Eu}\frac{\partial P}{\partial X} + \frac{1}{\mathrm{Re}}\left(\frac{\partial^2 U}{\partial X^2} + \frac{\partial^2 U}{\partial Y^2}\right) \quad (1)$$

$$\frac{\partial V}{\partial T} + \frac{\partial (VV)}{\partial Y} + \frac{(\partial UV)}{\partial X} = -\mathrm{Eu}\frac{\partial P}{\partial Y} + \frac{1}{\mathrm{Re}}\left(\frac{\partial^2 V}{\partial X^2} + \frac{\partial^2 V}{\partial Y^2}\right) \quad (2)$$

The continuity equation (for constant properties) is

$$\frac{\partial U}{\partial X} + \frac{\partial V}{\partial Y} = 0 \quad (3)$$

where Re and Eu are the Reynolds and Euler numbers, respectively. One should note that the characteristic length used in this study is the vertical size of the physical domain (h) while the time scale is determined by the division of this length by the free stream velocity U_o. Taking the divergence of the X- and Y-momentum equations, and using continuity for simplification, one obtains a pressure equation that appears under a Poisson-type format.

$$\mathrm{Eu}.\nabla^2 P = -\frac{\partial^2 (U^2)}{\partial X^2} - 2\frac{\partial^2 (UV)}{\partial X \partial Y} - \frac{\partial^2 (V^2)}{\partial Y^2} + \left\{-\frac{\partial \mathfrak{D}}{\partial T} + \frac{1}{\mathrm{Re}}\left(\frac{\partial^2 \mathfrak{D}}{\partial X^2} + \frac{\partial^2 \mathfrak{D}}{\partial Y^2}\right)\right\} \quad (4)$$

One can see that the dilation term, $\mathfrak{D} = \partial U/\partial X + \partial V/\partial Y$, is similar to the continuity equation, and during calculations represents the residual that has to become identically zero if the continuity is to be satisfied. This is a necessary but not a sufficient condition for the convergence of pressures in Eq. (4).

III.2 Boundary and Initial Conditions

The Momentum Equation. The boundary conditions on the lateral solid walls assume nonslip conditions and nonporous walls. At the pin array entrance the velocity is assumed to be uniform with $U = 1$, $V = 0$ (angle of incidence is zero). A reference pressure is assigned to one point on the inflow boundary. At the exit, the flow is allowed to develop naturally with the boundary conditions for velocities derived from the satisfaction of the continuity equation:

$$\frac{\partial U}{\partial X} = -\frac{\partial V}{\partial Y}; \quad \text{and} \quad \frac{\partial V}{\partial X} = 0 \tag{5}$$

Boundary Conditions for the Poisson Equation. The dynamic pressures on the inflow and outflow boundaries are allowed to float and were determined through the balance of the normal forces with the inertia and viscous forces. The effects of the terms $\partial U/\partial T$ and $\partial V/\partial T$ both at inflow and outflow have been considered negligible. Thus one obtains

$$\frac{\partial P}{\partial X} = -\frac{1}{\text{Eu}}\left[\frac{\partial(UU)}{\partial X} + \frac{\partial(UV)}{\partial Y}\right] + \frac{1}{\text{Re}\cdot\text{Eu}}\left(\frac{\partial^2 U}{\partial X^2} + \frac{\partial^2 U}{\partial Y^2}\right);$$
$$\text{at} \quad X = 0; \quad X = 1; \quad \text{and} \quad 0 < Y < 1 \tag{6}$$

On the noncontiguous internal boundaries of the pins, in addition to Eq. (6), one needs to add an expression for $\partial P/\partial Y$

$$\frac{\partial P}{\partial Y} = -\frac{1}{\text{Eu}}\left[\frac{\partial(UV)}{\partial X} + \frac{\partial(VV)}{\partial Y}\right] + \frac{1}{\text{Re}\cdot\text{Eu}}\left(\frac{\partial^2 V}{\partial X^2} + \frac{\partial^2 V}{\partial Y^2}\right) \tag{7}$$

This formulation is independent of the internal boundary configuration.

At the channel's upper and lower walls the pressure boundary condition takes a simplified form due to the fact that $U = V = 0$

$$\frac{\partial P}{\partial Y} = \frac{1}{\text{Re}\cdot\text{Eu}}\left(\frac{\partial^2 V}{\partial Y^2}\right);$$
$$\text{at} \quad Y = 0; \quad Y = 1; \quad \text{and} \quad 0 < X < 1 \tag{8}$$

Initial Conditions ($T = 0$). The velocities are given as $U = 1$, $V = 0$. The pressures are set initially to $P = P_{\text{ref}} =$ const.

III.3 Numerical Implementation and Solution Procedure.

The finite difference method applied here uses a collocated uniform grid throughout the entire domain. The geometric details of the grid and the layout of the array of pins are shown in Fig. 1(B). The discretization of the system of governing equations follows through the use of the alternating direction iteration method (ADI). The procedure uses the full direct approximation of each term within the differential equation on every half time step, $\Delta\tau/2$. One obtains the following system of linear algebraic equations:

$$\frac{u^{n+1/2} - u^n}{\Delta\tau/2} = \frac{1}{\text{Re}}\left[\Lambda_{xx}(u)^{n+1/2} + \Lambda_{yy}(u)^n\right] + \mathcal{C}_x(u)^{n+1/2} + \mathcal{C}_y(u)^n + \mathcal{Q}_x(p)^n \tag{9}$$

$$\frac{u^{n+1} - u^{n+1/2}}{\Delta\tau/2} = \frac{1}{\text{Re}}\left[\Lambda_{xx}(u)^{n+1/2} + \Lambda_{yy}(u)^{n+1}\right] + \mathcal{C}_x(u)^{n+1/2} + \mathcal{C}_y(u)^{n+1} + \mathcal{Q}_x(p)^n \tag{10}$$

$$\frac{v^{n+1/2} - v^n}{\Delta\tau/2} = \frac{1}{\text{Re}}\left[\Lambda_{xx}(v)^{n+1/2} + \Lambda_{yy}(v)^n\right] + \mathcal{C}_x(v)^{n+1/2} + \mathcal{C}_y(v)^n + \mathcal{Q}_y(p)^n \tag{11}$$

$$\frac{v^{n+1} - v^{n+1/2}}{\Delta\tau/2} = \frac{1}{\text{Re}}\left[\Lambda_{xx}(v)^{n+1/2} + \Lambda_{yy}(v)^n\right] + \mathcal{C}_x(v)^{n+1/2} + \mathcal{C}_y(v)^{n+1} + \mathcal{Q}_y(p)^n \tag{12}$$

$$\frac{p^{s+1/2,n+1} - p^{s,n+1}}{\sigma} = \Lambda_{xx}(p)^{s+1/2,n+1} + \Lambda_{yy}(p)^{s,n+1} + \mathcal{Q}(u,v)^{n+1} \tag{13}$$

$$\frac{p^{s+1,n+1} - p^{s+1/2,n+1}}{\sigma} = \Lambda_{xx}(p)^{s+1/2,n+1} + \Lambda_{yy}(p)^{s+1,n+1} + \mathcal{Q}(u,v)^{n+1} \tag{14}$$

All the spatial derivatives except those of the convection terms and cross-derivatives are approximated by a second-order central finite difference. For the convection terms we employed the first-order conservative scheme proposed by Torrance (1968). This scheme contributes to the stability of the whole computational process, and proves to handle well conditions of high and intermediate convection (Roach, 1982). While the computations presented herein use a first-order scheme, an alternate higher-order scheme for the treatment of convective terms was also considered. The deferred-correction (DC) concept utilizes a two-dimensional version of the third-order scheme proposed by Kudriavtsev (1991, 1992) and Hayase et al. (1992). The outflow boundary conditions for the momentum equations, Eq. (5), can be written in operator finite difference form as

$$\mathcal{C}_x(u)^{n+1} = -\mathcal{C}_y(v)^n \tag{15}$$

$$\mathcal{C}_x(v)^{n+1} = 0 \tag{16}$$

At the test section inlet the velocities are prescribed as

$$u_{1j} = 1; \quad v_{1j} = 0; \quad \text{for} \quad 1 < j < M \tag{17}$$

and on the channel walls as

$$u_{i1} = 0; \quad v_{i1} = 0; \quad \text{for} \quad 1 < i < N \tag{18}$$

$$u_{iM} = 0; \quad v_{iM} = 0; \quad \text{for} \quad 1 < i < N \tag{19}$$

On the internal boundaries (B) one can write generally the boundary condition as

$$u_{B,ij} = 0 \quad \text{and} \quad v_{B,ij} = 0 \tag{20}$$

The pressure boundary conditions represented by Eqs. (6) and (7) can be written in operator finite difference form as

$$\mathcal{Q}_x(p)^{n+1} = \frac{1}{\mathrm{Re}\cdot\mathrm{Eu}}\left[\Lambda_{xx}(u)^{n+1} + \Lambda_{yy}(u)^{n+1}\right] + \frac{1}{\mathrm{Eu}}\left[\mathcal{C}_x(u)^{n+1} + \mathcal{C}_y(u)^{n+1}\right] \quad (21)$$

$$\mathcal{Q}_y(p)^{n+1} = \frac{1}{\mathrm{Re}\cdot\mathrm{Eu}}\left[\Lambda_{xx}(v)^{n+1} + \Lambda_{yy}(v)^{n+1}\right] + \frac{1}{\mathrm{Eu}}\left[\mathcal{C}_x(v)^{n+1} + \mathcal{C}_y(v)^{n+1}\right] \quad (22)$$

while that of Eq. (8) takes the form of

$$\mathcal{Q}_y(p)^{n+1} = \frac{1}{\mathrm{Re}\cdot\mathrm{Eu}}\left[\Lambda_{yy}(v)^{n+1}\right] \quad (23)$$

Solution Procedure. When the boundary conditions are combined with Eqs. (9) through (14), the entire system of linear algebraic equations becomes self sufficient. The solution follows according to the time-dependent ADI method using a tridiagonal matrix algorithm (TDMA). The steps of the solution are as follows:

- solve in the X direction for the U velocity at the $n + 1/2$ time step, Eq. (9)
- solve in the Y direction for the U velocity at the $n + 1$ time step, Eq. (10)
- solve in the X direction for the V velocity at the $n + 1/2$ time step, Eq. (11)
- solve in the Y direction for the V velocity at the $n + 1$ time step, Eq. (12)
- solve the Poisson equation of pressure at the $n = 1$ time step by means of the pseudo-transient method: (*i*) in the X direction at the $s + 1/2$ time ste, Eq. (13), and (*ii*) in the Y direction at the $s + 1$ time step, Eq. (14).

The pseudo-time marching form of the Poisson equation allows a stable implicit implementation of the TDMA solver with the ADI method, thus enabling faster iterative convergence of the computations (Washpress, 1966).

IV Iterative Convergence and Accuracy Considerations

The code verifications were performed for start-up flows (low time T), on grids of 31 × 31 and 61 × 61 points, respectively, with a range of Reynolds numbers of $\mathrm{Re}_h = 2500, \ldots 25{,}000$ (or $\mathrm{Re}_d = 500, \ldots 5000$). The verification concerned the flow and pressure fields around a body of cylindrical cross section, of diameter 0.2, positioned in the center of a square channel ($h = 1.0$).

Table 1 Iterative convergence on 31 × 31 grid; $\mathrm{Re}_h = 25{,}000$ ($\mathrm{Re}_d = 5000$)

n_f	$p_{\mathrm{tr.edge}}$	$\Delta p_{\mathrm{tr.edge}}$	p_{in}	p_{out}	CPU
32	99.330	0.768	100.098	99.030	142.16
16	99.330	0.768	100.098	99.030	75.73
8	99.333	0.766	100.099	99.033	42.75
5	99.337	0.763	100.100	99.038	30.11
3	99.318	0.782	100.099	99.012	22.05
1	99.395	0.708	100.103	99.122	13.77

Table 2 Iterative convergence on 61 × 61 grid; $\mathrm{Re}_h = 25{,}000$ ($\mathrm{Re}_d = 5000$)

n_f	$p_{\mathrm{tr.edge}}$	$\Delta p_{\mathrm{tr.edge}}$	p_{in}	p_{out}	CPU
16	99.031	1.020	100.051	99.013	297.32
8	99.032	1.019	100.051	99.014	166.36
5	99.031	1.021	100.051	99.012	117.18
3	99.031	1.021	100.052	99.013	84.47
1	99.024	1.031	100.054	99.006	51.78

Table 3 Iterative convergence for $\mathrm{Re}_h = 2500$ ($\mathrm{Re}_d = 500$)

n_f	$p_{\mathrm{tr.edge}}$	$\Delta p_{\mathrm{tr.edge}}$	p_{in}	p_{out}
grid 31x31				
16	99.208	0.865	100.073	98.902
8	99.208	0.866	100.074	98.902
3	99.199	0.876	100.075	98.888
1	99.269	0.809	100.078	98.985
grid 61x61				
8	99.034	0.916	99.95	98.98

The iterative convergence was checked for both u and v velocities. The pressure field convergence was monitored through its calculated average value across the cross section. In order to obtain an optimal combination of accuracy, computational stability and computational costs, we used a pseudo-time step of $\sigma = 0.025$ (computations marched to time $T = 1$, with a $\Delta\tau = 0.005$). It was found that the computational process on the 61 × 61 grid was no longer stable at times approaching $T = 2$, if the time step remained the same as the one used for the 31 × 31 grid. To re-achieve stability it was necessary to reduce the time step in the same proportion as the space step. Tables 1 and 2 display average values of p_{in}, p_{out}, and $p_{\mathrm{tr.edge}}$, and the CPU time of a CRAY-YMP as a function of the number of internal iterations n_f, when a fixed pseudotime σ is used for the Poisson equation iterative solution. Generally, the pseudotime is chosen equal to the $\Delta\tau$ of the transient calculation. For the present calculations, the optimal σ was adjusted to be larger than $\Delta\tau$, based on trial and error that yielded the lowest CPU time. The results show that the average pressure field converges within 3–5 internal iterations for the 31 × 31 grid, and roughly in 1–2 iterations on the 61 × 61 grid. On inspection, it was found that the differences between the isobar fields for $n_f = 5$ and $n_f = 8$ are minimal (Kudriavtsev et al., 1993), thus mitigating our approach of judging the convergence by the average value of the field.

Table 3 presents comparisons of average pressure drops ($\Delta p = p_{\mathrm{in}} - p_{\mathrm{out}}$) for 31 × 31 and 61 × 61 grids. One can see that for $n_f = 8$, the difference in the calculated Δp is about 5.5 percent for $\mathrm{Re}_h = 2500$ ($\mathrm{Re}_d = 500$). If one further compares data from Table 1 and Table 2, for $n_f = 8$ and $\mathrm{Re}_h = 25{,}000$ ($\mathrm{Re}_d = 5000$), one can see changes in Δp as high as 24.8 percent. It becomes evident that the computational error increases considerably with the Reynolds number if the grid size is maintained constant. For all the numerical experiments presented below we have used a 139 × 139 computational grid, which provides a resolution that is identical to the one used in the discussion presented above.

A further code validation test was performed through the comparison of our numerical results with experimental visualization of flow around an impulsively started cylinder (Bouard and Coutanceau, 1980). The Reynolds number is $\mathrm{Re}_d = 5000$, and the nondimensional times considered were $T = 1.5$, 2, and 2.5. The results of this comparison are shown in Figs. 2(A), 2(B), and 2(C). The experimental and the numerical results show a good coincidence for the flow patterns, the size of the recirculation, and the position of the vortex center with respect to the moving cylinder.

V Results and Discussion

V.1 Numerical Results ($\mathrm{PTDR_L}$, $\mathrm{PTDR_T} = 1$). There is a wide body of numerical work treating the flow around a circular cylinder in crossflow (Kawamura et al., 1986; Fornberg, 1980; Ohya et al., 1992; Li et al., 1992). However, few researchers focused their attention on the nature of the flow changes when it interacts with a bank of tubes (Reynell et al., 1991). The effects of the cylinder arrangement and the array size on the flow structure are presently not fully understood, especially when the pitch-to-diameter-ratio (PTDR) is small (< < 1).

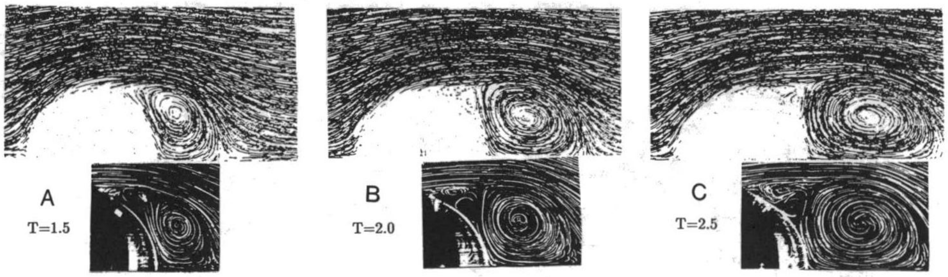

Fig. 2 Qualitative comparison between experimental (Bouard and Coutanceau, 1980) and numerical results for flow around a cylinder at $\mathrm{Re}_d = 5000$

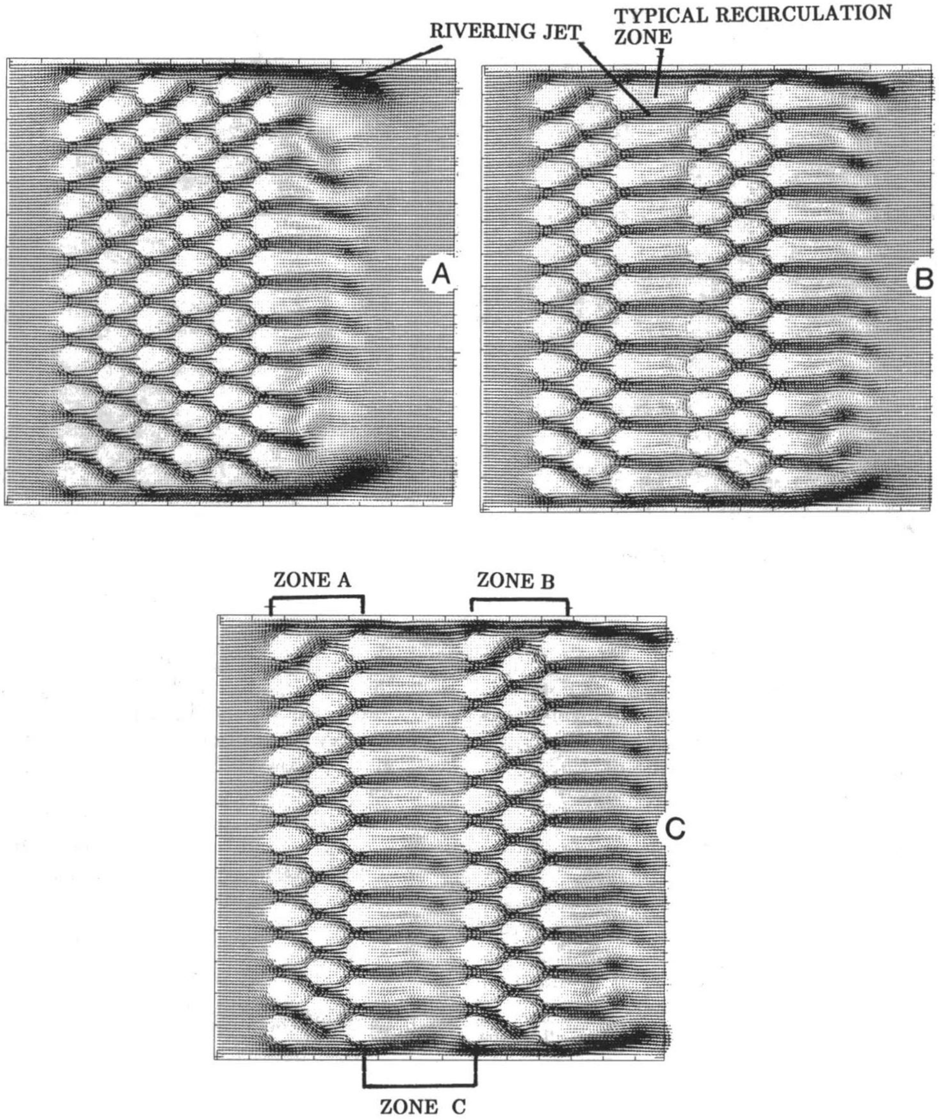

Fig. 3 Flow across array of pins at $\mathrm{Re}_h = 2000$, $\mathrm{PTDR}_L = 1$, $\mathrm{PTDR}_T = 1$: (A) six rows; (B) cascade of two elements (three rows each), $C = 3d$; (C) cascade of two elements (three rows each), $C = 5d$

Flow and Pressure Patterns. Figure 3(A) presents the flow, at $\mathrm{Re}_h = 2000$, for a staggered array of six rows of tubes with a $\mathrm{PTDR}_L = \mathrm{PTDR}_T = 1$. The flow enters the cross section with a symmetric velocity distribution, which completely changes its structure upon passing through the first row of tubes. One can notice the characteristic jetting between the pins, and the formation of recirculation zones in the wake of the pins. The nature of the PTDR does not allow the growth of the recirculation zones and forces their closure within one pin diameter. In the wake of the last row of pins one can notice the shedding of eddies as well as the formation of steady recirculation zones. The computed nondimensional pressure drop was 28.8. Figure 3(B) and 3(C) present for the same Reynolds number and nondimensional time ($T = 0.14$), the flow patterns between a cascade of two formations (A and B) of three rows of pins each. The spacing (C) between

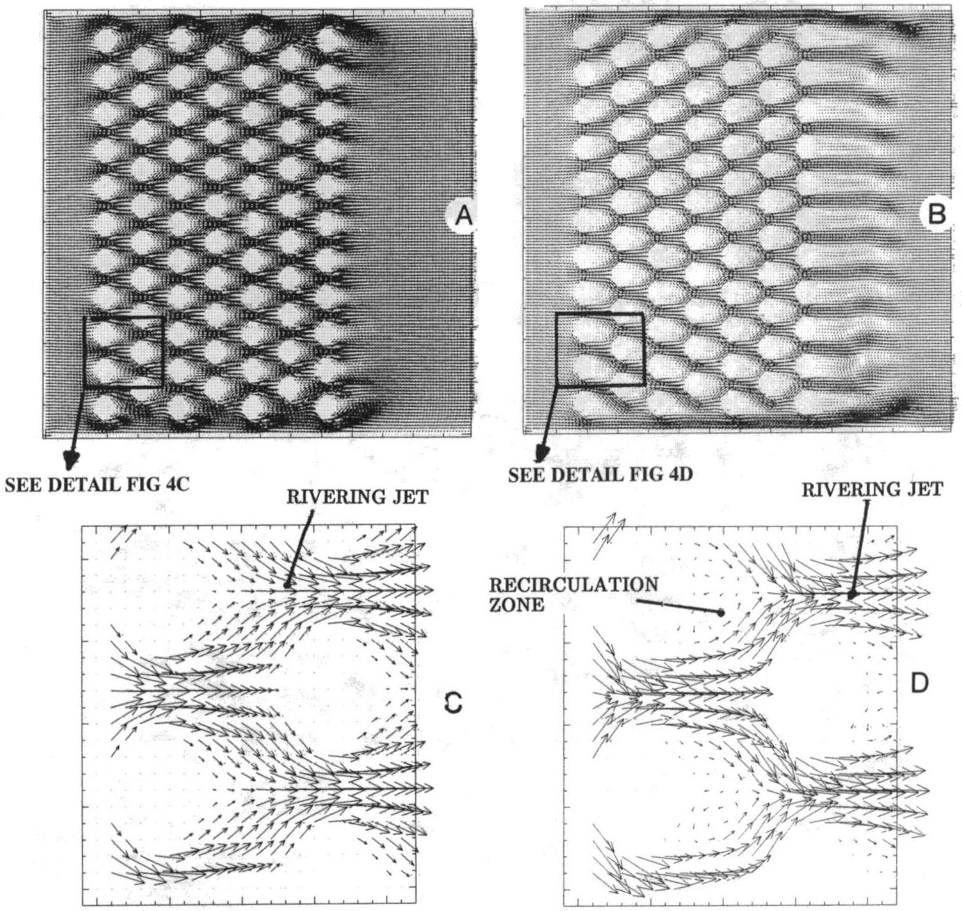

Fig. 4 Flow through basic array configuration 7 rows × 11 pins: (A) $\mathrm{Re}_h = 100$; (B) $\mathrm{Re}_h = 2000$; (C) detail of flow in the quadrant indicated in Fig. 4(A); (D) detail of flow in the quadrant indicated in Fig. 4(B)

the two formations of pins is different, $C = 3d$ (Fig. 3B) and $C = 5d$ (Fig. 3C) respectively. The recirculation zones between A and B, Fig. 3(B), occupy longitudinally the entire space C, while laterally they are limited by the rivering jets to one width diameter. The wake behind the last rows of pins is qualitatively similar to the one of Fig. 3(A), even though its length has increased and shows diminished shedding. The computed pressure drop was 29.08. The larger distance, $C = 5d$ (Fig. 3C), gives the jets the opportunity to expand and merge all across the cross section, only to re-accelerate upon entering the first row of pins of zone B. This phenomenon is associated with an additional expenditure of mechanical work that causes an increase in the pressure drop to 31.53. This effect can be crucial for design of more effective brush seal configurations.

Figures 4(A) and 4(B) present the development of flow in an array of 7 (rows) × 11 round pins with a $\mathrm{PTDR}_\mathrm{L} = \mathrm{PTDR}_\mathrm{T} = 1$. In Fig. 4(A), $\mathrm{Re}_h = 100$, while in Fig. 4(B), $\mathrm{Re}_h = 2000$. The same basic flow patterns of Fig. 3 are visible. The flow patterns in the regions marked in Figs. 4(A) and 4(B) are shown in detail in Figs. 4(C) and 4(D), respectively. One can see the lack of recirculation in the wake of the pins for $\mathrm{Re}_h = 100$ in Fig. 4(C), while for $\mathrm{Re}_h = 2000$, the formation of two standing vortices is clearly displayed.

Figure 5 presents the calculated pressure fields for the two cases considered in Fig. 4. Figure 5(A) exhibits the pressure distribution for the case of $\mathrm{Re}_h = 100$. The nondimensional pressure drop is 67.3. As the Reynolds number is increased to 2000, the pressure drop decreases to 35.3. One should keep in mind that the pressure nondimensionalization follows as $P = p/\rho U_o^2$, with U_o varying directly proportional with the Reynolds number. The same wavy pattern of pressure drops was reported by Braun et al. (1991a, 1991b).

Figure 6 shows the calculated pressure profiles upstream of, and in the wake of each one of the rows of pins. Figures 6(A) and 6(B) present the pressure variations at $\mathrm{Re}_h = 100$, while Figs 6(C) and 6(D) correspond to $\mathrm{Re}_h = 2000$. Analysis of these images indicates that the drop in pressure occurring at the leading edge of any given row is followed by a pressure recovery in the wake of the row, followed by a renewed drop in pressure as the fluid enters the next row of pins. The phenomena exhibited by these numerical experiments shed light on a mechanism of kinetic energy consumption that we believe is instrumental in the sealing process.

Figures 7 demonstrate the effect of PTDR_L decrease on the development of the flow pattern structure. The numerical experiments were performed at $\mathrm{Re}_h = 2000$ for $\mathrm{PTDR}_\mathrm{L} = 1$ (Fig. 7A), 0.66 (Fig. 7C), and 0.33 (Fig. 7E) respectively. The decrease in the PTDR_L engenders a contraction, and even complete disappearance (Fig. 7E) of the recirculation zones behind the inner cylinders (bold contours), but shows little influence on the size or shape of the wakes behind the last row of cylinders. A close view at the physical nature of the wakes shrinkage is detailed in Figs. 7(B), 7(D), and 7(F). The variations of the pressure drops associated with the events in Figs. 7 can be studied in Table 4, Part A. Part B contains the pressure drops in the same array of pins for $\mathrm{Re}_h = 100$. The pressure drops show a consistent increase with the decrease of PTDR_L. At low Re_h the lack of the recirculation zones eliminates one of the mechanisms responsible for the pres-

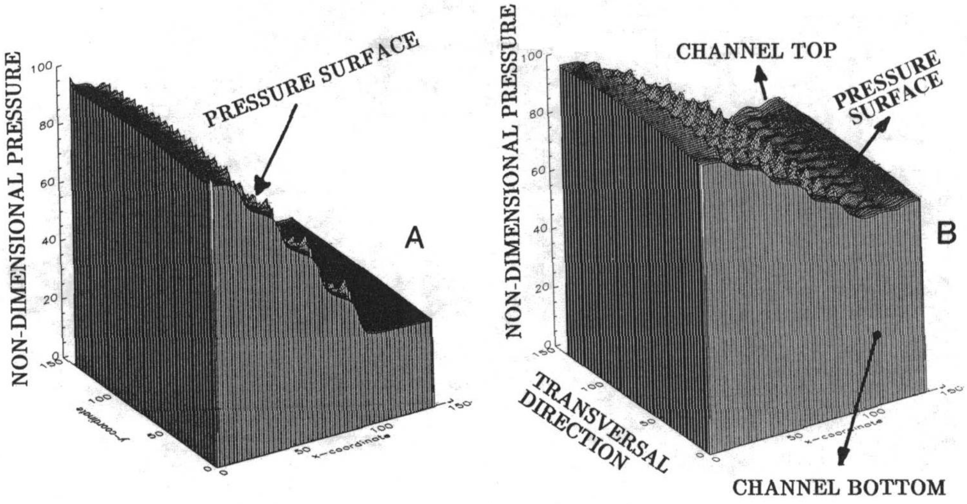

Fig. 5 Nondimensional pressure maps for pressure drops in the basic array configuration (7 rows × 11 pins): (A) $Re_h = 100$; (B) $Re_h = 2000$

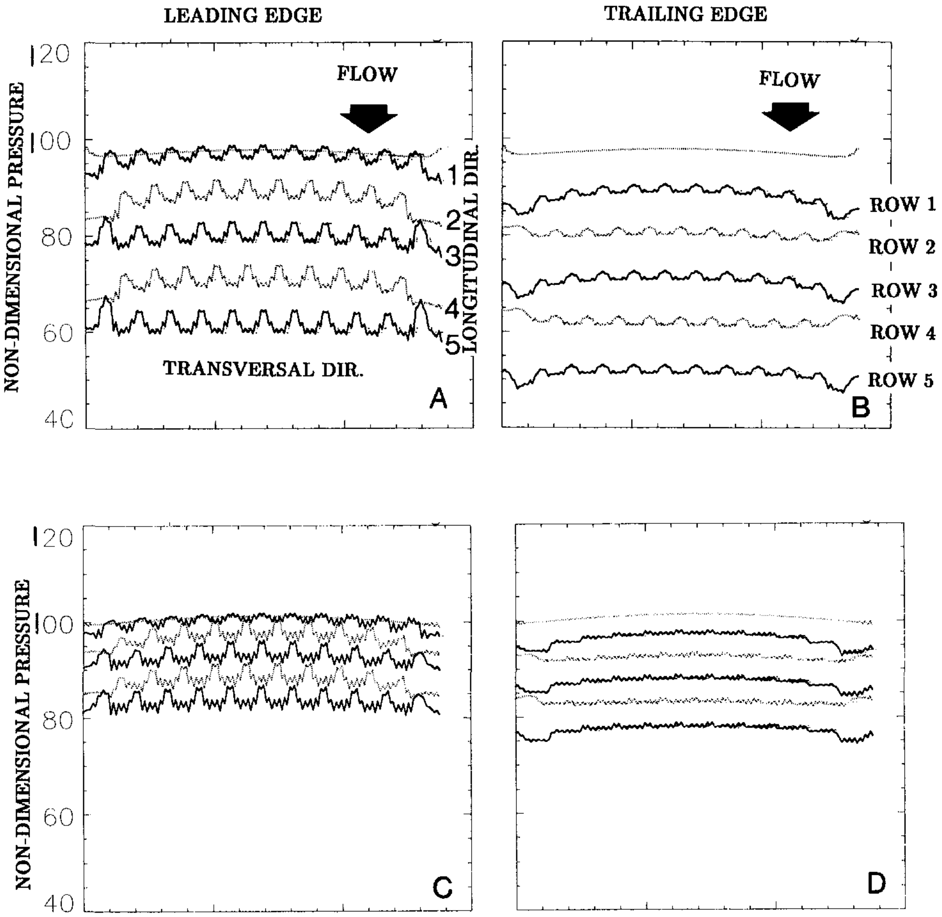

Fig. 6 Nondimensional pressure variation in the transverse direction: (A), (C) leading edge of the row, at $Re_h = 100$ and $Re_h = 2000$; (B), (D) trailing edge of the row, at $Re_h = 100$ and $Re_h = 2000$

sure drops, and leaves friction and fluid acceleration as the only responsible mechanisms.

Effect of the Numerical Scheme (Table 5). To ascertain the physical veracity of the results, the first-order upwind scheme used for the present analysis has been compared with the third-order deferred correction scheme (Kudriavtsev, 1991; Hayase et al., 1992). The comparison covers a range of Re_h between 500 and 2000. The flow patterns observed between the pins and in the wake of the array were similar for the two methods. The comparison of the corresponding pressure drops yielded by the two schemes has been found to be within a 4 percent envelope, Table 5. One can conclude that the amount of artificial viscosity introduced by the

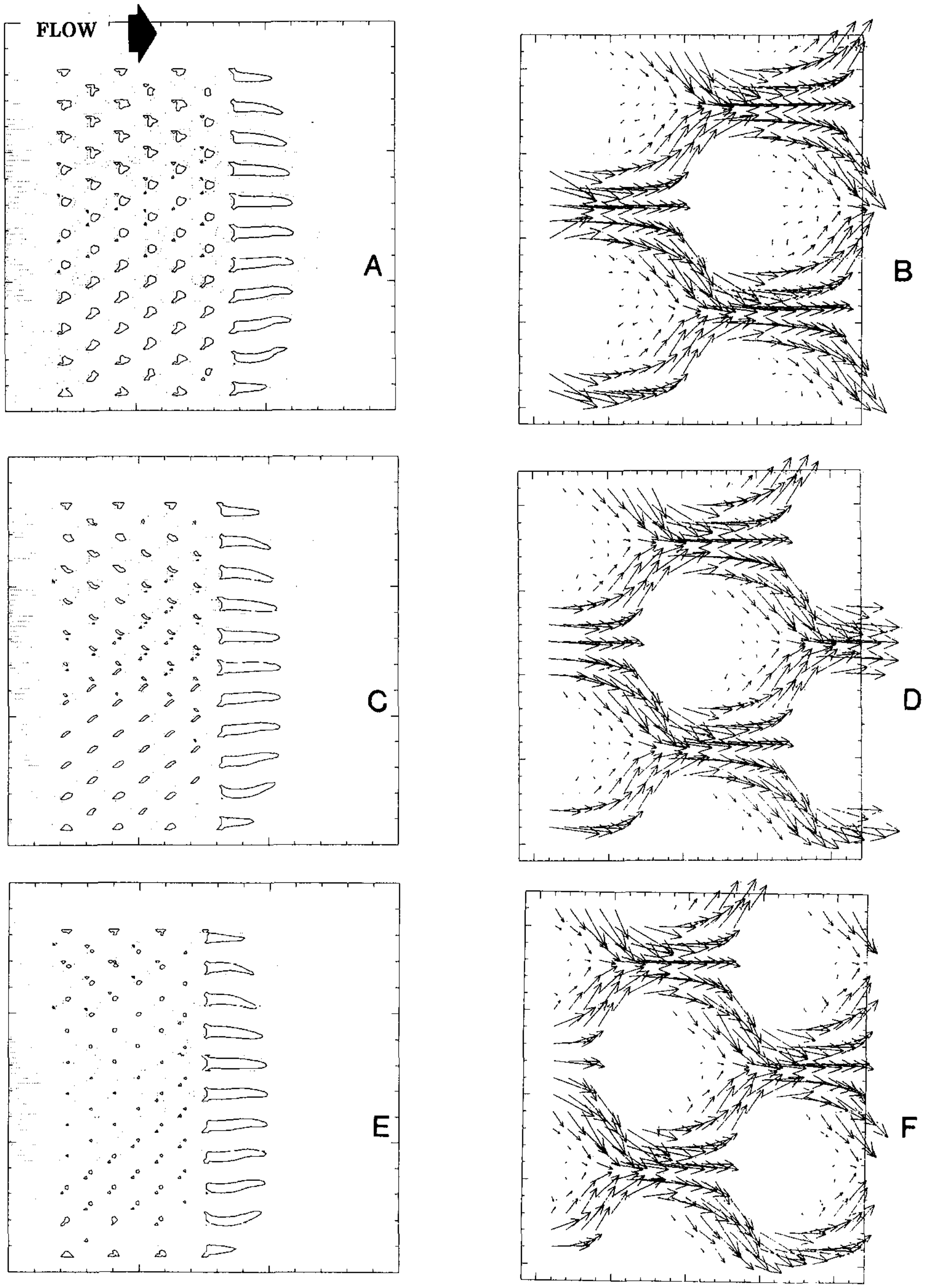

Fig. 7 Variation of the flow field structure with the change in the longitudinal pitch

Table 4 Effect of PTDR on the pressure drop

Part A	Re=2000				
$PTDR_L$	1	0.83	0.66	0.33	0.16
ΔP	35.33	35.01	34.73	34.57	49.1
Part B	Re=100				
$PTDR_L$	1	0.83	0.66	0.50	----
ΔP	67.3	70.84	74.56	81.13	----

conservative first-order upwind scheme does not deteriorate the truthfulness of the solution within the range of Reynolds numbers considered in this paper.

V.2 Experimental Results ($PTDR_L$, $PTDR_T < 0.1$). The

Table 5 Effect of the convective approximation on the pressure drop

Scheme	Upwind	Third-order PUI DC
Re=500		
ΔP_{7row}	38.54	40.19
ΔP_{out}	36.81	38.63
Re=1000		
ΔP_{7row}	36.21	37.83
ΔP_{out}	34.31	36.07
Re=2000		
ΔP_{7row}	35.13	36.42
ΔP_{out}	33.25	34.64

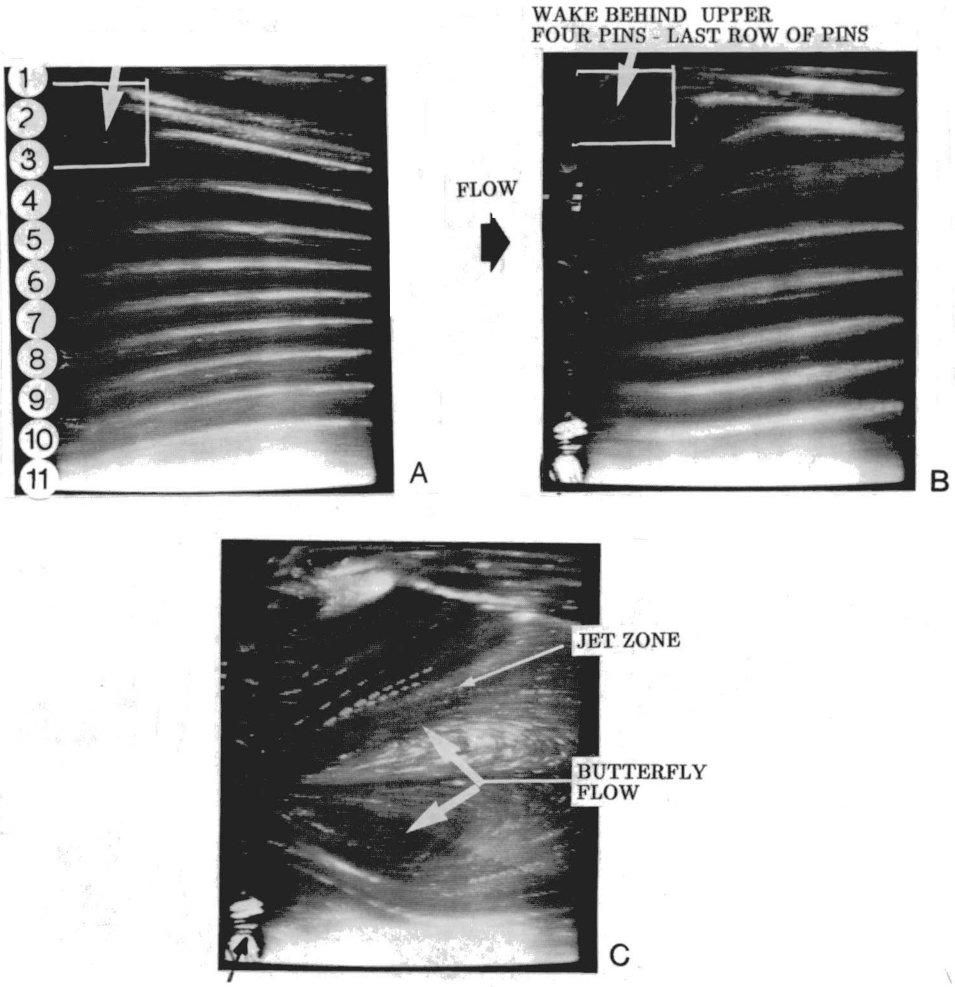

Fig. 8 Experimental flow visualization at $\mathrm{Re}_h = 197$ (A), 500 (B), 956 (C)

experiments were conducted in a test facility that is briefly described in the appendix.

Figure 8 presents qualitatively the flow in the wake of a 3 (rows) × 11 pin array, at $\mathrm{Re}_h = 197$ (Fig. 8A), $\mathrm{Re}_h = 500$ (Fig. 8B), and $\mathrm{Re}_h = 956$ (Fig. 8C). In Fig. 8(A) the exiting jets have a coherent structure interrupted by small recirculation zones behind the pins, Fig. 9(A). These zones close within 1/2 pin diameter and do not influence either the jet development or the unimpeded flow of mass through the array. As Re_h increases to 500 (Fig. 8B) and 956 (Fig. 8C), the flow changes its structure visibly, and one can observe a nonsymmetry situation between the flow near the upper and the lower walls. These structures are due to slightly nonequal pitches between the walls and the adjacent pins. Details of the local flow structures between pin 1 and the upper wall are shown in Figs. 9(B) and 9(C). The strong jet flowing adjacent to the upper wall generates a low-pressure zone that molds the S-shaped jet emerging from pins 2 and 3, and the associated vortex zones. The increase in the Re_h to 956 allows the development of two recirculation zones of butterfly-like structure that are symmetric with respect to pin 6. The low-pressure region engendered by the wall jet (Fig. 9C) becomes dominant across the entire section, and the jets emerging from the spaces between the pins deviate toward the zones of lower pressure. This situation is instrumental in creating both the structure of Fig. 9(C), and the butterfly effect, which can be seen in detail in Fig. 10. One notices the structure of the upper half of the butterfly as it is confined by the jet emerging from between the pins (zone A, Fig. 8). A similar flow formation was also reported in experiments performed by Zdravkovich and Stonebanks (1988). The butterfly, which appears due to an interplay of transverse low-pressure zones, and longitudinal pressure inversions has the net effect of "sealing" the exit of the array, thus preventing the flow from "leaking" downstream.

Comparison of Some Experimental and Numerical Results ($PTDR_L$, $PTDR_T < 0.1$). The magnitude and trends of the pressure drops across the array are very important parameters in the determination of the sealing effectiveness. The authors compared the measured pressure drops with their numerical counterparts. The physical configuration involved was identical to the one described in the section above, and the appendix. The results are detailed in Table 6. For $\mathrm{Re}_h = 195$ one can observe a difference of only 7 percent between the numerical and experimental results. As the Re_h increase to 327 this good coincidence deteriorates. The result can be mitigated through the consideration of the error introduced by the scaling factor ρU_o^2.

Figure 11 presents the flow pattern in the array of three rows discussed above when $\mathrm{Re}_h = 195$. This allows direct comparison between this figure and the experimental results presented in Figs. 8(A) and 9(A). Figure 11(A) models the same geometric asymmetry mentioned in the discussion of Figs. 8 and 9. The effect of this asymmetry is evident in the upward deviation of the inlet flow of Fig. 11(A). Experimen-

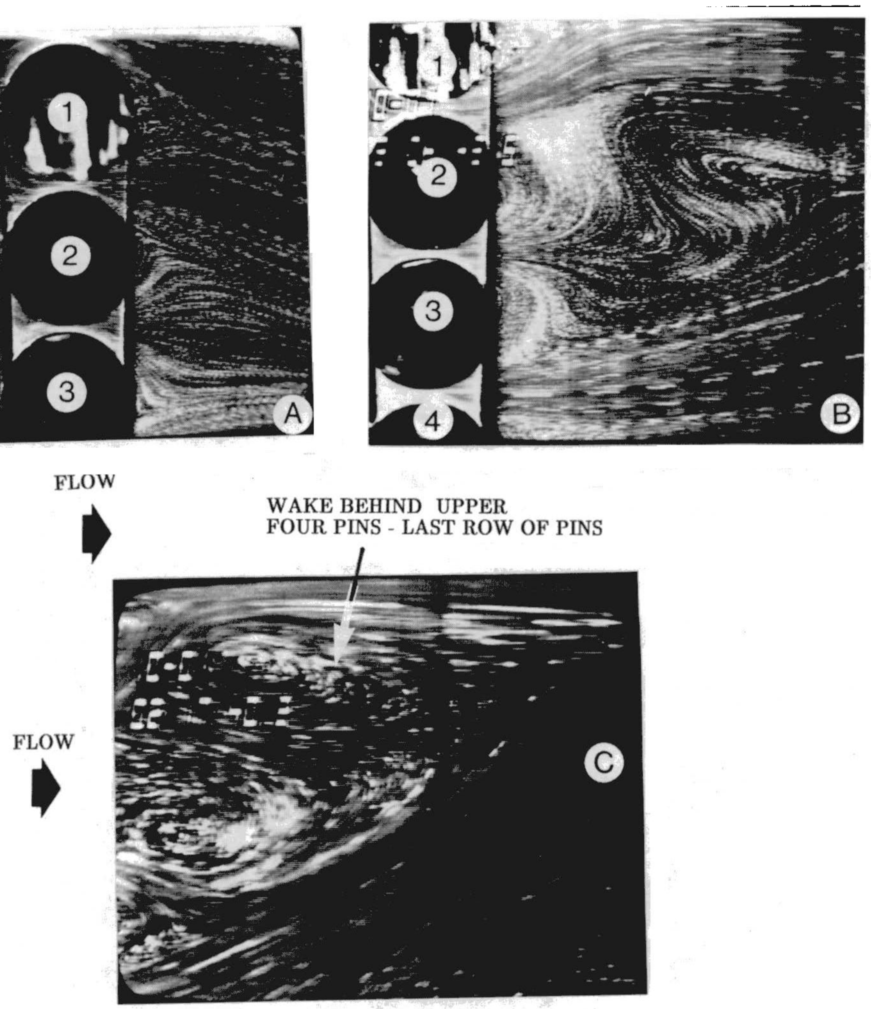

Fig. 9 Details of flow in the sections indicated in Fig. 8 at $\mathrm{Re}_h = 197$ (A), 500 (B), 956 (C)

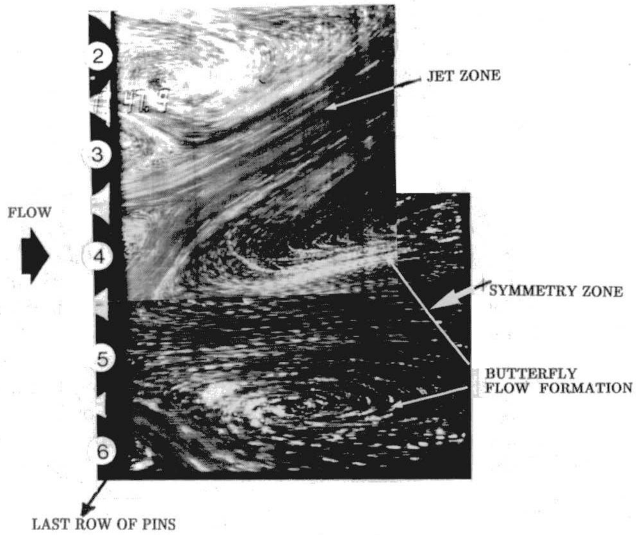

Fig. 10 Details of the butterfly recirculation zone of Fig. 8(C) at $\mathrm{Re}_h = 956$

Table 6 Comparison of experimental and numerical results; temperature $T \approx 70°\mathrm{F}$; $\rho = 950\ \mathrm{kg/m^3}$; fluid velocities: $U \approx 18.5$ cm/s ($\mathrm{Re}_h \approx 195$); $U = 31$ cm/s ($\mathrm{Re}_h = 327$)

Re_h	Δp(psi)	Δp(Pa)	ρU^2	ΔP(nondimensional)
195 (exp)	4.02	27,758	32.16	863
195(num)	4.31(ϵ=7%)			926
327(exp)	6.82	47,056	91.29	516
327(num)	8.6(ϵ=26%)			650

tal observation confirmed the same trend for the inlet flow as the one reproduced numerically. In the exit section of the array, a comparison of Fig. 11(A) and 8(A) shows good qualitative coincidence. One can see that the inlet flow asymmetry carries through, and in both figures the fluid jet adjacent to the upper wall is much stronger than the one flowing along the lower wall. The reader has an even more convincing comparison in the similarity of the flow structures presented in Figs. 11(B), 11(C), and 8(A). These figures show in detail the wall jet and adjacent flow formations in the upper exit corner of the pin array.

VI Conclusions

This paper presents an analysis and numerical simulation for flow in an array of pins with a PTDR varying between 0.1 and 1. The effects of the Reynolds number variation and array configuration have been studied. The experimentally obtained results concerning the jet rivering between the pins, and the formations of recirculation zones between cascades of pins have been confirmed numerically. It was found that

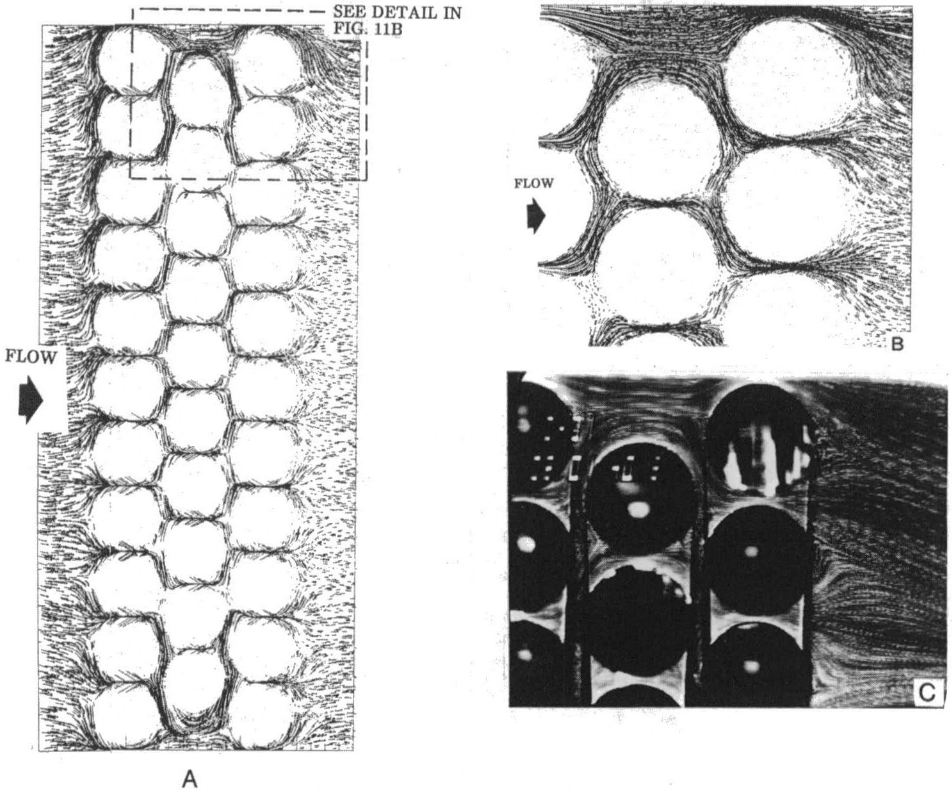

Fig. 11 Comparison of numerical and experimental flow patterns at $Re_h = 195$

the distance (zone *C*, Fig. 3) between zones of densely packed pins can be influential on the overall pressure drop. Contrary to expectations, an increase in zone *C* length can carry with it an increase in the pressure drops. This phenomenon has been attributed to the nature of the development of the recirculation zones in zone *C*. The interplay of successive pressure drops and partial pressure recovery, Fig. 8, inside the array of pins has also been found to contribute greatly to the overall pressure drop. Finally, the experimental results shown in Figs. 8, 9, and 10, indicate the onset of large recirculation zones in the wake of the array of pins that are associated with longitudinal and cross-sectional pressure inversions that contribute to the sealing effect.

Acknowledgments

The authors want to express their gratefulness to Dr. R. Bill and Mr. G. Bobula for their continued support. The work has been performed under the auspices of NASA Grant NAG 3-969, NASA Lewis Research Center.

References

Bouard, R., and Coutanceau, M.,1980, "The Early Stage of Development of the Wake Behind an Impulsively Started Cylinder for $40 < Re < 10^4$," *J. Fluid Mech.*, Vol. 101, Part 3, pp. 583–607.

Braun, M. J., Hendricks, R. C., and Canacci, V. A., 1990a, "Flow Visualization in a Simulated Brush Seal," ASME Paper No. 90-GT-217.

Braun, M. J., Hendricks, R. C., and Canacci, V. A., 1990b, "Non-intrusive Qualitative and Quantitative Flow Characterization and Bulk Flow Model for Brush Seals," *Proc. Japan International Tribology Conference*, Nagoya, Vol. II, pp. 1611–1616.

Braun, M. J., Canacci, V. A., and Hendricks, R. C., 1991a, "Flow Visualization and Quantitative Velocity and Pressure Measurements in Simulated Single and Double Brush Seals," *Tribology Transactions*, Vol. 34, No. 1, pp. 70–80.

Braun, M. J., Hendricks, R. C., and Yang, Y., 1991b, "Effects of Brush Seal Morphology on Leakage and Pressure Drops," Paper No. AIAA 91-2106.

Braun, M. J., Canacci, V. A., and Hendricks, R. C., 1992, "Flow Visualization and Motion Analysis for a Series of Four Sequential Brush Seals," *J. of Propulsion and Power*, Vol. 8, No. 3, pp. 697–702.

Chupp, R. E., Holle, G. F., and Dowler, C. A., 1991, "Simple Leakage Flow Model for Brush Seals," AIAA Paper No. 91-1913.

Chupp, R. E., and Dowler, C. A., 1993, "Performance Characteristics of Brush Seals for Limited-Life Engines," ASME *Journal of Engineering for Gas Turbines and Power*, Vol. 115, pp. 390–396.

Fergusson, J. G., 1988, "Brushes as High Performance Gas Turbine Seals," ASME Paper No. 88-GT-182.

Flower, R., 1990, "Brush Seal Development System," AIAA Paper No. 90-2143.

Fornberg, F., 1980, "A Numerical Study of Steady Viscous Flow Past a Circular Cylinder," *J. Fluid Mech.*, Vol. 98, Part 4, pp. 819–855.

Gorelov, G. M., Reznik, V. E., and Tsibizov, V. I., 1988, "An Experimental Study of the Rate Characteristics of Brush Seals in Comparison With Labyrinth Seals," *Aviatsonnaia Teknika*, No. 4, pp. 43–46.

Griner, H. F., 1991, "Seal Related Activities at EG & G," *Seal Flow Code Development*, A. Liang, ed., NASA CP-10070, NASA Lewis Research Center, Cleveland, OH, Mar.

Hayase, T., Humphrey, J. A. C., and Greif, R., 1992, "A Consistently Formulated QUICK Scheme for Fast and Stable Convergence Using Finite-Volume Iterative Calculation Procedures," *Journal of Computational Physics*, Vol. 98, pp. 108–118.

Hendricks, R. C., Proctor, M. P., Schlumberger, J. A., Braun, M. J., and Mullen, R. L., 1991a, "Some Preliminary Results of Brush Seal/Rotor Interference Effects on Leakage at Zero and Low rpm Using a Tapered Plug Rotor," NASA TM-104396; AIAA 91-3390.

Hendricks, R. C., Schlumberger, J. A., Braun, M. J., Choy, F. K., and Mullen, R. L., 1991b, "A Bulk Flow Model of a Brush Seal System," ASME Paper No. 91-GT-325.

Hendricks, R. C., Carlile, J. A., and Liang, A., 1992, "Some Sealing Concepts—A Review, Part B: Brush Seal Systems," presented at the *Fourth International Symposium on Transport Phenomena and Dynamics* of Rotating Machinery (ISROMAC-4), Apr. 5–8, Honolulu, HI.

Holle, G. F., and Krishnan, M. R., 1990, "Gas Turbine Engine Brush Seal Applications," AIAA Paper No. 90-2142.

Kawamura, T., Takami, H., and Kuwahara, K., 1986, "Computation of High Reynolds Number Flow Around Circular Cylinder," *Fluid Dynamics Research*, Vol. 1, pp. 145–162.

Kudriavtsev, V. V., 1991, "Comparison of Computational Performance of Implicit Higher-Order Deferred Correction Finite Difference Schemes for Unsteady Flows," *Fluid Transients and Fluid-Structure Interactions*, ASME PVP-Vol. 224/FED-Vol. 126, pp. 9–12.

Kudriavtsev, V. V., 1992, "Novel Nonhomogeneous Monotonic Finite-Difference Scheme for Thermo-Fluid Transport Phenomena," *The Fourth International Symposium on Transport Phenomena and Dynamics of Rotating Machinery* (*ISROMAC*-4), Vol. A, pp. 633–640.

Kudriavtsev, V. V., and Braun, M. J., 1993, "A Reynolds Number Parametric Numerical Investigation of Flow Structures and Pressure Distribution in a System of Cylinder Arrays," *ASME Int. Fluid Engineering Conference, Symposium on Separated Flows*, J. C. Duton and L. P. Purtell, eds., ASME FED-Vol. 149, pp. 83–93.

Li, J., Sun, J., and Roux, B., 1992, "Numerical Study of an Oscillating Cylinder in Uniform Flow and in the Wake of an Upstream Cylinder," *J. Fluid Mech.*, Vol. 273, pp. 457–478.

Liang, A., ed., 1991, "Seals Flow Code Development," NASA CP-10070, NASA Lewis Research Center, Cleveland, OH, Mar.

Ohya, Y., Nakamura, Y., Ozono, S., Tsuruta, H., and Nakayama, R., 1992, "A Numerical Study of Vortex Shedding From Flat Plates With Square Leading and Trailing Edges," *J. Fluid Mech.*, Vol. 236, pp. 445–460.

Reynell, M. J. W., Clark, I. W., and Rosten, H. I., 1991, "A Two-Level Micro/Macro Approach to the Simulation of Air Flow and Heat Transfer in Typical Convection-Cooled Electrical Systems," ASME Paper No. 91-WA-EEP-33.

Roach, P. J., 1982, *Computational Fluid Dynamics*, revised printing, p. 66, Hermosa Publishers.

Torrance, K. E., 1968, "Comparison of Finite-Difference Computations of Natural Convection," *J. of Research of the National Bureau of Standards*, Vol. 72B, No. 4, pp. 281–301.

Washpress, E. L., 1966, *Iterative Solution of Elliptic Systems*, Prentice-Hall, Englewood Cliffs, NJ.

Zdravkovich, M. M., and Stonebanks, K. L., 1988, "Intrinsically Non-uniform and Metastable Flow in and Behind Tube Arrays," *Flow Induced Vibrations in Cylindrical Structures: Solitary Cylinders and Arrays in Cross-Flow*, Vol. 1, pp. 61–73.

Zukauskas, A., 1972, "Heat Transfer From Tubes in Crossflow," *Adv. Heat Transfer*, Vol. 8, pp. 93–160.

APPENDIX

Description of the Test Facility

The test facility, Fig. A1, comprises four parts: the oil tunnel with the test section, the laser assembly and appropriate optical lenses, the low-luminosity TV camera with a modified front-end long distance microscope, and the computer-based image processing system. For interested readers a full description of the system and the experimental procedure is given by Braun et al. (1992, 1990a, b, 1991a, b).

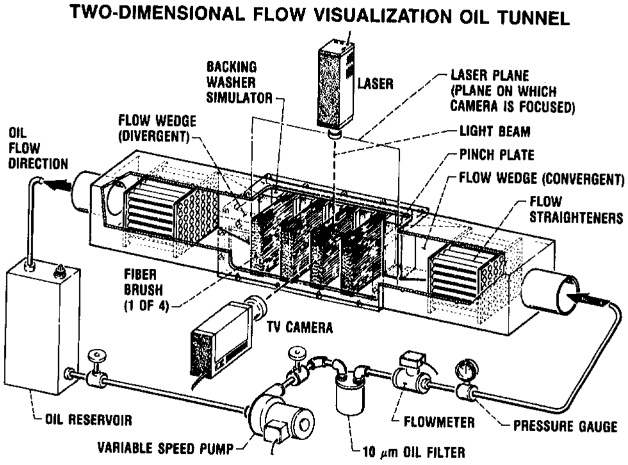

Fig. A1 Two-dimensional flow visualization oil tunnel

The Oil Tunnel

This facility is designed to study the behavior of one or more brushes in a pump pressurized environment at higher flow velocities. The tunnel is manufactured contains a lucite wall test section that is 333 mm (1 ft) long and 25.4 mm (1 in.) thick. The tunnel is 1524 mm (5 ft) long with a square cross section of 76.2 mm × 76.2 mm (3 in. × 3 in.). The test section contains a breadboard on which pins can be mounted in any arbitrary configuration. The board has pins that are 0.250 in. diameter and are spaced at $S_T = 0.020$ in. and $S_L = 0.020$ in. for a pitch-to-diameter ratio of $\mathrm{PTDR}_L = \mathrm{PTDR}_T = 0.08$.

Journal of Turbomachinery

Technical Briefs

A Note on Turbine Cooling Performance Characterization

D. A. Nealy[1]

Nomenclature

T_g = gas stream mean total temperature
T_{ge} = gas stream mean recovery temperature with film injection
T_w = cooled component mean surface temperature
T_c = coolant supply or sink temperature
ΔT_c = coolant temperature rise through internal cooling circuits
W_c = required component cooling flow rate
A_s = cooled component gas side surface area
h_g = mean gas to wall heat transfer coefficient
h_{ge} = mean gas to wall heat transfer coefficient with film injection
η_t = cooling system internal heat transfer efficiency, defined by Eq. (2)
ϵ = dimensionless level of cooling = $(T_g - T_w)/(T_g - T_c)$
W_g = gas stream flow rate
Cp_c = coolant mean specific heat
β = dimensionless cooling flow parameter, defined by Eq. (3)
K = overall cooling performance parameter, defined by Eq. (4)
Q/Q_o = heat flux ratio reflecting surface film injection effects

Introduction

Over the years, much has been written and presented regarding "efficiency" or "effectiveness" of active cooling systems for gas turbine engine hot-section components. It is clearly desirable to develop some measure of cooling performance that is simple enough to define and quantify from a practitioner's viewpoint, and yet universal enough to serve as a meaningful yardstick in comparing one cooling system design to another. It would be even better if such a parameter represented a physically meaningful interpretation of intrinsic cooling system performance, independent of other engine-unique aerodynamic and structural design parameters. Finally it would be very useful to develop a simple numerical measure of cooling performance, which could be compared to a generally agreed upon "best possible" level, yielding a simple yardstick measure of intrinsic cooling system efficacy somewhat akin to turbomachinery component efficiency level. Some thoughts on the combination of two commonly used parameters for this purpose follow.

Key Elements of the Problem

The cooling flow, W_c, required to maintain a desired wall temperature, T_w, in the presence of a hot gas environment characterized by temperature, T_g, is, in simplest terms, a function of effective gas to wall heat transfer coefficient, h_{ge}, effective gas to wall driving temperature, T_{ge}, cooled surface area, A_s, and coolant sink temperature, T_c. A simple formulation reflecting an overall, steady-state energy balance for the cooled component becomes

$$W_cCp_c[T_w - T_c]\eta_t = h_{ge}A_s[T_{ge} - T_w] \tag{1}$$

where η_t is a measure of cooling system internal heat transfer efficiency defined as

$$\eta_t = \Delta T_c/(T_w - T_c) \tag{2}$$

In the most general situation, where some form of spent coolant ejection onto the cooled surface occurs (e.g., film or transpiration-cooled surfaces), the driving parameters h_{ge} and T_{ge} would reflect those coolant film effects and would in general differ from the values (h_g, T_g) that would exist along an impermeable or non-film cooled surface.

A convenient and common way to characterize cooling performance is to express dimensionless cooling level $\epsilon = (T_g - T_w)/(T_g - T_c)$ as a function of percentage cooling flow or cooling flow ratio, W_c/W_g. This is a simple, useful measure, which at once provides a means of relating level of component cooling (ϵ) to system performance degradation (W_c/W_g). It is, however, a less than desirable measure of relative merit of one cooling system design to another because the parameter W_c/W_g merges intrinsic cooling system performance parameters $(\eta_t, h_{ge}/h_g, T_{ge}/T_g)$ with design-specific aerodynamic and operating point parameters that uniquely define, for example, the relationship between W_g and h_g (or W_g and A_s). The combined effect of component aerodynamic design, design point/off design point operation, and intrinsic cooling system efficiency on percentage cooling flow requirement (W_c/W_g) have been discussed elsewhere (Nealy and Lueders, 1976) and will not be elaborated on here. The basic point we make here is that however useful a trend of ϵ versus W_c/W_g may be from an engine performance perspective, it greatly clouds the issue of relative merit of one *cooling system design* to another at the same level of ϵ. Similarly, use of isolated cooling system efficiency parameters falls short of the mark. For example, comparing two systems solely on the basis of internal cooling

---

[1] Chief, Heat Transfer, Technology and Research Staff, Allison Gas Turbine Division, General Motors Corporation, Indianapolis, IN; present address: Consulting Engineer, Greenwood, IN.

Contributed by the International Gas Turbine Institute for publication in the JOURNAL OF TURBOMACHINERY. Manuscript received by the International Gas Turbine Institute May 1992; revision received September 1994. Associate Technical Editor: T. H. Okiishi.

efficiency (η_t) ignores the fact that one may provide much superior surface film cooling and hence much greater reduction in h_{ge} or T_{ge} (relative to h_g or T_g). Similarly comparison solely in terms of adiabatic film cooling effectiveness (a relationship between T_{ge} and T_g) ignores the complex interaction between T_{ge} and h_{ge} as well as the effect of internal cooling efficiency (η_t).

A More General Measure

The difficulties cited above lead to the consideration of a more universal measure of cooling system performance based on the widely used parameter

$$\beta = \frac{W_c Cp_c}{h_g A_s} \tag{3}$$

It can be readily shown that characterization of any given cooling system in terms of the pair of parameters (ϵ, β) leads to a simple dimensionless yardstick for comparing one system to another and each to a limiting theoretical maximum. The overall cooling performance parameter of interest here is defined as

$$K \equiv \left(\frac{\epsilon}{1-\epsilon}\right)(\beta)^{-1} \tag{4}$$

If the right-hand side of Eq. (1) is simplified to combine all surface film injection effects into a simple ratio of heat flux with injection to that without injection (Q/Q_o), then

$$h_{ge} A_s [T_{ge} - T_w] = h_g A_s [T_g - T_w](Q/Q_o) \tag{5}$$

and the parameter K can now be interpreted as a *measure of intrinsic cooling system efficacy*, namely

$$K \equiv \left(\frac{\epsilon}{1-\epsilon}\right)(\beta)^{-1} = \eta_t \left(\frac{Q}{Q_o}\right)^{-1} \tag{6}$$

Thus, at any level of cooling (ϵ), that cooling system which produces the "best" *combination* of high internal cooling efficiency (η_t) and reduction in gas to wall heat flux (Q/Q_o) will be characterized by the highest value of the parameter K. Note that the parameter K, as defined, is essentially a measure of intrinsic cooling system performance, (η_t, Q/Q_o) independent of application, operating point, aerodynamic design configuration, etc. Furthermore, for any systems dominated by forced convection heat transfer (most turbomachinery applications) it is possible to define limiting or maximum achievable levels of the parameter K at any given cooling level, ϵ. Those limiting levels are of course represented by ideal transpiration cooling and are readily quantified. For example, using the transpiration cooling results of Bartle and Leadon (1962) for a turbulent boundary layer, limiting (maximum) levels for the parameter K are given in Table 1.

Table 1 Cooling performance parameter limits (turbulent flow)

ϵ**	K
0.00	1.0
0.10	1.036
0.20	1.079
0.30	1.132
0.40	1.197
0.50	1.283
0.60	1.400
0.70	1.575
0.80	1.878
0.90	2.600
1.00	00

Data source: Bartle and Leadon (1962).
**Note: $\epsilon = 1 - (1 + \beta/3)^{-3}$.

It is worth noting that, since in ideal transpiration cooled systems, η_t = 1.0, the inverse of the parameter K at any given ϵ level in Table 1 is a measure of the gas to wall heat flux reduction Q/Q_o. Perhaps more importantly, comparison of demonstrated K levels for state-of-the-art combustor/turbine/exhaust nozzle cooling systems reveals that, in the meaningful advanced technology cooling regime of $\epsilon > 0.50$, the "best" current systems are characterized by K levels of the order of 70 percent of those achieved by ideal transpiration cooling.

Or alternatively, there exists at least a potential to reduce cooling air flows by about a third from today's "best" levels since for any given operational environment, required cooling flow (W_c) is inversely proportional to the parameter K.

In conclusion, the suggestion is made that any cooled component, whose overall cooling performance is represented by a given combination of ϵ and β, can be characterized by a unique, intrinsic cooling performance parameter K. The parameter K, in turn, provides a simple dimensionless yardstick for comparing one cooling system to another, and each to a limiting, theoretical maximum.

References

Bartle, E. R., and Leadon, B. M., 1962, "The Effectiveness as a Universal Measure of Mass Transfer Cooling for a Turbulent Boundary Layer," *Proceedings, 1962 Heat Transfer and Fluid Mechanics Institute*, Stanford Univ. Press, F. E. Ehlers et al., eds., pp. 27-41.

Nealy, D. A., and Lueders, H. G., 1976, "An Analytical Study of Turbine Variable Geometry Operation on Turbine Blade Cooling Requirements for Fixed Match Point Turbojet Application," SAE Paper No. 760916; also *SAE Transactions*, 1976.